GEORGINA FABREGAT JOVÉ

UNIVERSITAT POLITÈCNICA DE CATALUNYA

2014

CONDUCTING POLYMERS AND HYBRID DERIVATIVES WITH SPECIFIC APPLICATIONS AS SENSORS AND BIOACTIVE PLATFORMS

Presented by:

M.Sc. Georgina Fabregat Jové

Under direction of:

Dr. Carlos Alemán Lllansó

Dra. Elaine Armelin Diggroc

Realized at Departament d'Enginyeria Química (DEQ) of Escola Tècnica Superior d'Enginyeria Industrial de Barcelona (ETSEIB) of Universitat Politècnica de Catalunya (UPC)

Barcelona, April 2014

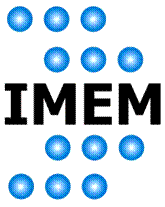

Agradecimientos

Des que vaig començar els estudis universitaris mai m'hagués imaginat cursar el doctorat. Encara tinc en ment aquelles converses amb ex-companys d'universitat, on la meva frase sempre era la mateixa: jo el doctorat ni de conya!...però vet aquí que ara em trobo en la recta final. Durant aquests anys, he après que la realització d'una tesi és un camí personal però sens dubte no es pot fer sol, per això en les pròximes línies m'agradaria agrair a tota aquella gent que m'ha acompanyat en aquest llarg camí, i que gràcies a ells m'ha sorgit l'estímul d'aprendre, de conèixer i descobrir.

En primer lloc, vull agrair als meus directors de tesis, Dr. Carlos Alemán i Dra. Elaine Armelin, per haver-me donat l'oportunitat de formar part del grup d'investigació IMEM. En aquesta tesi han demostrat tenir grans dosis de paciència amb mi, recolzant-me i orientant-me en tot moment, dedicant-me moltíssimes hores revisant els meus escrits i en moltes ocasions escrivint els meus escrits,...totes les facilitats proporcionades en tots els projectes han estat essencials per arribar fins aquí, sense els quals aquesta tesina no hauria vist mai la llum.

També vull donar les gràcies a tots els companys del grup, les persones amb qui al final he acabat passant més hores al llarg del dia, amb els quals he compartit feina però també amistat i bones estones: Bruno (mi português!! gracias por ser mi mejor compañero de laboratorio y por todos tus "foda-se!" que tanto me hacían reír), Mar (companyera del CrnE!! saps més del que et penses, ets una excel·lent científica i persona), Dani y Esther (Becarios beers!! amb vosaltres he tingut les millors converses, m'heu fet reflexionar en molt àmbits de la meva vida, científics i personals, i sempre heu estat allà fent-me de psicòlegs particulars quan us he necessitat...avui no seria ni la meitat del que sóc. Sou genials!), Guillem (qui pogués tenir un gram del teu coneixement al cervell!, i a sobre ets un tros de pa...si us plau no canviïs mai!), David (quins grans obsequis a l'hora de dinar amb els teus coneixements sobre història universal,...quin rollo!!, també t'haig de donar les gràcies per haver-me escoltat i donat consells sempre que ho necessitava), Silvana (nuestra nueva incorporación made in Italy! te deseo lo mejor en tu carrera como científica y estoy segura de que lo harás muy bien!).

També vull agrair a tots els companys del departament d'Enginyeria Química que he compartit dinars, sopars, cafès, xerrades,...: Elena (la meva nina! sempre ficada en mil històries), Sara (preocupada siempre por el dinero y con razón!), la gent de dalt (Ainhoa, Cristina, Antxon, Alberto,...especialmente a Abdel que me encanta su sentido del humor!, y Helena con la habilidad de tener siempre una sonrisa en la cara), Alex (me quito el sombrero, viva Brasil!), Viviane, Francielli, Anca, Rafel, etc.

En la mateixa línia, vull agrair la col·laboració oferta pels professors del departament de Enginyeria Química, que s'han interessat en els meus estudis i han contribuït al bon desenvolupament del present treball; Dr. Francesc Estrany (el gran guia davant els dubtes de electroquímica i el món del AFM), Dra. Mª Teresa Casas (gracias por enseñarme y ayudarme a obtener imágenes dignas con el TEM) i Dr. Luis J. Del Valle Lucho (te agradezco tu importante aporte y participación activa en todas las cuestiones biológicas). També vull agrair els tècnics del CRnE, Dr. Trifón Trifonov i Dra. Montserrat Dominguez, la seva disponibilitat incondicional com també tots els seus consells que m'han ajudat a fer ciència.

Per últim però no menys important, vull agrair a la meva família, especialment als meus pares, i a tota la colla d'Igualada que malgrat no entendre res del que explico sempre intenten preguntar-me com va la tesis. Us estimo moltíssim però si us plau no us vull sentir més!

Gràcies a tothom de tot cor!

Caminante, son tus huellas
el camino y nada más;
Caminante, no hay camino,
se hace camino al andar.
Al andar se hace el camino,
y al volver la vista atrás
se ve la senda que nunca
se ha de volver a pisar.
Caminante no hay camino
sino estelas en la mar.

Antonio Machado (Poeta espanyol, 1875-1939)

Abstract

In recent decades, the scientific community have been attracted by advanced research on conducting polymers, which display reversible redox behaviour and the unusual combination of properties of metals/semiconductor and plastics. As a result of the revolution in the field of polymers, a large number of chemical modifications on conventional structure of conducting polymers have been developed and extensively investigated. The principal focus of this Thesis is the development and design of promising hybrid nanocomposites based on conducting polymers with the main objective of achieving applications in the field of biotechnology and biomedicine. Furthermore, some of studies have been supported and corroborated by theoretical techniques based on quantum mechanical and molecular dynamics, which allows predict some electronic and structural properties of conjugated polymers, and helps the elucidating of the electronic properties not fully understood at experimental level.

One of the major contributions of this Thesis is reported in Chapter 4 which consists on the preparation, characterization and evaluation of *N*-substituted polypyrrole derivatives and poly(3,4-ethylenedioxythiophene) (PEDOT) for electrochemical detection of dopamine, one of the neurotransmitters associated to neurological disorders. In order to examine this purpose, different strategies have been taken into account such as, polymerization method using individual or even combined conducting polymers, the incorporation of gold nanoparticles, the use of soft templates, and other approachs. In general, the result of this chapter suggests that PEDOT is the most appropriated conducting polymer for the selective detection of dopamine.

Chapter 5 is devoted to the design of synthetic amino acids bearing an EDOT group to develop peptide-PEDOT hybrids materials based on chemical similarity concepts. The conjugates have shown that the electrical and electrochemical properties of the conducting polymers are preserved. Therefore, one of their potential applications would be as candidates for the development of platforms with bioactive and bioelectrocompatible properties. Within this similar context, Chapter 6 is focused on the preparation and characterization of organic hybrid materials formed by an all-conjugated polythiophene backbone and well-defined polyethylene glycol (PEG)

grafted chains, which have powerful applicability as active surfaces for the selective adsorption of proteins and as bioactive platforms. Among several factors which influence on the structure and properties of graft copolymers, one of the most important is the molecular weight of the PEG chains which provokes a considerably reduction in the backbone conjugation length. Therefore, it was one of the aspects taken to account in the Chapter 6.

Finally, the preparation and characterization of new bionanocomposites formed by PEDOT and CREKA, which is a biologically active linear pentapeptide, is studied in Chapter 7. The incorporation of CREKA into a PEDOT matrix has been carried out under different experimental conditions and has shown a positive effect on the electrochemical properties of conducting polymer and indicating a favourable cellular proliferation due to the ability to bind fibrin.

"The most beautiful thing we can experience is the mysterious. It is the source of all true art and all science. He to whom this emotion is a stranger, who can no longer pause to wonder and stand rapt in awe, is as good as dead: his eyes are closed."

Albert Einstein (German physicist, 1879-1955)

"La patience est amère mais son fruit est doux"

Jean Jacques Rousseau (French philosopher, 1712-1778)

TABLE OF CONTENTS

Agradecimientos ..... **i**
Abstract ..... **iii**
List of abbreviations ..... **xi**
List of symbols ..... **xiii**
List of scientific journals ..... **xv**
CHAPTER 1. Introduction **1**
1.1 Discovery and development of conducting polymer **3**
1.2 Importance of doping process in conducting polymers **4**
1.2.1 Electrical conductivity 4
1.2.2 Doping process 5
1.2.3 Charge tranfer mechanism 6
1.3 Synthesis of conducting polymers **7**
1.4 Properties of conducting polymers for biomedical applications **10**
1.5 Principal strategies to modify conducting polymers **11**
1.5.1 Non-covalent methods 13
1.5.2 Covalent methods 14
1.6 References **15**
CHAPTER 2. Objectives **19**
CHAPTER 3. Experimental Background **27**
3.1 Electrochemical techniques **28**
3.1.1 Chronoamperometry 28
3.1.1 Cyclic voltammetry 28
3.1.1 Recurrent galvanostatic pulse 28
3.1.1 Electrochemical impedance spectroscopy 29
3.2 Microscopy techniques **29**
3.2.1 Scanning electron microscopy 29
3.2.1 Atomic force microscopy 30
3.2.1 Transmission electron microscopy 30
3.3 Spectroscopic techniques **31**
3.3.1 Ultraviolet-visible spectroscopy 31
3.3.2 Fourier transform infrared spectroscopy 32
3.3.3 Raman spectroscopy 32
3.3.4 X-Ray photoelectron spectroscopy 33
3.4 Physical techniques **34**

3.3.1 Contact angle measurements....34
3.3.2 Sheet resistance method....34
3.5 Cellular biology and biochemistry 35
3.5.1 MTT cell growth assay....35
3.5.2 Bradford assay....35
CHAPTER 4. Conducting Polymer for Sensors Applications 37
4.1 Nanostructured conducting polymer for dopamine detection 39
4.1.1 Introduction....40
4.1.2 Methods....42
4.1.3 Results and Discussion....45
4.1.4 Conclusions....52
4.1.5 References....53
4.2 Controlling the morphology of Poly(N-cyanoethylpyrrole) 57
4.2.1 Introduction....58
4.2.2 Methods....59
4.2.3 Results and Discussion....62
4.2.4 Conclusions....70
4.2.5 References....70
4.3 Detection of dopamine using chemically synthesized multilayered hollow microspheres 73
4.3.1 Introduction....74
4.3.2 Methods....76
4.3.3 Results and Discussion....79
4.3.4 Conclusions....89
4.3.5 References....90
4.4 Ultrathin films of polypyrrole derivates for dopamine detection 93
4.4.1 Introduction....94
4.4.2 Methods....95
4.4.3 Results and Discussion....99
4.4.4 Conclusions....112
4.4.5 References....113
4.5 Selective electrochemical detection of dopamine combining multilayers of conducting polymer with gold nanoparticles 115
4.5.1 Introduction....116
4.5.2 Methods....118
4.5.3 Results and Discussion....120

4.5.4 Conclusions 146
4.5.5 References 147
4.6 A rational design for the selective detection of dopamine using conducting polymers 149
4.6.1 Introduction 150
4.6.2 Methods 152
4.6.3 Results and Discussion 156
4.6.4 Conclusions 172
4.6.5 References 173
CHAPTER 5. Peptide-Conducting Polymer Conjugates as Bioactive Platforms..... 175
5.1 Electroactive and biologically responsive hybrid conjugate based on chemical similarity 177
5.1.1 Introduction 178
5.1.2 Methods 180
5.1.3 Results and Discussion 185
5.1.4 Conclusions 203
5.1.5 References 203
5.2 Design of hybrid conjugates based on chemical similiraty 207
5.2.1 Introduction 208
5.2.2 Methods 211
5.2.3 Results and Discussion 216
5.2.4 Conclusions 241
5.2.5 References 242
CHAPTER 6. PEG-Conducting Polymer Conjugates as Bioactive Platforms 245
6.1 Hybrid materials consisting of all-conjugated polythiophene backbone and grafted hydrophilic poly(ethylene glycol) chains 247
6.1.1 Introduction 248
6.1.2 Methods 250
6.1.3 Results and Discussion 253
6.1.4 Conclusions 275
6.1.5 References 275
6.2 Polythiophene-*g*-poly(ethylene glycol) graft copolymers for electroactive scaffolds 279
6.2.1 Introduction 280
6.2.2 Methods 282
6.2.3 Results and Discussion 288

6.2.4 Conclusions 301
6.2.5 References 302
CHAPTER 7. PEDOT-CREKA Nanocomposites for Biomedical Applications 305
7.1 Impact of incorporating a clot-binding peptide into conducting polymer properties composites for biomedical applications 307
7.1.1 Introduction 308
7.1.2 Methods 310
7.1.3 Results and Discussion 316
7.1.4 Conclusions 334
7.1.5 References 335
CHAPTER 8. Conclusions 337
ANNEX I. 343
Captions for Figures 345
Captions for Tables 357

LIST OF ABBREVIATIONS

Abbreviation	Meaning
AA	Ascorbic acid
AFM	Atomic force microscopy
ATR	Attenuated total reflectance
AuNP(s)	Gold nanopaticle(s)
Boc	*Tert*-butoxycarbonyl
BSA	Bovine serum albumin
CA	Chronoamperometry
CE	Counter or auxiliary electrode
CFME	Cylindrical carbon-fiber microelectrodes
CP	Counterpoise
CP(s)	Conducting polymer(s)
CPE	Constant phase element
CV(s)	Cyclovoltametry(ies)
DA	Dopamine or 3,4-dihydroxyphenyl ethylamine
dAA	Dehydroascorbic acid
DBSA	Dodecylbenzene sulphonic acid
DC	Dopaminechrome
DFT	Density functional theory
DQ	Dopamine-*o*-quinone
DNA	Deoxyribonucleic acid
DMEM	Dulbecco's modified eagle medium
DU145	Human prostate carcinoma
EDOT	3,4-ethylenedioxythiophene
EDX	Energy dispersive X-ray spectroscopy
EIS	Electrochemical impedance spectroscopy
FIB	Focused Ion Beam
FRA	Frequency response analyzer
FWHM	Full-Width Half-Maximum
GAFF	Generalized AMBER force-field
GC	Glassy carbon
GPC	Gel permeation chromatography
GPES	General purpose electrochemical system
GRIM	Gridnard metathesis

Hep-2	Humane epidermoid cancer cell line
HOMO	Highest occupied molecular orbital
IP	Ionization potential
IP_{∞}	Infinite ionization potential
ITO	Indium-tin oxide
LbL	Layer-by-layer
LEA	Loss of electroactivity
LLC-MK2	Rhesus monkey kidney epithelial cell line
MDCK	Madin-Darby canine kidney epithelial cell line
MTT	3-(4,5-dimethylthiazol-2-yl)-2,5-diphenyltetrazolium
Me	Methyl
MD	Molecular Dynamics
NCPy	N-cyanoethylpyrrole
NMPy	N-methylpyrrole
OCP	Open circuit potential
PA	Polyacetylene
PBS	Phosphate buffer saline
PCM	Polarizable continuum model
PEDOT	Poly(3,4-ethylenedioxythiophene)
PEG	Poly(ethylene glycol)
PHMeDOT	Poly(hydroxymethyl-3,4-ethylenedioxythiophene)
PNCPy	Poly(N-cyanoethylpyrrole)
PNMPy	Poly(N-methylpyrrole)
PPy	Polypyrrole
PS	Polystyrene
PSS	Poly(styrene sulfonate)
PSSA	Poly(styrenesulfonic acid)
PT3M or P3MT	Poly(3-methylthiophene)
PTh	Polythiophene
Py	Pyrrole
qdU	Quinoid diimine
QM	Quantum mechanical
RE	Reference electrode
RESP	Restrained ElectroStatic Potential
SAGA	Specular aperture grazing angle

SCE	Saturated calomel electrodes
SDBS	Sodium dodecylbenzenesulfonate
SDS	Sodium dodecyl sulfate
SEM	Scanning electron microscopy
TBATFB	Tetrabutylammonium tetrafluoroborate
TCPS	Tissue culture polystyrene
TD-DFT	Time-dependent density functional theory
Th	Thiophene
Th_5	Pentathiophene
THF	Tetrahydrofuran
UA	Uric acid
UV-vis	Ultraviolet visible
Vero	African green monkey kidney epithelial cell line
VSI	Vertical scanning interferometry
WE	Working electrode

LIST OF SYMBOLS

Symbol	Meaning
A	Absorbance
C_F	Film capacitance
D_{app}	Apparent diffusion coefficient
D_0	Diffusion coefficient
δ	Chemical shifts
ΔE	Relative Energy
ΔE_{int}	Binding energy
ΔG	Gibbs Free energy
ΔQ	Electroactivity
ΔV	Potential window
Ep	Peak potential
E_g	π-π^* lowest transition energy or band gap energy
Ip	Peak intensity
j	Current density
J	Coupling constants
ℓ	Thickness

Q	Voltammetric charge
Q_{pol}	Polymerization charge consumed
P	Porosity
r_{AFM} and r_{op}	Root-mean-square roughness (determined by AFM and optical profilometer)
R_{ct}	Charge transfer resistance
R_p	Pore resistance
R_s	Ohmic resistance
SC	Specific capacitance
σ	Conductivity
θ	Polymerization time
Z	Impedance
Z'	Impedance: real component
Z''	Impedance: imaginary component
ZPVE	Zero-point vibrational energy
t	Time
W_{ox}	Mass of polymer deposited in the electrode

LIST OF SCIENTIFIC JOURNALS

Some of research articles provided in Chapters 4-7 have been published or accepted for publication in the following scientific journals.

Applied materials & Interfaces

Publisher: American Chemical Society (U.S.)

- *"Impact of incorporating a clot-binding peptide into conducting polymer properties: Composites for biomedical applications", (accepted for publication).*

Impact factor (2012): 5.008

Journal of Materials Chemistry

Publisher: Royal Society of Chemistry (U.K.)

- *"Nanostructured conducting polymer for dopamine",* J. Mater. Chem., **2010**, 20, 10652.

Impact factor (2010): 5.099

Journal of Materials Chemistry B

Publisher: Royal Society of Chemistry (U.K.)

- *"Polythiophene-g-poly(ethylene glycol) graft copolymers for electroactive scaffolds*", *J. Mater. Chem. B*, **2013**, 1, 4135.

Impact factor (2012): 6.101

Physical Chemistry Chemical Physics

Publisher: Royal Society of Chemistry (U.K.)

- *"A rational design for the selective detection of dopamine using conducting polymers", Phys. Chem. Chem. Phys.,* **2014**, 16, 7850.

Impact factor (2012): 3.829

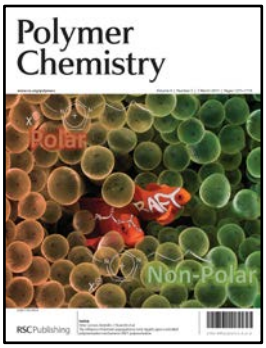

Polymer Chemistry

Publisher: Royal Society of Chemistry (U.K.)

- *"An electroactive and biologically responsive hybrid conjugate based on chemical similarity",* Polym. Chem**.**, **2013**, 4, 1412.

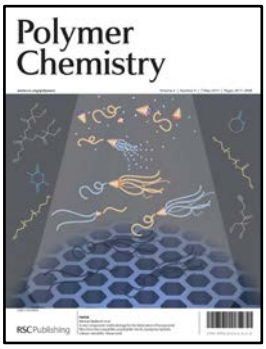

- *"Hybrid materials consistint of all-conjugated polythiophene backbone and grafted hydrophilic poly-(ethylene glycol) chain",* Polym. Chem., **2013**, 4, 2709.

Impact factor (2012): 5.231

RSC Advances

Publisher: Royal Society of Chemistry (U.K.)

- *"Design of hybrid conjugates based on chemical similarity***",** *RSC Adv.*, **2013**, 3, 21069.

Impact factor (Partial): 2.562

The Journal of Physical Chemistry B

Publisher: American Chemical Society (U.S.)

- *"Controlling the morphology of poly(N-cyanoethylpy-rrole)",* J. Phys. Chem. B, **2012**, 116, 5064.

- *"Selective electrochemical detection of dopamine combining multilayers of conducting polymer with gold nanoparticles", (accepted for publication).*
- *"Detection of dopamine using chemically synthesized multilayered hollow microsphere", (accepted for publication).*

Impact factor (2012): 3.607

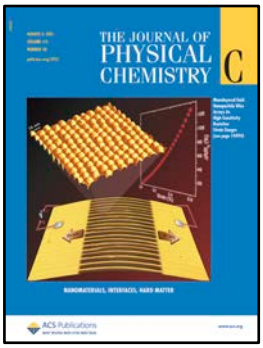

The Journal of Physical Chemistry C

Publisher: American Chemical Society (U.S.)

- *"Ultrathin films of polypyrrole derivatives for dopamine detection",* J. Phys. Chem. C, **2011**, 115,14933.

Impact factor (2011): 4.805

CHAPTER 1

INTRODUCTION

CHAPTER 1. Introduction

1.1 Dicovery and development of conducting polymer

Conducting polymers (CPs) are the most recent and promising generation of polymers. They display many of the desirable properties typically associated with conventional polymers while they also show electrical and optical properties similar to those of metals and inorganic semiconductors.

In 1862, Letherby reported the anodic oxidation of aniline in dilute sulphuric acid, which yielded an insoluble deep-blue shiny powdered deposit on a platinum (Pt) electrode [1]. That was the first reference describing the synthesis of a CP. From such initial discovery, further studies were reported [2-7] but little was understood about CPs at such time, the discovery being essentially disregarded. However, in 1977, Alan J. Heeger and Alan G. MacDiarmid from the United States and Hideki Shiraskawa from Japan discovered that an organic polymer could be altered to exhibit properties like metal [8]. Specifically, the conductivity of the polyacetylene (PA) films was enhanced a 10 million-fold by partial oxidation with iodine vapours or other similar reagents. In 2000, their research was distinguished with the Nobel Prize in Chemistry for the discovery and development of CPs [1]. In 1979, the electrochemical approach for the synthesis of CPs was recovered by Diaz et al., who synthesized electrochemically polypyrrole (PPy) films with good electrical and mechanical properties [9]. Simultaneously, Heeger reported that CPs submitted to chemical and electrochemical redox processes yield materials with relatively high electric conductivities [10].

In recent decades, CPs have attracted great interest within the scientific community and, as a result, a large number of these chemical compounds have been developed and extensively investigated [2,5,11]. Figure 1 shows a simple classification of CPs according to their chemical structure. In this memory, PPy and polythiophene (PTh) derivatives, as for example poly(N-methylpyrrole) (PNMPy) and poly(3,4-ethylenedioxythiophene) (PEDOT), have received much attention because of their excellent electrical and electrochemical properties, and their good chemical and thermal stabilities as well [1, 9,12-13].

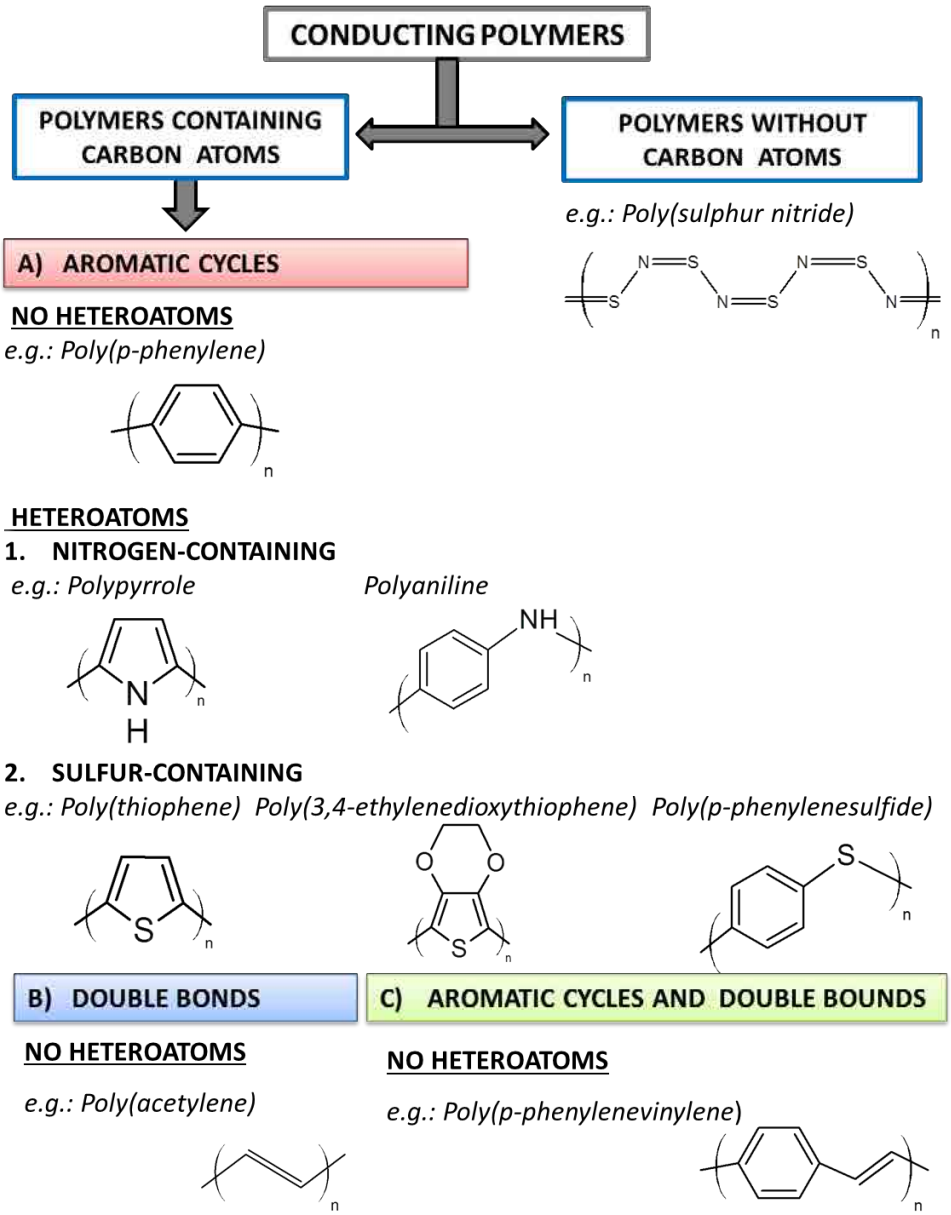

Figure 1. General classification of CPs according to their chemical structure.

1.2 Importance of doping process in conducting polymers

1.2.1 Electrical conductivity

Electrical conductivity is the term describing how well a given material allows electrons to flow through it, and is expressed in siemens per centimeter (i.e., S/cm). In general, materials are classified as insulators (< 10^{-8} S/cm), semiconductors (10^{-8} - 10^{3} S/cm) and conductors (> 10^{3} S/cm). CPs are usually associated with semiconductors materials, whose electrical properties are essentially due to the continuous and ordered distribution of their π- bonds along backbone (organic chains of alternating double- and single-bonded sp^2 hybridized atoms) [14]. The density and mobility of

electrons, which act as charge carriers along the conjugated backbone, determine the degree of conductivity of polymer [15].

1.2.2 Doping process

CPs in the neutral state are typically considered insulative or weak semiconductors. However, the electrical conductivity of CPs can be increased several orders of magnitude by reacting the conjugated polymer with an oxidizing (p-doped) or reducing (n-doped) agent. These processes, which are known as doping, result in highly delocalized polycations or polyanions, respectively [16-17]. In addition, the reactive species used to oxidize or reduce the CP leave behind an anion or cation, respectively. For example, when the doping is carried out with $FeCl_3$, the resulting doping agent is Cl^- or $FeCl_4^-$.

Doping can be carried out using chemical or electrochemical methods and is dependent on the oxidation potential [15]. It is known that the oxidation potential of oligomers decreases with the increasing number of monomers [18]. CPs can be doped or co-doped with a variety of molecules such as salt ions, DNA [19- 21] peptides [22-23], proteins [24-26] and polymers [24]. However, most of biological dopants are not appropriated for redox chemistry, for this reason their incorporation should be done via electrochemical methods, in which the synthetic and doping processes are conducted at the same time. These biological dopants are positively or negatively charged and can coexist with the monomer in the generation solution or can simply act as co-dopantd and be entrapped during the synthesis.

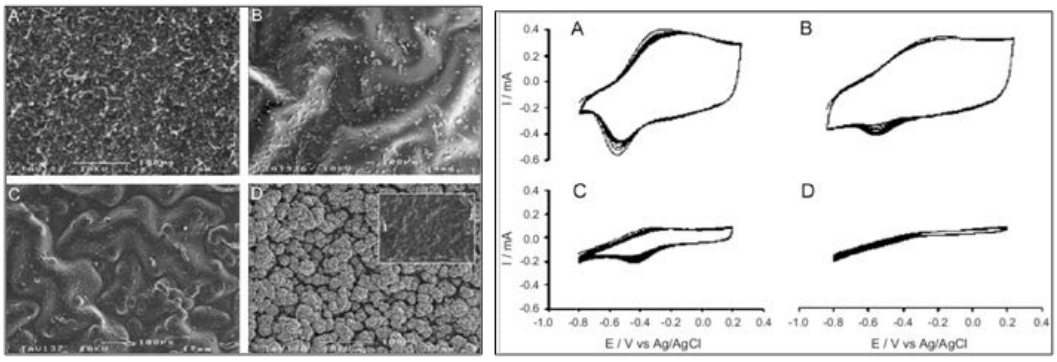

Figure 2. Surface morphology of thick PPy films assessed using scanning electron microscopy (SEM) (left) and the corresponding cyclic voltammograms (CV), indicating electrical activity of the polymers (right). A) doped with ions Cl-, B) doped with poly(vinyl sulfate), C) doped with

dermatan sulfate, D) doped with collagen (inset: thin film of collagen-PPy). (Data taken from reference 31)

In order to maintain the overall charge neutrality, when the CP is altered by gain or loss of electrons from the conjugated backbone, there is a movement of mobile dopant ions [27]. This movement is mainly affected by the chemical nature, size and steric properties of the dopant. For instance, it is reported the ability to release adenosine triphosphate (503 $g \cdot mol^{-1)}$ [28] and risperidone (410.5 $g \cdot mol^{-1}$) [29] from PPy films while release of nicoside is not possible (122 $g \cdot mol^{-1}$).[30] The chemical nature of the dopant does not only affect the electroactivity, but also affects surface and bulk structural properties of polymer as shown in the Figure 2 for the electrochemically doped PPy films with different dopants. [31].

1.2.3 Charge transfer mechanism

According to the charge transfer mechanism, CPs can be classified as degenerate or non degenerate. For example, PA presents a degenerated ground state. This means that its two geometric resonance structures correspond exactly to the same total energy. Figure 3 shows the two degenerated structures of *trans*-PA, the only difference between them being the exchange of the carbon-carbon single and double bonds. Charge carrier species in *trans*-PA are known as solitons, which may be neutral (radical), positive (carbocation) or negative (carbanion).

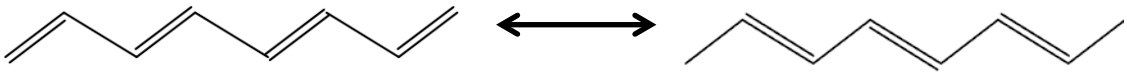

Figure 3. Two degenerated ground state structures of *trans*-PA.

CPs with a non degenerate ground state are usually heterocyclic polymers such as PTh and their derivatives. The ground state of such polymers corresponds to a single geometric structure (aromatic-like structure) with lower energy than that of the corresponding resonance quinoid-like structure (Figure 4). When the polymer is in the non-conductive state, the conjugated backbone is uncharged. On the other hand, when the polymer is oxidized, 'holes' or radical cations are created along the backbone through the removal of electrons. These radical cations, also known as polarons, are partially delocalized within the polymer segment. Quantum-chemical calculations revealed that the aforementioned segments are about four to five ring in

polyheterocycles systems.[32] In a higher conducting state of CPs, dications or bipolarons are formed, when a second electron is removed from the polymer. Finally, neighbouring electrons are free to move into these holes, allowing charge mobility along the polymer backbone and between adjacent chains. This kind of electron delocalization is limited by both disorder and Coulombic interactions between electrons and holes. The resulting conductivity depends on the polymer backbone, and also the chemical nature of the dopant and the doping level.

Figure 4 shows the formation of polaron and bipolaron in conducting polyheterocycles, such as PPy and PTh.

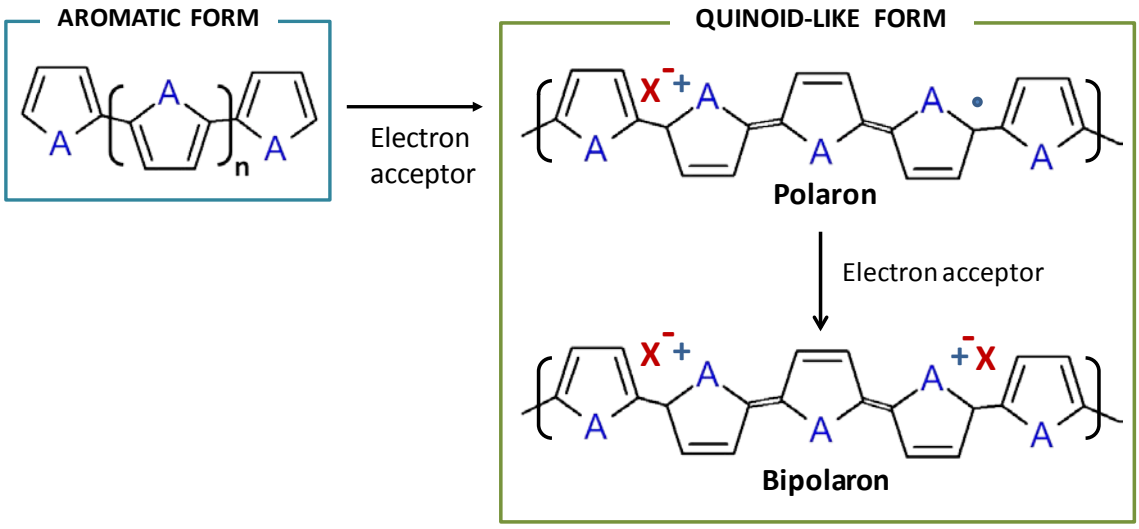

Figure 4. Formation of polarons and bipolarons (p-type doping) in polyheterocycles. A = S, NH or O.

1.3 Synthesis of conducting polymers

The oxidative synthesis of CPs can be achieved by two methods: chemical and electrochemical polymerization. Both methods involve the oxidative polymerization of monomers, which are dissolved in solution, being achieved through a chemical oxidant or applying an anodic potential at electrode, respectively. The polymerization process of heterocyclic polymers is summarized in Figure 5.

Although chemical synthesis provides many different possible routes to synthesize a variety of CPs, electrochemical synthesis is often a preferable alternative since this procedure is relatively straightforward and allows keeping control over the yielding, morphology and electrochemical properties of the resulting material.

Conventional CPs, such as PPy and PEDOT, have been polymerized by both chemical and electrochemical processes. The advantages and disadvantages of both strategies are summarized in Table **1**

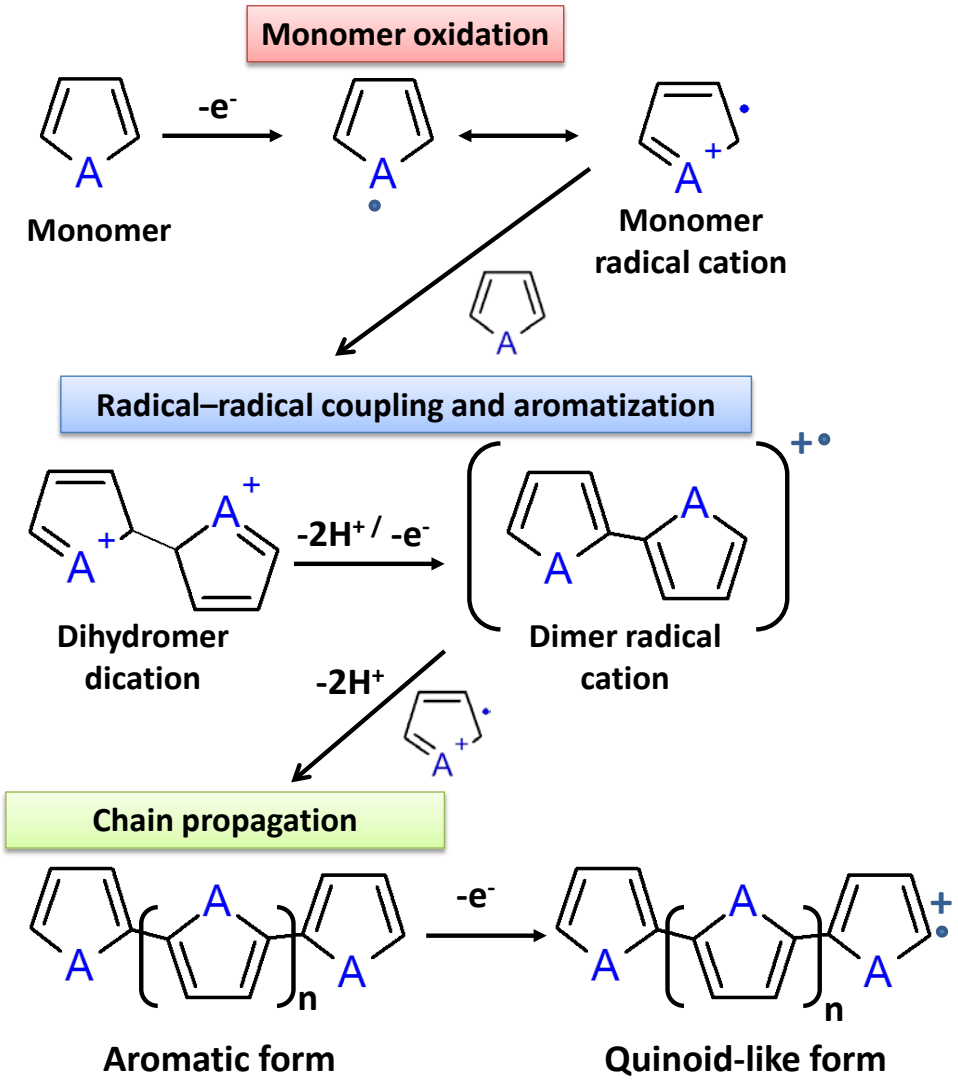

Figure 5. Mechanism for heterocycle polymerization. A = S, NH or O.

Chemical oxidative synthesis involves an appropiate solution mixture of monomer and oxidizing agent such as $FeCl_3$, H_2O_2, H_2SO_4 and some Lewis acids. Currently, the most popular method is the polymerization of thiophenes (Th) using $FeCl_3$, which was described by Sugimoto in 1986.[34] In addition, it is worth mentioning the synthetic procedure described by McCullough et al. in 1992.[35] Homogenous alkylated PThs were achieved by selective bromoniation producing 2-bromo-3-alkylthiophene, followed by transmetallation, and finally Kumada cross-coupling in

presence of a Ni catalyst. This process requires low temperature and careful exclusion of water, oxygen and brominated monomers.

Polymerization Method	Advantages	Disadvantages
Chemical polymerization	a) Larger-scale production b) Post-covalent modification of bulk CP c) More options to modify CP backbone covalently	a) Synthesis more complicated b) Difficult to make thin films
Electrochemical polymerization	a) Ease of synthesis b) Entrapment of molecules in polymer network c) Doping and synthesis are simultaneous d) Easy to make thin films	a) Difficult to remove film from electrodes surface b) Post-covalent modification of bulk CP is difficult

Table 1. Comparision of chemical and electrochemical CP polymerization. [33]

On the other hand, electrochemical polymerization is usually performed using a three-electrode cell containing a working electrode (WE), a counter or auxiliary electrode (CE), and reference electrode (RE). The WE and CE can be made of a variety of materials including steel, Pt, gold, glassy carbon (GC) and indium-tin oxide (ITO) coated glass. Silver|silver chloride (Ag|AgCl) or saturated calomel electrodes (SCE) are frequently used as reference electrodes. Electric current is passed through the solution, provoking the growing of insoluble polymer chainsat the surface of the electrode. Ideally, the selected system should be stable at the oxidation potential of the monomer, providing an ionically conductive medium. Electrochemical oxidation can be achieved using different electrical forms including constant current density (galvanostatic mode), constant potential (potentiostatic mode) and cyclic voltammetry (CV, potentiodynamic mode).

Besides, it should be mentioned that the, application of high potentials during the anodic polymerization may result in the formation of materials with poor properties because of the existence of overoxidation and other eventual degradation processes (*e.g.* polymer crosslinking). Thus, undesirable processes provoke a reduction in both the conductivity and electroactivity. Moreover, the loss of both mechanical properties and adhesion to the substrate have been also observed in overoxidized materials.[36-37]

Application of these two synthetic procedures involves consideration of many variables, such as temperature, polymerization time, stirring, solvent system and dopant. In addition, the potential and the electrodes system must be also considered in case of the electrochemical polymerization. For instance, electrochemical PPy films prepared using low anodic potentials (0.8 V) show a compact and homogeneous surfaces while porous and irregular surfaces are achieved at high potentials (> 0.9 V).[38-39] Each of these parameters also affects the electrochemical and morphological properties, and the performance the resulting materials for different applications (*e.g.* biological platform, organic battery, supercapacitor, etc).

1.4 Properties of conducting polymers for biomedical applications

Some properties such as biodegradability and biocompability must be taken into consideration in the biomedical field. More specifically, biocompatibility is an essential requirement for many biomedical applications. In vitro assays have shown that many CPs, such as PPy and PTh derivatives, do not exhibit toxicity, allowing adhesion and proliferation of different cell types.[40-45] By the mid-1990s, CPs were already used to monitor cellular activities (*e.g.* cell growth, DNA synthesis and protein secretion) through electrical stimulation.[46-48] In addition the biocompatibility of other compounds contained in CP samples, as for example the dopant and other excipients, must be properly considered. In order to improve its biocompability, two different strategies can be followed: **(1)** immobilize specific bioactive molecules into the polymer network; and **(2)** control cellular reactions by electrical signalling from the CP.

On the other hand, CPs are not biodegradable materials, which is an essential requirement for applications related with tissue engineering. However, several strategies can have been proposed to transform them into biodegradable materials. One approach consists in the incorporation of chemical modifications into the CP chain. For example, Rivers et al. prepared modified PPy with using Py-Th-Py oligomers bearing degradable ester linkages, which can be cleaved by enzymatic digestion and consequently removed by macrophages.[49] An alternative strategy is the physical mixture of the CP with an isolating biodegradable polymer. Within this context, biodegrable mixtures of PTh derivatives and biodegradable polyester were recently reported.[50]

Application	Advantages of CPs	Limitations of CPs
Tissue engineering	• Good conductivity • Possible modification to include chemical cues	• Not Biodegradable • Not highly porous • Hydrophobicity
Neural probes	• Good conductivity and stability • Electrochemical synthesis on metal electrodes • Increased surface area (decreased impedance)	• Decreased electrical contact at interface
Biosensors	• Ability to entrap biomolecules in films • Possible surface modification • Efficient electric charge transfer from bioreactions • Electrochemical synthesis on metal electrodes	• Hydrophobicity can denaturalize entrapped proteins • Diffusion barriers for entrapped enzymes
Drug Delivery	• Ability to entrap biomolecules • Controlled release with reduction	• Rapid release • Hydrophobicity can denaturalize entrapped proteins
Bio-actuators	• Ability to entrap biomolecules • Good conductivity • Can control dopant uptake/ release (control volume) • Lightweight • Work at body temperature and with body fluids	• Short-term redox stability • Delamination of CP films • Response limited by ion mobility

Table 2. Advantages and limitations of CPs in biomedical applications.[33]

Table 2 summarizes the advantages and limitations of CPs in biomedical applications, such as tissue-engineering, neural probes, biosensors, drug-delivery devices and bio-actuators.

1.5 Principal strategies to modify conducting polymers

The modification of CPs at chemical and biological level has become the most popular choice for many biomedical applications. CPs exhibit many advantages over other electroactive materials *(e.g.* electrets and piezoelectric materials*)* or other semiconductors and metals (*e.g.* silicon and gold). Specifically, CPs are inexpensive, easy to synthesize and versatile. In recent years, most research has been focused on

improving their electrochemical properties, morphology and biological characteristics, allowing the achievement of specific materials for the intended applications. The main strategies developed to design such improvements are classified in two groups, which correspond to those involving non-covalent and covalent modifications. As shown in Figure 6 non-covalent modifications include adsorption, physical entrapment and affinity binding while covalent modifications include chemical conjugation and copolymerization.

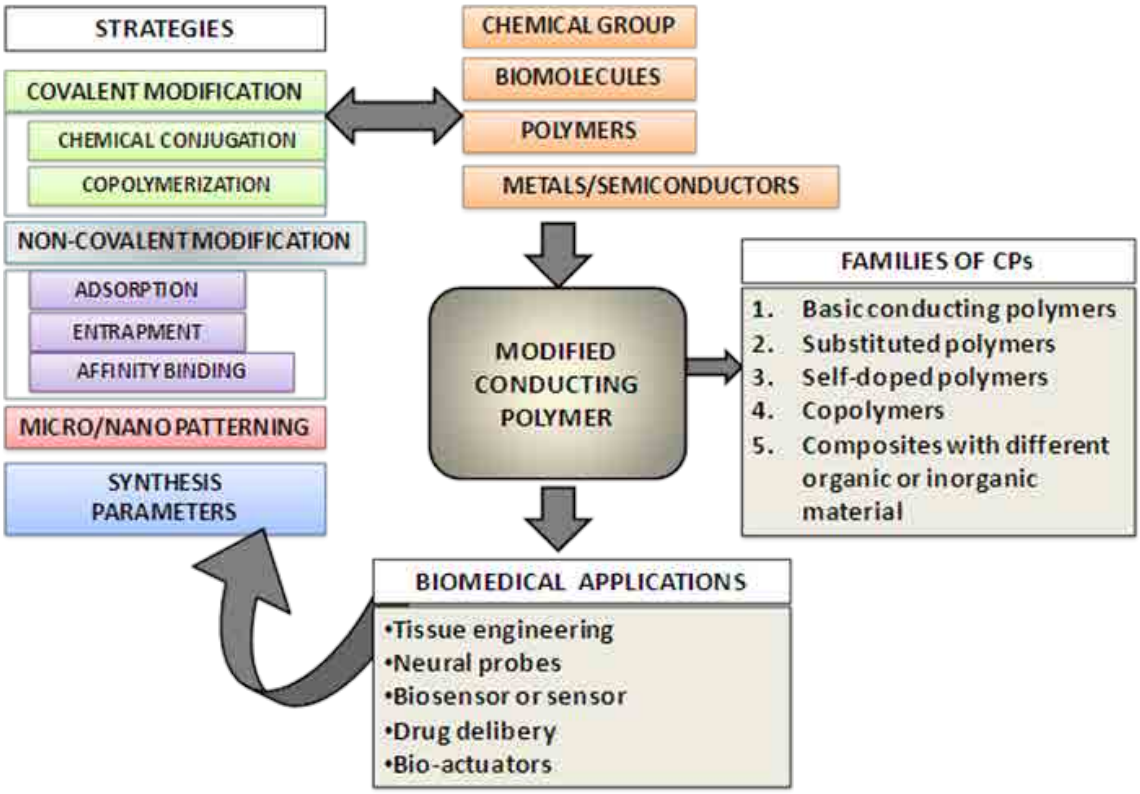

Figure 6. Principal strategies to modify CPs for biomedical applications.

Other strategies used to manipulate physical properties are micro- or nanopatterning, which include the use of templates that can be removed to yield free-standing structures, and modification of the parameters used for the electrochemical synthesis of CPs (*e.g.* dopant and deposition charge).

Also, CPs can be combined with a wide variety of materials (*e.g.* metal nanoparticles, living cells, polymers) to enhance the desired properties. As a result of these combinations, CPs can be categorized into five groups: basic polymers, substituted polymers, self-doped polymers, copolymers and composites.

1.5.1 Non-covalent methods

Physical adsorption is much used for biosensors because of its simplicity. Nevertheless, its main disadvantage is the difficulty of controlling the concentration of immobilized molecules. This is caused by weak forces (*e.g.* van der Waals, hydrogen bonding and electrostatic interaction), resulting in a low stability.[51] Another drawback is that the adsorption occurs as a monolayer, which limits the amount of sensing element, and with a random orientation on the surface. For example, the DNA biosensor reported by Fu et al. DNA was developed by indirect absorption of mercapto-oligonucleotide onto Au–Ag nanocomposites deposited on PPy.[52]

Entrapment is a simple non-covalent method, which can be achieved by having the desired molecule present in the polymerization medium. Entrapment can be also used as alternative doping process, replacing the conventional dopant by an appropriately charged biomolecule in the medium. The process is usually carried out under mild conditions (i.*e.* neutral pH, aqueous medium and low oxidation potentials) to avoid chemical reactions that could alter the bioactivity. CPs have been used to immobilize polymers [24], living cells [53-55], enzymes [24-26], antibodies [56] and DNA [56-57]. For instance, the polymerization of PPy in presence of cells extracted from banana pulp was used to detect dopamine (DA). This type of cells contains polyphenol oxidase, which catalyzes the conversion of DA to dopamine-*o*-quinone (DQ) [53,58].

The hydrophobic nature of CPs can negatively affect the bioactivity of the immobilized biomolecule. However, this drawback can be avoided by modifying the monomer with hydrophilic groups such as ether chains [59]. Other limitations are the high concentration of biomolecule required to have an optimum content and, if the case, the accessibility of analytes to form affinity complexes (*e.g.* antibody-antigen).

The affinity binding method is a non-covalent strategy used to overcome some of the limitations discussed above. This is based on the immobilization of molecules on the surface of CPs through strong cooperative effects that involve non-covalent interactions. For example, the avidin–biotin complex was formed through the covalent pre-immobilization of biotin on the CP and, subsequently, of avidin through non-covalent interactions by affinity with biotin[60]. The orientation of the immobilized

molecules can be controlled by optimizing the location of the binding elements; improving the activity and accessibility of the biological sensing elements. Pyrrole (Py) and biotinylated hydrophilic Py monomers were combined using electrochemical methods in recent studies. The modified monomer contained poly(ethylene glycol) (PEG), which acted as a spacer arm to link the biotin moiety to the PPy backbone. The amount of anchored avidin on the hydrophilic PPy was modulated by the immobilized biotin density and by the length of the PEG spacer.[61-62]

1.5.2 Covalent methods

The main advantage of covalent methods with respect to the non-covalent ones refers to the permanent functionalization, which is easier for the formers than for the latters. The desired functional group can be introduced into the polymer matrix using two different strategies: pre- and post-polymerization. The choice of one of these strategies is determined by the agreement balance between the difficulties associated to the incorporation of the functionalized component and the facilities for the desired application.

In the post-polymerization modification, the immobilization takes places on the polymer's surface, allowing independent optimization of the experimental conditions required in each stage of the whole process (*i.e.* polymerization and covalent immobilization).[63] In contrast, the hybrid materials that result from the pre-polymerization modification similar to expected from a chemical strategy similar to the copolymerization. Moreover, the process can be designed according to the desired organization of the different chemical components in the hybrid, which can be random, alternating, multiblock and grafted.

Besides the introduction of biomolecules or chemical groups via chemical conjugation, polymeric components with very different properties (*e.g.* topography, hydrophilicity, porosity, malleability, degradability) can also be incorporated. The resulting materials present the characteristics and properties of their individual components. For example, Liu *et al.* recently increased the surface hydrophilicity of PTh and poly(3-methylthiophene) (P3Th) films by incorporating PEG monomethacrylate through UV-light-induced graft copolymerization.[64]

However, it is worth noting that some incorporated functional groups can induce repulsive steric effects, breaking the planarity of the π-conjugated system typically associated to the backbone CP chains. This undesired effect usually results in a reduction of the electrical conductivity.

1.6 References

1. G. Inzelt, "Conducting Polymers: A new era in electrochemistry", Springer, Berlin (2008).

2. H. S. Nalwa, "Handbook of Advanced Electronic and Photonic Materials and Devices", Academic Press, USA (2011) 132.

3. B. A. Bolto, R. McNeil and D. E. Weiss, Aust. J. Chem., 1963, **16**, 1103.

4. Z. P. Li and B. H. Liu, J. Appl. Electrchem., 2010, **40**, 475.

5. A. Dall'Olio, Y. Dascola, V. Varacca and V. Bocchi, Compte Rendus, 1968, **C267**, 433.

6. D. D. Ateh, H. A. Navsaria and P. Vadgama, J. R. Soc. Interface, 2006, **3**, 741.

7. R. De Surville, M. Jozefowicz, L. T. Yu, J. Pepichon and R. Buvet, Electrochim. Acta, 1968, **13**, 1451.

8. H. Shirakawa, E.J. Louis, A.G. MacDiarmid, C.K. Chiang and A.J. Heeger, J. Chem. Soc. Chem. Commun., 1977, **16**, 578.

9. A. F. Diaz, K. K. Kanasawa and G. P. Gradini, J. Chem Soc. Chem. Comm., 1979, 635.

10. A. G. McDiarmid and A. J. Heeger, "Molecular Materials", Plenum, New York (1979) 1.

11. H. Peng, L. Zhang, C. Soeller and J. Travas-Sejdic, Biomaterials, 2009, **30**, 2132.

12. G. G. Wallace, G. M. Spinks, L. A. P. Kane-Maguire and P. R. Teasdale, "Conducting Electroactive Polymers: Intelligent Polymer Systems", New York : CRC Press (2008) 1.

13. C. Ocampo, E. Armelin, F. Estrany, L. J. Del Valle, R. Oliver, F. Sepulcre and C. Alemán, Macromol. Mater. Eng., 2007, **292**, 85.

14. D. M. Ivory, G. G. Miller, J. M. Sowa, L. W. Shacklette, R. R. Chance and R.H.Baughman, J. Chem. Phys., 1979, **71**, 1506.

15. Terje A., Skotheim and J.R. Reynolds, "Conjugated Polymers: Theory, Synthesis, Properties and Characterization" 3rd ed. Taylor & Francis Group, Florida, (2007).

16. U. Evans, O. Soyemi, M. S. Doescher, U. H. F. Bunz, L. Kloppenburg and M. L. Myrick, Analyst (Cambridge, U. K.), 2001, **126**(4), 508.

17. M. D. McClain and D. S. Dudis, Synth. Metals, 2001, **116**, 199.

18. T. Vernitskaya and O. Efimov, Russ. Chem. Rev. 66, 1997, **5**, 443.

19. Y. Fu, R. Yuan, Y. Chai, L. Zhou and Y. Zhang, Anal. Lett., 2006, **39**, 467.

20. X. Jiang and X. Lin, Anal. Chim. Acta, 2005, **537**, 145.

21. S. Cosnier, R. E. Ionescu, S. Herrmann, L. Bouffier, M. Demeunynck and R.S. Marks, Anal. Chem., 2006, **78**, 7054.

22. R. A. Green, N. H. Lovell and L. A. Poole-Warren, Biomaterials, 2009, **30**, 3637.

23. R. A. Green, N. H. Lovell and L. A. Poole-Warren, Acta Biomater, 2010, **1**, 63.

24. O. Ngamna, A. Morrin, S.E. Moulton, A.J. Killard, M.R. Smyth and G.G. Wallace, Synth. Met. 2005, **153**, 185.

25. L. Cen, K. G. Neoh and, E. T. Kang, Biosensors Bioelectron, 2003, **18**, 363.

26. S. Singh, A. Chaubey and B. D. Malhotra, J. Appl. Polym. Sci., 2004, **91**, 3769.

27. M. Pyo, G. Maeder, R. T. Kennedy and J. R. Reynolds, J. Electroanal. Chem., 1994, **368**, 329.

28. M. Pyo and J. R. Reynolds, Chem. Mater., 1996, **8**, 128.

29. D. Svirskis, B. E. Wright, J. Travas-Sejdic, A. Rodgers and S. Garg, Electroanalysis, 2010, **22**(4), 439.

30. K. Kontturi, P. Pentti and G. Sundholm, J. Electroanal. Chem., 1998, **453**, 231.

31. D. D. Ateh, P. Vadgama and H. A. Navsaria, Tissue Eng., 2006, **12**, 645.

32. C. Casanovas and C. Alemán, J. Phys. Chem. C, 2007, **111**, 4823.

33. N. K. Guimard et al., Prog. Polym. Sci., 2007, **32**, 876.

34. R. Sugimoto, S. Taketa, H. B. Gu and K. Yoshino, Chem. Express, 1986, **1**, 635.

35. R. D. McDullough and R. D. Lowe, J. Chem. Soc. Chem. Commun., 1992, 70.

36. B. C. Thompson, S. E. Moulton, J. Ding, R. Richardson, A. Cameron, S. O'Leary, G. G.Wallace and G. M. Clark, J. Control. Release, 2006, **116**, 285.

37. G. G. Wallace, G. M. Spinks, L. A. Kane-Maguire and P. R. Teasdale, "Conductive Electroactive Polymers: Intelligent Polymer Systems", 3rd ed.Taylor & Francis Group, Florida, 2009.

38. R. Wadhwa, C. F. Lagenaur and X. T. Cui,J. Control. Release, 2006, **110**, 531.

39. J.-M. Pernaut and J. R. Reynolds, J. Phys. Chem. B., 2000, **104**, 4080.

40. M. R. Abidian, J. M. Corey, D. R. Kipke and and D.C. Martin, Small, 2010, **6**, 421.

41. P. M. George, A. W. Lyckman, D. A. Lavan, A. Hegde, Y. Leung, R. Avasare, C. Testa,P. M. Alexander, R. Langer and M. Sur, Biomaterials, 2005, **26**, 3511.

42. S. J. Chen, C. W. Yuan, X. D. Wang, P. Y. Zhang and X. S. Gu, Prog. Biochem. Biophys., 2000, **27**, 212.

43. J. E. Collazos-Castro, J. L. Polo, G. R. Hernandez-Labrado, V. Padial-Canete and C. Garcia-Rama, Biomaterials, 2010, **31**, 9244.

44. H. Gerding, J. Neural Eng., 2007, **4**, S30.

45. X. Y. T. Cui and D. C. Martin, "Conducting IPN Fibers: a new design for linear actuation in open air" in Y. Bar-Cohen "Electroactive Polymers and Rapid Prototyping 2001", Materials Research Society, Boston (USA), (2002).

46. N. C. Foulds and C. R. Lowe, J. Chem. Soc. Faraday Trans., 1986, **82**,1259.

47. M. Umana and J. Waller, Anal. Chem., 1986, **58**, 2979.

48. J. Y. Wong, R. Langer and D. E. Ingber, Proc. Natl. Acad. Sci. USA, 1994, **91**, 3201.

49. T. J. Rivers, T. W. Hudsen and C. E. Schmidt, Adv. Funct. Mater., 2002, **12**, 33.

50. T. Ahuja, I.A. Mir, D. Kumar and Rajesh., Biomaterials, 2007, **28**, 791.

51 M. M. Perez-Madrigal, E. Armelin, L. J. del Valle, F. Estrany and C. Aleman., Polym. Chem., 2012, **3**, 979

52. Y. Fu, R. Yuan, Y. Chai, L. Zhou and Y. Zhang, Anal. Lett., 2006, **39**, 467.

53. M. V. Deshpande and E. A. Hall, Biosensors Bioelectron, 1990, **5**, 431.

54. A. J. Hodgson, M. J. John, T. Campbell, A. Georgevich, S. Woodhouse and T. Aoki, Proc. SPIE Int. Soc. Opt. Eng., 1996, **2716**, 164.

55. T. E. Campbell, A. J. Hodgson and, G. G. Wallace, Electroanalysis, 1999, **11**, 215.

56. C. M. Li, C.Q. Sun, S. Song, V. E. Choong, G. Maracas and X.J. Zhang, Front. Biosci., 2005, **10**, 180.

57. X. Jiang and X. Lin, Anal. Chim. Acta, 2005, **537**, 145.

58. J. S. Sidwell and G. A. Rechnitz, Biotechnol. Lett., 1985, **7**, 419.

59. J. Roncali, Chem. Rev., 1992, **92**, 711.

60. M. Wilchek and E.A. Bayer, Anal. Biochem., 1988, **171**, 1.

61. L. M. Torres-Rodriguez, M. Billon, A. Roget and G. Bidan, J. Electroanal. Chem., 2002, **523**, 70.

62. S. A. G. Evans, K. Brakha, M. Billon, P. Mailley and G. Denuault, Electrochem. Commun., 2005, **7**, 135.

63. J. C. Vidal, E. G. Ruiz and J. R. Castillo, Microchim. Acta, 2003, **143**, 93.

64. F. Liu, Y. Chen, Y. Wei, L. Li and S. Shang, J. Appl. Polym. Sci., 2012, **123**, 2582.

CHAPTER 2

OBJECTIVES

CHAPTER 2. Objectives

The general and specific objectives of this Thesis can be summarized as follows:

Objective 1

Preparation of ultra-thin hollow microsphere particles by self-assembly polymerization using different combinations of CPs for electrochemical detection of neurotransmitters.

- Determine the influence of the polymerization method in the morphology and thickness of *N*-substituted PPy derivatives chemically deposited onto soft templates.
- Optimize the experimental conditions for the preparation of hollow microspheres with mechanical integrity and tunable thickness. For this purpose, two *N*-substituted PPy derivatives, PNMPy and poly(N-cyanoethylpyrrole) (PNCPy), have been considered.
- Prepare and characterize hollow microspheres formed by a multilayered sequence of two different CPs, PEDOT and PNMPy, arranged alternatively.
- Examine the efficacy of 3-layered microspheres for the electrochemical detection of DA, compared to other CP systems prepared by self-assembly or electrochemical polymerizations.

Objective 2

Explore the detection of DA using films made with one or more CPs and examine the influence on the detection sensitivity of the incorporation of gold nanoparticles (AuNPs) to such films for the formation of hybrid nanocomposites.

- Examine the ability of films made of different *N*-substituted PPy derivatives to detect DA concentrations lower than the maximum concentration found for this neurotransmissor in the synaptic region and analyze the influence of the *N*-substituent in the detection response.
- Compare the selective sensing capacities of *N*-substituted PPy derivatives and PEDOT towards DA and use the results for the rational design of an optimized CP for the selective detection of DA (i.e. in presence of other biomolecules, which act as interferents).

- Test the ability of hybrid films formed by a CP coated by AuNPs to immobilize and detect DA, and compare the results with the films without AuNPs.
- Investigate the influence of internal interfaces created using multiple polymerization steps in the efficacy of CP films for the electrochemical detection of DA.
- Evaluate the sensitivity and resolution of multilayered films made by combining layers of two different CPs for the selective detection of DA and compare their efficacy with those of films prepared using individual CPs.
- Investigate the electrocatalytic role of AuNPs in the detection of DA when they are used to coat multilayered films.
- Check the efficiency of the materials with the better abilities to detect selectively DA when they are applied to real human fluids.

Objective 3

Development of a new approach based on chemical similarity for the design of peptide-CP hybrids, which are potential candidates for the development of platforms with bioactive and bioelectrocompatible properties. This strategy is expected to avoid, or at least to reduce, the peptide-induced detriment typically observed in the electrochemical, electronic and electrical properties of the CP.

- Design of new non-proteinogenic amino acids for the covalent incorporation of peptides to the surface of CPs, by applying chemical similarity concepts.
- Characterize the properties of the conjugates designed by chemical similarity, comparing them with those of the corresponding CP homopolymers.
- Analyze how small changes in the chemical structure of the peptide can affect the morphological, electrochemical, hydrophilic and electronic properties of the peptide-CP conjugate.
- Evaluate the performance of the new hybrid materials, in relation with the corresponding CP, as bioactive matrices to promote cell adhesion and proliferation.

Objective 4

Prepare and characterize organic hybrid materials formed by an all-conjugated PTh backbone and well-defined PEG grafted chains, as well as explore their potential use for biotechnological and biomedical applications.

- Select and apply a suitable strategy for the preparation of graft copolymers consisting of a PTh backbone and chains of PEG grafter to the backbone.
- Investigate and rationalize the influence of the length and the polymerization conditions of the grafted PEG chains on the structure and properties of graft copolymers.
- Examine the potential applicability of graft copolymers, based on PTh and PEG, as active surfaces for the selective adsorption of proteins and as bioactive platforms.

Objective 5

Prepare, characterize and apply as bioactive platform bio-nanocomposites formed by PEDOT, a very stable and electroactive CP, and CREKA, a biologically active linear pentapeptide.

- Select the most appropriated approach and conditions for the incorporation of CREKA into a PEDOT matrix.
- Determine the morphological, topographical, chemical and electrochemical properties of PEDOT-CREKA nanocomposites, evaluating the impact of the peptide on the intrinsic properties of the CP.
- Examine the ability of PEDOT-CREKA to promote both cell adhesion and proliferation and its ability to bind fibrin.

CHAPTER 3

EXPERIMENTAL BACKGROUND

CHAPTER 3. Experimental Background

The experimental procedures and methodology used to develop the tasks addressed in this Thesis are widely described in sub-sections explicitly included in each of the next Chapters. These sections provide all details needed to reproduce the results and well as the technical characteristics of the equipments used for measures. For this reason, the purpose of this Chapter is not to provide deep information about the experimental methods used during the development of the Thesis but only to briefly discuss the physicial and chemical principles associated to the most frequently used procedures and techniques. These basic concepts are expected to clarify eseential aspects of techniques that may be unfamiliar to the reader, facilitating the understanding of next Chapters.

It should be also mentioned that description of the employed polymerization techniques Thesis have been excluded from this Chapter since they were briefly discussed in Section 1.3. Chemical oxidative polymerization has been used to generate hollow microspheres because it provides a suitable coating for freestanding nanostructures using initially soft and not-conducting templates as substrates. Thus, the main advantage of chemical polymerization compared to the electrochemical one is related with the fact that the former enables the yielding of larger amounts of polymer (i.e. chemical polymerization allowed us to prepare large quantities of hollow). However, it should be remarked that most of the CPs used in the present Thesis have been produced by potentiostatic methods since electrochemical synthesis provides several advantages compared with chemical methods, as for example high doping level, absence of catalyst, control of the oxidation state, ease purification and lower solvent comsuption (see Table 1 in Chapter 1). As the electrochemical techniques used in this work for the electropolymerization of CPs have been also used to characterize the properties of the resulting materials, a brief discussion of the physical concepts associated to such procedures has been included in this Chapter (Section 3.1). However, details about their direct application on polymerization have omitted since, as was mentioned above, these are explicitly described in next Chapters.

3.1 Electrochemical techniques

The main electrochemical techniques employed for polymerization as well as for electrochemical studies once the CPs were prepared are based on potentiostatic (chronoamperometry, CA), potentiodynamic (cyclic voltammetry, CV) and galvanostatic (recurrent galvanostatic pulse, RGP) methods. Furthermore, a powerful surface technique, called electrochemical impedance spectroscopy (EIS), has been also used to get information about the influence of the electrolytic medium in the surface properties.

3.1.1 Chronoamperometry

The principle of CA is focused on applying a constant voltage during a period of time. The resulting current variation in the WE is recorded as a function of time. This technique is frequently used to synthesize polymer films onto the metallic substrates (WE), and in particular to obtain different redox states of CP using the access (doping process) or scape (undoping process) of anions.

3.1.2 Cyclic voltammetry

CV is one of the most common electrochemical techniques employed to characterize CPs. CV is based on measurement of the current obtained at the WE as a function of the applied potential. This technique provides information of the redox processes occurred in polymer and/or electroactive species in solution. Also, it is possible to evaluate the charge storage (electroactivity) and the loss of electroactivity versus the successive oxidation-reduction cycles (electrostability) of CPs.

3.1.3 Recurrent galvanostatic pulse

RGP involves applying a current density on the WE with successive charge–discharge cycles. The response consists of a potential as a function of time. The procedure has been used to determine the specific capacitance of CPs which is intended to be used as bioactive platform for the adhesion and proliferation of cells.

3.1.4 Electrochemical impedance spectroscopy

Electrochemical impedance spectroscopy (EIS) technique measures the dielectric properties of a medium as a function of frequency. The frequency response of the system reveals information about the interface process occurred at the surface among different materials, which provides information about the energy storage and dissipation properties. The response obtained by EIS is represented graphically in a Bode plot or a Nyquist plot. In a Bode plot the impedance is represented with log-frequency on the X-axis and both the absolute values of the impedance and the phase-shift on the Y-axis. A Nyquist plot consists on a graphical representation of the impedance, which is composed of a real and an imaginary part. More specifically, the real part is plotted on the X-axis and the imaginary part is plotted on the Y-axis.

3.2 Microscopy techniques

Microscopy studies were performed in order to evaluate the morphology and surface semi-quantitative composition of the prepared materials.

3.2.1 Scanning electron microscopy

Scanning electron microscopy (SEM) allows observing the surface of a material from images using a beam of electrons. The shorter wavelength of electrons offers a better resolution than conventional light microscopy. The detector equipment is very sensitive being able to reveal details up to 1-5 nm in size and, thus, must operate within an ultra-high vacuum for accurate measurement. When the beam impinges on the sample, many types of signals are generated and some of these can be displayed as an image but with different results for each. The two signals most often used to generate SEM topographical images are secondary electrons (inelastic collisions) and back-scattered electrons (elastic collisions), whereas for elemental analysis, X-rays radiation is employed. Each of these emissions is provoked by the different energy levels of the incident electron.

The samples were examined using a scanning microscope equipped with an energy dispersive X-ray (EDX) spectroscopy system, which provides qualitatively or semi-quantitatively information on the elemental composition of the polymers. Samples were mounted on aluminum studs using adhesive graphite tape. Insulator

materials, such as samples involved in cell adhesion and proliferation assays, were sputtered-coated with ultrathin layer of carbon or gold. This coating prevented the accumulation of static electric charge on the specimen during electron irradiation.

3.2.2 Atomic force microscopy

The atomic force microscope (AFM) is one of the most powerful tools for determining the topology of a sample in *x*, *y* as well as *z* direction. AFM involves a cantilever with a sharp tip that moves over the sample in a faster scan and bends in response to the small repulsive force (10^{-9} to $l0^{-8}$ N) between the atoms of the tip and the surface atoms of the sample. The tip radius of curvature is in the scale of nanometers. The bending response of the cantilever is mesured by the deflection of a laser beam focused on the back of the tip. Finally, laser deflections are recorded by a photodiode array, which translates these results into topographic features. The force is kept constant by means of a feed-back loop in the so-called 'constant force mode'.

The AFM can be operated in static (also called contact) and dynamic (non-contact and tapping) modes, the difference between them being the extent of tip-sample interaction during the measurement. Contact mode operation involves direct contact of the tip with the surface. The detected net force is the sum of the attractive and repulsive force between the tip and the sample. In non-contact mode the tip is oscillated at its resonating frequency and positioned over the surface at a distance, so that the two are no longer in contact. The detected force is the result of van de Waals, magnetic or electrostatic forces. Tapping mode consists of a cantilever that vibrates with larger amplitude and the vibrating tip contacts the sample surface many times per data point. This mode is generally used for soft samples because it causes less damage.

In the present Thesis, all the AFM imaging has been done in tapping mode, and operated at constant deflections. This technique was used to study in ambient conditions the rugosity and thickness of different materials.

3.2.2 Transmission electron microscopy

The principle of transmission electron microscopy (TEM) consists of an electron beam which is transmitted through an ultra-thin section of the sample. Electrons are

generated by the microscope through a process known as termionic emission from a tungsten filament. TEM image is formed from the intensity of the transmitted beam, which depends largely on the density and thickness of the material. The resolution of TEM imaging is significantly higher resolution than that of light microscopes. Furthermore, TEM images present varying contrast in which darker areas, with higher contrast, are those from where fewer electrons have been transmitted due to high density or thickness of the sample; while the areas of lower contrast indicates a higher number of transmitted electrons.

TEM has been employed in this work to observe the shape and size of the gold nanoparticles and to determine the thickness of hollow microspheres. Samples were prepared for TEM examination by dropping the corresponding material, which was previously dispersed in absolute ethanol or water, onto carbon coated copper grids.

3.3 Spectroscopic techniques

3.3.1 Ultraviolet-visible spectroscopy

Ultraviolet-visible spectroscopy (UV-vis) is used to obtain the absorbance or reflectance spectrum of materials in the UV-vis spectral region. UV-vis analyses are generally carried out in solution but solids and gases can also be studied. UV-vis technique is based on measuring the amount of light absorbed by a sample at a specific wavelength. The UV-vis region of energy for the electromagnetic spectrum covers 1.5-6.2 eV, which correspond to a wavelength range of 200-800 nm. Electrons are transferred from low-energy to high-energy atomic or molecular orbitals when the material is irradiated in this region of the electromagnetic spectrum. The UV-vis technique allows evaluation of different electronic transitions, which are associated to characteristic wavelengths (λ). Depending on the range of wavelength, specific transitions can take place. Thus, when a molecule absorbs energy an electron is excited from an occupied orbital to an unoccupied orbital of greater energy.

In this work, UV-vis technique has been employed to determine both electronic transitions and doping/undoping states in CPs. The extended system of alternating simple and double bonds of CPs can absorb light in the UV-vis region. The peaks in an UV-vis spectrum are commonly due to $n - \pi^*$ or $\pi - \pi^*$ transitions, which are

responsible for the color of the material. Specifically, $\pi - \pi^*$ transitions are one of the most important to determine the lowest electronic energy gap.

3.3.3 Fourier transform infrared spectroscopy

Fourier Transform Infrared Spectroscopy (FTIR) is a useful tool to evaluate and to determine functional groups in liquids, gases, powders and films. Sample is irradiated with an IR light source. When the IR light is passing through the sample, molecules can absorb the energy contained in the incident light to rotate and vibrate. That vibrations are only allowed when the dipole moment of molecule changes during the vibration. Vibrational modes can be divided into stretching (symmetric and asymmetric) and bending vibrations (in-plane and out-of plane). A detector registers the amount of light transmitted by a sample at a specific wavelength.

In this Thesis, FTIR spectroscopy has been employed to verify the polymerization process and to characterize chemically the corresponding CP. Additionally, the detection of the dopant agent has allowed evaluation of the changes induced in the polymeric structure by the oxidation (doping) – reduction (undoping) processes.

3.3.4 Raman spectroscopy

Raman spectroscopy is a non-destructive technique used to observe vibrational, rotational, and other low-frequency modes in a system. Raman spectroscopy studies the inelastic scattering of monochromatic light, usually from a laser in the visible, near IR, or near UV range. The intensity of the scattered light depends on the amount of the polarization potential required by a molecule to exhibit a Raman effect. A molecule can be transferred to an excited state through the absorption of a photon and, when the molecule recovers from this state, scattering reactions occur. Spontaneous Raman scattering is typically very weak, and as a result the main difficulty of Raman spectroscopy is the separation of the weak inelastically scattered light from the intense elastically scattered light (Rayleigh scattering). During this recovery process, the system can gain or lose energy depending on whether the system reaches a higher or lower energy state than it had before, respectively. However, the latter process is less common, since at room temperature most

molecules are in the ground state as opposed to a higher energy level. Stokes scattering (red shifted, low-energy) is provoked when the scattered light loses energy while the opposite situation results in Anti-Stokes scattering (blue shifted, high-energy). The Stokes bands are most commonly used due to their higher intensity.

This technique has been very useful to characterize CP nanostructures in the doped state.

3.3.5 X-Ray photoelectron spectroscopy

X-Ray Photoelectron spectroscopy (XPS) is a nondestructive and a surface-sensitive quantitative spectroscopic technique that analyze the elemental composition as well as both electronic and chemical states of the elements present in the surface of the material. XPS method can analyze elements that are present within the top 1-10 nm of the sample surface.

XPS spectra are obtained by irradiating a material with X-ray beam, data being analyzed by measuring the kinetic energy and the number of electrons that escape from the surface. When an X-ray beam impacts on the sample surface, the energy of the X-ray photon is adsorbed completely by the core electrons of an atom. The binding energy of the core electrons of each atom is equal to the ionization energie of those electrons. If the photon energy, *hv*, is large enough, the core electrons will then escape from the atom and are emitted out of the surface. The binding energy of a given core electron is expressed as:

$$E_{binding} = E_{photon} - E_{kinetic} - \Phi \qquad (1)$$

where $E_{binding}$ is the energy of the electron emitted from one electron configuration within the atom, E_{photon} is the energy of the X-ray photons being used, $E_{kinetic}$ is the kinetic energy of the emitted electron as measured by the instrument and Φ is the work function of the spectrometer.

In this thesis, XPS has been employed to determine the elements and the quantity of those elements that are present on the surface of CPs, as well as the electronic and chemical state of these elements.

3.4 Physical techniques

3.4.1 Contact angle

Wettability studies usually involve the measurement of contact angles as the primary data, which indicates the degree of wetting when a solid and a liquid interact. The contact between both the liquid and the solid surface exerts a force on each other that can be repelling or attracting, depending on the surface energy of the solid surface and surface tension of the liquid. The contact angle is defined geometrically as the angle formed by the intersection of the liquid-solid interface and the liquid-vapor interface (geometrically acquired by applying a tangent line from the contact point along the liquid-vapor interface in the droplet profile). Small contact angles (<90°) are observed when the liquid spreads on the surface of the sample, indicating high wettability. In contrast, large contact angles (>90°) correspond to low wettability and therefore the liquid forms a compact drop on the surface. Several techniques are used to measure contact angles, which can be classified into two main groups: optical tensiometry (goniometry), which analyze the shape of a drop of test liquid placed on solid, and force tensiometry, which measure the forces that are present when a sample of solid is brought into contact with a test liquid.

The Young's equation is used to describe the nature of the contact angle. The Young's equation (Eq.2) takes into account the surface energies of the solid, liquid and solid/liquid interfaces:

$$\gamma^{S} = \gamma^{L} \cos\theta + \gamma^{SL} \qquad (2)$$

where γ^{S} is the solid surface energy, γ^{L} is the liquid surface tension, γ^{SL} is the interface free energy for the solid/liquid interface, and θ is the contact angle.

In this work the contact angle measurements of CPs films have been perfomed using the static sessile drop method and measured by a goniometer.

3.4.2 Sheet resistance method

The conductivity (σ) has been measured from the sheet resistance method, which consists of measuring the resistance between the two silver terminals of a film.

According to the law of conductivity and both the geometric and physical properties of the material, the conductivity can be measured as follows:

$$\sigma = \frac{R \cdot l}{A} \qquad (3)$$

where l is the length between the two silver terminals of a film, *R* is the resistance and A is the cross-sectional area of the polymer film.

3.5 Cellular biology and biochemistry

3.5.1 MTT cell growth assay

Cell adhesion and proliferation has been evaluated using MTT (3-(4,5-dimethylthiazol-2-yl)-2,5-diphenyltetrazolium bromide) assay. The MTT colorimetric assay is a simple method for evaluating the cell viability using standard microplate absorbance readers. The MTT assay involves the conversion of the water soluble MTT to an insoluble formazan. The yellow tetrazole is reduced by metabolically active cells, in part by the action of mitochondrial dehydrogenase, to generate reducing equivalents such as NADH and NADPH. The resulting intracellular purple formazan is then solubilized and its concentration determined by optical density at 570 nm.

In this Thesis the biocompatibility of CPs has been evaluated using different cellular lines: HEp-2 (human Larynx carcinoma), DU145 (human prostate carcinoma), LLC-MK2 (rhesus monkey kidney), MDCK (Madin-Darby canine kidney) and Vero (African green monkey kidney).

3.5.2 Bradford assay

The Bradford assay is a colorimetric method used to determine the concentration of protein in solution. This method is based on an absorbance shift of the standard dye, Coomassie Brilliant Blue G-250. In acidic conditions the red form of the dye is converted into its blue form to bind to the assayed protein.

The formation of dye-protein complex involves two steps: 1) the disruption of the protein's native state to expose its hydrophobic pockets to the cationic form of the Coomassie dye; and 2) the formation of non-covalents bonds between the pockets of

the protein's tertiary structure and the non-polar region of the dye through van der Waals forces and hydrophobic interactions. Ionic interactions are also present in the complex formation. The binding of the protein stabilized with the anionic form of the Coomassie dye has an absorption maximum at 595 nm. The absorbance of light at 595nm increases linearly when the protein concentration increases. Although the absorbance of Coomassie blue dye at 595 nm is proportional to the amount of protein bound, it is necessary to establish a correspondence between absorbance values and known amounts of protein. The response is also protein dependent, and varies with the composition of the protein. On the other hand, its response is influenced by non protein sources such as detergents.

CHAPTER 4

CONDUCTING POLYMER FOR SENSOR APPLICATIONS

4.1 Nanostructured conducting polymer for dopamine*/**

In this work, we demonstrate the ability of PNMPy to form nanostructures and to detect very low concentrations of DA, an important neurotransmitter. PNMPy hollow particles of controlled thickness have been prepared using the Layer-by-Layer (LbL) assembly technique and polystyrene (PS) core-shell particles as template, which are subsequently eliminated to yield free-standing hollow microspheres with layer thickness of 30 nm. The morphology and composition of these structures have been evaluated by SEM, TEM, FTIR, Raman and XPS. Results demonstrate that intact hollow spheres can be obtained controlling the number of polymer deposition cycles. Furthermore, two kind of sensors were constructed by immobilizing PNMPy /Au nanocomposites and PNMPy nanomembranes on the surface of a glassy carbon electrode (GCE). Electrochemical techniques were employed to evaluate the ability of PNMPy to absorb/immobilize DA molecules. It was found that systems based on this CP are highly sensitivity to the neurotransmitter concentration, presenting a very fast response even when the concentration of the DA is very low.

*Results described in this section previously appeared in *J. Mater. Chem.*, 2010, **20**, 10652.

**Preparation and characterization of hollow microspheres were performed in collaboration with Dr. M. Martí.

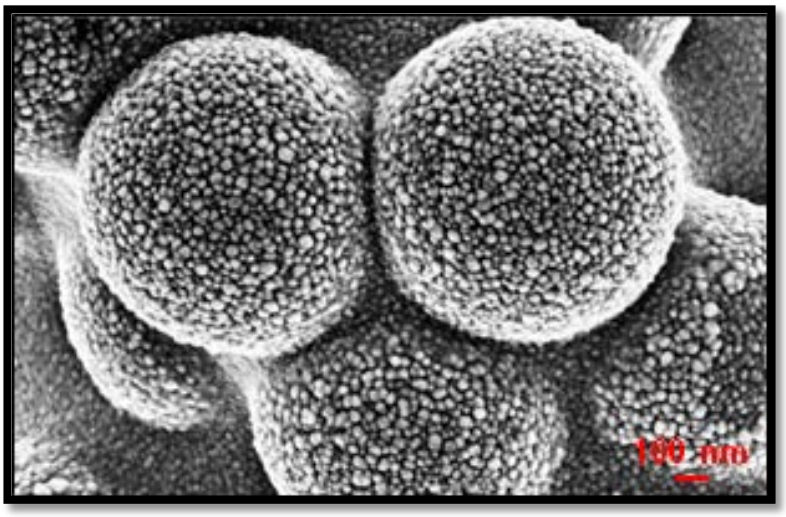

4.1.1 Introduction

DA is an important neurotransmitter involved in motor and cognitive functions. The loss of DA in neurons has been associated to neurological disorders, like Parkinson's disease and schizophrenia[1,2]. In neurons this dihydroxylated phenetylamine derivative and other neurotransmitters are stored in synaptic vesicles (or neurotransmitter vesicles), which are small balloon-like sacs able to transport material throughout the cell. When vesicles receive an electrical signal through a nerve impulse, they carry the DA molecules to the cell wall and release them into the synapse, which is the tiny gap between the axon ending and the dendrite of the next neuron.[3]

The development of sensors to measure the DA concentration in a single synapse is currently getting special attention because of the necessity of understanding the mechanisms that provoke neurological disorders, which is essential to achieve their complete control. Nevertheless, this is a very complex task due to the synapse nanoscale dimensions.[4] Electrochemical techniques have been extensively employed to monitor neurochemistry.[5] Nevertheless, this is frequently performed using cylindrical carbon-fiber microelectrodes (CFME) (~ 5 μm of diameter), which are larger than the synapse dimensions. Thus, to the best of our knowledge, dopamine detection at the nanometric scale has been only reported in the very recent work published by Tyagi *et. al.*, who fabricated gold-nanowire-based electrochemical sensors with diameters ranging from 30 to 1000 nm.[6] It is worth noting that detection at this scale opens new possibilities for controlled electrochemical recognition of DA *in vitro* and *in vivo*, as well as for innovative studies on sensitive and selective DA detection.

Nowadays, there are two options to detect DA with electrochemical techniques in a synapse scale: (i) minimizing the size of the electrodes,[6] or (ii) employing novel nanomaterials with properties highly sensitive to DA molecules.[7] Within the latter context, organic/inorganic nanocomposites, which are obtained by combining organic and inorganic materials, have attracted significant attention, novel materials with advanced structures being produced by the LbL templating technique.[8] The LbL method has become one of the more employed route to sequential deposition of a

broad range of templates, *e.g.* molecules (proteins, dyes, lipids, polymers, etc), biological cells and nanoparticles with inorganic compounds.[9] The general process involves the sequential deposition of species onto various templates, which are subsequently removed to yield free-standing structures. This technique offers two main possibilities for the generation of self-assembled monolayered films: (a) use solid planar substrates or (b) use core-shell particles. Since the pioneering studies of Decher[8] many research groups have successfully used this technology to prepare nanoscale materials. In this sense, we can emphasize the brilliant research developed by Caruso and co-workers with complex systems based on polymer capsules. The recent reviews written by Caruso *et. al* [9] presents the new advances on the LbL assembly technique, as well as the future research directions using planar, colloidal and naturally occurring templates.

One of the critical steps of this LbL approach is the removal of the templating substrate, which is necessary to obtain the free-standing nanostructured material. Thus, non desirable morphologies and functions may be obtained after the template removal because of the substrate rupture. Fortunately, after almost twenty years since the LbL self-assembly was firstly introduced by Decher and Hong,[8] such limitations have been partially or totally overcome as is reflected by the wide number of innovative materials reported in the last few years, *e.g.* nanofilms, microspheres, nanotubes, macroparticles, porous particles and biomimetic structures.[10] Many of the nanostructured materials currently under development are based on the CPs deposition in a core-shell particle. The major part of the works is related to PPy and PAni systems.[11-18] However, in the last years, PNMPy has attracted the attention of the researchers since its environmental stability and positive oxidation potential are higher than those of PPy.[19] Thus, despite the electrical conductivity of PNMPy electrodeposited films is lower than that of the PPy one, the former material has been postulated as a good alternative to replace PPy in some applications, like sensors,[20-25] batteries[26,27] or capacitors,[28,29] and drug delivery systems.[30,31]

In the present work, we report the preparation and characterization of a porous PNMPy nanocomposite and its ability to detect very low concentrations of DA. More specifically, we present the fabrication of hollow microspheres of controlled

nanolayer thickness using the LbL procedure and PS core-shell particles as template. The surface composition and morphology of these PNMPy nanostructures, which were doped with chloride and dodecylbenzenesultonate ions, have been analyzed using spectroscopy techniques (FTIR, Raman and UV-vis-NIR), XPS, SEM and TEM. Nanomembranes fabricated with this material have been used to monitor the interaction between PNMPy and DA, the detection being been based on the readily electrochemical oxidation of the latter. Results indicate that the gold-PNMPy nanomembrane-based sensors prepared in this work detect submicromolar concentrations of DA, the synaptic concentration of DA being reported to be around 1.6mM.[32]

4.1.2 Methods

Materials. Py and NMPy 99% were purchased from Aldrich and were used freshly distilled. Styrene was purchased from Aldrich and was purified after passing through an activated neutral alumina column. Poly(N-vinylpyrrolidone) (PVP) with M_w= 360,000 g/mol, α-azoisobutyronitrile (AIBN), iron (III) chloride hexahydrate 97% (ACS reagent) and dodecylbenzene sulphonic acid (DBSA) 70 wt. % were also purchased from Aldrich and used as received. All solvents or acid solutions were purchased from Panreac S.A., while aqueous solutions were prepared using doubly distilled deionized water.

DA hydrochloride and $HAuCl_4 \cdot 3H_2O$ were obtained from Sigma-Aldrich (Spain), whereas sodium citrate dihydrate was purchased from J.T. Baker. All other chemicals were of analytical-reagent grade and used without further purification. Phosphate buffer solution (PBS) 0.1 M with pH 3 was prepared as electrolyte solution by mixing four stock solutions of NaCl, KCl, $NaHPO_4$, KH_2PO_4, the pH being subsequently adjusted with HCl. High-purity nitrogen was used for deaeration of the prepared aqueous solutions.

Preparation of PNMPy core-shell and hollow microspheres. PNMPy core-shell and hollow microspheres were prepared following the procedure described by Lascelles *et. al.*[11] The complete synthesis procedure, including the doping of the

PNMPy/PSS and PPy/PSS microspheres and the extraction of the PSS core to obtain hollow spheres, is displayed in Figure 1.

Preparation of Au colloidal nanoparticles. Preparation of the Au colloidal nanopaticles (AuNPs) for deposition onto GCEs, which were used to fabricate the nanomembranes of CPs, was performed following the standard procedure described in the literature.[32-35] All glassware used in such preparation was thoroughly cleaned in aqua regia (3:1 HCl:HNO_3), rinsed in doubly distilled water, and oven-dried prior to use. In a 1 L round-bottom flask equipped with a condenser, 500 mL of 1 mM $HAuCl_4$ was brought to a rolling boil with vigorous stirring. Rapid addition of 50 mL of 38.8 mM sodium citrate to the vortex of the solution produced a colour change from pale yellow to burgundy. Boiling was continued for 15 min. After this, the heating mantle was removed while the stirring was continued for 30 min. When the solution reached the room temperature, it was filtered through a 0.2 µm membrane filter. The resulting solution of colloidal particles showed an absorption maximum at 520 nm indicating that the particle size ranged from 9 to 22nm. A spherical model for a particle size of 13 nm was used to determine approximately the concentration of mother solution from UV-vis absorption, which was estimated to be 7.4 nM.[44]

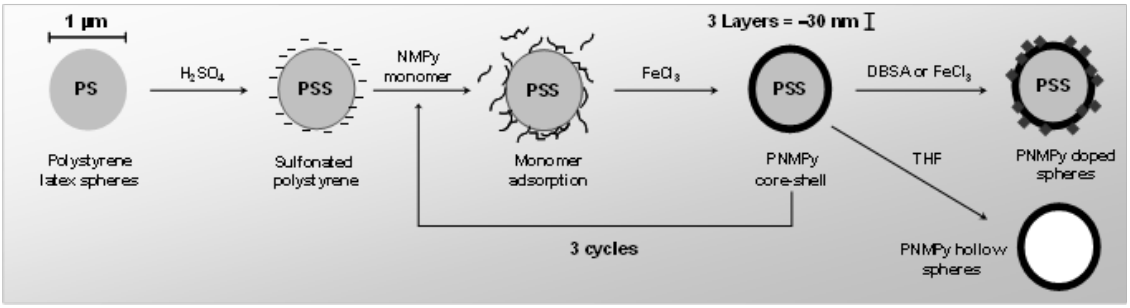

Figure 1. Scheme showing the synthesis of doped and hollow PNMPy spheres.

Analytical Techniques.

Raman. Raman spectroscopy was performed with a Dilor Jobin Yvon dispersive spectrometer equipped with a 1024 diodes multichannel detector using a He/Ne laser (20 mW) with 633 nm of excitation wavelength. The spectral interval ranged from 1200 to 2000 cm^{-1}.

XPS. XPS analyses were performed in a PHI 5500 Multitechnique System instrument (from Physical Electronics) equipped with a monochromatic Al Kα X-Ray

source (1486.6 eV, 350W), placed perpendicular to the analyzer axis and calibrated using the 3d5/2 line of Ag with a full width at half maximum (FWHM) of 0.8 eV. The X-ray spot size was 650 μm. The pass energy was set at 150 and 40 eV for the survey and the narrow scans, respectively. Charge compensation was achieved with a combination of electron and argon ion flood guns. The energy and emission current of the electrons were 4 eV and 0.35 mA, respectively. For the argon gun, the energy and the emission current were 0 eV and 0.1 mA, respectively. The partial pressure for the argon flood gun was $2 \cdot 10^{-8}$ mbar. These standard conditions of charge compensation resulted in a negative but perfectly uniform static charge. Data acquisition and processing were achieved with the Advantage Software. Spectral calibration was determined by setting the main C1s component at 285 eV. The surface composition was determined using the manufacturer's sensitivity factors.

TEM and SEM. SEM studies were carried out using a FIB Zeiss Neon40 scanning electron microscope equipped with an EDX spectroscopy system and operating at 30 kV. The samples were mounted on a double-sided adhesive carbon disc and sputter-coated with a thin layer of gold to prevent sample charging problems. The TEM images were collected with a Philips TECNAI 10 electron microscope operating at 80kV. Bright field micrographs were taken with an SIS MegaView II digital camera. A solution containing PS, sulfonated PS, PNMPy/PSS core-shell and PNMPy hollow spheres (1mg/10μL in water) were cast onto a carbon coated copper-grids (300 mesh) and the solvent was allowed to evaporate.

Electrochemical methods. CV studies were conducted with an Autolab PGSTAT302N equipped with the ECD module for measure very low current densities (100μA-100pA) (Ecochimie, The Netherlands). All electrochemical experiments were performed in a cell containing 20 mL of PBS 0.1M at room temperature and equipped with saturated Ag|AgCl as RE and Pt wire as CE. A GCE was used as the WE (1 mm diameter) and its surface was polished with alumina powder and cleaned by ultrasonication prior to the polymer electropolymerization.

PNMPy was electrochemically deposited on the GCE bare by CA in 0.1M using a NMPy solution (10 mM) with $LiClO_4$ as supporting electrolyte. The anodic

polymerization was carried out using an optimum potential of 1.30 V, which was kept constant, during 20 s. The thickness of the films prepared using this procedure ranged from 350 to 500 nm. In all cases, the solution was purged with nitrogen gas for 10 min prior electrochemical synthesis. Then, the AuNPs colloidal solution (2 µL) was dropped onto the PNMPy-modified GCE surface and allowed to dry under atmosphere conditions, this process was repeated twice. The AuNPs concentration in the electrode surface was estimated to be $22.6 \cdot 10^9$ nanoparticles/mm^2.

4.1.3 Results and Discussion

Chemical composition and morphology of the CP microspheres.

Characterization of CPs by spectroscopy is a difficult task compared to the conventional and insulating polymers, due to the charge of inorganic particles present in the polymer chains after the oxidative chemical polymerization. This task becomes worse when the concentration of CP is very low, as occurs in the structures investigated in this work: PSS microspheres coated with nanolayers of PNMPy or PPy. In this study we discuss the most usual spectroscopic techniques for the characterization of the CPs adapted to these systems.

Infrared spectroscopy is one of the most employed techniques for identification of organic compounds. However, despite many works describe the characterization of PTh and PPy derivatives using this spectroscopic method,[11,13] the application of this technique to our system present serious limitations. On the other hand, RAMAN spectroscopy has proved to be a useful technique for studying CP nanostructures, especially when they are in the doped state. The bands corresponding to the polymer are increased by the Raman resonant effect; while the bands of the dopant molecules are not in resonance conditions.[19] Therefore, we examined the presence of the PNMPy and PPy in microspheres doped systems with Raman spectroscopy. Figure 2 compares the Raman spectra of PNMPy-$FeCl_3$, PNMPy-DBSA, PPy-$FeCl_3$ and PPy-DBSA materials. The PNMPy core-shell was characterized by Raman analysis with the observation of strong bands at 1578 cm^{-1} ($C^{\alpha}=C^{\beta}$ ring stretching), 1425 and 1327 cm^{-1} (C-N antisymmetrical stretching) and 1170 cm^{-1} (C-H in plane deformation and ring stretching) referred to doped species. Interestingly, the peaks assigned to the C^{β}-H

bending vibrations at 1080-1040 cm^{-1} and the $C^{\beta}=C^{\beta}$ stretching are not detected in the Raman spectra of the PNMPy microspheres. The disappearance of peaks usually indicates loss of symmetry in the molecule.[36] In this case we attribute such disappearance to the polymer backbone overoxidation of the position C-H (β) in the Py aromatic ring (see inset arrow on Figure 2a and 2b). The origin of these CO groups is the oxidative process undergone by some five-membered rings during the preparation of the PNMPy. The peaks are also quite broad presenting much noise, which is due to both the very thin layer of conducting polymer coat (30nm) and the interactions with the dopant counterions.

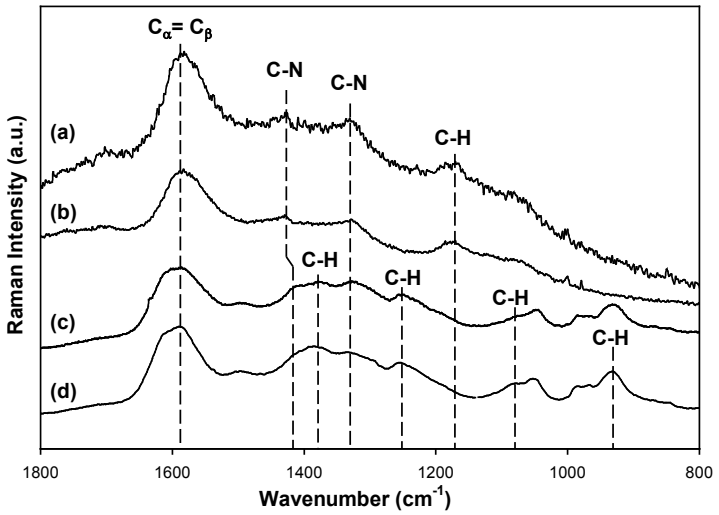

Figure 2. Raman spectra of (a) PNMPy-FeCl3, (b) PNMPy-DBSA, (c) PPy-FeCl3, and (d) PPy-DBSA core-shell particles. Inset arrow indicates the Cα=Cβ bond-stretching vibration associated to the loss of symmetry in the molecule due to the irreversible oxidation of the Py ring Exciting radiation: 632.8 nm.

On the other hand, it is worth noting that when polymer chains are partially doped some peaks should be duplicated. This is evidenced for PPy doped spheres in Figures 2c and 2d, which show not only a duplicated stretching mode of the C=C bonds at ca. 1600 cm^{-1} but also two additional bands at 1080 cm^{-1} (C-H in plane deformation) and 1380 cm^{-1} (ring stretching). These features should be attributed to the partially oxidized PPy backbone, as is indicated also by the presence of bipolaron (932 and 1080 cm^{-1}) and polaron (980 and 1045 cm^{-1}) C-H deformation and bending peaks. However, no relevant difference was found between the Raman spectra of the PNMPy microspheres doped with $FeCl_3$ and DBSA, or similarly between the spectra of the two

PPy systems. This is in agreement with the loss of Raman resonance effect in the dopant molecules discussed above.

Another interesting observation provided by the Raman analyses is the absence of absorption bands related with the PS molecules. This allowed us to confirm that the template was completely coated by the CP in all the prepared microspheres doped systems. Furthermore, the spectra displayed in Figure 2 are consistent with those reported in the literature.[37-38]

The CP composition of the coated PS microspheres was further characterized with XPS analysis. Elemental analyses showed the characteristic peaks of various elements with different binding energies corresponding to: Cl 2p (200.8 eV), C 1s (284.9 eV), N 1s (399.1 eV) and O 1s (532.2 eV). PNMPy XPS data reveals additional peaks compared to PS microspheres. These peaks indicate that the CP is partially doped by chloride anions and undergone partial surface oxidation by the high level of oxygen atoms. The presence of Cl 2p signals, which was already observed by Lascelles et. al.[11] for PPy coated PS particles, is observed when $FeCl_3$ oxidant is employed in the chemical polymerization process. The surface chemical composition determined by XPS for the coated PS studied in this work is: 87.65% C, 10.17 % N, 2.18 % Cl (considering C+N+Cl= 100%). The C/N ratio of PNMPy is 8.618 and the Cl/N ratio is 0.21; which is comparable with the doping level typically accepted for PPy.

High resolution spectra of C 1s, N 1s and Cl 2p are displayed in Figure 3. for both uncoated PS and PNMPy/PSS coated particles. As it can be seen, no signal associated to the aromatic ring of PS is observed in the spectra of the coated microspheres (Figure 3a), i.e. π-π* shake-up satellite peaks at 291.5-293.0 eV are not detected in the C 1s region. This indicates that the core-shell is well covered by 30 nm thickness of PNMPy. There is no evidence of Fe atoms (708-720 eV) at the surface of the material, indicating that the material is well purified after the polymerization process. The overall of the XPS results obtained in this work are in excellent agreement with those reported by Lascelles et. al.[11] and by Yang et. al.[15] for PPy/PS microspheres.

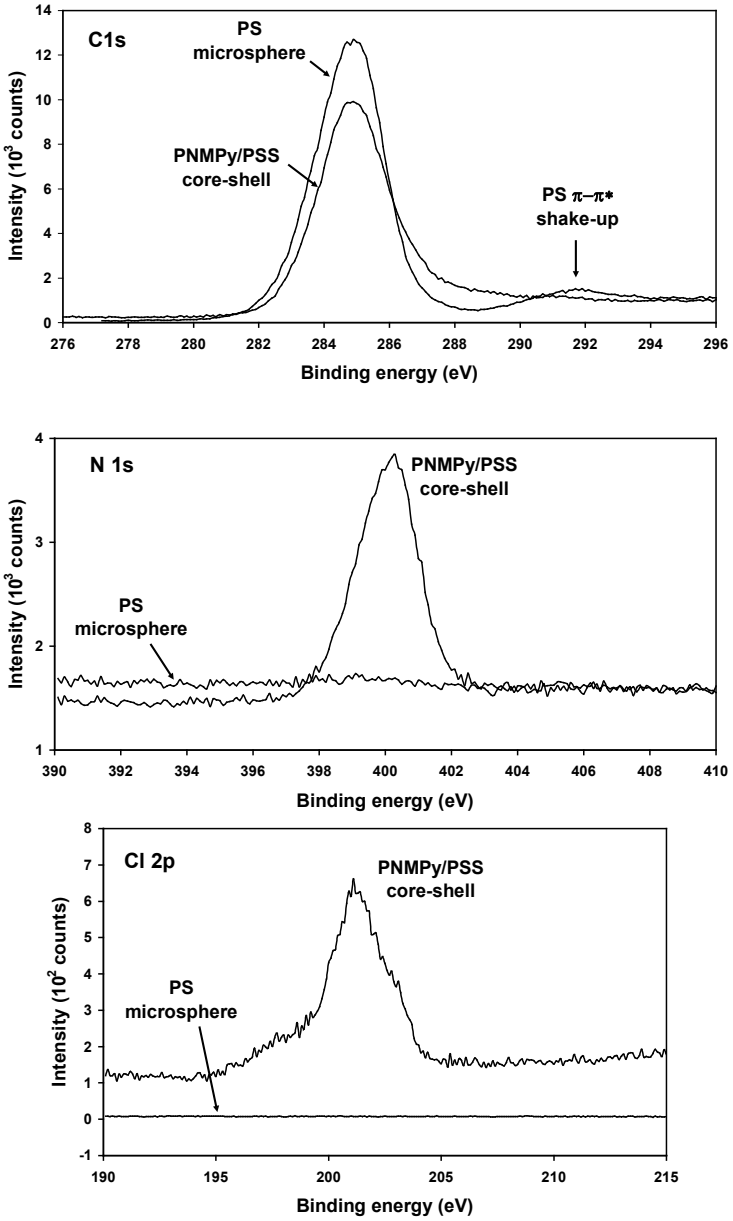

Figure 3. High resolution XPS spectra of PNMPy/PSS core-shell and PS uncoated microspheres: (a) C 1s region; (b) N 1s region; and (c) Cl 2p region.

Regarding to the overall procedure used to prepare nanolayers of CP, which is illustrated in Figure 1, solid PS spheres with an average diameter of 1.0±0.3 μm were obtained using the synthesis procedure developed by Lascelles et. al.[11] The SEM and TEM micrographs indicate that all the PS particles are spherical and their size distribution is homogeneous. The PNMPy/PS overlayer thickness average is 9±1.8 nm for one polymerization step, taken by TEM microscopy and assuming that the coating is uniform. After three polymerization cycles the PNMPy shell thickness increased to 30±2.5 nm. The surface of the PNMPy microspheres is more roughness than that of

the PPy ones,[39] and indeed the porosity of the bulk is higher in the former than in the latter. Previous studies on PPy and PNMPy confirm these observations.[40,41]

These nanostructures are expected to be useful to trap and/or delivery drugs or related biomolecules, as will be demonstrated in the next section with the fabrication of the PNMPy nanomembrane for detection of dopamine neurotransmitter.

Application of PNMPy nanomembranes to the detection of DA

Measurement of DA in the brain is not an easy task due to the dimensions of synapse. Ideally, DA concentration should be determined inside the ~100 nm synapse. This was not possible with PNMPy hollow spheres due to the difficulties in support the beads adhered to the surface electrode. One option and good approach was to prepare a PNMPy nanomembrane directly adhered to GCE surface by CA technique, described on the Methods section, and to compare this system with another that contains AuNPs deposited onto PNMPy-modified GCE. The thickness of the nanomembranes prepared by CA ranged from 350 to 500 nm, being only slightly larger than synapse diameter.

After construct the sensor, the minimum concentration of DA detected by this organic/inorganic nanocomposite was measured using CV. Figure 4 shows the control voltammograms of the neurotransmitter at isolated GCE, AuNPs-modified GCE, PNMPy-modified GCE and PNMPy/AuNPs-modified GCE systems. Voltammograms were recorded in the potential range from -0.40 to 0.80 V at a scan rate of $100 mV \cdot s^{-1}$, scanning being stopped after 10 oxidation-reduction cycles. All the modified electrodes were in contact with the electrolyte solution for 10 min prior to the CV measurements. Figures 4a and 4b evidence the lack of electrochemical response in absence of DA for GCE and the AuNPs-modified GCE in PBS solution, respectively. Furthermore, DA in direct contact with the GCE (Figure 4a) showed a less reversible electrochemical behavior than the GCE modified with AuNPs (Figure 4b), without an oxidation peak and showing a less positive reduction potential at 0.14V. In the case of AuNPs-modified GCE, we observed two oxidation peaks at 0.43 and 0.56V when the concentration of DA is 10mM, implying that AuNPs helps the system to oxidize and to reduce in a lower potential range and with higher current density. Therefore, AuNPs accentuates the

electrochemical oxidation response of the neurotransmitter, i.e. acting as a catalyst and lowering the oxidation peak of DA.[12] The first oxidation peak at 0.43V is attributed to the formation of a polaron, while the second oxidation peak (0.56 V) has been attributed to the oxidation of DA to DQ molecules (Figure 5), according to the studies reported by Lin and Zhang.[42] Voltammograms obtained using concentrations of DA higher than 10 mM showed in all cases oxidation peaks observed at very similar values with the PNMPy-modified GCE. This electrochemical behavior is produced by the electrostatic interactions between the modified GCE and the DA molecules dissolved in the PBS buffer. Therefore, the oxidation peaks move to lower potentials with respect to the results obtained with the no-modified GCE, while the reduction peaks show more positive potential. Moreover, DA voltammogram become more reversible and exhibit sharper peaks at AuNPs-modified GCE. This response is due to the unique electrical properties of the nanocomposite, which can act as a catalyst for the oxidation of DA, mentioned above.

The interaction of the PNMPy nanomembrane with DA is reflected in Figures 4c and 4d, which compare the oxidation potentials for two modified electrode systems, i.e. in absence and presence of AuNPs. In general, results reflect that the electrode kinetics for the PNMPy/AuNPs-modified GCE was better than for the PNMPy-modified GCE without AuNPs. However, the anodic current densities obtained for DA with the PNMPy nanomembrane were also higher than those achieved with the unmodified GCE. More specifically, a more positive potential (0.73V) and reversibility were observed for both PNMPy/AuNP-modified GCE and PNMPy-modified GCE systems. These results indicate that PNMPy is useful for the detection of very low DA concentrations since the anodic current density obtained in presence of this CP is one and a half higher. Thus, the PNMPy and PNMPy/AuNPs systems produce an anodic current density of 4.1 and 5.7 $mA \cdot cm^{-2}$ (Figure 4c and 4d), respectively, for a DA concentration of 10mM, whereas the AuNPs system yields a current density of 2.6 $mA \cdot cm^{-2}$(Figure 4b). This behavior suggests that PNMPy induces a catalytic effect on the oxidation of DA, which should be attributed to the influence of its electrochemical properties on the intensity of the sign.

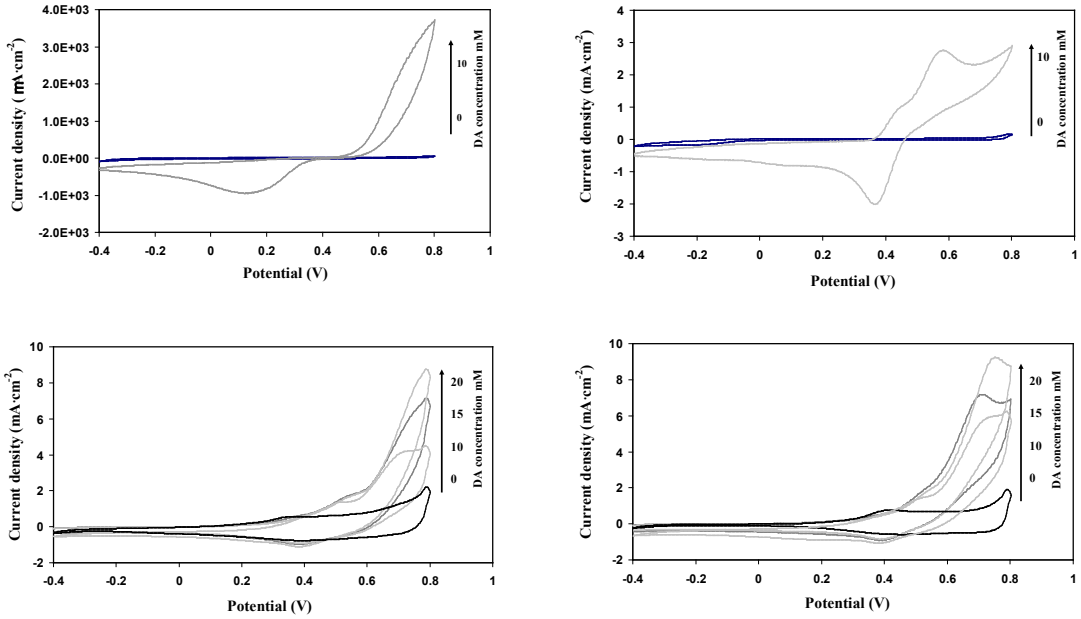

Figure 4. CVs of (a) GCE; (b) AuNPs-modified GCE, (c) PNMPy-modified GCE and (d) PNMPy/AuNPs-modified GCE in absence and presence of different DA concentrations. Scan rate: 100mV·s-1. Supporting electrolyte: 0.1M PBS. Voltammograms were obtained by scanning from -0.40 to 0.80V at a scan rate of 100 mV·s^{-1}.

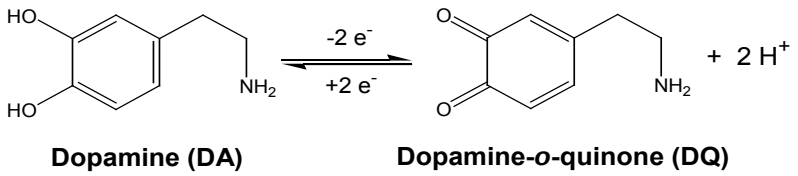

Figure 5. Electrochemical oxidation of DA to DQ.

Additionally, Figure 4c and 4d show that the current density increases with the concentration of DA, reflecting the catalytic property of the modified electrode in the detection of DA oxidation. At the same time, the improved electrocatalytic oxidation of DA in the PNMPy/AuNPs system should be attributed to the charge hopping through the metallic conductor in AuNPs, which mediated the effective charge migration through the polymer.[12] Thus, the AuNPs generate many active sites inside the electrode for the transfer of the charge through the interface, inducing good contact with the PNMPy matrix.

The calibration graph for the PNMPy/AuNPs-modified GCE, which was drawn considering DA concentrations ranging from 10 mM to 20 mM, provided a linear response with R^2= 0.98. To validate this linear model, a DA concentration of 1.5 µM was prepared and subsequently used for experimental measures. The value of the

current density experimentally determined was 1.81 mA·cm^{-2}, while that derived from the calibration model was 2.53 mA·cm^{-2} (Figure 6). These results clearly indicate that the PNMPy nanomembrane allows detect even very low concentrations of DA, which is due to the fact that the electrochemical properties of this CP are retained in the nanometric scale.

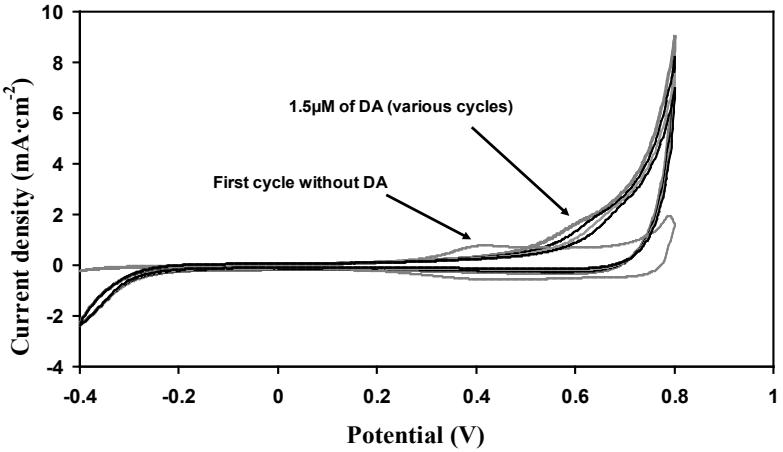

Figure 6. CVs of PNMPy/AuNPs-modified GCE without dopamine and with 1.5 μM (6, 7, 8 and 9 cycles).

It should be noted that PNMPy-based sensors could be also tested for the detection of other biomolecules, as for example enzymes, proteins or DNA, since this CP does not lose its electrochemical properties and stability in a nano- or micro-scale. Within this context, the efficiency of PPy or PNMPy nanocomposites to interact with biological cells or rodhamine molecules was already described by D.L. Feldheim and co-workers.[43]

4.1.4 Conclusions

This work reports an innovative study about the performance of a CP sensor, based on PNMPy nanomembrane, to detect the oxidation of DA molecules at very low concentrations. We presented a comprehensive study about the synthesis of PNMPy microspheres that have been prepared using the LbL self-assembly technique. The LbL templating technique has been proved to be a highly versatile method to produce nanostructured PNMPy. Raman and XPS are excellent tools for characterization of nanolayers made of CPs. After the successful preparation and characterization of PNMPy/PSS core-shell microspheres, we have examined the ability of this CP to detect

DA. For this purpose, sensors were prepared by coating GCE and AuNPs-GCE with a PNMPy nanomembrane. PNMPy has been demonstrated to be highly sensitive to this neurotransmitter, being able to detect DA concentrations lower than that estimated for the synapse (1.6 mM). Thus, the constructed PNMPy nanosensor was able to detect a DA concentration of 1.5 μM without loss of current density. Moreover, we found that AuNPs are not essential for the sensing abilities of PNMPy, which is an important advantage due to the difficult to employ a metallic nanocomposite based on gold inside the brain. Thus, this finding represents an alternative on the course to find an effective, fast and sensitive sensor to use in diagnosis detection of deficiency of DA in the neuron vesicle or the synaptic region or for future treatment of neurological disorders caused by irregular DA delivery on the synaptic region.

Extension of this work is being focused from two different points of view: (i) development of an experimental technique to adhere PNMPy hollow microspheres on the surface of GCE to check the sensing ability of this modified system; and (ii) encapsulation of DA in PNMPy hollow spheres for the preparation of a neurotransmitter delivery system.

4.1.5 References

1. E. R. Kandel, J. H. Schwartz and T. M. Jessel, "Principles of Neural Science", 4th ed. New York, McGraw-Hill, 2000**,** pp. 207-298.

2. B. J. Venton and R. M. Wightman, *Anal. Chem.*, 2003, **75**, 414A.

3. K. Powell, *J. Cell Biology*, 2005, **170**, 166.

4. T. Schikorski and C.F. Stevens, *J. Neurosci.*, 1997, **17**, 5858.

5. (*a*) R. N. Adams, *Anal. Chem.*, 1976, **48**, 1126A; (*b*) X. Huang, Y. Li, P. Wang and L. Wang, *Anal. Sci.,* 2008, **24**, 1563; (*c*) M. Ates and A. S. Saraç, *Prog. Org. Coat.*, 2009, **66**, 337; (*d*) Y. Li and X. Lin, *Sens. Actuators. B,* 2006, **115**, 134.

6. P. Tyagi, D. Postetter, D. L. Saragnese, C. L. Randall, M. A. Mirski and D. H. Gracias, *Anal. Chem.*, 2009, **81**, 9979.

7. C. Xu, K. Xu, H. Gu, R. Zheng, H. Liu, X. Zhang, Z. Guo and B. Xu, *J. Am. Chem. Soc.* 2004, **126**, 9938.

8. (*a*) G. Decher, J. D. Hong, *Ber. Bunsen-Ges*, 1991, **95**, 1430; (*b*) G. Decher, *Science*, 1997, **277**, 1232; (*c*) F. Caruso, R. A. Caruso and H. Möhwald, *Science*, 1998, **282**, 1111; (*d*) F. Caruso, K. Niikura, D.N. Furlong and Y. Okahata, *Langmuir*, 1997, **13**, 3427; (*e*) E. R. Kleinfeld and G. S. Ferguson, *Science*, 1994, **265**, 370; (*f*) G. B. Sukhorukov, H. Möhwald, G. Decher and Y. M. Lvov, *Thin Solid Films*, 1996, **285**, 220; (*g*) E. Donath, G. B. Sukhorukov, F. Caruso, S.A. Davis and H. Möhwald, *Angew. Chem. Int. Ed.*, 1998, **37**, 2201; (*h*) F. Caruso, H. Lichtenfeld, M. Giersig and H. Möhwald, *J. Am. Chem. Soc.*, 1998, **120**, 8523.

9. (*a*) B. Städler, A. D. Price, R. Chandrawati, L. Hosta-Rigau, A. N. Zelikin and F. Caruso, *Nanoscale*, 2009, **1**, 68; (*b*) Y. Wang, A. S. Angelatos and F. Caruso, *Chem. Mat.,* 2008, **20**, 848; (*c*) J.F. Quinn, A.P.R. Johnston, G.K. Such, A. N. Zelikin and F. Caruso, *Chem. Soc. Rev.,* 2007, **36**, 707.

10. P. Hammond, *Adv. Mat.*, 2004, **16**, 1271.

11. S. F. Lascelles, S. P. Armes, P. A. Zhdan, S. J. Greaves, A. M. Brown, J. F. Watts, S. R. Leadley and S. Y. Luk, *J. Mat. Chem.*, 1997, **7**, 1349.

12. X. Feng, C. Mao, G. Yang, W. Hou and J. J. Zhu, *Langmuir*, 2006, **22***,* 4384.

13. C. Mangeney and S. Bousalem, C. Connan, M. J. Vaulay, S. Bernard and M. M. Chehimi, *Langmuir*, 2006, **22**, 10163.

14. X. Yang, T. Dai, M. Wei and Y. Lu, *Polymer*, 2006, **47***,* 4596.

15. F. Yang, Y. Chu, S. Ma, Y. Zhang and J. Liu, *J. Coll. Interf. Sci.*, 2006, **301**, 470.

16. H. Yang, W. Jiang and Y. Lu, *Mat. Lett.*, 2007, **61**, 2789.

17. T. Yao, Q. Lin, K. Zhang, D. Zhao, H. Lv, J. Zhang and B. Yang, *J. Coll. Interf. Sci.*, 2007, **315**, 434.

18. C. Zhou, J. Han, G. Song and R. Guo, *J. Pol. Sci.Part A: Pol. Chem.*, 2008, **46**, 3563.

19. L. H. Dall'Antonia, M. E. Vidotti, S. I. Córdoba de Torresi and R. M. Torresi, *Electroanal.*, 2002, **14**, 1577.

20. D. T. McQuade, A. E. Pullen and T. M. Swager, *Chem. Rev.*, 2000, **100**, 2537.

21. J. Liu, Y. Lin, L. Liang, J. A. Voigt, D. L. Huber, Z. R. Tian, E. Coker, B. Mckenzie and M. J. Mcdermott, *Chem. Eur. J.*, 2003, **9**, 604.

22. J. X. Huang, S. Virji, B. H. Weiller and R. B. Kaner, *J. Am. Chem. Soc.*, 2003, **125**, 314.

23. J. X. Huang, S. Virji, B. H. Weiller and R. B. Kaner, *Chem. Eur. J.*, 2004, **10**, 1314.

24. S.Virji, J. X. Huang, R. B. Kaner and B. H. Weiller, *Nano Lett.*, 2004, **4**, 491.

25. L. Jiang, H. K. Jun, Y. S. Hohb, J. O. Lim, D. D. Lee and J. S. Huh, *Sens. Actuators B*, 2005, **105**, 132.

26. S. Y. Chew, Z. P. Guo, J. Z. Wang, J. Chen, P. Munroe, S. H. K. Ng, L. Zhao and H. K. Liu, *Electrochem. Commun.*, 2007, **9**, 941.

27. M. Sun, S. Zhang, T. Jiang, L. Zhang and J. Yu, J. *Electrochem. Commun.*, 2008, **10**, 1819.

28. M. Hughes, M. S. P. Shaffer, A. C. Renouf, C. Singh, G. Z. Chen, D. J. Fray and A. H. Windle, *Adv. Mater.*, 2002, **14**, 382.

29. A. S. Saraç*,* H. Geyik, E. A. Parlak and M. Serantoni, *Prog. Org. Coat.*, 2007, **59**, 28.

30. S. C. Wuang, K. G. Neoh, E. T. Kang, D. W. Pack and D. E. Leckband, *Macromol. Rapid Commun.*, 2007, **28**, 816.

31. B. C. Thompson, S. E. Moulton, J. Ding, R. Richardson, A. Cameron, S. O'Leary, G. G. Wallace and G. M. Clark, *J. Control. Releas.*, 2006, **116**, 285.

32. E. K. Richfield, J. B. Penney and A. B. Young, *Neuroscience*, 1989, **30**, 767.

33. R. G. Freeman, M. B. Hommer, K. C. Grabar, M. A. Jackson and M. J. Natan, *J. Phys. Chem.*, 1996, **100**, 718.

34. S. Link and M. A. El-Sayed, *J. Phys. Chem. B*, **1999**, **103**, 8410.

35. M. M. Maye, L. Han, N. N. Kariuki, N. K. Ly, W. B. Chan and C. J. Zhong, *Anal. Chim. Acta*, 2003, **406**, 17.

36. K. P. R. Nilsson, J. Rydberg, L. Baltzer and O. Inganäs, *Proc. Natl. Acad. Sci. USA*, 2004, **101**, 11197.

37. M. Li, J. Yuan and G. Shi, *Thin Solid Films*, 2008, **516**, 3836.

38. M. Li, Z. Wei and L. Jiang, *J. Mat. Chem.*, 2008, **18**, 2276.

39. Y. Yang, Y. Chu, F. Yang and Y. Zhang, *Mat. Chem. Phys.*, 2005, **92**, 164.

40. C. Alemán, J. Casanovas, J. Torras, O. Bertran, E. Armelin, R. Oliver and F. Estrany, *Polymer*, 2008, **49**, 1066.

41. D. Aradilla, F. Estrany, R. Oliver, E. Armelin and C. Alemán, *Thin Solid Films*, 2010, DOI: 10.1016/j.tsf.2009.12.079.

42. X. Q. Lin and L. Zhang, *Anal*. *Lett.*, 2001, **34**, 1585.

43. S. M. Marinakos, J. P. Novak, L. C. Brousseau, B. House, E. M. Edeki, J. C. Feldhaus and D. L. Feldheim, *J. Am. Chem. Soc.*, 1999, **121**, 8518.

44. M. M. Maye, L. Han, N. N. Kariuki, N. K. Ly, W. B. Chan and C. J. Zhong, *Anal. Chim. Acta*, 2003, **406**, 17.

4.2 Controlling the morphology of Poly(N-cyanoethylpyrrole)*

The morphology of poly(N-cyanoethylpyrrole) (PNCPy) has been controlled through the polymerization process. This polymer has been prepared by anodic polymerization, chemical oxidative polymerization in emulsion medium and LbL templating polymerization. Anodic polymerization using $LiClO_4$ as supporting electrolyte provides compact films, in which the oxidation degree is controlled through the thickness, useful for the microdetection of DA. Chemical polymerization using $FeCl_3$ as oxidant agent results in very well defined microspheres with porous internal structure, which may be useful in molecular loading and transport processes. Finally, the LbL templating technique produces core-shell particles of controlled size and thickness. Moreover, these core-shell particles can be easily converted in hollow microspheres by removing the template.

*Results described in this section previously appeared in *J. Phys. Chem. B*, 2012, **116**, 5064.

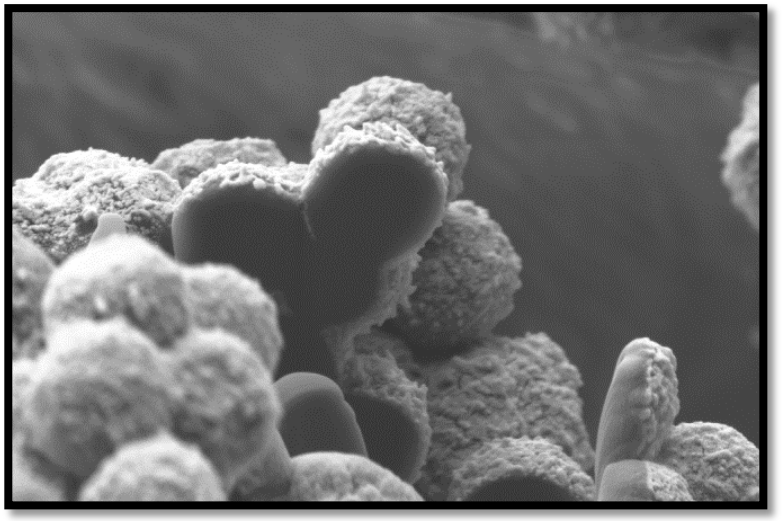

4.2.1 Introduction

Many of the nanostructured materials currently under development draw their inspiration from the structures found in nature.[1-3] Highly sophisticated morphologies and functions have been achieved using supramolecular architectures of polymer structures.[4] Within this context, micro- and nanostructures based on CPs is a field of current interest. CPs are a class of important materials with many potential applications because of their low density, large specific area, high stability and surface permeability, and good electrochemical properties.

In general, the structure of CPs is moderately affected by the experimental conditions used in the polymerization process. For example, the roughness, regularity and porosity of the spongy morphology of electrochemically produced PEDOT, an extensively studied CP with very important technological applications,[5,6] are known to depend on factors such as the applied potential, polymerization time (*i.e.* the thickness of the sample), the solvent, the supporting electrolyte that acts as doping agent, and the substrate used for polymer deposition.[7-13] Much higher variability can be obtained using alternative synthetic process based on templates. These approaches are typically described as the one-step electrochemical generation of CP in a solid substrate assisted by a solid or soft template mechanism. Thus, the generation of CP micro- and nanostructures can be carried out using solid templates with well defined shapes (*e.g.* porous alumina membranes or polystyrene colloidal nanoparticles) limiting the size of the materials,[14,15] or "soft" templates formed by assemblies of molecules (*e.g.* surfactants and gases).[16,17] This approach has been used to prepare microspheres, microcrocks, microbowls, microbarrels, micropunpkins, microbottles and micro-doughnuts of PPy and PNMPy.[19-23]

In this work we show how to exert a drastic control on the structure and morphology of PNCPy (Figure1), through the polymerization method. More specifically, we report the very different morphologies and microstructures found for this material when it is prepared by anodic polymerization, oxidative polymerization in emulsion medium, and LbL templating technique. PNCPy was found to be highly sensitive to DA, presenting a very fast and effective response even when the concentration of such neurotransmitter is of 100 μM only (*i.e.* the concentration of DA in the synaptic region

is 1.6 mM).[24] However, in spite of such promising biomedical application, the number of studies devoted to examine the structure of this CP is very scarce. Thus, although PNCPy has been obtained and characterized using anodic polymerization methods,[25-27] the structures of the materials prepared by the LbL procedure and oxidative polymerization have not been reported yet.

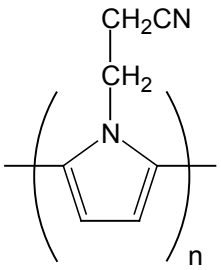

Figure 1. Molecular structure of PNCPy

4.2.2 Methods

Materials. N-(2-cyanoethyl)pyrrole (NCPy), acetonitrile and anhydrous $LiClO_4$ of analytical reagent grade were purchased from Sigma-Aldrich (Spain). The monomer was used freshly distilled.

Electrochemical synthesis of poly[N-(2-cyanoethyl)pyrrole] films. PNCPy films were prepared by CA under a constant potential of 1.40 V. Electrochemical experiments were performed on an Autolab PGSTAT302N equipped with the ECD module (Ecochimie, The Netherlands), which allows to measure very low current densities (100μA-100pA), using a three-electrode two-compartment cell under nitrogen atmosphere (99.995 % in purity) at room temperature. The RE was a saturated Ag | AgCl electrode, whereas Pt sheets of 0.50×0.70 cm^2 were used as CE. A GCE was used as the WE (4.11 mm^2), its surface being polished with alumina powder and cleaned by ultrasonication before each trial. PNCPy was electrochemically deposited on the GCE using 70 mL of the corresponding monomer solution (10 mM) in acetonitrile containing 0.1 M $LiClO_4$ as supporting electrolyte. The polymerization time (θ) varied from 20s to 300s.

Oxidative polymerization in emulsion medium. A solution of NCPy (0.63 mmol) in 4.2 mL of ethanol was added to deionized water (7.0 mL) under magnetic stirring. After the monomer was completely dispersed (15 min), an excess of oxidant agent,

0.696 g of $FeCl_3 \cdot 6H_2O$ (2.5 mmol in 2.8 mL of deionized water), was added slowly into the vessel at 25ºC. After oxidant addition, the temperature was increased to 70ºC and the reactants were stirred for 24h. The resulting product was washed repeatedly with deionized water and ethanol. Finally, PNCPy, which was obtained as a dark-brown powder, was dried under vacuum oven at 40 ºC for 48h.

Layer-by-layer assembly polymerization.

1) Preparation of PS microspheres. PS microspheres were prepared following the procedure described by Lascelles et. al.[28] In a three-necked round flask provided with magnetic stirring and a condenser, PVP stabilizer (3.8 g) dissolved in isopropyl alcohol (180 mL) was heated until 70ºC for 1 h under nitrogen atmosphere. After this, a solution of AIBN (0.25 g) and styrene monomer (25 g) was added dropwise to the reaction vessel. The mixture, which was vigorously stirred at 70 ºC for 24 h, was left for cooling at room temperature. The resulting emulsion was centrifuged several times, and washed repeatedly with deionized water to remove the PVP stabilizer excess. The chemical composition of the PS samples was evaluated with FTIR spectroscopy, while the size of the latex particles was determined by SEM and TEM.

2) Preparation of polystyrene sulfonated microspheres. PS microparticles (10% in deionized water, 3 mL) and concentrated sulfuric acid (H_2SO_4, 98%, 11 mL) were introduced into a 30 mL centrifuge tube. The sulfonation reaction was allowed to take place at 40ºC under magnetic stirring for 24 h and reflux. After this, the vessel was cooled to the room temperature. The product was separated by repeated centrifugation (6000 rpm) and washed with an excess of ethanol. Finally, a white fine powder made of PSS core-shell particles was obtained after drying under vacuum for 48 h.

3) Preparation of PNCPy/PSS. PSS powder (0.06 g) was dispersed in 3.5 mL of deionized water. Then, solution of NCPy (0.17 mmol) in 4.2 mL of ethanol was added to the PSS suspension under magnetic stirring. The monomer/PSS mixture was stirred during 15 minutes, then 0.19 g of $FeCl_3 \cdot 6H_2O$ (0.7 mmol in 2 mL of deionized water) was subsequently added. The polymerization process took place at 70 ºC during 24h. The resulting PNCPy/PSS particles were purified after several centrifugations washing with deionized water and ethanol. Finally, the material was dried under vacuum for

48h. This polymerization process was repeated three times to achieve a suitable PNCPy thickness.

4) Preparation of PNCPy hollow microspheres. The PSS core was removed from PNCPy/PSS core-shell particles by dispersing the latter into tetrahydrofuran (THF, 11 mL) under magnetic stirring for 48 h at room temperature. The resulting product was washed by repeated centrifugation with ethanol and afterwards was dried in vacuum at 40 ºC for 48 h.

Analytical techniques

SEM. SEM studies were carried out using a FIB Zeiss Neon40 scanning electron microscope equipped with an EDS system and operating at 5 kV. Samples were mounted on a double-sided adhesive carbon disc and sputter-coated with a thin layer of gold (samples obtained by LbL assembly polymerization) or carbon (samples obtained by anodic and chemical oxidative polymerizations) to prevent sample charging problems.

TEM. TEM images were collected with a Philips TECNAI 10 electron microscope operating at 80 kV. Bright field micrographs were taken with an SIS MegaView II digital camera. Solutions containing PS, PSS, PNCPy/PSS core-shell and PNCPy hollow spheres (1 mg/1 mL in absolute ethanol) were cast onto a carbon coated copper-grids (300 mesh), the solvent being allowed to evaporate.

FTIR. Spectra of samples obtained by chemical oxidative polymerization and LbL assembly polymerizations were recorded on a FTIR 4100 Jasco spectrophotometer with a resolution of 4 cm^{-1} in the transmittance mode. Samples were placed in an attenuated total reflection accessory with a diamond crystal (Specac model MKII Golden Gate Heated Single Reflection Diamond ATR). On the other hand, the spectra of the films generated by electrochemical polymerization were obtained using a Nicolet 6700 FT-IR spectrometer, equipped with a Smart SAGA (Specular Aperture Grazing Angle) accessory with an incidence angle of 80º, gold mirror for background calibration and Omnic software. The spectrum was taken using a resolution of 4 cm^{-1} in the transmittance mode.

UV-vis. Spectra of PNCPy electrochemically generated were obtained using a Shimadzu UV-vis-NIR UV3600 spectrophotometer and with an integrating sphere accessory. All spectra were collected in reflectance mode and converted to absorbance.

4.2.3 Results and Discussion

PNCPy films obtained by anodic polymerization using $LiClO_4$ as supporting electrolyte and a θ= 20 s show a compact, irregular and lumpy morphology with elliptical protuberances of nanometric dimensions homogeneously distributed in the surface (Figure 2a). Such protuberances suggest the formation of small and compact clusters of molecular aggregates. The morphology obtained by electropolymerization should be attributed to the combination of two factors: (i) the influence of the substrate on the growing of polymer chains imposing a directional preference; and (ii) PPy derivatives with substituents at the N-position of the Py ring tend to be cross-linked (*i.e.* consecutive pyrrole rings may form α-β and β-β linkages in addition of the conventional α-α ones),[29,30] providing branched molecules with many irregularities. The thickness of the films produced using θ= 20 s is 172$\pm$16 nm.

UV-vis absorption spectra (Figure 3) revealed that the oxidation level of PNCPy generated electrochemically can be precisely controlled through polymerization time. Thus, the polymer is highly oxidized when θ is higher than 100 s, while the oxidation degree level is very low for θ= 20 s. The first absorption band (before 500 nm) corresponds to the π-π^* transition of aromatic rings, the maximum absorption being 2.89-3.5eV. The second absorption band has been assigned to the formation of the polaron cation (~550 nm, 2.1-2.3eV), which is related with the first stages of the oxidation process, while dications or bipolaronic states (highest oxidation level) show a characteristic absorption at 684nm (1.81eV).[31] The UV-vis spectrum of PNCPy generated using θ= 300s shows a weak absorption at around 350 nm (3.6 eV) and strong absorption in the range of 500-900 nm, the latter being also displayed by the polymer obtained using θ= 100s. This broad free-carrier-tail band is characteristic of CPs with a high degree of doping. As it can be seen, this situation is completely different from that found for samples produced with lower polymerization time values.

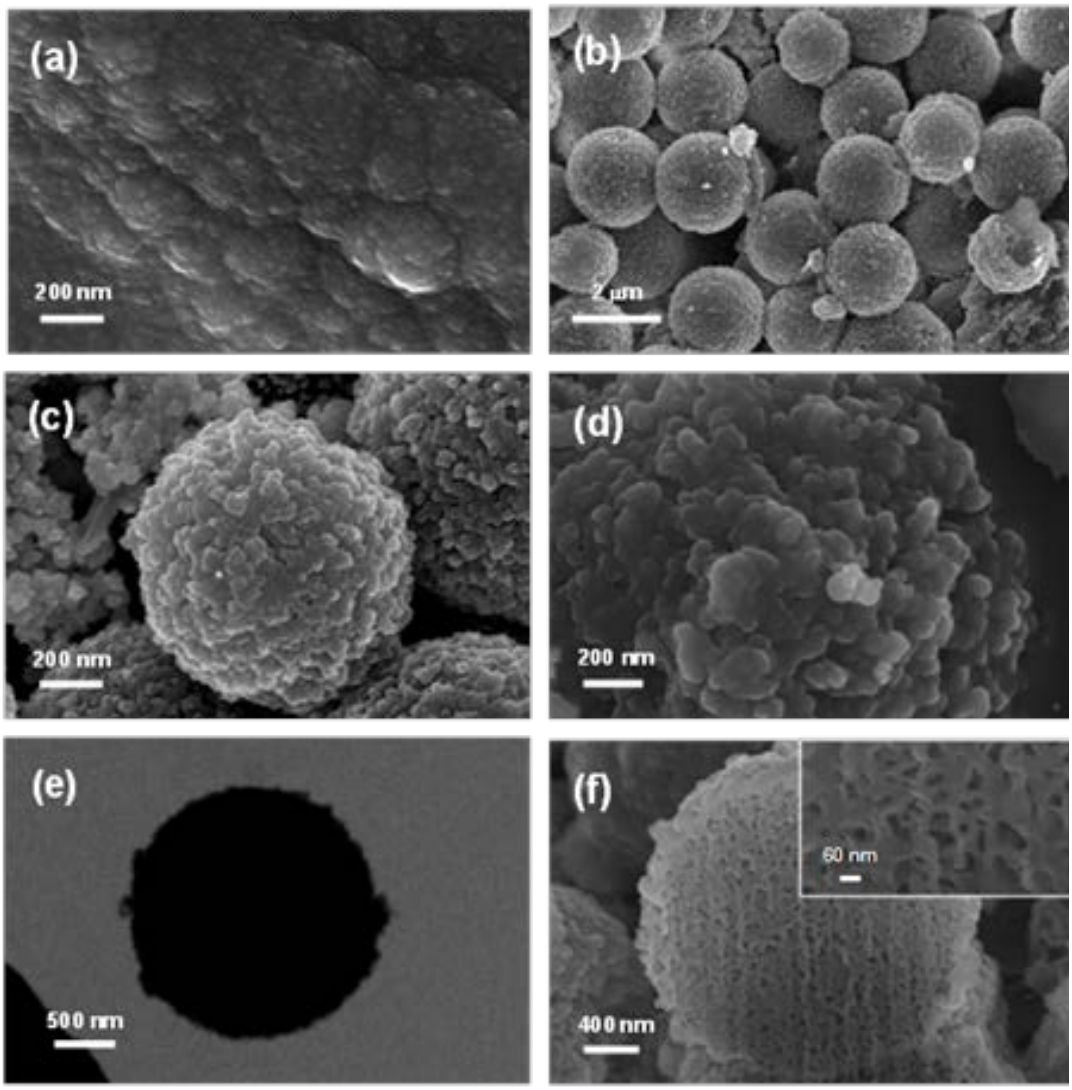

Figure 2. (a) SEM micrograph of the surface of a film prepared by anodic polymerization. (b) Low- and (c) high-resolution SEM images of microspheres obtained using oxidative polymerization in emulsion medium, the pseudo-spherical nanoaggregates coating the microspheres being displayed in (d). (e) TEM micrographs of an isolated microsphere. (f) SEM image of the FIB-section of a microsphere (inset: high resolution micrograph showing the remarkable porosity).

Chemical oxidative polymerization in emulsion medium yielded a powder that corresponds to an aggregation of very well defined microspheres (Figures 2b and 2c). The diameters of such microparticles, which were measured directly from the SEM images, ranged from 1.59 to 3.57 µm. The number-average and the volume-average diameters were calculated as $\overline{D}_n = \Sigma_i N_i D_i / \Sigma_i N_i$ and $\overline{D}_v = \Sigma_i N_i (D_i)^4 / \Sigma_i N_i (D_i)^3$, respectively, where D_i means the diameters of individual particles and N_i refers to number of particles corresponding to the diameters. Results indicate that PNCPy microspheres produced using this procedure follows a narrow diameter distribution, with $\overline{D}_n$ = 2.10 µm, $\overline{D}_v$ = 2.36 µm and $\overline{D}_v / \overline{D}_n$ = 1.12, which is expected to be particularly useful for

their possible technological applications (Figure 4). High resolution micrographs (Figure2d) obtained by SEM reveal that the surface is coated by compact aggregations of pseudospherical nanoparticles with small and relatively uniform sizes (*i.e.* $\overline{D}_n$ = 52 nm, $\overline{D}_v$ = 58 nm and $\overline{D}_v / \overline{D}_n$ = 1.11) (Figure 5). Local elemental analyses using EDS revealed the organic nature of such superficial aggregates (*i.e.* oligomer or polymer chains with a very low amount of iron chloride as dopant), allowing us to discard the deposition of crystalline inorganic iron salts on the surface of the microspheres (Figure 6). TEM micrographs showed that microspheres generated by oxidative polymerization are solid particles with irregular surfaces (Figure 2e).

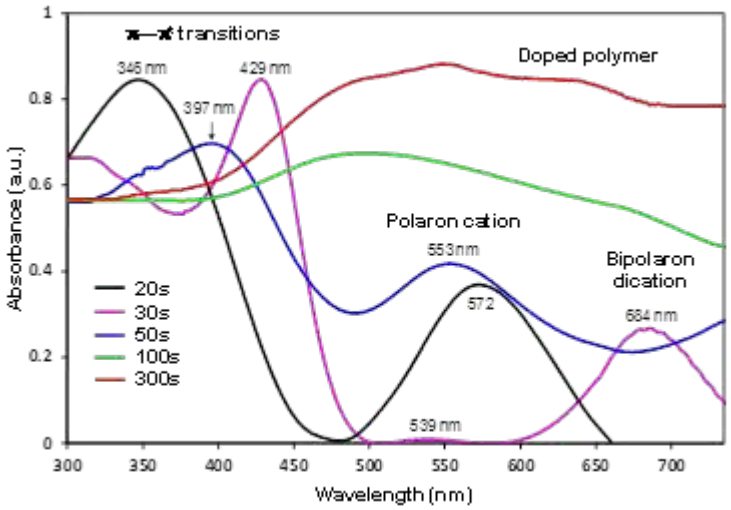

Figure 3. UV-vis spectra of PNCPy obtained using 20, 30, 50, 100 and 300 s of polymerization time and by CA. Numbers depicted on the graph are referred to the maximum wavelength obtained for each transition band.

The internal structure of the microspheres was investigated after cutting them with FIB microscopy and subsequent examination of the section by SEM. Micrographs proved the absence of hollow regions in the core of the microspheres (Figure 2f), which is consistent with the filled structure displayed in the TEM image (Figure 2e). Moreover, high resolution micrographs reveal a very remarkable porosity that is homogeneously distributed (Figure 2f). The formation of this particular morphology has been attributed to the co-existence of two independent driving forces. First, the formation of spherical microparticles is due to the immiscibility of the NCPy monomer and the mixture of water and ethanol used as emulsion medium. Thus, the micromicelles resulting from such immiscibility define the spherical shape of the polymer resulting from such immiscibility define the spherical shape of the polymer

microparticles. Second, as mentioned above, PPy derivates substituted at the N-position of the Py ring, including PNCPy,[29,30] tend to form cross-linked structures, giving place to the formation of branched molecules. In electrochemical processes, which are characterized by a directional growing preference (*i.e*. polymer chains grow perpendicularly to the substrate), cross-linking favors the formation of compact structures. However, the opposite effect is produced when polymer chains grow without any directional preference, as occurs in chemical oxidative polymerization processes. In these cases, cross-linking induces the formation of porous microstructures.

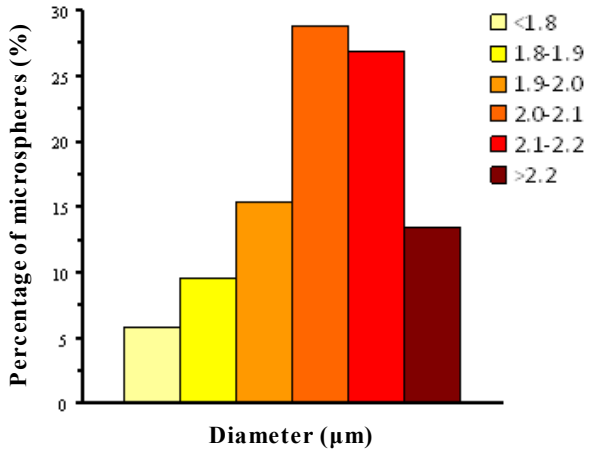

Figure 4. Particle size distribution of the PNCPy microspheres obtained by chemical oxidative polymerization in emulsion medium.

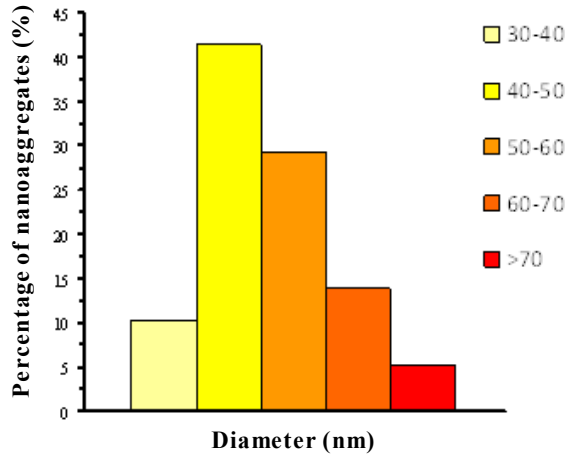

Figure 5. Size distribution of the nanoaggregates located at the surface of the PNCPy microspheres produced by chemical oxidative polymerization in emulsion medium.

The structural organization displayed in Figure 2b-2f suggests that the PNCPy polymerized chemically in emulsion medium may be considered as a potential candidate for technological applications related with molecular transport processes

(*i.e.* loading or encapsulation of molecules and their subsequent releasing through an electric potential). Thus, microspheres for loading and subsequent controlled delivery of therapeutic drugs are frequently prepared using biodegradable polyesters,[32-35] while PPy porous films are used for similar purposes.[36-38] The porous PNCPy microspheres described in this work could be considered as an electric field-stimulus responsive microparticle system for programmed drug loading/delivery. This potential application should be considered complementary to the use of the compact PNCPy films produced by electropolymerization as highly sensitive and effective detectors of dopamine.[24]

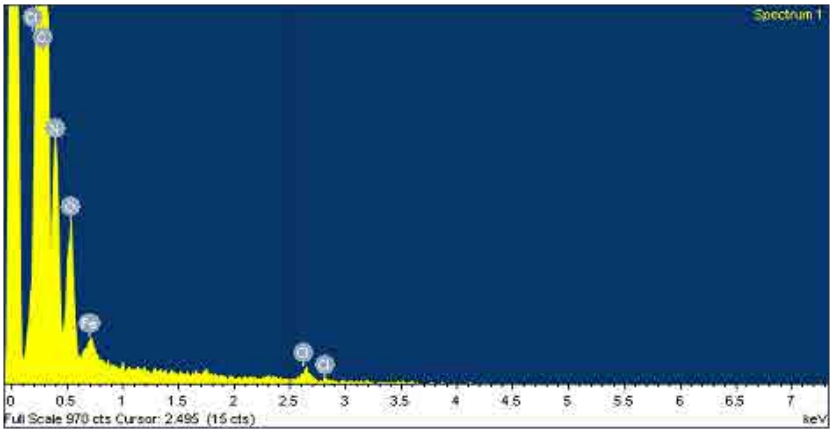

Element	% (w/w)
C	76.02
N	17.45
O	5.08
Cl	0.78
Fe	0.67

Figure 6. EDX analysis of the nanoaggregates located at the surface of the PNCPy microspheres produced by chemical oxidative polymerization in emulsion medium.

Homogeneous solid spherical PS microparticles with an average diameter of 1.0±0.3 μm were prepared using a previously reported procedure (Figure 7a).[28] PSS core/shell particles were obtained through a sulfonation reaction with concentrated H_2SO_4 (Figure 7b). It should be noted that surface-sulfonation produces a significant enhancement of the microparticles polarity, the behavior as surfactant of PSS core/shell particles in LbL assembly polymerization processes being reported to be better than that of PS microspheres.[39,40]

PSS microspheres were coated with PNCPy using the LbL assembly technique. More specifically, an ethanol solution of the NCPy monomer was added to the PSS aqueous suspension and, subsequently, stirred for the monomer adsorption on PSS surface. Then, PNCPy was obtained by chemical polymerization adding $FeCl_3$ as oxidant to the monomer/PSS mixture. This polymerization process was repeated three times to get the desired PNCPy shell thickness and mechanical integrity. The complete synthetic procedure is displayed in Figure 8. The resulting PNCPy/PSS core-shell particles (Figures

7c and 7d) show very sharp and thin structures on the surface, which are completely different from the compact nanoaggregates observed in the microspheres produced by chemical polymerization in emulsion medium (Figures 2c and 2d). This feature, which was corroborated by TEM (Figures 7e and 7f), has been attributed to a crystalline organization of oligomers at the surface of the microspheres. Thus, electron micrographs evidenced the presence of crystalline phases with morphology similar to "*losango*" forms (Figure 7f, inset).

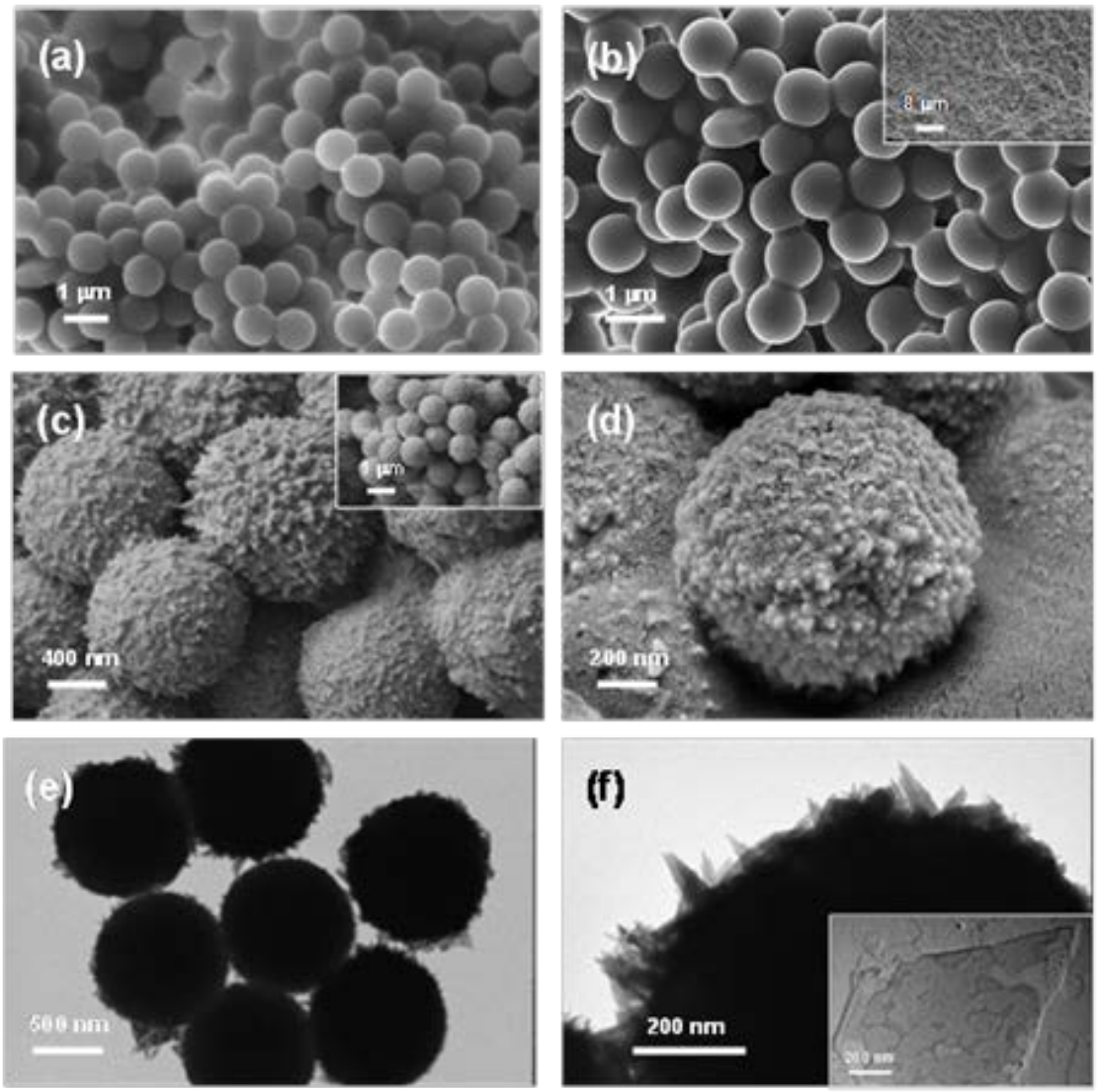

Figure 7. (a) and (b) SEM micrograph of PS microparticles before and after sulfonation reaction, respectively. (c-d) SEM and (e-f) TEM micrographs of PNCPy/PSS core-shell particles (inset: crystalline structure, shadowed with Pt).

The average thickness of the PNCPy/PSS shell is 54±5 nm after three polymerization cycles, which was taken by SEM from the FIB section (Figure 9a). PNCPy hollow particles were obtained after PSS extraction with tetrahydrofuran.[8] TEM images

evidenced that removal of PSS was carried out without produce major alterations in the spherical shape of the PNCPy shells (Figures 9b and 9c), even though some imperfections or defects are detected at the surface of such free-standing hollow microparticles. However, SEM images clearly show serious damages in the integrity of a significant amount of PNCPy microspheres (Figure 9d). Thus, the mechanical properties of PNCPy nanolayers are not good enough to guarantee the integrity of the microspheres once the PSS core-shell particles have been eliminated. Unfortunately, experiments devoted to increase the sell thickness of the PNCPy nanolayer deposition, which was achieved by enlarging the number of polymerization cycles to 4 and 5, did not improve this result. This feature suggests that PNCPy microspheres prepared by the LbL technique are formed by small oligomers, which is consistent with the electron micrograph displayed in Figure 7f. This is a drawback with respect to hollow microspheres produced using other CPs, like for example PNMPy,[41] even though the technological interest of the latter is smaller than that of PNCPy (*i.e.* PNMPy shows both lower sensitivity and worse response towards dopamine than PNCPy).[24]

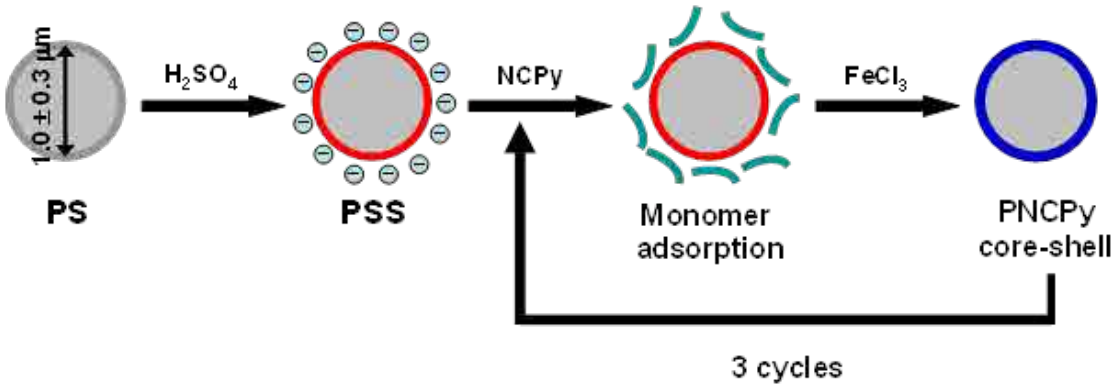

Figure 8. Scheme showing the synthesis of PNCPy core shell microspheres.

Despite such limitation in the mechanical properties, we would like to emphasize that polymerization of PNCPy using the LbL technique allows to obtain spherical particles coated with a shell of CP in which both the size of the particle and the thickness of the shell are precisely controlled. Specifically, the diameter of the particles is defined by the PS templates while the thickness of the shell is determined by the number of polymerization cycles. Accordingly, nanostructured PNCPy/PSS core-shell particles obtained by LbL may be used for technological applications based on achieve a good dispersion of the CP in a matrix. For example, CPs, including PPy

derivatives, have been successfully used as anticorrosive additives in the formulation of organic coatings (*i.e.* essentially epoxy and alkyd paints),[42-48] imparting corrosion protection to metal substrates when they are well dispersed in the resin. Furthermore, in very recent studies micro- and nanoparticles of PAni, a well known CP, were used to promote the corrosion protection imparted by epoxy paints.[49] Future studies investigating the potential applications proposed for PNCPy microspheres may allow not only to expand but also to complement the range of applications covered by this CP. Thus, such applications would depend on the morphology that in turn is controlled through the polymerization procedure.

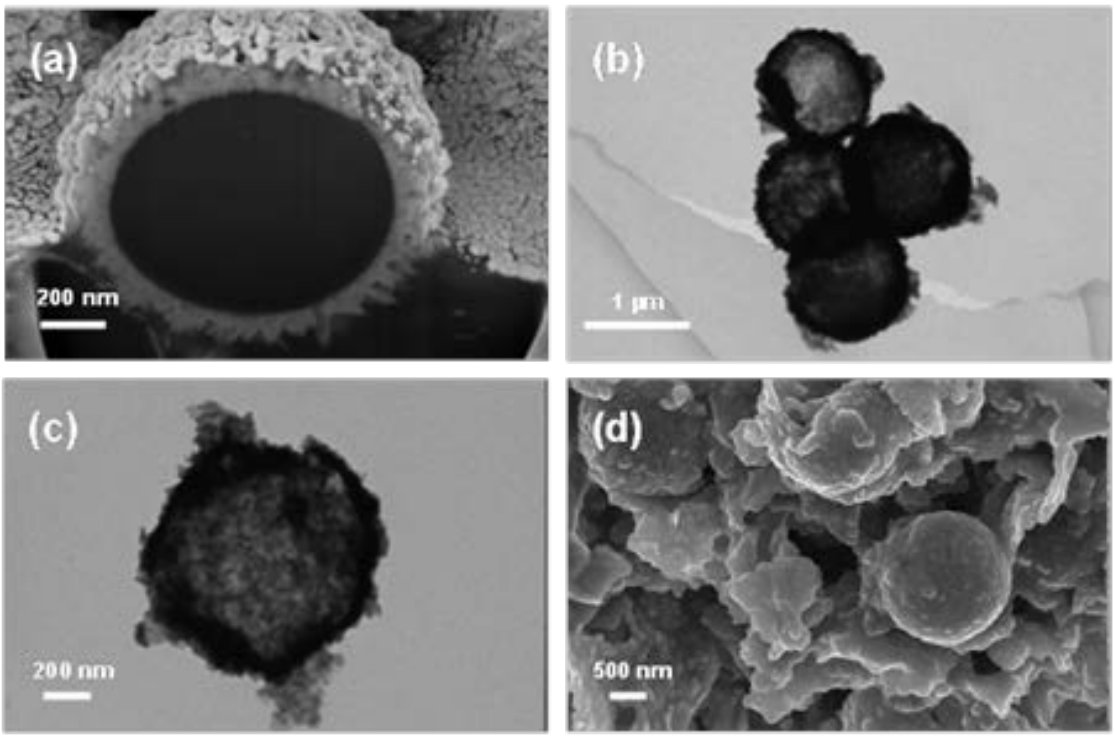

Figure 9. (a) SEM micrograph of the transversal section of a PNCPy/PSS core-shell particle. (b) and (c) TEM images of free-standing hollow PNCPy microspheres. (d) SEM micrograph of the damage produced by the removal of the PSS template in PNCPy/PSS core-shell microspheres.

Samples produced by the three polymerization methods were examined by FTIR spectroscopy. The FTIR spectra allowed us to confirm that -C≡N moiety was retained in the polymer structure after polymerization (Figure 10), stretching band at 2251cm^{-1}). However, the oxidation to -CH_2NH_2 of a small percentage of nitrile groups was observed in samples prepared using $FeCl_3$ as oxidant agent. Thus, the intensity of nitrile peak decreased while the stretching vibrations of amino group appeared at 3119 cm^{-1} and 3200-3500 cm^{-1} (free and hydrogen-bonding associated, respectively), and at 674

cm^{-1} (NH_2 bending). Although the NH_2 group was not observed in electrochemical samples, in which $LiClO_4$ was used as oxidant (strong stretching vibration at 1110 cm^{-1}), the appearance of an intense peak associated to the C=O stretching vibration (1700 cm^{-1}) revealed the overoxidation of the pyrrole ring, as expected.[40,45] Moreover, the absence of C-H^{α} absorption band at 728 cm^{-1} in all the spectra indicated that the polymerization reactions occurred through the formation of α-α' linkages.

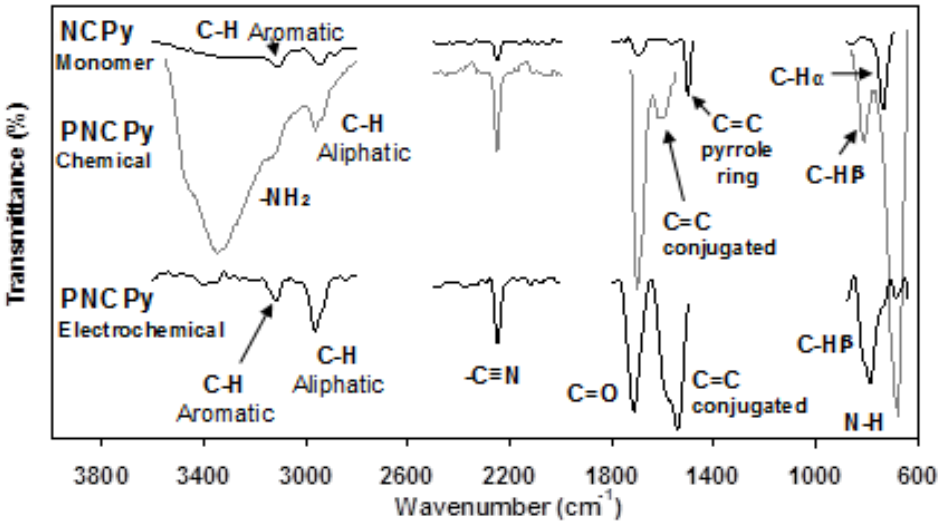

Figure 10. FTIR spectra of PNCPy synthesized by chemical and electrochemical polymerization methods compared to the monomer, NCPy, absorption bands.

4.2.4 Conclusions

Our results indicate that the morphology of PNCPy is precisely controlled through the polymerization method. Thus, compact films, solid microspheres with a porous internal structure and core-shell microspheres with an ultrathin shell have been prepared using anodic, chemical oxidative and LbL polymerization processes, respectively. Details of all these microstructures have been obtained using SEM and TEM. Each of these varied morphologies results particularly appropriated for a given technological application.

4.2.5 References

1. B. Städler, A. D. Price, R. Chandrawati, L. Hosta-Rigau, A. N. Zelikin and F. Caruso, *Nanoscale*, 2009, **1**, 68.

2. Y. Wang, A. S. Angelatos and F. Caruso, *Chem. Mater*., 2008, **20**, 848.

3. J. F. Quinn, A. P. R. Johnston, G. K. Such, A. N. Zelikin and F. Caruso, *Chem. Soc. Rev.,* 2007, **36**, 707.

4. M. Wan, *Macromol. Rapid Commun.,* 2009, **30**, 963.

5. T. A. Skotheim and J. R. Reynolds, Handbook of Conducting Polymers, 3rd ed.; A. L. Dyer, J. R. Reynolds, Eds.; CRC Press:Boca Raton, FL, 2007, Chapter 20.

6. M. A. Invernale, M. Acik and G. A. Sotzing, Handbook of Thiophene-Based Materials, I. F. Perepichka and D. F. Perepichka, Eds.; Wiley-VCH, Chichester, U.K., 2009; Chapter 20.

7. E. Poverenov, M. Li, A. Bitler and M. Bendikov, *Chem. Mater*., 2010, **22**, 4019

8. S. Patra, K. Barai and N. Munichandraiah, *Synth. Met.*, 2008, **158**, 430.

9. Kiefer, R.; Bowmaker, G. A.; Cooney, R. P.; Kilmartin, P. A.; Travas-Sejdic, K. *Electrochim. Acta* 2008, **53**, 2593.

10. D. Aradilla, F. Estrany, E. Armelin and C. Alemán, *Thin Solid Films*, 2010, **518**, 4203.

11. A. Bund and S. Neudeck, *J. Phys. Chem. B*, 2004, **108**, 17845.

12. J. Xia, N. Masaki, M. Lira-Cantu, Y. Kim, K. Jiang and S. Yanagida, *J. Phys. Chem. C*, 2008, **112**, 11569.

13. D. Aradilla, D. Azambuja, F. Estrany, J. I. Iribarren, C. A. Ferreira and C. Alemán, *Polym. Chem*., 2011, **2**, 2548.

14. R. V. Parthasarathy and C. R. Martin, *J. Appl. Polym. Sci.,* 1996, **62**, 875.

15. J. Jang, J. H. Oh and J. Li, *Mater. Chem.*, 2004, **14**, 2872.

16. J. Jang and J. H. Oh, *Adv. Mater.,* 2003, **15**, 977.

17. H. B. Xia, D. M. Cheng, C. Y. Xiao and H. S. O. Chan, *J. Mater. Chem.,* 2005, **15**, 4161.

18. L. Qu, G. Shi, F. Chen and J. Zhang, *Macromolecules*, 2003, **36**, 1063.

19. L. Qu and G. Shi, *Chem. Commun*., 2003, 206.

20. L. Qu and G. Shi, *J. Polym. Sci. Pol. Chem.,* 2004, **42**, 3170.

21. X. He, C. Li, F. Chen and G. Shi, *Adv. Funct. Mater.,* 2007, **17**, 2911.

22. C. Li, H. Bai and G. Shi, *Chem. Soc. Rev.,* 2009, **38**, 2397.

23. B. Teixeira-Dias, C. Alemán, F. Estrany, D. Azambuja and E. Armelin, *Electrochim. Acta,* 2011, **56**, 5836.

24. G. Fabregat, E. Córdova-Mateo, E. Armelin, O. Bertran and C. Alemán, *J. Phys. Chem. C* , 2011, **115**, 14933.

25. D. Aradilla, F. Estrany, E. Armelin, R. Oliver, J. I. Iribarren and C. Alemán, *Macromol. Chem. Phys.*, 2010, **211**, 1663.

26. Z. Deng, D. C. Stone, M. Thompson and *Can. J. Chem.,* 1995, **73**, 1427.

27. Z. Deng, D. C.Stone and M. Thompson, *Analyst,* 1997, **122**, 1129.

28. S. F. Lascelles, S. P. Armes, P. A. Zhdan, S. J. Greaves, A. M. Brown, J. F. Watts, S. R. Leadley and S. Y. Luk, *J. Mat. Chem.*, 1997, **7**, 1349.

29. C. Alemán, J. Casanovas, J. Torras, O. Bertran, E. Armelin, R. Oliver and F. Estrany, *Polymer*, 2008, **49**, 1066.

30. D. Aradilla, J. Torras and C. Alemán, *J. Phys. Chem. B,* 2011, **115**, 2882.

31. S. Okur and U. Salzner, *J. Phys. Chem. A,* 2008, **112**, 11842.

32. J. Lee, Y. J. Oh, S. K. Lee and K. Y. Lee, *J. Control Release*, 2010, **146**, 61.

33. G. Liu, X. Miao, W. Fan, R. Crawford and Y. Xiao, *J. Biomimetics Biomater. Tissue Eng.,* 2010, **6**, 1.

34. S. Freiberg and X. X. Zhu, *Int. J. Pharm.,* 2004, **28**, 1.

35. G. Crotts and T. G. Park, *J. Control Release*., 1995, **35**, 91.

36. G. Kang, B. Borgens and Y. N. Cho, *Langmuir*, 2011, **27**, 6179.

37. P. Ge, E. Neofytou, T. J. Cahill, R. E. Beygui and R. N. Zare, *ACS Nano*, 2012, **6**, 227.

38. S. Majumdar, K. Kargupta and S. Ganguly, *Polym. Eng. Sci.,* 2011, **51**, 2001.

39. Y. Yang, Y. Chu, F. Yang and Y. Zhang, Mat. Chem. Phys., 2005, **92**, 164.

40. G.-D. Fu, G. L. Li, K. G. Neoh and E. T. Kang, *Prog. Polym. Sci.,* 2011, **36**, 127.

41. M. Martí, G. Fabregat, F. Estrany, C. Alemán and E. Armelin, *J. Mat. Chem.,* 2010, **20**, 10652.

42. M. G. Hosseini, M. Jafari and R. Najjar, *Surf. Coat. Technol.,* 2011, **206**, 280.

43. M. Selvaraj, S. Palraj, K. Maruthan, G. Rajagopal and G. Venkatachari, *J. Appl. Polym. Sci*. 2010, **116**, 1524.

44. E. Armelin, M. Martí, F. Liesa, J. I. Iribarren and C. Alemán, *Prog. Org. Coat.* 2010, **69**, 26.

45. E. Armelin, A. Meneguzzi, C. A. Ferreira and C. Alemán, *Surf. Coat. Technol*., 2009, **203**, 3763.

46. M. Selvaraj, S. Palraj, K. Maruthan, G. Rajagopal and G. Venkatachari, *Synth. Metals,* 2008, **158**, 888.

47. E. Armelin, R. Pla, F. Liesa, X. Ramis, J. I. Iribarren and C. Alemán, *Corr. Sci.,* 2008, **50**, 721.

48. G. Tansug, T. Tuken, A. T. Ozyilmaz, M. Erbil and B. Yazici, *Curr. Appl. Phys.,* 2007, **7**, 440.

49. R. S. Jadhav, K. J. Patil, D. G. Hundiwale and P. P. Majulikar, *Polym. Adv. Technol.,* 2011, **22**, 1620.

4.3 Detection of dopamine using chemically synthesized multilayered hollow microspheres*

Microspheres made of alternating layers of two different CPs, PEDOT and PNMPy, have been found to be sensitive to DA oxidation, presenting a very well-defined and linear response in the range of DA concentrations from 0.5 to 2 mM. The novelty of the present study is the use of doped multilayered hollow microspheres, which are prepared by successive oxidative chemical polymerizations in $FeCl_3$ aqueous solution. The multilayered microspheres were characterized by FTIR, UV-visible, SEM, TEM and AFM. The UV-visible bands confirm that the multilayered system is not well doped with $FeCl_4^-$ counter-ions. Therefore, the doping level was increased by further oxidation with $LiClO_4$ before DA electrochemical detection. Despite the range of concentration detection was limited from 0.5mM to 2mM, doped hollow multilayered microspheres show a very good anodic peak current response compared to single-layer films fabricated with an individual CP and activated by AuNPs.

*Results described in this section has been accepted for publication in *J. Phys. Chem. B.*

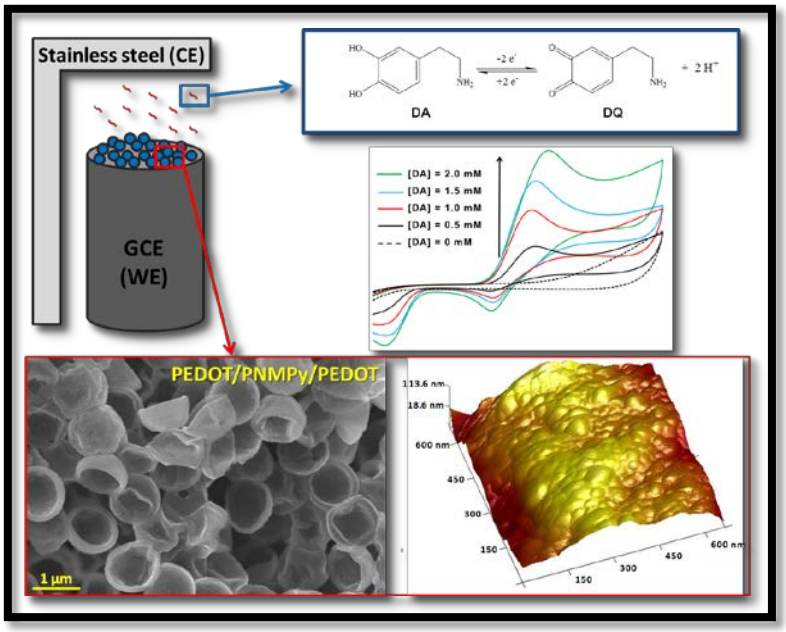

4.3.1 Introduction

In the struggle to find new compounds more effective, selective and sensitive for the detection of DA, many materials have been explored.[1-4] Detection of DA and control of the concentration released in the brain are very complex tasks due to the synapse nanometric dimensions (i.e. the small zone where the DA is released by the neurotransmitter vesicles).[5] DA is involved in motor and cognitive functions. The loss of DA in neurons has been associated to neurological disorders, like Parkinson's disease and schizophrenia.[6,7] Thus, DA detection at the nanometric scale is one of the main objectives to keep in mind since it would be of great help for monitoring patients with impaired release of this neurotransmitter *in vivo*.

Core–shell and gel particles, for example, are excellent candidates for the fabrication of stimuli-responsive switchable substrates for the control of DA concentrations in the synapse, due to the easiness of preparing them with dimensiond smaller than one micrometer. Within this context, micro- and nanostructures based on CPs is a field of current interest due to their low density, large electroactive area, high stability and surface permeability, and good electrochemical properties. Such surfaces can reversibly switch their properties between oxidized and reduced, charged or uncharged, loaded or unloaded states.

Nevertheless, before reach the nanoscale dimensions, efforts of the research community have focused on the response of new materials in the micrometric scale and in *in vitro* conditions. Detection is typically carried out with potentiostate-galvanostate equipment's using electrochemical techniques, such as CV,[8-12] differential pulse voltammetry[13] and EIS.[14] Within this strategy several studies have been published employing many kinds of conducting electrodes as support.[15-16] On the other hand, several kinds of materials have been proposed to the fast and quantitative detection of DA molecules. For example, the work reported by Palomar-Pardavé and co-workers[4] has shown that cheap carbon paste electrodes modified with sodium dodecyl sulfate (SDS) micelles, at pH 7, are able to provoke a drastic change in the DA oxidation potential peak, shifting it toward less positive values with a notorious increment in the oxidation peak intensity. This modified electrode was also selective

allowing a quantitative DA determination, even in the presence of high concentrations of both ascorbic acid and uric acid.

Some references mentioned before are related with the generation of micro- and nanostructures based on CPs using solid templates with well-defined shapes (*i.e.* typically gold, silver, Pt, GC or stainless steel substrates), which limite the size of the sensors.[17-19] However, "soft" templates formed by assemblies of molecules, as for examplelike surfactants, gas particles, PS or other polymers, has been used to prepare microspheres, microbowls, microdoughnuts and microfibers of CPs for sensor applications.[20-29]

The present study comprises the chemical preparation and characterization of core-shell and hollow microspheres formed by a multilayered sequence of two different CPs, which have been arranged alternatively. More specifically, microspheres have been produced using oxidative chemical polymerization and PS microspheres as soft template. This polymerization method provides randomly distributed polymers with small concentrations of chloride anions as well as a very low amount of iron, according to the well discussed deposition mechanism reported by Martí *et. al.*[30]. Other interesting oxidative reagents were reported by Ramanavicius and co-workers[31], whom proposed the mechanism reaction provided by the use of sodium dodecyl sulfate and hydrogen peroxide, both easily degradable and cheap materials, to the oxidative polymerization reaction to obtain polypyrrole nanoparticles. PPy nanoparticles prepared by their route were suggested for biomedical applications, just due to the low toxicity of PPy nanoparticles, reported late for the same research group.[32] In this work, the sequence of CPs selected for this study is of PEDOT/PNMPy/PEDOT, and therefore the resulting hollow microspeheres correspond to 3-layered systems. After characterization, multilayed microspheres have been used to detect low concentrations of DA through CV, as simple and fast electrochemical technique. Results have been compared with those obtained in our previous works using individual CPs, such as PNMPy and PNCPy, activated with AuNPs.[30,33] According to our previous experience, pyrrole and polythiophene derivatives are more stable, electrochemically and in contact with air, than the simplest and cheaper polymers. Thus, it is the reason they are subject of interest in the present work.

4.3.2 Methods

Materials. 3,4-ethylenedioxythiophene (EDOT) and NMPy 99% were purchased from Aldrich and were used freshly distilled. PS microparticles (10% in deionized water, 1 μm), PVP with Mw= 360,000 g/mol, iron (III) chloride hexahydrate 97% (ACS reagent) and sodium dodecyl benzenesulfonate (SDBS) were also purchased from Aldrich and used as received. All solvents were purchased from Panreac S.A., while aqueous solutions were prepared using doubly distilled deionized water.

DA hydrochloride was obtained from Sigma-Aldrich (Spain). All other chemicals were of analytical-reagent grade and used without further purification. PBS 0.1 M with pH 7.4 was prepared as electrolyte solution by mixing four stock solutions of NaCl, KCl, $NaHPO_4$, KH_2PO_4, the pH being subsequently adjusted with NaOH.

Layer-by-layer assembly polymerization.

1) Preparation of polystyrene sulfonated microspheres. Concentrated sulfuric acid (98%, 11 mL) was introduced in a 30 mL centrifuge tube. PS microparticles (10% in deionized water, 3 mL) were added drop-wise under magnetic stirring. The sulfonation reaction was allowed to take place at 40ºC during 24 h under reflux. When the vessel cooled to the room temperature, the solution was centrifuged and the solid was washed several times with an excess of ethanol. A white fine powder, made of PSS core/shell particles, was obtained after drying under vacuum for 48 h.

2) Preparation of PEDOT-PSS microspheres (1st layer). PSS microparticles (0.06 g) were dispersed in a solution of PVP (11 mg) and 4 mL of deionized water in a 30 mL centrifuge tube, and were allowed stirring for 1 h. A solution of 24 μL of EDOT (0.224 mmol) and 1 mL of ethanol was introduced into the PSS suspension under magnetic stirring. After 15 min, 240 mg of $FeCl_3 \cdot 6H_2O$ (0.887 mmol) and 1 mL of deionized water were added. The polymerization process took place at room temperature during 24 h. The resulting powder was washed by centrifugation with an excess of deionized water and with ethanol. Finally, the sample was dried under vacuum for 48 h. This polymerization step was repeated three times.

3) Preparation of PNMPy/PEDOT-PSS microspheres (2nd layer). PEDOT-PSS microparticles (0.06 g) were dispersed in a solution of PVP (11 mg) and 4 mL of

deionized water in a 30 mL centrifuge tube, and were allowed stirring for 1 h. A solution of 20 µL of NMPy (0.246 mmol) and 1 mL of ethanol was introduced into the PEDOT-PSS suspension under magnetic stirring. After 15 min, 100 mg of $FeCl_3 \cdot 6H_2O$ (0.369 mmol) and 1 mL of deionized water were added. The polymerization time, temperature, purification process and drying were the same that used for the first layer. This polymerization step was repeated twice in order to have the first layer completely covered.

4) Preparation of PEDOT/PNMPy/PEDOT-PSS microspheres (3rd layer). The same procedure and molar quantities described for first layer preparation were employed for the deposition of the third layer of CP, which was another layer of PEDOT. This polymerization step was repeated once. Therefore, from inner to outer layer of CP and after several polymerizations, the thickness obtained was about 40-50 nm in total (Figure 1), measured by TEM.

5) Preparation of PEDOT/PNMPy/PEDOT, PEDOT/PNMPy and PEDOT hollow microspheres. PEDOT/PNMPy/PEDOT-PSS core-shell microspheres (6.0 mg) were dispersed in 12mL of THF under magnetic stirring for 48 h at room temperature. The resulting mixture was purified by centrifugation, and the final product was dried in vacuum at 40ºC for 24 h before characterization. The same procedure was applied for the preparation of PEDOT and PEDOT/PNMPy hollow microspheres.

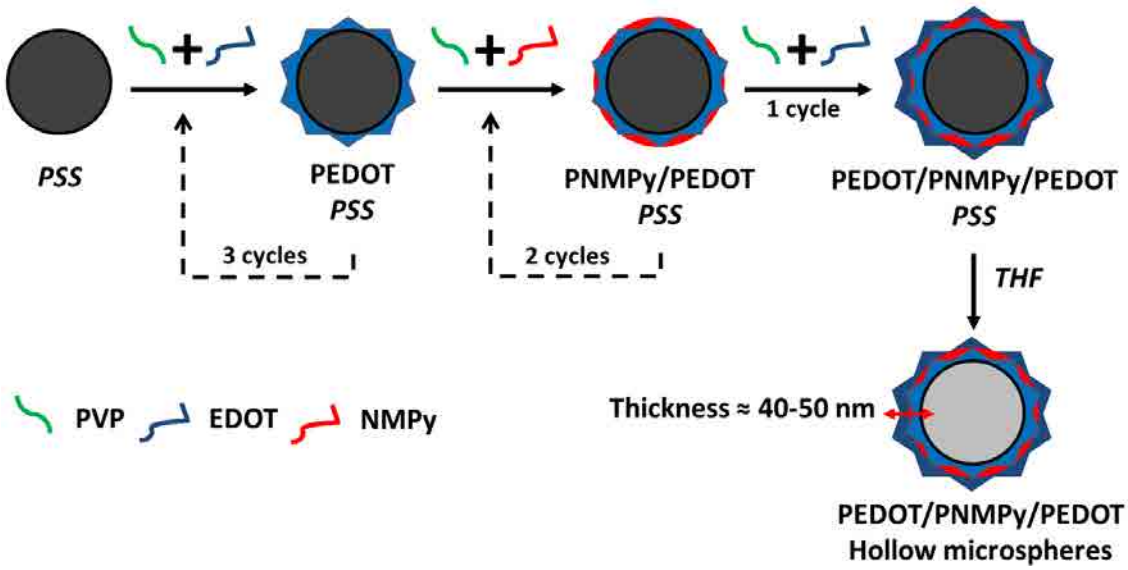

Figure 1. Scheme showing the synthesis of hollow PEDOT/PNMPy/PEDOT spheres.

Analytical techniques.

FTIR spectroscopy. Spectra of samples obtained by chemical oxidative polymerization and LbL assembly polymerizations were recorded on a FTIR 4100 Jasco spectrophotometer. Samples were placed in an attenuated total reflection accessory with a diamond crystal (Specac model MKII Golden Gate Heated Single Reflection Diamond ATR). Infrared spectra were measured in the range of 600–4000 cm^{-1}, taking 32 scans at a resolution of 4 cm^{-1} in the transmittance mode.

UV-vis. UV-Vis spectra of PEDOT/PNMPy/PEDOT hollow microspheres dispersed in distilled water to obtain a diluted solution (5 mg/mL), were recorded using a UV/Vis-NIR Shimadzu 3600 spectrophotometer. All the solutions had to be sonicated before analysis due to the low solubility of the microspheres in neutral water. The equipment contains a tungsten halogen visible source, a deuterium arc UV source, a photomultiplier tube UV-Vis detector, and an InGaAs photodiode and cooled PbS photocell NIR detectors. The wavelength range was from 200 to 900 nm. Single-scan spectra were recorded at a scan speed of 60 nm/min using the UVProbe 2.31 software in the absorbance mode.

SEM. SEM studies were carried out using a FIB Zeiss Neon40 scanning electron microscope equipped with an EDS system and operating at 5 kV. Samples were mounted on a double-sided adhesive carbon disc and sputter-coated with a thin layer of carbon to prevent sample charging problems.

TEM. TEM images were collected with a Philips TECNAI 10 electron microscope operating at 80 kV. Bright field micrographs were taken with an SIS MegaView II digital camera. Solutions containing PSS, PEDOT, PNMPy/PEDOT, PEDOT/PNMPy/PEDOT hollow spheres (1 mg/10 μL in water) were dispersed on carbon coated copper-grids (300 mesh), the solvent being allowed to evaporate before analysis.

AFM. Topographic AFM images were obtained with a Dimension 3100 Nanoman AFM and Multimode from Veeco using a NanoScope IV controller under ambient conditions in tapping mode. The root-mean-square roughness was determined using the statistical application of the Nanoscope software, which

calculates the average considering all the values recorded in the topographic image with exception of the maximum and the minimum. The scan window size was 600×600nm to 5×5 μm^2.

Electrochemical assays. Detection of DA was performed by CV using a glass cell containing 40 mL of a PBS solution at room temperature and considering DA concentrations ranging from 0.5 mM to 2 mM. GCE with a diameter of 2 mm, modified PEDOT/PNMPy/PEDOT hollow microspheres were employed as WE for DA electro-catalytic oxidation. Stainless steel AISI 316 sheets, with an area of 1 cm^2, were employed as CE, while Ag|AgCl (KCl, 3M) was used as RE. CVs were recorded at a scan rate of 50 $mV \cdot s^{-1}$. The surface of the GCE was polished with alumina slurry and cleaned by ultrasonication prior to the deposition of the polymer microspheres. Electrochemical measurements were conducted on a PGSTAT302N AUTOLAB potenciostat-galvanostat (Ecochimie) equipped with the ECD module to measure very low current densities (100 μA-100 pA), and employing NOVA 1.6 software.

Preparation of doped PEDOT/PNMPy/PEDOT hollow microspheres. PEDOT/ PNMPy/PEDOT hollow microspheres were dispersed in distilled water to form a 10 mg/mL solution and ultrasonically treated for 30 min. The dispersed solution (4μL) was dropped onto the pre-treated GCE surface and allowed to dry under ambient conditions. The hollow microspheres deposited were subjected to 10 cycles of oxidation-reduction in acetonitrile containing 0.1 M $LiClO_4$ as supporting electrolyte and doping reactive. CVs were recorded at a scan rate of 50 $mV \cdot s^{-1}$, using the same reference and counter-electrode mentioned above.

4.3.3 Results and Discussion

Core-shell and hollow PEDOT/PNMPy/PEDOT microspheres characterization.

The chemical deposition of several layers of CP was monitored by FTIR spectroscopy and by SEM. Figure 2 shows the overlapped FTIR absorption curves for the pure PSS microsphere, the second PNMPy layer and the outer PEDOT layer. The first PEDOT layer is not displayed due to its similarity with the third layer. The main absorption bands regarding the presence of PSS microsphere was reported in our previous work[30] and, therefore, are not be repeated here. However, it should

remarked that PS presents intense and sharp peaks corresponding to mainly C-H aromatic and aliphatic stretching, C=C aromatic stretching and C-H in-plane and out-of-plane bending, whereas sulfonic groups are evidenced at 1158 and 1029 cm^{-1} as two neighboring bands. When microspheres incorporate the first CP PEDOT layer, PSS absorption bands do not disappear due to the poor covering, three polymerizations being necessary to obtain a complete coverage of PS microsphere by PEDOT. The CP color obtained at this stage is slightly bluish, whereas the PS and PSS microspheres are white and beige, respectively.

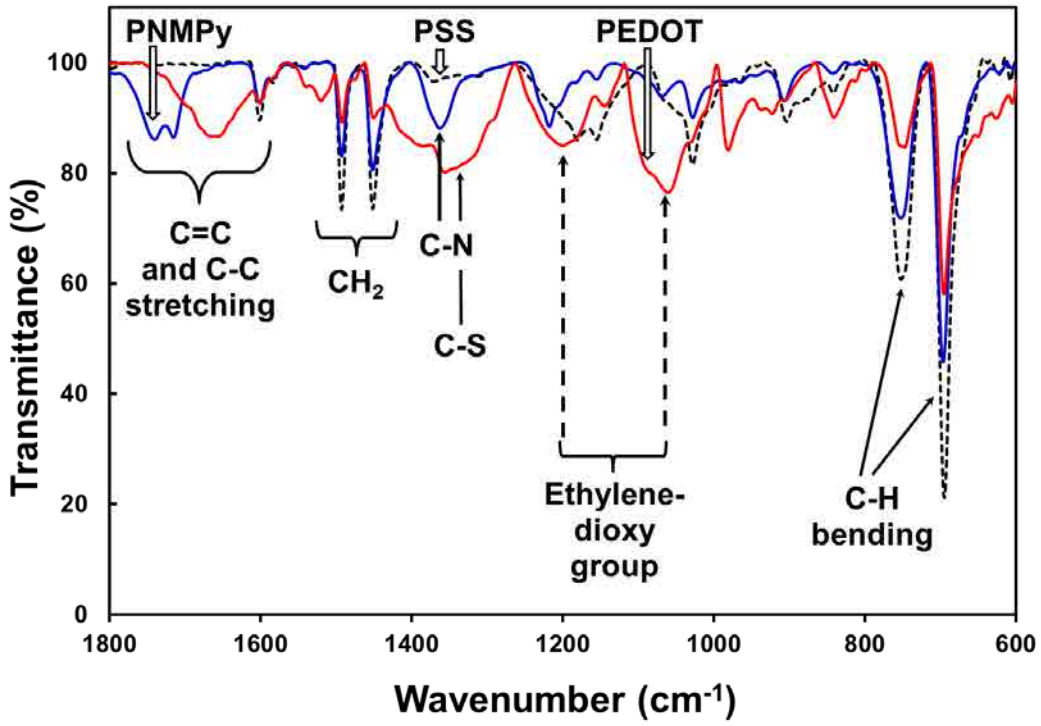

Figure 2. FTIR spectra of PSS microspheres (black dashed curve), PNMPy (blue curve) and PEDOT (red curve) synthesized by oxidative chemical polymerization.

The second layer shows absorption bands at 1734, 1711 and 1597 cm^{-1}, which are typically attributed to the presence of Py ring. Thus, the first band is associated to the overoxidation promoted by water solvent, giving a carbonyl band coupled to the ring, as was reported in previous works.[27,34,35] The second corresponds to the C=C conjugated bonds formed after NMPy polymerization and the third is associated to the ring deformation. Absorption bands corresponding to $N–CH_3$ groups are seen at 1175cm^{-1} and 1250cm^{-1}. Furthermore, bands observed at 1449 and 1356cm^{-1} have been attributed to C–N antisymmetrical stretching. The dark green color of the second layer is clearly distinguishable from first blue polymer.

Finally, the third PEDOT layer deposition has been evidenced by the presence of the main absorption peaks from Th ring, which were also reported previously.[34] Stretching modes of C=C in the Th ring are observed at 1650 and 1559 cm^{-1}, whereas CH_2 stretching modes are detected at 1490 and 1449 cm^{-1}. On the other hand, the presence of ether groups is reflected by the bands at about 1186 and 1054 cm^{-1}, which are not detected in the spectra of PSS or PNMPy. Therefore, these results allow us to conclude that multilayered films were successfully obtained.

The layer-by-layer deposition was also followed by SEM, the corresponding micrographs being displayed in Figure 3. PS microspheres are excellent templates for CP deposition due to their completely smooth surface, as was evidenced in our previous studies.[30,37] PEDOT chemically deposited on PSS, as first layer, shows a flat stairs-like morphology (Figures 3a-c), which is consistent with the directional growing preference usually found in PEDOT films.[38,39] It should be remarked that the morphology obtained for PEDOT using this oxidative chemical polymerization strategy is completely different from described for ultra-thin films produced by anodic polymerization in acetonitrile with $LiClO_4$ as supporting electrolyte.[38] Thus, the morphology electropolymerized PEDOT typically consists on packing of sticks (i.e. fiber-like organizations), which results in a very porous material. High magnification micrographs showed in Figures 3b and c, show how microspheres electrostatically attract one another. This is probably due to the large charge density at the PEDOT surface film. Thus, this phenomenon was also observed for PNCPy/PSS core-shell particles synthesized using a similar chemical procedure.[37]

In contrast, the morphology of chemically polymerized PNMPy shows the formation of granular aggregates. PPy derivatives with substituents at the N-position of the Py ring tend to be cross-linked, *i.e.* consecutive Py rings may form α-β and β-β linkages in addition of the conventional α-α ones;[40,41] causing the appearance of a rough surface (Figures 3d-f). Finally, the third and outer PEDOT layer does not present the appearance of flat stairs, as observed in PEDOT first layer, neither a granular aspect found at the PNMPy intermediate layer. Indeed, the surface morphology of the third layer is half way between those of the first- and second-layers, as is reflected in Figures 3g-i. In accordance with FTIR results, SEM micrographs evidence that the surface is

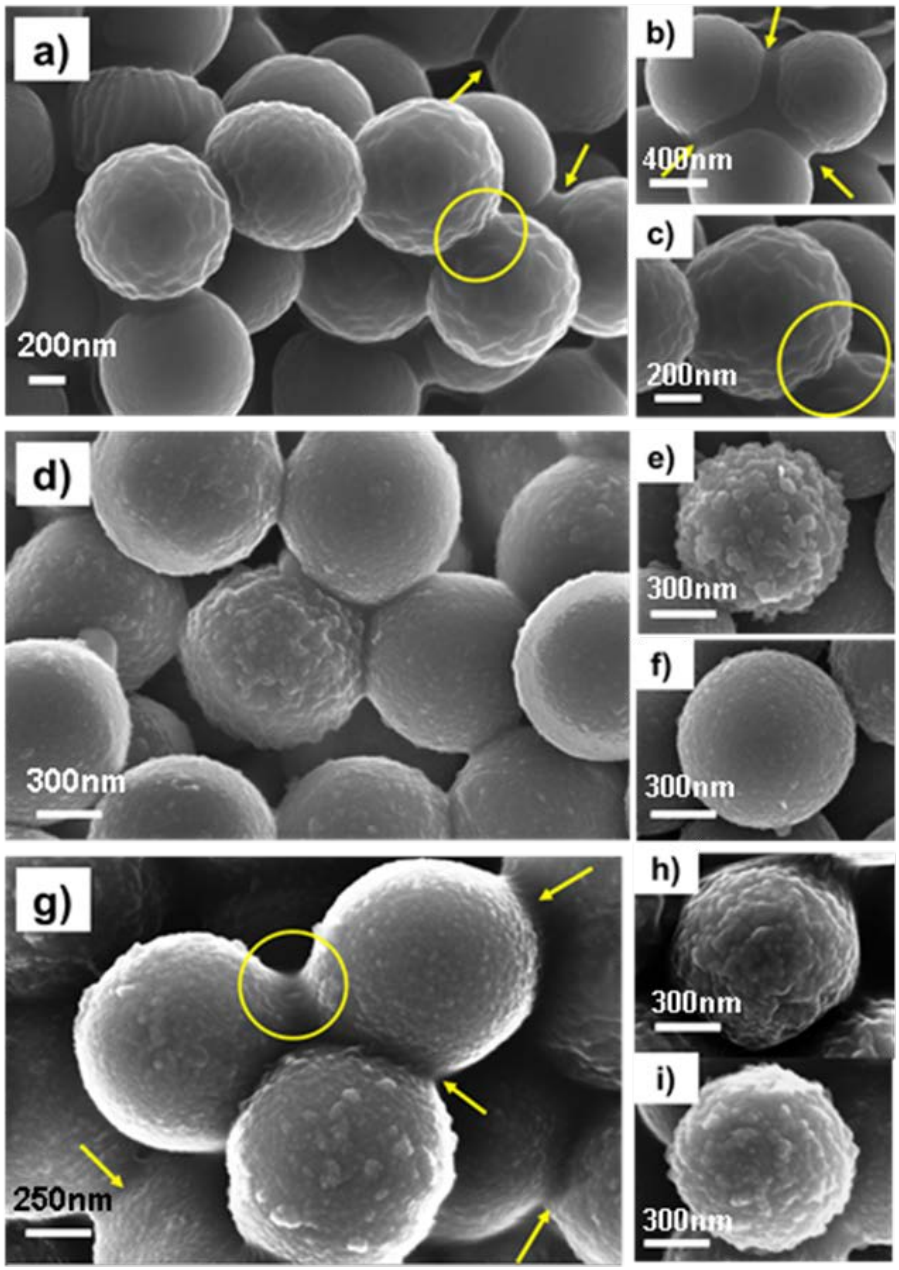

Figure 3. SEM micrographs of PS core-shell particles with one layer of PEDOT (a-b-c), PEDOT/PNMPy bilayers (d-e-f) and PEDOT/PNMPy/PEDOT trilayers (g-h-i).

well-covered using several oxidative chemical polymerizations on the deposition of the multilayered CP systems. After removal of PS core, microspheres lose the spherical form and some layers bent over each other (Figure 4), which has been attributed to the high weight provoked by the final thickness reached after many polymerization cycles and/or to the effect of the high vacuum applied to operate the SEM equipment. The final thickness obtained after take out the PS template was about 45±5 nm, considering that part of the layer was collapsed into de microsphere.

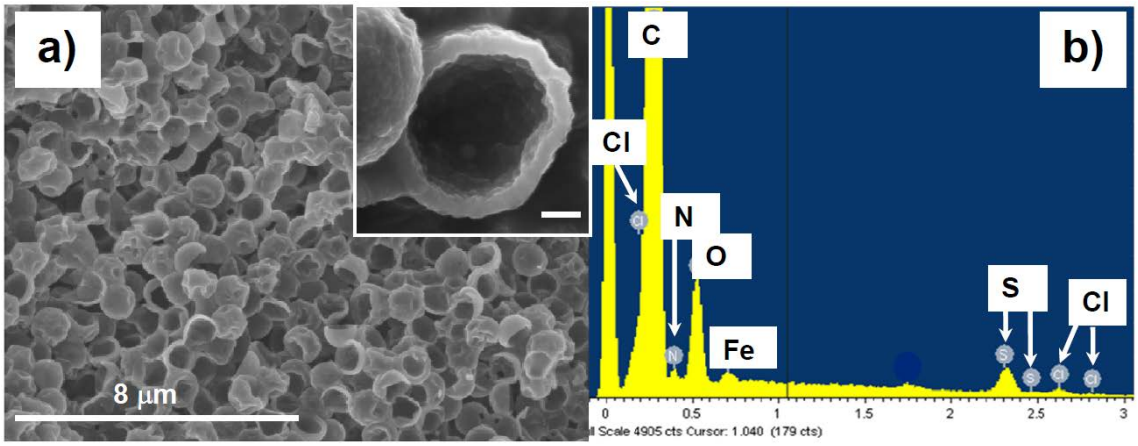

Figure 4. (a) SEM micrographs and (b) EDX analyses of the hollow and open microspheres composed by PEDOT/PNMPy/PEDOT multilayered films. Scale bar of inset corresponds to 100 nm.

EDX analyses were carried out for each CP layer deposited. In general, elemental analyses corroborate the generation of doped CPs with $FeCl_4^-$, from the oxidative reactive, acting as dopant agent. Figure 4b, shows the results from semi-quantitative analyses of C, O, N, S, Fe and Cl ions from an area with several hollow microspheres.

Inspection of the TEM images from hollow microspheres after each layer deposition, allow us to realize that the number of polymerization cycles affect both the concentration of dopant ions at the surface and he integrity of the spheres. The micrograph displayed in Figure 5a shows a high density of elongated particles among polymer chains, which has been attributed to the $FeCl_4^-$ dopant ions. Moreover, detailed inspection of outline sphere helps us to check the flat stairs surface observed by SEM for the first PEDOT layer deposition. Furthermore, after PNMPy deposition, the elongated particles become aggregates uniformly distributed on the film surface (Figure 5b). In the third PEDOT layer these aggregates disappear and the elongated particles are hardly appreciated (Figure 5c), even though elongated particles are detected in some other microspheres (Figure 5d). TEM images clearly show that the hollow-multilayered microspheres were preserved after the removal of the PS cores, confirming the effects observed by SEM. Thus, as was discussed above, vacuum has a negative effect in integrity of the microspheres and the shell is not rigid enough to keep the original shape, provoking a collapse.

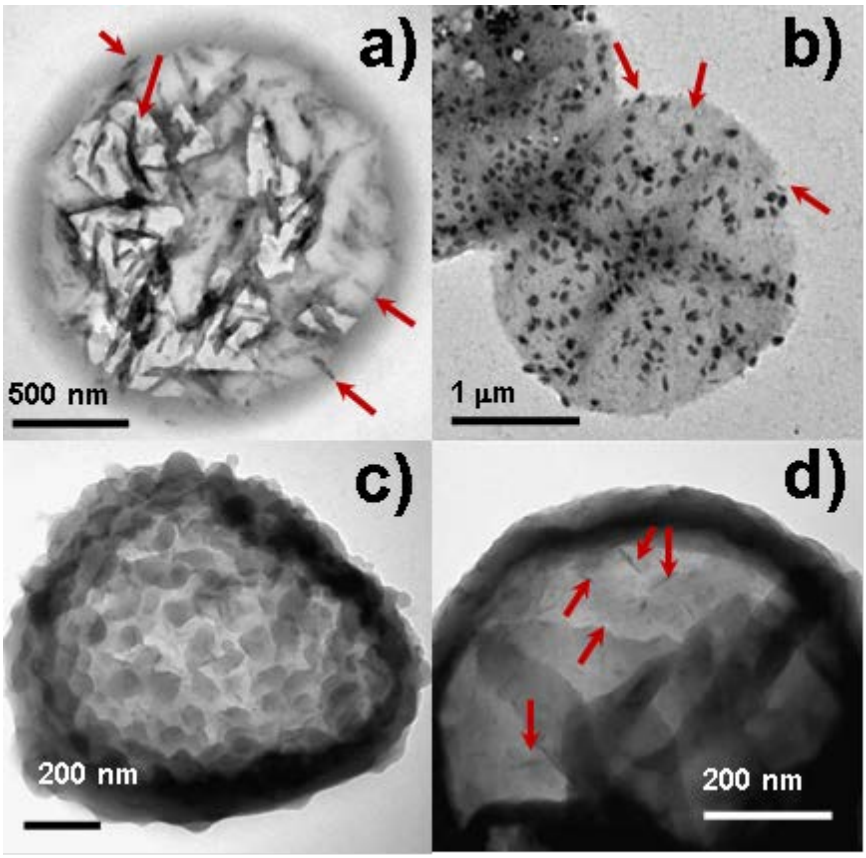

Figure 5. TEM images of (a) PEDOT, (b) PEDOT/PNMPy and (c and d) PEDOT/PNMPy/PEDOT hollow spheres doped with $FeCl_4$.PEDOT/PNMPy/PEDOT spheres are partially collapsed.

Similarly, AFM images evidenced very similar surface topologies for PEDOT/PNMPy/PEDOT multilayered spheres (Figure 6) than those observed by SEM and TEM microscopies. When the PS is maintained as a template, this consists on relatively dense distribution of sharp spheres that group through electrostatic interaction (Figure 6a). As PEDOT molecules exclusively involve α–α linkages (*i.e.* the β positions of the Th ring are occupied by the fused dioxane ring), the electrostatic interaction has been attributed to the formation of a compact structure with linear chains that are stabilized by the iron chloride dopant ions. This surface topology is better illustrated in Figures 6b and 6c, which display an AFM image of PEDOT/PNMPy/PEDOT hollow microspheres. The RMS roughness (*r*) determined for PEDOT/PNMPy/PEDOT hollow microspheres is extremely low, *r*= 4.8 ±1.5 nm. Ultra-thin PEDOT films synthesized by electrochemical techniques using acetonitrile and $LiClO_4$ as solvent and dopant agent,[38] respectively, show a relatively high roughness as compared to the material generated in this work by chemical synthesis.

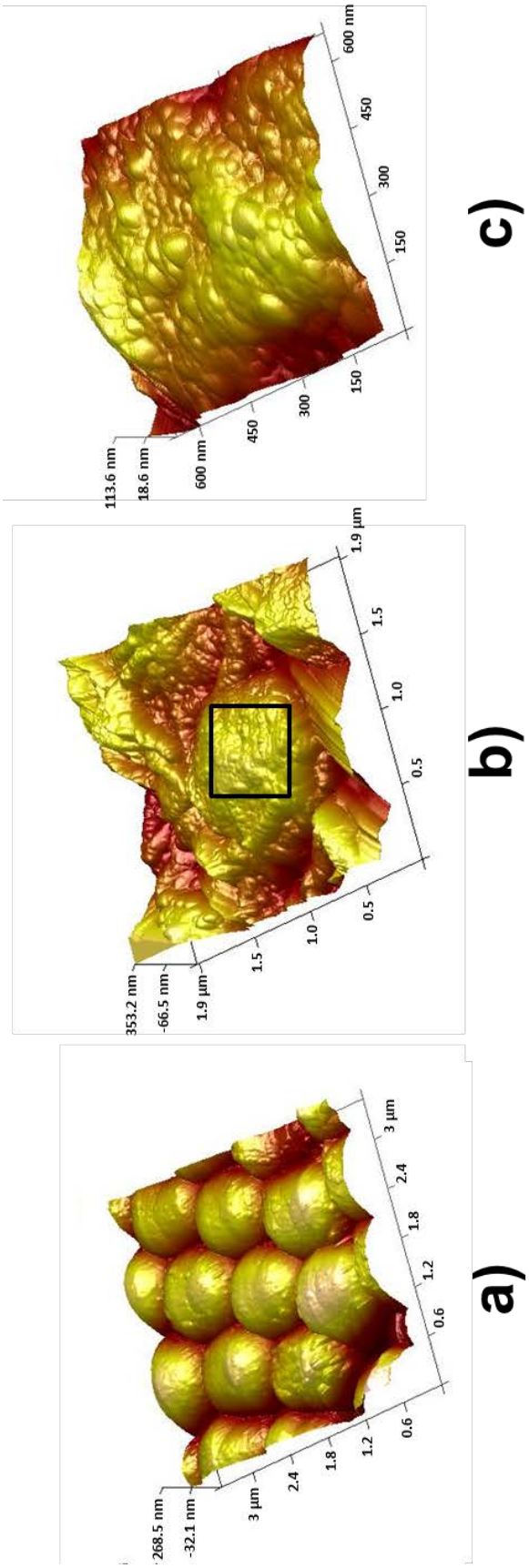

Figure 6. AFM images of: (a) PEDOT/PNMPy/PEDOT core-shell microspheres and (b and c) PEDOT/PNMPy/PEDOT hollow microspheres. The image displayed in (c) corresponds to a detailed view of the region selected in (b), which was used to determine the RMS roughness.

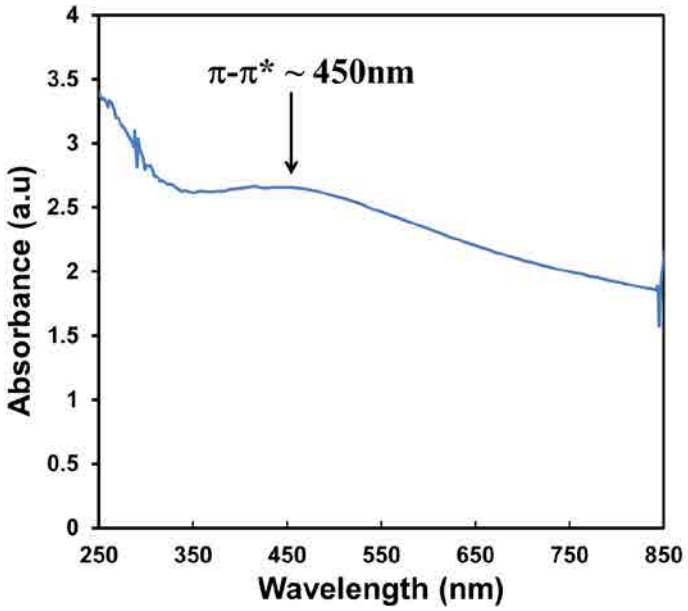

Figure 7. UV-vis spectra of PEDOT/PNMPy/PEDOT hollow microspheres obtained by oxidative chemical synthesis.

In order to prove if the hollow 3-layered spheres are doped, the UV-vis-NIR spectrum was recorded. The $\pi \rightarrow \pi^*$ transition associated to the Th conjugated ring, which is typically observed at about 450 nm for PEDOT, is showed in the (Figure 7). However, dopant transition response is not detected at the region from 500 to 800 nm. Therefore, we conclude that the 3-layered microsphere is not fully doped with $FeCl_4^-$ ions. This feature is essential for the studies devoted to investigate the potential application of multilayered microspheres as biosensor for DA detection. Thus, further doping process using CV was necessary in order to achieve the good electrochemical response from the CP system.

Using PEDOT/PNMPy/PEDOT hollow microspheres for Dopamine detection.

In recent studies we investigated the properties of multilayered films formed by two, or even more CPs.[42-46] More specifically, we found that multilayered films show better electrochemical properties and higher ability to store charge than each of the individual CPs. This improvement is due to a synergistic effect produced by favorable interactions at the interfaces, which increase with the structural differences between the CPs (*i.e.* in terms of morphology, porosity and roughness). Within this context, properties of multilayered films made of alternated PEDOT and PNMPy nanometric layers were found to be particularly enhanced with respect to those of the corresponding individual polymers.[42-46] However, multilayered core-shell and hollow

microspheres made of two CPs were not reported before. Similarly, although CP films alone or composed with metallic nanoparticles have been used in sensing applications,[12-17,30,33] the efficacy of multilayered microspheres as sensors remain untested. In the specific field of DA detection employing CP films, the actuation of alone and combined with AuNPs was found to be excellent in terms of sensitivity.[16,47] In this section we evaluate the sensing ability of PEDOT/PNMPy/PEDOT hollow microspheres towards DA, results being compared with those reported for electrochemically produced PEDOT films[16,47] and PNMPy films obtained by electrochemical polymerization.[30,33] For this purpose, PEDOT/PNMPy/PEDOT microspheres were previously re-doped with CV using $LiClO_4$ as dopant agent, using a protocol identical to that employed in our previous studies with PNMPy films.[30] In order to avoid the CP multilayered system oxidation, experiments were performed in a potential range below 0.8 V (vs. Ag|AgCl RE). Thus, Figure 8a indicates that the oxidation of the microspheres occurs at about 0.86V. As can be seen, pure electrodes do not have electrochemical activity in PBS solutions; whereas conducting polymers are well known by their ability to reverse oxidation-reduction cyclic reactions due to the equilibrium between entry and exit of dopant molecules inside the polymer chain.

Figure 8b shows the results obtained after the addition of 0.5-to-2 mM DA to 0.1 M PBS solution. According to previous works[16,17,30], conducting polymers are able to catalyse the oxidation of DA molecules in a low potential range, which means that in cellular systems, the voltage applied would be the minimal required to detect this kind of biomolecule *in vivo*. As expected, from Figure 8b, the anodic peak current increases with the concentration of DA. Nevertheless, the anodic peak potential remains almost constant (0.27 V) for low concentrations, showing a good rectilinear behaviour. In opposition, high concentrations usually show a non-rectilinear behaviour, reaching an oxidation potential of 0.33 V for 2 mM DA. The response of DA is apparently lost for concentrations below 0.5 mM. Despite this concentration limit detection is not the lowest that would be desirable; the response of the multilayered hollow microspheres is better than that of PNMPy single films activated with AuNPs[30] because the anodic current peak associated to the DA oxidation is better defined and sharper for PEDOT/PNMPy/PEDOT system than for the PNMPy homopolymer one.

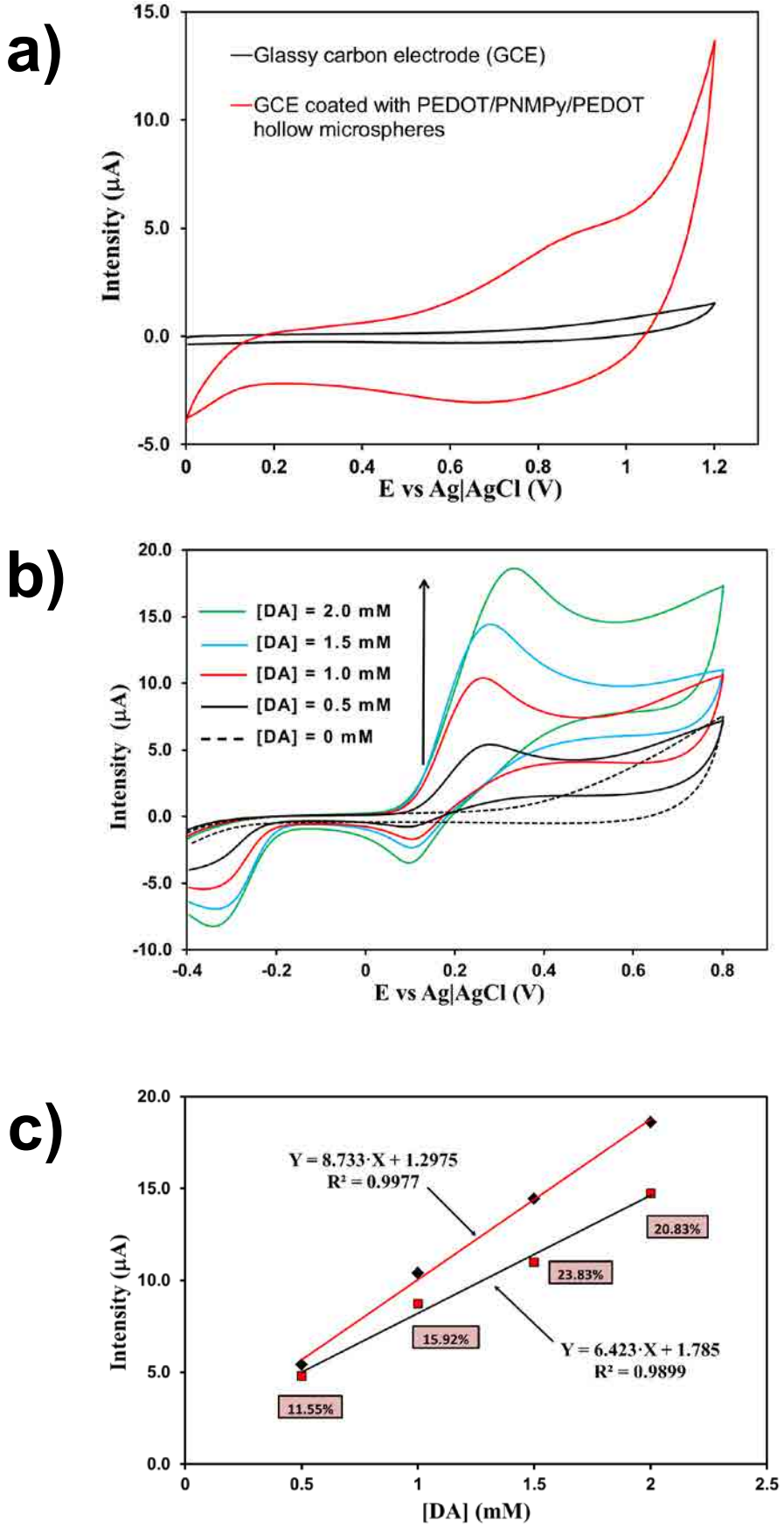

Figure 8. (a) Control voltammograms of GCEs uncoated and coated with PEDOT/PNMPy/PEDOT hollow microspheres after re-doping with $LiClO_4$. (b) Comparison of DA detection intensity

from 0 to 2 mM in 0.1M PBS, employing PEDOT/PNMPy/PEDOT microspheres re-doped with $LiClO_4$. (c) Calibration curve for DA detection in the concentration range from 0.5 to 2 mM in 0.1M PBS with PEDOT/PNMPy/PEDOT hollow microspheres. Red and black lines correspond to the first and fifth oxidation-reduction cycles, respectively. Numbers inside rectangular forms indicate the loss of intensity from the first to the fifth redox cycle, in percentage.

The calibration curve (Figure 8c) shows a linear behaviour with correlation coefficient of 0.9977 for the 1st oxidation-reduction cycle, the anodic peak current determined for 0.5 and 2 mM DA being 5.41 and 18.6 μA, respectively. On the other hand, the CGE coated with PEDOT/PNMPy/PEDOT microspheres gradually deteriorate with increasing number of consecutive oxidation-reduction cycles, the correlation coefficient decreasing to 0.9899 after five redox cycles. It is probably due to the irreversible polymerization of dopamine molecules after oxidation-reduction cycles, after interaction with the tri-layer CP. This effect is relevant with increased DA concentration, as can be seen on Figure 8c. In spite of this inconvenience for the first cycle, the loss of current intensity from after five cycles is relatively low (~10-20%) for 2 mM of DA. These results demonstrate that 3-layered PEDOT/PNMPy/PEDOT microspheres can be successfully used for the detection of DA in the range of concentrations from 0.5 to 2 mM, taking to account the results obtained after first redox cycle. The influence of AuNPs in the capabilities of multilayered microspheres to detect DA will be investigated in a near future. Thus, after prepare and characterize 3-layered microspheres and check their intrinsic ability to detect DA, future research will be oriented towards the detection of lower concentrations of DA as is desirable for the *in vivo* sensing applications.

4.3.4 Conclusions

CPs electrochemically adhered to the electrode surface show an excellent response towards DA oxidation. The main disadvantage of this technique is the variability of both the amount and morphology of the polymer in electrode if the coating thickness is not perfectly controlled. Polymer morphology is considered an important factor for the fabrication of DA sensors. In the present study, we moved from electrochemical synthesis to chemical synthesis for obtaining multilayered systems for DA detection, obtaining better anodic oxidation peaks than systems prepared by electrochemical synthesis. Characterization assays proved that chemical synthesis was effective to cover PS microspheres used as template and the extraction

of PS template is effective with tetrahydrofuran solvent; despite the microspheres were partially destroyed when subjected to strong vacuum.

One disadvantage of the oxidative chemical polymerization is related to the oxidizing agent ($FeCl_3$) used, it does not actuate as a good dopant for the multilayered microspheres and the microspheres had to be re-doped with electrochemical technique before DA detection assays. Therefore, $LiClO_4$-doped hollow microspheres, which were well adsorbed onto GCEs, were used for electrochemical DA detection experiments. CV results proved that PEDOT/PNMPy/PEDOT hollow microspheres are able to detect DA, in the concentration range from 0.5mM to 2mM. The response of the 3-layered system towards the oxidation of DA is better than obtained for PNMPy single layer films activated with AuNPs in terms of resolution of the anodic peak oxidation. The overall of the results allow us to conclude that multilayered systems are better sensors than monolayer systems.

4.3.5 References

1. P. Tyagi, D. Postetter, D. L. Saragnese, C. L. Randall, M. A. Mirski and D. H. Gracias, *Anal. Chem.,* 2009, **81**, 9979.

2. A. N. Shipway, E. Katz and I. Willner, *Chem. Phys. Chem*., 2000, **1**, 18.

3. M. Ates and A. S. Saraç, *Prog. Org. Coat*., 2009, **66**, 337.

4. E. Colín-Orozco,M. T. Ramírez-Silva, S. Corona-Avendaño, M. Romero-Romo and M. Palomar-Pardavé, *Electrochim. Acta,* 2012, **85**, 307.

5. T. Schikorski and C. F. Stevens, *J. Neurosci.,* 1997, **17**, 5858.

6. E. R. Kandel, J. H. Schwartz and T. M. Jessel, "Principles of Neural Science", 4th ed. New York, McGraw-Hill, 2000**,** pp. 207-298.

7. B. J. Venton and R. M. Wightman, *Anal. Chem.,* 2003, **75**, 414A.

8. D. L. Robinson, B. J. Venton, M. L. A. V. Heien and R. M. Wightman, *Clinical Chem*., 2003, **49**, 1763.

9. R. N. Adams, *Anal. Chem*., 1976, **48**, 1126A.

10. X. Huang, Y. Li, P. Wang and L. Wang, *Anal. Sci.,* 2008, **24**, 1563.

11. Y. Li and X. Lin, *Sens. Actuators. B,* 2006, **115**, 134.

12. N. F. Atta, A. Galal and R. A. Ahmed, *Electroanalysis,* 2011, **23**, 737.

13. N. F.Atta, A. Galal and S. M. Azab, *Int. J. Electrochem. Sci*., 2011, **6**, 5066.

14. N. F. Atta and M. F. El-Kady, *Talanta,* 2009, **79**, 639.

15. C. Wang, R. Yuan, Y. Chai, S. Chen, Y. Zhang, F. Hu and M. Zhang, *Electrochim. Acta,* 2012, **62**, 109.

16. N. F. Atta, A. Galal and R. A. Ahmed, *Bioelectrochemistry,* 2011, **80**, 132.

17. X. Huang, Y. Li, P. Wang and L. Wang, *Anal. Sci.,* 2008, **24**, 1563.

18. R. V. Parthasarathy and C. R. Martin, *J. Appl. Polym. Sci.,* 1996, **62**, 875.

19. J. Jang, J. H. Oh and Y. Li, *J. Mater. Chem*., 2004, **14**, 2872.

20. J. Jang and J. H. Oh, *Adv. Mater.,* 2003, **15**, 977.

21. H. B. Xia, D. M. Cheng, C. Y. Xiao and H. S. O. Chan, *J. Mater. Chem.,* 2005, **15**, 4161.

22. L. Qu, G. Shi, F. Chen and J. Zhang, *Macromolecules,* 2003, **36**, 1063.

23. L. Qu and G. Shi, Chem. Commun., 2003, **2**, 206.

24. L. Qu and G. Shi, *J. Polym. Sci. Pol. Chem*., 2004, **42**, 3170.

25. X. He, C. Li, F. Chen and G. Shi, *Adv. Funct. Mater*., 2007, **17**, 2911.

26. C. Li, H. Bai and G. Shi, *Chem. Soc. Rev*., 2009, **38**, 2397.

27. B. Teixeira-Dias, C. Alemán, F. Estrany, D. Azambuja and E. Armelin, *Electrochim. Acta,* 2011, **56**, 5836.

28. M-Y. Bai and Y. Xia, *Macromol. Rapid Commun.,* 2010, **31**, 1863.

29. S-C. Luo, H-H. Yu, A.C.A. Wan, Y. Han and J. Y. Ying, *Small*, 2008, **4**, 2051.

30. M. Martí, G. Fabregat, F.Estrany, C. Alemán and E. Armelin, *J. Mat. Chem*., 2010, **20**, 10652.

31. K. Leonavicius, A. Ramanaviciene and A. Ramanavicius, *Langmuir,* 2011, **27**, 10970.

32. A. Vaitkuvienea, V. Kaseta, J. Voronovic, G. Ramanauskaite, G. Biziuleviciene, A. Ramanaviciene and A. Ramanavicius, *J. Haz. Mater.*, 2013, **250-251**, 167.

33. G. Fabregat, E. Cordova-Mateo, E. Armelin, O. Bertran and C. Alemán, *J. Phys. Chem. C* 2011, **115**, 14933.

34. L.H. Dall'Antonia, M.E. Vidotti, S.I. Córdoba de Torresi and R. M. Torresi, *Electroanalysis,* 2002, **14**, 1577.

35. A. Cambra, M. I. Redondo and M. J. Gonzalez-Tejera, *Synth. Met.,* 2003, **139**, 21.

36. F. Alvi, M. K. Ram, P. A. Basnayaka, E. Stefanakos, Y. Goswami and A. Kumar, *Electrochimica Acta,* 2011, **56**, 9406.

37. G. Fabregat, C. Alemán, M. T. Casas and E. Armelin, *J. Phys. Chem. B,* 2012, **116**, 5064.

38. D. Aradilla, F. Estrany, E. Armelin and C. Alemán, *Thin Solid Films,* 2012, **520**, 4402.

39. G. Fabregat, G. Ballano, E. Armelin, L. J. del Valle, C. Cativiela and C. Alemán, *Polym. Chem.*, 2013, **4**, 1412.

40. C. Alemán, J. Casanovas, J. Torras, O. Bertran, E. Armelin, R. Oliver and F. Estrany, *Polymer,* 2008, **49**, 1066.

41. D. Aradilla, J. Torras and C. Alemán, *J. Phys. Chem. B,* 2011, **115**, 2882.

42. D. Aradilla, F. Estrany and C. Alemán, *J. Phys. Chem. C,* 2011, **115**, 8430.

43. D. Aradilla, F. Estrany, R. Oliver and C. Alemán, *Eur. Polym. J.*, 2010, **46**, 2222.

44. F. Estrany, D. Aradilla, R. Oliver, E. Armelin and C. Alemán, *Eur. Polym. J.*, 2008, **44**, 1323.

45. D. Aradilla, F. Estrany, E. Armelin and C. Alemán, *Thin Solid Films,* 2010, **518**, 4203.

46. D. Aradilla, M. M. Pérez-Madrigal, F. Estrany, D. Azambuja, J. I. Iribarren and C. Alemán, *Org. Electron*., 2013, **14**, 1483.

47. N. F. Atta, A. Gala and E. H. El-Ads, *Electrochim. Acta,* 2012, **69**, 102.

4.4 Ultrathin films of polypyrrole derivatives for dopamine detection*/**

Ultrathin films of PNCPy and PNMPy, and their composites with AuNPs, were used for the electrochemical detection of small concentrations (10 mM-100 μM) of DA, a neurotransmitter related with neurological disorders. Results indicated that AuNPs improve the sensing abilities of the two polymers, even though they are not essential to obtain effective and fast responses towards the presence of DA. Furthermore, although both polymers have been found to be highly sensitive to low concentrations of DA, the response of PNCPy is better and more effective than the response of PNMPy. Experimental results were corroborated with quantum mechanical (QM) calculations on model systems, which also indicated that the interaction of oxidized DA with PNCPy is stronger than with PNMPy. This behavior has been attributed to two different factors: (i) the flexibility of the cyanoethyl groups, which allows maximize the number of attractive van der Waals interactions; and (ii) the dipole of the cyano group, which interacts favorably with the dipole of the C=O bonds of oxidized DA. Finally, theoretical results were used to propose an atomistic model that explains the interaction behavior between the oxidized DA and the CPs.

*Results described in this section previously appeared in *J. Phys. Chem. C*, 2011, **115**,14933.
**QM calculations were performed by E. Córdova-Mateo.

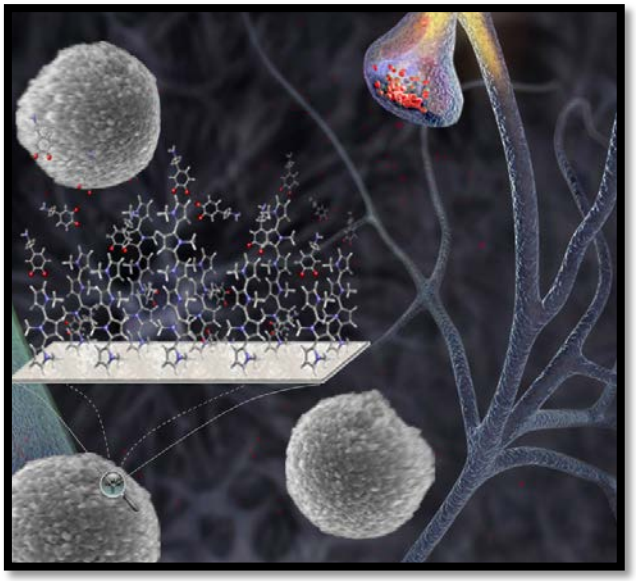

4.4.1 Introduction

DA is one of the most important neurotransmitters in the mammalian central nervous system. The deficiency or excess of DA may result in serious diseases related with neurological disorders, including Parkinson's disease and schizophrenia.[1,2] In neurons DA is stored in synaptic vesicles with other neutrotrasmiters. When synaptic vesicles receive an electrical stimulus produced by a nerve impulse, the DA molecules are transported to the cell wall releasing them to the synapse, which is the tiny gap between the axon ending and the dendrite of the next neuron.[3] Accordingly, the development of sensors to measure the DA concentration in a single synapse is receiving special attention because of the necessity of both the understanding the mechanisms that provokes neurological disorders and the prevention to numerous diseases. Furthermore, detection of DA contained in samples plays also a crucial role in the clinical diagnoses.

Electrochemical techniques have been developed to monitor the concentration of DA.[4-15] Within this context, conducting polymer modified electrodes have been used to for the determination of DA in biological fluids. Among others, electrodes coated with PPy,[9-11] PNMPy,[12] PAni[13,14] and PEDOT[7] have been used to detect DA. In a very recent study, we prepared DA sensors by coating GCE and AuNPs deposited on GCE with an ultrathin film of PNMPy.[12] Results indicated that PNMPy is highly sensitive to this neurotransmitter, being able to detect DA concentration lower than that estimated for the synapse (1.6 mM). Thus, the constructed PNMPy sensor detected DA concentrations of 1.5 μM without loss of current density. Moreover, we found that AuNPs are not essential for the sensing abilities of PNMPy, which represents an important practical advantage.[12] These findings suggested that PNMPy based detectors should be considered as good candidates for the development of effective, fast and sensitive systems to be used in diagnosis detection of deficiency or excess DA.

On the other hand, we recently reported the synthesis and characterization PNCPy,[16] a N-substituted PPy derivative able to form thin and ultrathin films with some properties close to those of PNMPy. Specifically, the electrochemical stability and the electrical conductivity of PNCPy and PNMPy prepared using identical experimental conditions are very similar, while the current productivity and the doping level are

lower for the former material. PNCPy shows a negligible flow of current density through the electrode for potentials lower than a given threshold (~1.10 V), while this flow increases rapidly and significantly after such potential. The incorporation of the cyano to N-position of the PPy has been only used to improve the sensing and detection abilities of PPy. Specifically, early PNCPy studies, in which the material was only preliminary characterized by CV and scanning electron microscopy, were focused on the utility of PNCPy to detect organic vapors,[17-19] to develop impedimetric immunosensors[20] and to prepare membranes for ions separation.[21] It is worth noting that, as far as we know, PNCPy has never been used for the detection of biomolecules like DA, even though the cyano functionality is able to participate in a wide number of intermolecular interactions (*e.g.* hydrogen bond and dipole···dipole).[17] Furthermore, strong electron-withdrawing cyano groups incorporated at positions relatively close to the π-system of conjugated CPs induce the reduction of the barrier for electron injection, increase the oxidation potential and improve the electron transporting properties.

In this work we compare the affinity and sensitivity of PNMPy and PNCPy towards DA molecules. More specifically, the abilities of these two PPy derivatives to immobilize and identify DA molecules have been investigated using the electrochemical oxidation of the neurotransmitter for the detection process. The sensitivity of these two PPy derivatives has been examined by considering submicromolar concentrations of biomolecules. In addition, QM calculations have been carried out to examine the geometry and strength of the binding between the CPs and the oxidized DA. Results have allowed us to propose a model that explains the different behaviors experimentally observed for PNMPy and PNCPy.

4.4.2 Methods

Materials. NCPy, acetonitrile, anhydrous $LiClO_4$, DA hydrochloride and $HAuCl_4 \cdot 3H_2O$ of analytical reagent grade were purchased from Sigma-Aldrich (Spain), whereas sodium citrate dihydrate was obtained from J.T. Baker. All other chemicals were of analytical-reagent grade and used without further purification. PBS 0.1 M with pH 7.4 was prepared as electrolyte solution by mixing four stock solutions of NaCl, KCl,

$NaHPO_4$ and KH_2PO_4. High-purity nitrogen was used for deaeration of the prepared aqueous solutions.

Electrochemical synthesis, polymerization kinetics and thickness of the films. PNMPy and PNCPy films were prepared by CA under a constant potential of 1.40 V. Electrochemical experiments were performed on an Autolab PGSTAT302N equipped with the ECD module for measure very low current densities (100µA-100pA) (Ecochimie, The Netherlands) using a three-electrode two-compartment cell under nitrogen atmosphere (99.995 % in purity) at room temperature. The RE was a saturated Ag | AgCl electrode, whereas Pt sheets of 0.50×0.70 cm^2 were used as CE. A GCE was used as the WE (4.11 mm^2), its surface being polished with alumina powder and cleaned by ultrasonication before each trial. PNMPy and PNCPy were electrochemically deposited on the GCE using 70 mL of the corresponding monomer solution (10 mM) in acetonitrile containing 0.1 M $LiClO_4$ as supporting electrolyte. The polymerization time was 3 s for PNMPy and PNCPy.

In addition, the polymerization kinetics of PNCPy and PNMPy was investigated considering the same electrochemical conditions discussed above with exception of: (1) the working and counter electrodes, which were made of steel AISI 316 L sheets of 2.0×2.0 cm^2; and (2) the polymerization time, which ranged from 5 to 70 s. The difference between the masses of the coated and uncoated electrodes was measured with a Sartorius analytical balance with a precision of 10^{-6} g.

The thickness of the films (ℓ) was estimated using the procedure reported by Schirmeisen and Beck.[22] Accordingly, the current productivity, (m/Q) was determined through the following relation:

$$W_{OX} = Q_{pol}\left(\frac{m}{Q}\right) \qquad (1)$$

where Q_{pol} is the polymerization charge consumed in the generation of each layer and W_{ox} is the mass of polymer deposited in the electrode. The current productivity was determined as the slope of a plot representing the variation of reproducible film weights (in $mg \cdot cm^{-2}$) against the polymerization charge consumed in each process (in $mC \cdot cm^{-2}$), which was directly obtained from each CA. The volume of polymer deposited

in the electrode, V_{pol}, was obtained using the values of W_{ox} and the density. The densities of PNMPy (1.52 g·cm^{-3}) and PNCPy (1.42 g·cm^{-3}) were determined in previous works.[23,24]

Preparation of AuNPs. In order to remove any adsorbed substance on the GCE surface, prior to the CP deposition, it was polished repeatedly with alumina slurry, followed by successive sonication in ethanol and doubly distilled water for 5 min, and dried under a nitrogen flow.

Preparation of the AuNPs for deposition onto GCEs, which were used to fabricate the nanomembranes of PNCPy and PNMPy, was performed following the standard procedure described in the literature.[25,26] All glassware used in such preparation was thoroughly cleaned in aqua regia (3:1 HCl:HNO_3), rinsed in doubly distilled water, and oven-dried prior to use. In a 1 L round-bottom flask equipped with a condenser, 500 mL of 1 mM $HAuCl_4$ was brought to a rolling boil with vigorous stirring. Rapid addition of 50 mL of 38.8 mM sodium citrate to the vortex of the solution produced a colour change from pale yellow to burgundy. Boiling was continued for 15 min. After this, the heating mantle was removed while the stirring was continued for 30 min. When the solution reached the room temperature, it was filtered through a 0.2 μm membrane filter. The resulting solution of colloidal particles showed an absorption maximum at 520 nm indicating that the particle size ranged from 9 to 22 nm. A spherical model for a particle size of 13 nm was used to determine approximately the concentration of mother solution from UV-vis absorption, which was estimated to be 7.4 nM.[27]

Detection assays. Detection of DA was performed by CV using a glass cell containing 40 mL of PBS 0.1 M at room temperature, and considering DA concentrations ranging from 100 μM to 10 mM. Detection was studied considering PNCPy, PNMPy, PNCPy/AuNP and PNMPy/AuNP modified GCE systems. PNCPy and PNMPy GCEs were prepared by depositing the CP on the GCE bare using CA. PNCPy/AuNP and PNMPy/AuNP modified GCEs were prepared by dropping the AuNPs colloidal solution (2 μL) onto the PNCPy and PNMPy modified GCE surface, respectively, and allowing dry under atmosphere conditions, this process being

repeated twice. CVs were recorded in the potential range from -0.40 to 0.80 V at a scan rate of 100 mV/s, scanning being stopped after 10 oxidation-reduction cycles. All the modified electrodes were in contact with the electrolyte solution for 10 min prior to the CV measurements.

QM calculations. Calculations were performed using the Gaussian 03[28] computer program. PNCPy and PNMPy were modelled considering small oligomers in the radical cation state (charge= +1 and spin multiplicity= 2) made of *n* repeating units (*n*-NCPy and *n*-NMPy, respectively, with *n*= 1, 2 and 3). DA was considered in its oxidized form DQ, in Figure 1). It is worth noting that the selection of DQ and the oxidized oligomers was based on our own experimental results (see Results and Discussion section), which indicate that at the detection potential the oxidation from DA to DQ has occurred and the polymer is oxidized. Although the length of the alkyl group has a negligible effect on the electronic properties of N-substituted PPy derivatives, as was found in recent studies on poly[N-(2-cyanoalkyl)pyrrole]s[29] and poly(N-hydroxyalkylpyrrole)s[30] bearing short alkyl groups (*i.e.* alkyl= methyl, ethyl and propyl), the ethyl group of PNCPy was considered explicitly because it may play a crucial role in the detection process.

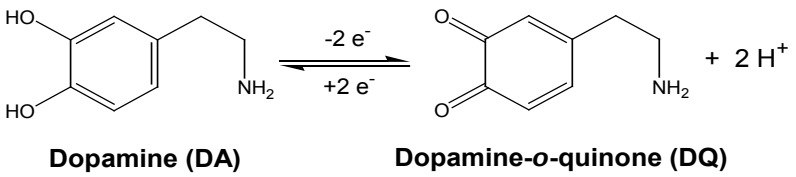

Figure 1. Electrochemical oxidation of DA to DQ.

The structures of the *n*-NMPy···DQ and *n*-NCPy···DQ complexes were determined by full geometry optimization in the gas-phase at the Hartree-Fock level using the 6-31+G(d,p) basis set.[31,32] Single point energy calculations were performed on the HF/6-31+G(d,p) geometries at the B3LYP/6-311++G(d,p) level.[33,34] The binding energy (ΔE_{int}) was calculated at the B3LYP/6-311++G(d,p) level as the difference between the total energy of the optimized complex and the energies of the isolated monomers with the geometries obtained from the optimization of the complex. The counterpoise (*CP*) method[35] was applied to correct the basis set superposition error from the ΔE_{int}.

4.4.3 Results and Discussion

Electropolymerization kinetics.

The kinetics of oxidation-polymerizations yielding PNCPy and PNMPy have been studied by electrogenerating films under a constant potential of 1.40 V and considering θ= 5, 10, 20, 30, 40, 50, 60 and 70 s. Figure 2 represents the variation of W_{ox} against Q_{pol} for the two PPy derivatives, each value of both Q_{pol} and W_{ox} corresponding to the average of three measures from independent experiments. The linear correlations showed regression coefficient R^2 larger than 0.98 in both cases, which is consistent with the existence of Faradaic processes. The slope of each plot, 0.411 and 0.355 mg·C^{-1} for PNCPy and PNMPy, respectively, corresponds to the current productivity, (m/Q), of the polymer. These values are significantly different from those obtained for micrometric films using identical experimental conditions but higher polymerization times (*i.e.* θ ranged from 300 to 1500 s): 0.531 and 0.619 mg·C^{-1} for PNCPy[16] and PNMPy,[36] respectively. Such differences affect not only the numerical values but also the relative order in the mass of polymer produced by Coulomb of charge consumed during the anodic polymerization process. These features are fully consistent with previous observations, which evidenced that the growing mechanism, morphology and properties of ultrathin films of CPs (*i.e.* those produced using $\theta \leq$ 70 s) are significantly different from those of micrometric thin films (*i.e.* $\theta \geq$ 300 s).[24,37,38]

The current productivities determined for nanometric PNMPy and PNCPy coatings were used to estimate the thickness of the films used for detection assays, which were produced using a θ= 3 s. The average thickness, which resulted from 12 independent measures, were ℓ= 54±11 nm and 78±14 nm for PNMPy and PNCPy, respectively. It should be noted that measurement of DA concentration in the brain is not an easy task due to the dimensions of the synapse. However, for both polymers the thickness of the films is smaller than the synapse diameter, ~ 100 nm.

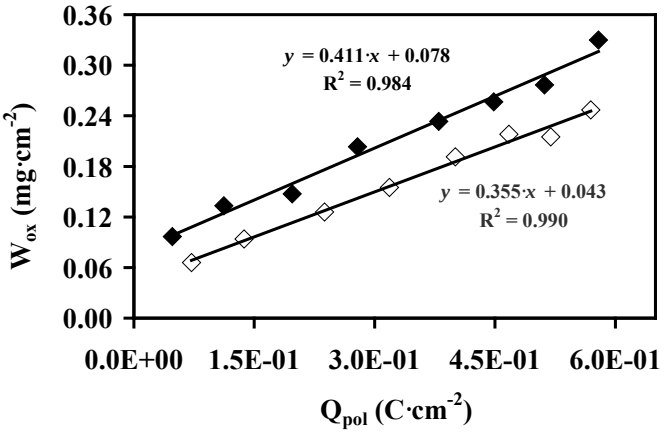

Figure 2. Variation of the Wox per unit of area of PNCPy (filled diamonds) and PNMPy (empty diamonds) deposited on stainless steel from 10 mM monomer solutions in acetonitrile with 0.1 M LiClO4 at a constant potential of 1.40 V, against the Qpol.

Detection of dopamine.

Control voltammograms of the neurotransmitter at isolated GCE and AuNP-modified GCE were reported in our previous study[12] and, therefore, they have not been repeated here. The electrochemical behavior of the DA in direct contact with the GCE was found to be less reversible than that with AuNP-modified GCE. Two oxidation peaks were observed for the latter in presence of DA at 0.43 and 0.56 V, which were attributed to the formation of a polaron and the oxidation of DA molecules to DQ (Figure 1), respectively. This enhancement of the electrochemical response of the DA was attributed to the catalytic role of the AuNPs: the electronic transference between the redox pair and the AuNPs provokes the lowering of the oxidation peak of the neurotransmitter.

Figure 3 shows CVs of PNMPy and PNMPy/AuNP modified GCEs in the absence and presence of DA concentrations ranging from 1 to 10 mM, while Figure 4 displays the results corresponding to the PNCPy and PNCPy/AuNP modified GCEs. Figures 5a and 5b represent the variation of the oxidation potential and the current density of the neurotransmitter against the DA concentration for the four systems. Results indicate that in both cases AuNPs improve the electrochemical oxidation response of the neurotransmitter. The oxidation potential of DA is clearly lower for the PNMPy/AuNP system than for the PNMPy without AuNPs (Figure 5a). This effect is not so evident when PNCPy/AuNP and PNCPy are compared, even though the oxidation peak is much more pronounced in the former than in the latter (Figure 4). On the other hand,

cathodic and anodic current densities are significantly higher for PNCPy/AuNP than for the PNCPy (Figure 5b). However, although detectable, this effect is much less pronounced for PNMPy-containing systems. This difference should be attributed to the fact that the interaction of AuNPs with PNCPy is better than with PNMPy, which is probably due to the combination of two effects: the higher roughness of former polymeric matrix[16] and the electron withdrawing behavior of the cyano group. In addition to the catalytic role mentioned above, the favorable effects produced by AuNPs in DA detection process should to be attributed to the fact that charge migration through PNMPy and PNCPy is facilitated by the charge hopping in the conductor AuNPs.[39]

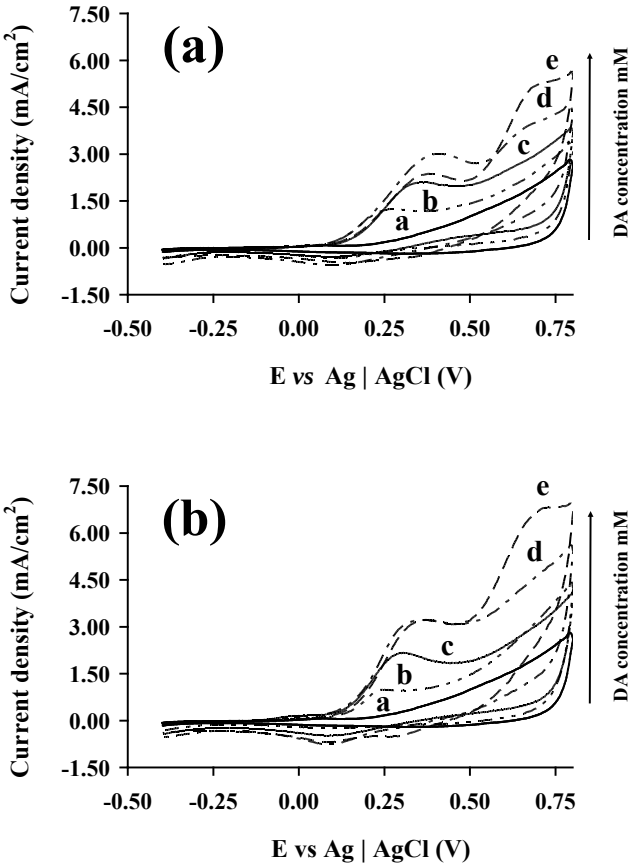

Figure 3. CVs for the oxidation of (a) PNMPy and (b) PNMPy/AuNP modified GCEs in the absence and presence of different DA concentrations (from 1 to 10 mM). Scan rate: 100 mV/s. Initial and final potential: -0.40 V; reversal potential: +0.80 V. For each graphic, labels a, b, c, d and e refer to DA concentrations of 0, 1, 3, 6 and 10 mM, respectively.

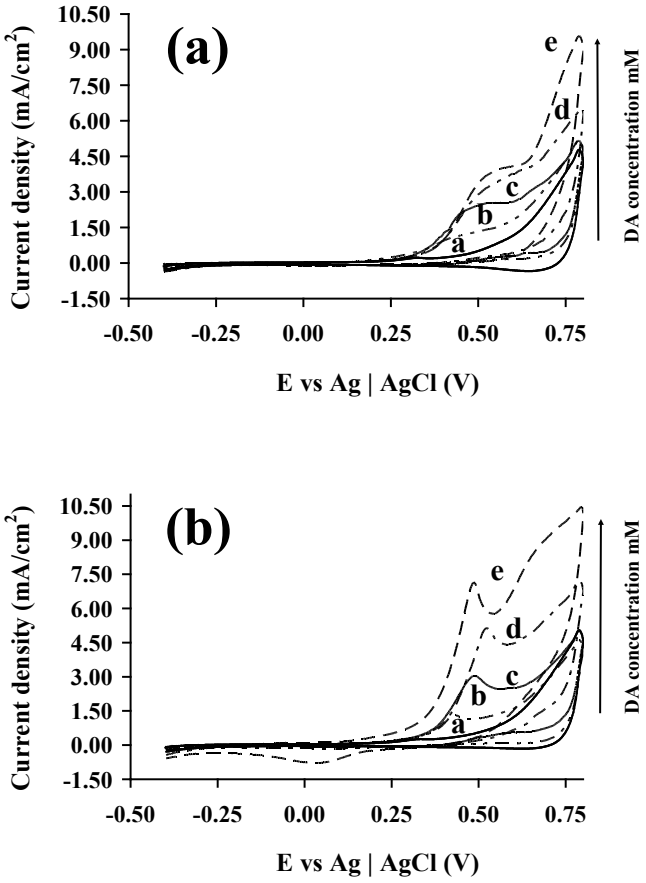

Figure 4. CVs for the oxidation of (a) PNCPy- and (b) PNCPy/AuNP-modified GCEs in the absence and presence of different DA concentrations (from 1 to 10 mM). Scan rate: 100 mV/s. Initial and final potential: -0.40 V; reversal potential: +0.80 V. For each graphic, labels a, b, c, d and e refer to DA concentrations of 0, 1, 3, 6 and 10 mM, respectively.

Comparing the oxidation and reduction processes, we evidence that the oxidation of DA is a not completely reversible process due to the polymerization of DA.[40] In spite of this, some reduction peaks, which should be attributed to the reduction of the CP chains, are observed. This behavior is evidenced by the anodic current density of the first oxidation peak, which is higher than the cathodic current density of the corresponding reduction peak. For the PNCPy modified GCE the current density ranges from 1.10 to 3.80 mA/cm^2 when the DA concentration ranges from 1 to 10 mM, while the cathodic current density of the corresponding reduction peak is of only ~ -0.1 mA/cm^2. In the case of PNCPy/AuNP modified GCE, there is no reduction peak in the CVs with exception of that recorded for a DA concentration of 10 mM, which shows a current density of -0.13 mA/cm^2. Additionally, the oxidation potential increases with the concentration of DA for the four modified electrode systems (Figure 5a). This behavior is very evident for concentrations up to 6 mM but practically

inexistent when DA increases from 6 to 10 mM, which should be attributed to the saturation of the electrode. Thus, after a threshold (6 mM), the accumulation of oxidized DA molecules in the surface makes difficult, or even precludes, the oxidation of other neurotransmitter molecules.

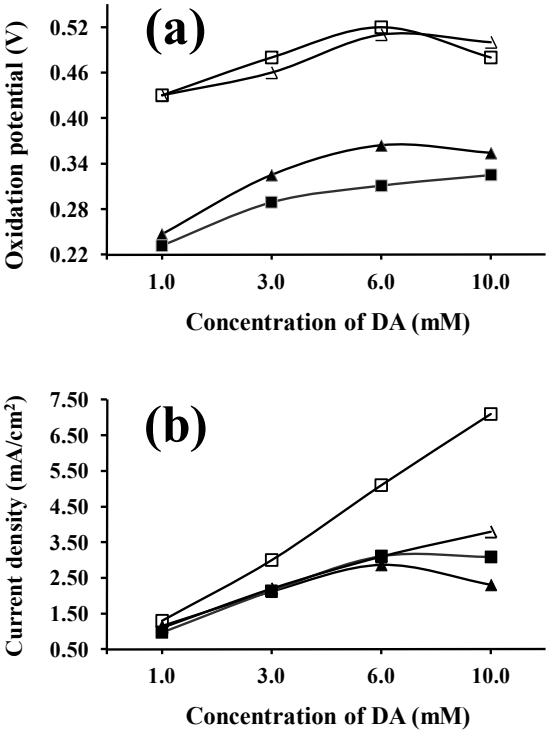

Figure 5. Variation of (a) the oxidation potential and (b) the current density for the oxidation peak of DA against the neurotransmitter concentration measured using PNMPy (filled triangles), PNMPy/AuNP (filled squares), PNCPy (empty triangles) and PNCPy/AuNP modified GCEs (empty squares).

Figures 3b and 4b show the presence of a second oxidation peak (0.67 and 0.65 V, respectively) and the corresponding reduction peak (0.30 and 0.52 V, respectively) when the concentration of DA is 10 mM. The same behavior is also displayed by the PNMPy system for concentrations of 6 and 10 mM (Figure 3a), whereas such second peak is not observed in the voltammograms recorded using the PNCPy modified GCE. The second peak has been attributed to the oxidation of DQ molecules to dopaminechrome (DC in Figure 6).[41]

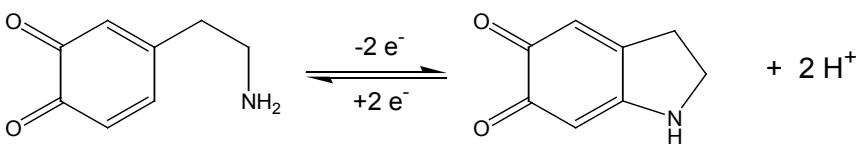

Dopamine-*o*-quinone (DQ) **Dopaminechrome (DC)**

Figure 6. Electrochemical oxidation of DQ to DC.

In a previous study, we reported that PNCPy films prepared by CA under a constant potential of 1.40 V undergo, upon reduction, an oxidative process in some Py rings.[16] As a consequence of this process, a carbonyl group appears in such rings. This overoxidation process is typically found in PPy derivatives, included PNMPy.[42,43] The onset of overoxidation of PPy derivatives is typical observed at ~1.30 V.[16,42,43] As the CVs used for DA detection were recorded in the potential range from -0.40 to 0.80 V, the proportion of oxidized five membered rings is expected to be considerably low. Accordingly, although the C=O groups may attract oxidized DA molecules, this interaction has been neglected in our subsequent modeling studies (see below).

Stability and limit of detection.

Figure 7 displays the control voltammograms recorded for 10 consecutive oxidation-reduction cycles of PNMPy/AuNP and PNCPy/AuNP systems in presence of a concentration of DA equal to 10 mM. For the two modified electrodes, the DA oxidation peak moves towards higher potentials when the number of oxidation-reduction cycles increases, whereas the current density decreases significantly. Furthermore, the cathodic and anodic areas decrease when the number of cycles increases, the electroactivity determined for the 10^{th} cycle being about 52-54 % lower than that of the first one. Accordingly, the electrostability showed by two AuNP containing CP films was relatively low. Figure 8 represents the variation of the loss of electroactivity (LEA) after 10 consecutive redox cycles for the PNMPy, PNMPy/AuNP, PNCPy and PNCPy/AuNP modified GCEs against the concentration of DA. As it can be seen, the loss of electroactivity decreases when the DA concentration increases. Although the behavior of the four systems is very similar, the electrostability of the electrodes modified with PNCPy is slightly higher than that of the coatings with PNMPy, independently of the presence or absence of AuNPs. Moreover, differences are more remarkable for DA concentrations lower than 6 mM.

Figure 9a shows the response of the PNMPy and PNMPy/AuNP modified GCEs in presence of a 100 μM DA concentration. Oxidation of DA molecules is immediately detected by the latter system (0.19 V and 0.30 mA/cm^2), whereas two consecutive oxidation-reduction cycles are required for the electrode without AuNPs. In contrast the oxidation peak at 0.37 V is clearly detected by both PNCPy and PNCPy/AuNP

systems (Figure 9b). These results combined with those previously displayed (Figures 3-9) indicate that, although the two CPs allow the detection of very low concentration of DA (*i.e.* lower than that estimated for the synapse), the response of the PNCPy is better and more effective than the response of PNMPy.

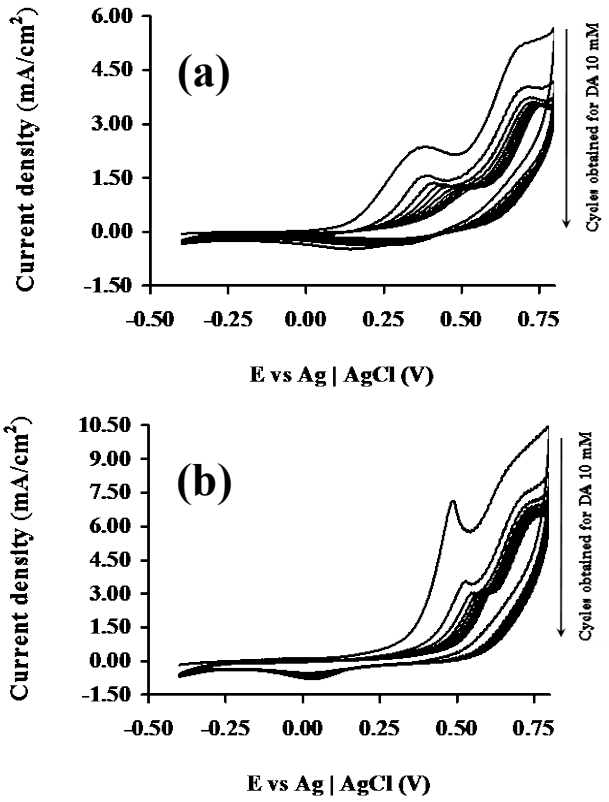

Figure 7. Control voltammograms for 10 consecutive oxidation-reduction cycles of (a) PNMPy/AuNP and (b) PNCPy/AuNP modified GCEs in presence of 10 mM DA.

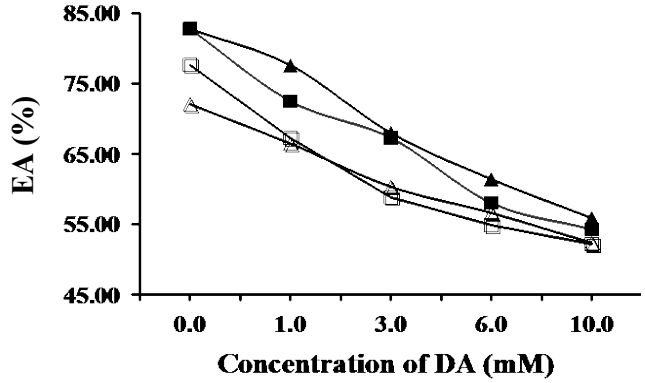

Figure 8. Variation of EA after 10 consecutive oxidation-reduction cycles for PNMPy (filled triangles), PNMPy/AuNP (filled squares), PNCPy (empty triangles) and PNCPy/AuNP modified GCEs (empty squares) against the DA concentration

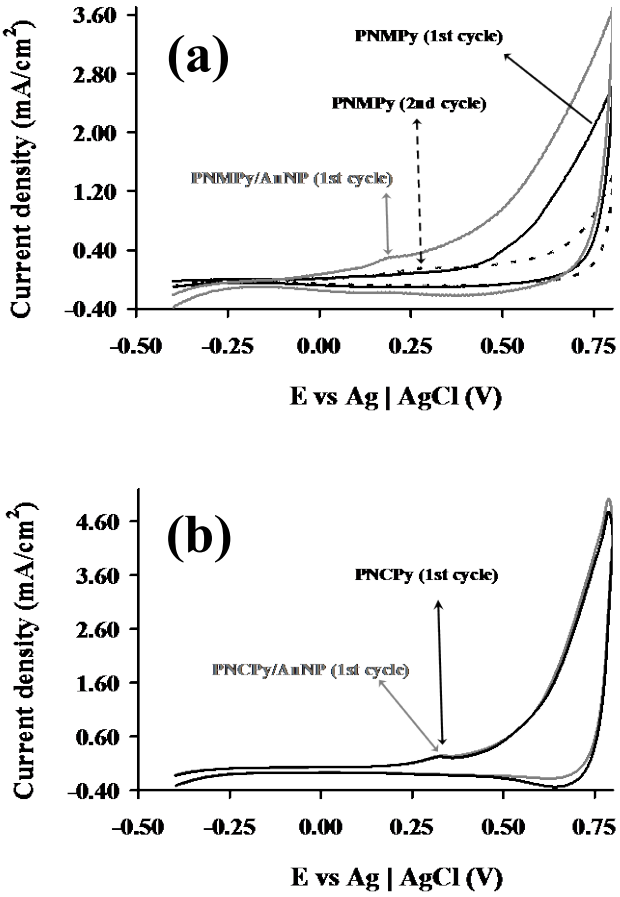

Figure 9. CVs for the oxidation of (a) PNMPy and PNMPy/AuNP modified GCEs and (b) PNCPy and PNCPy/AuNP modified GCE in presence of a 100 μM DA concentration. Scan rate: 100 mV/s. Initial and final potential: -0.40 V; reversal potential: +0.80 V. The second consecutive oxidation-reduction cycle is also displayed for the PNMPy modified GCE.

Modeling of the interaction PNMPy···DQ.

The interaction between PNMPy and the oxidized DA was modeled using a build-up scheme. Specifically, the interaction between 1-NMPy and DQ was examined in a first stage, the resulting complexes being used to construct the starting structures for 2-NMPy···DQ. Finally, starting arrangements for 3-NMPy···DQ were constructed using the optimized structures of 2-NMPy···DQ.

Geometry optimizations of 40 starting structures led to 17 1-NMPy···DQ complexes, which were categorized in four groups according to the interaction patterns. The most stable structure of each group is displayed in Figure 10a. As it can be seen, complexes 1-Ma, 1-Mb and 1-Mc are stabilized by interactions involving the C-H moieties of the Py ring and the oxygen atoms of DQ, whereas the two rings interact through a π-π stacking in complex I-Md. The C-H···O contacts with a H···O

distance (d_{H-O}) lower than 2.65 Å are explicitly indicated in Figure 10a. The most stable arrangement corresponds to 1-Ma, the relative energy (ΔE) of 1-Mb, 1-Mc and 1-Md calculated at the B3LYP/6-311++G(d,p) level being 2.9, 15.5 and 26.2 kcal/mol. Inspection to the ΔE_{int} between 1-NMPy and DQ, which are listed in Table 1, indicate C-H···O interactions are significantly more attractive than the π-π stacking (*i.e.* ~ 17 kcal/mol).

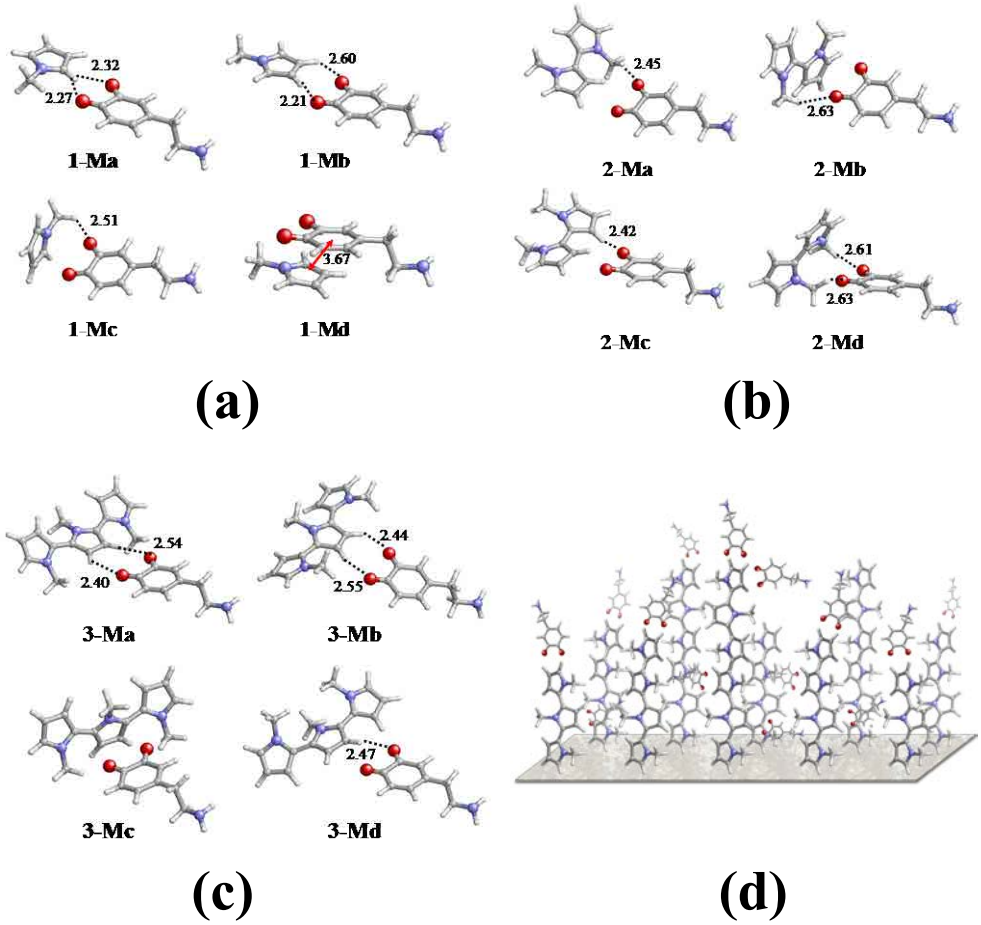

Figure 10. Four structures of lower energy derived from QM calculations for (a) 1-NMPy···DQ, (b) 2-NMPy···DQ and (c) 3-NMPy···DQ complexes. (d) Atomistic model proposed for the detection of DA by PNMPy.

The four structures selected for the 1-NMPy···DQ complex were used to construct eight starting structures of 2-NMPy···DQ by adding a new NMPy repeating unit to 1-NMPy, both *trans* and *cis* arrangements being considered for the inter-ring dihedral angle (*i.e.* θ_A= 180º and θ_B= 0º, respectively). The four structures of lower energy obtained after geometry optimization are displayed in Figure 10b. As it can be seen, the four complexes are essentially stabilized by intermolecular C-H···O interactions. It should be noted that in the past fifteen years, a multitude of close

contacts between the C-H group and the electronegative oxygen atom were identified as hydrogen bonds, this interaction being found in an enormous variety of chemical systems.[44-49] According to the literature, the thresholds chosen for the distance in C-H···O stabilizing hydrogen bonds was ~ 2.6 Å. It should be noted that although C-H···O interactions play a crucial role in the detection of oxidized DA, their chemical nature (*i.e.* hydrogen bonds or van der Waals contacts) is out of the scope of this work. The θ_A and θ_B in the two complexes of lower energy, 2-Ma and 2-Mb, corresponds to an *anti-gauche*$^-$ conformation (~ -160^o), while structures with the 2-NMPy molecule arranged in *syn-gauche*$^+$ (~ +20^o), 2-Mc and 2Md, are destabilized by around 4-5 kcal/mol with respect to the global minimum. On the other hand, ΔE_{int} values are relatively similar in the four complexes, ranging from -13.5 to -14.6 kcal/mol. The reduction in the ΔE_{int} values with respect to those obtained for 1-NMPy···DQ complexes, is consistent with the fact that the d_{H-O} values are shorter in the latter than in 2-NMPy···DQ.

Complex	ΔE (Kcal/mol)	ΔE_{int} (Kcal/mol)	θ_A (º)	θ_B (º)
1-Ma	0.0[a]	-21.9		
1-Mb	2.9	-16.5		
1-Mc	15.5	-20.6		
1-Md	26.2	-2.6		
2-Ma	0.0[b]	-13.8	-164.0	
2-Mb	2.4	-13.7	-163.5	
2-Mc	4.4	-13.5	21.2	
2-Md	5.4	-14.6	23.2	
3-Ma	0.0[c]	-12.3	158.9	-159.9
3-Mb	1.8	-12.8	159.0	-159.9
3-Mc	3.3	-11.3	-158.7	157.8
3-Md	8.2	-11.6	22.5	-37.6-

[a] E= -764.856211 a.u. [b] E= -1013.243780 a.u. [c] E= -1261.612486 a.u

Table 1. Relative energy, binding energy and inter-ring dihedral angles of the four structures of lower energy calculated for *n*-NMPy···DQ complexes, where *n* ranges from 1 to 3. Molecular geometries have been obtained at the HF/6-31+G(d,p) level, while ΔE and ΔE_{int} were derived from single point calculations at the B3LYP/6-311++G(d,p) level.

The four structures displayed in Figure 10b for the 2-NMPy···DQ complex were used to built the starting structures of 3-NMPy···DQ using the procedure previously described (*i.e.* the third repeating unit was added to the 2-NMPy molecule considering both the *trans* and *cis* arrangements for the θ_B). The four structures of lower energy,

which expand within a ΔE interval of 8.2 kcal/mol, are displayed in Figure 10c. The two θ_A and θ_B of the three structures of lower energy, 3-Ma, 3-Mb and 3-Mc, which only differ in 3.3 kcal/mol, adopt *anti-gauche* arrangements. In contrast, structure 3-Md shows two consecutive *syn-gauche* rotamers, which result in a destabilization of 4.9 kcal/mol with respect to 3-Mc.

The ΔE_{int} values range from -11.3 to -12.8 kcal/mol confirming that the strength of the interaction decreases with the length of the polymer chain. The overall of the calculations on *n*-NMPy···DQ complexes indicate that PNMPy detects oxidized DA molecules mainly through the formation of C-H···O interactions. The C-H moieties involved in such interactions belong to the rigid Py rings or to the methyl (Met) groups, whose deformability is null or very limited. Accordingly, the strength interaction is determined by the molecular rigidity of both the polymer chains and the neurotransmitter. Figure 10d provides a schematic representation of the model proposed to explain the detection of DQ by PNMPy.

Modeling of the interaction PNCPy···DQ.

The structures displayed in Figures 11a-11c for *n*-NMPy···DQ complexes were modified by replacing the Met by the cyanoethyl at the N-position of each Py ring, being subsequently used as starting structures for geometry optimization of *n*-NCPy···DQ complexes. The optimized structures of 1-NCPy···DQ are displayed in Figure 11a while their corresponding ΔE and ΔE_{int} values are listed in Table 2. As it can be seen, C-H···O interactions are more important than in 1-NMPy···DQ complexes, which explains the reduction of the ΔE interval with respect to the latter. This feature is particularly evident in 1-Ca, in which the C-H···O interactions involving the Py ring (with $d_{H-O} < 2.40$ Å) are reinforced by other attractive C-H···O contacts produced by the two methylene units. On the other hand, ΔE_{int} values indicate that the binding with DQ is stronger for 1-NCPy than for 1-NMPy. The four 2-NCPy···DQ complexes are displayed in Figure 11b while ΔE and ΔE_{int} values are listed in Table 2. As it can be seen, the 2-NCPy tends to surround the DQ favoring the formation of attractive van der Waals interactions in the four structures. This interaction pattern is consistent the fact that the ΔE interval expands by less than 1 kcal/mol. The binding of DQ with 2-NCPy is

about 4-5 kcal/mol more favorable than with 2-NMPy. Thus, the flexibility of the cyanoethyl group, which participates actively in the interaction with DQ, avoids a significant the reduction of ΔE_{int} when *n* grows from 1 to 2. It should be noted that the opposite behavior was predicted for *n*-NMPy···DQ complexes (Table 1), where ΔE_{int} increases considerably with *n*.

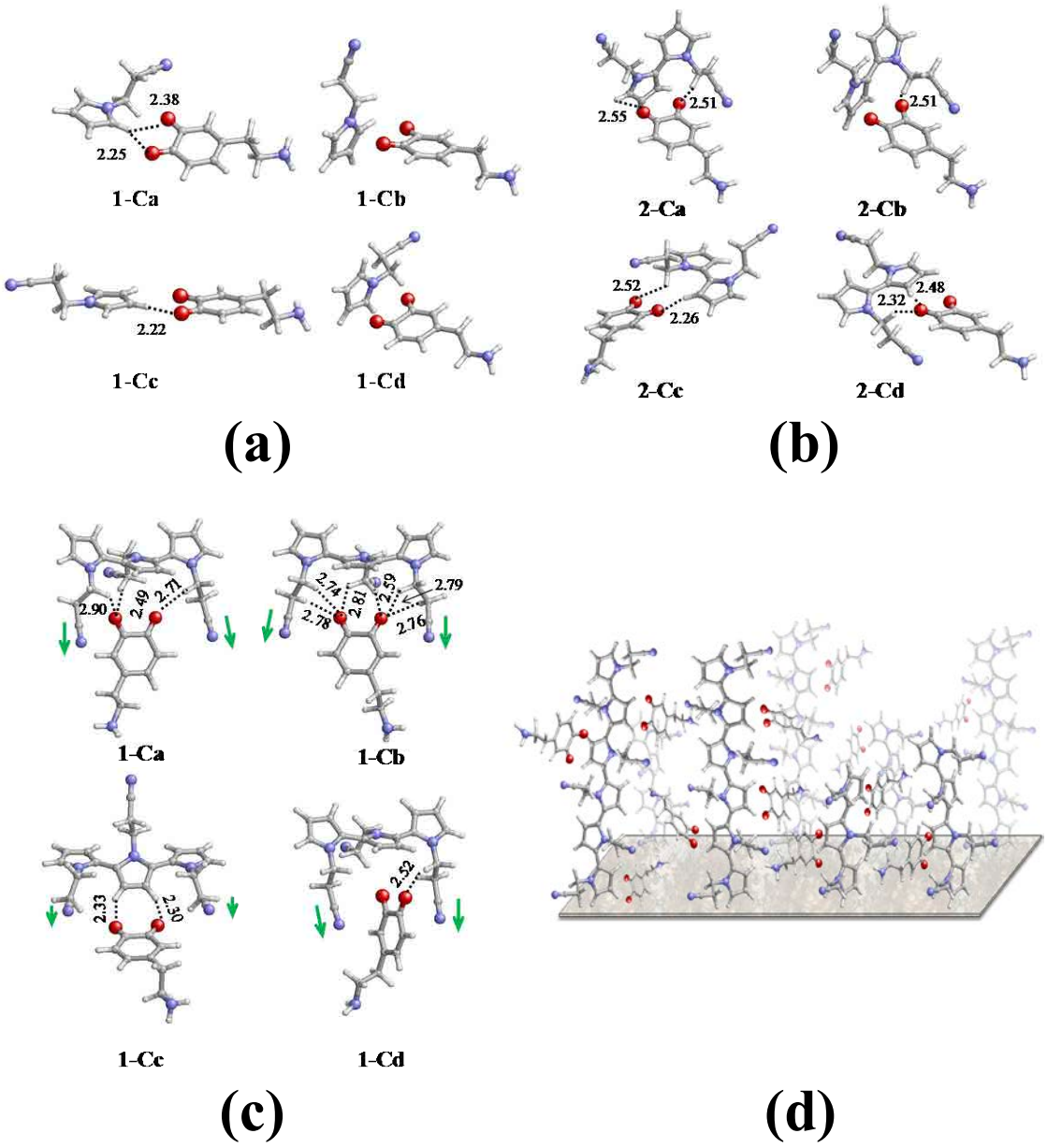

Figure 11. Structures derived from QM calculations for (a) 1-NCPy···DQ, (b) 2-NCPy···DQ and (c) 3-NCPy···DQ complexes. (d) Atomistic model proposed for the detection of DA by PNCPy.

Complex	ΔE (Kcal/mol)	ΔE_{int} (Kcal/mol)	θ_A (º)	θ_B (º)
1-Ca	0.0[a]	-24.3		
1-Cb	2.1	-22.2		
1-Cc	5.3	-19.1		
1-Cd	14.2	-19.6		
2-Ca	0.0[b]	-16.0	159.0	
2-Cb	0.1	-19.1	157.1	
2-Cc	0.3	-16.4	-166.4	
2-Cd	0.9	-17.1	163.3	
3-Ca	0.0[c]	-19.1	158.6	-158.0
3-Cb	0.1	-19.2	158.9	-159.1
3-Cc	0.8	-17.7	-155.7	157.3
3-Cd	1.8	-17.2	152.1	-155.5

[a] E= -896.434644 a.u. [b] E= -1276.398028 a.u. [c] E= -1656.350539 a.u

Table 2. Relative energy, binding energy and inter-ring dihedral angles of the four structures calculated for *n*-NCPy···DQ complexes, where *n* ranges from 1 to 3. Molecular geometries have been obtained at the HF/6-31+G(d,p) level, while ΔE and ΔE_{int} were derived from single point calculations at the B3LYP/6-311++G(d,p) level.

Finally, Figure 11c depicts the optimized structures of 3-NCPy···DQ, which confirm the trends previously observed for 2-NCPy···DQ. Thus, the four structures are comprised within a ΔE interval of 1.8 kcal/mol only and ΔE_{int} values, which are similar to those obtained for 2-NCPy···DQ, indicate that DQ forms stronger interactions with 3-NCPy than with 3-NMPy. Thus, the cyanoethyl groups wrap the DQ molecule forming many attractive C-H···O interactions that stabilize the complex. In addition, the orientation adopted by the cyano groups allows the formation of attractive dipole-dipole interactions with the C=O bonds of the DQ molecule. These interactions are explicitly represented in Figure 11c using green arrows. On the other hand, Figure 11d describes the model proposed for the interaction between PNCPy and oxidized DA, which is based on the flexibility provided by the methylene units of the substituent at the N-position of the polymer. It is worth noting that the models provided in Figures 10d and 11d are fully consistent with the experimental observations reported in the previous sections. Thus, the relative efficacy of PNCPy and PNMPy as DA detectors is explained by the fact that the interactions of the former polymer are stronger than those of the latter, which in turn is consequence of the flexibility of the cyanoethyl group.

4.4.4 Conclusions

Nanometric films of PNMPy and PNCPy have been used to examine and compare the abilities of these two CPs to detect small concentrations of DA. Control voltammograms for the oxidation of PNMPy, PNCPy, PNMPy/AuNP and PNCPy/AuNP modified GCEs in presence of DA concentrations ranging from 100 μM to 10 mM evidenced the sensing abilities of both polymers. AuNPs, which interact more favourably with PNCPy than with PNMPy, enhance the electronic transference and the charge migration processes of the DA oxidation. In spite of this, AuNPs are not essential for the detection because of the powerful sensing abilities showed by both PNCPy and PNMPy. The response of the two polymers against a DA concentration of only 100 μM, which is significantly lower than the concentration found in the synapse (1.6 mM), were crucial to discern that the electrochemical response of the PNCPy is more effective than that of PNMPy and facilitating the possible application of these materials to biomedical applications.

QM calculations allowed us to propose atomistic models that explain the interaction of oxidized DA with PNMPy and PNCPy systems. Calculations on *n*-NMPy···DQ and *n*-NCPy···DQ complexes with *n* ranging from 1 to 3 indicate that C-H···O interactions play a crucial role in the detection process. The strength of the interaction between the *n*-NMPy and DQ molecules decreases when *n* increases. Thus, the low deformability of the Met group precludes the re-accommodation of the oxidized DA molecule without energy penalty when the length of the *n*-NMPy increases. This limitation is also reflected by the distances between the interacting atoms, $d_{H\text{-}O}$, which grow with *n*. These features allow us to conclude that, although PNMPy interacts very satisfactorily with DA molecules, the molecular rigidity of this polymer limits the detection process with respect to other materials. In contrast, analysis of the calculated *n*-NCPy···DQ complexes indicate that the flexibility of the cianoethyl group favours not only the rearrangement of the interacting molecules when *n* increases but also the maximization of the number of attractive C-H···O intermolecular interactions. Consequently, calculations predict that PNCPy interacts more strongly with DQ than PNMPy, which is fully consistent with experimental observations.

4.4.5 References

1. E. R. Kandel, J. H. Schwartz and T. M. Jessel, *Principles of Neural Science*, New York, McGraw-Hill, 4th Edn, 2000, pp. 207–298.

2. B. J. Venton and R. M. Wightman, *Anal. Chem.*, 2003, **75**, 414A.

3. K. J. Powell, *Cell Biol.,* 2005, **170**, 166.

4. B. D. Bath, H. B. Martin, R. M. Wightman and M. R. Anderson, *Langmuir,* 2001, **17**, 7032.

5. B. J. Venton, K. P. Troyer and R. M. Wightman, *Anal. Chem.,* 2002, **74**, 539.

6. C. R. Raj and T. J. Ohsaka, *Electroanal. Chem.,* 2001, **496**, 44.

7. L. Zhang, J. Jia, X. Zou and S. Dong, *Electroanalysis,* 2004, **16**, 1413

8. V. S. Vasantha and S.-M. Chen, *J. Electroanal. Chem.,* 2006, **592**, 77.

9. K. Pihel, Q. D. Walker and R. M. Wightman, *Anal. Chem.,* 1996, **68**, 2084.

10. C. C. Harley, A. D. Rooney and C. B. Breslin, *Sensors and Actuators B,* 2010, **150**, 498.

11. S. Shahrokhian and H. R. Zare-Mehrjardi, *Electroanalysis*, 2001, **21**, 157.

12. M. Martí, G. Fabregat, F. Estrany, C. Alemán and E. Armelin, *J. Mat. Chem.,* 2010, **20**, 10652.

13. X. Feng, C. Mao, G. Yang, W. Hou and J. J. Zhu, *Langmuir,* 2006, **22**, 4384.

14. J. Mathiyarasu, S. Senthikumar, K. L. N. Phani and V. Yegnaraman, *J. Appl. Electrochem.,* 2005, **35**, 513.

15. J. Mathiyarasu, S. Senthikumar, K. L. N. Phani and V. Yegnaraman, *J. Nanosci. Nanotech.*, 2007, **7**, 2206.

16. D. Aradilla, F. Estrany, E. Armelin, R. Oliver and J. I. Iribarren, *Macromol. Chem. Phys.,* 2010, **211**, 1663.

17. Z. Deng, D. C. Stone and M. Thompson, *Can. J. Chem.* 1995, **73**, 1427.

18. Z. Deng, D. C. Stone and M. Thompson, *Analyst.,* 1997, **122**, 1129.

19. Z. Deng, D. C. Stone and M. Thompson, *Analyst.,* 1996, **121**, 1341.

20. O. Ouerghi, A. Senillou, N. Jaffrezic-Renault, C. Martelet, H. Ben Ouada and S. Cosnier, *J. Electroanal. Chem.,* 2001, **501**, 62.

21. A. Naji, C. Marzin, G. Tarrago, M. Cretin, C. Innocent, M. Perzin and J. Sarrazin, *J. Appl. Electrochem.,* 2001, **31**, 547.

22. M. Schirmeisen and F. J. Beck, *J. Appl. Electrochem.,* 1989, **19**, 401.

23. R. Oliver, A. Muñoz, C. Ocampo, C. Alemán and F. Estrany, *Chem. Phys.,* 2006, **328**, 299.

24. D. Aradilla, F. Estrany, R. Oliver and C. Alemán, *Eur. Polym. J.,* 2010, **46**, 2222.

25. E. K. Richfield, J. B. Penney and A. B. *Young, Neuroscience,* 1989, **30**, 767.

26. R. G. Freeman, M. B. Hommer, K. C. Grabar, M. A. Jackson and M. J. Natan, *J. Phys. Chem.,* 1996, **100**, 718.

27. M. M. Maye, L. Han, N. N. Kariuki, N. K. Ly, W. B. Chan and C. J. Zhong, *Anal. Chim. Acta,* 2003, **496**, 17.

28. Gaussian 03, Revision B.02, M. J. Frisch, G. W. Trucks, H. B. Schlegel, G. E. Scuseria, M. A. Robb, J. R. Cheeseman, J. A. Montgomery, T. Vreven, K. N. Kudin, J. C. Burant, J. M. Millam, S. S. Iyengar, J. Tomasi, V. Barone, B. Mennucci, M. Cossi, G. Scalmani, N. Rega, G. A. Petersson, H. Nakatsuji, M. Hada, M. Ehara, K. Toyota, R. Fukuda, J. Hasegawa, M. Ishida, T. Nakajima, Y. Honda, O. Kitao, H. Nakai, M. Klene, X. Li, J. E. Knox, H. P. Hratchian, J. B. Cross, V. Bakken, C. Adamo, J. Jaramillo, R. Gomperts, R. E. Stratmann, O. Yazyev, A. J. Austin, R. Cammi, C. Pomelli, J. W. Ochterski, P. Y. Ayala, K. Morokuma, G. A. Voth, P. Salvador, J. J. Dannenberg, V. G. Zakrzewski, S. Dapprich, A. D. Daniels, M. C. Strain, O. Farkas, D. K. Malick, A. D. Rabuck, K.

Raghavachari, J. B. Foresman, J. V. Ortiz, Q. Cui, A. G. Baboul, S. Clifford, J. Cioslowski, B. B. Stefanov, G. Liu, A. Liashenko, P. Piskorz, I. Komaromi, R. L. Martin, D. J. Fox, T. Keith, M. A. Al-Laham, C. Y. Peng, A. Nanayakkara, M. Challacombe, P. M. W. Gill, B. Johnson, W. Chen, M. W. Wong, C. Gonzalez and J. A. Pople, Gaussian, Inc., Wallingford CT, 2004.

29. D. Aradilla, J. Torras and C. Alemán, *J. Phys. Chem. B,* 2011, **115**, 2882.

30. J. Casanovas, L. Y. Cho, C. Ocampo and C. Alemán, *Synth. Met.,* 2005, **151**, 239.

31. P. C. Hariharan and J. A. Pople, *Theor. Chim. Acta,* 1973, **28**, 213.

32. A. D. McLean and G. S. Chandler, *J. Chem. Phys.,* 1980, **72**, 5639.

33. K. Burke, J. P. Perdew and Y. Wang, *In Electronic Density Functional Theory: Recent Progress and New Directions*; J. F. Dobson, G. Vignale and M. P. Das, Eds. Plenum Press: New York, 1998, pp 81-111.

34. M. J. Frisch, J. A. Pople and J. S. Binkley, *J. Chem. Phys.,* 1984, **80**, 3265.

35. S. F. Boys and F. Bernardi, *Mol. Phys.,* 1970, **19**, 553.

36. C. Ocampo, C. Alemán, R. Oliver, M. L. Arnedillo, O. Ruíz and F. Estrany, *Polym. Int.,* 2007, **56**, 803.

37. F. Estrany, D. Aradilla, R. Oliver, E. Armelin and C. Alemán, *Eur. Polym. J.,* 2008, **44**, 1323.

38. D. Aradilla, F. Estrany, E. Armelin and C. Alemán, *Thin Solid Films,* 2010, **518**, 4203.

39. X. Feng, C. Mao, G. Yang, W. Hou and J. J. Zhu, *Langmuir,* 2006, **22**, 4384.

40. P. Wei, F. Zhang, J. Li, B. Li and C. Zhao, *Polym. Chem.,* 2010, **1**, 1430.

41. F. Yu, S. Chen, Y. Chen, H. Li, L. Yang, Y. Chen and Y. Yin, *J. Mol. Struct.,* 2010, **982**, 152.

42. M. Skompska and M. A. Vorotyntsev, *J. Solid. State Electrochem.,* 2004, **8**, 360.

43. I. Fernández, M. Trueba, C. A. Nuñez and J. Rieumont, *Surf. Coat. Technol.,* 2005, **191**, 134.

44. G. R. Desiraju, *Acc. Chem. Res.,* 1996, **29**, 441.

45. T. Steiner, *J. Phys. Chem. A*, 2000, **104**, 433.

46. E. S. Meadows, S. L. De Wall, L. J. Barbour, F. R. Fonczek, M.-S. Kim and G. W. Gokel, *J. Am. Chem. Soc.,* 2000, **122**, 3325.

47. A. Ghosh and M. Bansal, *J. Mol. Biol.,* 1999, **294**, 1149.

48. K. N. Houk, S. Menzer, S. P. Newton, F. M. Raymo, J. F. Stoddart and D. J. Williams, *J. Am. Chem. Soc.*, 1999, **121**, 1479.

49. C. Alemán, J. Casanovas, D. Zanuy and Jr. H. K. Hall, *J. Org. Chem.,* 2005, **70**, 2950.

4.5 Selective Electrochemical Detection of Dopamine Combining Multilayers of Conducting Polymer with Gold Nanoparticles*

Electrodes based on the combination of 3-layered films formed by two different CPs and AuNPs have been developed for the selective voltammetric determination of dopamine in mixtures with ascorbic acid (AA) and uric acid (UA) and human urine samples with real interferents. Voltammetric studies of solution mixtures indicate that electrodes formed by alternated layers of PEDOT (internal and external layer) and PNMPy (intermediate layer) show the best performance in term of sensitivity and resolution. Furthermore, the sensitivity of such 3-layered electrode increases only slightly after coating its surface with AuNPs, indicating that the catalytic effect typically played by AuNPs in the oxidation of DA is less effective in this case. Electrochemical pre-treatments based on the application of consecutive oxidation-reduction cycles to electrodes before of the detection process have been found to improve the selectivity without alter the sensitivity. On the other hand, the flux of DA to the 3-layered surface increases linearly with the scan rate. The detection limit for these electrodes is around 10 μM DA in mixtures with UA and AA, decreasing to 2-3 μM in absence of such interferents. The utility of 3-layered electrodes as sensors has been also demonstrated by determining DA in human samples with real interferents.

*Results described in this section has been accepted for publication in *J. Phys. Chem. B.*

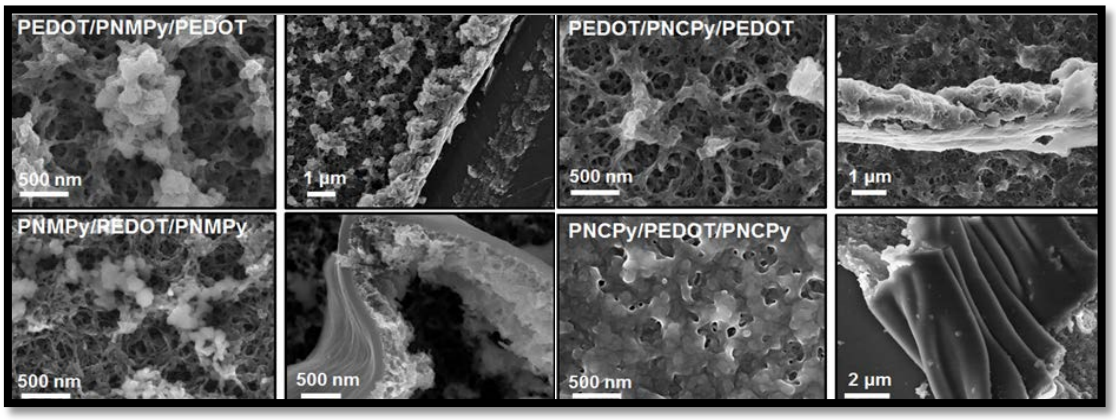

4.5.1 Introduction

AuNPs have potential applications in the construction of electrochemical sensors and biosensors due to their advantages of enhanced diffusion, good stability and biocompatibility in biomolecules detection, high effective surface area, improved selectivity and sensitivity, outstanding electrocatalytic activity, good conductivity, and high signal-to-noise ratio.[1-6] AuNPs act channeling electrons between the electrode and the electroactive species promoting better electron transfer between the electrode surface and the electrolyte.[5] Electrochemical sensors based on AuNPs alone or dispersed on a variety of substrates have been used for the determination of different species, such as carcinoembryonic antigen,[7] proteins,[8] neurotransmitters[9-11] and metallic ions.[12,13]

CPs with π-conjugated backbones, which represent a particularly intriguing type of environment for AuNPs due to their remarkable electronic and optical properties, have been used to prepare metallic-organic nanocomposites with multiple applications.[14-17] Several kinds of chemical and electrochemical methods have been used to prepare CP-AuNPs composites.[17] Generally, chemical methods involve the in situ reduction of AuNPs in the polymer matrix or the preparation of the AuNPs followed by the chemical polymerization of the CP around the particles. For example, the former strategy has been used to obtain nanocomposites with PAni[18] and PEDOT[19], where the corresponding monomers acted as reductant species, while the second procedure has been used to prepare PPy by adding the monomer after the AuNPs were synthesized.[20] Electrochemical methods are based on the oxidation of individual monomers, the incorporation of metallic species occurring via deposition in the same or a subsequent step. Electrochemical synthesis has been successfully used to incorporate AuNPs in the matrix of different PTh derivatives.[21,22] Composites made of AuNPs coating the surface of CP films, hereafter denoted CP/AuNP, have also been prepared by electrochemical deposition[23,24] or simply by dropping of an AuNPs colloidal solution onto the film.[10,11]

CP/AuNP composites have been successfully used to detect DA,[10,11,24] which is an important neurotransmitter of catecholamine in the human brain.[25] The very low concentration of DA in the extracellular fluid[26] provides a huge challenge for the

detection of this analyte. The temporal fluctuation of the DA concentration in the human brain has a critical effect on several neurological disorders such as Harrington's disease and Parkinson disease. Electrochemical sensors are among the most convenient methods for the detection of DA because of their reliability for the rapid determination of analytes. DA concentrations significantly lower than the synaptic one (1.6 mM) were recently detected using PNMPy/AuNP[10] and PNCPy/AuNP[11] deposited on glassy carbon electrodes. More recently, PEDOT/AuNP gold electrodes were used for the selective determination of very low DA concentrations in presence of UA and AA.[15,24]

On the other hand, in recent studies we investigated the properties of multilayered systems formed by two, or even more, CPs.[27-32] More specifically, we found that multilayered materials prepared using the LbL electrodeposition technique show better electrochemical properties and higher ability to store charge than each of the individual CPs. This improvement is due to a synergistic effect produced by favorable interactions at the interfaces, which increase with the structural differences between the CPs (*i.e.* in terms of morphology, porosity and roughness). Within this context, properties of multilayered films made of alternated PEDOT and PNMPy, or even unsubstituted PPy, nanometric layers were found to be particularly enhanced with respect to those of the corresponding individual polymers.[29,30,32]

The present study reports on the first development of advanced sensing templates fabricated by combining multilayers of CPs with an AuNPs coating, which have been used to enhance the electrochemical detection of DA in presence of interferents such as UA and AA. More specifically, the sensitivity and resolution of eight different 3-layered systems fabricated by combining PEDOT with PNMPy or PNCPy have been tested as electrochemical sensors as prepared and coated with AuNPs, results being compared with those obtained for the individual CPs. The effects of AuNPs, consecutive oxidation-processes, presence/absence of interferents and scan rate in the selectivity, sensitivity and limit of detection of DA at the 3-layered electrodes with the best performance have been exhaustively examined. Furthermore, the ability of 3-layered films coated with AuNPs as electrodes for DA detection has been demonstrated by direct analysis in human urine samples.

4.5.2 Methods

Materials. EDOT, NMPy, NCPy, acetonitrile, $LiClO_4$, DA hydrochloride , AA (L-configuration, crystalline), UA (crystalline) and $HAuCl_4 \cdot 3H_2O$ of analytical reagent grade were purchased from Sigma-Aldrich (Spain), whereas sodium citrate dehydrate was obtained from J. T. Baker. All chemicals were used without further purification. PBS 0.1 M with pH= 7.4 was prepared as electrolyte solution by mixing four stock solutions of NaCl, KCl, $NaHPO_4$ and KH_2PO_4. High-purity nitrogen was used for de-aeration of the prepared aqueous solutions.

Synthesis of 3-layered films. 3-layered films were prepared by CA under a constant potential of 1.40 V[27-32] using a three-electrode two-compartment cell under nitrogen atmosphere (99.995% in purity) at 25 ºC. A bare of GC with a diameter of 2 mm was used as WE while a steel AISI 316 sheet with an area of 1 cm^2 was employed as CE. The surface of the GC electrode was polished with alumina powder and cleaned by ultrasonication prior to the deposition of the polymer. The RE was an Ag|AgCl electrode containing a KCl saturated aqueous solution (Eº = 0.222 V *vs.* standard hydrogen electrode at 25 ºC), which was connected to the working compartment through a salt bridge containing the electrolyte solution. All electrochemical experiments were conducted on a PGSTAT302N AUTOLAB potenciostat-galvanostat (Ecochimie, The Netherlands) equipped with the ECD module to measure very low current densities (100 μA-100 pA), which was connected to a PC computer controlled through the NOVA 1.6 software.

The electrochemical LbL technique was used to prepare 3-layered $CP_A/CP_B/CP_A$ films, where the first and last CP_A refers to the CP used for internal and external layer, respectively, while CP_B corresponds to the CP of the intermediate layer. In this work CP_A and CP_B can be PEDOT, PNMPy or PNCPy. For the generation of each layer the WE was immersed for a period of time θ_A or θ_B (both in seconds) in 50 mL cells filled with 10 mM acetonitrile solution of the corresponding monomer (EDOT, NMPy or NCPy) and 0.1 M $LiClO_4$ as supporting electrolyte. Accordingly, the total polymerization time for each 3-layered film is: $2\times\theta_A + 1\times\theta_B$ s. In order to obtain thin films, θ_A and θ_B ranged from 1 to 5 s in all cases.

Preparation of AuNPs. Preparation of the AuNPs was performed following the standard procedure described in the literature.[33,34] All glassware used in such preparation was thoroughly cleaned in aqua regia (3:1 HCl:HNO_3), rinsed in doubly distilled water, and oven-dried prior to use. In a 1 L round-bottom flask equipped with a condenser, 500 mL of 1 mM $HAuCl_4$ was brought to a rolling boil with vigorous stirring. Rapid addition of 50 mL of 38.8 mM sodium citrate to the vortex of the solution produced a color change from pale yellow to burgundy. Boiling was continued for 15 min. After this, the heating mantle was removed while the stirring was continued for 30 min. When the solution reached the room temperature, it was filtered through a 0.2 μm membrane filter. The resulting solution of colloidal particles showed an absorption maximum at 520 nm indicating that the particle size ranged from 9 to 22 nm (Figure 1). A spherical model for a particle size of 13 nm was used to determine approximately the concentration of mother solution from UV-vis absorption, which was estimated to be 7.4 nM.

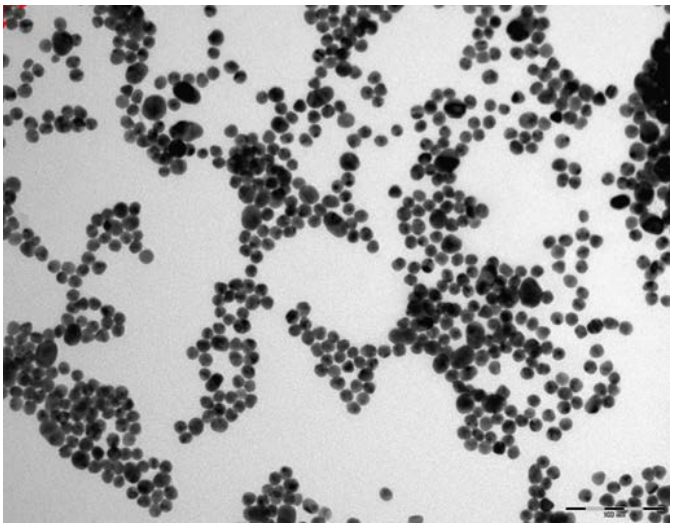

Figure 1. TEM micrograph of AuNPs (scale bar: 100 nm).

Preparation of AuNPs-modified GC electrodes. Deposition of the AuNPs onto the modified GCEs to fabricate PEDOT/PNMPy/PEDOT/AuNP, PNMPy/PEDOT/PNMPy/AuNP, PEDOT/PNCPy/PEDOT/AuNP and PNCPy/PEDOT/PNCPy/AuNP composites was performed using a previously used procedure.[10] More specifically, 4 μL of the AuNPs colloidal solution were dropped onto the external layer of the 3-layered films surface, drying under atmosphere conditions being subsequently allowed. The AuNPs concentration in the modified electrode surface was determined to be ~$23 \cdot 10^9$

nanoparticles/mm^2, assuming that all the AuNPs were well adhered to the 3-layered-modified GCE, since no absorption band at 520 nm was identified in the electrochemical solution after tests.

TEM and SEM. TEM images were collected with a Philips TECNAI 10 electron microscope operating at 80-100 kV. Bright field micrographs were taken with an SIS MegaView II digital camera. Solutions of AuNPs were cast onto a carbon coated copper-grids (300 mesh), the solvent being allowed to evaporate.

SEM studies were carried out using a FIB Zeiss Neon40 scanning electron microscope operating at 5 kV, equipped with an EDX spectroscopy system. The samples were mounted on a double-sided adhesive carbon disc.

Profilometry. The thickness of the films was determined through profilometry measurements using a profilometer Dektack 6 from Veeco.

Electrochemical measurements for detection of DA. Electrochemical detection was carried out by CV using the Autolab PGSTAT302N equipment described above. All electrochemical experiments were performed in a glass cell containing 10 mL of 0.1 M PBS (pH=7.4) at room temperature and equipped with saturated Ag|AgCl as RE and Pt wire as CE. The DA concentration used in this work ranged from 1μM to 1 mM. Voltammograms were recorded in the potential range from -0.40 to 0.80 V at a scan rate of 50 $mV \cdot s^{-1}$ unless other scan rate is explicitly specified. All the modified electrodes were in contact with the electrolyte solution for 5 min prior to CV measurements.

4.5.3 Results and Discussion

Preparation and characterization of 3-layered films.

As the diffusion coefficient of EDOT monomers[36] is higher than those of NMPy[37] and NCPy,[38] the polymerization time used to prepare PNMPy and PNCPy layers was higher than that employed for PEDOT ones. More specifically, 3-layered films were generated using θ= 3 s for PEDOT layers and θ= 5 s for PNMPy and PNCPy layers. Accordingly, the total polymerization time for PEDOT/PNMPy/PEDOT and

PEDOT/PNCPy/PEDOT films was (2×3)+(1×5)= 11 s while it was (2×5)+(1×3)= 13 s for PNMPy/PEDOT/PNMPy and PNCPy/PEDOT/PNCPy films.

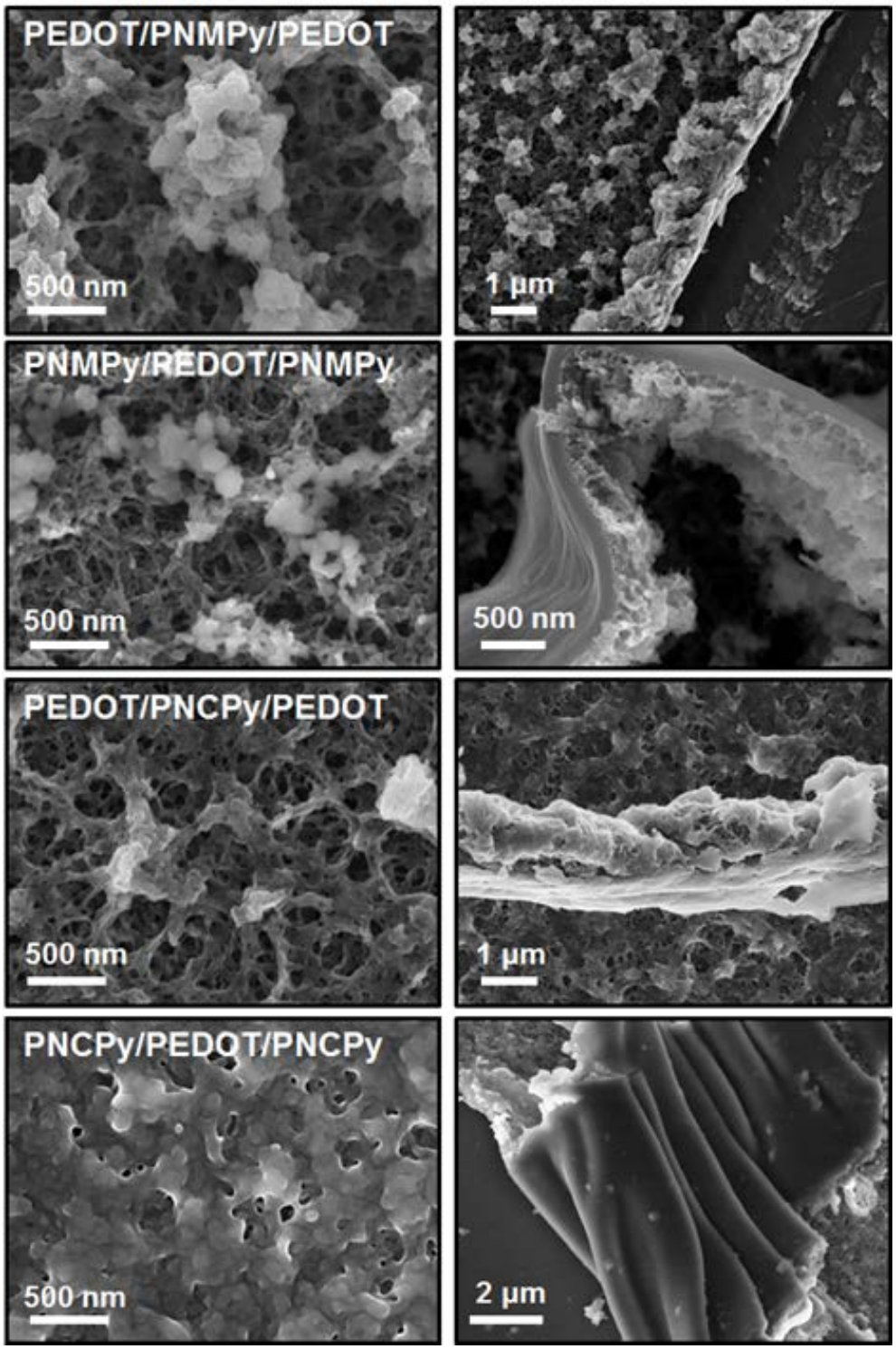

Figure 2. SEM micrographs of PEDOT/PNMPy/PEDOT, PNMPy/PEDOT/PNMPy, PEDOT//PNCPy/ PEDOT and PNCPy/PEDOT/PNCPy 3-layered films: surface (left) and cross-section (right).

SEM high-resolution micrographs of the 3-layered films studied in this work are displayed in Figure 2. As it can be seen, the external PEDOT layer in PEDOT/PNMPy/

PEDOT and PEDOT/PNCPy/PEDOT films exhibits a fibre-like morphology produced by the aggregation of sticks, which gives place to the formation of relatively narrow and tortuous pores. The presence of porous is expected to facilitate the mobility of dopant ions in oxidation (access of ions into the CP matrix) and reduction (escape of ions from the CP matrix) processes, facilitating the electrochemical detection with respect to CPs with more compact structures. This morphology is similar to that previously reported for individual PEDOT films that were generated using short polymerization times.[39] In contrast, the central PEDOT layer seems to affect the morphology of the external layer in PNMPy/PEDOT/PNMPy films. The surface of individual PNMPy films was found to present very compact morphologies, which makes difficult the access of the ions into the polymeric matrix during the Faradaic process.[27,31] However, the surface of PNMPy/PEDOT/PNMPy is very porous, indicating that the morphology of the external PNMPy layer is apparently conditioned by the intermediate PEDOT layer. Indeed, the surface morphology of PNMPy/PEDOT/PNMPy largely resembles that of PEDOT/PNMPy/PEDOT and, therefore, the mobility of the ions across the polymeric matrix is expected to be similar in both cases. This effect is much less pronounced in PNCPy/PEDOT/PNCPy films, which show a relatively compact morphology.

The compact morphology reported for individual PNMPy films of sub-micrometric and micrometric thickness was attributed to the formation of crosslinks (*i.e.* chemical couplings involving the β and β' positions of NMPy monomers).[27,31] However, morphological and electrochemical studies of PNMPy films deposited onto steel electrodes demonstrated that electropolymerization process is dominated by the formation of crosslinks for $\theta \geq 30$ s only.[31] As the θ used in the systems studied in this work was of only 5 s, the morphological behaviour of the external PNMPy layer should be attributed not only to the intermediate PEDOT layer but also to its ultra-thin nature. Thus, the PEDOT layer acts as a template for the growing of PNMPy chains, which in absence of crosslinks retain the same morphology rather than form the compact surfaces observed for larger polymerization times. This effect is practically inexistent in PNCPy due its particular chemical characteristics. Thus, PNCPy exhibits secondary oxidative processes in the five-membered rings that extend up to ~9 repeat units, giving place to the apparition of a carbonyl group attached to the Pyring.[38,40] This

phenomenon is independent of the polymerization time and induces the formation of a cross-linked structure with compact morphology formed by small but frequent branches.

The thickness of the films was estimated by cross-sectional SEM (Figure 2). The thickness of the two 3-layered films with PEDOT at the external and internal layers was ~1 μ, whereas the thickness of the films with PEDOT at the intermediate layer is ~350 nm. This result indicates that GC significantly promotes the polymerization of EDOT monomers, the thickness of the PEDOT layer directly deposited on the electrode being significantly higher than those deposited on PNMPy or PNCPy (*i.e.* intermediate or external layers). This is a very striking observation since the thickness of PEDOT films produced using the same experimental conditions (*i.e.* fixed potential at 1.40 V, acetonitrile solvent and $LiClO_4$ as supporting electrolyte) and a θ of 5 s is ~50 nm when deposited on steel or ITO electrodes,[39] θ slightly lower than 100 s being required to obtain ~1 μ thick films.[27]

Electrochemical behaviour of DA at bare GC and GC/AuNP electrodes.

Figure 3 compares the first control voltammograms of 0.1 M PBS (pH= 7.4) with and without 1 mM DA at bare GC and modified GC/AuNP electrodes. The electrochemical response to DA at bare GC and GC/AuNP electrodes is poor, even though the reversibility of the electrochemical processes is higher in the latter than in the former. The DA in contact with the GC shows a less reversible electrochemical behaviour than the GC/AuNP with oxidation and reduction peak potentials at 0.35 and 0.08 V, respectively. The GC/AuNP electrode shows oxidation and reduction processes with peak potentials at 0.19 and 0.14 V, respectively, indicating that AuNPs provokes an enhancement of the intensity and accentuates the electrochemical oxidation of the neurotransmitter. The detected process (Figure 4) corresponds to the oxidation of DA to DQ.[41] The peak intensity (I_p) for the oxidation is lower than 4 and 8 μA for GC and GC/AuNP, respectively. The catalyst role played by AuNPs in the oxidation of DA was described in previous works.[10,42] On the other hand, different trials showed that the selective determination of DA, AA and UA using GC and GC/AuNP electrodes is impossible because the oxidation peaks of these analytes are very close.

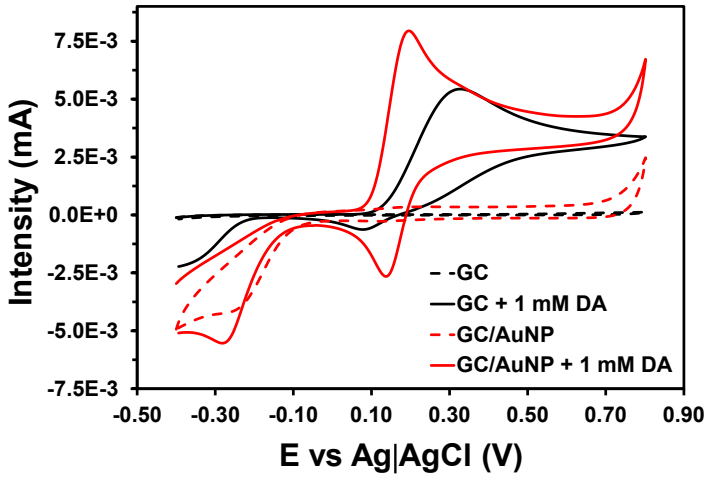

Figure 3. First control voltammograms of bare GC and modified GC/AuNP electrodes in the absence and presence of 1 mM DA. Supporting electrolyte: 0.1 M PBS. Voltammograms were obtained by scanning from -0.40 to 0.80 V at a scan rate of 50 $mV \cdot s^{-1}$.

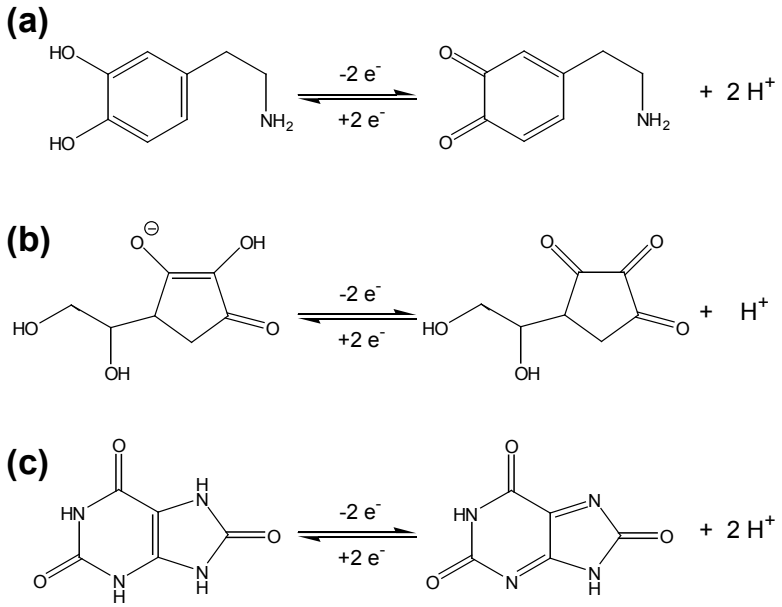

Figure 4. Electrochemical oxidation reactions for (a) DA, (b) AA and (c) UA.

Oxidation of DA, AA and UA at PEDOT, PNMPy and PNCPy electrodes.

DA, AA and UA coexist in extracellular fluids of the central nervous system and, therefore, the selective determination of these species is a major goal for the biomedical application of sensors. Before to check the performance of 3-layered and 3-layered/AuNP systems, the oxidation peaks of DA, AA and UA in GCEs modified with an individual CP were examined by CV. More specifically, the electrochemical behavior of a solution mixture with 100 μM DA, 200 μM AA and 100 μM UA in 0.1 M PBS was studied using PEDOT, PNMPy, PNCPy, PEDOT/AuNP, PNMPy/AuNP and PNCPy/AuNP

electrodes, which were prepared using θ of 6 (PEDOT and PEDOT/AuNP) and 10 s (PNMPy, PNCPy, PNMPy/AuNP and PNCPy/AuNP).

Results are summarized in Table 1. The oxidation peaks were well resolved at PEDOT and PEDOT/AuNP electrodes with peak potentials at 0.15, -0.03 and 0.28 V for the oxidation of DA, AA and UA, respectively. However, the I_p for DA oxidation does not increase when the PEDOT film is coated with AuNPs, indicating that the latters do not play any electrocatalytic activity in this case. Thus, AuNPs abilities to promote electron transfer between the electrode surface and the electrolyte are not necessary for PEDOT because of their excellent electrochemical properties (*i.e.* electroactivity and electrostability).[36] On the other hand, detection of AA was not possible with PNMPy, PNCPy, PNMPy/AuNP and PNCPy/AuNP electrodes since the oxidation peak was inappreciable. Furthermore, the oxidation peaks of DA and UA are weak and partially overlapped at PNMPy- and, especially, PNCPy-containing electrodes making difficult the selective and simultaneous determination of such species. This behavior did not change when the concentration of analyte was increased. In spite of such limitation, it should be noted that the anodic intensities determined for the oxidation of DA, independently of the concentration, are one order of magnitude higher for PNMPy/AuNP and PNCPy/AuNP electrodes than for PEDOT and PEDOT/AuNP.

Electrode	DA		AA		UA	
	E_p (V)	I_p (μA)	E_p (V)	I_p (μA)	E_p (V)	I_p (μA)
PEDOT	0.15	0.44	-0.03	2.11	0.28	3.93
PNMPy	0.15	0.51	-	-	0.32	0.10
PNCPy	0.37	0.04	-	-	0.46	0.31
PEDOT/AuNP	0.15	0.53	-0.03	1.82	0.28	2.88
PNMPy/AuNP	0.21	2.50	-	-	0.31	0.03
PNCPy/AuNP	0.42	2.48	-	-	0.47	0.01

Table 1. Summary of the electrochemical behavior of a solution mixture with 100 μM DA, 200 μM AA and 100 μM UA in 0.1 M PBS at CP and CP/AuNP electrodes. Both the peak potential and the peak intensity for the oxidation of each analyte are displayed.

3-Layered systems for the detection of DA.

The oxidation behaviour of 1mM DA in 0.1 M PBS at 3-layered and 3-layered/AuNP electrodes is shown in Figure 5. In all cases the two-electron oxidation of DA to DQ is detected. When compared to modified electrodes made of individual CPs (Table 1), a shift in the anodic peak is detected. This shift is higher for systems with PEDOT at the intermediate layer than for those with a PPy derivative. The oxidation peak potential (E_p) of DA at 3-layered electrodes ranges from 0.19 (PEDOT/PNCPy/PEDOT) to 0.28 V (PNMPy/PEDOT/PNMPy), this interval extending from 0.19 (PEDOT/PNMPy/PEDOT/AuNP and PEDOT/PNCPy/PEDOT/AuNP) to 0.33 V (PNCPy/PEDOT/PNCPy) at 3-layered/AuNP electrodes. Similarly, AuNPs affect the I_p which varies from 2.0 (PNMPy/PEDOT/PNMPy) to 13.4 μA (PEDOT/PNMPy/PEDOT) and from 3.4 (PEDOT/PNCPy/PEDOT/AuNP) to 12.3 μA (PNMPy/PEDOT/PNMPy/AuNP) at 3-layered and 3-layered/AuNP electrodes, respectively. The values of the E_p and the anodic I_p associated to the DA oxidation at 3-layered and 3-layered/AuNP electrodes are listed in Table 2.

The stability of the three 3-layered and 3-layered/AuNP electrodes for detection was examined by investigating the variation of the E_p and the I_p against the number of consecutive oxidation-reduction cycles for 1 mM DA in 0.1 M PBS. Results are represented in Figure 6 while Figure 5 includes the voltammogram of the fifth redox cycle for comparison with the first one. In general, the variation of the oxidation E_p is higher for electrodes with PEDOT as intermediate layer than for those with PNMPy or PNCPy (Figure -6a), indicating that the formers are less stable than the latters. Furthermore, the potential required for the oxidation of DA is lower for electrodes with PNMPy or PNCPy at the intermediate layer. On the other hand, PEDOT/PNMPy/PEDOT is the most sensitive electrode to the oxidation of DA (Figure 6b), the I_p at such electrode being the highest during the five redox cycles. In terms of intensity, the electrodes with lower stability are the PNMPy/PEDOT/PNMPy and the PNCPy/PEDOT/PNCPy/AuNP because of the large and progressive variation of anodic I_p with the number of redox cycles. Furthermore, the reduction of DQ to DA was identified in all cases with exception of PNMPy/PEDOT/PNMPy and PNMPy/PEDOT/

PNMPy/AuNP (Figure 5), even though the reversibility of the process was higher for the electrodes with PEDOT at the external and internal layers.

CVs of a solution mixture with 100 μM DA, 200 μM AA and 100 μM UA in 0.1 M PBS were recorded at 3-layered and 3-layered/AuNP electrodes. Sensitivity and resolution parameters, which have been expressed as the ratio between the I_p for the oxidation of a given specie and its concentration in the mixture (μA/mM) and the difference between the oxidation E_p of two species (V), respectively, for the eight investigated electrodes are listed in Table 3. Peak intensities and oxidation peak potentials at all the investigated 3-layered electrodes are provided in Table 4. The oxidation peaks of the three species are well-resolved in all cases with exception of PNCPy/PEDOT/PNCPy and PNCPy/PEDOT/PNCPy/AuNP electrodes. The sensitivity of these electrodes is very poor with respect to the other ones. More specifically, the I_p signals are very weak for the oxidation of the three species (*i.e.* < 0.1 μA) in PNCPy/PEDOT/PNCPy while in PNCPy/PEDOT/PNCPy/AuNP this limitation only affects to the response of AA (0.097 μA). The sensitivity improves significantly for PNMPy/PEDOT/PNMPy and PNMPy/PEDOT/PNMPy/AuNP electrodes, evidencing a favourable synergy with respect to the electrode with a monolayered film of PNMPy (see Table 1). This synergy must be attributed to the interaction between PNMPy and PEDOT layers,[27,29,30] which was reported to be more favourable than the interaction between PNCPy and PEDOT layers.[28] In general, PEDOT/PNMPy/PEDOT and its homologous coated with AuNPs show the highest performance for the selective determination of DA, AA and UA. These electrodes not only maintain the separation of the peak potentials observed for individual PEDOT and PEDOT/AuNP but also enhance the I_p with respect to the latter individual films. Thus, oxidation phenomena are clear enough to identify the response of individual species in the mixture. Furthermore, it is worth noting that the peak currents obtained at the PEDOT/PNMPy/PEDOT/AuNP electrode are higher than those at PEDOT/PNMPy/PEDOT (*i.e.* 15%, 28% and 49% for DA, AA and UA, respectively). This feature reflects the catalytic effect played by AuNPs in such 3-layered system, even though this effect was not detected in individual PEDOT films (see Table 1) due to its excellent electrochemical properties.[36] However, the external layer in PEDOT/PNMPy/PEDOT is very thin and, therefore, AuNPs act

improving the electron transfer between the electrolyte and the PNMPy intermediate layer, which is very close to the surface and also interact with the electrolyte.

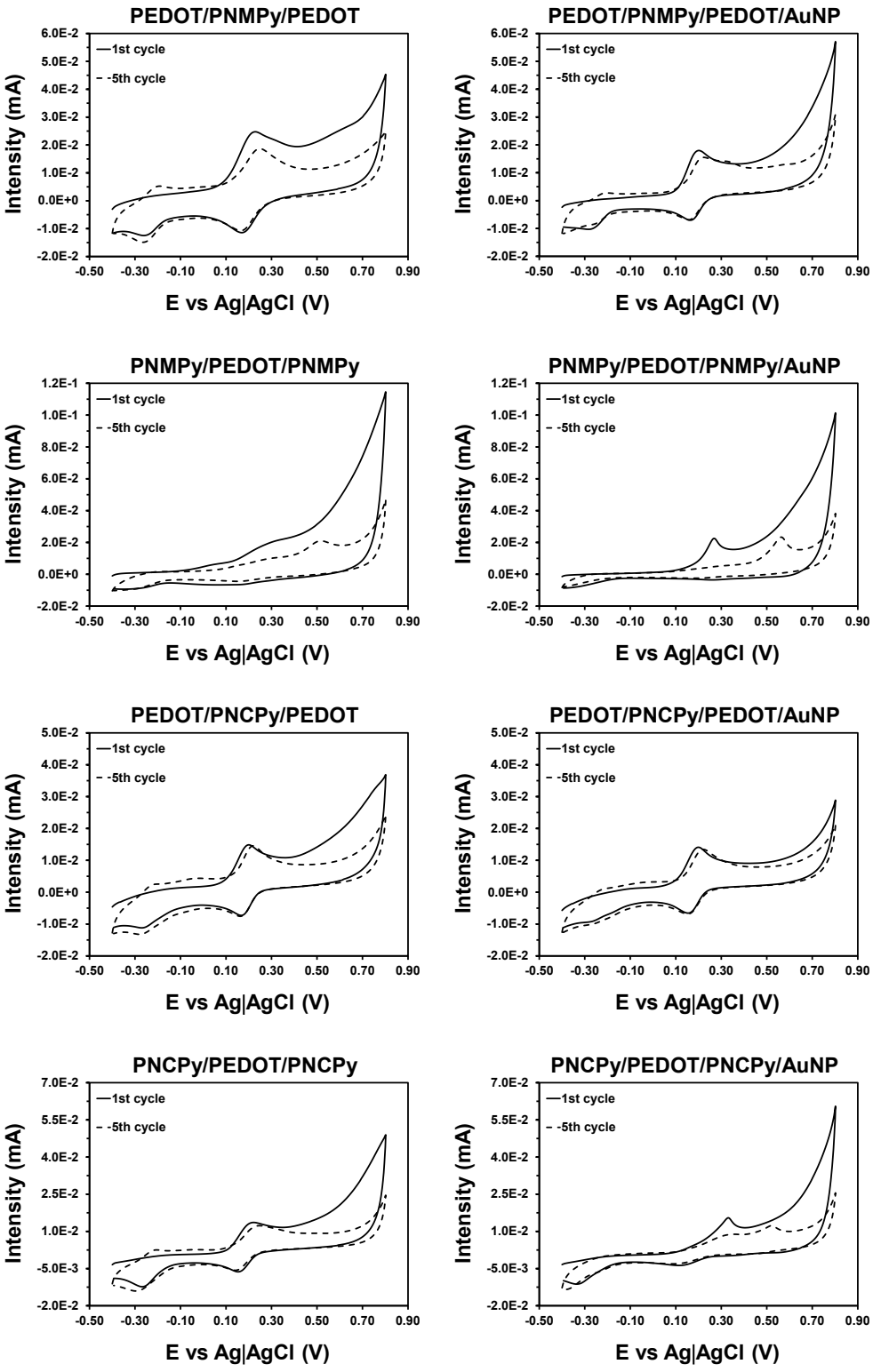

Figure 5. Control voltammograms of 1 mM DA in 0.1 M PBS at 3-layered and 3-layered/AuNP electrodes after one and five consecutive oxidation-reduction cycles (solid and dashed line, respectively). Voltammograms were obtained by scanning from -0.40 to 0.80 V at a scan rate of 50 $mV \cdot s^{-1}$.

Electrode	E_p (V)	I_p (μA)
PEDOT/PNMPy/PEDOT	0.219	13.4
PEDOT/PNMPy/PEDOT/AuNP	0.195	11.3
PNMPy/PEDOT/PNMPy	0.278	2.0
PNMPy/PEDOT/PNMPy/AuNP	0.267	12.3
PEDOT/PNCPy/PEDOT	0.195	8.8
PEDOT/PNCPy/PEDOT/AuNP	0.195	3.4
PNCPy/PEDOT/PNCPy	0.207	7.7
PNCPy/PEDOT/PNCPy/AuNP	0.326	6.8
3l-5s [a]	0.201	8.0
3l-5s/AuNP-4[b]	0.192	8.8
3l-5s/AuNP-8[b]	0.189	8.8
3l-5s (electrochemically degraded) [a,c]	0.208	9.0
3l-5s/AuNP-4 (electrochemically degraded) [b,c]	0.202	9.6

[a] Submicrometric PEDOT/PNMPy/PEDOT film (see text). [b] Submicrometric PEDOT/PNMPy/PEDOT film coated with AuNPs (see text). [c] Electrochemical degradation was provoked by applying 50 consecutive oxidation-reduction cycles (see text).

Table 2. Summary of the electrochemical behavior of 1 mM DA in 0.1 M PBS at micrometric and submicrometric 3-layered and 3-layered/AuNP electrodes (see text for nomenclature). Both the peak potential and the peak intensity for the oxidation of DA to DQ are displayed.

Electrode	Sensitivity (μA/mM)			Resolution (V)	
	DA	AA	UA	AA-DA	UA-DA
PEDOT/PNMPy/PEDOT	5.3	4.5	24.5	0.185	0.136
PEDOT/PNMPy/PEDOT/AuNP	6.1	5.7	36.5	0.173	0.142
PNMPy/PEDOT/PNMPy	6.7	4.1	11.9	0.178	0.119
PNMPy/PEDOT/PNMPy/AuNP	6.2	4.8	16.6	0.184	0.119
PEDOT/PNCPy/PEDOT	5.5	5.5	25.0	0.172	0.137
PEDOT/PNCPy/PEDOT/AuNP	6.2	3.8	18.2	0.172	0.131
PNCPy/PEDOT/PNCPy	0.8	0.2	0.6	0.196	0.161
PNCPy/PEDOT/PNCPy/AuNP	2.1	0.5	10.0	0.184	0.185

Table 3. Sensitivity and resolution obtained for the determination of DA, AA and UA in 0.1 M PBS using different 3-layered and 3-layered/AuNP electrodes. CVs are displayed in Figure 5 while the values of the peak current and peak potentials are listed in Table 4.

Electrode	DA		AA		UA	
	E_p (V)	I_p (μA)	E_p (V)	I_p (μA)	E_p (V)	I_p (μA)
PEDOT/PNMPy/PEDOT	0.15	0.53	-0.03	0.90	0.29	2.45
PEDOT/PNMPy/PEDOT/AuNP	0.15	0.61	-0.02	1.15	0.30	3.65
PNMPy/PEDOT/PNMPy	0.17	0.67	-0.01	0.83	0.29	1.19
PNMPy/PEDOT/PNMPy/AuNP	0.18	0.62	-0.01	0.97	0.30	1.66
PEDOT/PNCPy/PEDOT	0.16	0.55	-0.01	1.10	0.30	2.50
PEDOT/PNCPy/PEDOT/AuNP	0.16	0.62	-0.01	0.77	0.29	1.82
PNCPy/PEDOT/PNCPy	0.18	0.08	-0.01	0.04	0.34	0.06
PNCPy/PEDOT/PNCPy/AuNP	0.18	0.21	-0.01	0.09	0.34	0.36

Table 4. Summary of the electrochemical behavior of a solution mixture with DA (100 μM), AA (200 μM) and UA (100 μM) in 0.1 M PBS at 3-layered and 3-layered/AuNP electrodes. Both the peak potential and the peak intensity for the oxidation of each analyte are displayed.

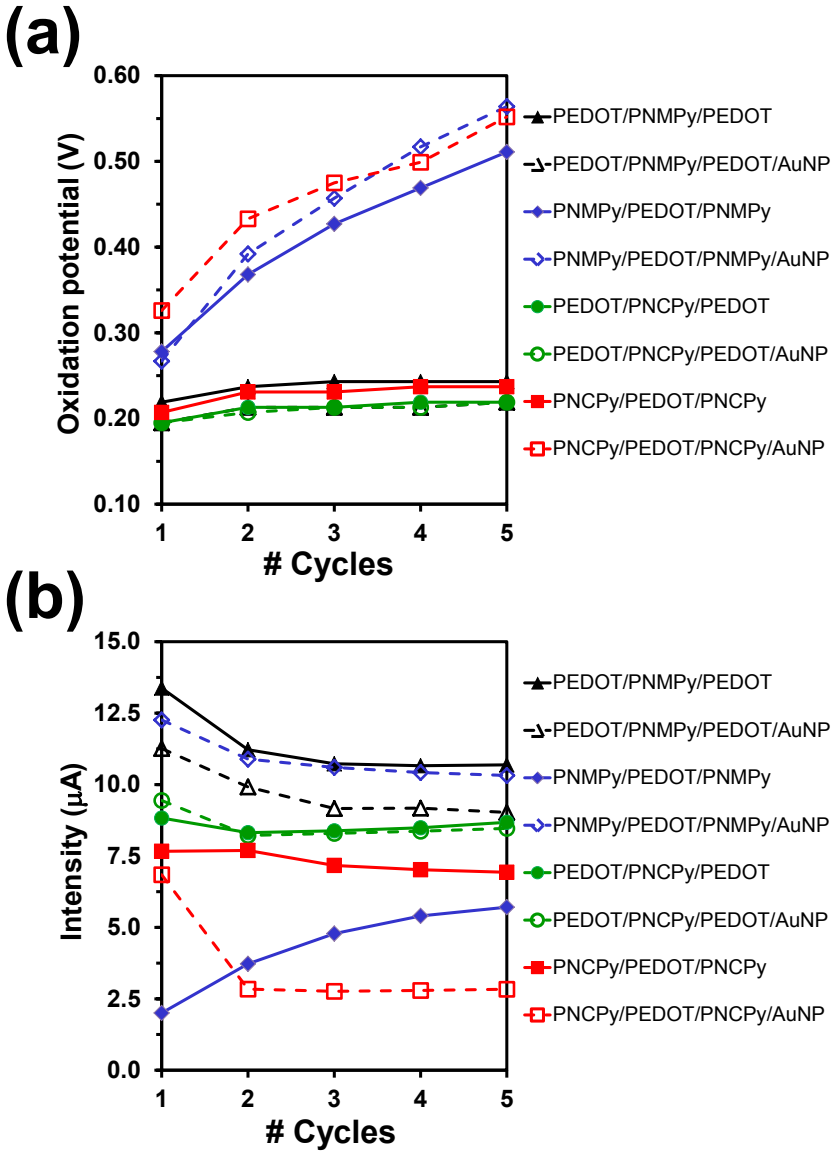

Figure 6. Variation of the (a) peak oxidation potential and the (b) peak intensity at 3-layered and 3-layered/AuNP electrodes against the number of consecutive oxidation-reduction cycles of 1 mM DA in 0.1 M PBS.

The diffusion coefficient (D_0) of DA has been estimated using the Randless-Sevcik equation, which at 298 K can be written as follows:[43]

$$i_p = 2.687 \cdot 10^{-5} n^{3/2} \upsilon^{1/2} \mathrm{D_0}^{1/2} A C_0 \qquad (1)$$

where i_p is the peak current density (A·cm^{-2}), n is the number of electrons appearing in half reaction for the redox couple, υ is the rate at which the potential is swept (V·s^{-1}), A is the area of the electrode (0.12566 cm^2), C_0 is the DA concentration (1 mM or 100 μM) and the constant 2.687·10^5 (C·mol^{-1}·V$^{-1/2}$) results from $0.4663(F^3/RT)^{1/2}$ (F= Faraday's constant in C·mol^{-1}, R= universal gas constant in J·mol^{-1}·K^{-1} and T= 298 K).

Figure -7a represents the D_0 of 1 mM DA in 0.1 M PBS determined from the voltammograms recorded using a scan rate of 50 mV·s^{-1} at different 3-layered and 3-layered/AuNP systems. As it can be seen, the highest value of D_0 corresponds to PEDOT/PNMPy/PEDOT (2.15·10^{-2} cm^2·s^{-1}), evidencing the efficacy of this 3-layered system. Interestingly, the values of D_0 for PNCPy-containing systems are one order of magnitude lower than those obtained for PNMPy-containing systems. Furthermore, the graphic displayed in Figure 7a clearly shows that AuNPs only promotes the DA diffusion when the external and internal layers are made with PNMPy or PNCPy, even though D_0 is still very low for the later systems (~10^{-3} cm^2·s^{-1}). The D_0 values for DA derived from the voltammograms (50 mV·s^{-1}) of the solution mixture with 100 μM DA, 200 μM AA and 100 μM UA in 0.1 M PBS are displayed in Figure 7b. The D_0 values decrease one order of magnitude in all cases with exception of PNCPy/PEDOT/PNCPy that, as discussed above, is not able to detect such low DA concentration. However, the most remarkable difference with respect to Figure 7a refers to the role of AuNPs. More specifically, the D_0 of each 3-layered system, which should be considered as the average of the diffusion process in the bulk defined by the DA-containing solution and the layer of DA, AA and UA molecules adsorbed at the surface of such electrode, is relatively similar to that of the corresponding 3-layered/AuNP.

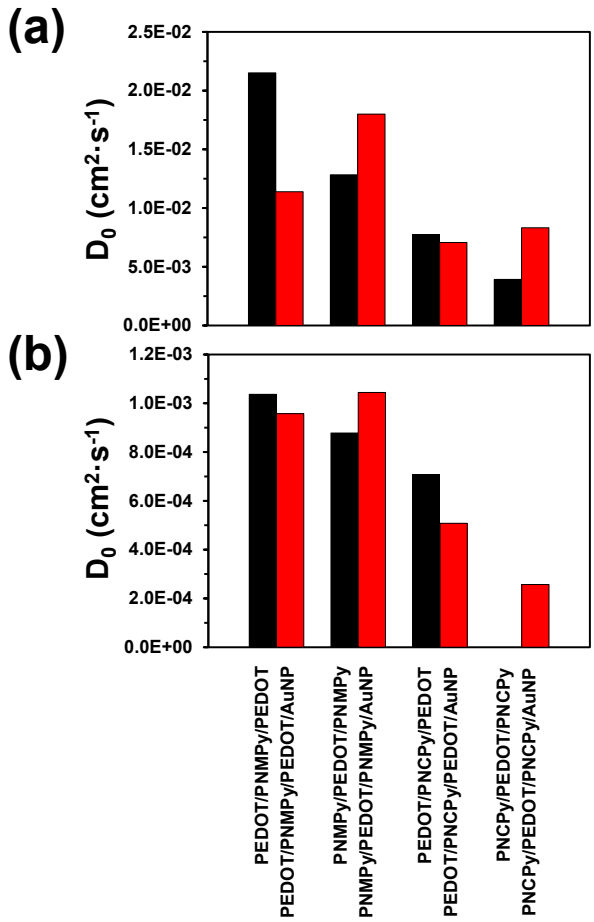

Figure 7. Representation of the D_0 (Eqn 1) derived from the CVs (scan rate: 50 mV·s^{-1}) recorded at 3-layered and 3-layered/AuNP electrodes for the following solutions: (a) 1 mM DA in 0.1 M PBS; and (b) mixture with 100 μM DA, 200 μM AA and 100 μM UA in 0.1 M PBS.

Submicrometric PEDOT/PNMPy/PEDOT films for the detection of DA.

Results obtained in the previous section clearly indicate that 3-layered and 3-layered/AuNP systems with PEDOT located at both the internal and external layers are the most appropriated for the detection of DA. Among those systems, those with PNMPy at the intermediate layer exhibit the highest performance. Accordingly, the rest of this work is focussed on the ability of PEDOT/PNMPy/PEDOT and PEDOT/PNMPy/PEDOT/AuNP electrodes to detect DA. In order to improve these systems, the following two modifications have been introduced: *i)* the micrometric ℓ of the films, which as mentioned above is due to the high affinity of EDOT monomers towards the bare GCE (*i.e.* the internal PEDOT layer), has been reduced to submicrometric by decreasing the θ; and *ii)* the concentration of AuNPs has been increased to enhance their catalytic role. More specifically, the following three systems

have prepared for deeper investigations on the selective detection of DA using 3-layered systems:

1. PEDOT/PNMPy/PEDOT films in which the internal and external PEDOT layers are obtained using a polymerization time of 1 s while the time employed to generate the intermediate PNMPy layer is 3 s (*i.e.* the total polymerization time is 2×1+1×3= 5 s).
2. PEDOT/PNMPy/PEDOT/AuNP films prepared by dropping 4 μL of the AuNPs colloidal solution onto the surface of the 3-layered film produced as in 1).
3. PEDOT/PNMPy/PEDOT/AuNP films prepared like in 2) but increasing the amount of AuNPs colloidal solution to 8 μL.

Hereafter, the systems prepared using the conditions indicated in 1), 2) and 3) are denoted 3l-5s, 3l-5s/AuNP-4 and 3l-5s/AuNP-8, respectively, where 3l-5s refers to 3-layered film prepared using a total polymerization time of 5 s. The thickness of the films prepared using such conditions, which was determined by prolifometry, ranged from 612 to 847 nm, the average value being 713±103 nm. This represent a reduction of ~300 nm with respect to the PEDOT/PNMPy/PEDOT films prepared using a total polymerization time of 11 s.

Figure 8a shows the voltammograms recorded for 1 mM DA in 0.1 PBS at 3l-5s, 3l-5s/AuNP-4 and 3l-5s/AuNP-8 electrodes (see also Table 2). The anodic peak associated to the oxidation of DA to DQ appears at 0.19-0.20 V in the three systems while the value reached by the anodic I_p is 7.96, 8.84 and 8.81 μA for 3l-5s, 3l-5s/AuNP-4 and 3l-5s/AuNP-8, respectively. Thus, AuNPs enhance the current response of DA at submicrometric PEDOT/PNMPy/PEDOT electrodes. However, such enhancement is moderate and does not increase with the concentration of AuNPs, corroborating that the improved electrocatalytic oxidation of DA provoked by AuNP-coating is significantly lower for PEDOT than for PNMPy.[10,11] For the latter, AuNPs were proposed to facilitate the effective charge migration through the CP by generating many active sites inside the electrodes.[10,11] However, this catalytic role is much less effective in PEDOT because of the excellent electrochemical and electrical properties of this CP. Comparison with the micrometric films discussed in previous sections (Table

2) indicates that the E_p undergoes a small shift to less positive value and the oxidation current response reduces about 20-40% only when the total polymerization time decreases from 13 s to 5 s. On the other hand, Figure 8a indicates that the oxidation of DA to DQ is a reversible process, the cathodic peak potential appearing at 0.15-0.16 V in all cases.

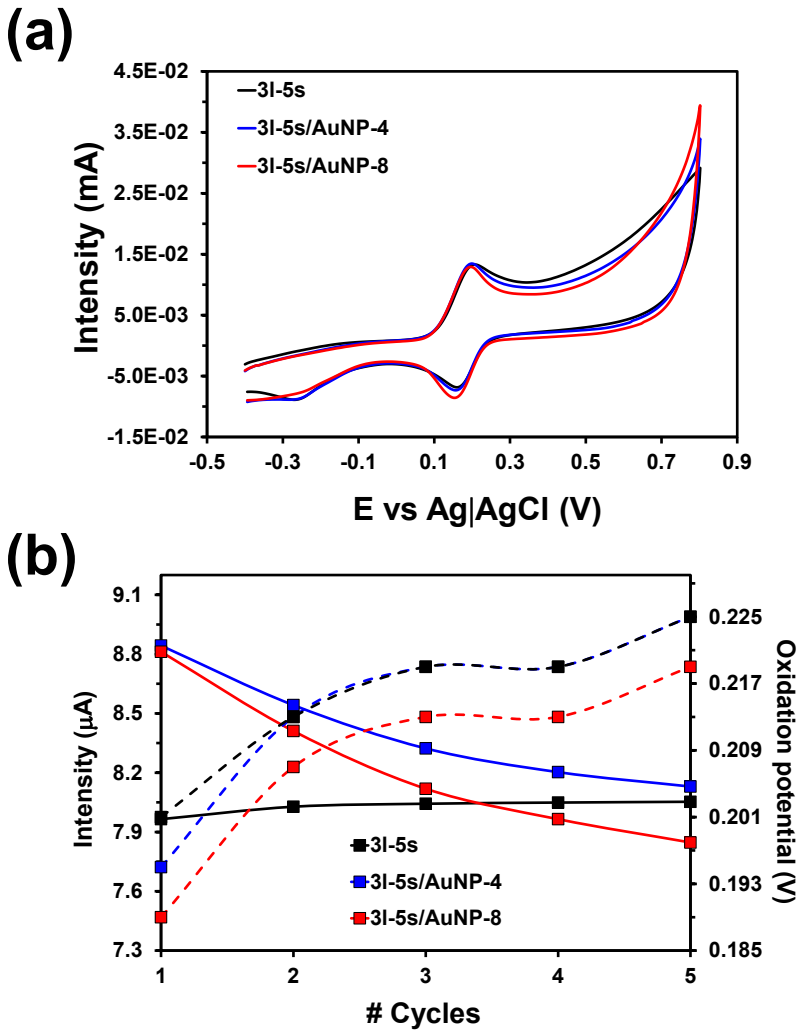

Figure 8. (a) Control voltammograms of 1 mM DA in 0.1 M PBS at submicrometric electrodes based on PEDOT/PNMPy/PEDOT films. (b) Variation of the peak intensity (solid lines) and peak oxidation potential (dashed lines) of 1 mM DA in 0.1 M PBS at submicrometric electrodes based on PEDOT/PNMPy/PEDOT films against the number of consecutive oxidation-reduction cycles.

Figure 8b represents the response of 3l-5s, 3l-5s/AuNP-4 and 3l-5s/AuNP-8 electrodes against the number of consecutive oxidation-reduction cycles for 1 mM DA in 0.1 M PBS (Figure 9). The behaviour of the three electrodes is very similar in terms of oxidation peak potential, a shift towards higher values being observed in all cases. However, this change represents ~0.03 V only. Amazingly, the sensitivity of the two

AuNPs-containing submicrometric electrodes reduces when the number of redox cycles increases, the I_p decreasing after five cycles. This should be attributed to the formation of aggregates made of oxidized species on the surface of AuNPs. In contrast, the I_p determined at the 3l-5s electrode remains practically unaltered during the five redox cycles. It is worth noting that application of a few redox cycles to provoke small changes in the oxidation E_p while the sensitivity remains constant is a potential strategy to enhance the resolution and, therefore, the selectivity of electrochemical sensors. This strategy is further explored below.

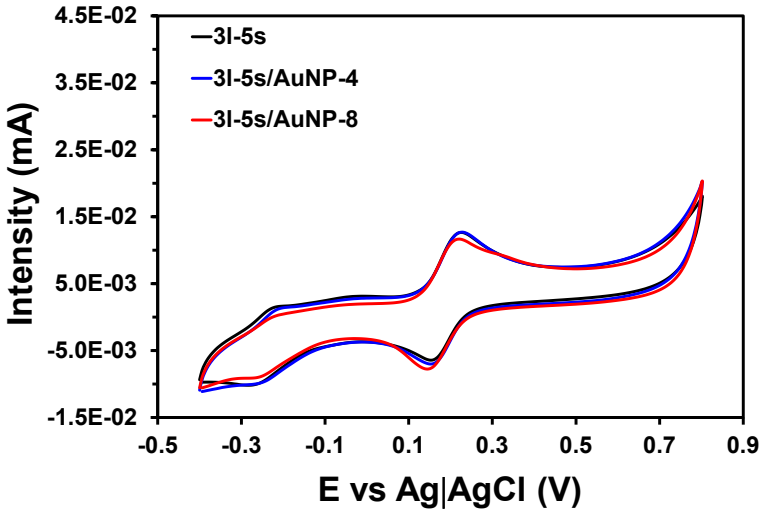

Figure 9. Voltammograms of 1 mM DA in 0.1 M PBS after five consecutive oxidation-reduction cycles recorded at electrodes based on submicrometric PEDOT/PNMPy/PEDOT films. Voltammograms were obtained by scanning from -0.40 to 0.80 V at a scan rate of 50 $mV \cdot s^{-1}$.

Stability of DA detection by using electrochemically aged electrodes.

In order to examine the stability of submicrometric electrodes based on PEDOT/PNMPy/PEDOT films for DA detection, 3l-5s and 3l-5s/AuNP electrodes were submitted to 50 consecutive oxidation-reduction cycles in 0.1 PBS solution using a potential interval comprised between -0.40 V (initial and final potential) and +0.80 V (reversal potential). It is well known that application of this aggressive treatment provokes electrochemical degradation, which is reflected by a reduction of the electroactivity. In spite of this, Atta and co-workers[24] reported that the current response towards DA of PEDOT and PEDOT/AuNP electrodes reaches a steady sate stabilizes once the *LEA* reaches a steady state, obtaining good reproducibility (*i.e.* the oxidation E_p and anodic I_p remained practically unaltered for consecutive detection cycles). In this work the *LEA* for 3l-5s and 3l-5s/AuNP-4 films has been determined as:

$$LEA = \frac{\Delta Q}{Q_{ii}} 100 \qquad (2)$$

where *ΔQ* is the difference of voltammetric charge between the second cycle and the last cycle and Q_{ii} is the voltammetric charge corresponding to the second cycle.

Figure 10a, which represents the evolution of the *LEA* with the number of redox cycles, indicates that the electrochemical stability of 3l-5s and 3l-5s/AuNP-4 is very similar, the loss of *LEA* after 50 cycles being of 83% and 85%, respectively. The first cycles provokes a drastic reduction of electroactivity, a steady state-like behaviour being obtained after ~15 cycles. Figure 10 includes the voltammograms recorded for 1 mM DA in 0.1 PBS at 3l-5s and 3l-5s/AuNP-4 electrodes previously submitted to 50 consecutive redox cycles. The voltammograms recorded in absence of DA are also displayed for comparison. Despite of the electrochemical degradation, DA is clearly detected by both 3l-5s and 3l-5s/AuNP-4, the E_p appearing at 0.21 and 0.20 V, respectively. The I_p for the oxidation of DA at 3l-5s and 3l-5s/AuNP-4 electrodes is 9.0 and 9.6 μA, respectively, indicating that, as occurred above, the catalytic role played by AuNPs in the detection of DA is moderate. Moreover, these anodic I_p are slightly higher than those obtained for as prepared electrodes (see Table 2).

Comparison of the voltammograms recorded for first and fifth detection cycles at electrodes previously submitted to 50 consecutive redox cycles (Figure 11) evidences a slight reduction of the I_p. Thus, the I_p of electrochemically degraded 3l-5s and 3l-5s/AuNP-4 undergoes a small reduction after five detection cycles (*i.e.* from 9.0 to 6.9 μA and from 9.6 to 7.2 μA, respectively). However, the E_p of the first and fifth cycles at 3l-5s and 3l-5s/AuNP-4 electrodes remains very close (*i.e.* 0.22 and 0.21 V, respectively, for the fifth cycle). These results indicate that the electrochemical treatment of the electrodes may be used to improve the selectivity of the 3-layered PEDOT/PNMPy/PEDOT electrodes without produce significant variations in the sensibility. This information has been successfully used at the end of this section to detect DA in real human urine samples.

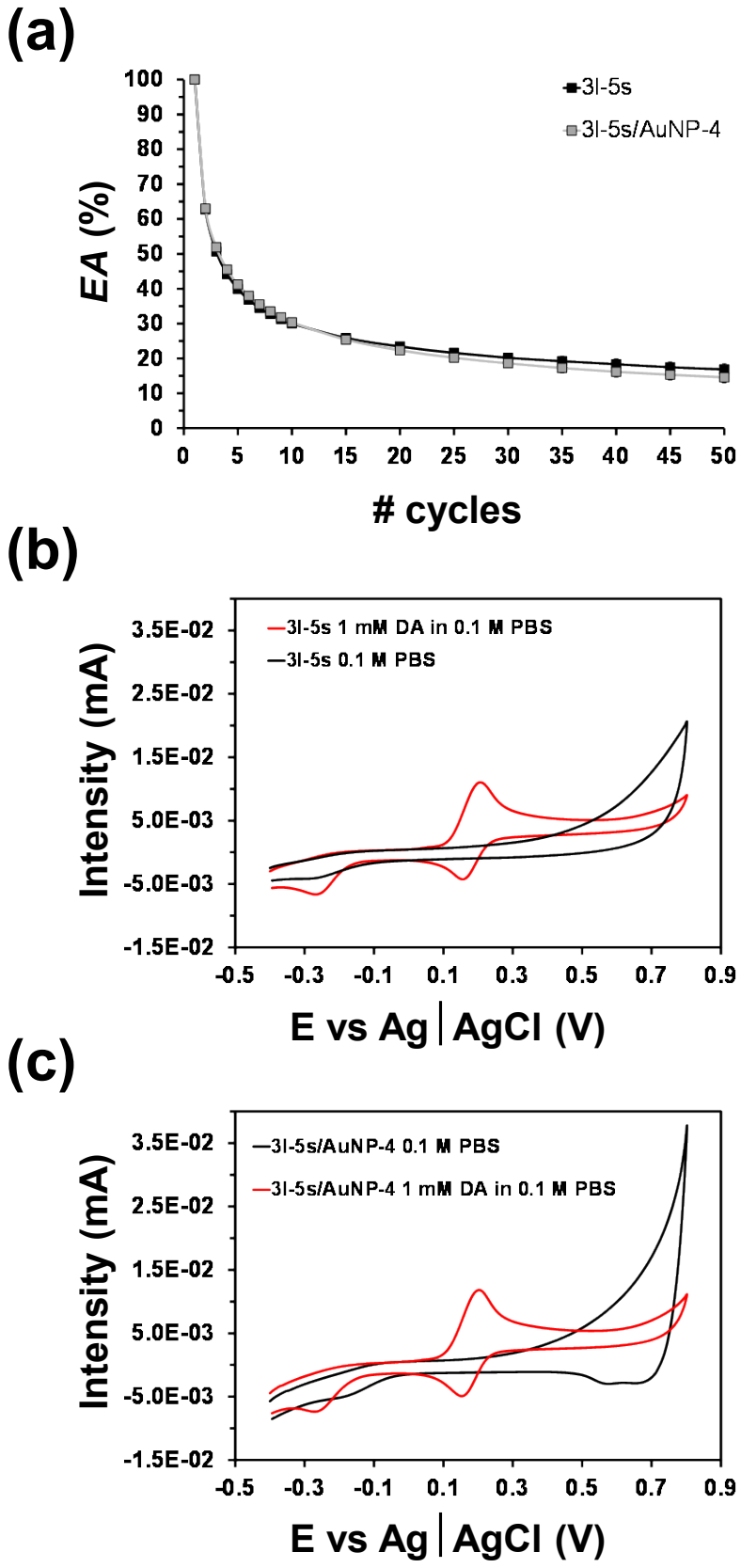

Figure 10. (a) Variation of the *EA* (in %) against the number of consecutive oxidation-reduction cycles for submicrometric 3l-5s and 3l-5s/AuNP-4 films in 0.1 M PBS. Control voltammograms at electrochemically degraded (b) 3l-5s and (c) 3l-5s/AuNP-4 electrodes of 1 mM DA in 0.1 M PBS (red line) and of 0.1 M PBS (black line).

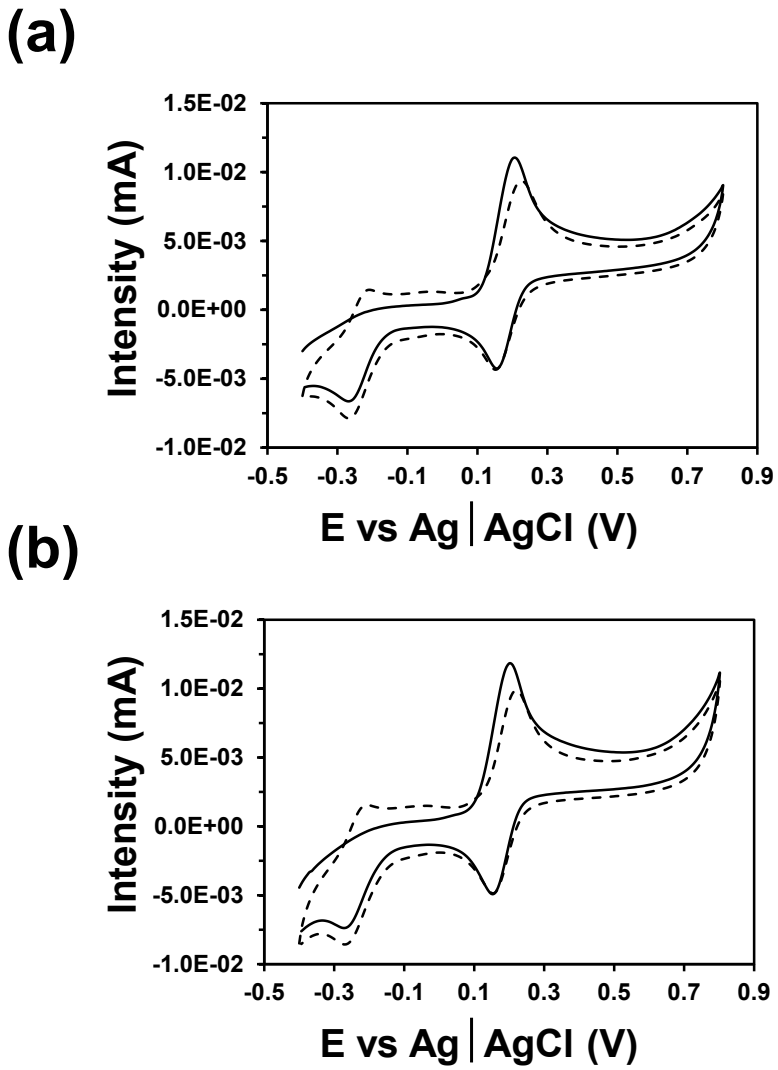

Figure 11. Control voltammograms of 1 mM DA in 0.1 M PBS at electrochemically degraded (a) 3l-5s and (b) 3l-5s/AuNP-4 electrodes after one and fifth consecutive detection cycles (solid and dashed line, respectively). Voltammograms were obtained by scanning from -0.40 to 0.80 V at a scan rate of 50 $mV \cdot s^{-1}$.

Effect of scan rate on the voltammetric detection of DA using 3-layered films.

CVs of 1 mM DA in 0.1 PBS at 3l-5s and 3l-5s/AuNP-4 electrodes recorded using scan-rates of 50, 100, 200, 400, 600 and 1200 $mV \cdot s^{-1}$ are displayed in Figure 12. Representation of the oxidation E_p, anodic I_p, reduction E_p and cathodic I_p against the square root of the scan rate for 3l-5s and 3l-5s/AuNP-4 (Figures 13a and 13b, respectively) indicates a linear behavior in all cases. The anodic I_p and the oxidation E_p increase linearly with the following equations:

Anodic peak current:	3l-5s	$y = 1.18 \cdot x - 0.86$	(3)
	3l-5s/AuNP-4	$y = 1.74 \cdot x - 2.95$	(4)
Oxidation peak potential:	3l-5s	$y = 0.0047 \cdot x + 0.1639$	(5)
	3l-5s/AuNP-4	$y = 0.0038 \cdot x + 0.1625$	(6)

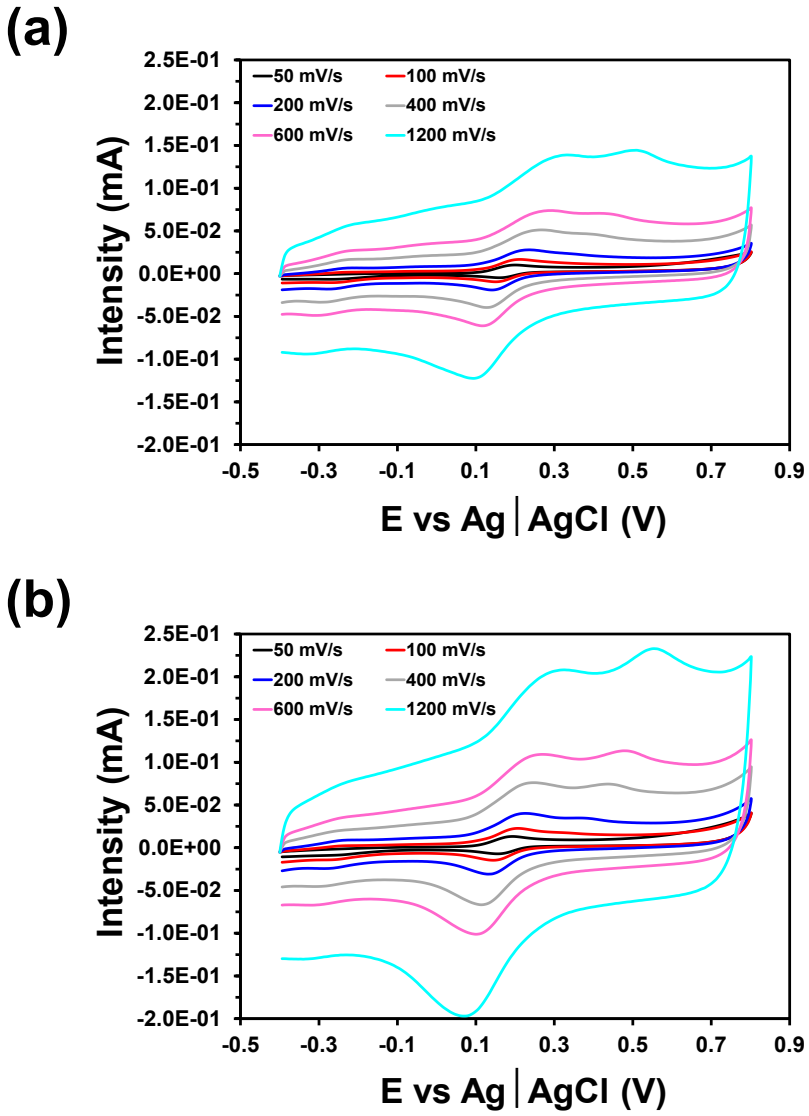

Figure 12. Control voltammograms at (a) 3l-5s and (b) 3l-5s/AuNP-4 electrodes of 1 mM DA in 0.1 M PBS obtained by scanning from -0.40 to 0.80 V at a scan rate of 50, 100, 200, 400, 600 and 1200 $mV \cdot s^{-1}$.

For the anodic I_p the slope is slightly higher for 3l-5s/AuNP-4 than for 3l-5s indicating that AuNPs enhance the sensitivity of the 3-layered electrode. In contrast, for the oxidation E_p the slope is slightly higher for 3l-5s than 3l-5s/AuNP-4 evidencing that AuNPs intensify the stability. However, differences between the slopes indicate that such effects are moderate. On the other hand, the cathodic I_p and the reduction E_p decrease linearly for the two electrodes, according to these equations:

Cathodic peak current:	3l-5s $y = -1.95 \cdot x + 11.09$	(7)
	3l-5s/AuNP-4 $y = -3.39 \cdot x - 22.20$	(8)
Reduction peak potential:	3l-5s $y = -0.0023 \cdot x + 0.1773$	(9)
	3l-5s/AuNP-4 $y = -0.0030 \cdot x + 0.1809$	(10)

Although AuNPs improve the sensitivity in terms of cathodic current, as occurred above for the anodic process, the stability of the reduction potential is slightly higher for 3l-5s than for 3l-5s/AuNP-4.

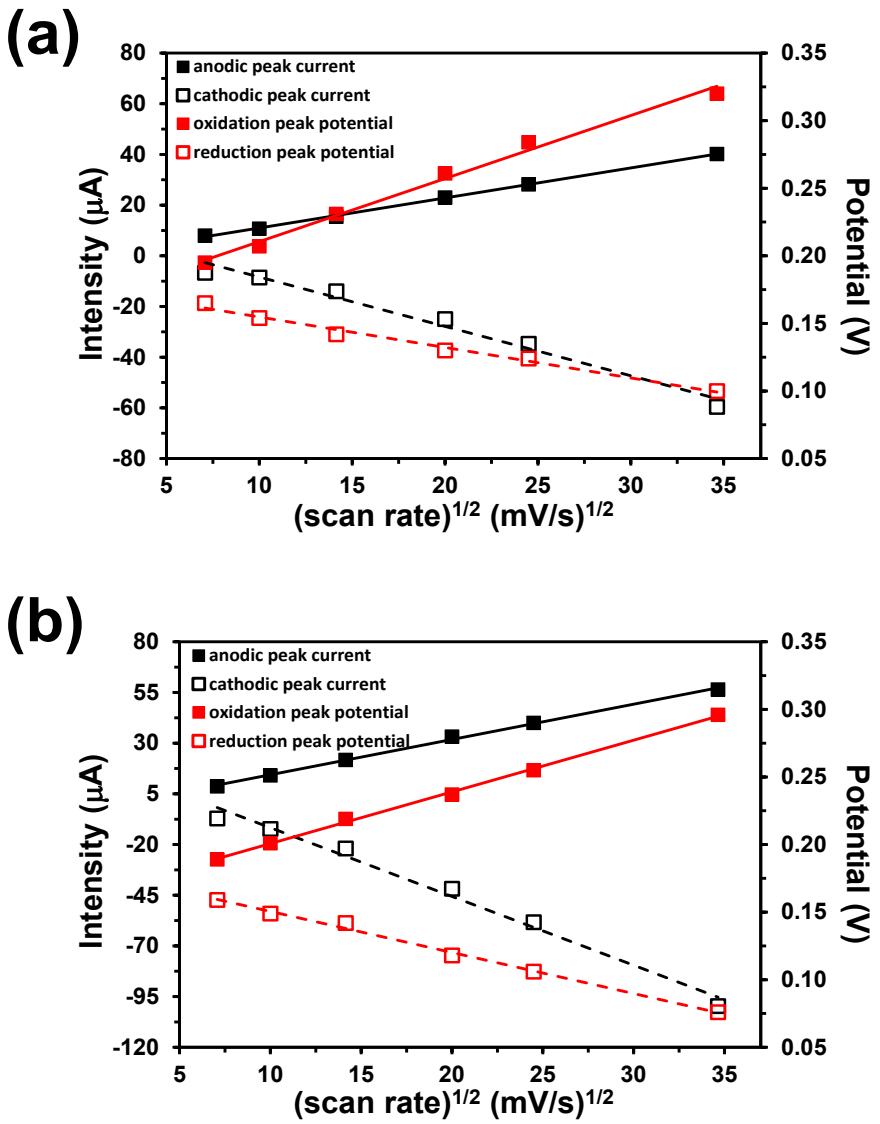

Figure 13. Variation of the anodic peak intensity, oxidation peak potential, cathodic peak intensity and reduction peak potential against the square root of the scan rate for (a) 3l-s5 and (b) 3l-5s/AuNP-4 in presence of 1 mM DA in 0.1 M PBS.

Figure 14 represents the variation of the D_0 (Eqn 1) against the scan rate. The flux to the electrode surface increases linearly with the scan rate, this increment being slightly higher for 3l-5s/AuNP-4 than for 3l-5s. The apparent diffusion coefficient (D_{app}) of DA is $2.7 \cdot 10^{-3}$ and $4.6 \cdot 10^{-3}$ $cm^2 \cdot s^{-1}$ for 3l-5s and 3l-5s/AuNP-4, respectively. This behaviour indicates that the charge transfer is under a diffusion control process.

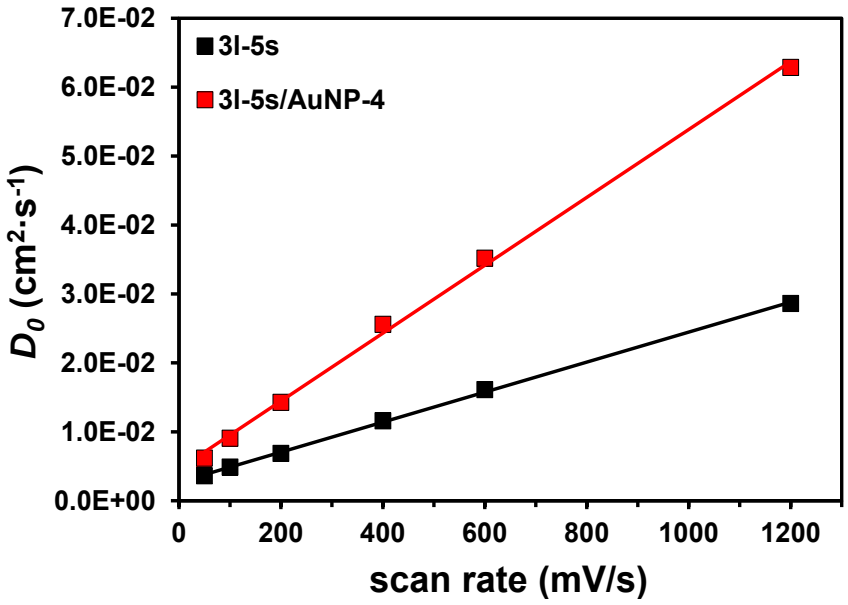

Figure 14. Variation of the D_0 (Eqn 1) against the scan rate.

Calibration curve.

The detection limit of 3l-5s and 3l-5s/AuNP-4 was determined by CV using a scan rate of 50 mV·s^{-1}. Figures 15a and 16 show the results of standard addition of 10 μL DA to 10 mL of 0.1 M PBS (*i.e.* a linear range of 1-100 μM DA). The anodic I_p increases with the concentration of DA for the two electrodes. The response of DA is apparently improved by the incorporation of AuNPs, even though such improvement is relatively small. The detection limit, which was determined using a calibration curve for DA concentrations from 1 to 10 μM (inset in Figure 15a), was 3 μM (0.037 μA) and 2 μM (0.015 μA) for 3l-5s and 3l-5s/AuNP-4, respectively.

Figures 15b and 17 display the voltammetric response of DA (1 to 100 μM) in presence of interferents (*i.e.* 200 μM AA and 100 μM UA in 0.1 M PBS) at 3l-5s and 3l-5s/AuNP-4 electrodes. As it was observed in Figure 15a, CV results show that the anodic I_p increases with DA concentration, indicating that the adsorption of oxidized DA molecules in surface of the electrode is favoured with respect to the adsorption of AA and UA. This effect is more pronounced for 3l-5s/AuNP-4 than for 3l-5s. However, the limit of detection decreases considerably in presence of interferents. Thus, the anodic I_p obtained for a solution of 10 μM DA in 0.1 M PBS without any interferent is 0.270 and 0.379 μA for 3l-5s and 3l-5s/AuNP-4, respectively, these values decreasing to 0.027 and 0.075 μA in presence of 200 μM AA and 100 μM UA.

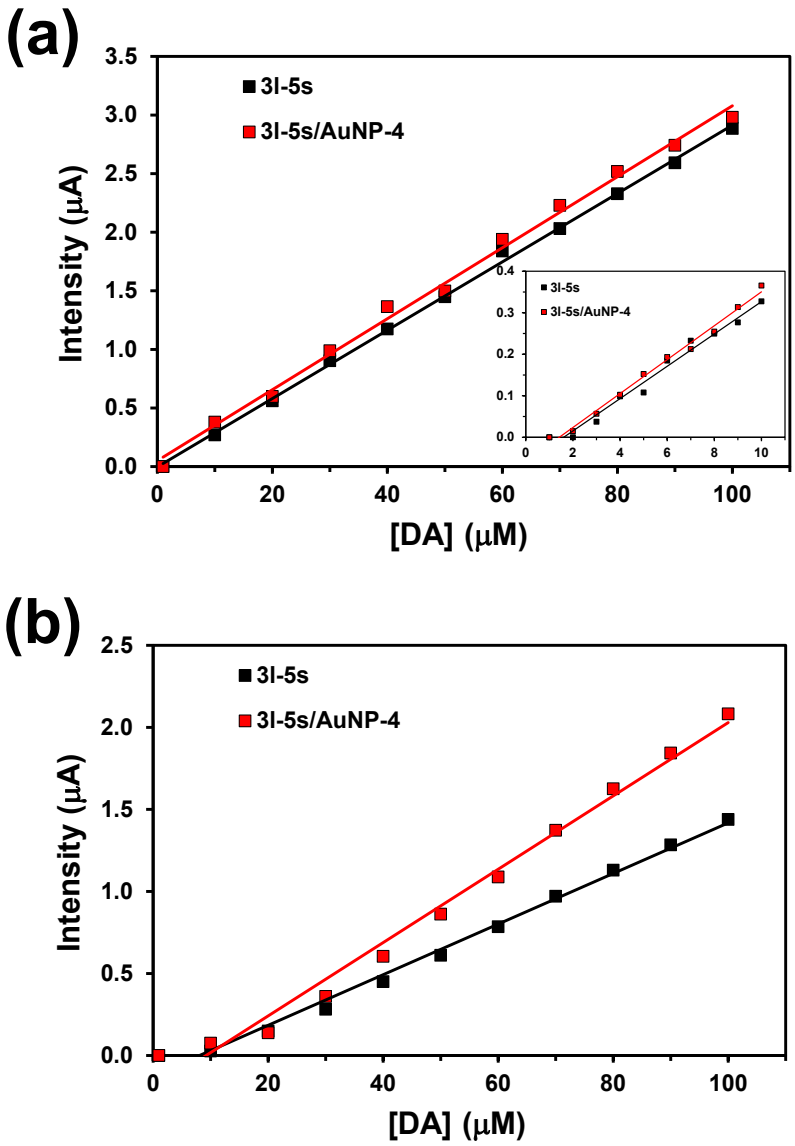

Figure 15. (a) Calibration curve for DA concentrations ranging from 1 to 100 μM (inset: from 1 to 10 μM) in 0.1 M PBS at 3l-5s and 3l-5s/AuNP-4 electrodes. (b) Calibration curve for DA concentrations ranging from 1 to 100 μM in 0.1 M PBS with 200 μM AA and 100 μM UA, acting as interferents, at 3l-5s and 3l-5s/AuNP-4 electrodes. CVs are displayed in Figures 16 and 17.

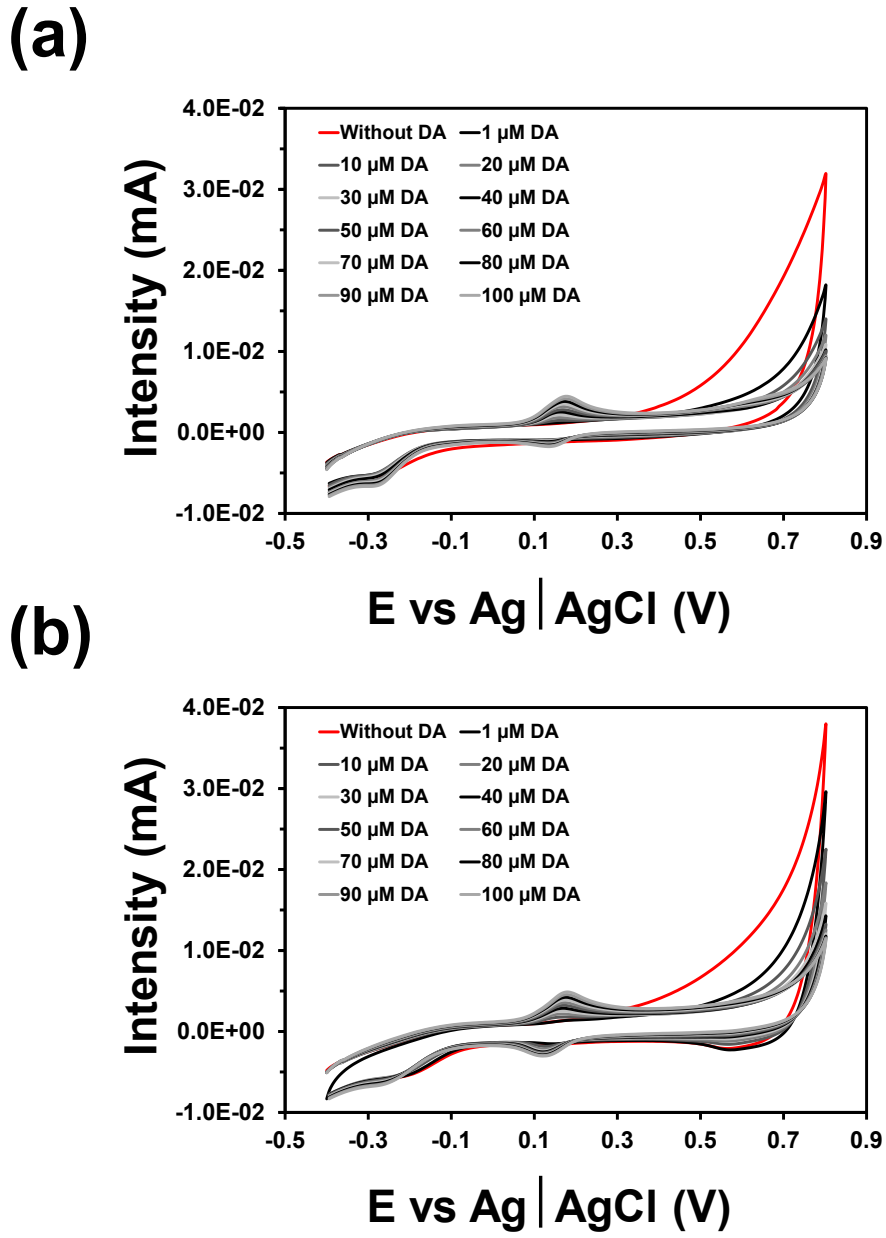

Figure 16. Control voltammograms at (a) 3l-5s and (b) 3l-5s/AuNP-4 electrodes of DA concentrations ranging from 1 to 100 µM in 0.1 M PBS. The voltammogram in absence of DA is also displayed (red line). Voltammograms were obtained by scanning from -0.40 to 0.80 V at a scan rate of 50 $mV \cdot s^{-1}$. These results were used for the calibration curves displayed in Figure 15a.

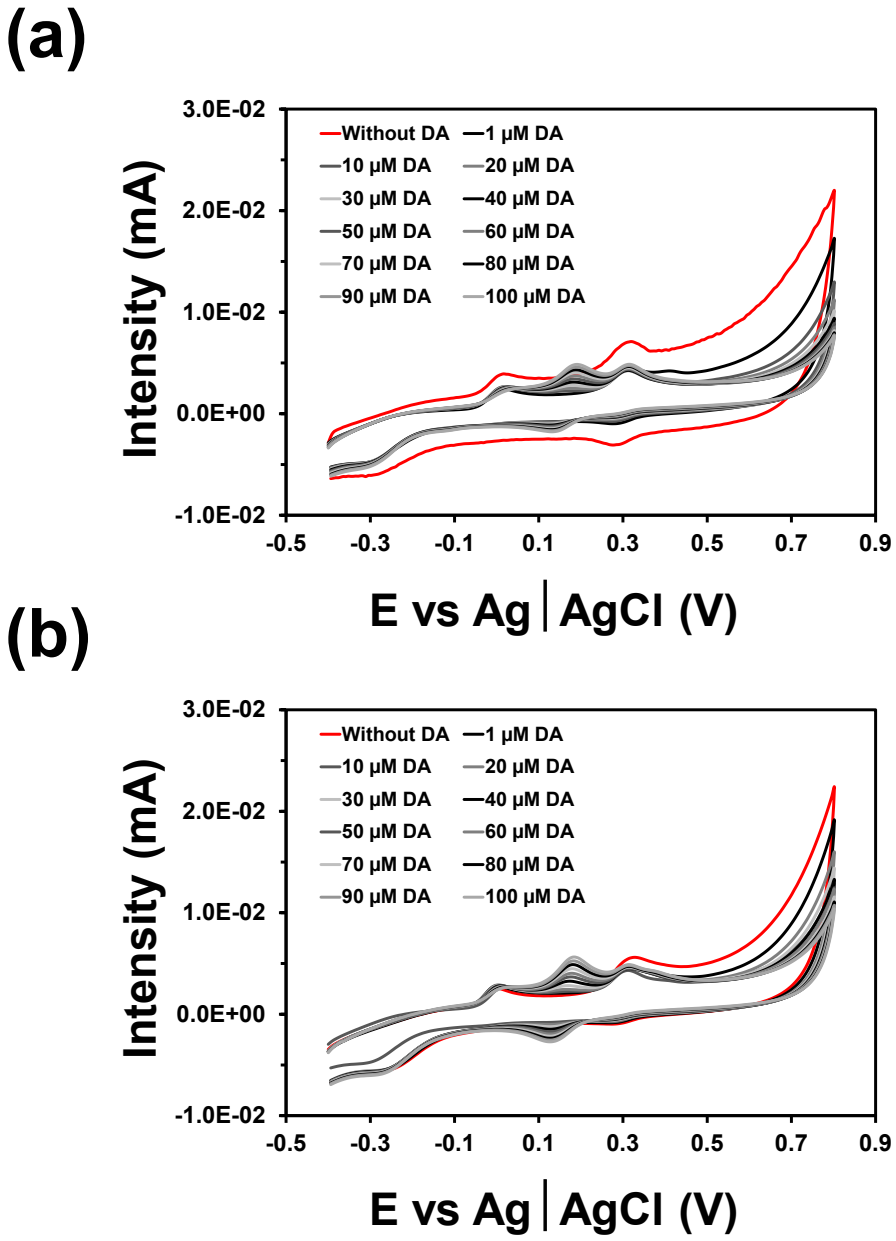

Figure 17. Control voltammograms at (a) 3l-5s and (b) 3l-5s/AuNP-4 electrodes of DA concentrations ranging from 1 to 100 µM in 0.1 M PBS with 200 µM AA and 100 µM UA acting as interferents. The voltammogram in absence of DA is also displayed (red line). Voltammograms were obtained by scanning from -0.40 to 0.80 V at a scan rate of 50 $mV \cdot s^{-1}$. These results were used for the calibration curves displayed in Figure 15b.

Detection of DA in human urine.

Human urine was successfully used to evaluate the reliability of 3l-5s/AuNP-4 films to detect DA in real samples. Initially, pH of urine was adjusted to 7.4 by adding NaOH and, subsequently, suspended solids were eliminated by centrifugation (5 minutes at 4000 rpm). As the oxidation peak of urea was found to overlap the detection potential of DA, the electrode was stabilized by applying four consecutive oxidation-reduction cycles, which enabled to shift the oxidation peak of urea towards higher potentials.

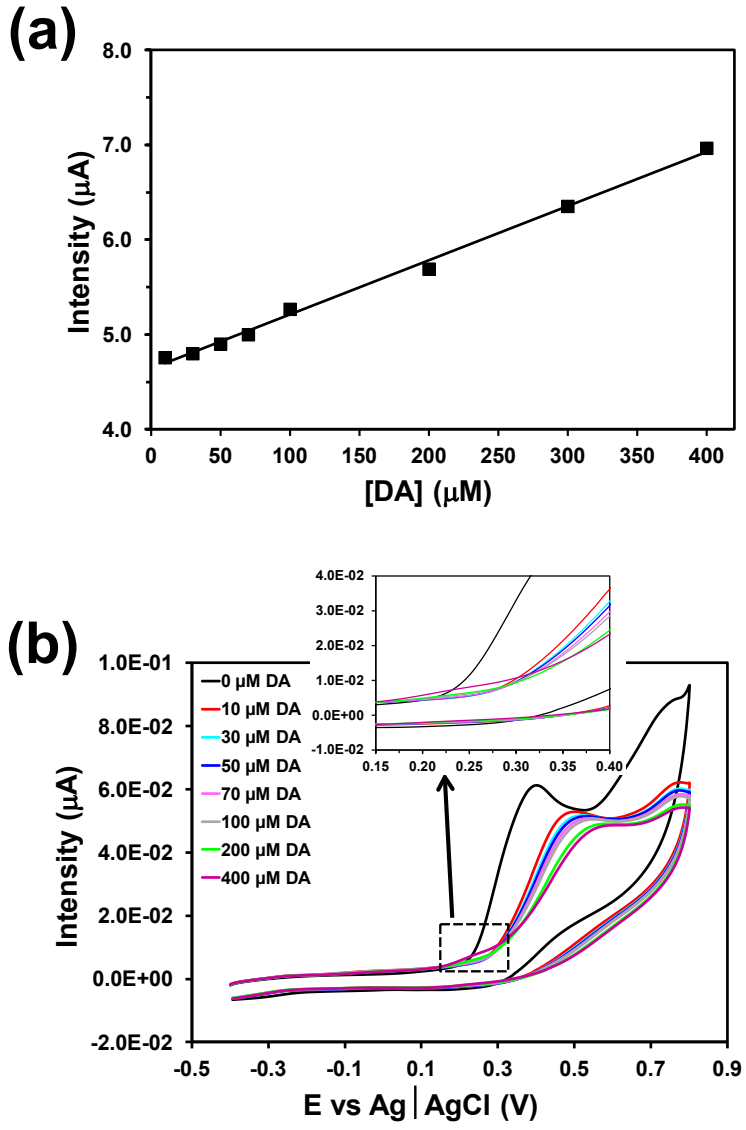

Figure 18. (a) Calibration curve for DA concentrations ranging from 10 to 400 μM in human urine samples at 3l-5s and 3l-5s/AuNP-4 electrodes. (b) Control voltammograms at 3l-5s/AuNP-4 electrode of DA concentrations ranging from 10 to 400 μM in human urine samples. Voltammograms were obtained by scanning from -0.40 to 0.80 V at a scan rate of 50 $mV \cdot s^{-1}$.

Figure 18 summarizes the voltammetric response results determined for samples prepared through the standard addition of 10, 30, 50, 70, 100, 200, 300 and 400 μM DA to 10 mL of urine. The results are very satisfactory considering the interference of urea. Thus, the anodic peak associated to the oxidation of DA is clearly identified for concentrations ≥ 100 μM DA (Figure 18b). The calibration curve (Figure 18a) shows a linear behaviour with correlation coefficient of 0.996, the anodic I_p determined for 10 and 100 μM DA being 4.76 and 5.27 μA. These results demonstrate that submicrometric 3-layered PEDOT/PNMPy/PEDOT electrodes coated with AuNPs can be successfully used for the selective detection of an excess DA in real urine samples, preventing the neurological disorders associated to high concentrations of such neurotransmitter.

4.5.4 Conclusions

PEDOT/PNMPy/PEDOT, PEDOT/PNCPy/PEDOT, PNMPy/PEDOT/PNMPy and PNCPy/PEDOT/PNCPy 3-layered films have been prepared to evaluate the performance of 3-layered films for the sensitive and selective detection of DA. SEM studies indicate that all 3-layered films with exception of PNCPy/PEDOT/PNCPy, which is compact, present a porous surface morphology that is expected to facilitate the access and escape of ions into the polymeric matrix during oxidation and reductions processes, respectively. The thickness of the films prepared using a total θ of 11-13 s ranged from 350 nm (those with PEDOT in the intermediate layer) to ~1 μm (those with PEDOT in the external and internal layers), indicating that GC considerably promotes the polymerization of EDOT monomers.

Voltammetric studies on individual CPs indicated that, independently of the AuNPs coating, PEDOT is more appropriated for the selective detection of DA than PNMPy and PNCPy (*i.e.* the oxidation peak of AA is indistinguishable while the oxidation peaks of DA and UA overlap). Similar voltammetric studies to examine the electrochemical behaviour of a solution mixture with 100 μM DA, 200 μM AA and 100 μM UA in 0.1 M PBS at 3-layered and 3-layered/AuNP electrodes indicate that the PEDOT/PNMPy/PEDOT and PEDOT/PNMPy/PEDOT/AuNP show the best performance in terms of both sensitivity and resolution. Furthermore, the D_0 of DA is also very high

for such two electrodes. The capabilities of PEDOT/PNMPy/PEDOT and PEDOT/PNMPy/PEDOT/AuNP electrodes for the detection of DA have been found to remain practically unaltered when the thickness of the film decreases from ~1 μ to ~700 nm. AuNPs improve moderately the sensitivity of submicrometric PEDOT/PNMPy/PEDOT electrodes, even though this catalytic activity does not increase with the concentration of nanoparticles and is considerably lower than that reported for individual PNMPy films.[10,11]

The influence on the detection process of an electrochemical pre-treatment based on the application of consecutive oxidation-reduction cycles to the 3-layered electrodes has been examined. Results indicate that, although application of redox cycles before of the detection provokes a LEA, the anodic peak density associated to the DA oxidation does not undergo significant changes while the oxidation E_p shifts to higher values. Consequently, this electrochemical pre-treatment can be used as a strategy to improve the selectivity of 3-layered electrodes without alters their sensibility.

The anodic I_p increases with the concentration of DA for submicrometric PEDOT/PNMPy/PEDOT electrodes with and without AuNPs. The limit of detection for such electrodes is around 10 μM in presence of AA and UA, decreasing to 2-3 μM in absence of the interferents. The submicrometric PEDOT/PNMPy/PEDOT film coated with AuNP has been successfully used to identify DA in samples with real interferents made of human urine.

4.5.5 References

1. J. Li, H. Xie and L. Chen, *Sens. Actuators B*, 2011, **153**, 239.
2. J. Wang and W.-D. Zhang, *J. Electroanal. Chem.*, 2011, **654**, 79.
3. M. Chen and G. Diao, *Talanta*, 2009, **80**, 815.
4. G.-Z. Hu, D.-P. Zhang, W.-L. Wu and Z.-S. Yang, *Colloids Surf. B*, 2008, **62**, 199.
5. R. N. Goyal, V. K. Gupta, M. Oyama and N. Bachheti, *Talanta*, 2007, **72**, 976.
6. Y. Song, Y. Ma, Y. Wang, J. Di and Y. Tu, *Electrochim. Acta*, 2010, **55**, 4909.
7. X. Li, R. Yuan, Y. Chai, L. Zhang, Y. Zhuo and Y. Zhang, *J. Biotechnol.*, 2006, **123**, 356.
8. S. Liu, Z. Yang, Z. Liu and L. Kong, *Anal. Biochem.*, 2006, **353**, 108.
9. C. R. Raj, T. Okajima and T. Ohsaka, *J. Electroanal. Chem.*, 2003, **543**, 127.
10. M. Martí, G. Fabregat, F. Estrany, C. Alemán and E. Armelin, *J. Mat. Chem.,* 2010, **20**, 10652.

11. G. Fabregat, E. Córdova-Mateo, E. Armelin, O. Bertran and C. Alemán, *J. Phys. Chem. C*, 2011, **115**, 14933.

12. S. O. Obare, R. E. Hollowell and C. J. Murphy, *Langmuir*, 2002, **18**, 10407.

13. Y. Kim, R.C. Johnson and J.T. Hupp, *NanoLett.*, 2001, **1**, 165.

14. A. Berlin, B. Vercelli and G. Zotti, *Polym. Rev.*, 2008, **48**, 493.

15. C. Zanardi, F. Terzi and R. Seeber, *Sens. Actuators B*, 2010, **148**, 277.

16. P. Englebieene and A. Van Hoonacker, *Curr. Nanosci.,* 2005, **1**, 97.

17. C. B. Sih and M. O. Wolf, *Chem. Commun.* 2005, **27**, 3375.

18. Z. Xian, Y. Hu, F. Liu, Y. Xian, H. T. Wang, and L. T. Jin, *Biosens. Bioelectr.*, 2006, **21**, 1996.

19. X. Li, Y. Li, Y. Tan, C. Yang and Y. Li, *J. Phys. Chem. B*, 2002, **108**, 5192.

20. M. Marinakos, L. C. Brousseau, III, A. Jones and D. L. Feldheim, *Chem. Mater.*, 1998, **10**, 1214.

21. B. C. Sih, A. Teichert and M. O. Wolf, *Chem. Mater.,* 2004, **16**, 2712.

22. O. Zhang, Y. Wen, J. Xua, L. Lua, X. Duana and H. Yua *Synth. Met.* 2013, **164**, 47.

23. E. Spain, T. E. Keyes and R. J. Forster, *Biosens. Bioelectr.*, 2013, **41**, 65.

24. N. F. Atta, A. Galal and E. H. El-Ads, *Electrochim. Acta,* 2012, **69**, 102.

25. E. R. Kandel, J. H. Schwartz and T. M. Jessel, Principles of Neural Science, New York, McGraw-Hill, 4th edn, 2000, 207.

26. E. K. Richfield, J. B. Penney and A. B. Young, *Neuroscience*, 1989, **30**,767.

27. D. Aradilla, F. Estrany and C. Alemán, *J. Phys. Chem. C*, 2011, **115**, 8430.

28. D. Aradilla, F. Estrany, R. Oliver and C. Alemán, *Eur. Polym. J.*, 2010, **46**, 2222.

29. F. Estrany, D. Aradilla, R. Oliver, E. Armelin and C. Alemán, *Eur. Polym. J.,* 2008, **44**, 1323.

30. F. Estrany, D. Aradilla, R. Oliver and C. Alemán, *Eur. Polym. J.,* 2007, **43**, 1876.

31. D. Aradilla, F. Estrany, E. Armelin and C. Alemán, *Thin Solid Films*, 2010, **518**, 4203.

32. D. Aradilla, M. M. Pérez-Madrigal, F. Estrany, D. Azambuja, J. I. Iribarren and C. Alemán, *Org. Electr.,* 2013, **14**, 1483.

33. R. G. Freeman, M. B. Hommer, K. C. Grabar, M. A. Jackson and M. J. Natan, *J. Phys. Chem.,* 1996, **100**, 718.

34. S. Link and M. A. El-Sayed, *J. Phys. Chem. B*, 1999, **103**, 8410.

35. M. M. Maye, L. Han, N. N. Kariuki, N. K. Ly, W. B. Chan and C. J. Zhong, *Anal. Chim. Acta,* 2003, **496**, 17.

36. C. Ocampo, R. Oliver, E. Armelin, C. Alemán and F. Estrany, *J. Polym. Res.*, 2006, **13**, 193.

37. R. Oliver, A. Muñoz, C. Ocampo, C. Alemán, E. Armelin and F. Estrany, *Chem. Phys.*, 2006, **328**, 299.

38. D. Aradilla, F. Estrany, E. Armelin, R. Oliver, J. I. Iribarren and C. Alemán, *Macromol. Chem. Phys.*, 2010, **211**, 1663.

39. D. Aradilla, F. Estrany, E. Armelin and C. Alemán, *Thin Solid Films,* 2012, **520**, 4402.

40. D. Aradilla, D. Torras and C. Alemán, *J. Phys. Chem. B*, 2011, **115**, 2882.

41. X. Q. Lin and L. Zhang, *Anal. Lett.*, 2001, **34**, 1585.

42. X. Feng, C. Mao, G. Yang, W. Hou and J. J. Zhu, *Langmuir*, 2006, ***22***, 4384.

43. N. F. Atta, A. Galal and R. A. Ahmed, *Bioelectrochemistry*, 2011, **80**, 132.

4.6 A rational design for the selective detection of dopamine using conducting polymers */**

PNMPy, PNCPy and PEDOT films have been prepared using both single and two polymerization steps for the selective determination of low concentrations of DA, AA and UA in tertiary mixtures. Analysis of the sensitivity and resolution parameters derived from the electrochemical response of such films indicates that PEDOT is the most appropriated for the unambiguous detection of the three species. Indeed, the performance of PEDOT is practically independent of the presence of both AuNPs at the surface of the film and interphases inside the film, even though these two factors are known to improve the electroactivity of CPs. QM calculations on model complexes have been used to examine the intermolecular interaction involved in complexes formed by PEDOT chains and oxidized DA, AA and UA. Results show that such complexes are mainly stabilized by C–H···O interactions rather than by conventional hydrogen bonds. In order to improve the sensitivity of PEDOT through the formation of specific hydrogen bonds, a derivative bearing a hydroxymethyl group attached to the dioxane ring of each repeat unit has been designed. Poly(hydroxymethyl-3,4-ethylenedioxythiophene) (PHMeDOT) has been prepared and characterized by FTIR, UV-vis, CV, SEM and AFM. Finally, the performance of PHMeDOT and PEDOT for the selective detection of the species mentioned above has been compared.

*Results described in this section previously appeared in *Phys. Chem. Chem. Phys.* 2014, **16**, 7850.

**The QM calculations were performed by Dr. J. Casanovas.

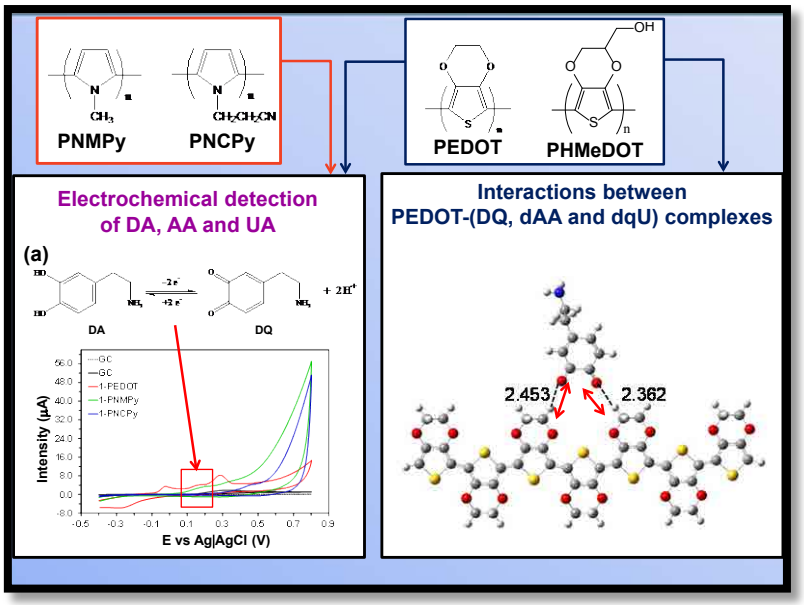

4.6.1 Introduction

π-Conjugated CPs, such as PPy and PTh derivatives, have been subject of intense research due to their interesting electronic and optical properties.[1-3] Among PTh derivatives, PEDOT deserves special attention because of a combination of properties. This CP, which was originally described by researchers at the Bayer company, exhibits moderate band gap, low oxidation potential, high conductivity, good optical transparency, and exceptional environmental stability.[4-6] PEDOT attracted considerable interest, and many electronic applications based on these properties were rapidly developed (*e.g.* electrode material in supercapacitors, hole injection layer in organic light-emitting diodes and solar cells).[7-10] Recently, some potential biotechnological applications for this CP have also been proposed (*e.g.* biosensor for the detection of specific nucleotide sequences,[11] neurotransmitters[12] and amino acids,[13] biocondenser with bactericide properties,[14,15] bioactive substrate for cell adhesion and proliferation[16,17]).

CPs have been successfully used to detect DA,[18-23] which is an important neurotransmitter of catecholamine in the human brain.[24]The very low concentration of DA in the extracellular fluid[25] provides a huge challenge for the detection of this analyte. The temporal fluctuation of the DA concentration in the human brain has a critical effect on several neurological disorders, such as Harrington's disease and Parkinson disease.[25] In recent studies we detected DA concentrations significantly lower than the synaptic one (1.6 mM) using PPy derivatives.[18,19] More specifically, PNMPy and PNCPy, deposited on GCEs were found to be highly sensitive to the DA concentration, presenting a very fast response even when the concentration of neurotransmitter is very low.[18,19] Furthermore, such response was enhanced by adding AuNPs to PNMPy or PCNPy films (*i.e.* forming PNMPy/AuNP and PNCPy/AuNP composites), even though metallic nanoparticles were not essential for the sensing abilities of such CPs. QM calculations indicated that intermolecular C–H···O interactions play a crucial role in the detection of DA using such two PPy derivatives.[19] More recently, PEDOT and PEDOT/AuNP deposited on different types electrodes were used for the selective determination of very low DA concentrations in presence of UA and AA.[20-23] It should be mentioned that DA, AA and UA coexist in extracellular fluids of

the central nervous system and, therefore, the selective determination of these species is a major goal for the biomedical application of sensors.

Despite of the accrued interest for selective sensing of DA using electrochemical methods, the abilities of PPy and PTh derivatives mentioned above have not been compared yet. This seems a crucial requirement for the rational design of CPs with optimized sensing capacities. In this work we compare the sensing ability of PEDOT, PNMPy and PNCPy (Figure 1) for the electrochemical detection of DA in tertiary mixtures with UA and AA. For this purpose, sensing templates based on such three CPs have been prepared by applying both a single and two polymerization steps. Recent studies evidenced that the electrochemical properties of CPs produced using multiple polymerization steps are significantly better than those of materials yielded through a continuous polymerization process,[26] which was attributed to the existence of favorable interactions at the interfaces induced by the former procedure. Accordingly, the impact of such interactions in the sensing ability of CPs has been examined by comparing materials produced using a single continuous process (*i.e.* 1-CP, where CP= PEDOT, PNMPy or PNCPy) and two polymerization steps (*i.e.* 2-CP). On the other hand, the synergy between AuNPs and CPs has been ascertained by comparing the sensitivity and resolution of 1-CP and 2-CP sensors with those of composites prepared by coating the surface of CP films with AuNPs (*i.e.* 1-CP/AuNPs and 2-CP/AuNPs). Furthermore, QM methods based on Density Functional Theory (DFT) calculations have been applied to investigate the interactions involved in the binding between PEDOT and the oxidized analytes. Results have been compared with those reported for PNMPy and PNCPy.[19] Overall of the results has been used to improve the selectivity and sensitivity of PEDOT by engineering some chemical modifications essentially oriented to enhance the binding between the CP and the analytes. Experimental development of such rational design has allowed us to identify a CP that has been proved to show optimized selectivity and sensitivity for the separation of DA, AA and UA in tertiary mixtures.

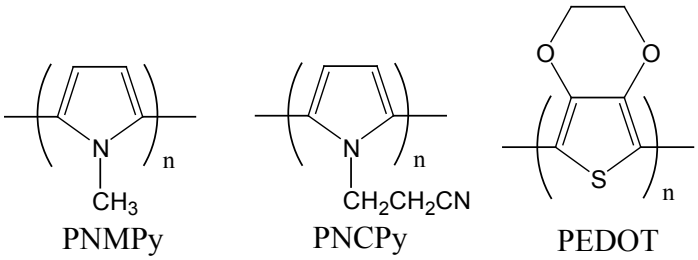

Figure 1. Molecular structure of PNMPy, PNCPy and PEDOT.

4.6.2 Methods

Materials. EDOT, NMPy, NCPy, acetonitrile, anhydrous $LiClO_4$, DA hydrochloride, AA (L-configuration, crystalline), UA (crystalline) and $HAuCl_4 \cdot 3H_2O$ of analytical reagent grade were purchased from Sigma-Aldrich (Spain), whereas sodium citrate dehydrate was obtained from J. T. Baker. All chemicals were used without further purification. PBS 0.1 M with pH=7.4 was prepared as electrolyte solution by mixing four stock solutions of NaCl, KCl, $NaHPO_4$ and KH_2PO_4. High-purity nitrogen was used for de-aeration of the prepared aqueous solutions.

Synthesis of CPs. PEDOT, PNMPy and PNCPy films were prepared by CA under a constant potential of 1.40 V[27-29] using a three-electrode two-compartment cell under nitrogen atmosphere (99.995% in purity) at 25 ºC. A bare of GC with a diameter of 2 mm was used as WE while a steel AISI 316 sheet with an area of 1 cm^2 was employed as CE. The surface of the GCE was polished with alumina powder and cleaned by ultrasonication prior to the deposition of the polymer. The RE was an Ag|AgCl electrode containing a KCl saturated aqueous solution (Eº = 0.222 V *vs.* standard hydrogen electrode at 25 ºC), which was connected to the working compartment through a salt bridge containing the electrolyte solution. All electrochemical experiments were conducted on a PGSTAT302N AUTOLAB potenciostat-galvanostat (Ecochimie, The Netherlands) equipped with the ECD module to measure very low current densities (100 μA-100 pA), which was connected to a PC computer controlled through the NOVA 1.6 software.

1-PEDOT, 1-PNMPy and 1-PNCPy films (*i.e.* CPs prepared with a single polymerization step) were obtained using a 10 mM monomer solution in acetonitrile with 0.1 M $LiClO_4$ and a polymerization time $\theta_{1\text{-}CP}$= 6, 10 and 10 s, respectively. The

generation of 2-CP films was performed with two polymerization steps. In the first step, the WE was immersed in a cell filled with a 10 mM monomer solution in acetonitrile with 0.1 M $LiClO_4$ for a period of time (θ_1). After this, the polymerization was interrupted and the electrode coated with the first layer of CP was immersed in a fresh solution identical to the previous one during a period of time (θ_2). Accordingly, the total polymerization time for each 2-layered film is: $\theta_{2\text{-}CP}= \theta_1 + \theta_2$ s. In order to obtain thin films, $\theta_1=\theta_2=$ 3 s for 2-PEDOT and $\theta_1=\theta_2=$ 5 s for both 2-PNMPy and 2-PNCPy. Thus, $\theta_{1\text{-}CP}=\theta_{2\text{-}CP}=$ 6, 10 and 10 s for all films based on PEDOT, PNMPy and PNCPy, respectively.

Preparation of AuNPs. Preparation of the AuNPs was performed following the standard procedure described in the literature.[30,31] All glassware used in such preparation was thoroughly cleaned in aqua regia (3:1 $HCl:HNO_3$), rinsed in doubly distilled water, and oven-dried prior to use. In a 1 L round-bottom flask equipped with a condenser, 500 mL of 1 mM $HAuCl_4$ was brought to a rolling boil with vigorous stirring. Rapid addition of 50 mL of 38.8 mM sodium citrate to the vortex of the solution produced a color change from pale yellow to burgundy. Boiling was continued for 15 min. After this, the heating mantle was removed while the stirring was continued for 30 min. When the solution reached the room temperature, it was filtered through a 0.2 μm membrane filter. The resulting solution of colloidal particles showed an absorption maximum at 520 nm indicating that the particle size ranged from 9 to 22nm. A spherical model for a particle size of 13 nm was used to determine approximately the concentration of mother solution from UV-vis absorption, which was estimated to be 7.4 nM.[31]

Preparation of AuNPs-modified GCEs. Deposition of the AuNPs onto the modified GCEs to fabricate 1-CP/AuNP and 2-CP/AuNP composites was performed using a previously used procedure.[18] More specifically, 4 μL of the AuNPs colloidal solution were dropped onto the 1-CP and 2-CP films surface, drying under atmosphere conditions being subsequently allowed. The AuNPs concentration in the modified electrode surface was determined to be $\sim 23 \cdot 10^9$ nanoparticles/mm^2, assuming that all the AuNPs were well adhered to the 1-CP and 2-CP modified GCE, since no absorption band at 520 nm was identified in the electrochemical solution after tests.

Profilometry. The thickness of the films was determined through profilometry measurements using a profilometer Dektack 6 from Veeco.

Electrochemical measurements for detection of DA. Electrochemical detection was carried out by CV using the Autolab PGSTAT302N equipment described above. All electrochemical experiments were performed in a glass cell containing 10 mL of 0.1 M PBS (pH=7.4) at room temperature and equipped with saturated Ag|AgCl as reference electrode and Pt wire as CE. Voltammograms were recorded in the potential range from -0.40 to 0.80 V at a scan rate of 50 $mV \cdot s^{-1}$ unless other scan rate is explicitly specified. All the modified electrodes were in contact with the electrolyte solution for 5 min prior to CV measurements.

FTIR and UV-vis. FTIR spectra were recorded on a Bruker Vertex 70 FTIR spectrometer, equipped with a diamond ATR device (Golden Gate, Bruker) in transmission mode, by using KBr pellets.

UV-vis absorption spectra were obtained using a UV-vis-NIR Shimadzu 3600 spectrophotometer equipped with a tungsten halogen visible source, a deuterium arc UV source, a photomultiplier tube UV-vis detector, and a InGaAs photodiode and cooled PbS photocell NIR detectors. Spectra were recorded in the absorbance mode using the integrating sphere accessory (model ISR-3100), the range wavelength being 200–900 nm. The interior of the integrating sphere was coated with highly diffuse $BaSO_4$ reflectance standard. Single-scan spectra were recorded at a scan speed of 60 nm/min. Measurements, data collection and data evaluation were controlled by the computer software UVProbe version 2.31.

Electrochemical properties. The electrochemical properties (i.e. electroactivity and stability) of the polymer designed in this work were determined by CV using a PBS solution (pH= 7.4). The initial and final potentials were -0.4 V, and the reversal potential was 0.8 V. A scan rate of 50 $mV \cdot s^{-1}$ was used.

SEM. SEM studies were carried out using a FIB Zeiss Neon40 scanning electron microscope operating at 5 kV, equipped with an EDX spectroscopy system. The samples were mounted on a double-sided adhesive carbon disc.

AFM. Topographic images were obtained with a Molecular Imaging PicoSPM using a NanoScope IV controller in ambient conditions. The root-mean-square roughness (r_{AFM}) was determined considering a 5×5 μm^2 window size.

QM calculations. Calculations were performed using the Gaussian 09[32] computer package. PEDOT was modeled considering small oligomers in the radical cation state (charge= +1 and spin multiplicity= 2) made of *n* repeat units (*n*-EDOT with *n*= 1, 3 and 5). DA, AA and UA were considered as oxidized species (Figure 2): DQ, dehydroascorbic acid (dAA) and quinoid diimine form (qdU), respectively. It is worth noting that the selection of DQ, dAA, qdU and the oxidized oligomers was based on our own experimental results (see Results and Discussion section), which indicate that at the detection potential the oxidation from DA to DQ, AA to dAA, and UA to qdU has occurred and the polymer is oxidized.

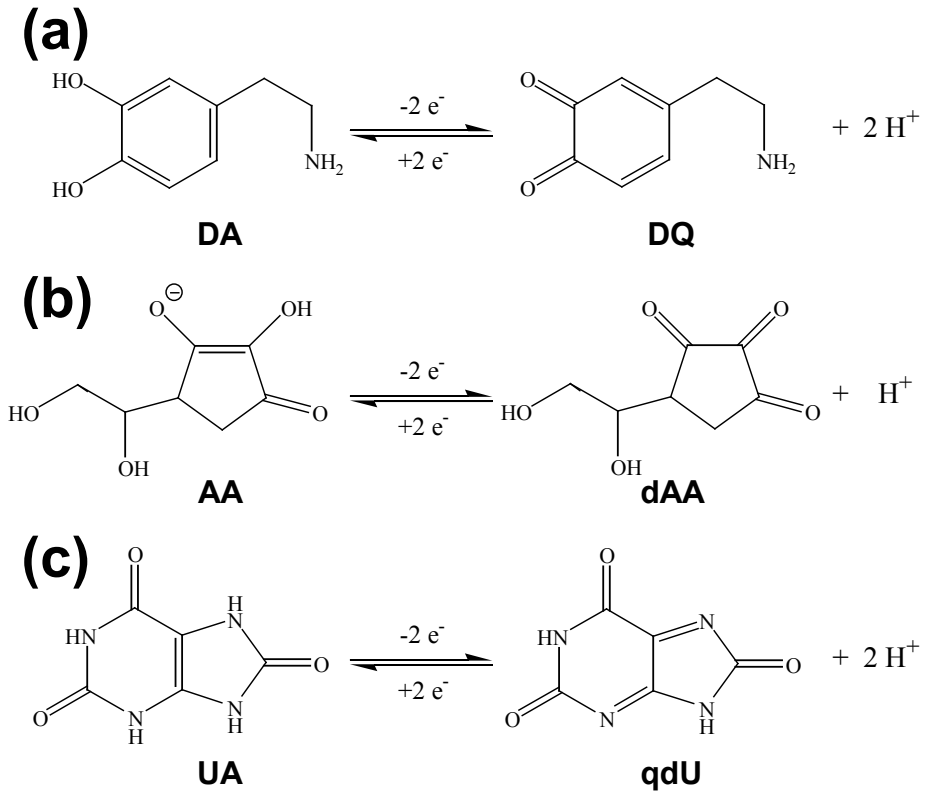

Figure 2. Electrochemical oxidation reactions for (a) DA, (b) AA and (c) UA.

The structures of the *n*-EDOT···DQ, and *n*-EDOT···dAA and *n*-EDOT···qdU complexes were determined by full geometry optimization in the gas-phase at the UB3LYP[33,34] level using the 6-311++G(d,p) basis set.[35,36] ΔE_{int} was calculated as the difference between the total energy of the optimized complex and the energies of the

isolated monomers with the geometries obtained from the optimization of the complex. The *CP* method[37] was applied to correct the basis set superposition error from the ΔE_{int}.

4.6.3 Results and discussion

Oxidation of DA, AA and UA at 1-CP and 1-CP/AuNP electrodes.

1-CP and 1-CP/AuNPs were electrodeposited potentiostatically on GCEs using the experimental conditions described in the Methods section. The thickness of the resulting films, which was estimated by profilometry, was ~0.7 μm for 1-PEDOT and ~0.3 μm for both 1-PNMPy and 1-PNCPy. This result indicates that GC significantly promotes the polymerization of EDOT monomers, which is a very striking observation. Thus, the thickness of PEDOT films produced using the same experimental conditions (*i.e.* fixed potential at 1.40 V, acetonitrile solvent and $LiClO_4$ as supporting electrolyte) and a polymerization time of 5 s is ~50 nm when deposited on steel or ITO electrodes.[38]

The voltammetric behavior of DA in PBS at electrodes modified with PEDOT, PNMPy, PNCPy and their composites with AuNPs was reported in previous studies[18-23] and, therefore, the comparison between the three modified electrodes has been focused on the selective determination of DA, AA and UA in tertiary mixtures. Figure 3 shows the voltammograms recorded for the solution mixture with 100 μM DA, 200 μM AA and 100 μM UA in 0.1 M PBS at GCEs modified with 1-CP or 1-CP/AuNP films. The electrochemical response to the tertiary mixture at bare GC and GC/AuNP electrodes, which is included in Figure 3, is very poor.

The anodic E_p for the oxidation of DA at 1-PNMPy electrode is 0.15 V while the anodic I_p associated to such process is 0.51 μA. Both E_p and, especially, I_p change significantly when the 1-PNMPy electrode is coated with AuNPs. Thus, the E_p and I_p values for the oxidation of DA at 1-PNMPy/AuNP are 0.21 V and 2.50 μA, respectively. These results are fully consistent with the behavior previously reported for the same electrodes in 0.1 M PBS with 100 μM DA (*i.e.* solution without interferents).[18,19] The electrocatalytic activity imparted by AuNPs to these electrodes should be attributed to their well-known ability for channeling electrons between the electrode and the

electroactive species, promoting better electron transfer between the electrode and the electrolyte.[39] Thus, AuNPs facilitates the effective charge migration through the 1-PNMPy films by generating many active sites inside this CP-electrode. Figure 3 also evidences that, unfortunately, the detection of AA is problematic with 1-PNMPy and 1-PNMPy/AuNP electrodes since the oxidation peak is inappreciable. Furthermore, the oxidation peaks of DA and UA overlap at PNMPy-containing electrodes making difficult the selective and simultaneous determination of such two species. This behavior does not change when the concentration of analyte is increased (data not shown).

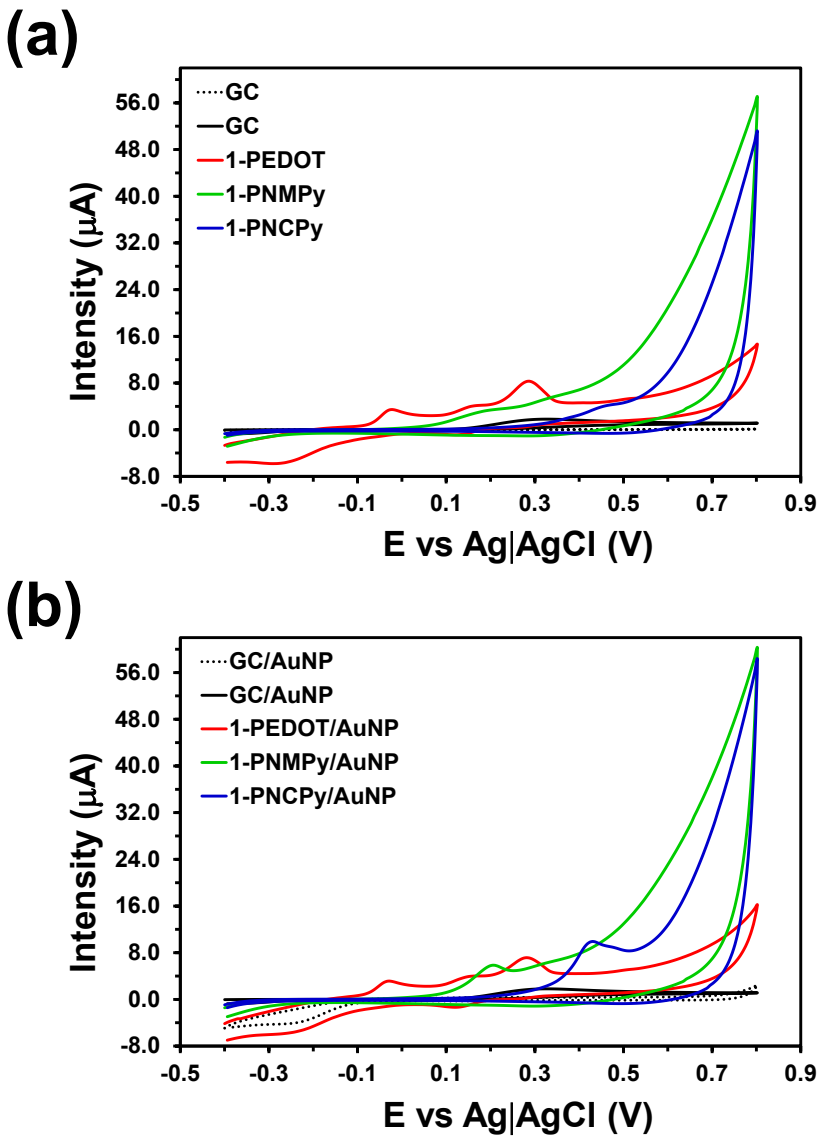

Figure 3. Control voltammograms of a solution mixture with 100 μM DA, 200 μM AA and 100 μM UA in 0.1 M PBS at (a) 1-CP and 1-CP/AuNP electrodes. The electrochemical response to the same solution mixture (solid black line) and to 0.1 M PBS (dotted black line) at bare (a) GC and (b) GC/AuNP electrodes is also displayed. All voltammograms were obtained by scanning from -0.40 to 0.80 V at a scan rate of 50 $mV \cdot s^{-1}$.

In contrast, the oxidation peaks for DA, AA and UA are very well resolved at 1-PEDOT and 1-PEDOT/AuNP electrodes. Amazingly, AuNPs do not play any electrocatalytic activity in this case. Thus, the E_p for oxidation of DA, AA and UA is 0.15, -0.03 and 0.28 V, respectively, at both 1-PEDOT and 1-PEDOT/AuNP electrodes. Similarly, the influence of AuNPs in the I_p values is small: 0.44 / 0.53, 2.11 / 1.82 and 3.93 / 2.88 μA for the oxidation of DA, AA and UA, respectively, at 1-PEDOT / 1-PEDOT/AuNP. Thus, AuNPs are inefficient for PEDOT, which should be attributed to the excellent electrochemical and electrical properties of this CP. Thus, the intrinsic porous morphology and linear molecular structure of PEDOT facilitate the transfer of charged species and electrons between the surface and the electrolyte,[4-6,27,38] the benefits typically provided by AuNPs being ineffective in this case.

Electrode	Sensitivity (μA/mM)			Resolution (V)	
	DA	AA	UA	AA-DA	UA-DA
1-PEDOT	4.4	10.5	39.3	0.179	0.130
1-PNMPy	5.1	-	1.0	-	0.166
1-PNCPy	3.0	-	3.0	-	Overlap
1-PEDOT/AuNP	5.3	9.1	28.8	0.179	0.130
1-PNMPy/AuNP	25.0	-	0.3	-	0.101
1-PNCPy/AuNP	24.8	-	24.8	-	Overlap

Table 1. Sensitivity and Resolution obtained for the determination of DA, AA and UA in 0.1 M PBS using different 1-CP and 1-CP/AuNP electrodes. CVs are displayed in Figure 3.

Sensitivity and resolution parameters, which have been expressed as the ratio between the peak intensity for the oxidation of the specie and its concentration in the mixture (μA/mM) and the difference between the peak oxidation potentials of two species (V), respectively, for the six electrodes investigated in this section are listed in Table 1. As it can be seen, 1-PEDOT and its homologous coated with AuNPs show the highest performance for the selective determination of DA, AA and UA. These electrodes provide separation of the peak potentials and, additionally, present peak currents high enough for unambiguous detection. In contrast, electrodes based on 1-PNMPy and 1-PNCPy, which were found to be very effective for the detection of DA in solutions without interferents,[18,19] show important disadvantages for the selective determination of DA in real biological fluids.

Oxidation of DA, AA and UA at 2-CP and 2-CP/AuNP electrodes.

In order to examine the effect of the interphase created in 2-layered films in the selective detection of DA, the electrochemical behavior of the solution mixture with 100 μM DA, 200 μM AA and 100 μM UA in 0.1 M PBS was studied at 2-CP and 2-CP/AuNP electrodes. Figure 4 displays the recorded voltammograms while Table 2 compares the resulting sensitivity and resolution parameters.

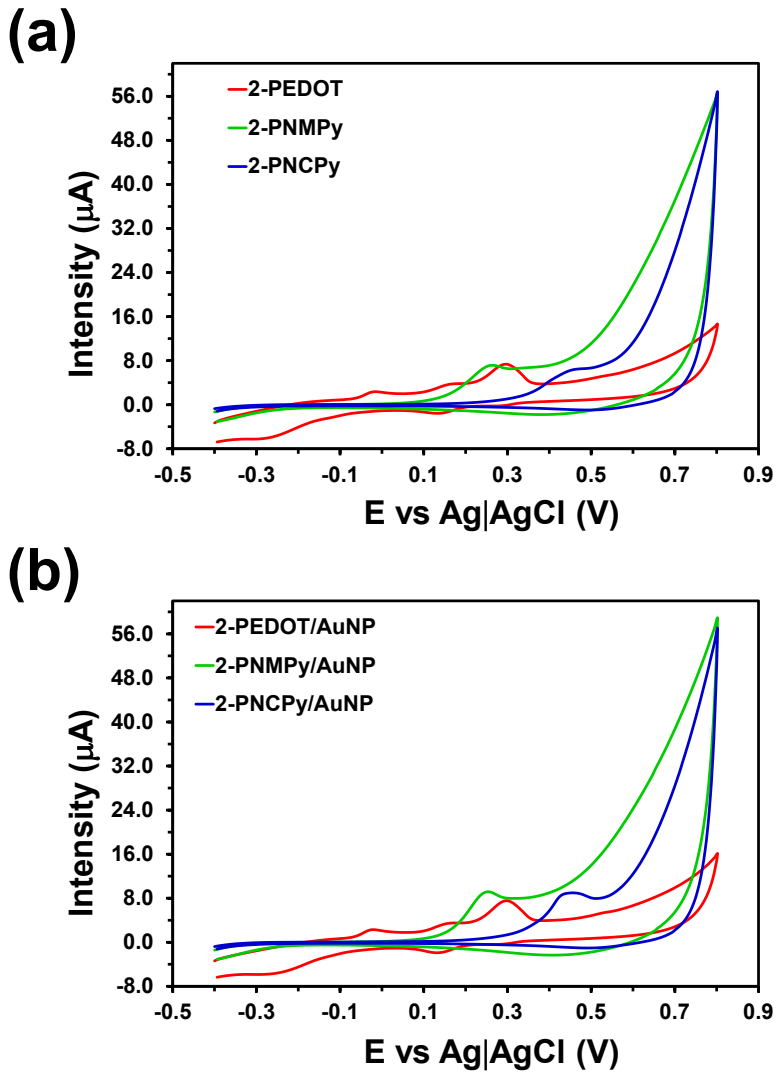

Figure 4 Control voltammograms of a solution mixture with 100 μM DA, 200 μM AA and 100 μM UA in 0.1 M PBS at (a) 2-CP and 2-CP/AuNP electrodes. All voltammograms were obtained by scanning from -0.40 to 0.80 V at a scan rate of 50 $mV \cdot s^{-1}$.

The oxidation peaks of the three species are clearly identified in the CVs recorded at 2-PEDOT and 2-PEDOT/AuNP, which are very similar to those displayed in Figure 3 for 1-PEDOT and 1-PEDOT/AuNP. Thus, the largest effect produced by the interphase created inside the PEDOT film corresponds to the peak intensity for the

oxidation of AA, which decreases from ~10 μA to ~5 μA. The variation of the I_p for the oxidation of the other two species is < 23% while the largest shift in the resolution parameter is 0.010 V. As occurred above for 1-PEDOT films, the influence of AuNPs in the sensitivity and resolution is practically negligible. The overall of these results indicate that ability of PEDOT for the selective determination of DA is due to the intrinsic electrochemical properties of the material. Moreover, such ability remains practically unaltered upon the application of external physical modifications (*e.g.* AuNPs coating and incorporation of an interphase inside the film through a two steps polymerization process).

Electrode	Sensitivity (μA/mM)			Resolution (V)	
	DA	AA	UA	AA-DA	UA-DA
2-PEDOT	4.6	4.6	35.1	0.169	0.140
2-PNMPy	15.3	-	15.3	-	Overlap
2-PNCPy	6.2	-	6.2	-	Overlap
2-PEDOT/AuNP	5.3	5.6	37.6	0.175	0.140
2-PNMPy/AuNP	21.8	-	21.8	-	Overlap
2-PNCPy/AuNP	17.7	-	17.7	-	Overlap

Table 2. Sensitivity and Resolution obtained for the determination of DA, AA and UA in 0.1 M PBS using different 2-CP and 2-CP/AuNP electrodes. CVs are displayed in Figure 4.

Although the interphase enhances the peak intensity for the oxidation of DA and UA at 2-PNMPy and 2-PNCPy, the overlapping of the oxidation peaks and the lack of signal for AA preclude the application of such two CPs for the separation of the species contained in the mixture. Overlapping of the oxidation peaks of DA and UA is also detected at 2-PNMPy/AuNP and 2-PNCPy/AuNP, in which surface AuNPs cancel the benefit induced by the interphase at the peak intensities. On the other hand, it is worth noting that sensitivity towards DA of 2-PNCPy is significantly higher than that of 1-PNCPy, evidencing an improvement when the film with submicrometric thickness (*i.e.* ~0.3 μm) transforms into two nanometric layers separated by an interphase.

Modeling the interactions between PEDOT and oxidized DA, AA and UA.

In a recent study QM calculations were used to explain the interaction of oxidized DA with PNMPy and PNCPy systems at the molecular level.[19] For such purpose, calculations on *n*-NMPy···DQ and *n*-NCMPy···DQ complexes, where *n*-NMPy and *n*-NCPy refer to oligomers with *n* repeat units of NMPy and NCPy, respectively,

were carried out considering *n* values ranging from 1 to 3. Results indicated that C–H···O non-conventional hydrogen bonds are responsible of the interaction between DQ molecules and these two PPy derivatives, playing a crucial role in the detection process.[19]

In order to examine the molecular affinity of PEDOT towards DA, AA and UA, QM calculations have been used to examine the chemical nature and strength of intermolecular interactions in *n*-EDOT···X complexes with X= DQ, dAA and qdU. A build-up scheme, similar to that previously used to model *n*-NMPy···DQ and *n*-NCPy···DQ complexes,[19] has been applied for such purpose. Specifically, the interactions between 1-EDOT and DQ, dAA or qdU were examined in a first stage. The resulting structures were used to construct the starting geometries for 3-EDOT···X, which after optimization were employed to build the starting geometries of 5-EDOT···X and 7-EDOT···X.

A total of 29, 38 and 25 starting geometries were constructed for 1-EDOT···X complexes with X= DQ, dAA and qdU, respectively, considering the different types of intermolecular interactions: conventional and non-conventional hydrogen bonds (*i.e.* N–H···O, O–H···O, C–H···O and N–H···S), dipole···π–cloud (*i.e.* N–H···π) and π–π stacking interactions. From the resulting geometry optimizations, only 6 (DQ), 7 (dAA) and 8 (dqU) structures were considered for the construction of the starting geometries for the corresponding 3-EDOT···X complexes. The remaining optimized structures were discarded due to at least one of the following reasons: (i) they were significantly destabilized with respect to the global minimum showing ΔE higher than 10 kcal/mol; or (ii) they were not appropriated for the growing of the *n*-EDOT oligomer (*i.e.* steric conflicts and/or the elimination of the intermolecular interactions resulted from the enlargement of *n* from 1 to 3). Regarding to the latter, for example some 1-EDOT···DQ structures with $\Delta E \leq 10$ kcal/mol were stabilized through non-conventional hydrogen bonds between the C=O of DQ and one of the α-hydrogen atoms of 1-EDOT, the latter disappearing in the polymerization process.

The structures selected for the 1-EDOT···X complexes were used to construct the starting geometries of 3-EDOT···X by replacing each α-hydrogen atom of 1-EDOT by

another EDOT repeat unit. Additionally, new starting geometries in which the analyte interact simultaneously with two repeat units of 3-EDOT were constructed. The resulting optimized structures (5, 9 and 10 for X=DQ, dAA and dqU respectively) were then used to construct the starting geometries of 5-EDOT···X complexes using the procedure previously described. Geometry optimizations led to 4 (DQ), 7 (dAA) and 6 (qdU) different structures with $\Delta E \leq 1.5$ kcal/mol, which were subsequently used to build the starting geometries of 7-EDOT···X. Optimized structures of 7-EDOT···DQ, 7-EDOT···dAA and 7-EDOT···qdU with $\Delta E \leq 1.5$ kcal/mol are displayed in Figures 5a, 5b and 5c, respectively. Furthermore, Table 3 lists the ΔE and ΔE_{int} for these optimized structures of the three complexes.

The lowest energy structure of 7-EDOT···DQ, denoted 7Ea/DQ in Table 3 and Figure 5a, shows two C–H···O interactions, which involve the CH_2 groups located at the dioxane ring of the same EDOT unit and the two C=O groups of DQ. The most stable local minimum, 7Eb/DQ, is unfavored by 0.5 kcal/mol only. Although this structure also presents two C–H···O interactions, it differs from 7Ea/DQ in the CH_2 groups, which belong to consecutive EDOT repeat units. The only difference between the other two structures, 7Ec/DQ and 7Ed/DQ, and the global minimum refers to the relative orientation of the DQ with respect to 7-EDOT. These results corroborate that C–H···O interactions play a crucial role in the detection process of DA, as was suggested in our previous study.[19] The ΔE_{int} of 7Ea/DQ-7Ed/DQ structures ranges from -7.5 to -6.7 kcal/mol indicating that, despite of two binding sites identified in each structure, the strength of the interaction between PEDOT and oxidized DA is moderate.

Regarding the interaction between the oxidized AA molecule and the 7-EDOT chain, the lowest energy structure (7Ea/dAA in Figure 5b and Table 3) is stabilized by two C–H···O interactions involving consecutive EDOT units. The most stable local minimum, 7Eb/dAA, which also presents two C–H···O interactions involving CH_2 groups of consecutive EDOT repeat units, is practically isoenergetic to 7Ea/dAA ($\Delta E <$ 0.1 kcal/mol). In both cases, intermolecular interactions involve one C=O and one O-H groups of dAA. The second local minimum, 7Ec/dAA, that is destabilized 0.9 kcal/mol with respect to the global minimum, shows intermolecular interactions between two C=O groups of dAA and CH_2 groups located at the dioxane ring of two non-consecutive

EDOT repeat units. The ΔE_{int} values obtained for 7-EDOT···dAA range from -5.4 to -2.2 kcal/mol (results obtained for structures with ΔE > 2.0 kcal/mol not detailed), evidencing that the strength of the interaction between PEDOT and oxidized AA is weaker than that calculated between the same CP and oxidized DA. This fact may be attributed to the markedly different relative orientation of the analyte and the 7-EDOT chain.

The lowest energy structure of 7-EDOT···dqU, 7Ea/dqU (Figure 5c), is also stabilized by two C–H···O interactions, which involve two C=O groups of dqU and two different and non-consecutive EDOT repeat units. The relative orientation of the oxidized UA and the EDOT chain is similar to that showed by 7-EDOT···DQ minima. Accordingly, the ΔE_{int} predicted for 7Ea/dqU (-7.1 kcal/mol) is very close to that calculated for 7Eb/DQ (Table 3). The first local minimum, 7Eb/dqU, is destabilized by only 0. 6 kcal/mol with respect to 7Ea/dqU. This structure also presents two C–H···O contacts with alternated EDOT units, the only difference being one C–H group. The other structures obtained for 7-EDOT···dqU present ΔE > 2.5 kcal/mol and ΔE_b values ranging from -4.4 to -4.0 kcal/mol, detailed description being omitted.

Complex	Structure	ΔE (kcal/mol)	ΔE_{int} (kcal/mol)
7-EDOT···DQ	7Ea/DQ	0.0	-7.5
	7Eb/DQ	0.5	-7.0
	7Ec/DQ	0.7	-6.9
	7Ed/DQ	0.9	-6.7
7-EDOT···dAA	7Ea/dAA	0.0	-5.4
	7Eb/dAA	< 0.1	-5.4
	7Ec/dAA	0.9	-4.5
7-EDOT··· qdU	7Ea/qdU	0.0	-7.1
	7Eb/qdU	0.6	-6.5

Table 3. Relative energy and binding energy of the structures of lower energy calculated for 7-EDOT···X complexes with X= DQ, dAA and qdU. Molecular geometries and energy parameters have been obtained at the B3LYP/6-31++G(d,p) level.

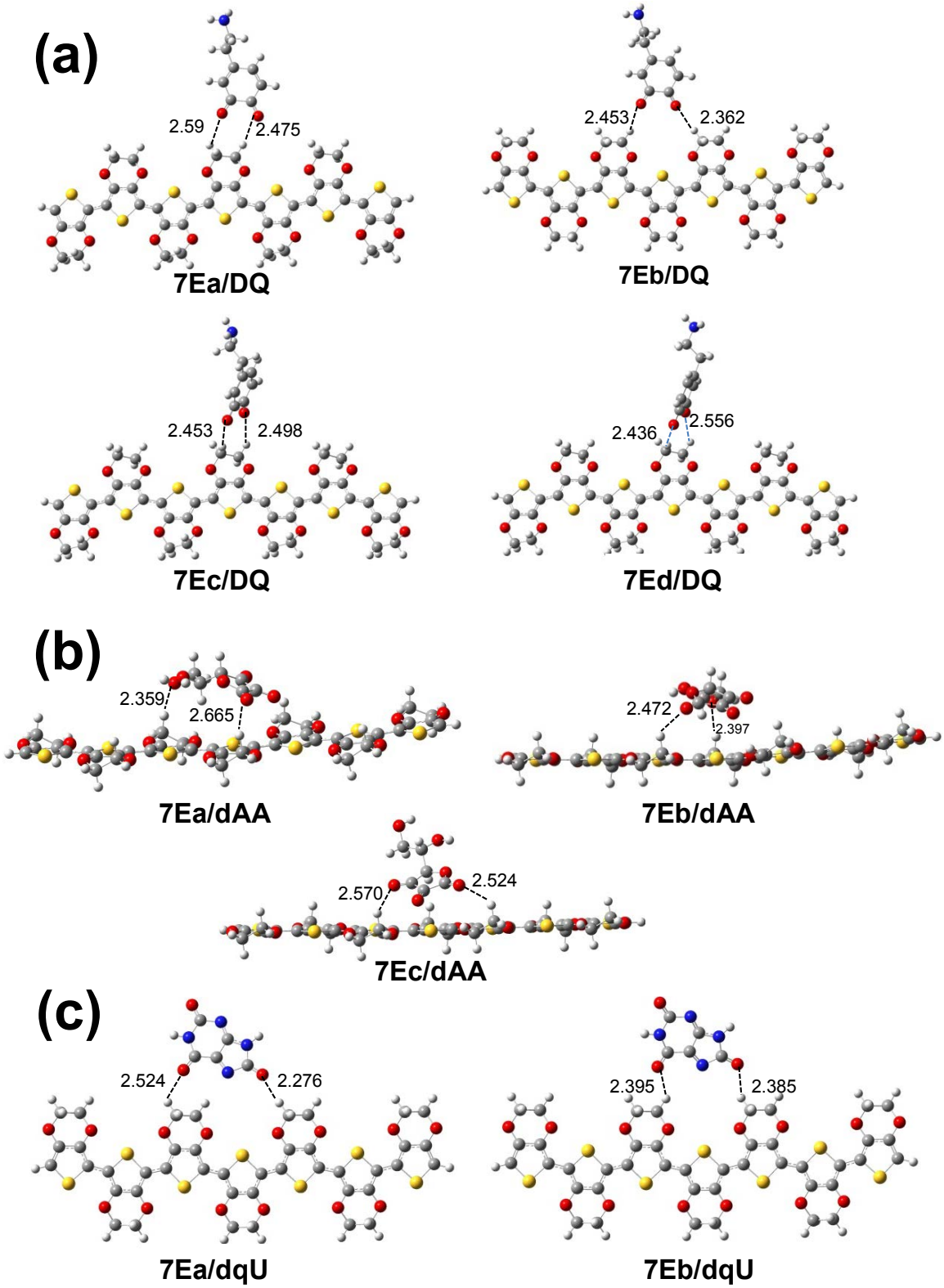

Figure 5. Optimized structures for (a) 7-EDOT···DQ, (b) 7-EDOT···dAA and (c) 7-EDOT···dqU complexes with $\Delta E \leq 1.5$ kcal/mol. Intermolecular C–H···O interactions are indicated. Distances are listed in Å.

Improving the selective detection of DA through rational design.

Results displayed in previous sections evidenced that, although the sensitivity of PEDOT towards DA is lower than that of N-substituted PPy derivatives, the former CP is the only able to detect simultaneously DA, AA and UA in tertiary mixtures. Furthermore, the interaction of PEDOT with the oxidized analytes is dominated by C–H···O interactions, involving hydrogen atoms that are not located at the π-system of the CP. These results suggest that sensitivity of PEDOT towards the three species could be improved by incorporating a substituent able to form intermolecular interactions stronger than C–H···O non-conventional hydrogen bonds. Thus, the grafting of an appropriated polar pendant side group onto the PEDOT backbone is expected to preserve the ability of the latter to separate DA, AA and UA in mixtures and, simultaneously, to produce a significant increase in the tendency to form intermolecular hydrogen bonds.

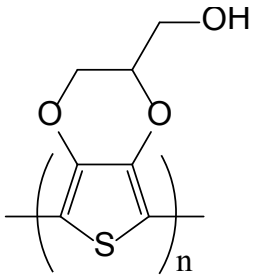

PHMeDOT

Figure 6. Molecular structure of PHMeDOT.

Within the vast palette of PEDOT derivatives developed in the last decade,[40,41] those based on the functionalization of the dioxane ring with small and flexible polar substituents are expected to fulfill the already mentioned conditions (*i.e.* ability to interact with other molecules through conventional hydrogen bonds and to retain the selectivity of PEDOT for the simultaneous detection of DA, AA and UA). Within this context and due to its simplicity, PHMeDOT (Figure 6), has been considered to be a suitable candidate for the selective determination of the DA in ternary mixtures. Thus, the electronic characteristics of PEDOT, that are mainly defined by π-conjugated system and the oxygen atoms of the dioxane ring, should remain unaltered by the exocyclic hydroxymethyl group, which in turn may easily form intermolecular hydrogen bonds with other species. Another important advantage of PHMeDOT with respect to

other PEDOT derivatives is that the experimental conditions required for successful electrochemical polymerization were previously examined.[42-45]

Experimental conditions for the generation of PHMeDOT films were taken from previous studies reported by Roncali and co-workers.[42,45] Specifically, 1-PHMeDOT films (where by analogy with 1-PEDOT the number one indicates a single polymerization step) was electrodeposited potentiostically on both ITO and GC electrodes under a constant potential of 1.50 V using an acetonitrile solution containing 0.1 M monomers with 0.1 M tetrabutylammonium tetrafluoroborate (TBATFB). Replacement of $LiClO_4$, which was used as supporting electrolyte for the synthesis of PEDOT, by TBATFB was carried out to improve the electrochemical properties of PHMeDOT.[42] The polymerization time used for the electrodeposition of polymer films on ITO and GC electrodes was θ=100 and 6 s, respectively. The choice of these times was based on the thickness of the films. Thus, the thickness of 1-PHMeDOT films, which show dark blue color, deposited on ITO and GC is ~0.8 and ~0.7 μm, respectively. These values are consistent with the thickness of 1-PEDOT deposited in GC using $\theta_{1\text{-CP}}$ =6 s. These results illustrate the significant role of the working electrode on the characteristics of the electrodeposited film. Thus, GC significantly promotes the polymerization of EDOT monomers and its derivatives with respect to steel and ITO substrates.[38]

The FTIR spectra of 1-PHMeDOT and the corresponding monomer, HMeDOT, are displayed in Figure 7a. The main bands in the spectrum of the monomer are centered at 3215 cm-1 (O–H stretching), 3101 cm-1 (=C–H stretching), 2939 cm-1 (–C–H stretching), 1578 cm-1 (C=O stretching) and 1484 cm-1 (C=C aromatic stretching). The most relevant bands in the 1-PHMeDOT spectrum are observed at 3671 cm1 (O–H stretching) and 2982 cm-1 (–C–H stretching). Regarding the O–H stretching vibration, the red shift observed after polymerization evidences a reduction of intermolecular polymer···polymer hydrogen bonding associations.46 This is expected to facilitate the formation of hydrogen bonds between hydroxyl groups of the polymer and oxidized DA, which would be consistent with the rational design proposed in this study. On the other hand, detailed inspection of the spectrum recorded for the polymer reveals the absence of the absorption band at 3101 cm-1, which is consistent with the absence of

hydrogen atoms at the Cα-position. This proves that the anodic polymerization of HMeDOT occurs at the α-α' position of the thiophene rings, providing linear molecules.

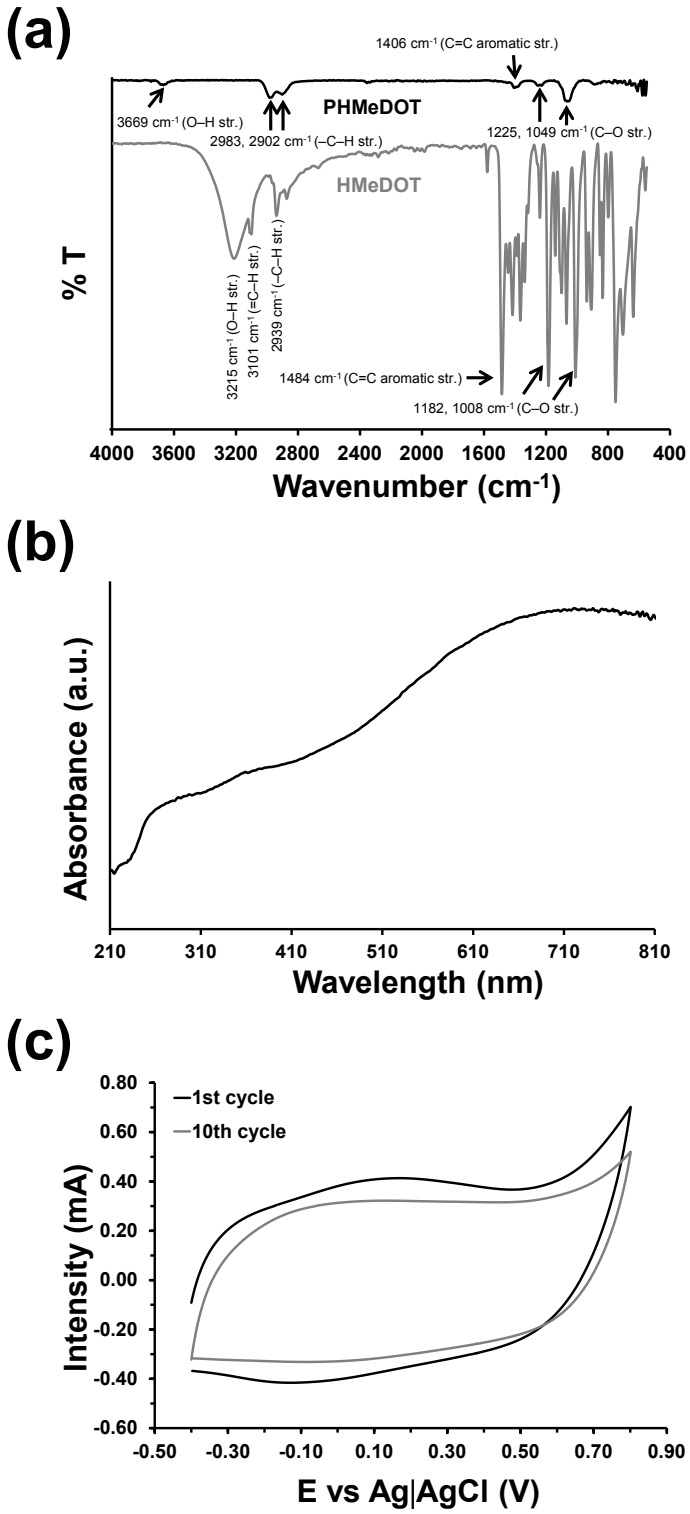

Figure 7. (a) FTIR spectra of PHMeDOT and HMeDOT. (b) UV-vis spectrum of PHMeDOT electrodeposited on ITO. (c) Voltammograms for PHMeDOT films deposited on ITO after one

and ten consecutive oxidation-reduction cycles. Voltamograms were recorded in water with 0.1 M PBS at 50 mV/s and 25ºC.

In order to corroborate our initial assumption (*i.e.* the exocyclic hydroxymethyl group does not provoke important changes in the properties of the material, which are essentially defined by the π-conjugated backbone), the main properties of PHMeDOT have been evaluated and compared with those reported for PEDOT. Figure 8a shows SEM micrographs of the typical morphologies found at the surface of 1-PHMeDOT films deposited on ITO. This CP presents a relatively porous cauliflower morphology formed by the aggregation of sticks with fiber-like morphology, giving place to relatively narrow pores with and tortuous channels. This morphology, which is very similar to that reported for PEDOT,[38] facilitates the mobility of dopant ions in oxidation and reduction processes (see below). The topology of 1-PHMeDOT films, which is illustrated in the AFM image displayed in Figure 8b, is fully consistent with the morphology showed in SEM micrographs. Thus, the topology of 1-PHMeDOT can be described as a dense and uniform distribution of clusters that resemble mountains, which in turn are formed by the compact aggregation of a few peaks, separated by narrow valleys. This reflects that the growing of the PHMeDOT chains is accompanied by an aggregation phenomenon, which is in concordance with cauliflower morphology observed by SEM. The RMS roughness of the 1-PHMeDOT films is *r*= 106 nm, this value being fully consistent with that of 1-PEDOT films obtained using polymerization times of 50 and 300 s (*i.e.* 97 and 123 nm, respectively).[38]

The optical properties of 1-PHMeDOT have been analyzed on films deposited on ITO. The UV-vis spectrum displayed in Figure 7b exhibits an absorption peak at 250 nm due to *n*-π electronic transitions of the aromatic rings and a broad absorption tail between ~500 and ~800 nm ascribed to the polaronic band of the conductive quinoid form.[47] The optical transitions of 1-PHMeDOT are very similar to those reported for PEDOT and several of its derivatives, which were recently discussed in detail.[48,49] On the other hand, the intrinsic electrochemical properties of PHMeDOT were examined by CV. Figure 7c shows the typical control voltammogram in PBS (pH= 7.4), a potential range from -0.40 to 0.80 V being considered. An anodic peak is detected at 0.15 V, which should be interpreted as the formation of polarons in the polymer chains. The electroactivity refers to the amount of charge reversibly exchanged under the used

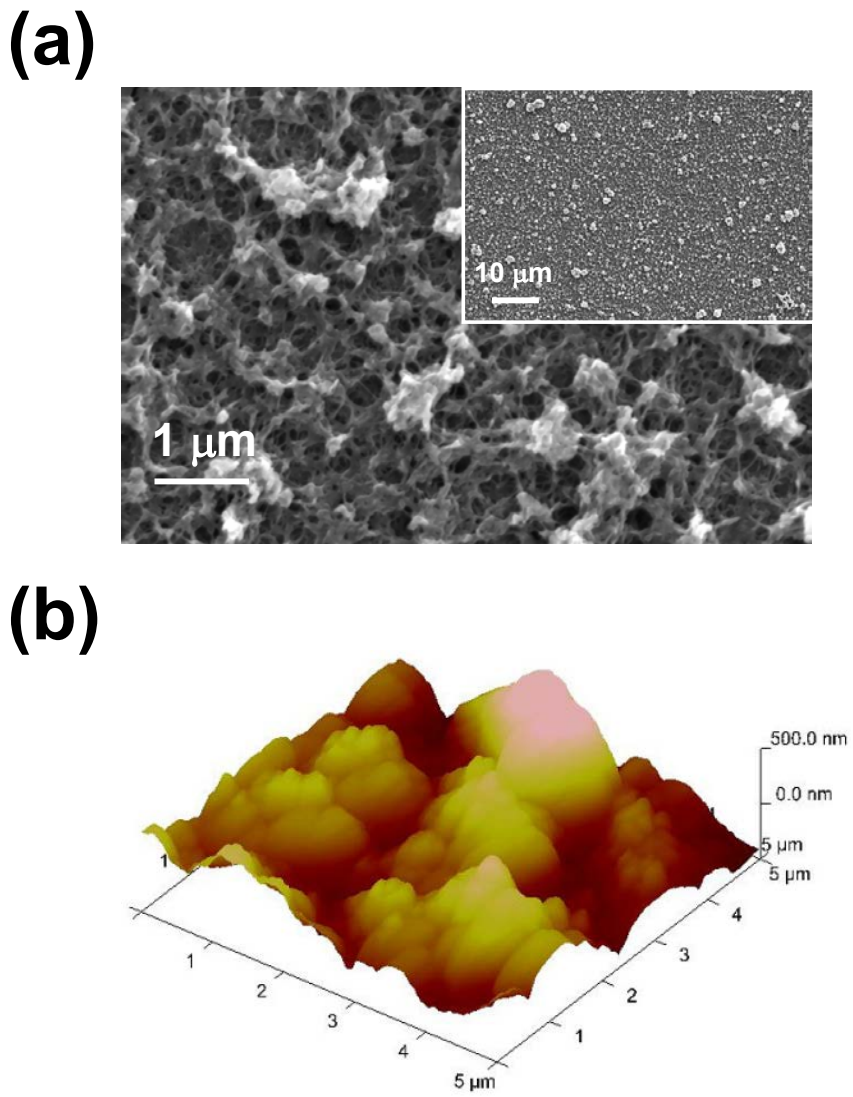

Figure 8. (a) High and low (inset) resolution SEM micrographs and (b) AFM image of PHMeDOT films electrodeposited on GC under a constant potential of 1.50 V using an acetonitrile solution containing 0.1 M monomers with 0.1 M TBATFB and a θ=6 s.

experimental conditions and, therefore, increases with the similarity between the anodic and cathodic areas of the control voltammogram. The voltammogram displayed in Figure 7c evidences that the electroactivity of 1-PHMeDOT is very high and similar to that reported for 1-PEDOT in the same environment.[50] Figure 7c also includes the voltammogram recorded for the same 1-PHMeDOT film after ten consecutive oxidation-reduction cycles, which has been used to evaluate the electrochemical stability. The latter, which decreases with the oxidation and reduction areas of consecutive control voltammograms, has been found to be also very high. Thus, although the electrochemical stability of CPs in PBS is usually moderate or even low,[51] the loss of electroactivity observed for both 1-PEDOT[49] and 1-PHMeDOT films after 10

consecutive redox cycles in this physiological environment is of only ~8%. The overall of the results displayed in Figures 7 and 8 suggests that the properties of 1-PEDOT and 1-PHMeDOT are very similar.

Figure 9a displays shows the voltammogram recorded for the solution mixture with 100 μM DA, 200 μM AA and 100 μM UA in 0.1 M PBS at 1-PHMeDOT electrodeposited onto GC, the electrochemical response to the tertiary mixture at 1-PEDOT generated using GC being also displayed for comparison. Furthermore, the sensitivity and resolution parameters obtained for such two electrodes are listed in Table 4. Unfortunately, incorporation of the hydroxymethyl substituent does not provoke any improvement in the sensitivity parameters, which are very similar to those obtained for 1-PEDOT (with exception of UA that decreases 20.2 μA/mM). Furthermore, the interactions induced by the new substituent reduce by 46% the resolution parameter to discriminate between AA and UA. These unexpected results suggested that the favorable synergy between PEDOT chains and the GC substrate decreases upon the incorporation of the hydroxymethyl group to the dioxane ring, which should be attributed to the alterations induced by intermolecular interactions between PHMeDOT chains. In order to corroborate the latter assumption, the voltammetric response of the solution mixture at ITO substrates modified with 1-PEDOT and 1-PHMeDOT was also investigated.

Figure 9b compares the voltammograms recorded for the solution mixture with 100 μM DA, 200 μM AA and 100 μM UA in 0.1 M PBS at both 1-PHMeDOT and 1-PEDOT deposited on ITO substrates. The generation of 1-PEDOT film was carried out using experimental conditions identical to those employed for the electrodeposition onto GC (see Methods section) with exception of the polymerization time, which was $\theta_{1\text{-CP}}$= 100 s rather than $\theta_{1\text{-CP}}$= 6 s. Utilization of ITO substrates provokes that the selective detection of the three species improves upon the incorporation of the hydroxymethyl substituent. This is numerically illustrated in Table 4, which includes the sensitivity and resolution parameters of the two ITO-modified electrodes. It should be emphasized that the sensitivity of the two 1-CPs deposited onto ITO is remarkably higher than observed for the same 1-films deposited onto GC. Furthermore, the sensitivity of 1-PHMeDOT towards oxidized UA and, especially, AA is significantly

higher than that of 1-PEDOT, while the former CP is slightly less sensitive towards DQ than the latter one. On the other hand, incorporation of hydroxymethyl groups results in a small approach of the oxidation potentials, the corresponding loss of resolution being relatively unimportant from a practical point of view. Further investigation on the sensitivity evidenced that, as expected, the reduction is practically negligible after five 5 redox cycles. This is reflected in Figure 9b, which included the voltammograms obtained after five consecutive redox cycles for the 0.1 M PBS solution mixture at both 1-PHMeDOT and 1-PEDOT deposited on ITO substrates.

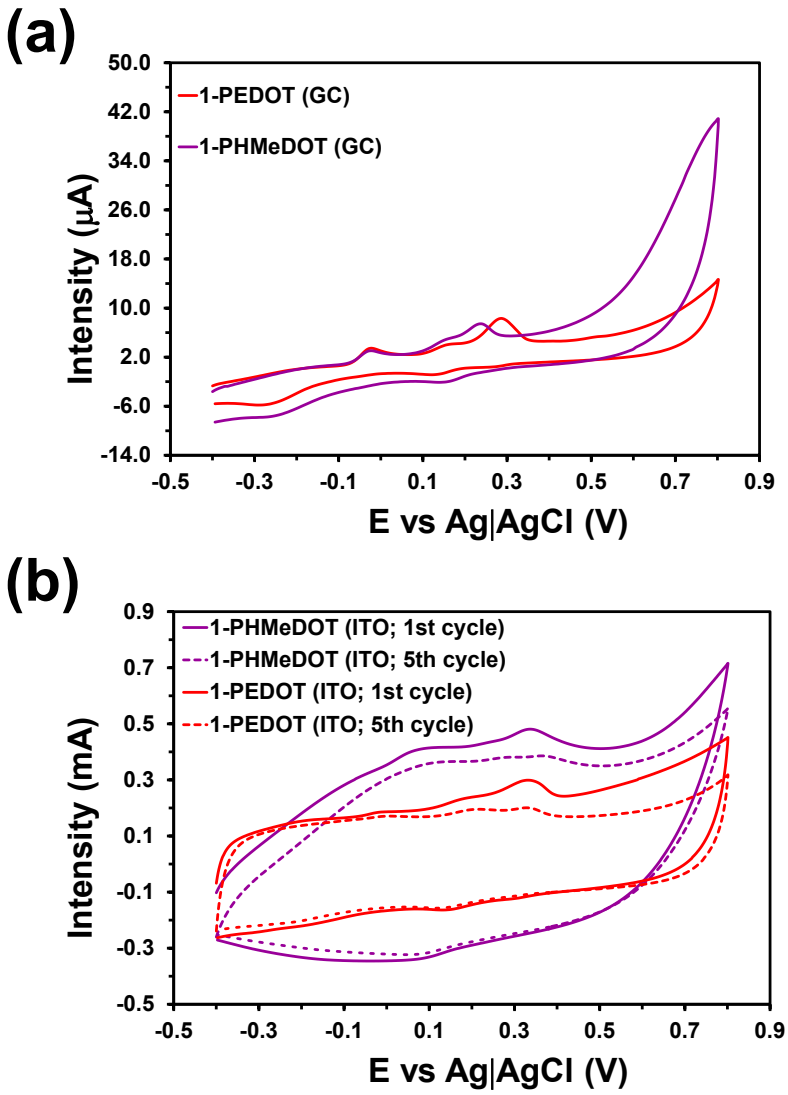

Figure 9. Control voltammograms of a solution mixture with 100 μM DA, 200 μM AA and 100 μM UA in 0.1 M PBS at 1-PEDOT and 1-PHMeDOT deposited on (a) GC and (b) ITO. The electrochemical response to the same solution mixture at the modified ITO electrodes after five consecutive oxidation-reduction cycles is also displayed in (b). All voltammograms were obtained by scanning from -0.40 to 0.80 V at a scan rate of 50 $mV \cdot s^{-1}$.

Electrode	Sensitivity (μA/mM)			Resolution (V)	
	DA	AA	UA	AA-DA	UA-DA
1-PEDOT (GC)	4.4	10.5	39.3	0.179	0.130
1-PHMeDOT (GC)	2.7	7.4	19.1	0.173	0.089
1-PEDOT (ITO)	60.9	36.1	519.3	0.193	0.153
1-PHMeDOT (ITO)	31.5	154.1	604.0	0.186	0.117

Table 4. Sensitivity and Resolution obtained for the determination of DA, AA and UA in 0.1 M PBS using 1-PEDOT and 1-PHMeDOT electrodeposited on GC and ITO. CVs are displayed in Figure 9.

4.6.4 Conclusions

The voltammetric behavior of DA-, AA- and UA-containing tertiary mixtures at GCEs modified with 1-CP, 1-CP/AuNP, 2-CP and 2-CP/AuNP submicrometric films, where CP= PEDOT, PNMPy or PNCPy, indicated that PEDOT is most appropriated for the selective determination of low concentrations of such species. Thus, the sensitivity and resolution provided by PEDOT is significantly better than those obtained using PNMPy and PNCPy, which show overlapping of the oxidation peaks of DA and UA. Unfortunately, the performance of PEDOT for the selective detection of DA cannot be improved by adding a coating of AuNPs at the surface or by incorporating interphases inside the film through multiple step polymerization techniques. However, this improvement can be achieved through a rational design strategy oriented to enhance the binding affinity of PEDOT towards the three investigated species.

QM calculations indicate that complexes formed by *n*-EDOT oligomers and the oxidized forms of DA, AA and UA are essentially dominated by C–H···O interactions. This suggests that the sensing abilities of PEDOT may be improved by incorporating substituents able to facilitate the formation of intermolecular hydrogen bonds with such species. For this purpose, PHMeDOT, which incorporates a hydroxymethyl substituent attached to the dioxane ring of every repeat unit, has been synthesized and subsequently characterized. However, the sensitivity and resolution parameters of GC modified with 1-PHMeDOT are worse than those found for GC coated with 1-PEDOT, suggesting that such substrate promotes the formation of intermolecular interactions between PHMeDOT chains through the exocyclic substituent. In contrast, the sensitivity and resolution parameters of both 1-PHMeDOT and 1-PEDOT improve considerably when the CPs are deposited onto ITO surfaces. Moreover, the sensitivities

of 1-PHMeDOT towards AA and UA are significantly higher than that of 1-PEDOT, evidencing that intermolecular interactions are stronger in the former than in the latter.

4.6.5 References

1. Roncali, *J. Chem. ReV.*, 1997, **97**, 173.

2. T. A. Skotheim, R. L. Elsenbaumer and J. R. Reynolds, *Handbook of conducting polymers*; Marcel Dekker: New York, 1998.

3. R. J. Kline and M. D. McGehee, *Polym. Rev.*, 2006, **46**, 27.

4. F. Jonas and L. Shrader, *Synth. Met.*, 1991, **83**, 141.

5. G. Heywang and F. Jonas, *Adv. Mate*r., 1992, **4**, 116.

6. M. Dietrich, J. Heinze, G. Heywang and F. Jonas, *J. Electroanal. Chem.*, 1994, **369**, 87.

7. C. J. Brabec, N. S. Sariciftci and J. C. Hummelen, *Adv. Funct. Mater.,* 2001, **11**, 15.

8. M. Granström, M. Berggren and O. Inganäs, *Science*, 1995, **267**, 1479.

9. L. Groenendaal, F. Jonas, V. Freitag, H. Pielartzik and J. R. Reynolds, *Adv. Mater.*, 2000, **12**, 481.

10. L. Groenendaal, G. Zotti, P.-H. Aubert, S. M. Waybright and J. R. Reynolds, *Adv. Mater.*, 2003, **15**, 855.

11. B. Teixeira-Dias, D. Zanuy, J. Poater, M. Solà, F. Estrany, L. J. del Valle and C. Alemán, *Soft Matter*, 2011, **7**, 9922.

12. V.S. Vasantha, S.M. Chen, *J. Electroanal. Chem.,* 2006, **592**, 77.

13. W.Y. Su and S.H. Cheng, *Electrochem. Commun.,* 2008, **10**, 899.

14. D. López-Pérez, D. Aradilla, L. J. del Valle and C. Alemán, *J. Phys. Chem. C*, 2013, **117**, 6607.

15. B. Teixeira-Dias, L. J. del Valle, D. Aradilla, F. Estrany and C. Alemán, *Macromol. Mater. Eng.*, 2012, **297**, 427.

16. L. J. Del Valle, D. Aradilla, R. Oliver, F. Sepulcre, A. Gamez, E. Armelin, C. Alemán and F. Estrany, *Eur. Polym. J.*, 2007, **43**, 2342.

17. L. J. Del Valle, F. Estrany, E. Armelin, R. Oliver and C. Alemán, *Macromol. Biosci.* 2008, **8**, 1144.

18. M. Martí, G. Fabregat, F. Estrany, C. Alemán and E. Armelin, *J. Mat. Chem.*, 2010, **20**, 10652.

19. G. Fabregat, E. Córdova-Mateo, E. Armelin, O. Bertran and C. Alemán, *J. Phys. Chem. C,* 2011, **115**, 14933.

20. N. F. Atta, A. Galal and E. H. El-Ads, *Electrochim. Acta*, 2012, **69**, 102.

21. S.S. Kumar, J. Mathiyarasu and K.L. Phani, *J. Electroanal. Chem.*, 2005, **578**, 95.

22. N. F. Atta, A. Galal and R. A. Ahmed, *Bioelectrochemistry*, 2011, **80**, 132.

23. C. Zanardi, F. Terzi and R. Seeber, *Sens. Actuators B*, 2010, **148**, 277.

24. E. R. Kandel, J. H. Schwartz and T. M. Jessel, *Principles of Neural Science*; New York, McGraw-Hill, 4th edn, 2000.

25. E. K. Richfield, J. B. Penney and A. B. Young, *Neuroscience*, 1989, **30**, 767.

26. D. Aradilla, F. Estrany, C. Alemán, *J. Appl. Polym. Sci.*, 2011,**121**, 1982.

27. C. Ocampo, R. Oliver, E. Armelin, C. Alemán and F. Estrany, *J. Polym. Res.*, 2006, **13**, 193.

28. R. Oliver, A. Muñoz, C. Ocampo, C. Alemán, E. Armelin and F. Estrany, *Chem. Phys.*, 2006, **328**, 299.

29. D. Aradilla, F. Estrany, E. Armelin, R. Oliver, J. I. Iribarren, C. Alemán, *Macromol. Chem. Phys.*, 2010, **211**, 1663.

30. R. G. Freeman, M. B. Hommer, K. C. Grabar, M. A. Jackson and M. J. Natan, *J. Phys. Chem.*, 1996, **100**, 718.

31. S. Link and M. A. El-Sayed, *J. Phys. Chem. B*, 1999, **103**, 8410.

32. M. J. Frisch, G. W. Trucks, H. B. Schlegel, G. E. Scuseria, M. A. Robb, J. R. Cheeseman, G. Scalmani, V. Barone, B. Mennucci, G. A. Petersson, H. Nakatsuji, M. Caricato, X. Li, H. P. Hratchian, A. F. Izmaylov, J. Bloino, G. Zheng, J. L. Sonnenberg, M. Hada, M. Ehara, K. Toyota, R. Fukuda, J. Hasegawa, M. Ishida, T. Nakajima, Y. Honda, O. Kitao, H. Nakai, T. Vreven, J. A. Jr Montgomery, J. E. Peralta, F. Ogliaro, M. Bearpark, J. J. Heyd, E. Brothers, K. N. Kudin, V. N. Staroverov, R. Kobayashi, J. Normand, K. Raghavachari, A. Rendell, J. C. Burant, S. S. Iyengar, J. Tomasi, M. Cossi, N. Rega, J. M. Millam, M. Klene, J. E. Knox, J. B. Cross, V. Bakken, C. Adamo, J. Jaramillo, R. Gomperts, R. E. Stratmann, O. Yazyev, A. J. Austin, R. Cammi, C. Pomelli, J. W. Ochterski, R. L. Martin, K. Morokuma, V. G. Zakrzewski, G. A. Voth, P. Salvador, J. J. Dannenberg, S. Dapprich, A. D. Daniels, O. Farkas, J. B. Foresman, J. V. Ortiz, J. Cioslowski and D. J. Fox, Gaussian 09, revision A.01, Gaussian, Inc.: Wallingford, CT, 2009.

33. A. D. Becke, *J. Chem. Phys.*, 1993, **98**, 1372.

34. C. Lee, W. Yang and R. G. Parr, *Phys. Rev. B*, 1988, **37**, 785.

35. P. C. Hariharan and J. A. Pople, *Theor. Chim. Acta*, 1973, **28**, 213.

36. A. D. McLean and G. S. Chandler, *J. Chem. Phys.*, 1980, **72**, 5639.

37. S. F. Boys and F. Bernardi, *Mol. Phys.*, 1970, **19**, 553.

38. D. Aradilla, F. Estrany, E. Armelin and C. Alemán, *Thin Solid Films*, 2012, **520**, 4402.

39. R.N. Goyal, V.K. Gupta, M. Oyama and N. Bachheti, *Talanta*, 2007, **72**, 976.

40. J. Roncali, P. Blanchar and P. Frère, *J. Mater. Chem.*, 2005, **15**, 1589.

41. D. Demeter, T, Rousseau and J. Roncali, *RSC Adv.*, 2013, **3**, 704.

42. S. Akoudad and J. Roncali, *Electrochem. Commun.*, 2000, **2**, 72.

43. Y. Xiao, X. Cui, J. M. Hancock, M. Bouguettaya, J. R. Reynolds and D. C. Martin, *Sens. Actuators B*, 2004, **99**, 437.

44. Y. Shi, S.-C. Luo, W. Fang, K. Zhang, E. M. Ali, F.Y.C. Boey, J. Y. Ying, J. Wang, H.-h. Yu and L.-J. Li, *Org. Electr.*, 2008, **9**, 859.

45. H. Brisset, A.-E. Navarro, C. Moustrou, I. Perepichka and J. Roncali, *Electrochem. Commun.*, 2004, **6**, 249.

46. J. Casanovas, O. Bertran, E. Armelin, J. Torras, F. Estrany and C. Alemán, J. Phys. Chem. A, 2008, **112**, 10650.

47. S. Garreau, G. Louarn, J. P. Buisson, G. Froyer and S. Lefrant, *Macromolecules*, 1999, **32**, 6807.

48. G. Fabregat, G. Ballano, J. Casanovas, A. D. Laurent, E. Armelin, L. J. del Valle, C. Cativiela, D. Jacquemin and C. Alemán, *RSC Adv.,* 2013, **3**, 21069.

49. G. Fabregat, G. Ballano, E. Armelin, L. J. del Valle, C. Cativiela and C. Alemán, *Polym. Chem.*, 2013, **4**, 1412.

50. L. J. del Valle, D. Aradilla, R. Oliver, F. Sepulcre, A. Gamez, E. Armelin, C. Alemán and F. Estrany, *Polym. Eur. J.*, 2007, **43**, 2342.

51. M. M. Pérez-Madrigal, E. Armelin, L. J. del Valle, F. Estrany and C. Alemán, *Polym. Chem.*, 2012, **3**, 979.

CHAPTER 5

PEPTIDE-CONDUCTING POLYMER CONJUGATES AS BIOACTIVE PLATFORM

5.1 An electroactive and biologically responsive hybrid conjugate based on chemical similarity*/**

Synthetic amino acids have become very important tools for the design of new materials. In this work, an electroactive polymer-amino acid hybrid material has been synthesized by conjugating PEDOT, a well known CP, with a synthetic amino acid bearing EDOT, which has been explicitly designed and prepared for such purpose. Nanometric films have been electrochemically generated using a two-steps procedure to evaluate the properties and potential applications of the resulting hybrid material. The successful incorporation of the amino acid as end-capping of the PEDOT chains has been proved by FTIR, EDX and XPS. The fabrication of the hybrid material using an engineered a has allowed us to preserve not only morphological and structural characteristics of the CP but also, and mostly important, to preserve the electrical conductivity, electroactivity, electrochemical stability and specific capacitance. Finally, the behavior of the hybrid material as cellular matrix has been compared with that of PEDOT using cellular adhesion and proliferation assays. Results obtained in this work represent the success of a new strategy for the preparation of peptide-CP hybrid materials, which is currently being improved by transforming the EDOT-containing amino acid into a cell adhesive peptide.

*Results described in this section previously appeared in *Polym. Chem.*, 2013, **4**, 1412.

**The synthesis and characterization of 2-(N-tert-butoxycarbonyl)amino-3-(3,4-ethylenedioxy-2-thienyl) propanoate were performed by Dr. G. Ballano and Dr. C. Cativiela.

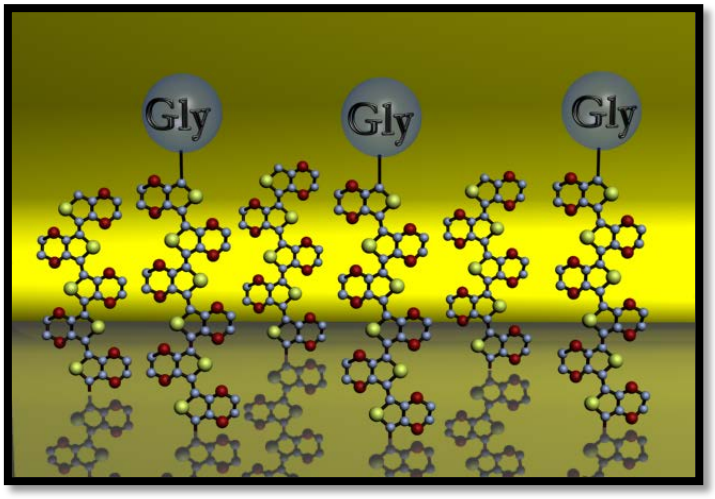

5.1.1 Introduction

Interaction of CPs with peptides/proteins is receiving an increasing amount of attention because of the interest for the development of biomedical and biotechnological devices with controlled electro-optical properties.[1-4] For example, PTh derivatives have been used to prepare smart biomaterial surfaces that can be resistant or susceptible to protein adhesion by a simple potential switching[1] or by changing the hydrophobicity of the substituents,[2] neural interfaces tailored for cell interaction by incorporation of bioactive factors,[3,4] electroactive composites with nanoscale organization in which the peptide form conducting pathways,[5] amperometric biosensors by covalent immobilization of enzymes or viruses,[6,7] quantitative colorimetric sensors based on protein-induced aggregation phenomena,[8] and films with bactericidal activity.[9] However, the more important applications of CP···peptide interactions are related with the fabrication of supports or platforms for the adhesion and growth of cells in tissue engineering.[10-20]

Fabrication of CP-containing bioactive platforms can be achieved by incorporating the peptide molecules into the polymeric matrix or coating the polymeric surface with a peptide layer. Cell attachment properties improve when the incorporated peptides present an overall anionic behavior, which has been attributed to role exerted by such anionic biomolecules as dopant agents of the CPs.[10-16] The use of anionic peptides as dopants is achieved through their incorporation into the monomer medium, where the polymerization process occurs. Unfortunately, this particular class of dopants frequently produces significant undesirable changes in the bulk properties of the CP, as for example a reduction in the electrical conductivity, the electroactivity or the electrochemical stability.[10-16] Besides using anionic peptides as dopants to modify CPs properties, there are other emerging non-covalent approaches to further modify CPs for biomedical applications. For instance, one approach was achieved by screening a bacteriophage library to find peptides that selectively bind to a CP.[17] Such study demonstrated that the surface of the electrically conductive chlorine-doped PPy can be functionalized by immobilizing the T59 peptide through selective binding. Moreover, the cell attachment on the PPy surface was promoted by joining the T59 peptide to a cell adhesive sequence (*i.e.* the Arg-Gly-Asp, RGD). An

advantage of this approach is that, apparently, it should not modify the intrinsic properties of the CP and could be used with a wide range of different biomolecules that do not need to be negatively charged.

In addition to the non-covalent approaches, modification of CPs via covalent bonds has been also explored. Multiple techniques have been used, like for example: the modification of the β-position on PPy to create strong disulfide bonds with the Cys of Arg-Gly-Asp-Cys (RGDS), enhancing osteoblast adhesion;[18,19] and the modification of the surface to immobilize peptides through covalent bonds, which have been successfully used to immobilize nerve growth factor to the surface of CPs through a photo-crosslinker.[20] Another possibility is the chemical synthesis of monomers and oligomers functionalized with peptides. For example, recently Cristopherson and co-workers reported the biological activities of different thiophenes and furanes substituted by amino acids,[21] while McTiernan and Chahma[22,23] reported the chemical synthesis of oligothiophenes functionalized with alanine or leucine (*i.e.* the amino acids were linked to the β-position on Th rings), which were subsequently electropolymerized to produce substituted PTh derivatives.

The present study, in which we present an alternative strategy for the covalent incorporation of amino acids and peptides to the surface of CPs, is focused on PEDOT (Figure 1). PEDOT is a widely studied CP because of its impressive properties, such as high electrical conductivity (up to 500 $S \cdot cm^{-1}$), moderate band-gap, low oxidation potential and good thermal and environmental stability.[24,25] Consequently, PEDOT has been recently employed in different technological applications related, among others, with bioelectrochemistry (*e.g.* electrochemical biological sensors),[26-28] corrosion inhibition,[29-31] and electronic and optoelectronic devices.[32-34] Furthermore, PEDOT has been also successfully used as bioactive platform for the adhesion and proliferation of cells, showing a good behaviour as cellular matrix.[35-37]

In this work we present the design of a synthetic amino acid bearing EDOT which is the monomer used to prepare PEDOT, as side group for the subsequent preparation of a hybrid CP. In order to avoid undesirable secondary reactions during the incorporation of the amino acid into the polymer chain, its N- and C-terminus have

been blocked with a *tert*-butoxycarbonyl (Boc) and a methyl (Me) group, respectively. The resulting product, methyl 2-(*N*-*tert*-butoxycarbonyl)amino-3-(3,4-ethylenedioxy-2-thienyl) propanoate (**I** in Figure 1), has been incorporated at the end of PEDOT chains through an anodic polymerization process. After detailed chemical characterization, the electrochemical properties (*i.e.* electroactivity, electrostability and specific capacitance) and the behavior as cellular matrix of the resulting hybrid material (PEDOT-I in Figure 1) have been examined and compared with PEDOT. Results indicate that the strategy presented in this work is very promising for the development of CP-containing advanced hybrid materials able to combine the cell-adhesion properties of specific peptides with the electrical, optical and electrochemical properties of CPs, without any significant detriment with respect to the individual counterparts.

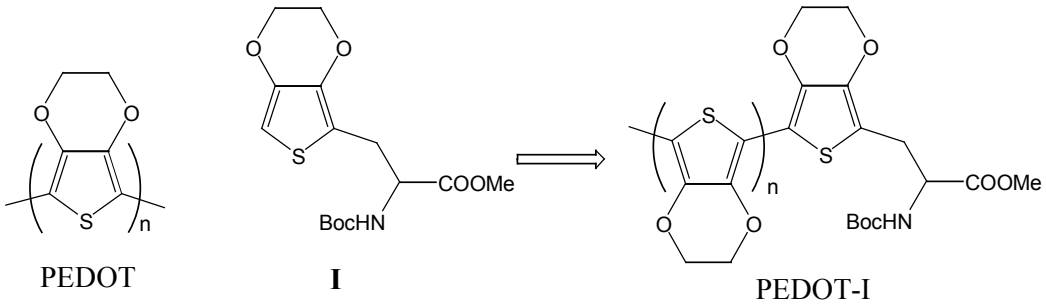

Figure 1. Scheme showing the preparation of PEDOT-I

5.1.2 Methods

General data for the synthesis of I. Melting points were determined on a Gallenkamp apparatus and are uncorrected. IR spectra were registered on a Mattson Genesis FTIR spectrophotometer; ν_{max} is given for the main absorption bands. ^{1}H and ^{13}C NMR spectra were recorded on a Bruker AV–400, ARX–300 or Varian Gemini 300 instrument at room temperature unless otherwise indicated, using the residual solvent signal as the internal standard. Chemical shifts (δ) are expressed in ppm and coupling constants (*J*) in Hertz. High-resolution mass spectra were obtained on a Bruker Microtof-Q spectrometer.

Anodic polymerizations and electrochemical assays. All electrochemical assays, including polymerizations, were carried out in a standard three electrode cell of 50 mL using steel AISI 316 sheets of 4 cm^2 area as WE and CE. The RE was an Ag|AgCl electrode containing a KCl saturated aqueous solution (Eº = 0.222 V at 25ºC). CA, CV

and galvanostatic charge-discharge cyclic assays were performed with a Autolab PGSTAT302N equipped with the ECD module (Ecochimie, The Netherlands). Each trial was performed under nitrogen atmosphere at room temperature.

Thickness by profilometry and electrochemical measurements. The thickness of the films was determined using electrochemical and profilometry measurements. Electrochemical estimations of the thickness were obtained by determining the current productivity through the mass-charge ratio and, subsequently, the W_{ox}. The latter procedure was detailed in previous works.[38,39] Profilometry measurements were conducted using a profilometer Dektack 6 from Veeco. On the other hand, the thickness of PEDOT and PEDOT-I films was also measured by scratch AFM, as is dicussed below.

FTIR. FTIR spectra of PEDOT and PEDOT-I were recorded on a Nicolet 6700 spectrophotometer. For this purpose, films were scrapped off from the electrode and dried under vacuum. FTIR spectra were recorded using KBr discs at a 6 cm^{-1} resolution (60 scans).

SEM *and* EDX. EDX spectroscopy and SEM studies were performed to examine the composition of PEDOT-I and to investigate the effect of **I** on the surface morphology of PEDOT, respectively. Dried samples were placed in a FIB Zeiss Neon 40 scanning electron microscope operating at 5 kV, equipped with an EDX spectroscopy system. Samples were mounted on a double-side adhesive carbon disc and sputter-coated with a thin layer of carbon to prevent sample charging problems.

AFM. Topographic AFM images were obtained with a Dimension 3100 Nanoman AFM and Multimode from Veeco using a NanoScope IV controller under ambient conditions in tapping mode. The r_{AFM} was determined using the statistical application of the Nanoscope software, which calculates the average considering all the values recorded in the topographic image with exception of the maximum and the minimum. AFM measurements were performed on various parts of the films, which produced reproducible images similar to those displayed in this work. The scan window size was 5×5 μm^2.

The AFM scratching technique was used to measure the thickness of the films. Specifically, contact mode AFM was used to intentionally scratch the film deposited on the steel substrate. Thus, the force was set to completely remove the layer in a scratch area of 0.7×0.7 μm^2. A line profile determined across the scratch with tapping mode AFM was used to determine the film thickness from the depth of the scratch. It should be noted that such topographic image was taken of a region bigger than the scratch area so as to accurately measure the step between the coated and the uncoated surface.

XPS. XPS analyses were performed in a SPECS system equipped with a high-intensity twin-anode X-ray source XR50 of Mg/Al (1253 eV / 1487 eV) operating at 150 W, placed perpendicular to the analyzer axis, and using a Phoibos 150 MCD-9 XP detector. The X-ray spot size was 650 μm. The pass energy was set to 25 and 0.1 eV for the survey and the narrow scans, respectively. Charge compensation was achieved with a combination of electron and argon ion flood guns. The energy and emission current of the electrons were 4 eV and 0.35 mA, respectively. For the argon gun, the energy and the emission current were 0 eV and 0.1 mA, respectively. The spectra were recorded with a pass energy of 25 eV in 0.1 eV steps at a pressure below 6×10^{-9} mbar. These standard conditions of charge compensation resulted in a negative but perfectly uniform static charge. The C 1s peak was used as an internal reference with a binding energy of 284.8 eV. High-resolution XPS spectra were acquired by Gaussian/Lorentzian curve fitting after S-shape background subtraction. The surface composition was determined using the manufacturer's sensitivity factors.

UV-vis. Measurements were performed on a UV/Vis-NIR Shimadzu 3600 spectrophotometer, which contains a tungsten halogen visible source, a deuterium arc UV source, a photomultiplier tube UV-vis detector, and an InGaAs photodiode and cooled PbS photocell NIR detectors. The wavelength range is 200–810 nm. All the spectra were collected in the reflectance mode using the integrating sphere accessory (Model ISR-3100) and converted to absorbance (Kubelka-Munk transformation). The total reflectance measured by this device involves both specularly and diffusely reflected light. Single-scan spectra were recorded at a scan speed of 60 nm min^{-1} using the UVProbe 2.31 software.

Electrical conductivity. The electrical conductivity was determined using the sheet resistance method with a previously described procedure.[40]

Electrochemistry. The electrochemical properties of PEDOT-I and PEDOT were studied by CV. The electroactivity and electrostability were determined using a 0.1 M PBS solution (pH= 7.4 adjusted with NaOH). The initial and final potentials were –0.40 V, and the reversal potential was 0.60 V. A scan rate of 25 mV/s was used in all cases. The electroactivity and electrostability were determined through direct measure of the anodic and cathodic areas in the control voltammograms using the GPES software. The electroactivity increases with the similarity between the anodic and cathodic areas of the first control voltammogram, whereas the electrostability decreases with the oxidation and reduction areas of consecutive control voltammograms. Specifically, the electrostability (LEA; in %) was expressed as the loss of electroactivity using the following Eqn:

$$LEA = \frac{\Delta Q}{Q_{II}} 100 \qquad (1)$$

where ΔQ is the difference of voltammetric charges (in C) between the second and the last cycle, and Q_{II} is the voltammetric charge corresponding to the second cycle.

The specific capacitance (SC; in F/g) of PEDOT and PEDOT-I were determined by CV:

$$SC = \frac{Q}{\Delta V \times m} \qquad (2)$$

where Q is the voltammetric charge, which is determined by integrating either the oxidative or reductive parts of the cyclic voltammetry curve, ΔV is the potential window (in V), and m is the mass of polymer on the surface of the WE (in g).

Galvanostatic charge/discharge curves were used as an alternative method to evaluate the SC:

$$SC = \frac{i\Delta t}{\Delta V} \qquad (3)$$

where ΔV is the difference between the potential at the beginning and at the end of the discharge, *i* is the applied current intensity (0.2 mA), and Δt is the time interval required for the change in voltage ΔV.

Cellular adhesion and proliferation. HEp-2 (human epidermoid cancer cell line), LLC-MK2 (rhesus monkey kidney epithelial cell line), MDCK (Madin-Darby canine kidney epithelial cell line) and Vero (African green monkey kidney epithelial cell line) cells were cultured in Dulbecco's modified Eagle medium (DMEM) supplemented with 10% fetal bovine serum, 1% penicillin/streptomycin and 2 mM L-glutamine at 37ºC in a humidified atmosphere of 5% CO_2 in air. The cultured media were changed every two days. For sub-culture, cell monolayers were rinsed with PBS and detached by incubating them with 0.25% trysin/EDTA for 5 min at 37ºC. Cells concentrations were determined by counting at the Newbauer camera using 4% trypan blue as dye vital.

The detached cells were cultured following the conditions for the adhesion and proliferation assays. PEDOT and PEDOT-I films deposited onto steel AISI 316 sheets of 1 cm^2 were placed in plates of 24 wells and sterilized using UV irradiation for 15 min in a laminar flux cabinet. An aliquot of 50 mL containing 5×10^4 cells (adhesion assays) or 2×10^4 cells (proliferation assays) was deposited on the substrate of each well. The plate was incubated under culture conditions for 60 min to promote the cell attachment to the film surface. Finally, 1 mL of the culture medium was added to each well. Controls of adhesion and proliferation were simultaneously performed by culturing cells on the surface of the tissue culture polystyrene (TCPS) plates and uncoated steel. Cell adhesion and proliferation were evaluated after 24 hours and 7 days of culture, respectively, using the MTT assay, which determines the cell viability.[41] This assay measures the ability of the mitochondrial dehydrogenase enzyme of viable cells to cleave the tetrazolium rings of the MTT and form formazan crystals, which are impermeable to cell membranes and, therefore, are accumulated in healthy cells. This process is detected by a colour change: the characteristic pale yellow of MTT transforms into the dark blue of formazan crystals. The viability results were normalized to TCPS control as relative percentages.

Results were derived from the average of four replicates (*n*= 4) for each independent experiment. ANOVA and Turkey tests were performed to determine the statistical significance, which was considered at a confidence level of 95% ($p < 0.05$).

Before the carbon coating for examination by SEM, samples covered with cells were fixed in a 2.5% glutaraldehyde PBS solution overnight at 4ºC. Then, they were dehydrated by washing in an alcohol battery (30º, 50º, 70º, 90º, 95º and 100º) at 4ºC for 30 minutes per wash. Finally, samples were air-dried, and sputter-coated with carbon before SEM observation.

5.1.3 Results and Discussion

Synthesis of methyl 2-(N-tert-butoxycarbonyl)amino-3-(3,4-ethylenedioxy-2-thienyl) propanoate (I).

The synthetic route used to obtain I is summarized in Figure 2, details for each step being provided in this section.

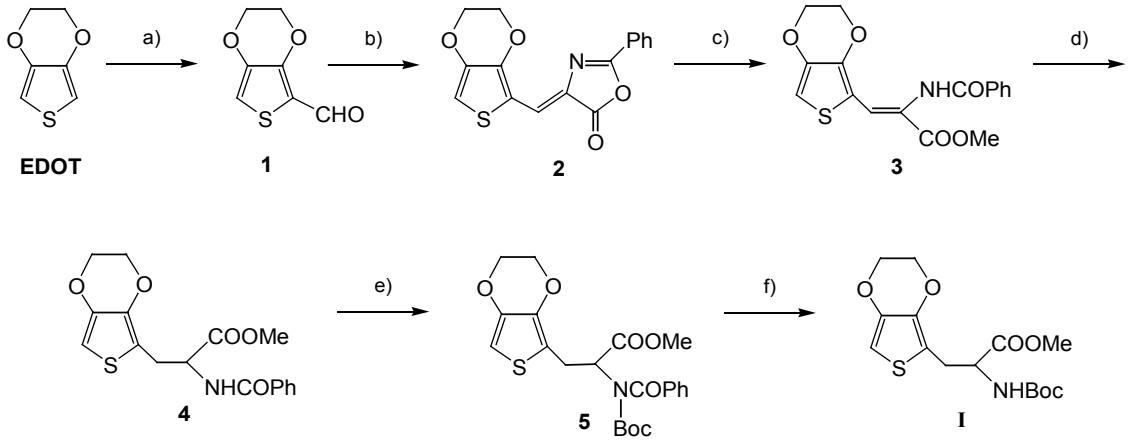

Figure 2. Reagents and conditions for the synthesis of I: (a) $POCl_3$, DMF, 0ºC 2h, rt overnight, 94%; (b) Hippuric acid, NaOAc, Ac_2O, rt 30 min, 1, 80ºC 4h, 68%; (c) MeONa, MeOH, rt 30 min, 97%; (d) H_2, Wilkinson's catalyst, MeOH/CH_2Cl_2 8/2, 45ºC 12h, 99%; (e) Boc_2O, DMAP, THF, 35ºC 24h, 95%; (f) NH_2-NH_2, THF/MeOH 1/1, rt 24h, 93%.

3,4-Ethylenedioxythienyl-2-carbaldehyde (1). EDOT (5.0 g, 35.17 mmol) was dissolved in dry dimethylformamide (20 mL). The mixture was cooled to 0ºC and phosphorus oxychloride (3.61 mL, 38.68 mmol) was added drop-wise. The reaction mixture was stirred for 2 hours at 0ºC. Then, ice water (50 mL) was added and the mixture was allowed to warm to room temperature and stirred overnight. After that, ethyl acetate (100 mL) was added and the organic layer was washed with water (3 x 30

mL). The organic phase was dried with magnesium sulphate and evaporated to dryness. Purification was carried out by column chromatography (eluent: hexane/dichloromethane/ethyl acetate 4/5/1) on silica gel to provide 1 as a white solid (5.65 g, 33.23 mmol, 94% yield). Mp 142-143 ºC. IR (nujol) ν: 1649 cm^{-1}. ^{1}H NMR ($CDCl_3$, 400 MHz): δ 4.25 (m, 2H), 4.35 (m, 2H), 6.77 (s, 1H), 9.88 (s, 1H). ^{13}C NMR ($CDCl_3$, 100 MHz): δ 64.5, 65.4, 110.9, 118.5, 141.9, 148.6, 180.2. HRMS (ESI) $C_7H_6O_3SNa$ $[M+Na]^+$: calcd. 192.9930, found 192.9938.

2-Phenyl-4-(3,4-ethylenedioxy-2-thenylidene)-5(4H)-oxazolone (2). A mixture of hippuric acid (3.16 g, 17.65 mmol) and anhydrous sodium acetate (1.45 g, 17.65 mmol) in acetic anhydride (20 mL) was stirred at room temperature for 30 minutes. 3,4-ethylenedioxythienyl-2-carbaldehyde (1) (3.0 g, 17.65 mmol) was then added and the reaction mixture was heated at 80ºC for 4 hours. After cooling to room temperature, water (20 mL) was added. The resultant precipitate was filtered, washed with water and taken up in dichloromethane (100 mL). The solution was washed with saturated aqueous sodium bicarbonate (3 $\times$ 30 mL) and brine (3 $\times$ 30 mL). After being dried and filtered, removal of the solvent furnished a solid, which was chromatographed (eluent: hexane/dichloromethane/ethyl acetate 4/5/1) to provide 2 as an orange solid (3.76 g, 12.0 mmol, 68% yield). Mp 224-225ºC. IR (nujol) ν: 1785 (C=O, oxazolone ring), 1763 (C=O, oxazolone ring), 1640 (C=N, oxazolone ring) cm^{-1}. ^{1}H NMR ($CDCl_3$, 300 MHz): δ 4.26 (m, 2H), 4.35 (m, 2H), 6.79 (s, 1H), 7-47-7.59 (m, 4H), 8.12-8.15 (m, 2H). ^{13}C NMR ($CDCl_3$, 75 MHz): δ 64.6, 65.5, 110.9, 114.7, 121.3, 126.0, 128.2, 128.9, 129.0, 132.9, 141.8, 146.1, 161.5, 167.1. HRMS (ESI) $C_{16}H_{11}NO_4SNa$ $[M+Na]^+$: calcd. 336.0301, found 336.0275.

Methyl 2-benzoylamino-3-(3,4-ethylenedioxy-2-thienyl) propenoate (3). A 2% solution of sodium methoxide in absolute methanol (10 mL) was added to 2 (2.81 g, 8.98 mmol), and the reaction mixture was vigorously stirred at room temperature for 30 minutes. The solvent was removed and the residue chromatographed (eluent: hexane/ethyl acetate 1/1) to give 3 as a white solid (3.0 g, 8.71 mmol, 97% yield). Mp 190-191ºC. IR (nujol) ν: 3232 (NH), 1706 (C=O, ester), 1644 (C=O, amide) cm^{-1}. ^{1}H NMR ($CDCl_3$, 400 MHz): δ 3.79 (s, 3H), 4.18 (m, 2H), 4.26 (m, 2H), 6.46 (s, 1H), 7.45-7.55 (m,

3H), 7.57 (bs, 1H), 7.81 (s, 1H), 7.93 (d, 2H, J = 7.3 Hz). ^{13}C NMR ($CDCl_3$, 100 MHz): δ 52.5, 64.6, 65.3, 105.5, 112.3, 119.8, 125.1, 127.7, 128.8, 132.3, 134.1, 141.7, 143.6, 165.6, 166.8. HRMS (ESI) $C_{17}H_{15}NO_5NaS$ $[M+Na]^+$: calcd. 368.0563, found 368.0576.

Methyl 2-benzoylamino-3-(3,4-ethylenedioxy-2-thienyl) propanoate (4). A solution of 3 (2.25 g, 6.52 mmol) in a mixture of methanol/dichloromethane 8:2 v/v (60 mL) was hydrogenated at 45ºC in the presence of 2% chlorotris(triphenylphosphine)rhodium(I) (Wilkinson's catalyst). After 12 hours, the solvent was evaporated and the obtained residue was purified by column chromatography (eluent: hexane/ethyl acetate 1/1) giving 4 as a white solid (2.24 g, 6.45 mmol, 99% yield). Mp 111-112ºC. IR (nujol) ν: 3343 (NH), 1736 (C=O, ester), 1637 (C=O, amide) cm^{-1}. ^{1}H NMR ($CDCl_3$, 300 MHz): δ 3.25 (dd, 1H, J = 15.1 Hz, J = 5.1 Hz), 3.36 (dd, 1H, J = 15.1 Hz, J = 5.1 Hz), 3.78 (s, 3H), 4.06-4.13 (m, 4H), 4.98 (dt, 1H, J = 7.1 Hz, J = 5.1 Hz), 6.18 (s, 1H), 6.95 (d, 1H, J = 7.1 Hz), 7.41-7.53 (m, 3H), 7.80 (d, 2H, J = 6.9 Hz). ^{13}C NMR ($CDCl_3$, 75 MHz): δ 28.7, 52.6, 53.4, 64.6, 64.9, 97.9, 110.5, 127.2, 128.6, 131.8, 134.2, 139.5, 141.5, 167.0, 171.7. HRMS (ESI) $C_{17}H_{17}NO_5NaS$ $[M+Na]^+$: calcd. 370.0720, found 370.0723.

Methyl 2-(N-tert-butoxycarbonyl)benzoylamino-3-(3,4-ethylenedioxy-2-thienyl) propanoate (5). A mixture of 4 (2.24 g, 6.52 mmol), 4-(dimethylamino)pyridine (120 mg, 0.98 mmol) and di-tert-butyl dicarbonate (2.13 g, 9.78 mmol) in tetrahydrofuran (40 mL) was stirred at 35 ºC for 24 hours. The solvent was removed and the residue chromatographed (eluent: hexane/ethyl acetate 6/4) to give 5 as a colorless oil (2.77 g, 6.19 mmol, 95% yield). IR (nujol) ν: 1734 (C=O, ester), 1682 (C=O, urethane) cm^{-1}. ^{1}H NMR ($CDCl_3$, 400 MHz): δ 1.12 (s, 9H), 3.51 (d, 2H, J = 8.1 Hz), 3.77 (s, 3H), 3.99-4.06 (m, 4H), 5.49 (t, 1H, J = 8.1 Hz), 6.14 (s, 1H), 7.30-7.46 (m, 5H). ^{13}C NMR ($CDCl_3$, 100 MHz): δ 26.5, 27.4, 52.6, 57.3, 64.5, 64.7, 83.5, 96.8, 111.9, 127.7, 128.0, 131.2, 137.4, 139.4, 141.7, 152.7, 170.6, 172.8. HRMS (ESI) $C_{22}H_{25}NO_7SNa$ $[M+Na]^+$: calcd. 470.1244, found 470.1262.

Methyl 2-(N-tert-butoxycarbonyl)amino-3-(3,4-ethylenedioxy-2-thienyl) propanoate (I). A solution of 5 (2.50 g, 5.59 mmol) in tetrahydrofuran/methanol 1:1 v/v (20 mL) was treated with hydrazine monohydrate (0.27 mL, 5.59 mmol), and the

reaction mixture was stirred at room temperature for 24 hours. After evaporation of the solvent, the residue was triturated with a mixture of hexane/diethyl ether 3:1 v/v (50 mL). The filtrate was concentrated to a thick oil, which was purified by chromatography (eluent: hexane/ethyl acetate 7/3) to provide I as a colorless oil (1.78 g, 5.20 mmol, 93% yield). IR (neat) ν: 3379 (NH), 1746 (C=O, ester), 1716 (C=O, urethane) cm^{-1}. ^{1}H NMR ($CDCl_3$, 400 MHz, 60 °C): δ 1.42 (s, 9H), 3.06 (dd, 1H, J = 15.0 Hz, J = 5.7 Hz), 3.15 (dd, 1H, J = 15.0 Hz, J = 5.7 Hz), 3.71 (s, 3H), 4.13 (m, 4H), 4.46 (m, 1H), 5.16 (m, 1H), 6.14 (s, 1H). ^{13}C NMR ($CDCl_3$, 100 MHz, 60 °C): δ 28.5, 29.1, 52.2, 54.2, 64.7, 64.8, 79.9, 97.5, 110.9, 139.6, 141.6, 155.1, 171.9. HRMS (ESI) $C_{15}H_{21}NO_6SNa$ $[M+Na]^+$: calcd. 366.0982, found 366.0982.

As the chirality of I is expected to have a negligible effect in the properties of PEDOT-I, no subsequent treatment was applied to separate the two enantiomers. Consequently, PEDOT-I was prepared (see next subsection) using a racemic mixture of I.

Synthesis of PEDOT and PEDOT-I

A two-steps process, which is schematically depicted in Figure 3a, was used for the anodic polymerization of PEDOT-I. In the first step, PEDOT was prepared by CA using a 0.01 M monomer solution in acetonitrile containing 0.1 M $LiClO_4$ as supporting electrolyte and a constant potential of 1.40 V was used.[42] The polymerization time (θ_1) was 10 s in all cases. It should be mentioned that such experimental conditions were found to produce films of nanometric thickness and roughness (i.e. ~90 and ~73 Å, respectively).[43] PEDOT films were deposited at the electrode surface, exhibiting the typical blue color. After this, films were washed with acetonitrile to eliminate the excess monomer, dopant or contaminants.

Figure 3b compares the control voltammograms recorded for the oxidation of the resulting PEDOT films in a 0.1 M $LiClO_4$ acetonitrile solution containing or not containing 1mM of compound I. As it can be seen, the oxidation potential of PEDOT-I is detected at 1.34 V while the degradation of PEDOT films occurs at around 1.6 V.

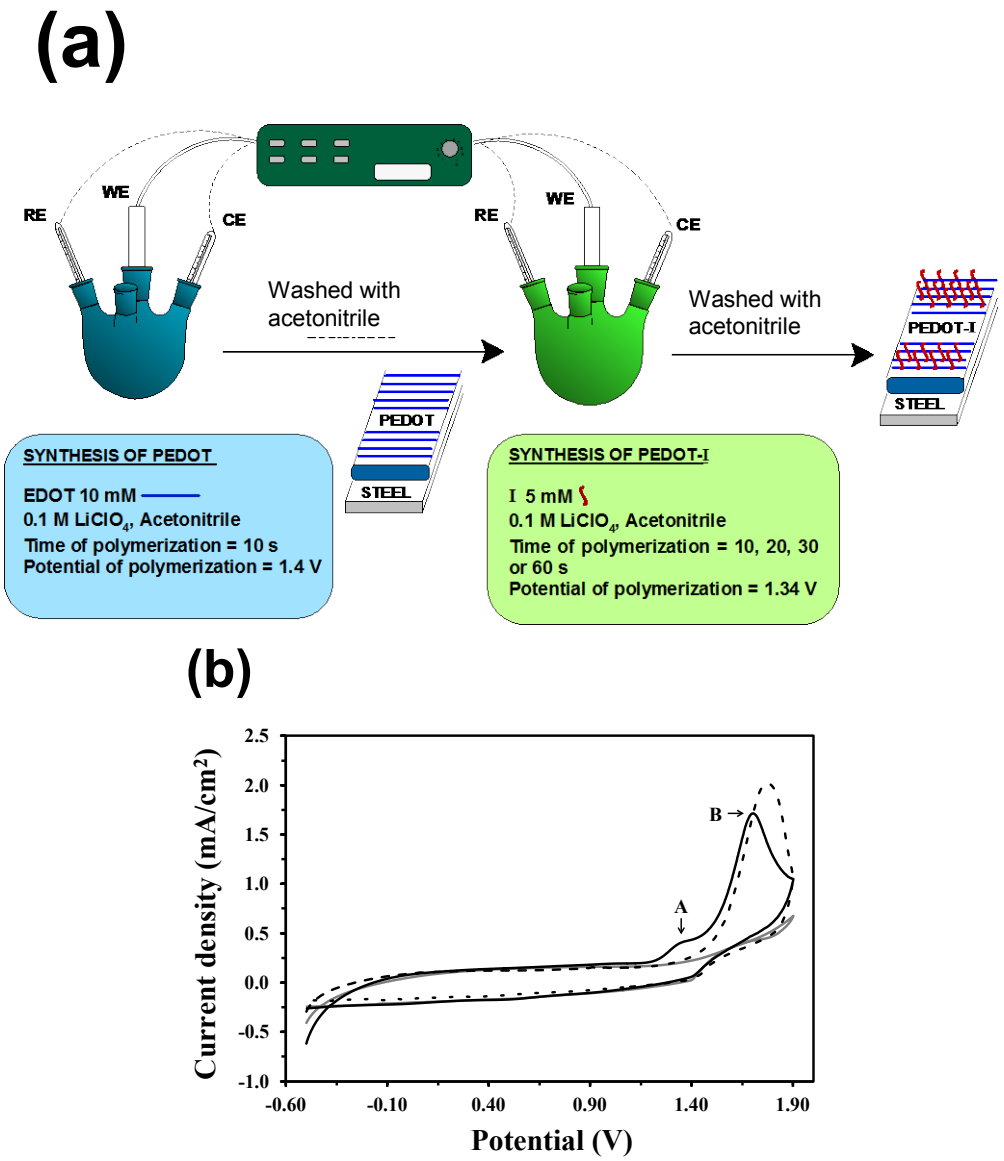

Figure 3. (a) Scheme displaying the synthetic process used to prepare PEDOT-I (see text). The first step corresponds to the generation of nanometric PEDOT films while the second one consists on the incorporation of I to the end of the PEDOT chains. (b) Control voltammograms for the oxidation of PEDOT films deposited on steel electrodes in a 0.1 M $LiClO_4$ acetonitrile solution containing (solid black line) and non-containing (dashed black line) 1 mM I. Initial and final potentials: –0.50 V; reversal potential: 1.90 V. Scan rate: 10 mV s^{-1}. Temperature: 25ºC. The control voltammogram of an uncoated steel electrode in a 0.1 M $LiClO_4$ acetonitrile solution containing 1 mM I (solid gray line) is also displayed. The oxidation potentials related with the formation of PEDOT-I and the electrochemical degradation of the films are labeled as A and B, respectively.

According to these observations, PEDOT films were transformed into PEDOT-I by CA under a constant potential of 1.34 V (second step in Figure 3a). For this purpose, the electrode coated with PEDOT was introduced in a cell filled with 50 mL of a 5 mM I solution in acetonitrile containing 0.1 M of $LiClO_4$. Four polymerization times (θ_2) were considered at this stage: 10, 20, 30 and 60 s (i.e. the value of θ_2 used to prepare the

samples for the different assays presented in this work is explicitly indicated in each case). It should be noted that the advantage of this procedure resides in the incorporation of I at the end of PEDOT chains, which is expected to induce minimum changes not only in the thickness and roughness but also in the electrochemical and electrical properties of the CP.

Thickness.

The thickness of PEDOT-I and PEDOT films was practically identical, independently of the technique used for the analysis. For example, the average thickness (25 samples) determined by profilometry for PEDOT-I (θ_2= 20 s) and PEDOT was 280±44 and 275±37 nm. This remarkable similarity is consequence of the role played by the amino acid in PEDOT-I, which can be thought as a simple end-capping of the polymer chains. The average thickness determined for PEDOT-I (θ_2= 20 s) by AFM scratch was 333 nm, which is fully consistent with the estimations obtained from profilometry. In contrast, the thickness estimated by electrochemical measurements [i.e. 136±9 and 138±11 nm for PEDOT and PEDOT-I (θ_2= 20 s), respectively] is considerably underestimated in comparison to profilometry and AFM scratch techniques. This was an expected result since the electrochemical method is based in two drastic approaches: (i) the whole electrode surface is completely and uniformly coated by the polymer; and (ii) the two sides of the electrode are coated by the same amount of polymer. The first approach is unrealistic for small polymerization times, like those in this work, and the film adhered to the side of the WE exposed to the CE is thicker than that adhered to the other one.

Chemical composition

The incorporation of I to the PEDOT chains was examined by FTIR, EDX and XPS spectroscopies. The FTIR-ATR spectra of PEDOT and PEDOT-I (θ_2= 20 s) films are superimposed in Figure 4. The two spectra are qualitatively comparable, even though the amino acid is easily detectable in the PEDOT-I spectrum because of the presence of Boc (urethane) and ester (COOMe) in the absorptions at the 1710-1760 cm^{-1} region. Unfortunately, the amide II (1600-1500 cm^{-1}) region and the N–H stretching (free: 3500-3300 cm^{-1}; hydrogen bonded: 3350-3070 cm^{-1}) are not recognizable because of

the overlapping with the bands associated to the Th ring (C=C and C–C stretching) and water (O–H stretching) bands, respectively. Regarding to the latter, it should be mentioned that hydration occurred despite samples were stored two days in a desiccator evidencing the hydrophilicity of the materials, as was already reported.[44] On the other hand, the IR band at 837 cm^{-1} can be assigned to the C–S stretching vibration in the Th rings of PEDOT and PEDOT-I.[45,46] The bands at 1141 and 1057 cm^{-1} are ascribed to the stretching mode of the ethylenedioxy group, and the band at 922 cm^{-1} is due to the ethylenedioxy ring deformation mode.[43,46,47]

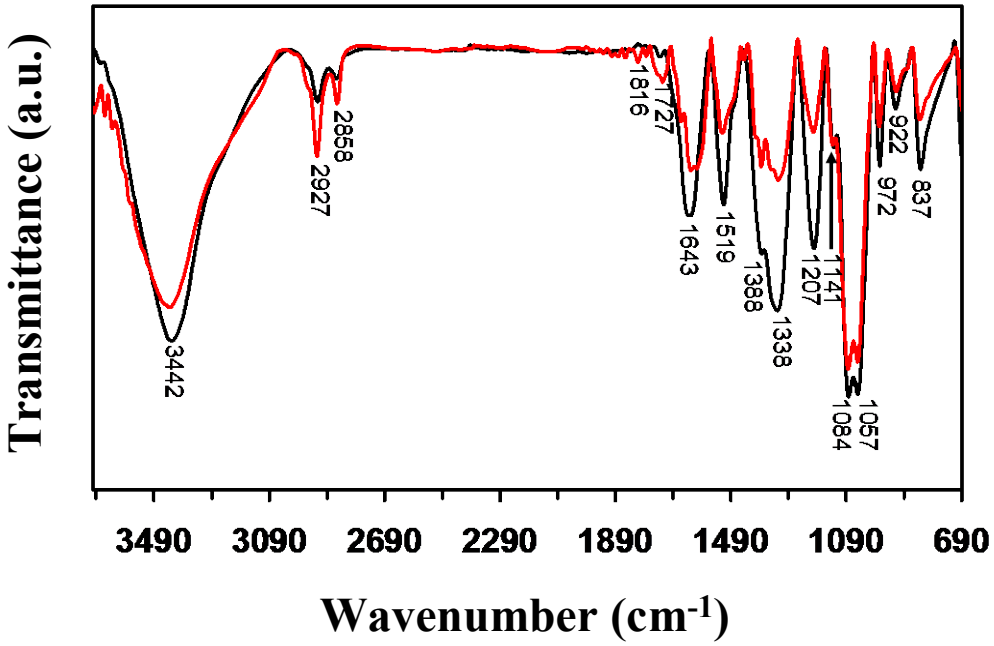

Figure 4. FTIR spectra of PEDOT (black line) and PEDOT-I (θ_2= 20 s; red line).

The composition of PEDOT and PEDOT-I (θ_2= 30 s) films as obtained from energy dispersive EDX spectroscopy analyses are compared in Table 1. Semi-quantitative elemental analyses of C, O and N reflect the successful incorporation of the amino acid into the PEDOT-I films, which display an appreciable concentration of N (i.e. this element was undetectable for PEDOT films). Similarly, EDX spectroscopy analyses of PEDOT-I films with θ_2= 10, 20 and 60 s (not shown) evidenced the presence of N at the surface.

PEDOT and PEDOT-I films on steel AISI 316 were further characterized by XPS, as shown in Table 2 and Figure 5. In general, the atomic compositions obtained using the conditions described in the Methods section correspond to the surface, the

penetration of the X-ray radiation being expected to be of ~10 nm. However, in the present study the penetration of the radiation is unknown since the thickness of the film was within the nanometric scale and examination of the surface morphology revealed abundant pores (SEM micrographs below) in both PEDOT and PEDOT-I films.

Electrode	C	O	N
PEDOT	91.14±0.48	8.86±0.44	-
PEDOT-I	95.70±0.31	1.68±0.17	2.62±0.26

Table 1. Weight percent composition (C, O and N) obtained by EDX spectroscopy analyses at the surface of PEDOT and PEDOT-I (θ_2= 30 s) films.

This explains the detection of nitrogen in PEDOT films (Table 2), which cannot be attributed to traces of acetonitrile solvent since samples were stored in a desiccator under vacuum conditions during one week before XPS analyses. Thus, detailed interpretation of the N1s and S2p spectra (see below) allowed us to conclude that the nitrogen detected in the composition of PEDOT comes from the AISI 316 steel. Despite of this, the N1s increases from 0.43% in PEDOT to 0.66% in PEDOT-I with θ_2= 10 s, and from the latter to 1.05% in PEDOT-I with θ_2= 60 s. On the other hand, for the PEDOT film the C/S ratio is 6.22, which is slightly larger than the theoretical value of 6.00. For PEDOT-I, this ratio increases to 6.6-7.4, depending on θ_2, which is consistent with the fact that the content of C increases with the incorporation of the amino acid.

Figure 5 depicts characteristic XPS spectra in the C1s, O1s and N1s regions for PEDOT-I (θ_2= 20 s). As it can be seen, deconvolution of the C1s peak led to a six Gaussian curves that have been attributed to saturated and conjugated C–C (284.5 eV), C–S (285.6 eV), C=C–O (286.5 eV) and C–O–C (287.2 eV) bonds of PEDOT chains,[48-50] and to the C=O of amide (288.5 eV) and ester (289.5 eV) groups of I.[51-53] It should be mentioned that the peaks of the amino acid may be influenced by those of the polymer and vice versa, explaining the small deviations found in some peaks with respect to the values reported in the literature.[48-53] The O1s signal consists of four components with the first centered at 532.3 eV, corresponding to the overlap of the oxygen of perchlorate anions[54] and of C=O groups in I.[55] The peak centered at 533.5 eV is attributed to the C–O of the Boc and the COOMe groups of I.[55] The other components at 533.8 and 535.9 eV are assigned to the oxygen of the C–O–C bonding in the ethylene bridge[48,54] and the C=O groups of contamination products. The latter was

also found by Sakmeche et al.[54] in PEDOT produced by anodic polymerization and doped with sodium dodecyl sulfate and lithium perchlorate.[54]

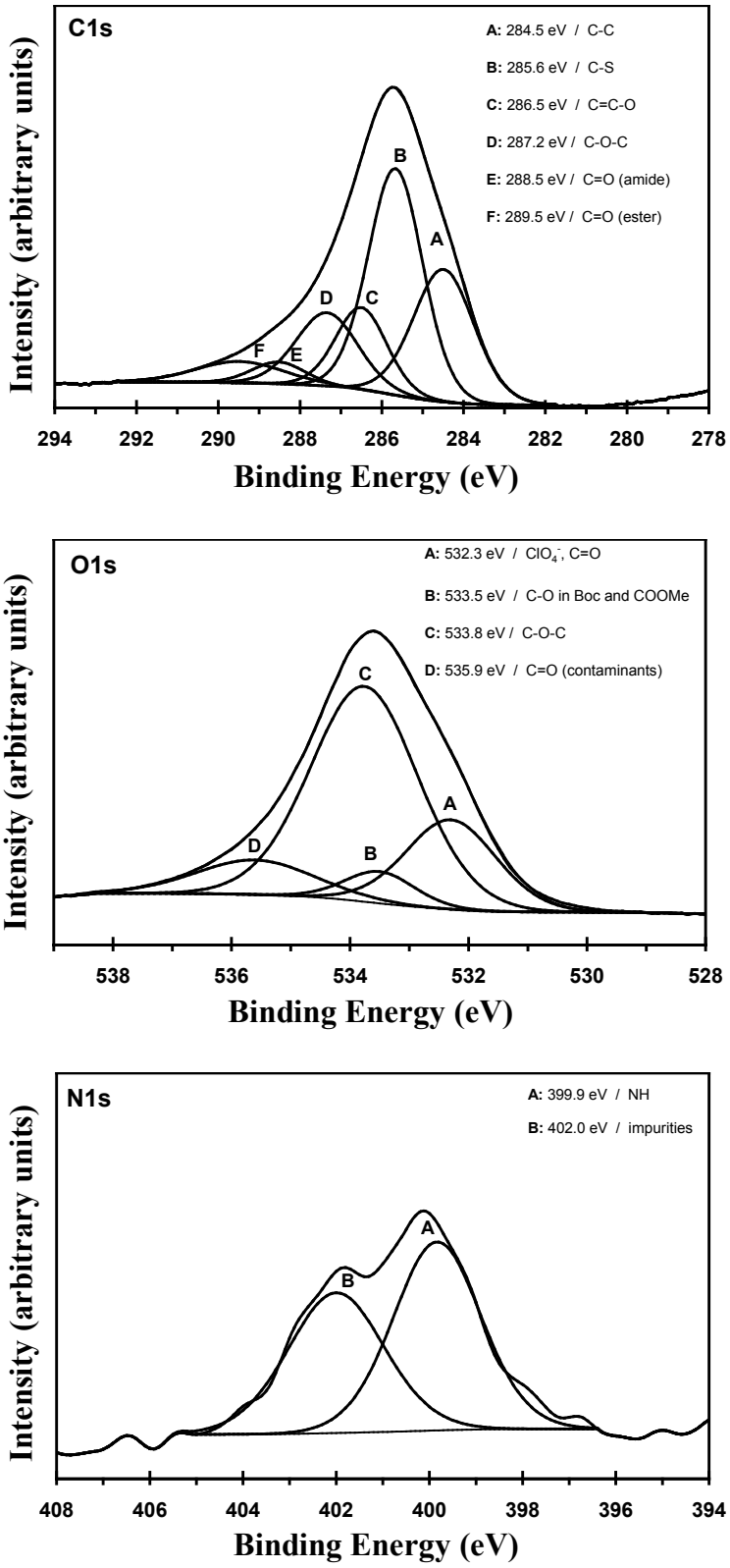

Figure 5. High-resolution XPS spectra for PEDOT-I (θ_2= 20 s): C1s (top), O1s (middle) and N1s (bottom) regions. Peaks from deconvolution are also displayed.

Electrode	C1s	N1s	O1s	S2p	Cl2p
PEDOT	50.56	0.43	36.90	8.12	3.99
PEDOT-I (θ_2= 10 s)	56.15	0.66	32.55	8.47	2.16
PEDOT-I (θ_2= 20 s)	54.49	0.75	33.93	8.33	2.50
PEDOT-I (θ_2= 30 s)	55.52	0.85	33.57	7.50	2.56
PEDOT-I (θ_2= 60 s)	53.34	1.05	34.96	7.64	3.00

Table 2. Atomic percent composition (C1s, O1s, N1s, S2p and Cl2p) obtained by XPS for PEDOT and PEDOT-I nanometric films.

The high resolution N1s spectrum in Figure 5, which shows two peaks centered at 399.9 and 402.0 eV, is crucial to prove the immobilization of I at the surface of the CP. In a recent study, Bhattacharyya and Gleason attributed the presence of N1s characteristic peaks at 399.7 eV (–NH) and 400.4 eV (N–C=O) to bovine serum albumin (BSA) attached to the surface of a copolymer of thiophene-3-acetic acid and EDOT.[51] Similarly, the XPS N–H signal of Boc-Val-Gly-Gly-Val-Gly-OEt and poly(Val-Gly-Gly-Val-Gly) were identified at 400.0 and 400.2 eV, respectively.[55] On the other hand, the N1s XPS spectra of the Boc-protected 10-aminodec-1-ene showed two broad overlapping signals, one at a binding energy of 400.2 eV, and a second at 401.9 eV.[56] These were assigned to the free unprotonated amine (NH–Boc) and the free protonated amine, respectively, the latter indicating the removal of the Boc protecting moiety. However, the coexistence of the two peaks indicated that the deprotection reaction did not go to completion.[56] Two peaks were also detected in the high resolution N1s spectrum of an adhesive peptide reproducing the 351-359 sequence of human vitronectin, which was covalently attached to TiO_2.[52] The first peak (399.6 eV) was attributed to the N–H while the second (401.7 eV) suggested a partial protonation of the terminal amino groups. These observations support the successful attachment of I to the PEDOT chains and indicate the existence of Boc protected N–H groups (399.9 eV). However, as was mentioned above, the detection of N1s in PEDOT films (Table 1) indicates that the peak centred at 402.0 eV is consequence of impurities in the AISI 316 steel substrate rather than to unprotected N–H groups. In order to prove that, in this particular case, the 402 eV peak is due to impurities and not to the removal of the Boc groups, we examined the variation of the contribution associated to the 399.9 and 402.0 peaks with θ_2. It should be noted that, if exists, the deprotection reaction is probably induced by the applied potential and, therefore, its effect on the 402.0 eV peak should grow with θ_2.

Results, which are provided in Table 3, reflect that the contribution of the 402.0 eV remains practically constant (i.e. 45.0%-49.6%) for all the PEDOT-I samples. This feature combined with the fact that, as mentioned above, it was also detected in PEDOT samples corroborates that the 402.0 eV peak is due to impurities of the substrate.

Electrode	399.9 eV	402.0 eV
PEDOT	0	100
PEDOT-I (θ_2= 10 s)	50.4	49.6
PEDOT-I (θ_2= 20 s)	55.0	45.0
PEDOT-I (θ_2= 30 s)	54.2	45.8
PEDOT-I (θ_2= 60 s)	53.9	46.1

Table 3. Contribution (in %) of the N1s peaks at 399.9 and 402.0 eV obtained by XPS for PEDOT and PEDOT-I films.

The high resolution XPS of the S2p region for PEDOT-I (θ_2= 20 s) is very similar to that recently reported for PEDOT[31] and by this reason has not been included in Figure 5. The main observations refer to the spin-split sulphur coupling, $S2p_{3/2}$ (164.0 eV) and the $S2p_{1/2}$ (165.1 eV), with a separation of 1.16 eV and to the higher energy broad tail produced by positively charged sulphur within the Th ring. Oxidized species are due to the fact that samples were repeatedly exposed to the atmosphere after their preparation. These results are fully consistent with results reported by other authors for PEDOT.[57-59]

Surface morphology

Figure 6a shows SEM micrographs of the typical morphology found at the surface of PEDOT films deposited on steel using a θ= 10 s. Although low magnification micrographs indicates a compact structure, high magnification images evidences a sponge-like morphology, which can be described as a structure with abundant narrow and tortuous pores. Such pores are formed by the aggregation of sticks with a fiber-like morphology. The length of each of these sticks typically range from 25 to 50 nm, decreasing when the level of aggregation increases. This morphology is fully consistent with those reported in the literature for films generated in the same conditions and $\theta \leq$ 30 s.[60] The influence of I in the morphology of PEDOT was negligible, independently of the polymerization time. This is illustrated in Figure 6b, which shows SEM micrographs

of PEDOT-I (θ_2= 30 s). The morphology and the electrochemical properties of CPs are frequently related and, therefore, these results suggest that the excellent electrochemical properties of PEDOT are not altered by the incorporation of the amino acid at the surface (see below).

Similarly, AFM images evidenced very similar surface topologies for PEDOT and PEDOT-I. This consists on relatively dense distribution of sharp peaks that are grouped forming small and well-defined clusters that resemble mountain ranges. As PEDOT molecules exclusively involve α–α linkages (i.e. the β positions of the Th ring are occupied by the fused dioxane ring), the clusters has been attributed to the formation of compact molecular aggregates of linear chains that are stabilized by the perchlorate dopant ions. This surface topology is illustrated in Figure 6c, which displays an AFM image of PEDOT. Similarly, no significant effect has been detected in the roughness of the films by the incorporation of I to the surface, independently of θ_2. Thus, the r_{AFM} of PEDOT and PEDOT-I (θ_2= 30 s) films is 151 and 134 nm, respectively.

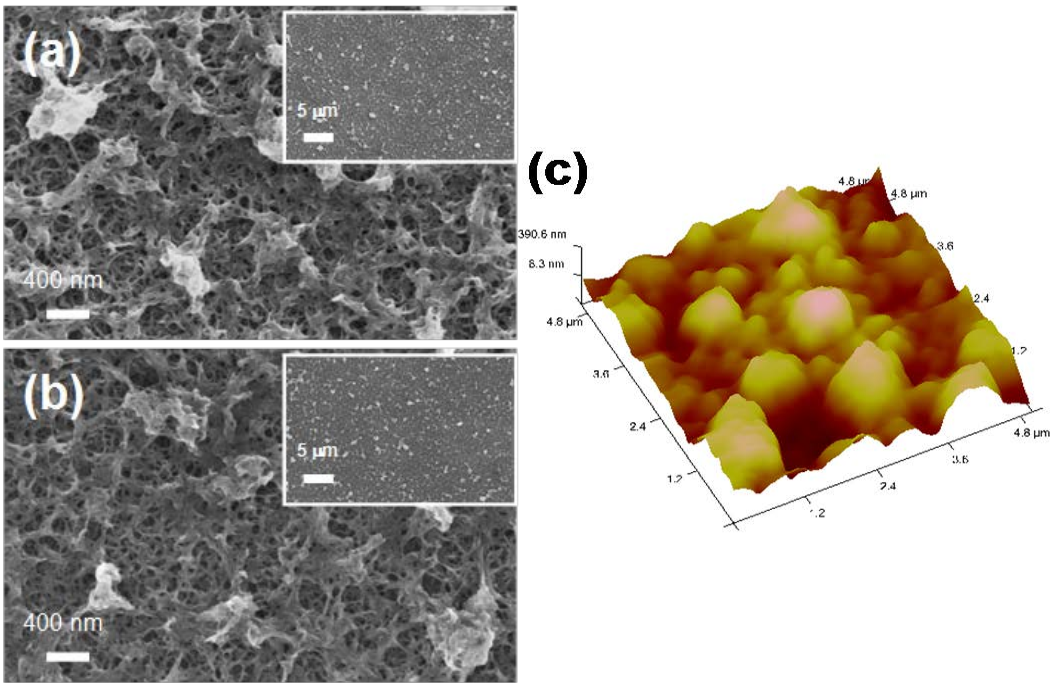

Figure 6. SEM micrographs of (a) PEDOT and (b) PEDOT-I (θ_2= 30 s). (c) AFM image of PEDOT.

UV-vis reflectance spectroscopy

Figure 7a shows the absorption spectrum recorded for I, which presents two important transitions at $\lambda^{(1)}$= 256 and $\lambda^{(2)}$= 246 nm. By analogy with a recent study on EDOT monomer,[61] these absorption bands have been attributed to the HOMO $\rightarrow$

LUMO and HOMO-1→ LUMO transitions, respectively. The $\lambda^{(1)}$-$\lambda^{(2)}$ gap (Δ) found for EDOT diluted in dimethyl sulfoxide (Δ=7 nm)[61] is in good agreement with that of I (Δ= 10 nm), evidencing the small influence of the amino acid skeleton on the electronic transitions of the heterocyclic side group.

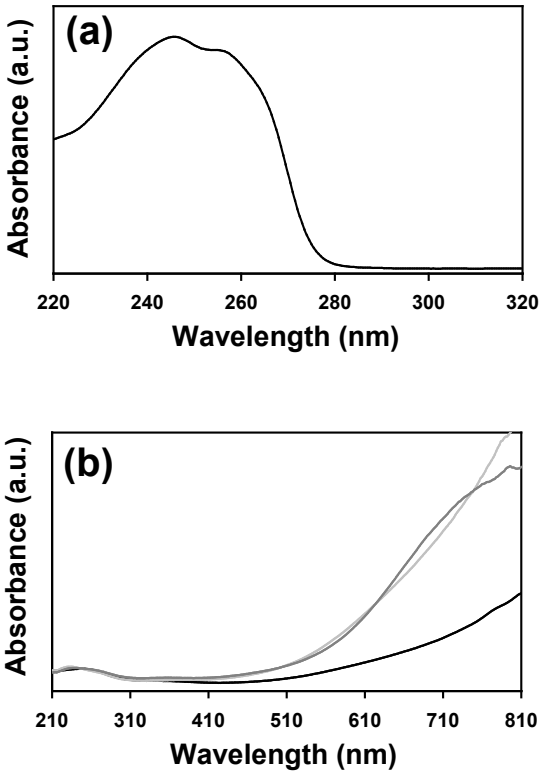

Figure 7. UV-vis spectra of: (a) I; and (b) PEDOT (black line), PEDOT-I (θ_2= 20 s; dark gray) and doped PEDOT (additional 20 s of oxidation at 1.34 V; light gray).

Figure 7b compares the UV-vis spectra of PEDOT and PEDOT-I (θ_2= 20 s). As it can be seen, both spectra exhibit an absorption peak at 240 nm due to the π–π electronic transitions of the aromatic rings and a broad absorption tail between 500 and 800 nm ascribed to the polaronic band of the conductive quinoid form.[47] As expected, the slope of such tail is more pronounced for PEDOT-I than for PEDOT. Thus, the doping level of polymer chains is higher for PEDOT-I than for PEDOT. This increment was provoked by the fact the hybrid material is affected more time by the 1.34 V potential than PEDOT (i.e. $\theta_1 + \theta_2$= 30 s for PEDOT-I while θ_1= 10 s for PEDOT). In order to prove this feature, Figure 7b includes the UV-vis spectrum of doped PEDOT, which was produced by applying a potential of 1.34 V during 20 s to the film obtained using θ_1= 10 s. It is worth nothing that the spectra of PEDOT-I (θ_2= 20 s) and doped PEDOT are very similar.

Electrical conductivity

The electrical conductivity of PEDOT and PEDOT-I (θ_2= 20 s) was measured on four independent samples. The average value was 507±13 and 466±14 S/cm for PEDOT and PEDOT-I, respectively. These results indicate that the amino acid-polymer linkages localized at the surface film does not alter appreciably the electrical conductivity of the bulk polymer, which decreases by 8% only.

Electrochemical behavior

The electroactivity (i.e. ability to store charge), which increases with the similarity between the anodic and cathodic areas of the first control voltammogram, was determined by CV in an aqueous buffered medium. Figure 8a compares the control voltammograms recorded for PEDOT and PEDOT-I (θ_2= 20 s) in the potential range from –0.40 to +0.60 V. Inspection of the curves indicates that the electroactivity of PEDOT-I, which shows an anodic peak (O_1) with E_p^a (O_1)≈ –0.1 V and a cathodic peak (R_1) with E_p^c(R_1)= –0.3 V, is higher than that of PEDOT. This feature is fully consistent with the current densities (j in Figure 8a), which reflect that the concentration of oxidized molecules is larger for PEDOT-I than for PEDOT. The different electrochemical behavior of PEDOT-I with respect to PEDOT has been attributed to the higher doping level of the former material that, as mentioned above, is consequence of the application of the external potential during an additional period of time (i.e. θ_2). This feature is corroborated in Figure 8a, which includes the CV recorded for doped PEDOT.

The electrochemical degradation of PEDOT and PEDOT-I (θ_2= 20 s) in water with 0.1 M PBS is compared in Figure 8b, which represents the variation of the LEA against the number of consecutive oxidation-reduction cycles. The electroactivity of PEDOT and PEDOT-I decreases 8% and 18%, respectively, after 100 cycles. In order to examine, the influence of the oxidation of the polymer chains during θ_2 is reflected in Figure 8b, which includes the variation of the LEA for doped PEDOT. The electroactivity of the latter decreases by 14% after 100 cycles, indicating that the electrochemical stability of PEDOT-I is consequence of both I and the doping of the PEDOT chains (i.e. 4% each one

Table 4 compares the SC values determined by CV (Eqn 2) using different scan rates (i.e. from 25 to 100 mV/s) for PEDOT, doped PEDOT and PEDOT-I. The SC of the three materials increases with the scan rate, even though such systematic behavior was lost at the highest scan rate. On the other hand, the SCs measured for PEDOT films range from 130 to 194 F/g when the scan rate varies between 50 and 100 mV/s, the order of magnitude of these values being identical to that reported for nanometric PEDOT using different experimental conditions.[34,60]). On the other hand, doped PEDOT undergoes a reduction of the SC, which is drastic at the highest (22%) scan rate and only moderate at the intermediate scan rates (~5%). Finally, the SC of PEDOT-I is very similar to that of doped PEDOT evidencing that attachment of I is not in detriment of the ability showed by the polymer to store charge, this feature being consistent with the CVs displayed in Figure 8a. This is also corroborated by the SCs obtained from galvanostatic charge/discharge curves, which are 221, 229 and 215 F/g for PEDOT, doped PEDOT and PEDOT-I, respectively.

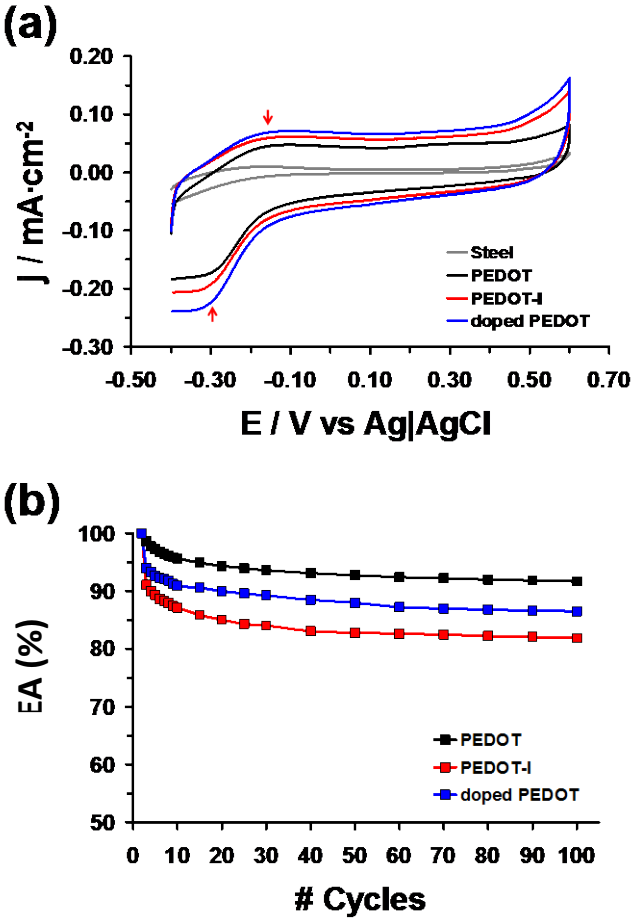

Figure 8. (a) Control voltammograms for the oxidation of PEDOT and PEDOT-I (θ_2= 20 s) and doped PEDOT films. The voltammogram of the bare steel AISI 316 substrate is also displayed

for reference. Voltammograms were recorded in water with 0.1 M PBS at 25 mV/s and 25ºC. Initial and final potentials: –0.40 V; reversal potential: +0.60 V. (b) Variation of the *EA* (in %) against the number of consecutive oxidation-reduction cycles for PEDOT, PEDOT-I (θ_2= 20 s) and doped PEDOT in water with 0.1 M PBS.

Scan rate (mV/s)	PEDOT (F/g)	doped PEDOT (F/g)	PEDOT-I (F/g)
25	72	93	90
50	130	124	121
75	164	157	157
100	194	152	154

Table 4. Specific capacitance for PEDOT, doped PEDOT and PEDOT-I (θ_2= 20 s) obtained from CV assays (Eqn 2) using different scan rates.

Cell adhesion and proliferation

The responses of PEDOT-I (θ_2= 20 s) towards different cellular lines were compared with those of PEDOT and doped PEDOT. Cellular adhesion and proliferation assays were performed considering four different lines of eukaryotic cells: Hep-2, LLC-MK2, MDCK and Vero. These cell lines were selected due to their adherent growth and epithelial-like characteristics. Quantitative results of cellular adhesion assays are displayed in Figure 9a, steel and TCPS being used as control substrates. The steel was considered as a control since the nanometric PEDOT-I were deposited in such substrate. As it can be seen, the number of cells by area onto the controls is similar for the four cellular lines. PEDOT supports a large number of cells adhered to its surface as compared to controls.[35-37] The behavior of PEDOT-I and doped PEDOT as supportive matrix for the adhesion of the four cellular lines is considerably better than that of controls. Regarding to the good results achieved for doped PEDOT, it should be mentioned that previous studies evidenced that overoxidation processes favor cell-polymer interactions because of the higher dopant ion concentration in the polymeric matrix.[62] Moreover, adhesion of Vero and MDCK cells onto PEDOT-I is significantly favored with respect to doped PEDOT. This should be attributed to the combination of two effects: the concentration of dopant and the specific benefits introduced by the amino acid.

After 7 days of culture, the cellular activity on the materials was evaluated. Cellular proliferation results, which are displayed in Figure 9b, show that the number of viable cells per area of steel (control) decreased considerably, evidencing the limited

biocompatibility of such substrate. However, the number of proliferated cells in PEDOT, doped PEDOT and PEDOT-I was considerably higher than in the controls, even though the tendencies were similar to those discussed above for cellular adhesion. The overall of the results reflects the good behavior of PEDOT-I as cellular matrix, evidencing that the attachment of the amino acid as end capping of PEDOT chains does not inhibit but promotes cell adhesion and proliferation.

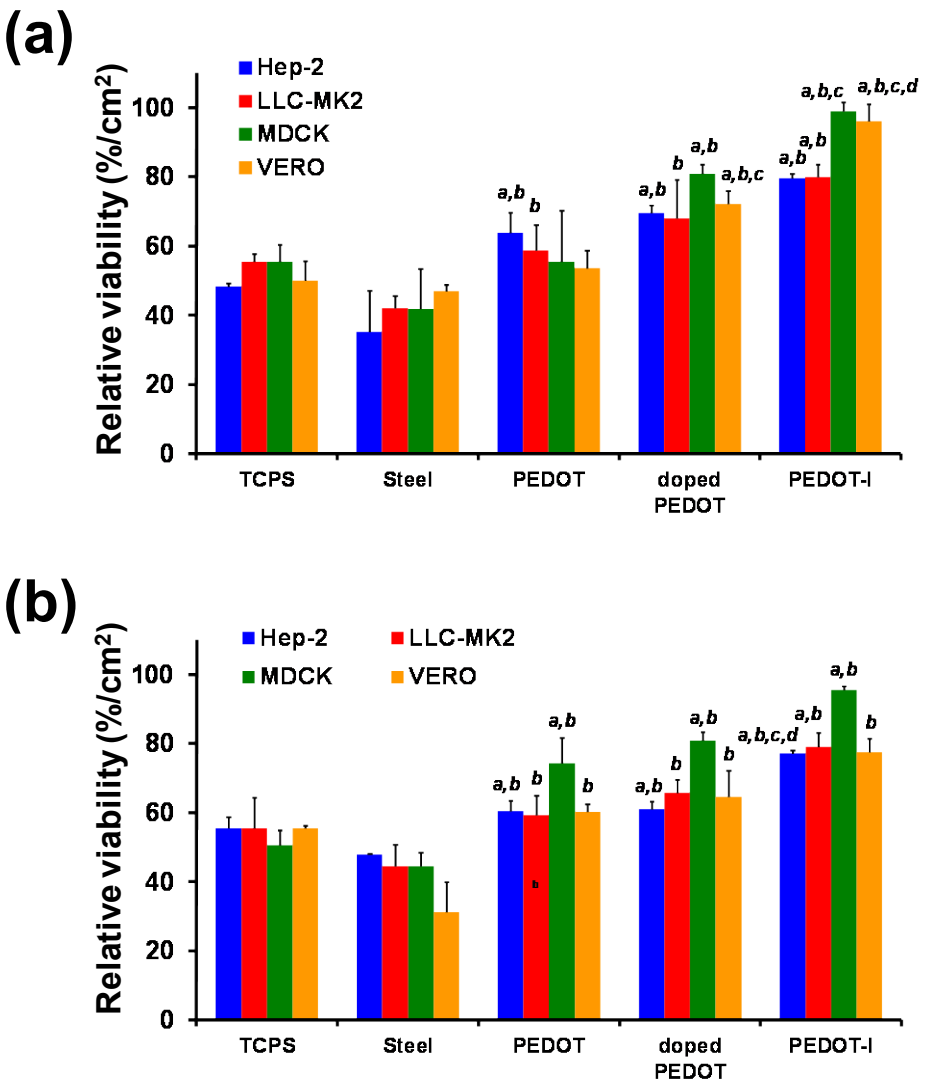

Figure 9. Cellular adhesion (a) and cellular proliferation (b) on PEDOT, doped PEDOT and PEDOT-I (θ_2= 20 s) using HEp-2, LLC-MK2, MDCK and Vero eukaryotic cell lines. The relative viability was established in relation to the TCPS control. Steel was also considered as a control substrate because the individual polymers and the blend were deposited on this material. $p < 0.05$ vs a) TCPS, b) Steel, c) PEDOT, and d) doped PEDOT.

SEM micrographs displayed in Figure 10 show the characteristics of cell cultured onto the surface of PEDOT-I (θ_2= 20 s) nanofilms. In general, there is a

significant spreading of cells for the formation of cellular monolayers on the surface of the substrate. The connection sites between the cells and the surface of PEDOT-I have been marked with arrows in Figures 10a and 10d, details about the stress fibers formed by the cells to move along the substrate being also displayed. The latter correspond to lamellipodia, which are thin but broad projections at the edge of a mobile cell. Lamellipodia contain extensively branched arrays of actin filaments, oriented with their barbed ends towards the film surface. These filaments for local adhesion are known as fillopodia (insets in Figures 10a and 10d). On the other hand, insets of Figures 10b and 10c show a typical eukaryotic cell connection process to establish cell-cell communication, which is a crucial step in the coordination of differentiation processes. These observations corroborate that PEDOT-I surface stimulates the cellular proliferation.

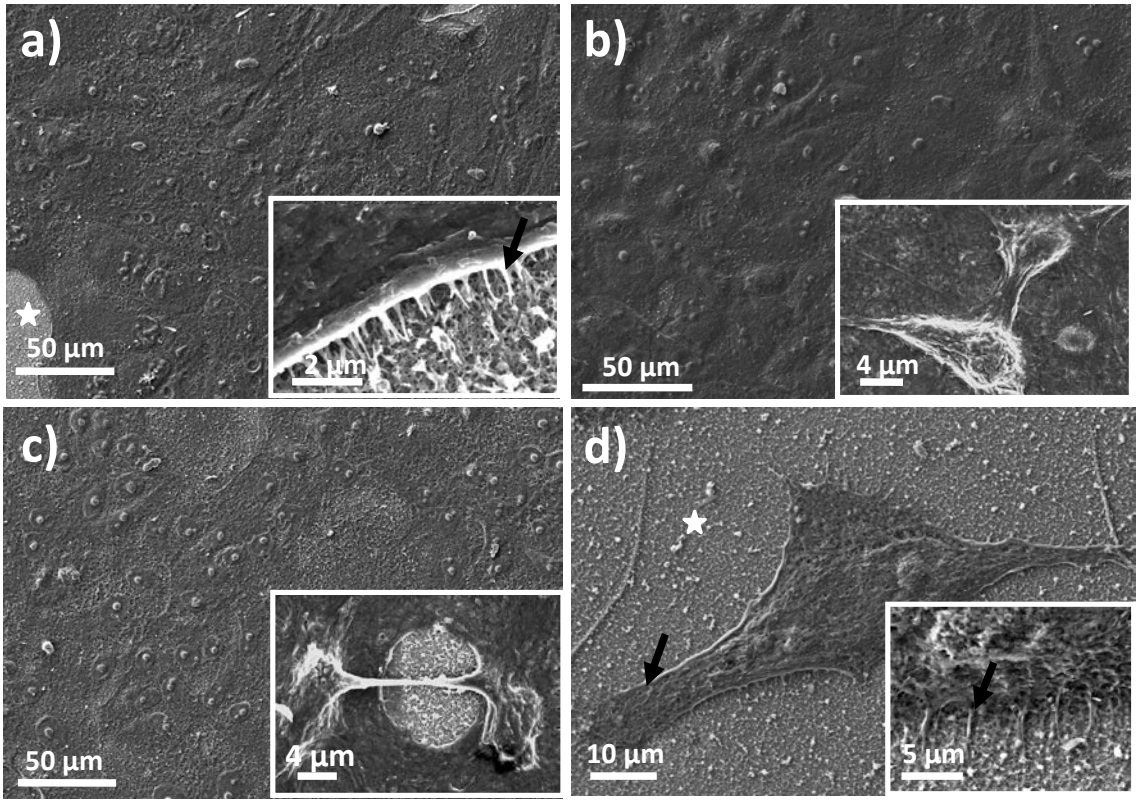

Figure 10. SEM micrograps of (a) MDCK, (b) LLC-MK2, (c) Vero and (d) Hep-2 cells cultured for seven days on the surface of PEDOT-I (θ_2= 20 s). The substrate surfaces (domains without cells) are marked with asterisks (*). The connections or interactions between the cell and the surface are indicated by arrows: lamedipodia in the low resolution image of (d) and fillopodia in the insets of (a) and (d). Insets in (b) and (c) display intercellular communication processes.

5.1.4 Conclusions

A synthetic amino acid bearing a EDOT group have been designed and synthesized. This amino acid has been conjugated with PEDOT to produce a hybrid material through a two-steps potentiostatic procedure. The successful incorporation of the amino acid as end capping of the polymer chains have been corroborated by FTIR, EDX and XPS. The hybrid material preserves the excellent electrical and electrochemical properties of such CP. Moreover, cell adhesion and proliferation assays indicate that the behavior of PEDOT-I as cellular matrix is better than that of PEDOT.

PEDOT-I represents the success of a new strategy for the preparation of peptide-CP hybrid materials. Such strategy is based on the design of peptides bearing chemical groups similar to those of the CP, which are used to join the two components of the hybrid. This approximation avoids any detriment in the electrical and electrochemical behavior of the CP matrix, being much more efficient than non-covalent approaches. Within this topic, our current research is focused on the development of electrically and electrochemically-active hybrid materials with an enhanced behavior as cellular matrix using PEDOT-I as starting point. Specifically, we are developing a cell adhesive sequence by adding Arg and Asp to the N- and C-terminus of **I**, which will be incorporated as end capping to the PEDOT chains. The behavior as bioactive substrate of the resulting hybrid material is expected to be significantly higher than that of PEDOT and PEDOT-I.

5.1.5 References

1. R. B. Pernites, C. M. Santos, M. Maldonado, R. R. Ponnapati, D. F. Rodrigues and R. C. Advincula, *Chem. Mater.,* 2012, **24**, 870.

2. D. F. Li, H. J. Wang, J. X. Fu, W. Wang, X. S. Jia and J. Y. Wang, *J. Phys. Chem. B,* 2008, **112**, 16290.

3. R. A. Green, N. H. Lovell and L. A. Poole-Warren, *Acta Biomat.* 2010, **6**, 63.

4. Y. H. Xiao, C. M. Li, S. Q. Wang, J. S. Shi and C. P. Ooi, *J. Biomed. Mater. Res. Part A,* 2010, **92A**, 766.

5. M. Hamedi, J. Wigenius, F.-I. Tai and D. Aili, *Nanoscale,* 2012, **2**, 2058.

6. M. Hiller, C. Kranz, J. Huber, P. Bäuerle and W. Schuhmann, *Adv. Mater,* 1996, **8**, 219.

7. J. A. Arter, D. K. Taggart, T. M. McIntire, R. M. Penner and G. A. Weiss, *Nano Letters,* 2010, **10**, 4858.

8. D. Y. Yu, Y. Zhang and B. Liu, *Macromolecules,* 2008, **11**, 4003.

9. B. Teixeira-Dias, L. J. del Valle, D. Aradilla, F. Estrany and C. Alemán, *Macromol. Mater. Engin.,* 2012, **297**, 427.

10. N. K. Guimard, N. Gomez and C. E. Schmidt, *Prog. Polym. Sci.,* 2007, **32**, 876.

11. Y. Zhong, X. Yu, R. Gilbert and R. V. Bellamkonda, *J. Rehabil. Res. Dev.*, 2001, **38**, 627.

12. X. Cui, J. Wiler, M. Dzaman, R. A. Altschuler and D. C. Martin, *Biomaterials*, 2003, **24**, 777.

13. B. Garner, A. J. Hodgson, G. G. Wallace and P. A. Underwood, *J. Mat. Sci. Mater. Med.,* 1999, **10**, 19.

14. R. A. Green, N. H. Lovell and L. A. Poole-Warren, *Biomaterials,* 2009, **30**, 3637.

15. X. Y. Cui and D. C. Martin, *Sensors Actuators B*, 2003, **89**, 92.

16. Y. H. Xiao, X. Y. Cui, J. M. Hancock, M. Bouguettaya, J. R. Reynolds and D. C. Martin., *Sensors Actuators B*, 2004, **99**, 437.

17. B. Sanghvi, K. P.-H. Miller, A. M. Belcher and C. E. Schmidt., *Nat. Mater*., 2005, **4**, 496.

18. E. De Giglio, L. Sabbatini and G. Zambonin, *J. Biomater. Sci. Polym.,* 1999, **10**, 845.

19. E. De Giglio, L. Sabbatini, S. Colucci and G. Zambonin, *J. Biomater. Sci. Polym.,* 2000, **11**, 1073.

20. N. Gomez and C. E. Schmidt, *J. Biomed. Mater. Res. A*, 2007, **81**, 135.

21. R. I. Christopherson, S. D. Lyons and P. K. Wilson, *Acc. Chem. Res.*, 2002, **35**, 961.

22. C. D. McTiernan and M. Chahma, *New J. Chem.,* 2010, **34**, 1417.

23. C. D. McTiernan, K. Omri and M. Chahma, *J. Org. Chem.,* 2010, **75**, 6096.

24. S. Kirchmeyer and K. Reuter, *J. Mater. Chem.,* 2005, **15**, 2077.

25. L. Groenendaal, F. Jonas, V. Freitag, H. Pielartzik and J. R. R. Reynolds, *Adv. Mater.,* 2000, **12**, 481.

26. K. C. Lin, T. H. Tsai and S. M. Chen, *Biosens. Bioelectron.,* 2010, **26**, 608.

27. J. Liu, M. Agarwal and K. Varahramyan, *Sens. Actuators B,* 2008, **135**, 195.

28. K. Krishnamoorthy, R. S. Gokhale, A. Q. Contractor and A. Kumar, *Chem. Commun.,* 2004, **7**, 820.

29. S. J. R. Prabakar and M. Pyo, *Corros. Sci.,* 2012, **57**, 42.

30. E. Armelin, A. Meneguzzi, C. A. Ferreira and C. Alemán, *Surf. Coat. Technol.,* 2009, **203**, 3763.

31. D. Aradilla, D. Azambuja, F. Estrany, J. I. Iribarren, C. A. Ferreira and C. Alemán, *Polym. Chem.,* 2011, **2**, 2548.

32. D. Aradilla, F. Estrany and C. Alemán, *J. Phys. Chem. C,* 2011, **115**, 8430.

33. J. Ouyang, C. W. Chu, F. C. Chen, Q. Xu and Y. Yang, *Adv. Funct. Mater.,* 2005, **15**, 203.

34. D. Aradilla, D. Azambuja, F. Estrany, M. T. Casas, C. A. Ferreira and C. Alemán, *J. Mat. Chem.,* 2012, **22**, 13110.

35. L. J. del Valle, F. Estrany, E. Armelin, R. Oliver and C. Alemán, *Macromol. Biosci.,* 2008, **8**, 1144.

36. L. J. del Valle, D. Aradilla, R. Oliver, F. Sepulcre, A. Gamez, E. Armelin and C. Alemán, F. Estrany, *Eur. Polym. J.,* 2007, **43**, 2342.

37. B. Teixeira-Dias, L. J. del Valle, F. Estrany, J. F. Mano, R. Reis and C. Alemán, *Macromol. Mater. Eng.,* 2012, **97**, 359.

38. F. Estrany, D. Aradilla, R. Oliver and C. Alemán, *Eur. Polym. J.,* 2007, **43**, 1876.

39. F. Estrany, D. Aradilla, R. Oliver, E. Armelin and C. Alemán, *Eur. Polym. J.,* 2008, **44**, 1323.

40. J. Carrasco, E. Brillas, V. Fernández, P. L. Cabot, J. A. Garrido, F. Centellas and R. M. Rodríguez, *J. Electrochem. Soc.,* 2001, **148**, E19.

41. T. Mosmann, *J. Immunol. Methods,* 1983, **65**, 55.

42. C. Ocampo, R. Oliver, E. Armelin, C. Alemán and F. Estrany, *J. Polym. Res.*, 2006, **13**, 193.

43. C. Li and T. Imae, *Macromolecules*, 2004, **37**, 2411.

44. C. Sivakumar and K. L. Phani, *Chem. Commun,* 2011, **47**, 3535.

45. S. Liu, H. Liu, K. Bandyopadhyay, Z. Gao and L. Echegoyen, *J. Org. Chem.*, 2000, **65**, 3292.

46. C. Kvarnstrom, H. Neugebauer, S. Blomquist, H.J. Ahonen, J. Kankare and A. Ivaska, *Electrochim. Acta*, 1999, **44**, 2739.

47. S. Garreau, G. Louarn, J. P. Buisson, G. Froyer and S. Lefrant, *Macromolecules,* 1999, **32**, 6807.

48. S. Ahmad, M. Deepa and S. Singh, *Langmuir,* 2007, **23**, 11430.

49. G.-F. Wang, X.-M. Tao, J. H. Xin and B. Fei, *Nanoscale Res. Lett.,* 2009, **4**, 613.

50. S. A. Spanninga, D. C. Martin and Z. Chen, *J. Phys. Chem. C,* 2010, **114**, 14992.

51. D. Bhattacharyya and K. K. Gleason, *Chem. Mater.,* 2011, **23**, 2600.

52. G. Iucci, M. Dettin, C. Battocchio, R. Gambaretto, C. Di Bello and G. Polzonetti, *Mater. Sci. Engin. C,* 2007, **27**, 1201.

53. Y. Zubavichus, M. Zharnikov, A. Shaporenko, O. Fuchs, L. Weinhardt, C. Heske, E. Umbach, J. D. Denlinger and M. Grunze, *J. Phys. Chem. A,* 2004, **108**, 4557.

54. N. Sakmeche, S. Aeiyach, J.-J. Aaron and M. Jouini, *Langmuir,* 1999, **15**, 2566.

55. R. Flamia, G. Lanza, A. M. Salvi, J. E. Castle and A. M. Tamburro, *Biomacromolecules,* 2005, **6**, 1299.

56. T. Strother, R. J. Hamers and L. M. Smith, *Nucleic Acids Res.,* 2000, **28**, 3535.

57. G. Greczynski, T. Kugler and W. R. Salaneck, *Thin Solid Films,* 1999, **354**, 129.

58. E. T. Kang, K. G. Neoh and K. L. Tan, *Phys. Rev. B: Condens. Matter,* 1991, **44**, 10461.

59. G. Zotti, S. Zecchin, G. Schiavon, F. Louwet, L. Groenendaal, X. Crispin, W. Osikowicz, W. Salaneck and M. Fahlman, *Macromolecules,* 2003, **36**, 3337.

60. D. Aradilla, F. Estrany, E. Armelin and C. Alemán, *Thin Solid Films,* 2012, **520**, 4402.

61. J. Preat, B. Teixeira-Dias, C. Michaux, E. A. Perpète and C. Alemán, *J. Phys. Chem. A,* 2011, **115**, 13642.

62. B. Teixeira-Dias, D. Zanuy, L. J. del Valle, F. Estrany, E. Armelin, C. Alemán, *Macromol. Chem. Phys.,* 2010, **211**, 1117.

5.2 Design of hybrid conjugates based on chemical similarity*/**

CP-amino acid hybrid materials have been prepared by conjugating PEDOT and an amino acid bearing a EDOT ring as side group. Two amino acids have been designed, synthetized and characterized. These compounds differ in the presence or not of a methylene group between the EDOT ring and the backbone (*i.e.* **I** and **II**, respectively). The electrochemical properties of PEDOT and their conjugates with **I** and **II** (PEDOT-I and PEDOT-II) have been determined by CV and EIS, and subsequently compared. Incorporation of end capping amino acids has been found to increase the hydrophilicity of PEDOT surface, which is consistent with the better behaviour of the conjugates as cellular matrix. The electronic properties of both the amino acids and the conjugates have been investigated by UV-vis spectroscopy. Results indicate that elimination of the methylene group of **I** provokes a reduction of 0.13 eV in the π-π^* lowest transition energy (E_g) of the conjugate. This decrease is explained by the larger structural flexibility due to the methylene group in **I**. Calculations of the electronic properties of the two hybrids at the molecular level using QM methods suggest that the end capping amino acid essentially affect the electronic intermolecular effects.

*Results described in this section previously appeared in *RSC Adv.*, 2013, **3**, 21069.

**QM calculations were performed by Dr. J. Casanovas , Dr. A. Laurent and Dr. D. Jacquemin.

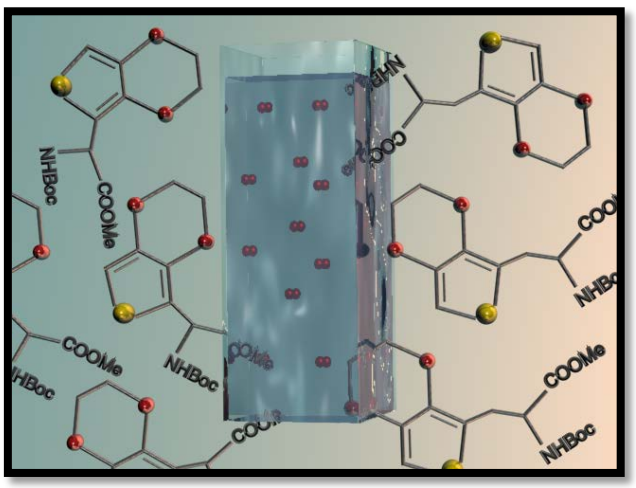

5.2.1 Introduction

Peptide-polymer conjugates combine the precise chemical structure of biomolecules and the stability and processability of synthetic polymers, prospectively exhibiting the potentials for diverse applications from nanotechnology to tissue engineering.[1-10] This arises from their ability to organize in hierarchical assemblies and well-defined nanostructures,[11-16] combined with a remarkable control of chemical functionalities and potentials to actively interact with biological systems.[17-19]

Within this field, conjugates based on peptides covalently bonded to CPs are receiving increasing attention due to the interest for the development of biomimetic materials with controlled electro-optical properties. Multiple techniques have been explored for the development of peptide-CP hybrid materials and they can be categorized in two main approaches. The first is based on the attachment of peptides to already formed CP chains using, for example, disulfide bonds[20,21] or photo-crosslinkers.[22] The second possibility is the chemical synthesis of monomers and oligomers functionalized with peptides, as for example Th or furane rings substituted by amino acids at the 3-position,[23-25] which are subsequently electropolymerized.

In a recent study[26] we reported an alternative strategy for the preparation of peptide-CP hybrid materials, which is based on the chemical similarity of the two components of the hybrid. More specifically, methyl 2-(*N*-*tert*-butoxycarbonyl)amino-3-(3,4-ethylenedioxy-2-thienyl) propanoate (**I** in Figure 1a), a synthetic amino acid bearing a EDOT side group, was designed and subsequently incorporated at the end of PEDOT chains by electrochemical methods to produce the hybrid PEDOT-I (Figure 1a). The advantage of peptide-CP conjugates based on chemical similarity is that this approximation avoids significant detriment in the electrical and electrochemical behavior of the bulk CP matrix. Thus, PEDOT-I was found to preserve the impressive electrical and electrochemical properties of PEDOT (*i.e.* the two materials show electrical conductivities of ~500 S/cm, high ability to store charge and excellent electrochemical stability).[26] In addition, cell adhesion and proliferation assays showed that the behavior of PEDOT-I as a cellular matrix is better than is PEDOT counterpart due to the presence of the amino acid.[26]

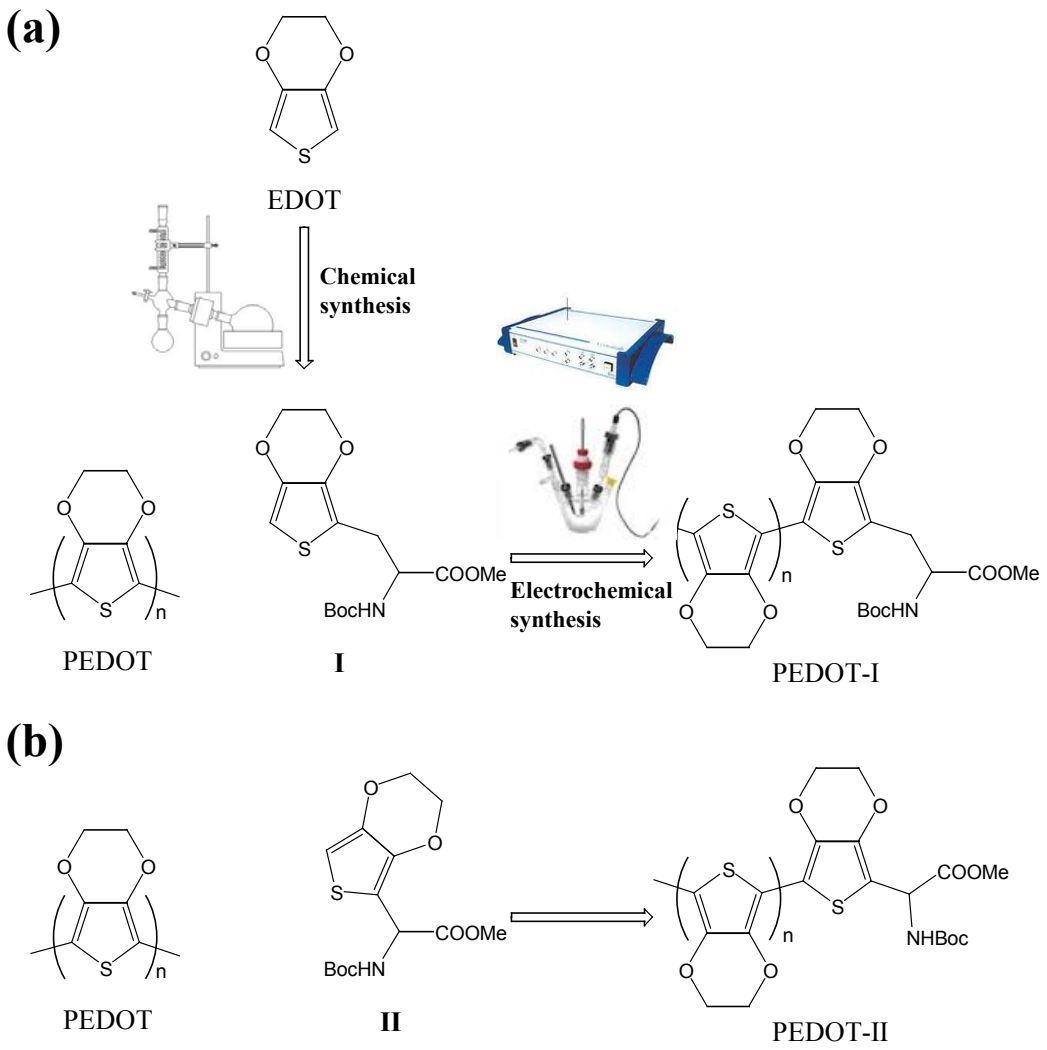

Figure 1. Schematic description of the process used for obtaining the conjugates designed by chemical similarity in this work: (a) PEDOT-I and (b) PEDOT-II.

This work tried to go a step further on the importance of hybrid's design based on chemical similarity. More specifically, this paper is focused on the influence of the linker that joins the two components of the conjugates on the electrochemical and electronic properties. For this purpose, a new blocked amino acid, methyl 2-(*N*-*tert*-butoxycarbonyl)amino-2-(3,4-ethylenedioxy-2-thienyl) acetate (**II** in Figure 1b), has been designed and synthesized. It should be noted that in **II** the EDOT side group is directly attached to the backbone, which implies the elimination of the methylene unit used as linker **I**. This blocked amino acid has been incorporated at the end of PEDOT chains to produce PEDOT-II (Figure 1b) using the procedure and conditions previously employed to prepare PEDOT-I.[26] After this, the electrochemical, morphological, hydrophilic and electronic properties of PEDOT-I and PEDOT-II have been investigated using CV, EIS, SEM, contact angle measurements and UV-vis spectrospy, results being

also compared with those achieved for PEDOT. Furthermore, the intrinsic conformational properties **I** and **II** have been investigated using QM calculations. For this purpose two different systems have been considered; (*i*) the *N*-acetyl-*N'*-methylamide blocked derivatives of the amino acids (Figure 2a), which allowed us to determine the intrinsic preferences of the amino acids when they are inserted in a peptide sequence; and (*ii*) **I** and **II** as they are displayed in Figure 1. It should be noted that the results obtained have been used not only to rationalize the experimental UV-vis spectra of these new compounds, but also to perform additional calculations on PEDOT-I and PEDOT-II and to explain the features related with the most relevant electronic transition of the hybrids, which corresponds to the E_g.

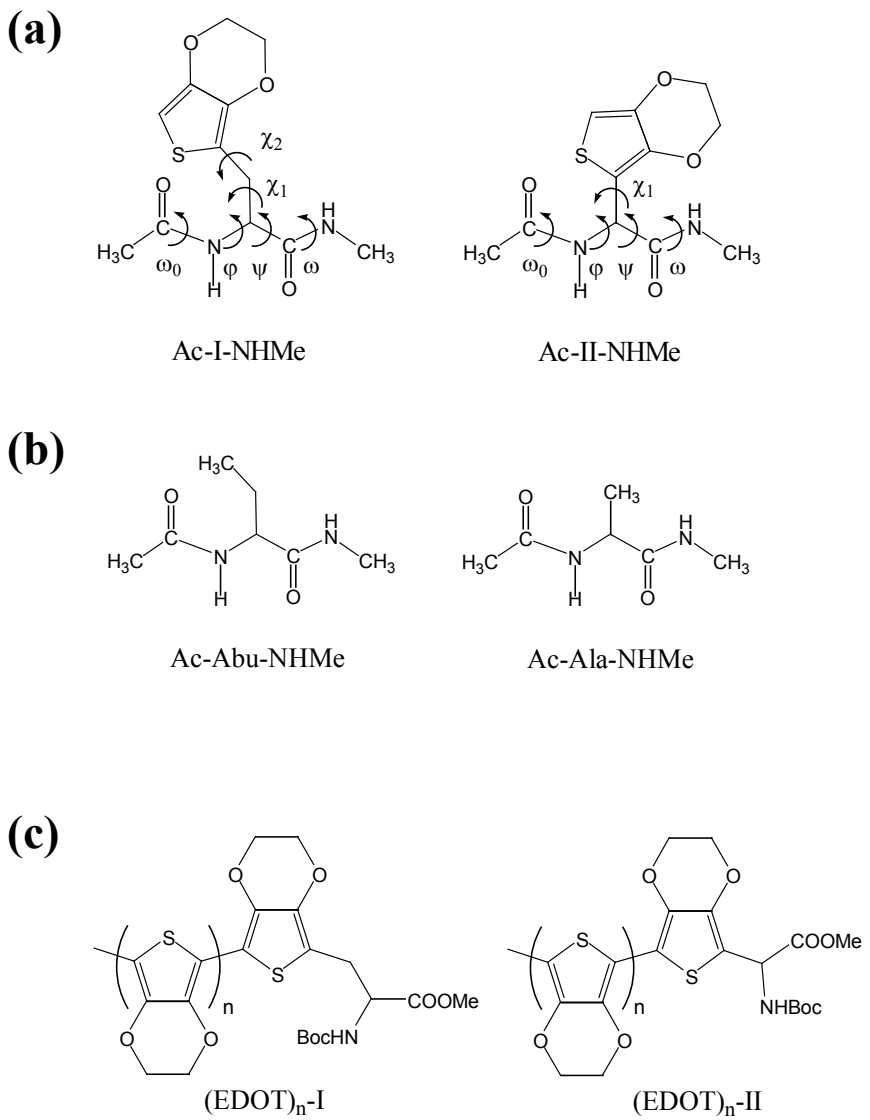

Figure 2. Chemical structure of: (a) Ac-**I**-NHMe and Ac-**II**-NHMe; (b) Ac-Abu-NHMe and Ac-Ala-NHMe; and (c) $(EDOT)_n$-I and $(EDOT)_n$-II.

5.2.2 Methods

Materials. EDOT were purchased from Aldrich and used as received. Anhydrous $LiClO_4$, analytical from Aldrich, analytical reagent grade, was stored in an oven at 80 ºC before use in the electrochemical trials. All organic reactants, with exception of EDOT, and solvents for the chemical synthesis of **II** were purchased from Panreac Quimica S.A.U. (Spain) and used as received.

***General data for the synthesis of* II.** Melting points were determined on a Gallenkamp apparatus and are uncorrected. IR spectra were registered on a Mattson Genesis FTIR spectrophotometer; υ_{max} is given for the main absorption bands. ^{1}H and ^{13}C NMR spectra were recorded on a Bruker AV400, ARX-300 or Varian Gemini 300 instrument at room temperature unless otherwise indicated, using the residual solvent signal as the internal standard. Chemical shifts are expressed in ppm and coupling constants in Hertz. High-resolution mass spectra were obtained on a Bruker Microtof-Q spectrometer.

Anodic polymerization and electrochemical assays. All electrochemical assays, including polymerizations, were carried out in a standard three electrode cell of 50 mL using steel AISI 316 sheets of 4 cm^2 area (surface roughness determined by AFM: 11.4 Å) as WE and CE. It should be noted that the electrochemical response obtained using AISI 316 sheets is very similar to that recorded using more sophisticated electrodes.[27] The RE was an Ag|AgCl electrode containing a KCl saturated aqueous solution (E^0 = 0.222 V at 25ºC).

PEDOT-I and PEDOT-II were prepared by anodic polymerization using a two-steps strategy, which was previously described.[26] This can be summarized a follows. In the first step, PEDOT was prepared by CA under a constant potential of 1.40 V using a 0.01 M EDOT solution in acetonitrile containing 0.1 M $LiClO_4$ as supporting electrolyte. The polymerization time was 10 s for all systems. The resulting PEDOT films were washed with acetonitrile to eliminate the excess of monomer and dopant. In the second step, the electrode coated with the PEDOT film was introduced in a cell filled with 50 mL of a 5 mM **I** (or **II**) solution in acetonitrile containing 0.1 M $LiClO_4$. Then, PEDOT films were transformed into PEDOT-I (or PEDOT-II) applying a constant

potential of 1.34 V during 20 s. It should be mentioned that the time used for such CA was optimized for PEDOT-I in our previous work[26] by comparing the properties of the hybrid materials obtained from processes that took 10, 20, 30 and 60 s. The success of this two-steps strategy to produce the desired hybrid materials was previously proved by XPS, EDX spectroscopy, and FTIR spectroscopy.[26]

Properties evaluated for PEDOT-I and PEDOT-II have been compared with those of doped PEDOT (hereafter denoted PEDOT*), which was obtained in the same conditions that the hybrids. Specifically, PEDOT films were produced using the identical procedure described above for the first stage. After this, the electrodes coated with PEDOT films were immersed in cell filled with 50 mL of an acetonitrile solution containing 0.1 M $LiClO_4$, and a potential of 1.34 V was applied during 20 s. It is worth to mention that, we demonstrated in our previous work,[26] this process ensures approximately the same doping level for PEDOT*, PEDOT-I and PEDOT-II films. Thus, the doping level essentially depends on the applied potential, the time used to apply the potential, and the concentration of dopant agent, these three parameters being exactly the same for PEDOT*, PEDOT-I and PEDOT-II (*i.e.* 1.34 V, 10 s + 20 s = 30 s and 0.1 M $LiClO_4$ in acetonitrile).

CA, CV and EIS assays were performed with an Autolab PGSTAT302N equipped with the ECD module (Ecochimie, The Netherlands), controlled by the GPES 4.9 software. Each trial was performed under nitrogen atmosphere at room temperature. All the electrochemical experiments were carried out in a 0.1 M PBS (pH= 7.4 adjusted with NaOH). The surface of the WE was exposed to such PBS solution during 5 minutes before each assay.

The initial and final potentials for CV experiments were -0.50 V; and the reversal potential was 0.80 V. A scan rate of 25 $mV{\cdot}s^{-1}$ was used in all cases. The electrochemical stability has been expressed as LEA (in %) using the following Eqn:

$$LEA = \frac{\Delta Q}{Q_{ii}} 100 \qquad (1)$$

where ΔQ is the difference of voltammetric charges (in C) between the second and the last cycle, and Q_{II} is the voltammetric charge corresponding to the second cycle.

On the other hand, EIS measurements were performed using the FRA2 module controlled by FRA 4.9 software. Experiments were done at open circuit potential (OCP). A frequency range of 100 KHz – 10mHz was used. The amplitude of the AC perturbation was set to 10mV.

Thickness and porosity The thickness of the films was determined by profilometry measurements, which were conducted using a profilometer Dektack 6 from Veeco.

The porosity was indirectly quantified through the parameter P[28]:

$$P = \frac{\ell_o - \ell_{50}}{\ell_o} 100 \qquad (2)$$

where ℓ_0 and ℓ_{50} refer to the thickness before applying any oxidation–reduction cycle and after 50 consecutive oxidation–reduction cycles. This procedure is based on the fact that the degree of com-pactness induced by consecutive redox cycles depends on the porosity of the fresh sample, both the degree of com-pactness and porosity of the films being related with their thickness.

SEM. SEM studies were performed to investigate the surface morphology of PEDOT-II. Dried samples were placed in a Focussed Ion Beam Zeiss Neon 40 scanning electron microscope operating at 5 kV, equipped with an EDX spectroscopy system. Samples were mounted on a double-side adhesive carbon disc and sputter-coated with a thin layer of carbon to prevent sample charging problems.

Contact angle. Contact angle measurements for steel, PEDOT*, PEDOT-I and PEDOT-II were obtained using the water drop method. Images of 0.5 µL distillated water drops were recorded after stabilization with the equipment OCA 20 (DataPhysics Instruments GmbH, Filderstadt). The software SCA20 was used to analyze the images and determine the contact angle value, which was obtained as the average of ten independent measures for each sample.

UV-vis. UV-vis absorption spectra of EDOT, **I**, **II**, PEDOT*, PEDOT-I and PEDOT-II were obtained using a UV-vis-NIR Shimadzu 3600 spectrophotometer equipped with a tungsten halogen visible source, a deuterium arc UV source, a photomultiplier tube

UV-vis detector, and a InGaAs photodiode and cooled PbS photocell NIR detectors. Spectra were recorded in the absorbance mode using the integrating sphere accessory (model ISR-3100), the range wavelength being 200-900 nm. The interior of the integrating sphere was coated with highly diffuse $BaSO_4$ reflectance standard. Single-scan spectra were recorded at a scan speed of 60 nm/min. Measurements, data collection and data evaluation were controlled by the computer software UVProbe version 2.31.

The deconvolution of the UV-Vis spectra was performed using the PeakFit V4.0 software and applying a Gaussian deconvolution method with a width of 2 nm in Full-Width Half-Maximum (FWHM) mode and with scan amplitude of 1.5%.

The band gap energy was determined for PEDOT[*], PEDOT-I and PEDOT-II using the following expression:

$$E_g(eV) = \frac{h \cdot c}{1.6 \cdot 10^{-19} \cdot \lambda_{onset}} \qquad (3)$$

where h is the Plank's constant, *c* is the speed of light and λ_{onset} is the cut off wavelength for the absorption spectra.

QM calculations. The conformational preferences of (i) the *N*-acetyl-*N*'-methylamide derivatives of the amino acids, hereafter denoted Ac-**I**-NHMe and Ac-**II**-NHMe (Figure 2a) and of (ii) **I** and **II** (Figure 1) have been determined using the ωB97X-D[29] exchange-correlation functional combined with the 6-311++G(d,p)[30,31] atomic basis set. ωB97X-D is a range-separated hybrid functional with empirical atom pair-wise dispersion corrections that was satisfactorily used to determine the conformational preferences of small dipeptides.[32] The major difference between both systems (Ac-**I**-NHMe vs **I** and Ac-**II**-NHMe vs **II**) is the nature of the blocking terminal group (*i.e.* Ac and NHMe blocking groups are replaced by COOMe and NH-tert-Butyloxycarbonyl (NHBoc), respectively).

The conformational search was performed considering a built-up procedure (see below) using the minimum energy conformations reported for the *N*-acetyl-*N*'-methylamide derivatives of alanine[33,34] and α-aminoisobutyric acid[35] (Ac-Ala-NHMe and Ac-Abu-NHMe, respectively; Figure 2b). Frequency analyses were carried out to

verify the nature of the minimum energy state of all the stationary points obtained as well as to calculate the zero-point vibrational energy (ZPVE) and both thermal and entropic corrections using the harmonic rigid-rotor approximation. These statistical terms were then used to compute the relative Gibbs free energies at 298 K (ΔG). The *trans* state was considered for both ω_0 and ω in all cases since for non-proline α-amino acids it is considered as the most energetically favored isomer. All calculations were performed considering L-amino acids. Optical spectra have been computed for each minimum of **I** and **II** with the Time-dependent density functional theory (TD-DFT),[36] which is the most widely used model for studying UV/Vis spectra of organic and biological molecules. This method is well-known to describe low-lying states with robustness and accuracy.[37-39] The CAM-B3LYP/6-311++G(d,p) level of theory[40] has been employed to compute these electronic properties in acetonitrile, solvent effects being modeled by the Polarizable Continuum Model(PCM)[41]. For the lowest-lying excited states of **I** and **II**, a complex orbital mix is provided by TD-DFT, making a MO-based analysis cumbersome. We choose to bypass this difficulty through the calculation of electronic density differences between states.[42,43]

The three most stable conformations obtained from calculations on **I** and **II** were used to build up the molecular models for the hybrids, hereafter denoted $(EDOT)_n$-I and $(EDOT)_n$-II, respectively (where *n* refers to the number of EDOT units in the model oligomer linked to the amino acid, as is indicated in Figure 2c). EDOT rings were added to the models by considering an all-anti (*i.e.* all-trans) arrangement with inter-ring dihedral angles set at 180.0°, which was found to be its preferred conformation.[44-46] Molecular geometries of $(EDOT)_n$-I and $(EDOT)_n$-II with *n* ranging from 2 to 14 were fully optimized using the ωB97X-D/6-311++G(d,p) method. The ionization potential (IP) of each calculated model was estimated using the Koopmans' theorem,[47] according to which the IPs were taken as the negative of the highest occupied molecular orbital (HOMO) energy (*i.e.* $IP= -\varepsilon_{HOMO}$). Although Koopman's theorem does not apply to DFT, Janak's theorem[48] was used by Perdew[49] to show the connection between the IP and ε_{HOMO}. The E_g was estimated using two different strategies. In the first, E_g was approximated as the difference between the energies of the frontier orbitals: $E_g= \varepsilon_{LUMO} - \varepsilon_{HOMO}$, where ε_{LUMO} refers to the energy of the lowest

unoccupied molecular orbital. In an early work, Levy and Nagy showed that, in DFT calculations, E_g can be correctly estimated using this procedure.[50] The second estimation of E_g for $(EDOT)_n$-I and $(EDOT)_n$-II was also derived from the excitation energies provided by TD-DFT calculations. Electronic excitations were evaluated with the ωB97X-D functional combined with the 6-311++G(d,p) basis set. In addition, the IP and E_g values were estimated in acetonitrile solution. Solvent effects were included by means of the PCM, single point calculations being carried out using geometries optimized in the gas-phase.

All the quantum mechanical calculations were performed with the Gaussian 09 computer program.[51]

5.2.1 Results and discussion

Synthesis of methyl 2-(N-tert-butoxycarbonyl)amino-2-(3,4-ethylenedioxy-2-thienyl) acetate (II).

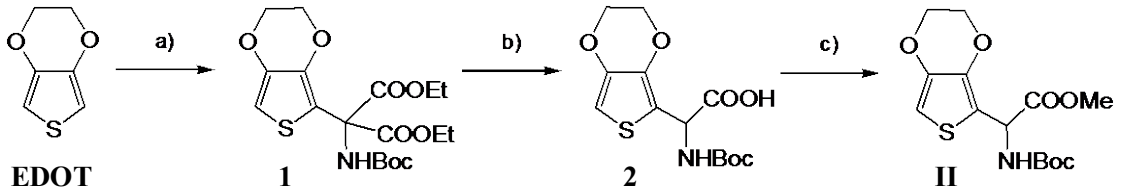

Figure 3. Reagents and conditions used to obtain **II**: (a) *n*-BuLi 1.6M, THF, -78ºC 10 min, diethyl-(*N-tert*-butoxycarbonyl)-iminomalonate, THF, -78ºC 1h, 58%; (b) i): KOH 2N/MeOH, rt 2h, ii): Δ50ºC 30 min, 99%; (c) $TMSCH_2N_2$, Toluene/MeOH, rt 30 min, 97%.

Figure 3 summarizes the synthetic route used to obtain II, detailed description of each for each step being given below.

Diethyl 2-(N-tert-butoxycarbonyl)amino-2-(3,4-ethylenedioxy-2-thienyl) malonate (1). A hexane solution of n-BuLi 1.6 M (6.46 mL, 10.34 mmol) was added dropwise to a solution EDOT (1.13 g, 7.95 mmol) in anhydrous tetrahydrofuran (30 mL) at –78 ºC. The mixture was stirred for 15 minutes at this temperature. Then, a solution of diethyl-(N-tert-butoxycarbonyl)-iminomalonate[52] (2.17 g, 7.95 mmol) in anhydrous tetrahydrofuran (10 mL) was added. Stirring was continued for 1 hour at –78 ºC before quenching cold with water (30 mL). The reaction mixture was extracted with diethyl ether (3 × 30 mL). The combined organic layers were washed with brine (30 mL), dried over magnesium sulphate, filtered and concentrated to dryness. The remaining residue

was chromatographed (eluent: hexane/ethyl acetate 7/3) to provide 1 as a colourless oil which solidifies on standing (1.91 g, 4.61 mmol, 58% yield). Mp 67–68 ºC. IR (neat) ν: 3415, 1747, 1711 cm^{-1}. ^{1}H NMR ($CDCl_3$, 400 MHz, 60 °C): δ 1.25 (t, 6H, J = 7,1 Hz), 1.39 (s, 9H), 4.12 (bs, 4H), 4.19–4.34 (m, 4H), 6.26 (bs, 1H), 6.31 (s, 1H). ^{13}C NMR ($CDCl_3$, 100 MHz, 60 °C): δ 14.0, 28.3, 62.8, 64.5, 64.9, 65.2, 80.6, 100.7, 112.6, 139.6, 140.6, 153.8, 165.5. HRMS (ESI) $C_{18}H_{25}NO_8NaS$ $[M+Na]^+$: calcd. 438.1193, found 438.1192.

2-(N-tert-butoxycarbonyl)amino-3-(3,4-ethylenedioxy-2-thienyl) acetic acid (2). A 2N solution of KOH in ethanol (15 mL) was added to 1 (1.60 g, 3.86 mmol) and the reaction mixture was stirred at room temperature for 2 hours. After evaporation of the solvent, the remaining residue was redissolved in water (15 mL), neutralized with HCl 2N and extracted with ethyl acetate (3 × 15 mL). The combined organic layers were dried over magnesium sulphate and filtered. The resulting solution was stirred at 50ºC for 30 minutes. After that, the solvent was evaporated to dryness to afford pure 2 (1.20 g, 3.82 mmol, 99% yield). IR (neat) ν: 3500–2500, 1722, 1711 cm^{-1}. ^{1}H NMR ($CDCl_3$, 400 MHz, 60 °C): δ 1.45 (s, 9H), 4.15–4.19 (m, 2H), 4.21–4.26 (m, 2H), 5.49 (m, 1H), 5.54 (m, 1H), 6.29 (s, 1H). ^{13}C NMR ($CDCl_3$, 100 MHz, 60 °C): δ 28.5, 51.0, 64.8, 65.1, 81.0, 99.3, 111.2, 140.0, 141.7, 155.2, 172.8. HRMS (ESI) $C_{13}H_{17}NO_6NaS$ $[M+Na]^+$: calcd. 338.0669, found 338.0658.

Methyl 2-(N-tert-butoxycarbonyl)amino-2-(3,4-ethylenedioxy-2-thienyl) acetate (II). To a solution of 2 (1.05 g, 3.34 mmol) in toluene/methanol 3:1 v/v (15 mL) cooled to 0ºC was added slowly trimethylsilyldiazomethane (2.5 mL, 5.01 mmol). Strong evolution of nitrogen occurred during the addition of trimethylsilyldiazomethane. The reaction mixture was stirred at this temperature for 10 minutes. Excess of trimethylsilyldiazomethane was destroyed by the addition of a small quantity of silica gel. Evaporation of the solvent followed by chromatographic purification (eluent: hexane/ethyl acetate 7/3) afforded 3 as an oil (1.07 g, 3.24 mmol). IR (neat) ν: 3374, 1749, 1716 cm^{-1}. ^{1}H NMR ($CDCl_3$, 300 MHz, 60 °C): δ 1.46 (s, 9H), 3.75 (s, 3H), 4.13–4.24 (m, 4H), 5.35–5.50 (m, 2H), 6.26 (s, 1H). ^{13}C NMR ($CDCl_3$, 75 MHz, 60 °C): δ 28.5, 51.1, 52.8, 64.8, 65.1, 80.5, 99.0, 112.0, 139.9, 141.7, 154.9, 170.7. HRMS (ESI) $C_{14}H_{19}NO_6NaS$ $[M+Na]^+$: calcd. 352.0825, found 352.0822.

Electrochemical behavior of conjugates

PEDOT-I, PEDOT-II and PEDOT* (i.e. doped PEDOT) films were prepared using the procedure described in the Methods section. The thickness of the films was determined by profilometry, being very similar in all cases. This should be attributed to that fact that the conjugates and PEDOT* only differ in the small capping group at the end of polymer chains. Specifically, the values of the thickness ranged from ~240 to ~310 nm for the three systems, no differential trend being detected among them.

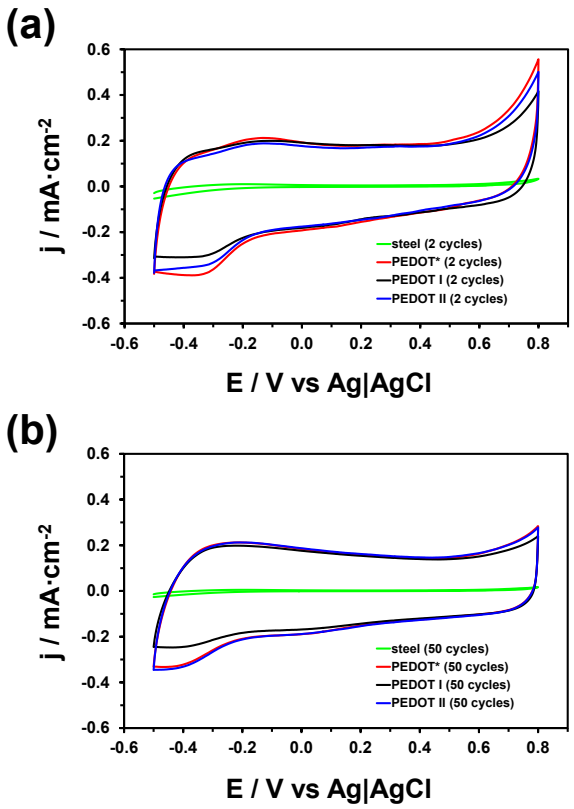

Figure 4. (a) Control voltammograms for PEDOT*, PEDOT-I and PEDOT-II after (a) 2 and (b) 50 consecutive oxidation-reduction cycles. Voltammograms were recorded in a 0.1 M PBS solution at 25 mV/s and 25ºC. Initial and final potentials: –0.50 V; reversal potential: +0.80 V. The reduction peak at -0.4 V has been attributed to the reduction of oxygen.

The electroactivity, which refers to the charge storage ability, and electrochemical stability were determined by CV using a 0.1 M PBS solution. The electroactivity increases with the similarity between the anodic and cathodic areas of the control voltammogram. Figure 4a compares the control voltammograms recorded after two consecutive oxidation-reduction processes in the potential range of -0.50 to 0.80 V. As it can be seen, the electroactivity is very high for the three systems. However, Figure 4a enables the detection of the effect of methylene group in the side

chain of the end-capping amino acid. Thus, the electroactivity of PEDOT-II is slightly higher and closer to that of PEDOT* than that of PEDOT-I, indicating that the elimination of the methylene group from the amino acid side group favors the flux of charge towards/from the surface during the oxidation/reduction processes. This phenomenon becomes more pronounced when the oxidation-reduction cycles increases, as is reflected in Figure 4b, which compares the voltammograms for three materials after 50 consecutive oxidation-reduction cycles. Thus, the PEDOT-II voltammogram practically matches that of PEDOT* while the electroactivity of PEDOT-I undergoes a small but non negligible reduction.

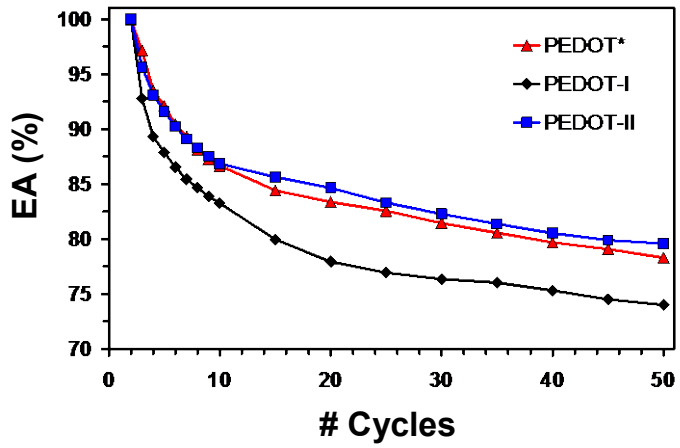

Figure 5. Variation of *EA* (in %) against the number of consecutive oxidation-reduction cycles for PEDOT*, PEDOT-I and PEDOT-II in a 0.1 M PBS solution.

The electrochemical stability of a CP during oxidation-reduction cycles is one of the essential parameters for practical use in applications related with energy storage and electrochromic properties. The electrochemical stability is typically determined by examining the LEA with the number of consecutive oxidation-reduction cycles (i.e. reduction of the similarity between the oxidation and reduction areas in the recorded voltammograms). Figure 5 represents the variation of the LEA against with the number of cycles for PEDOT*, PEDOT-I and PEDOT-II. It is worth noting that the electrochemical stability of the three systems in 0.1 M PBS is lower than that reported for PEDOT in other solvents. Thus, the electroactivity of PEDOT*, PEDOT-I and PEDOT-II decreases 22-25% after 50 redox cycles in PBS using potential interval ranging from -0.5 V (initial and final potential) to 0.8 V (reversal potential). In contrast, the electroactivity of PEDOT in water with 0.1 M $LiClO_4$ was reported to decrease by only 15% after 100 redox cycles using a potential window very similar to the one used in this work (i.e.

from -0.5 to 1.0 V).[54] In spite of this, the electrostability of PEDOT-II was found to be similar to that of PEDOT and larger than that of PEDOT-I, differences becoming more apparent after 15 cycles. Specifically, the LEA of PEDOT*, PEDOT-I and PEDOT-II is 87%, 83% and 87%, respectively, after 10 cycles, decreasing to 78%, 74% and 80%, respectively, after 50 cycles.

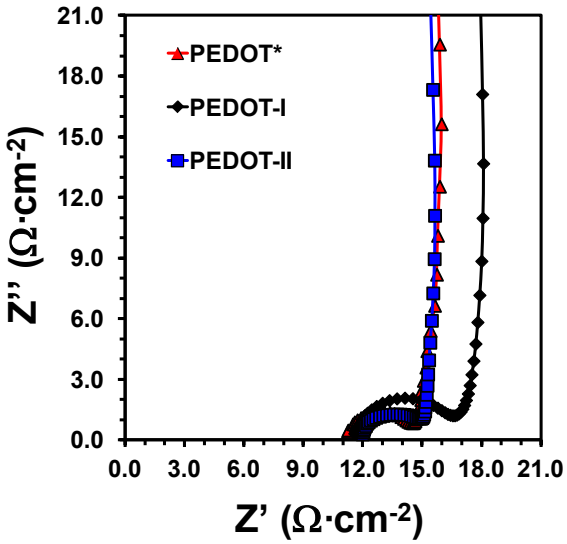

Figure 6. EIS spectra (Nyquist impedance plots) over a frequency of 100 kHz to 10 mHz of PEDOT*, PEDOT-I and PEDOT-II in a 0.1 M PBS solution.

EIS was further employed to compare the electrochemical behavior of PEDOT*, PEDOT-I and PEDOT-II. Typical Nyquist diagrams are displayed in Figure 6. The impedance curves of the three systems show two well-characterized regions. A capacitive semicircle related with the polymer (or hybrid)/electrolyte interface is observed at high frequencies, whereas a nearly vertical line is found in the low frequency region. The latter is due to the faradaic pseudocapacitance of the films.[53,54] According to the shape of these spectra, at higher frequencies the process is charge-transfer controlled while at lower frequencies the diffusion of charges in the hybrid or doped PEDOT films determines the impedance response. Although the spectra of the three systems fit to the equivalent circuit previously reported for PEDOT (not shown),[55] a simple qualitative analysis is presented in this work to show the differences between hybrid and doped PEDOT films in terms of resistance and capacitance only.

The intercept of the semicircle with the real axis (Z') at high frequencies is the measure of the ohmic resistance (R_S) between the working and the reference electrodes. The R_S is 11.0, 11.6 and 10.2 $\Omega \cdot cm^{-2}$ for PEDOT*, PEDOT-I and PEDOT-II

films, respectively. The pore resistance (R_P), which is given by the diameter of the semicircle along the real axis Z', is associated to the film resistance in parallel with the film capacitance (C_F). The R_P determined for PEDOT*, PEDOT-I and PEDOT-II is 3.9, 5.8 and 4.0 $\Omega \cdot cm^{-2}$. These low resistances should be also related with the high porosity of the films, which favors the kinetics of the electron transfer through redox processes. Thus, thin films of PEDOT typically present a sponge-like morphology with abundant pores.[56] The incorporation of I and II at the end of PEDOT chains does not alter such porous structure and, therefore, does not affect the access and escape of dopant anions into the polymeric matrix. Accordingly, the porosity, which has been determined using the procedure indicated in Eqn 2, is very high for the three systems: P = 40%, 41% and 37% for PEDOT*, PEDOT-I and PEDOT-II, respectively.

The film capacitance is expressed as constant phase element (CPE) that describes a non-ideal capacitor when the phase angle is different from -90º. The CPE impedance was expressed as:

$$Z_{CPE} = [Q\ (j \cdot \omega)^n]^{-1} \qquad (4)$$

The CPE represents a capacitor and a resistor for n= 1 and n= 0, respectively, while it is associated with a diffusion process when n= 0.5. The CPE impedance is attributed to the distributed surface reactivity, surface heterogeneity and roughness of the current and potential distribution, which are, in turn related with the electrode geometry and the electrode porosity.[57] The CPE for PEDOT*, PEDOT-I and PEDOT-II is 179, 138 and 911 $\mu F \cdot cm^{-2} \cdot s^{n-1}$, respectively, while n is 0.78 in all cases.

The CPE impedance is higher for PEDOT-II than for PEDOT* and PEDOT-I, indicating that the effective surface area for interfacial charge transport is highest for the former two than for the latter. Moreover, it should be remarked that for all three systems the imaginary part of the impedance Z'' at low frequencies is almost perpendicular to the real part Z'. This feature proves that, as expected, the amino acids do not affect the good capacitive behavior of PEDOT.

Morphology and wettability

The SEM micrograph displayed in Figure 7a indicates that, as foreseen, the morphology of PEDOT-II is practically identical those reported for PEDOT* and PEDOT-I.[26] Thus, the incorporation of I or II at the surface does not introduce changes in the spongy-like morphology of PEDOT. Moreover, Figure 7a shows a structure with abundant narrow and tortuous pores, which is fully consistent with the excellent electrochemical properties discussed in the above section.

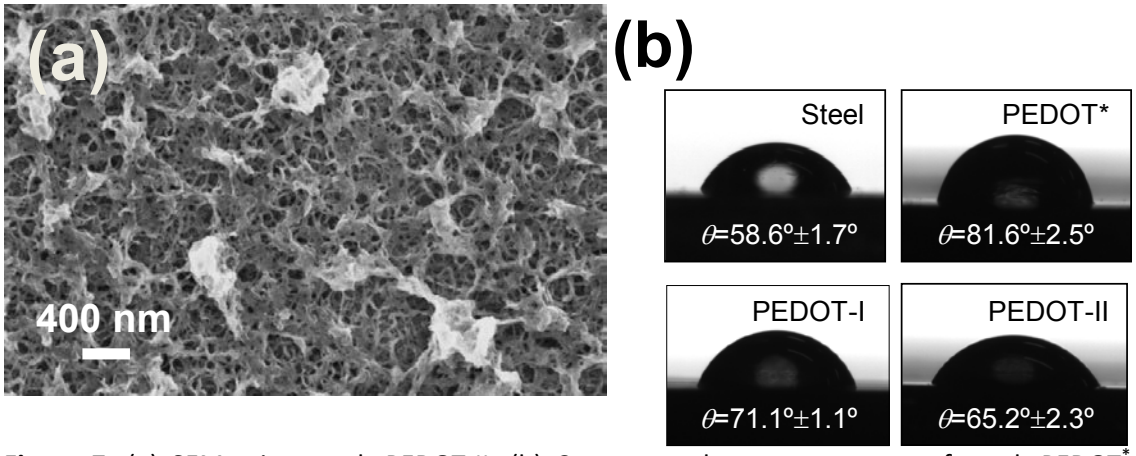

Figure 7. (a) SEM micrograph PEDOT-II. (b) Contact angle measurements of steel, PEDOT*, PEDOT-I and PEDOT-II.

In contrast, Figure 7b evidences that the wettability of the films is drastically altered by the incorporation of both I and II, at the end of the PEDOT chains. The hydrophobicity of PEDOT* surface is significantly higher than that of steel, the difference in the contact angles being of $\Delta\theta$=23º. However, incorporation of I and, especially, II increases the hydrophilicity, producing a reduction in the contact angle of 10º and 16º, respectively. This enhancement of the hydrophilicity at the surface of the hybrid conjugates represents an important benefit for their application as substrates for cellular growth. Indeed, contact angles displayed in Figure 7b explains our previous observations based on cell adhesion and proliferation assays, which evidenced that the behavior of PEDOT-I as cellular matrix is better than that of PEDOT*.[26]

Conformational preferences of Ac-I-NHMe and Ac-II-NHMe dipeptides

In order to ascertain the intrinsic conformational preferences of the two EDOT-containing amino acids, a systematic study has been performed considering the corresponding N-acetyl-N'-methylamide blocked derivatives (i.e. Ac-I-NHMe and Ac-II-

NHMe in Figure 2a). To explore conformational preferences of Ac-II-NHMe, 72 starting geometries were constructed by combining the backbone dihedral angles (φ,ψ) of the six minima reported for Ac-Ala-NHMe[33,34] with 12 different values for the dihedral angle χ_1, which was varied between 0 and 360º in steps of 30º. Geometry optimizations of such initial structures led to 13 different minimum energy conformations, the geometrical parameters and energetic properties being listed in Table 1. Inspection of the ΔG values indicates that the 13 minima are within a gap of 8.6 kcal/mol. Table 2 shows the six minima reported for the Ac-Ala-NHMe dipeptide after geometry re-optimization at the ωB97X-D/6-311++G(d,p) level. Comparison with the results displayed in Tables 1 and 2 evidences the remarkable influence of the EDOT ring in the backbone preferences.

The lowest energy minimum of Ac-Ala-NHMe corresponds to the C_{7eq} conformation (equatorial seven membered hydrogen bonded ring to the backbone). This structure is 0.4 and 0.2 kcal/mol more stable than the C_5 (five membered hydrogen bonded ring) and β_2 conformations, respectively, whereas the ΔG of rest of backbone conformations (i.e. C_{7ax}, α_L and α') ranges from 2.0 to 5.6 kcal/mol (Table 2). In contrast, inspection of Table 1 reveals that the only two minima of Ac-II-NHMe with $\Delta G < 1.5$ kcal/mol show a C_5 backbone conformation (C_5-1 and C_5-2 in Table 1). These structures, which are displayed in Figure 8a, only differ in the orientation of the EDOT ring. Thus, the two minima shows the intramolecular N–H···O hydrogen bond typically involved in the extended secondary structure.[58,59] In addition, the geometric parameters associated to this backbone···backbone interaction are very similar for the two conformations: the H···O distance ($d_{H\text{-}O}$) and the $\angle$N–H···O angle are 2.143 Å/2.156 Å and 108.1º/107.0º for C_5-1/C_5-2, respectively. However, C_5-1 shows a stabilizing N–H···O hydrogen bond between the NHMe blocking group and the dioxane ring ($d_{H\text{-}O}$= 2.129 Å and $\angle$N–H···O= 149.4º), whereas C_5-2 does not present any backbone···side group intramolecular interaction. As a consequence of such difference, C_5-2 results unfavored by 1.3 kcal/mol with respect to C_5-1.

#	φ (º)	ψ (º)	χ_1 (º)	ΔE (kcal/mol)	ΔG (kcal/mol)
C_5-1	-151.3	170.3	23.2	0.0	0.0
C_5-2	-152.7	-173.0	-109.7	2.1	1.3
C_{7eq}-1	-85.2	75.0	-141.2	1.7	2.8
C_{7eq}-2	-85.7	78.2	92.4	2.2	3.3
C_{7eq}-3	-86.1	81.6	3.5	4.5	4.2
β_2-1	-118.4	16.9	-127.2	4.2	3.8
β_2-2	-82.1	-18.1	69.2	5.0	5.0
β_2-3	-114.8	14.8	123.6	5.7	5.8
C_{7ax}-1	77.5	-59.3	120.1	4.9	6.1
C_{7ax}-2	77.7	-43.6	-58.2	5.7	6.4
α'	-149.9	-61.6	-128.3	6.0	6.5
α_L-1	67.5	32.2	126.1	7.5	7.9
α_L-2	63.3	31.6	70.3	8.0	8.6

Table 1. Dihedral angles, relative energy and free energy of the minimum energy conformations obtained for Ac-II-NHMe (Figure 2a) at the ωB97X-D/6-311++G(d,p) level. The dihedral angles associated to the amide moieties (ω_0 and ω) remained close to 180º in all cases (not shown).

#	φ (º)	ψ (º)	ΔE (kcal/mol)	ΔG (kcal/mol)
C_{7eq}	-83.3	74.1	0.0	0.0
C_5	-158.0	165.7	1.2	0.4
C_{7ax}	73.9	-57.3	2.1	2.0
β_2	-110.6	19.9	3.0	0.2
α_L	68.3	24.0	4.9	4.2
α'	-166.0	-44.9	6.4	5.6

Table 2. Dihedral angles, relative energy and free energy of the minimum energy conformations obtained for Ac-Ala-NHMe (Figure 2b) at the ωB97X-D/6-311++G(d,p) level. The dihedral angles associated to the amide moieties (ω_0 and ω) remained close to 180º in all cases (not shown).

Inspection of the rest of minima displayed in Table 1 reveals the existence of the stabilizing backbone···side group hydrogen bond between the NHMe blocking group and the dioxane ring in C_{7eq}-1 ($d_{H\text{-}O}$= 2.174 Å and ∠N–H···O= 127.7º), β_2-1 ($d_{H\text{-}O}$= 2.346 Å and ∠N–H···O= 122.5º), C_{7ax}-1 ($d_{H\text{-}O}$= 2.174 Å and ∠N–H···O= 127.7º), α' ($d_{H\text{-}O}$= 2.040 Å and ∠N–H···O= 153.9º) and α_L-1 ($d_{H\text{-}O}$= 2.457 Å and ∠N–H···O= 108.5º), which are respectively destabilized by 2.8, 3.8, 6.5 and 7.9 kcal/mol compared to the lowest energy minimum. These large ΔG values indicate that the EDOT ring of Ac-II-NHMe restricts significantly the conformational flexibility of the backbone with respect to Ala, which may represent a significant advantage from an electronic point of view.

In a very recent study we reported the B3LYP/6-31+G(d,p) energy landscape of Ac-Abu-NHMe (Figure 2b).[35] We characterized 15 minimum energy structures, seven of them showing $\Delta G \leq$ 1.5 kcal/mol. More specifically, these representative minima, which are the only populated at 298 K, involved the following backbone conformations: C_5 (3 minima), C_{7eq} (3 minima) and δ_L (1 minimum). Starting geometries for Ac-I-NHMe (Figure 2a) were generated by combining the dihedral angles φ, ψ and χ_1 of the 7 representative minima of Ac-Abu-NHMe with 12 different values for the dihedral angle χ_2, which was varied between 0 and 360^o in steps of 30^o. 84 starting geometries have been optimized to eventually provide 18 different minima for Ac-I-NHMe, Table 3 showing the dihedral angles, ΔE and ΔG values. On the other hand, the 15 minima found at the B3LYP/6-31+G(d,p) level for Ac-Abu-NHMe were also re-optimized using the ωB97X-D/6-311++G(d,p) method (see Table 4).

Geometry re-optimization at the ωB97X-D/6-311++G(d,p) level of the B3LYP/6-31G(d) minima obtained for Ac-Abu-NHMe led practically to the same results (Table 4). Thus, 5 of the 7 conformations considered for the conformational search of Ac-I-NHMe kept $\Delta G \leq 1.5$ kcal/mol, whereas, for the other two the ΔG increases by ca. 1 kcal/mol. Furthermore, the dihedral angles provided by the ωB97X-D and B3LYP methods are very similar. The lowest energy minimum corresponds to a C_{7eq} backbone conformation, the C_5 and δ_L being destabilized by at least 0.2 and 1.1 kcal/mol, respectively. Substitution of the methyl side group by the EDOT ring results in small conformational changes. Thus, inspection of the minima displayed in Table 3 for Ac-I-NHMe indicates that the C_{7eq} is the most stable backbone conformation while the C_5 and δ_L conformations are higher in energy by 0.2 and 1.5 kcal/mol, respectively. Figure 8b depicts the most stable minimum for each backbone conformation of Ac-I-NHMe (i.e. C_{7eq}-1, C_5-1 and δ_L-1).

#	φ (º)	ψ (º)	χ_1 (º)	χ_2 (º)	ΔE (kcal/mol)	ΔG (kcal/mol)
C_{7eq}-1	-86.7	71.3	-58.5	-95.0	0.0	0.0
C_{7eq}-2	-86.6	71.6	-54.8	113.1	1.3	0.0
C_{7eq}-3	-83.2	59.0	44.5	76.6	1.2	1.0
C_{7eq}-4	-83.1	84.5	-168.7	-108.9	2.9	1.9
C_{7eq}-5	-80.5	46.1	56.8	96.2	1.4	2.1
C_{7eq}-6	-83.6	85.3	-174.6	57.7	4.0	3.0
C_{7eq}-7	-79.6	36.4	38.7	-132.5	4.5	3.5
C_{7eq}-8	-85.4	73.0	56.9	-76.0	3.6	3.6
C_5-1	-161.1	157.9	-176.4	78.7	0.6	0.2
C_5-2	-159.9	-172.7	73.5	-72.8	1.0	1.1
C_5-3	-137.1	151.5	-57.4	108.9	2.3	1.1
C_5-4	-157.3	149.2	177.1	-135.6	2.5	1.1
C_5-5	-159.0	158.9	-177.8	-110.5	1.5	1.2
C_5-6	-165.5	160.4	55.1	-97.2	0.9	1.3
C_5-7	166.7	171.6	62.9	91.7	2.1	1.7
C_5-8	-143.0	152.5	-81.6	-96.4	4.0	3.4
δ_L-1	-113.7	10.3	-54.4	-90.9	2.3	1.5
δ_L-2	-132.6	18.2	-51.0	109.3	2.1	2.0

Table 3. Dihedral angles, relative energy and free energy of the minimum energy comformations obtained for Ac-I-NHMe (Figure 2a) at the ωB97X-D/6-311++G(d,p) level. The dihedral angles associated to the amide moieties (ω_0 and ω) remained close to 180º in all cases (not shown).

The lowest energy minimum, C_{7eq}-1, is stabilized not only by the backbone···backbone hydrogen bond but also by a backbone···side group N–H···O interaction involving the N–H moiety of the amino acid and the oxygen atom of the dioxane ring (Figure 8a). This represents a significant difference with respect to Ac-II-NHMe, in which backbone···side group hydrogen bonds always involved the N–H of the blocking groups. Therefore, the conformational flexibility imparted by the methylene side group is crucial for the formation of interactions with the amino acid backbone since it facilitates the adequate orientation of the EDOT ring. In contrast, the C_5-I minimum shows a N–H···π interaction between the NHMe blocking group and the π cloud of the thiophene ring. Although this intramolecular interaction is relatively frequent in dipeptides bearing aromatic rings at the side chain,[60-63] it was not detected in the minima identified for Ac-II-NHMe because of the its molecular rigidity. However, N–H···π interactions have been found in other three minima of Ac-I-NHMe (i.e. C_5-4,

C_{7eq}-3 and C_{7eq}-7). The most stable minimum with the third representative backbone conformation, δ_L-1, is not stabilized by a backbone···backbone hydrogen bond but by a backbone···side group N–H···O interaction similar to that found for C_{7eq}-1.

#	φ (°)	ψ (°)	χ_1 (°)	ΔE (kcal/mol)	ΔG (kcal/mol)
C_{7eq}-1	-84.6	75.0	-63.9	0.3	0.0
C_{7eq}-2	-83.0	80.9	-171.5	0.0	0.4
C_{7eq}-3	-84.2	65.7	54.0	1.3	2.1
C_5-1	-157.6	171.1	63.6	0.8	0.2
C_5-2	-154.1	148.4	-173.5	1.4	1.2
C_5-3	-135.6	157.5	-61.2	1.4	1.7
δ_L-1	-119.5	15.1	-63.8	2.6	1.1
δ_L-2	-116.5	12.4	63.0	2.8	2.2
C_{7ax}-1	75.5	-57.6	-56.8	1.7	2.4
C_{7ax}-2	73.5	-65.3	-174.5	2.0	2.5
C_{7ax}-3	62.6	-38.3	74.9	4.8	5.1
α_L-1	65.5	33.0	-155.8	6.3	5.7
δ_D-1	-157.8	-56.6	179.9	6.3	5.7
δ_D-2	-170.5	-32.3	58.7	6.5	6.9
ε_D-1	44.6	-134.2	54.4	7.6	8.6

Table 4. Dihedral angles, relative energy and free energy of the minimum energy conformations obtained for Ac-Abu-NHMe (Figure 2b) at the ωB97X-D/6-311++G(d,p) level. The dihedral angles associated to the amide moieties (ω_0 and ω) remained close to 180° in all cases (not shown).

On the other hand, detailed inspection of Tables 3 and 4 indicates that the conformational flexibility of Ac-I-NHMe is higher than that of Ac-Abu-NHMe. Thus, the number of minima with C_5, C_{7eq} and δ_L backbone conformation, which is 3, 3 and 2 for Ac-Abu-NHMe (Table 4), increases to 8, 8 and 2 when the methyl group Abu is replaced by the EDOT ring (Table 3). Accordingly, the EDOT ring of Ac-I-NHMe is able to adopt multiple arrangements with respect to each backbone conformation. Moreover, these minima are within a ΔG gap of only 3.6 kcal/mol.

These results indicate that the conformational preferences of Ac-I-NHMe and Ac-II-NHMe are significantly different. Indeed, the conformation of the latter is severely restricted by the short distance between the EDOT ring and the backbone. This results in a reduction of the flexibility with respect to Ac-Ala-NHMe, the C_5 being the only representative backbone structure for Ac-II-NHMe (i.e. with ΔG < 1.5

kcal/mol). In contrast, the methylene group of Ac-I-NHMe induces an enhancement of the conformational flexibility. This latter outcome is due not only to the existence of multiple orientations of the ring with respect to the backbone but also to the stabilization of different backbone structures (i.e. C_{7eq}, C_5 and δ_L) within a ΔG gap of 1.5 kcal/mol. It should be noted that these results are fully consistent with the contact angle measurements reported in the previous subsection. We note that the polar groups of the amino acid (i.e. amide moieties and oxygen atoms of the dioxane ring) are completely exposed to the environment in the extended C_5 conformation while they are less accessible in the C_{7eq} and δ_L. Accordingly, the hydrophilicity of PEDOT-II should be larger than that of PEDOT-I, and this corroborates experimental findings.

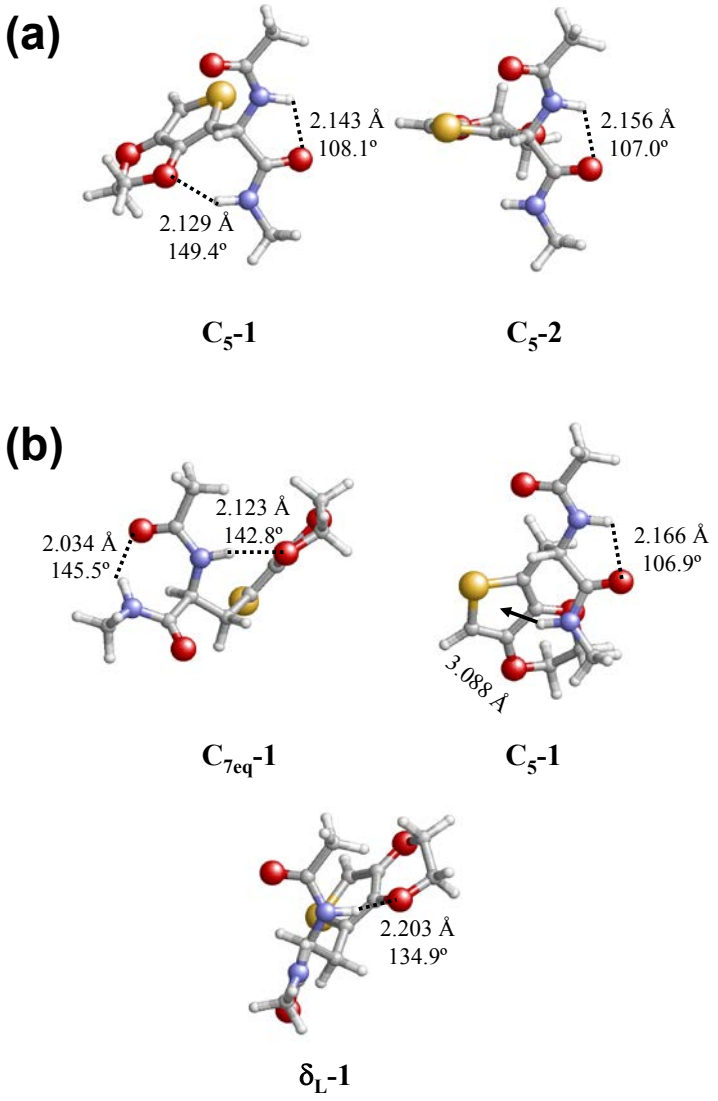

Figure 8. Minimum energy conformations of representative minima of (a) Ac-II-NHMe and (b) Ac-I-NHMe calculated at the ωB97X-D/6-311++G(d,p) level. The intramolecular hydrogen bonds and N–H···π interactions are indicated by dashed lines and arrows, respectively.

Geometric parameters associated to these interactions (*i.e.* H···O distance and ∠N–H···O angle in hydrogen bonds and the distance between the H and the center of mass of the Th ring in N–H···π) are indicated.

Conformational preferences of I and II

As a starting point, the 13 minima of Ac-II-NHMe and the 18 minima of Ac-I-NHMe have been selected, modified by replacing the Ac- and -NHMe blocking groups by -COOMe and NH-tert-butyloxycarbonyl (-NHBoc) and re-optimized. Table 5 and Table 6 contain the essential geometrical parameters (φ,ψ,χ_1 and χ_2), ΔE and ΔG for the 10 minima of II and the 11 minima of I, respectively. As for Ac-II-NHMe and Ac-I-NHMe, ΔG values of the minima are close in the energetic scale (e.g. 6.35 kcal/mol for II and only within 2.97 kcal/mol for I).

Similarly to Ac-II-NHMe, the two C_5 minima (Figure 9) possess a $\Delta G \leq 1.5$ kcal/mol for II. The lowest energy structure (C_5-1) has similar backbone geometrical properties (φ,ψ) that the lowest C_5-1 conformation of Ac-II-NHMe, Ac-II-NHMe (-149.8°,177.8°) and (-151.3°,170.3°) but with a more constraint C_5 ring characterized by $d_{O\text{-}H}$ and ∠N–H···O of 2.3 Å and 100.0° for II and of 2.1 Å and 108.1° for Ac-II-NHMe. We also notice that the χ_1 dihedral angle is significantly larger for II (-101.6°) than for Ac-II-NHMe (23.2°). The modification of the blocking group when going from -NHMe to -NHBoc induced a flip of the dioxane ring preventing the hydrogen bond which was present in Ac-II-NHMe. In contrast to the C_5-1 geometry of Ac-II-NHMe, C_5-1 of II does not present any backbone···side group stabilizing hydrogen bond interaction; however the -NHBoc presents two interactions between the oxygen and two hydrogen atoms of the methyl group (observed in all conformation of I and II).

The C_5-2 structure is energetically close C_5-1 with a $\Delta G = 0.1$ kcal/mol but its geometry differs by its χ_1=49.3° for which the dioxane is oriented in the same direction as in the C_5-1 conformation of Ac-II-NHMe (see Figure 9). However, C_5-2 exhibits a weak backbone···side group hydrogen bond interaction between the hydrogen bonded to C^{α} and one of the oxygen of the dioxane ($d_{O\text{-}H}$=2.6 Å and ∠N–H···O = 104.6°). Figure 9 remarkably shows that, for both structures, the interactions between the side group (EDOT) and the backbone are minimized forming a T-shape-like arrangement without any hydrogen bond between the EDOT and the blocking groups. Other backbone

conformations listed in Table 5 exhibit weak hydrogen bond between the hydrogen of -NHBoc and one of the oxygen atoms of the dioxane, as the α_L-3 (d_{O-H}=2.5 Å and ∠N–H···O = 110.9°), α' (d_{O-H}=2.5 Å and ∠N–H···O = 110.1°) and the β_2–1 (d_{O-H} =2.9 Å and ∠N–H···O=109.7°) which are destabilized by 5.2, 3.7 kcal/mol and 2.0 kcal/mol, respectively. Compared to Ac-II-NHMe, hydrogen bonds are weaker in II (with d_{O-H} =2.3-2.5 Å) mainly due to the steric effect of Boc. Thus, the EDOT ring tends to minimize the interaction with the Boc blocking group.

#	φ (°)	ψ (°)	χ_1 (°)	ΔE (kcal/mol)	ΔG (kcal/mol)
C_5-1	-149.8	177.8	-101.6	0.71	0.00
C_5-2	-167.0	167.3	49.3	0.00	0.09
C_{7eq}	-85.2	75.0	-141.2	2.56	2.00
β_2-1	-80.9	2.0	-105.7	1.60	2.00
β_2-2	73.6	-11.7	-75.8	5.81	6.35
α_L-1	-58.0	-30.8	70.3	1.71	2.70
α_L-2	53.0	38.0	60.5	3.70	4.06
α_L-3	57.2	42.6	117.8	3.90	5.17
α'	-155.5	-33.1	-137.0	2.07	3.69
C_{7ax}	86.8	-46.6	105.0	7.71	7.30

Table 5. Dihedral angles, relative energy and free energy of the minimum energy conformations obtained for **II** (Figure 1) at the ωB97X-D/6-311++G(d,p) level. The dihedral angles associated to the amide moieties (ω_0 and ω) remained close to 180° in all cases (not shown).

#	φ (°)	ψ (°)	χ_1 (°)	χ_2 (°)	ΔE (kcal/mol)	ΔG (kcal/mol)
C_5-1	169.9	-165.1	-52.4	98.5	0.02	0.00
C_5-2	140.8	-160.1	54.6	-109.3	0.92	0.24
C_5-3	141.7	-159.1	49.1	88.3	0.00	0.44
C_5-4	164.2	-175.7	-61.9	-92.6	0.39	0.48
C_5-5	155.7	-147.5	-175.3	107.1	2.68	0.98
C_5-6	161.2	-154.5	176.0	-86.3	2.16	1.11
α_L-1	62.4	20.2	-70.5	-100.9	1.61	0.61
α_L-2	68.7	17.3	-52.3	101.0	2.68	2.97
δ_L-1	138.9	32.6	54.7	-110.0	1.92	1.55
δ_L-2	139.4	27.8	49.5	88.5	0.80	1.63
δ_L-3	162.9	18.3	-69.7	71.3	2.87	2.37

Table 6. Dihedral angles, relative energy and free energy of the minimum energy conformations obtained for **I** (Figure 1) at the ωB97X-D/6-311++G(d,p) level. The dihedral angles associated to the amide moieties (ω_0 and ω) remained close to 180° in all cases (not shown).

For I, the ΔG values of the minima are within 3.0 kcal/mol (Table 6) with respect to the lowest energy conformation (C_5-1). As for Ac-I-NHMe this small energy gap between all conformations demonstrates the ability of I to present numerous stable structures. In opposition to the EDOT-CH_2 pattern inserted into a peptidic sequence, i.e. Ac-I-NHMe (Table 3), no C_{7eq} backbone conformations have been found while they were the most stable peptidic sequence. The lowest energy minimum is the C_5-1 conformation of I that was the second lowest energy structure for Ac-I-NHMe (after C_{7eq}). A total of six C_5 minima and one α_L minimum are characterized by a ΔG below the 1.5 kcal/mol threshold. The number of minima below this limit has considerably decreased compared to Ac-I-NHMe (8 C_5, 8 C_{7eq} and 2 δ_L) due to the strong repulsive and steric characters of the Boc and OMe blocking groups. C_5 minima are characterized by an intramolecular backbone interaction forming the 5 membered hydrogen bond ring and by dihedral angles close to 180° which yield to a "zig-zag planar" structure of the backbone. Additionally C_5-1 possesses one weak backbone···EDOT group interaction and one blocking group···EDOT group interaction between one hydrogen of dioxane and the oxygen atom of the carboxyl backbone (d_{OH} =2.99 Å and ∠C–H···O=111.2°) and between one hydrogen of the Boc group and the oxygen atom of the dioxane (d_{OH} =2.72 Å and ∠C–H···O=122.2°, see Figure 9b), respectively. Another interaction is observed for two conformations (C_5-2 and δ_L-1) between the hydrogen atom bonded to C_α and one of the oxygen atom of the dioxane. No N–H···π interaction between the NHBoc blocking group and π-electronic cloud of the dioxane have been observed for I.

To summarize the conformational studies of I and II, we conclude as for Ac-I-NHMe that I is more flexible than II, however, due to the repulsive blocking group, less conformations possess a ΔG <1.5 kcal/mol. For both I and II molecules, the C_5 backbone conformations lead to the lowest free energy conformations which is related to the fact that the polar blocking groups are much more exposed to the solvent.

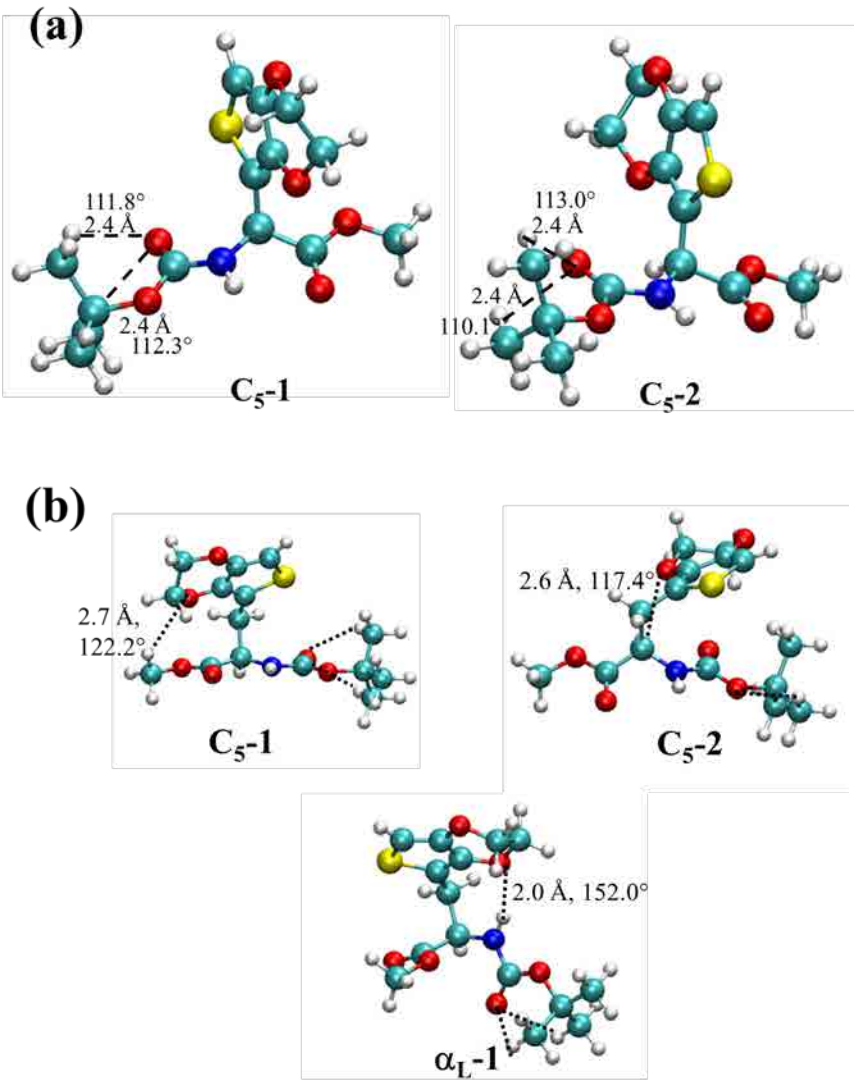

Figure 9. Minimum energy conformations of representative minima of (a) **II** and (b) **I** calculated at the ωB97X-D/6-311++G(d,p) level. The intramolecular interactions are indicated by dashed lines. Geometric parameters associated to these interactions (*i.e.* H···O distance and ∠N/C–H···O angle in hydrogen are indicated.

Experimental and Theoretical Electronic properties of I and II

Figure 10 shows the UV-vis spectra of I and II recorded in diluted acetonitrile solutions ($1 \cdot 10^{-5}$ M). As it can be seen, the spectra of the two compounds are apparently similar with two overlapped broad bands centered at 247 / 248 and 255 / 259 nm for I / II. The peaks should be essentially attributed to electronic transitions involving the EDOT substituent, as will be shown below by comparing the observed and the calculated spectra. The spectrum of EDOT in diluted acetonitrile solution with transition maxima at $\lambda^{(1)}$= 264 nm, $\lambda^{(2)}$= 255 nm (not shown) is very similar to that recently reported in diluted DMSO solution, which showed absorptions at $\lambda^{(1)}$= 266

nm, $\lambda^{(2)}$= 259 nm.[64] Recent TD-DFT calculations on EDOT in DMSO allowed us to conclude that the absorptions of lower energy $\lambda^{(1)}$ and $\lambda^{(2)}$ [i.e. 237 nm (5.23 eV) and 230 nm (5.39 eV), respectively] correspond to HOMO→LUMO and HOMO-1→LUMO transitions.[64] The effect of the solvent on EDOT is negligible for $\lambda^{(1)}$ and $\lambda^{(2)}$ computed in acetonitrile as the present experimental results are in this solvent. Figure 11 shows the difference between the excited and ground states electronic density for both electronic transitions. $\lambda^{(1)}$ is characterized by an increase/decrease of the electronic density on the oxygen atoms/CH of the dioxane/thiophene and the second electronic transition shows an increase of the density on the sulfur atom and on the C–C bond linking the thiophene and the dioxane moieties.

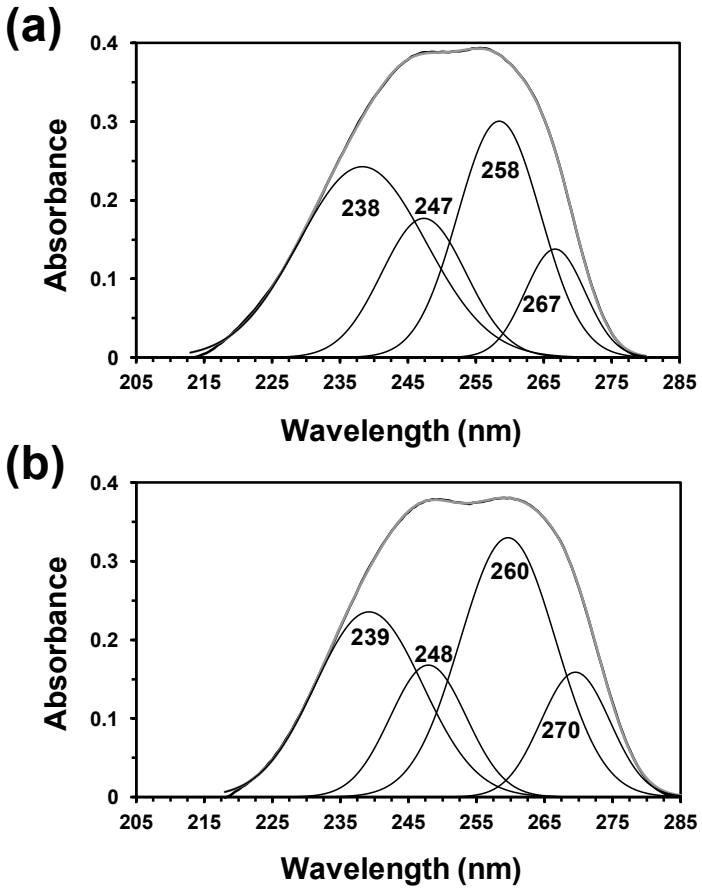

Figure 10. Absorption (absorbance expressed within an arbitrary unit) spectra of (a) **I** and (b) **II**. For each system, thick black and grey lines represent the experimentally recorded and simulated spectra, respectively. The curves (thin black lines) and wavelength (in nm) at the maxima resulting from the deconvolution process are also shown.

Deconvolution of the UV-vis spectra is essential to obtain information about the specific transitions that contribute to each observed peak and also to compare the calculated spectra with the experimental ones (see below). Results from deconvolution

(included in Figure 10) indicate that the incorporation of the EDOT ring into the amino acids produces some changes in the spectra, which also depend on the presence or the absence of the methylene group. Satisfactory statistical parameters (i.e. correlation coefficient, R^2 > 0.999, and standard error, s.e. < 0.005) were obtained for the deconvolution of the spectrum recorded for I (Figure 10a) by considering four peaks centered on 238, 247, 258 and 267 nm. Thus, the most significant changes with respect to the spectrum of EDOT is the apparition of a new transition at 247 nm and a very small red shift of the HOMO→LUMO transition, which increases by 2 nm (0.04 eV). The latter shift is significantly larger in the spectrum of II, which contains four peaks centered at 239, 248, 260 and 270 nm (Figure 10b). Therefore, the HOMO→LUMO transition in II arises at 270 nm, which represents an addition of 6 nm with respect to EDOT. The effect induced by the CH_2 side group in the HOMO→LUMO transition is fully consistent with the electrochemical behavior described above for PEDOT-I and PEDOT-II.

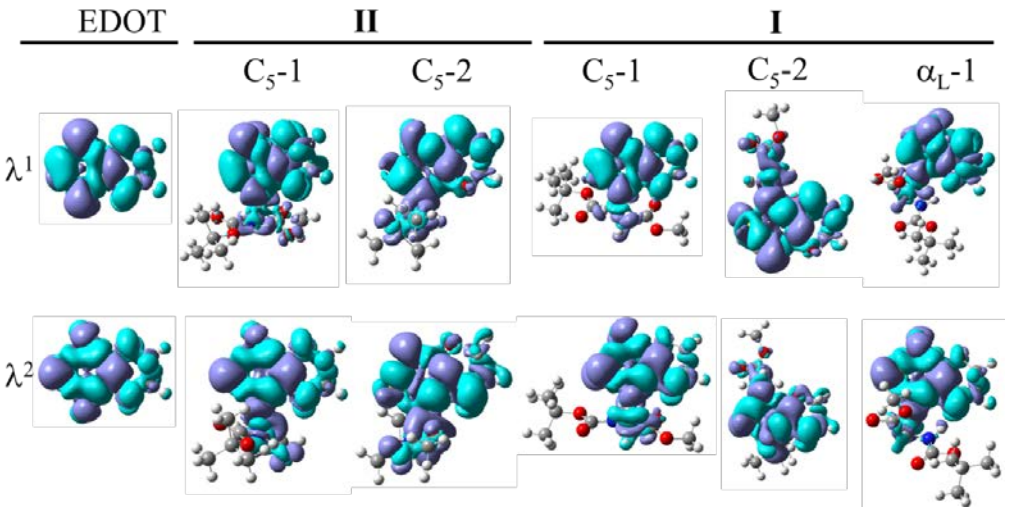

Figure 11. Difference of the total electronic densities (excited - ground) corresponding to the first two electronic transitions (λ^1 and λ^2). Blue (green) regions indicate an increase (decrease) of electron density upon electronic transition.

Optical spectra have been computed for each conformation of I and II (Table 7 and Figure 12) with TD-DFT. As for EDOT, only two electronic transitions have been observed and the differences of electronic density of both electronic transitions are shown in Figure 11. For a ΔG < 1.5 kcal/mol, I possesses 7 possible conformations with $\lambda^{(1)}$ going from 239 nm to 232 nm and $\lambda^{(2)}$ varying between 235 nm and 230 nm depending on the considered conformation (Figure 12a). This indicates that the largest

gap obtained theoretically between the two humps is 9 nm. C_5-2 has a $\lambda^{(1)}$ = 239 nm while α_L-1 is characterized by the lowest $\lambda^{(2)}$ (230 nm). Comparing to EDOT a red shift of 2 nm is theoretically observed for $\lambda^{(1)}$ and, as within the experiment, while $\lambda^{(2)}$ remains unchanged. We can conclude here that the experimental shift between EDOT and I can only be explained by a combination of several conformations with low free energy and not by multiple transitions present in a single conformation. The observed flexibility of I plays a significant role in the absorption spectrum. We point out that the variation between $\lambda^{(1)}$ and $\lambda^{(2)}$ is rather small (1-2 nm) for most of the lowest energetic conformations but for the C_5-2 which displays a variation of 6 nm due to the increase of a larger value of $\lambda^{(1)}$. This is explained by the presence of an interaction between the H bonded to C^{α} and one of the oxygen atoms of the dioxane. Actually the difference between the excited and ground states electronic density for both electronic transitions (Figure 11) for the conformers without such H bond interactions is similar to the one of EDOT while the presence of such interaction modifies the difference of electronic density between both states of EDOT, due to the extension of the density to the backbone. We observe a similar variation between both electronic transitions (5 nm) for the δ_L-1 conformation that also possesses such interaction. Compared to EDOT, the experimental absorption spectra of II exhibits red-shifts of 6 nm and 5 nm for the first and the second electronic transitions, respectively. Accounting for the lowest energetically C_5-1 and C_5-2 conformations of II (Figure 12b), $\lambda^{(1)}/\lambda^{(2)}$ are respectively 235/232 nm and 239/235 nm for C_5-1 and C_5-2. Again here the C_5-2 is characterized by the interaction between the H bonded to C^{α} and one of the oxygen of the dioxane. Qualitatively, the red-shifts compared to EDOT are well reproduced by theory with +2 nm and +2 nm. Comparing I and II, theoretical computations shows that it is essential to consider the dynamic behavior of the structure, here done by accounting for several conformations when mimicking absorption spectra (Figure 12).

	Conformations	λ^1_{max} (nm)	*f*	λ^2_{max} (nm)	*f*
EDOT[a]	--	237	0.24	230	0.10
II	C_5-1	235	0.21	232	0.19
	C_5-2	239	0.14	235	0.24
	C_{7eq}	234	0.20	231	0.20
	β_2-1	234	0.21	229	0.21
	β_2-2	237	0.20	233	0.19
	α_L-1	239	0.18	233	0.26
	α_L-2	239	0.18	232	0.23
	α_L-3	234	0.18	232	0.18
	α'	239	0.18	239	0.20
	C_{7ax}	239	0.16	234	0.23
I	C_5-1	233	0.20	232	0.17
	C_5-2	239	0.19	233	0.16
	C_5-3	236	0.16	235	0.20
	C_5-4	234	0.21	233	0.18
	C_5-5	234	0.23	232	0.18
	C_5-6	234	0.26	233	0.18
	α_L-1	232	0.19	230	0.18
	α_L-2	233	0.21	232	0.17
	δ_L-1	238	0.19	233	0.16
	δ_L-2	236	0.17	235	0.20

Table 7. Maximum vertical absorption wavelengths (λ_{max}) and oscillator strengths (*f*) of EDOT, **I** and **II** computed at the PCM(acetonitrile)/CAM-B3LYP /6-311++G(d,p) level of theory. The conformations with ΔG<1.5kcal/mol are highlighted by a light grey background.

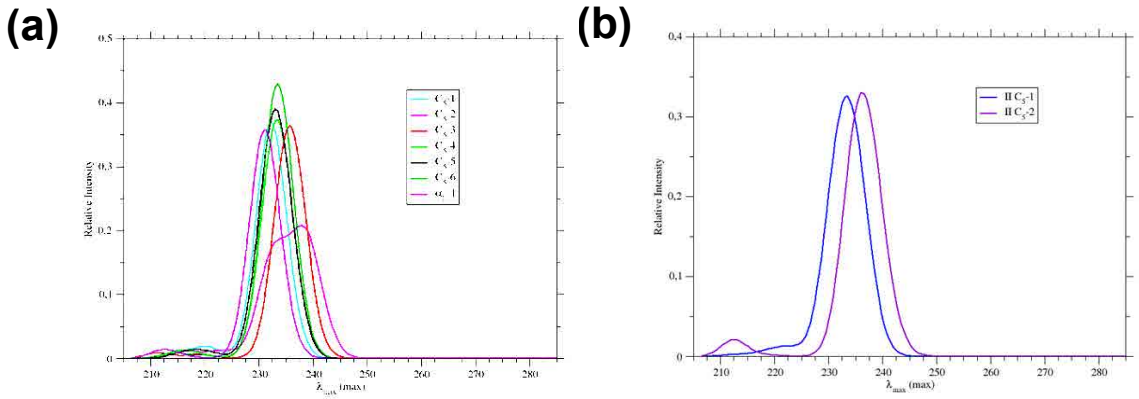

Figure 12. Electronic spectra calculated for the more stable conformations (*i.e.* ΔG < 1.5 kcal/mol; see Tables 5 and 6) of **I** (a) and **II** (b).

Electronic properties of PEDOT-I and PEDOT-II

Figure 13 compares the UV-vis spectra of PEDOT*, PEDOT-I and PEDOT-II films in both doped and dedoped states. Doped films refer to the materials prepared using the two-steps anodic polymerization strategy discussed in the Methods section, whereas dedoped films were obtained by reducing the doped materials in acetonitrile with 0.1 M $LiClO_4$ applying a constant potential of -1.50 V for 50 s. All the materials show two absorption bands. The highest energy band appears at λ_{max}=250 nm in all cases (i.e. independently of the oxidation state and the incorporation of end-capping amino acid), which is typically assigned to the n-π^* transition in the polymer backbone.[65]

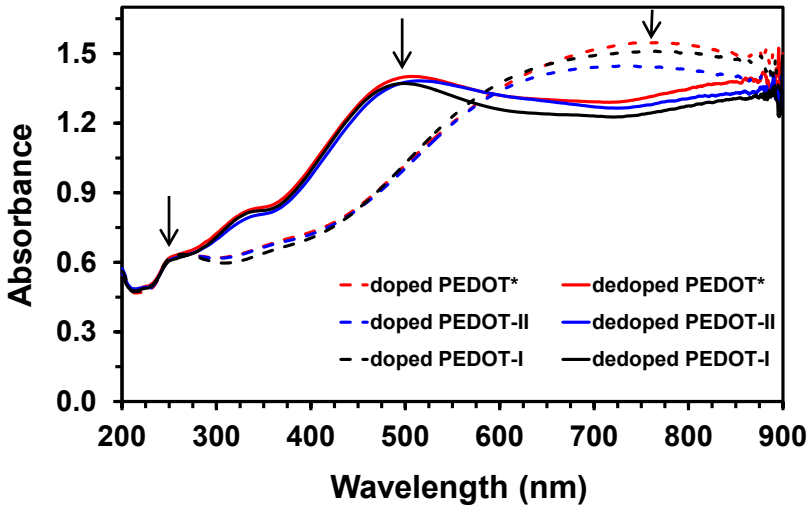

Figure 13. Absorption (absorbance expressed within an arbitrary unit) spectra of doped and dedoped PEDOT*, PEDOT-I and PEDOT-II. The main absorbance peaks are indicated by arrows.

The λ_{max} of the second absorbance peak occurs at ~500 nm in the dedoped systems. This absorption corresponds to the π-π^* transition,[66,67] showing also a small dependence on the presence or absence of end-capping amino acid. Thus, the E_g was determined for the different systems from the onset wavelength of the UV-vis displayed in Figure 13. The E_g values of dedoped PEDOT*, PEDOT-I and PEDOT-II are 1.99, 1.99 and 1.86 eV, respectively. It is worth noting that the E_g determined in this work for dedoped PEDOT* and PEDOT-I (i.e. 1.99 eV) are fully consistent with the value recently reported for PEDOT using electrochemical procedures (i.e. 1.98 V).[68] Moreover, the comparison of the results obtained for PEDOT-I and PEDOT-II reflects the importance of the methylene unit at the side chain of the end-capping amino acid.

Thus, the E_g decreases by 0.13 eV when the PEDOT chain is directly attached to the amino acid backbone. On the other hand, the large absorption band at ~750 nm in doped systems has been ascribed to the formation of polarons.[66]

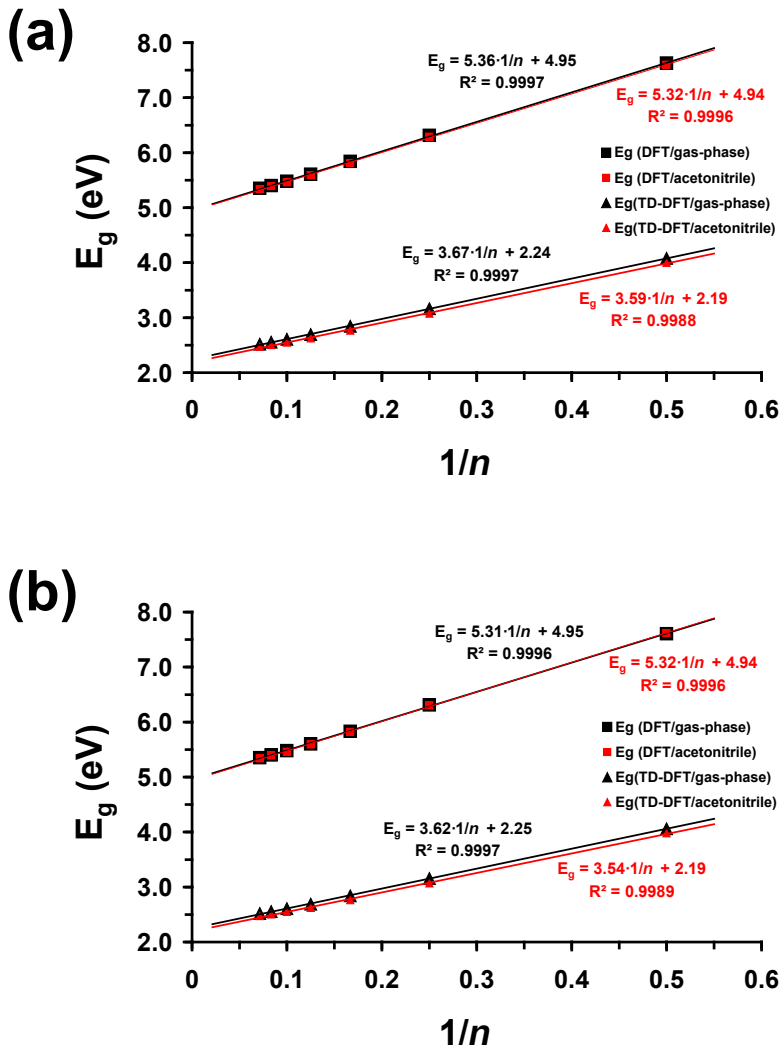

Figure 14. Variation of the E_g derived from both DFT and TD-DFT calculations in the gas-phase (black) and acetonitrile solution (red) against 1/*n*, where *n* is the number of EDOT units, in (a) $(EDOT)_n$-I and (b) $(EDOT)_n$-II. The solid lines correspond to the linear regressions used to extrapolate this electronic property towards conjugates with infinite PEDOT chains.

QM methods have been used to investigate the E_g of PEDOT-I and PEDOT-II at the molecular level. More specifically, the molecular geometries of $(EDOT)_n$-I and $(EDOT)_n$-II oligomers with n= 2, 4, 6, 8, 10, 12 and 14 (Figure 2c) were optimized using the ωB97X-D/6-311++G(d,p) method. In all cases, the amino acid was positioned according to the lowest energy structure found previously. For each oligomer, the E_g was estimated using two different procedures: (i) the difference between the energies of the frontier orbitals (E_g^{DFT}); and (ii) the excitation energies calculated with TD-DFT (

$E_g^{TD\text{-}DFT}$). In addition to calculations in the gas-phase, the E_g values of all oligomers were obtained in acetonitrile solution, bulk solvent effect being treated with the framework of the PCM model in both DFT and TD-DFT calculations. However, it should be mentioned that this solvation model did not represent the effect of the high hydrophobic PEDOT bulk phase, which is also expected to affect the electronic properties of PEDOT-I and PEDOT-II.

The E_g values predicted at the DFT and TD-DFT levels for infinite polymer chains ($E_{g,\infty}^{DFT}$ and $E_{g,\infty}^{TD\text{-}DFT}$, respectively) in the gas-phase and acetonitrile solution were obtained by extrapolating the linear variation of such electronic property against 1/n. Figure 14 represents the variation of E_g^{DFT} and $E_g^{TD\text{-}DFT}$ in the gas-phase and acetonitrile solution against 1/n for $(EDOT)_n$-I and $(EDOT)_n$-II.

Although the E_g^{DFT} values follow a linear behavior, the values extrapolated for an infinite polymer chain are considerably overestimated with respect to the experimental ones (i.e. by ~ 3 eV), independently of the environment. On the other hand, the $E_g^{TD\text{-}DFT}$ values are systematically lower than the E_g^{DFT} ones, which results in a reduction of ~2.7 eV in the $E_{g,\infty}^{TD\text{-}DFT}$ with respect to the $E_{g,\infty}^{DFT}$ estimations. Moreover, the $E_{g,\infty}^{TD\text{-}DFT}$ values obtained in the gas-phase are practically identical for the two polymers (i.e. 2.24 and 2.25 eV for PEDOT-I and PEDOT-II, respectively). Thus, although TD-DFT calculations on a single molecule provide an accurate description of the experimental E_g values (i.e. they are overestimated by 0.25 and 0.39 eV for PEDOT-I and PEDOT-II, respectively), they do not represent satisfactorily the experimental differences found between the two conjugates despite the selection of a range-separated hybrid that should allow consistent evaluation of systems of different sizes. The $E_{g,\infty}^{DFT}$ obtained in acetonitrile solution is 2.19 eV for the two conjugates, evidencing that solvent effects improve the quantitative description of the experimental E_g values by ~0.06 e. However, the differences between the two systems are not reflected by calculations in acetonitrile, as occurred in the gas-phase. This limitation should not be attributed to the TD-DFT methodology, which has been

demonstrated to be very reliable,[35] but to the fact that calculations were carried out in a single molecule. Indeed, theoretical results displayed in Figure 14 suggest that the end capping peptides essentially affect the electronic intermolecular effects, which

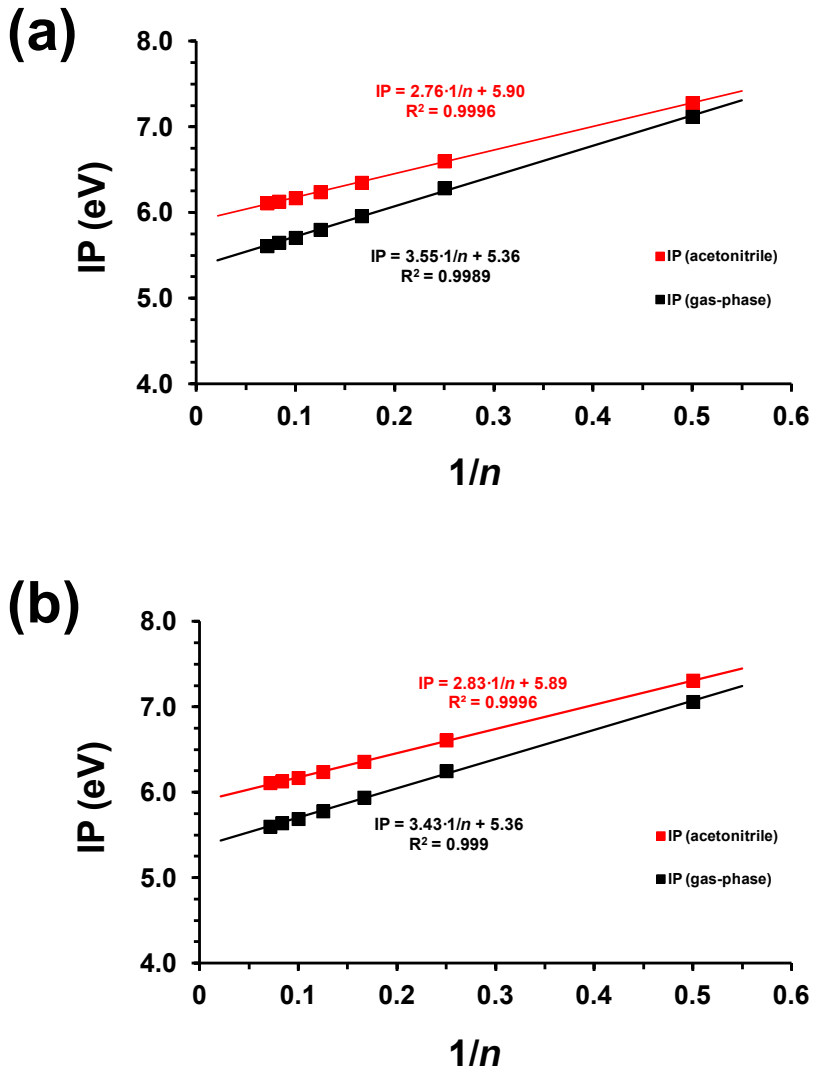

were reported to play an important role in the properties of PTh derivatives.[69-71]

Figure 15. Variation of the IP derived from DFT calculations in the gas-phase (black) and acetonitrile solution (red) against 1/*n*, where *n* is the number of EDOT units, in (a) $(EDOT)_n$-I and (b) $(EDOT)_n$-II. The solid lines correspond to the linear regressions used to extrapolate this electronic property towards conjugates with infinite PEDOT chains.

Figure 15 represents the variation of the IP in the gas-phase and acetonitrile solution against 1/n for $(EDOT)_n$-I and $(EDOT)_n$-II. As it can be seen, the influence of the amino acid is also trifling, the value obtained for infinite polymer chains (IP_∞) being 5.36 eV for both PEDOT-I and PEDOT-II. Nevertheless, the IP behavior shows a significant difference with respect to E_g. This refers to the effect of the acetonitrile

solvent, which produces an increment in the IP_∞ of ~0.5 eV with respect to the gas-phase. Thus, oxidation becomes a more difficult process in solution.

5.2.4 Conclusions

A new amino acid (**II**), in which the EDOT side group is directly linked to the backbone, has been synthesized and characterized. The elimination of the methylene group of **I** allows a direct connection between the PEDOT chains and the amino acid-containing surface in the conjugate. Consequently, the electrochemical behavior of PEDOT-II and PEDOT* has been found to be practically identical, and slightly different to that of PEDOT-I. Thus, the latter conjugate is less electroactive and electrostable than PEDOT-II. On the other hand, incorporation of end capping amino acids has been observed to increase the hydrophilicity of the PEDOT* surface, this increment being slightly higher for PEDOT-II than for PEDOT-I.

The conformation of Ac-II-NHMe is more restricted than that of Ac-I-NHMe since the distance between the rigid EDOT ring and the backbone is shorter in the former than in the latter. Accordingly, the extended C_5 is the only representative backbone conformation for Ac-II-NHMe while the conformational flexibility of Ac-I-NHMe is even higher than that of Ac-Abu-NHMe. Examination of the electronic properties of **I**, **II**, PEDOT-I and PEDOT-II using both UV-vis spectroscopy and quantum mechanical calculations have provided important information about the effect of the side methylene group. The red shift of **I** and **II** compared to EDOT has been reproduced only by considering all conformations with $\Delta G < 1.5$ kcal/mol. The variation between the spectra of **I** and **II** has been related to the structural fluctuations which is more favorable in the former. On the other hand, the E_g measured for PEDOT-I and PEDOT* are practically identical and higher than that of PEDOT-II by 0.13 eV, evidencing that the influence of methylene group is not negligible. Moreover, the E_g values predicted by quantum mechanical calculations, which are very similar to the experimental ones, suggest that the influence of the amino acid in the electronic properties occur at the intermolecular level.

5.2.5 References

1. T. S. Burkoth, T. L. S. Benzinger, V. Urban, D. G. Lynn, S. C. Meredith and P. Thiyagarajan, *J. Am. Chem. Soc.*, 1999, **121**, 7429.
2. O. Rathore and D. Y. Sogah, *J. Am. Chem. Soc.*, 2001, **123**, 5231.
3. A. Rosler, H. A. Klok, I. W. Hamley, V. Castelletto and O. O. Mykhaylyk, *Biomacromolecules*, 2003, **4**, 859.
4. J. M. Smeenk, M. B. J. Otten, J. Thies, D. A. Tirrell, H. G. Stunnenberg and J. C. M. van Hest, *Angew. Chem., Int. Ed.*, 2005, **44**, 1968.
5. J. H. Collier and P. B. Messersmith, *Adv. Mater.*, 2004, **16**, 907.
6. D. Eckhardt, M. Groenewolt, E. Krause and H. G. Börner, *Chem. Commun.*, 2005, 2814.
7. J. Hentschel, E. Krause, and H. G. Börner, *J. Am. Chem. Soc.*, 2006, **128**, 7722.
8. V. Castelletto, J. E. McKendrick, I. W. Hamley, U. Olsson and C. Cenker, *Langmuir*, 2010, **26**, 11624.
9. E. S. Place, N. D. Evans and M. M. Stevens, *Nat. Mater*., 2009, **8**, 457.
10. E. S. Place, J. H. George, C. K. Williams and M. M. Stevens, *Chem. Soc. Rev*., 2009, **38**, 1139.
11. H. W. Jun, S. E. Paramonov and J. D. Hartgerink, *Soft Matter*, 2006, **2**, 177.
12. M. S. Lamm, K. Rajagopal, J. P. Schneider and D. J. Pochan, *J. Am. Chem. Soc.*, 2005, **127**, 16692.
13. M. R. Ghadiri, J. R. Granja, R. A. Milligan, D. E. McRee and N. Khazanovich, *Nature*, 1993, **366**, 324.
14. J. Y. Shu, Y.-J. Huang, C. Tan, A. D. Presley, J. Chang and T. Xu, *Biomacromolecules*, 2010, **11**, 1443.
15. R. Chapman, K. A. Jolliffe and S. Perrier, *Polym. Chem.*, 2011, **2**, 1956.
16. H. G, Börner, B. M. Smarsly, J. Hentschel, A. Rank, R. Schubert, Y. Geng, D. E. Discher, T. Hellweg and A. Brandt, *Macromolecules*, 2008**, 41***,* 1430.
17. S. E. Paramonov, H.-W. Jun and J. D. Hertgerink, *J. Am. Chem. Soc.*, 2006, **128**, 7291.
18. M. Tirrell, E. Kokkoli and M. Biesalski, *Surf. Sci.*, 2002, **500**, 61.
19. S. Garty, N. Kimelman-Bleich, Z. Hayouka, D. Cohn, A. Friedler, G. Pelled and D. Gazit, *Biomacromolecules*, 2010, **11**, 1516.
20. E. De Giglio, L. Sabbatini and G. Zambonin, *J. Biomater. Sci., Polym. Ed.*, 1999, **10**, 845.
21. E. De Giglio, L. Sabbatini, S. Colucci and G. Zambonin, *J. Biomater. Sci., Polym. Ed.*, 2000, **11**, 1073.
22. N. Gomez and C. E. Schimdt, *J. Biomed. Mater. Res., Part A*, 2007, **81**, 135.
23. R. I. Christopherson, S. D. Lyons and P. K. Wilson, *Acc. Chem. Res.*, 2002, **35**, 961.
24. C. D. McTiernan and M. Chahma, *New J. Chem.*, 2010, **34**, 1417.
25. C. D. McTiernan, K. Omri and M. Chahma, *J. Org. Chem.,* 2010, **75**, 6096.
26. G. Fabregat, G. Ballano, E. Armelin, L. J. del Valle, C. Cativiela and C. Alemán, *Polym. Chem.*, 2013, **4**, 1412.
27. C. Ocampo, R. Oliver, E. Armelin, C. Alemán and F. Estrany, *J. Polym. Res.*, 2006, **13**, 193.
28. D. Aradilla, M. M. Pérez-Madrigal, F. Estrany, D. Azambuja, J. I. Iribarren and C. Alemán, *Org. Electr.*, 2013, **14**, 1483.
29. J.-D. Chai and M. Head-Gordon, *Phys. Chem. Chem. Phys.*, 2008, **10**, 6615.
30. A. D. McLean and G. S. Chandler, *J. Chem. Phys.*, 1980, **72**, 5639.
31. M. J. Frisch, J. A. Pople and J. S. Binkley, *J. Chem. Phys.*, 1984, **80**, 3265.
32. Y. K. Kang and B. J. Byun, *J. Comput. Chem.*, 2010, **31**, 2915.
33. Y. Bouteiller, J. C. Poully, C. Desfrançois and G. Grégoire, *J. Phys. Chem. A*, 2009, **113**, 6301.
34. R. Vargas, J. Garza, B. P. Hay and D. A. Dixon, *J. Phys. Chem. A*, 2002, **106**, 3213.
35. J. Casanovas, G. Revilla-López, M. Crisma, C. Toniolo and C. Alemán, C. *J. Phys. Chem. B*, 2012, **116**, 13297.

36. M. E. Casida, Time-Dependent Density-Functional Response Theory for Molecules, in Recent Advances in Density Functional Methods, Part I (ed. D. P. Chong), World Scientific, Singapore, 1995, pp: 155-192.
37. D. Jacquemin and C. Adamo, *Chem. Soc. Rev*., 2013, **42**, 845.
38. L. Goerigk and S. Grimme, *J. Chem. Phys*., 2010, **132**, 184103.
39. E. E. Dahlke, R. M. Olson, H. R. Leverentz and D. G. Truhlar, *J. Phys. Chem. A*., 2008, **112**, 3976.
40. T. Yanai, D. Tew and N. A. Handy, *Chem. Phys. Lett.*, 2004, **393**, 51.
41. J. Tomasi, B. Mennucci and R. Cammi, *Chem. Rev.*, 2005, **105**, 2999.
42. T. Le Bahers, C. Adamo and I. Ciofini, I. *J. Chem. Theory Comput*., 2011, **7**, 2498.
43. D. Jacquemin, T. Le Bahers, C. Adamo and I. Ciofini, I. *Phys. Chem. Chem. Phys.*, 2012, **14**, 5383.
44. C. Alemán and J. Casanovas, *J. Phys. Chem. A*, 2004, **108**, 1440.
45. C. Alemán and J. Casanovas, *J. Phys. Chem. C*, 2007, **111**, 4823.
46. J. Poater, J. Casanovas, M. Solà and C. Alemán, *J. Phys. Chem. A*, 2010, 114, 1023.
47. T. Koopmans, *Physica*, 1934, **1**, 104.
48. J. F. Janak, *Phys. Rev. B*, 1978, **18**, 7165.
49. J. P. Perdew, In Density Functional Methods in Physics; R. M. Dreizler and J. Providenca, Eds.; Plenum Press: New York and London, **1985**.
50. M. Levy and A. Nagy. *Phys. Rev. A*, 1999, **59**, 1687-1689.
51. M. J. Frisch, G. W. Trucks, H. B. Schlegel, G. E. Scuseria, M. A. Robb, J. R. Cheeseman, G. Scalmani, V. Barone, B. Mennucci, G. A. Petersson, H. Nakatsuji, M. Caricato, X. Li, H. P. Hratchian, A. F. Izmaylov, J. Bloino, G. Zheng, J. L. Sonnenberg, M. Hada, M. Ehara, K. Toyota, R. Fukuda, J. Hasegawa, M. Ishida, T. Nakajima, Y. Honda, O. Kitao, H. Nakai, T. Vreven, J. A. Jr Montgomery, J. E. Peralta, F. Ogliaro, M. Bearpark, J. J. Heyd, E. Brothers, K. N. Kudin, V. N. Staroverov, R. Kobayashi, J. Normand, K. Raghavachari, A. Rendell, J. C. Burant, S. S. Iyengar, J. Tomasi, M. Cossi, N. Rega, J. M. Millam, M. Klene, J. E. Knox, J. B. Cross, V. Bakken, C. Adamo, J. Jaramillo, R. Gomperts, R. E. Stratmann, O. Yazyev, A. J. Austin, R. Cammi, C. Pomelli, J. W. Ochterski, R. L. Martin, K. Morokuma, V. G. Zakrzewski, G. A. Voth, P. Salvador, J. J. Dannenberg, S. Dapprich, A. D. Daniels, O. Farkas, J. B. Foresman, J. V. Ortiz, J. Cioslowski and D. J. Fox, *Gaussian 09, revision A.01*, Gaussian, Inc.: Wallingford, CT, 2009.
52. P. Calí and M. Begtrup, *Synthesis*, 2002, 63.
53. W.-C. Chen, T.-C. When, C.-C. Hu and A. Golapan, *Electrochim. Acta*, 2002, **47**, 1305.
54. P. Sem and A. De, *Electrochim. Acta*, 2010, **55**, 4677.
55. D. Aradilla, D. Azambuja, F. Estrany, M. T. Casas, C. A. Ferreira and C. Alemán, *J. Mat. Chem.*, 2012, **22**, 13110.
56. D. Aradilla, F. Estrany, E. Armelin and C. Alemán, *Thin Solid Films*, 2012, **520**, 4402.
57. J.-B. Jorcin, M. E. Orazem, N. Pebere and B. Tribollet, *Electrochim. Acta*, 2006, **51**, 1473.
58. C. Toniolo, *CRC Crit. Rev. Biochem.*, 1980, **9**, 1.
59. M. T. Cung, M. Marraud and J. Néel, *Ann. Chim. France*, 1972, **7**, 183.
60. C. Alemán, A. I. Jiménez, C. Cativiela, J. J. Pérez and J. Casanovas, *J. Phys. Chem. B*, 2002**, 106***,* 11849.
61. J. Casanovas, A. I. Jiménez, C. Cativiela, J. J. Pérez and C. Alemán. *J. Org. Chem.*, 2003, **68**, 7088.
62. J. Casanovas, D. Zanuy, R. Nussinov and C. Alemán, *J. Org. Chem.*, 2007, **72**, 2174.
63. J. Casanovas, A. I. Jiménez, C. Cativiela, R. Nussinov and C. Alemán, *J. Org. Chem.*, 2008, **73**, 644.
64. J. Preat, B. Teixeira-Dias, C. Michaux, E. A. Perpète and C. Alemán. *J. Phys. Chem. A*, 2011, **115**, 13642.
65. D. Hohnholz, A. G. MacDiarmid, D. M. Sarno and W. E. Jones, *Chem. Commun.*, 2001, 2444.
66. S. L. McFarlane, B. A. Deore, N. Svenda and M. S. Freund, *Macromolecules*, 2010, **43**, 10241.

67. J. Ouyang, Q. Xu, Ch.-W. Chu, Y. Yang, G. Li and J. Shinar, *Polymer*, 2004, **45**, 8443.
68. D. Aradilla, F. Estrany and C. Alemán, *J. Appl. Polym. Sci.*, 2011, **121**, 1982.
69. L. Miller and K. R. Mann, *Acc Chem Res*, 1996, 29, 417.
70. T. A. Skotheim, In Handbook of Conducting Polymers; Marcel Deker: New York, 1986.
71. F. Rodríguez-Ropero, J. Casanovas and C. Alemán, *J. Comput. Chem.*, 2008, **29**, 69.

CHAPTER 6

PEG-CONDUCTING POLYMER CONJUGATES AS BIOACTIVE PLATFORMS

6.1 Hybrid materials consistint of all-conjugated polythiophene backbone and grafted hydrophilic poly(ethylene glycol) chains*/**

Organic hybrid materials formed by an all-conjugated PTh backbone and well-defined PEG grafted chains have been prepared by anodic polymerization of chemically synthesized macromonomers. The latter consist of a pentathiophene (Th_5) sequence in which the central ring bears a PEG chain with M_w=1000 or 2000 at the 3-position. The influence of the polymerization potential, the length of the PEG branches and the dopant agent on the structure and properties of the graft copolymers has been examined. The chemical structure of the grafted materials has been corroborated by FTIR and XPS. SEM and AFM studies reveal that the morphology and topography of these materials are influenced by the above mentioned factors, even though homogeneous films showing a compact distribution of nanoaggregates, very flat surfaces (*i.e.* roughness < 15 Å) and nanometric thickness (*i.e.* 100-500 nm) were obtained in all cases. CV assays have been used to determine the presence of charged species, the electroactivity, the electrostability and the formation of cross-links. The electrochemical stability of the copolymer with grafted PEG chains of M_w=1000 has been found to increase with the number of consecutive oxidation-reduction cycles (self-electrostabilizing behavior). Finally, a preliminary investigation about the applicability of these hybrid materials as active surfaces for the selective adsorption of proteins is presented.

*Results described in this section previously appeared in *Polym. Chem.*, 2013, **4**, 2709.

**The synthesis and characterization of macromonomers described in this section were provided by Dr. Bendrea, L. Cianga and I. Cianga.

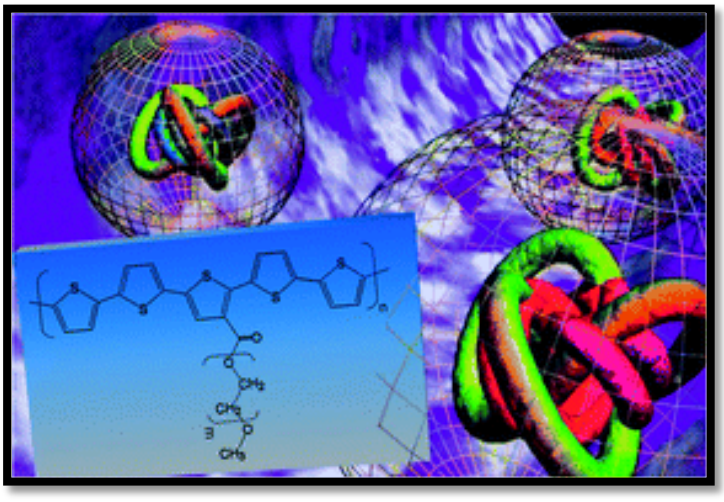

6.1.1 Introduction

Among CPs, PTh is particularly relevant due to its high stability, easy of chemical and structural modification, and controllable electrochemical behavior.[1] However, practical applications of this CP were limited for some time because of its serious problems of solubility and processability. These problems were resolved by incorporating substituents (*e.g.* alkyl chains) at the 3-position of the Th ring, which produced not only processable materials but also facilitated their complete chemical and physical characterization.[2] Moreover, the stability of poly(3-alkylthiophene)s in the doped state is achieved by introducing alkoxy groups, which in addition improve the solubility in polar solvents.[3-6]

Incorporation of polar substituents at the 3-position of the Th ring can be used for purposes other than improve solubility and processability. Specifically, in this work we design and prepare 3-substituted Th monomers to fabricate a new hybrid material based on conducting PTh and the isolating PEG, a well-characterized and readily available linear polyether diol. Although PEG is not biodegradable,[7] their characteristics as biocompatible and non-ionic hydrophilic polymer have motivated many applications in biology, biotechnology and biomedicine.[8,9] Moreover, in the last years PEG has become the most commonly used polymer in hybrid materials (*e.g.* combined with peptides and proteins,[10-12] other polymers,[13,14] and inorganic substrates[15-17]).

Both multiblock and graph copolymers made of two polymeric components with very different properties are considered polymer-polymer hybrid materials able to effectively amplify the characteristics and properties of their individual components. Within this context, some PTh derivatives have been recently combined with PEG to produce hybrid materials with particular properties. A very recent example is the all conjugated diblock PTh copolymer independently prepared by Hayward and co-workers[18] and Park and coworkers,[19-21] which contains non polar hexyl and polar triethylene glycol side groups blocks. This amphiphilic material, denoted P(3HT-*b*-3EGT) (Figure 1), was synthesized using Gridnard Metathesis (GRIM) polymerization methods, which allowed a very narrow molecular weight distribution ($M_w/M_n \approx 1.06$). In polar solvent conditions P(3HT-*b*-3EGT) was found to assemble into polymeric

vesicles with a hydrophobic crystalline interior and a hydrophilic amorphous exterior, which were used to encapsulate a hydrophobic guest polyfluorene.[19,20] In contrast, in very poor solvent conditions P(3HT-b-3EGT) formed suspended crystalline fibrils that upon the addition of potassium ions drives the formation helical nanowires able to bundle into superhelical structures.[18] On the other hand, in a very recent study, Liu *et al.*[22] modified the surface of PTh and poly(3-methylthiophene) films, which were produced by anodic polymerization, using UV-light-induced graft copolymerization with PEG monomethacrylate. The surface hydrophilicity of the grafted materials was found to be significantly higher than those of the two CPs.

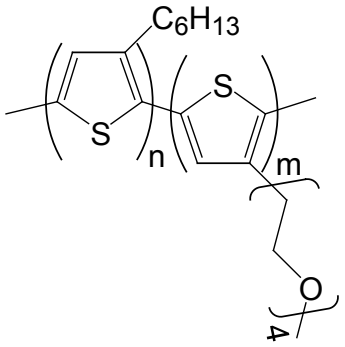

Figure 1. Molecular structure of P(3HT-*b*-3EGT).

In this work we used a strategy that combines chemical and electrochemical procedures to synthesize all conjugated hybrid materials that consists on graft copolymers with a PTh backbone and chains of PEG grafted to the backbone. Two copolymers, which differ in the molecular weight of PEG chains, have been prepared. These materials have been denoted PTh-*g*-PEG_{1000} and PTh-*g*-PEG_{2000} (Figure 2), where the sub-index refer to the molecular weight of the PEG chains (*i.e.* M_w=1000 and 2000, respectively). The fabrication of these two materials has allowed us to examine and rationalize the influence of the length of the grafted PEG chains on the structure and properties as well as to establish relationships with possible biotechnical applications, such as the ability to adsorb proteins.

The macromonomers needed to produce PTh-*g*-PEG_{1000} and PTh-*g*-PEG_{2000} have been prepared using a chemical route that started from 3-thiophene carboxylic acid. The products obtained at each step of such chemical route have been characterized by ^{1}H-NMR, FTIR and gel permeation chromatography (GPC). The macromonomers have

been anodically polymerized to produce the corresponding graft copolymers, which have been characterized using FTIR and XPS. Moreover, the morphology and electrochemical properties of these hybrid materials have been investigated in detail using SEM, AFM and CV. Finally, the ability of the two hybrid materials to adsorb both extracellular and plasma proteins have been examined, results allowing us to propose the biotechnical application of these hybrid materials.

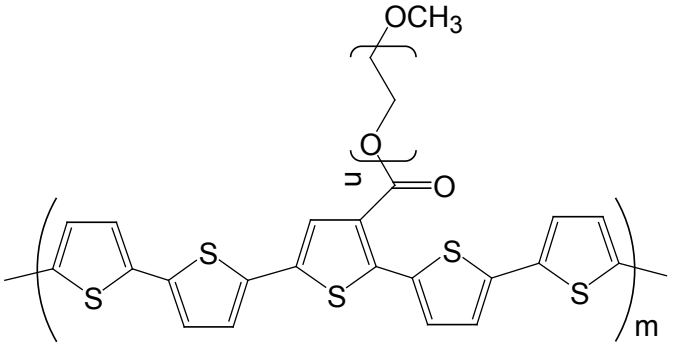

PTh-*g*-PEG_{1000}: *n*= 22

PTh-*g*-PEG_{2000}: *n*= 44

Figure 2. Molecular structure of PTh-g-PEG_{1000} and PTh-g-PEG_{2000}.

6.1.2 Methods

Materials. PEG methyl ether M_w=2000 (PEG_{2000}; Aldrich), PEG methyl ether M_w=1000 (PEG_{1000}; Aldrich), 3-thiophene carboxylic acid (Aldrich), N,N'-dicyclohexylcarbodiimide (DCCI; Merk), 4-dimethylamino pyridine (DMAP; Aldrich), 2,2'-bithiophene-5-boronic acid pinacol ester (Aldrich) and $Pd(PPh_3)_4$ (Aldrich) were used as received. All the solvents were purified and dried by usual methods.

^{1}H-NMR. spectra were recorded at room temperature on a Bruker Avance DRX-400 spectrometer (400 MHz) as solutions in acetone d_6. Chemical shifts are reported in ppm and referenced to TMS as internal standard.

GPC. The relative molecular weights were determined by GPC using a PL-EMD instrument, PS standards for the calibration plot and THF as elution solvent.

FT-IR spectroscopy. Spectra were recorded on a Bruker Vertex 70 FTIR spectrometer, equipped with a diamond ATR device (Golden Gate, Bruker) in transmission mode, by using KBr pellets.

Anodic polymerization and electrochemical assays. All electrochemical experiments were carried out in a standard three-electrode cell under nitrogen atmosphere (99.995% in purity) at room temperature. The anodic compartment was filled with 15 mL of a 1mM monomer solution in a mixture of acetonitrile:dichloromethane (50:50 v/v) containing 0.1 M of a supporting electrolyte, while the cathodic compartment was filled with 10 mL of the same electrolyte solution. The two electrolytes used in this work were $LiClO_4$ and Bu_4NPF_6. Steel AISI 316 and ITO sheets of 1.0×0.5 and 0.5×0.5 cm^2, respectively, were employed as WE. The CE was a Pt sheet of 1.0×0.50 cm^2 while the RE was an Ag|AgCl electrode containing a KCl saturated aqueous solution (Eº = 0.222 V at 25ºC), which was connected to the working compartment through a salt bridge containing the electrolyte solution. CA and CV assays were performed with an Autolab PGSTAT302N equipped with the ECD module (Ecochimie, The Netherlands).

The electroactivity, which refers to the charge storage ability, and the electrochemical stability (electrostability) were determined by CV. Specifically, the electrostability was evaluated by determining the loss of electroactivity with the number of consecutive oxidation-reduction cycles (*LEA*, in %):

$$LEA = \frac{\Delta Q}{Q_I}\ 100 \qquad (1)$$

where ΔQ is the difference between the voltammetric charges (in C) of the second and the last oxidation-reduction cycle, and Q_I is the voltammetric charge corresponding to the first cycle. Both the electroactivity and the *LEA* were determined in acetonitrile solution with 0.1 M $LiClO_4$, a scan rate of 50 $mV{\cdot}s^{-1}$ being employed in all cases.

XPS. XPS analyses were performed in a SPECS system equipped with a high-intensity twin-anode X-ray source XR50 of Mg/Al (1253 eV / 1487 eV) operating at 150 W, placed perpendicular to the analyzer axis, and using a Phoibos 150 MCD-9 XP detector. The X-ray spot size was 650 μm. The pass energy was set to 25 and 0.1 eV for the survey and the narrow scans, respectively. Charge compensation was achieved with a combination of electron and argon ion flood guns. The energy and emission current of the electrons were 4 eV and 0.35 mA, respectively. For the argon gun, the

energy and the emission current were 0 eV and 0.1 mA, respectively. The spectra were recorded with a pass energy of 25 eV in 0.1 eV steps at a pressure below 6×10^{-9} mbar. These standard conditions of charge compensation resulted in a negative but perfectly uniform static charge. The C 1s peak was used as an internal reference with a binding energy of 284.8 eV. High-resolution XPS spectra were acquired by Gaussian/Lorentzian curve fitting after S-shape background subtraction. The surface composition was determined using the manufacturer's sensitivity factors.

SEM. SEM studies were carried out using a FIB Zeiss Neon 40 scanning electron microscope operating at 6 kV, equipped with an EDX spectroscopy system. Samples were mounted on a double-side adhesive carbon disc and sputter-coated with a thin layer of carbon to prevent sample charging problems.

AFM. Topographic AFM images were obtained with a Molecular Imaging PicoSPM using a NanoScope IV controller under ambient conditions. The tapping mode AFM was operated at constant deflection. The row scanning frequency was set to 1 Hz and the physical tip-sample motion speed was 10 $\mu m\cdot s^{-1}$. The r_{AFM} was determined using the statistical application of the Nanoscope software, which calculates the average considering all the values recorded in the topographic image with exception of the maximum and the minimum. AFM measurements were performed on various parts of the films, which produced reproducible images similar to those displayed in this work. The scan window sizes used in this work were 5×5 and 2×2 μm^2.

Optical profilometry. The thickness and roughness (r_{op}) of the films was determined using a WYKO 9300NT optical profiler (Veeco, Plainview, NY). Different scratches were intentionally provoked on PTh-*g*-PEG_{1000} and PTh-*g*-PEG_{2000} films and measured to allow statistical analysis of data. Imaging of the films was conducted using the following optimized settings: vertical scanning interferometry (VSI) mode, full resolution, 5-mm back scan and 10-mm primary scan, 10× and 50× Michelson LR objective lens (fields of view of 2.0×) for image sizes of 237×315 μm^2 and 64×48 μm^2, respectively.

Adsorption of proteins. Analyses to examine the adsorption of proteins onto the surface of PTh-*g*-PEG_{1000} and PTh-*g*-PEG_{2000} films were performed using BSA

(Fraction V) and collagen type I (from Sigma Chemical Co., USA). Materials were incubated with 500 μL of 10% protein solution prepared in milli-Q water for 24 h. Samples were washed three times with PBS solution. Adsorbed proteins were removed by adding 100 μL of extraction buffer (0.32 M sucrose, 3 mM $CaCl_2$, 2 mM $MgCl_2$, 0.1 mM EDTA, 1 mM DTT, 0.5 mM PMSF and 0.5 % NP-40).

Adsorbed proteins were measured using a commercial protein quantification reagent (BioRad, USA) based on Bradford method by colorimetric detection of the cuprous cation obtained by protein Cu^{2+} reduction in an alkaline medium. The absorbance was read at 590 nm against a calibration curve using a BSA working range of 1.25-25 μg/mL. Steel sheets were used as protein binding controls.

6.1.3 Results and Discussion

Synthesis and characterization of macromonomers

A two-steps process, which is schematically depicted in Figure 3a, has been used for the preparation of PTh-g-PEG_{1000} and PTh-g-PEG_{2000}. The first step consists in the chemical synthesis of the corresponding macromonomers, hereafter denoted Th_5-PEG_{1000} and Th_5-PEG_{2000}, respectively, while the second step refers to the anodic polymerization of such macromonomers. The chemical route used to obtain Th_5-PEG_{1000} and Th_5-PEG_{2000} is summarized in Figure 3b, details for each step being provided in this section.

2,5-Dibromothiophene-3-carboxylic acid (**1**). The reaction was performed using a method adapted from the literature.[23,24] 8.15 g (0.0637 mol) of 3-thiophene carboxylic acid were placed in a 500 mL round-bottom flask equipped with a magnetic stirrer, condenser, dropping funnel and N_2 inlet-outlet. 159.8 mL of glacial acetic acid were added. Then, 17.6 mL Br_2 were added from the dropping funnel in about 30 minutes. The reaction was maintained at 60°C overnight. After that time, the reaction mixture was placed in an ice-bath and about 300 mL of deionized cold water and some Na_2SO_3 was added to decolorize. The mixture was filtered and the white solid was recrystallized twice from a mixture of water-ethanol 2/1 (v/v).

^{1}H-NMR (acetone d_6): 10.86 ppm (COOH), 7.4 ppm (TiH).

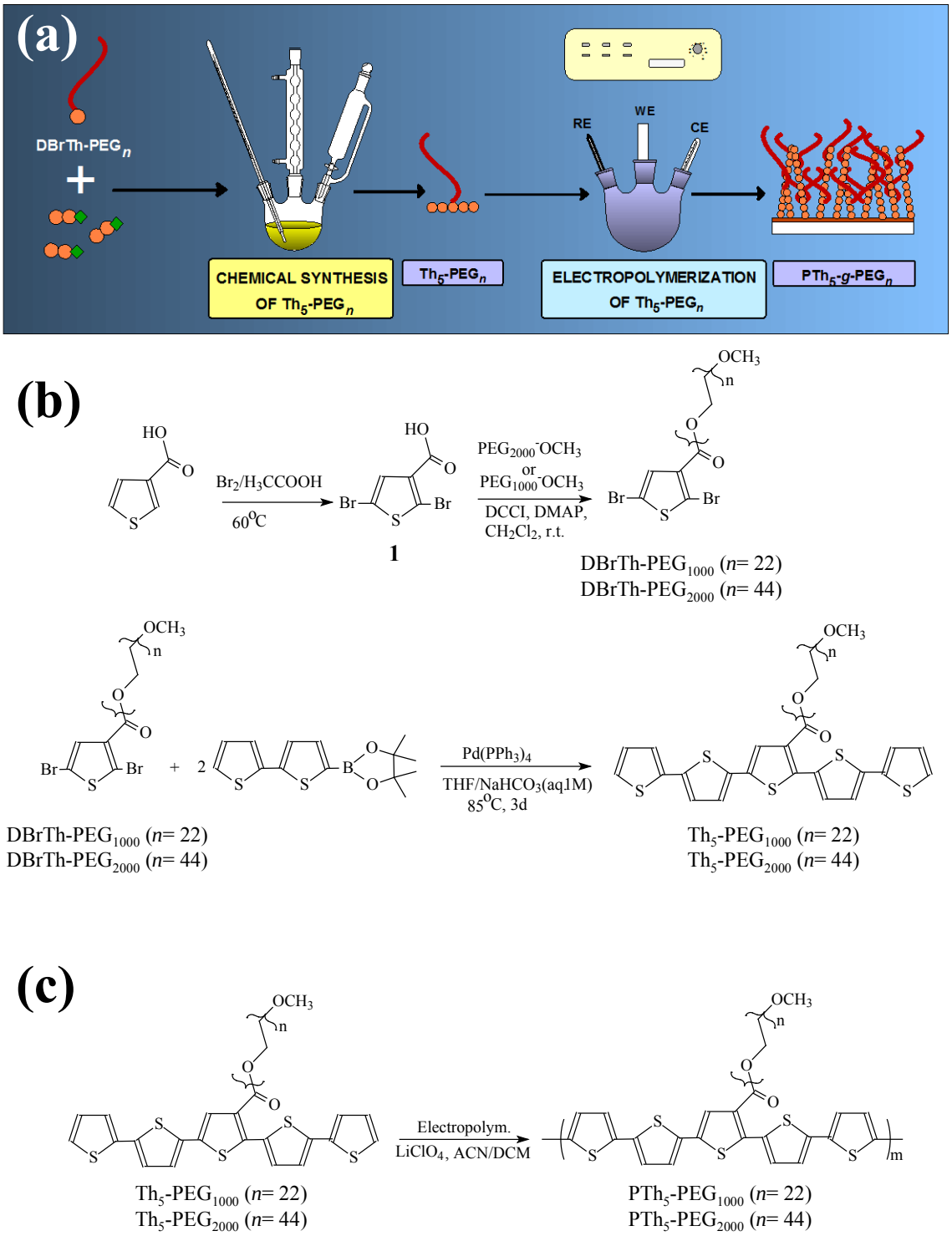

Figure 3. (a) Scheme displaying the processes used to prepare PTh-g-PEG1000 and PTh-g-PEG2000. (b) Reagents and conditions for the synthesis of Th_5 macromonomers. (c) Conditions used for the preparation of the graft copolymers by electropolymerization.

Synthesis of PEG macromonomers functionalized with 2,5 dibromothiopene moieties (DBrTh-PEG$_{1000}$ and DBrTh-PEG$_{2000}$). 8 g (0.004 mol) of PEG_{1000} and 3.432 g

(0.012 mol) of 1 were placed into a three-neck round-bottom flask equipped with a dropping funnel, under N_2. 70 mL of CH_2Cl_2 and 0.1452 g (0.0012 mol) of DMAP were added to the flask. 2.4624 g (0.012 mol) of DCCI in 6 mL CH_2Cl_2 were placed in the dropping funnel and added in about 15 minutes. The mixture was stirred at room temperature for three days. The resulting solution was filtered and precipitated in cold diethyl ether to remove the catalyst and non-reacted reagents. After filtration and drying a white solid (DBrTh-PEG_{1000}) was obtained.

DBrTh-PEG_{2000} was obtained in a similar way using 8 g (0.004 mol) of PEG_{2000}, 1.716 g (0.006 mol) of 1, 0.0726g (0.0006 mol) of DMAP and 1.2312g (0.006 mol) of DCCI.

Synthesis of PEG substituted Th_5 (Th_5-PEG_{1000} and Th_5-PEG_{2000}). The macromonomers Th_5-PEG_{1000} and Th_5-PEG_{2000} were synthesized via a Suzuki coupling reaction between the PEG macromonomers obtained in the previous step (DBrTh-PEG_{1000} and DBrTh-PEG_{2000}, respectively) and 2, 2'-bithiophene-5-boronic acid pinacol ester (Figure 3b). In order to assure a fully functionalization, a big excess of the boronic compound and long reaction time were used.

A 100 mL three neck round bottom flask equipped with a condenser, a rubber septum, nitrogen inlet-outlet and magnetic stirrer was charged with 10 mL 1 M $NaHCO_3$ aqueous solution and 15 mL THF. The solvents were previously desaerated by bubbling nitrogen over a period of 30 minutes and the mixture was refluxed under nitrogen for 3 hours.

A 20 mL three neck round bottom flask equipped in the same way as the previous one was charged under inert atmosphere with 0.416 mmol PEG macromonomer (DBrTh-PEG_{1000} or DBrTh-PEG_{2000}), 1.368 mmol 2,2'-bithiophene-5-boronic acid pinacol ester and 0.0166 mmol $Pd(PPh_3)_4$. The mixture of solvents was introduced with a syringe through the septum. The reaction was maintained under vigorous stirring and with the exclusion of oxygen and light. The mixture was refluxed under nitrogen for 3 days. After that period the reaction was stopped and the mixture was extracted several times with CH_2Cl_2. The organic layer was dried over $MgSO_4$, concentrated at rotaevaporatory and precipitated in cold diethyl ether. After filtration

and drying under vacuum, Th_5-PEG_{1000} and Th_5-PEG_{2000} were obtained as reddish (Th_5-PEG_{1000}) and orange (Th_5-PEG_{2000}) powders. The product were passed through a silica-gel filled column and reprecipitated in cold diethyl ether using CH_2Cl_2 as solvent.

Th_5-PEG_{1000} ^{1}H-NMR (acetone d_6): 7.7-7.06 ppm (aromatic protons of penta-thiophene), 4.45-4.38 ppm (CO–OCH_2); 3.9-3.44 ppm (CH_2O from PEG); 3.40 ppm (OCH_3). M_n(GPC)= 2120, P.D.=1.03. Th_5-PEG_{2000} ^{1}H-NMR (acetone d_6): 7.8-7.05 ppm (aromatic protons of pentathiophene), 4.48-4.36 ppm (CO–OCH_2); 3.9-3.44 ppm (CH_2O from PEG); 342 ppm (OCH_3). M_n(GPC)= 3140, P.D.=1.04.

Chemical characterization of macromonomers

In the ^{1}H-NMR spectrum of Th_5-PEG_{2000} (Figure 4) the ratio between the integrals of the peaks at 4.4 ppm and the aromatic ones is $I_{4.4}/I_{Ar}$=2/11, as expected, proving that the success of the coupling reaction. Due to the multitude of proton types in the new formed Th_5 sequence, the aromatic region of the ^{1}H-NMR spectrum is complex. In spite of this, individual signals were identified as shown in Figure 4. The ^{1}H-NMR spectrum of Th_5-PEG_{1000} (Figure 4) is very similar to that of Th_5-PEG_{2000}, even though some differences in the intensities of the peaks at the aromatic region are noticed.

The GPC traces of all the macromonomers using THF as eluent were unimodal and narrow. GPC measurements of Th_5-PEG_{1000} and Th_5-PEG_{2000} show slightly high molecular weights as compared with the expected theoretical values (assuming the value of M_n= 1000 and 2000 for the commercial PEG used as starting materials). For example, measurements for Th_5-PEG_{2000} led to $M_{n,GPC}$= 3130 and P.D.= 1.04 while the theoretical molecular weight is $M_{n,Th}$= 2430. The same observation could be made for the GPC data of Th_5-PEG_{1000}: $M_{n,GPC}$= 2407, PDI= 1.035 and $M_{n,Th}$= 2282. Generally, GPC measurements of PEGs using columns calibrated with PSt standards furnish overestimated molecular weights due to the difference in polarity of the two polymers. Moreover, the macromonomers architecture has a negative influence on the GPC results since the presence of both the Th_5 rigid sequence and the PEG branch can also induce errors on the measurements. On the other hand, molecular weights obtained from ^{1}H-NMR spectra are also susceptible of errors due to the eventual

presence of adsorbed water or solvents traces, which can affect the overall value of CH_2O protons integral. Taken in account these facts, further calculations we carried out using the theoretical values for the molecular weights of the macromonomers.

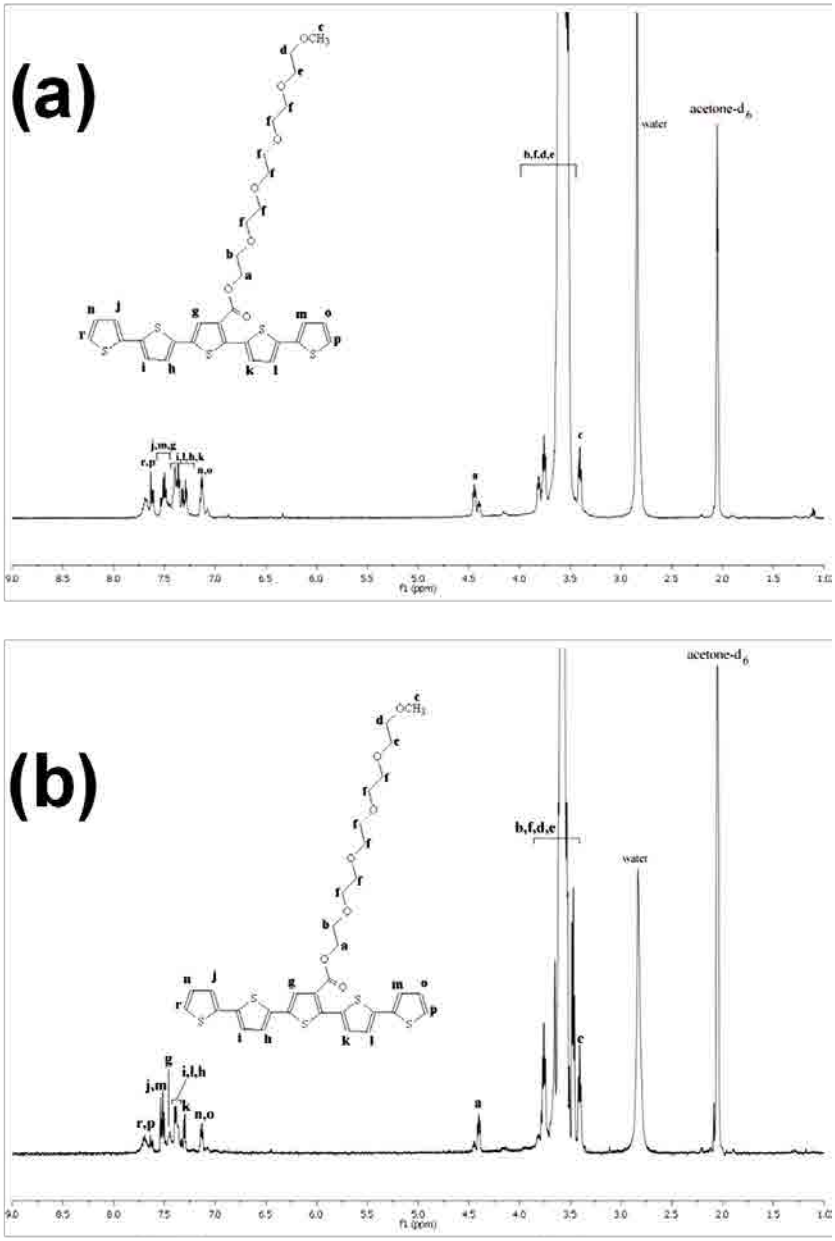

Figure 4. 1H-NMR spectrum in acetone-d6 of (a) Th5-PEG1000 and (b) Th5-PEG2000 macromonomers.

FTIR spectra of DBrTh-PEG_{1000} and DBrTh-PEG_{2000} (Figure 5) present strong absorptions originated by the PEG component at 2884 ($\nu_{as}CH_2$), 2738 (ν_sCH_2), 1464 (δCH_2), 1361, 1342 (CH_2 wagging), 1277 (CH_2 twisting), 1241 (CH_2 twisting and C–O–C stretching), 1150 (ν CO), 1114 (C–O–C stretching), 1061 (CH_2 rocking and C–O–C stretching), 964 (CH_2 rocking), 841 (r (CH_2)+ ν(C–O–C)) and 528 cm^{-1}.[24,25] Additional

peaks (that are missing in the IR spectra of the starting PEG_{1000} or PEG_{2000}), which have been attributed to the 2,5-bromo-thiophene moiety, appear at 3091 (shoulder), 1524, 1423, 1005 (shoulder), 765 and 497 cm^{-1}. The last signal has been assigned to the νC–Br bonds. The strong peak from 1728 cm^{-1} has been attributed to the ν(C=O) from the new formed ester group.

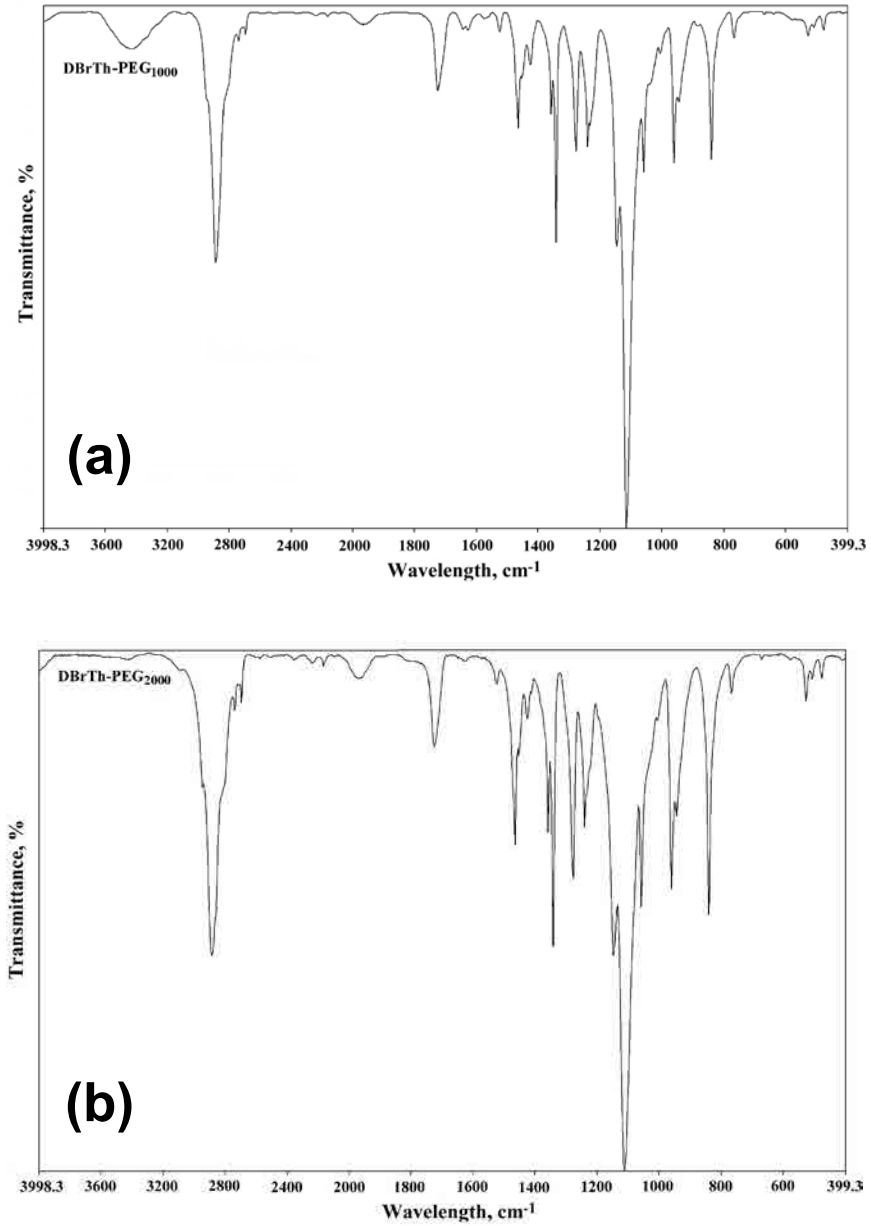

Figure 5. FTIR spectra of: (a) DBrTh-PEG_{1000}; and (b) DBrTh-PEG_{2000}.

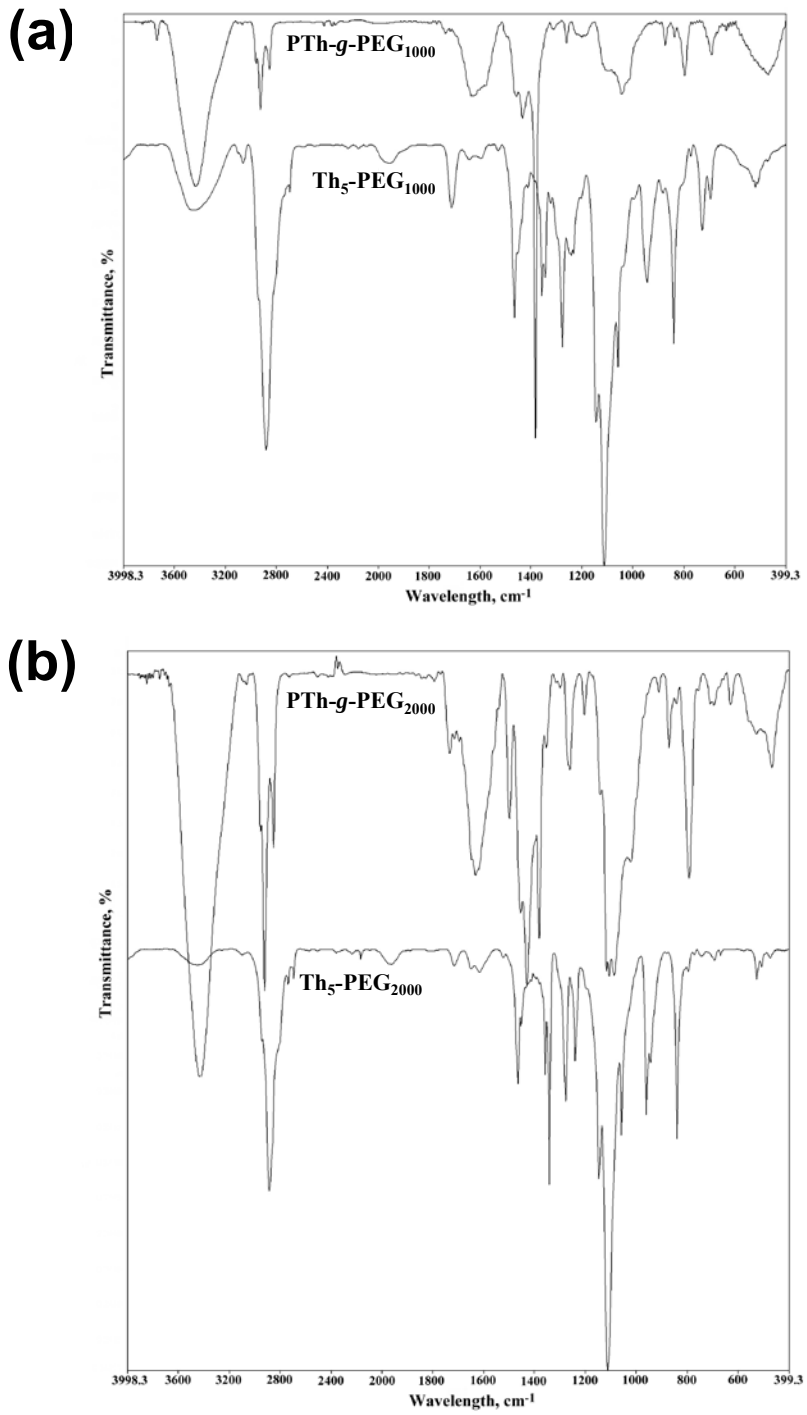

Figure 6. FTIR spectra of: (a) Th5-PEG1000 and PTh-g-PEG1000; and (b) Th5-PEG2000 and PTh-g-PEG2000.

The specific absorptions of PEG mentioned for DBrTh-PEG_{1000} and DBrTh-PEG_{2000} are also present in the FTIR spectra of Th_5-PEG_{1000} and Th_5-PEG_{2000}, which are displayed in Figures 6a and 6b, respectively. The bands of the thienyl rings are also present but with a lower intensity. The peaks attributed to the ν(C=O) in the ester linkage between the Th rings and PEG side chains are present in the spectra of both

macromonomers at 1712 cm^{-1}. Moreover, characteristic absorbances of the Th rings are present in the spectra of macromonomers. Specifically, in the spectrum of Th_5-PEG_{1000} the signals belonging to the aromatic C_α–H and C_β–H stretching vibrations appear at 3100 and 3056 cm^{-1}, respectively. In the spectrum of Th_5-PEG_{2000} absorptions corresponding to similar stretching vibrations are present at 3106 and 3073 cm^{-1}. Peaks indicating a conjugation between the Th rings along the main chain[25] are detected at 1641 / 1650 and 1594 / 1616 cm^{-1} in the spectra of Th_5-PEG_{1000} / Th_5-PEG_{2000}. The absorptions corresponding to the antisymmetric and symmetric stretching vibrations of the thienyl rings[26,27] appear at 1527 / 1524 and 1390 / 1434 cm^{-1}, respectively, in the spectra of Th_5-PEG_{1000} / Th_5-PEG_{2000}. On the other hand, the absorptions due to to C–S bending vibrations are found at 696 cm^{-1} in the spectrum of Th_5-PEG_{1000} and at 694 and 671 cm^{-1} in the spectrum of Th_5-PEG_{2000}.

Polymerization and chemical characterization of the polymers

Figure 3c summarizes the anodic polymerization process used to produce PTh-g-PEG_{1000} and PTh-g-PEG_{2000}. Figure 7a compares the cyclic voltammogram recorded in ITO electrodes for the anodic oxidation of Th_5-PEG_{2000} in a mixture of acetonitrile:dichloromethane with 0.1 M $LiClO_4$ (black line) and 0.1 M Bu_4NPF_6 (grey line). Five anodic processes with anodic peak potentials of 0.73 (O_1), 0.90 (O_2), 1.12 (O_3), 1.50 (O_4) and 1.68 V (O_5) were detected in the voltammogram with $LiClO_4$, while the peaks of anodic and cathodic processes in the oxidation and reduction scans of the mixture with Bu_4NPF_6 appear at 0.77 (O_1), 1.12 (O_2), 1.29 (O_3) and 1.70 (O_4) (i.e. the anodic process at ~ 0.9 V is not detected in the latter electrolyte). All these processes are clearly identified in Figure 7b, which shows the derivative of the potential for the two systems.

The difference between $LiClO_4$ and Bu_4NPF_6 electrolytes should attributed to the different mobility of the ClO_4^- and PF_6^- anions. Previous works showed that ClO_4^- moves more easily in PTh films than other species such as PF_6^-.[28-30] This difference was essentially associated to the interactions between the anions and the polymeric matrix but not to the size of the anions since they are similar (i.e. the radius of ClO_4^- and PF_6^- is 2.90 and 3.01 Å, respectively). Furthermore, the interactions between the polymer and the cations should be also taken into account since in some cases they contribute

to the redox processes. Within this context, it should be noted that the ionic radius of Li^+ is smaller than that of NBu_4^+ and, therefore, the interaction with the ether groups of PEG are expected to be easier for the former than for the latter. On the other hand, Figure 7a includes the CVs of Th_5-PEG_{1000} in acetonitrile:dichloromethane with 0.1 M $LiClO_4$ (dashed line) while the derivative of the potential is displayed in Figure 7c. The six anodic processes with anodic peak potentials of 0.67 (O_1), 0.85 (O_2), 0.97 (O_3), 1.11 (O_4), 1.49 (O_5) and 1.68 V (O_6) are similar to those detected in the voltammogram of Th_5-PEG_{2000} with $LiClO_4$.

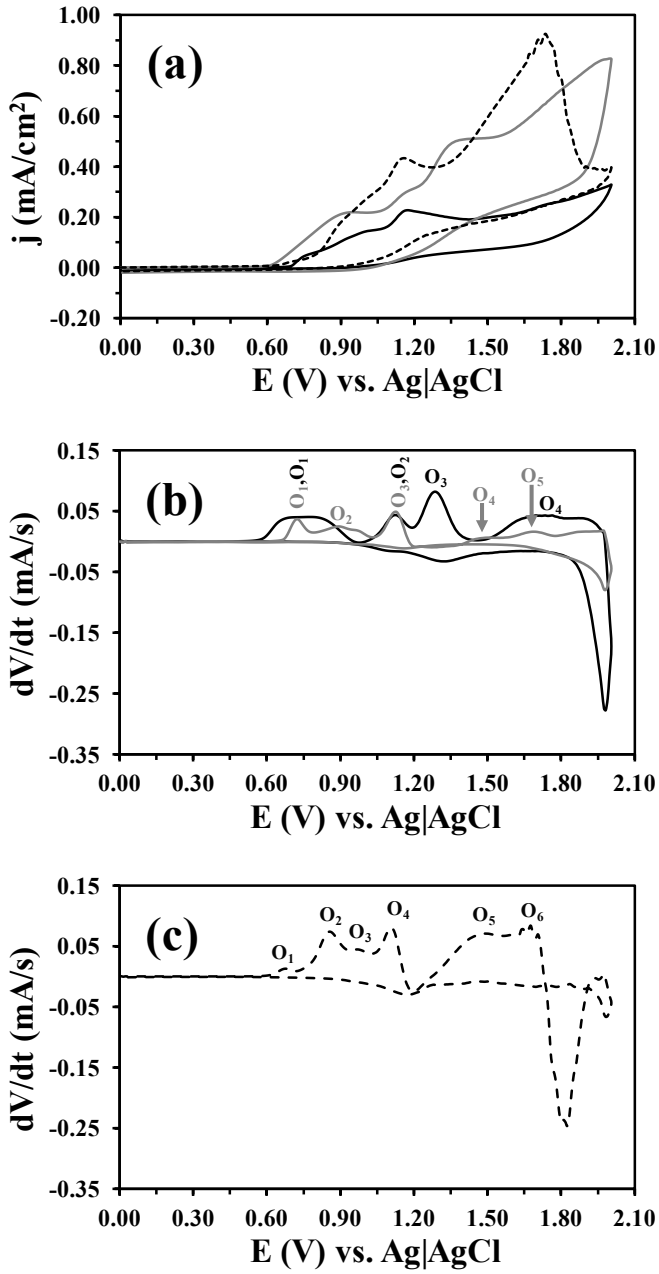

Figure 7. (a) Control voltammograms for the oxidation of a 1 mM of Th_5-PEG_{2000} solution in acetonitrile:dichloromethane (50:50 v/v) with 0.1 M $LiClO_4$ (black line) or 0.1 M Bu_4NPF_6 (gray

line), and of 1 mM of Th_5-PEG_{1000} solution in acetonitrile:dichloromethane (50:50 v/v) with 0.1 M $LiClO_4$ (black dashed line). Voltammograms were recorded using a 0.5×0.25 cm^2 ITO electrode. Initial and final potentials: 0.00 V; reversal potential: 2.00 V. Scan rate: 50 mV/s. The derivative of the potential for the voltammograms recorded for the Th_5-PEG_{2000} and Th_5-PEG_{1000} solutions are displayed in (b) and (c), respectively. The anodic (O) processes are indicated for each case.

According to the results displayed in Figure 7, the potentials considered for the anodic generation of PTh-g-PEG_{1000} and PTh-g-PEG_{2000} in presence of $LiClO_4$ were 0.70 and 75 V, respectively, while PTh-g-PEG_{2000} was also prepared using Bu_4NPF_6 as supporting electrolyte at a potential of 0.80 V. These potentials are very close to the oxidation potential O_1 discussed above (Figure 7) allowing us to maximize the velocity of polymerization process and to avoid the undesirable overoxidation of the generated materials. The two generated materials were deposited on ITO electrodes for spectroscopic, morphological and electrochemical studies, whereas steel AISI 316 electrodes were used for all the biological assays. Although the velocity of the polymerization process was maximized through the choice of the potential, very large polymerization times were required to completely cover the electrodes. Thus, the polymerization time for ITO and steel AISI 316 electrodes was 3000 and 1500 s, respectively, independently of both the length of the PEG branches and the electrolyte.

The FTIR spectrum of PTh-g-PEG_{1000} and PTh-g-PEG_{2000} obtained at 070 and 0.75 V, respectively, using $LiClO_4$ are included in Figure 6. As it can been seen, the weak band associated to the aromatic C_α–H stretching at 3100 cm^{-1}, which was clearly identified for the macromononers, should be attributed to the to the thienyl end groups of conjugated PTh chains, reflecting the success of the polymerization process. The disappearance of the C_α–H out of plane ring deformation absorption in the spectra of the polymers, which was detected at 727 and 745 cm^{-1} in the spectra of Th_5-PEG_{1000} and Th_5-PEG_{2000}, respectively, reflects the same conclusion. In contrast, the C_β–H stretching and C_β–H out of plane bending vibrations are detected at 3068 and 844 cm^{-1}, respectively, for the two polymers. The intensity of the peaks found at 1641/1650 and 1594/1616 cm^{-1} in Th_5-PEG_{1000}/Th_5-PEG_{2000} increases after polymerization, indicating an enhancement of the conjugation along the main chain. Moreover, these peaks shift to 1630/1636 cm^{-1} in PTh-g-PEG_{1000}/PTh-g-PEG_{2000}. The absorption due to

the antisymmetric and symmetric stretching of the thienyl rings appear at 1582 and 1389 cm^{-1} in the PTh-g-PEG_{1000} spectrum and at 1556 and 1389 cm^{-1} in the PTh-g-PEG_{2000} one. On the other hand, the peak associated with the C=O group of the ester linkage between the all conjugated PTh backbone and the PEG chain appears at 1738 cm^{-1}, indicating a shift of $\Delta\nu$= +26 cm^{-1} with respect to the macromonomers.

Figure 8 depicts the characteristic XPS spectra in the C1s, O1s, S2p and Cl2p regions for PTh-g-PEG_{1000} and PTh-g-PEG_{2000} prepared using $LiClO_4$ as electrolyte, whereas Table 1 summarizes the main information related with the peaks obtained from the deconvolution and the atomic percent composition. Deconvolution of the C1s peak, which was very similar for the two polymers, led to a five Gaussian curves that have been attributed to the O–C=O (289.3 eV), C–O (288.4 eV), C–O–C (286.7 eV), C–S (285.7 eV) and C–C/C=C (284.8 eV) linkages in PTh backbone and PEG branches.[31-34]

The O1s signal consists of four components. The small peaks centered at 529.8 and 528.0 eV correspond to the inorganic oxides of the ITO electrode,[35-37] the presence of these signals reflecting the existence of cracks in the films. The components at 533.2 and 531.9 eV are attributed to the oxygen atoms of the C–O–C and O=C–O bonding, respectively.[34,38] The high resolution XPS of the S2p region for PTh-g-PEG_{1000} and PTh-g-PEG_{2000} is very similar to that recently reported for different PTh derivatives.[33,39-41] The main observations refer to the spin-split sulphur coupling, $S2p_{3/2}$ (164.0-164.1 eV) and the $S2p_{1/2}$ (165.2-165.3 eV), with a separation of 1.2 eV and to the relatively high energy broad tail produced by positively charged sulphur within the thiophene ring. Oxidized species are due to the fact that samples were repeatedly exposed to the atmosphere after their preparation. These results are fully consistent with results reported by other authors for PTh derivatives.[42,43] Finally, the peaks centred at 208.2-208.4 and 209.7-210.0 of the Cl2p region has been attributed to the $Cl2p_{3/2}$ and $Cl2p_{1/2}$ of the perchlorate anion,[41,44] the separation being 1.6 and 1.5 eV for PTh-g-PEG_{1000} and PTh-g-PEG_{2000}, respectively. Interestingly, the high resolution XPS spectrum of the Cl2p region recorded for PTh-g-PEG_{2000} evidences the degradation of the dopant, as is shown by the peaks centred at 200.5 ($Cl2p_{3/2}$) and 202.0 eV ($Cl2p_{1/2}$).[35,45]

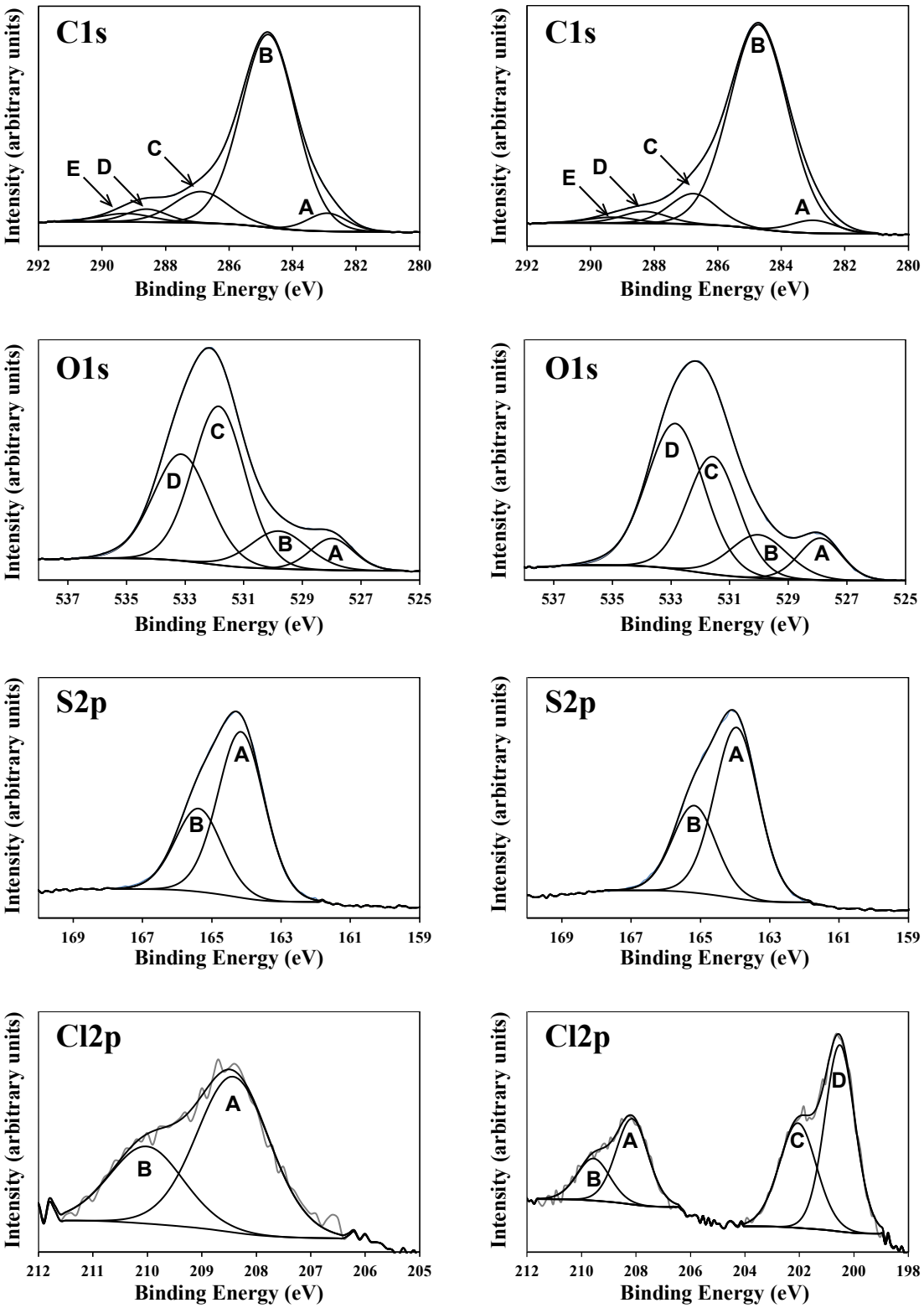

Figure 8. High-resolution XPS spectra for PTh-g-PEG_{1000} (left) and PTh-g-PEG_{2000} (right): C1s, O1s, S2p and Cl2p regions. Peaks from deconvolution, which are labeled with letters, are discussed in Table 1.

Atom	Peak		Center of the peak		Atomic composition	
			***k*= 1000**	***k*= 2000**	***k*= 1000**	***k*= 2000**
C1s	E	O–C=O	289.2	289.3	61.4%	67.4%
	D	C–O	288.6	288.4		
	C	C–O–C	286.8	286.7		
	B	C–S	285.7	285.7		
	A	C–C/C=C	284.8	284.8		
O1s	D	C–O–C	533.2	533.2	30.8%	23.7%
	C	O=C–O	531.9	531.9		
	B	ITO oxides	529.8	529.8		
	A	ITO oxides	528.0	528.0		
S2p	B	C–S ($S2p_{1/2}$)	165.3	165.2	7.0%	7.0%
	A	C–S ($S2p_{1/2}$)	164.1	164.0		
Cl2p	D	ClO_4^- ($Cl2p_{1/2}$)	210.0	209.7	0.8%	1.9%
	C	ClO_4^- ($Cl2p_{3/2}$)	208.4	208.2		
	B	Cl ($Cl2p_{1/2}$)	-	202.0		
	A	Cl ($Cl2p_{3/2}$)	-	200.5		

Table 1. Assignment of the peaks obtained in the high-resolution XPS spectra recorded for PTh-g-PEG_k with k= 1000 and 2000 (Figure 8) and atomic percent composition (C1s, O1s, S2p and Cl2p).

A feature that deserves mention is the detection of Br in the XPS spectra of both PTh-g-PEG_{1000} and PTh-g-PEG_{2000}. Although the peak of Br (Figure 9), which appears at 71.4 eV (C–Br bonding), is not important for the identification of the chemical structure of the two graft copolymers, the existence of this element is very relevant for the polymerization process. Thus, residual C–Br bonds, which arise from the chemical synthesis of the DBrTh-PEG_{1000} and DBrTh-PEG_{2000}, are expected to preclude the growing of the polymer chains during the anodic polymerization. The S/Br ratio obtained using the atomic percent compositions recalculated with Br led is 3.6 and 5.2 for PTh-g-PEG_{1000} and PTh-g-PEG_{2000}, respectively. These values are fully consistent with the fact that anodic polymerization was more difficult and slow for the latter copolymer than for the former one.

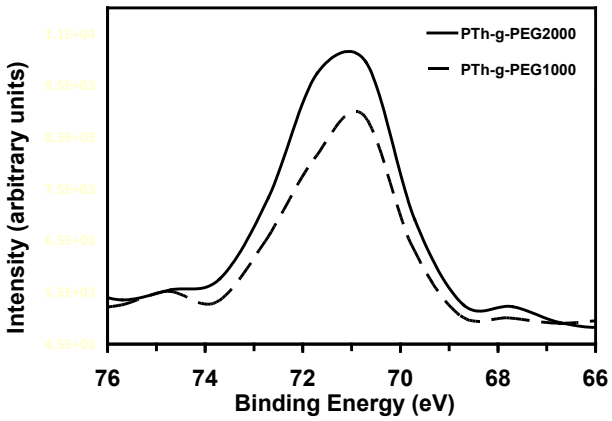

Figure 9. XPS spectra in the Br3d region for PTh-*g*-PEG_{1000} and PTh-*g*-PEG_{2000} prepared using $LiClO_4$ as electrolyte.

Morphology and thickness of the films

SEM micrographs of PTh-g-PEG_{1000} and PTh-g-PEG_{2000} obtained in an acetonitrile:dichloromethane solution with 0.1 M $LiClO_4$ under a constant potential of 0.70 and 0.75 V, respectively, are displayed in Figures 10a and 10b. As it can be seen, the morphology is very similar for the two materials, consisting of a compact distribution of aggregates. Despite such similarity, the size and frequency of the nanometric aggregates is different in the two hybrid materials, suggesting that the influence of the molecular weight of the grafted PEG chains is not negligible. Specifically, nanoaggregates are smaller and more abundant in PTh-g-PEG_{1000} than in PTh-g-PEG_{2000}. These differences are corroborated by the 2D height and 3D topographic AFM images displayed in Figures 12a and 12b for PTh-g-PEG_{1000} and PTh-g-PEG_{2000}, respectively. The latter material shows a very irregular topography, consisting in a dense distribution of sharp peak. In contrast, the surface of PTh-g-PEG_{1000} is more leveled with a few broad peaks randomly dispersed into it. Despite of this difference, the root-mean-square roughness (r_{AFM} in Table 2) of PTh-g-PEG_{1000} and PTh-g-PEG_{2000} are very similar and noticeably low (Table 2).

In order to ascertain if the differences in the topography and morphology are exclusively due to the molecular weight of PEG chains or are also influenced by the anodic potential used for the polymerization processes, the polymerization of PTh-g-PEG_{1000} was repeated considering identical experimental conditions but using a constant potential of 0.75 V. Amazingly, the AFM images of the resulting material, which are displayed in Figure 12c, indicated that these graft copolymers are largely

influenced by the potential used in the polymerization process. Thus, the AFM images of PTh-g-PEG_{1000} and PTh-g-PEG_{2000} produced at 0.75 V are practically identical. Moreover, the r_{AFM} of PTh-g-PEG_{1000} increased by ~25% when the polymerization potential grew from 0.70 to 0.75 V (Table 2). A similar behavior was found for the morphology, the nanometric aggregates observed in the SEM micrographs of the PTh-g-PEG_{1000} films obtained at 0.75 V (Figure 11) being larger than those displayed in Figure 10a.

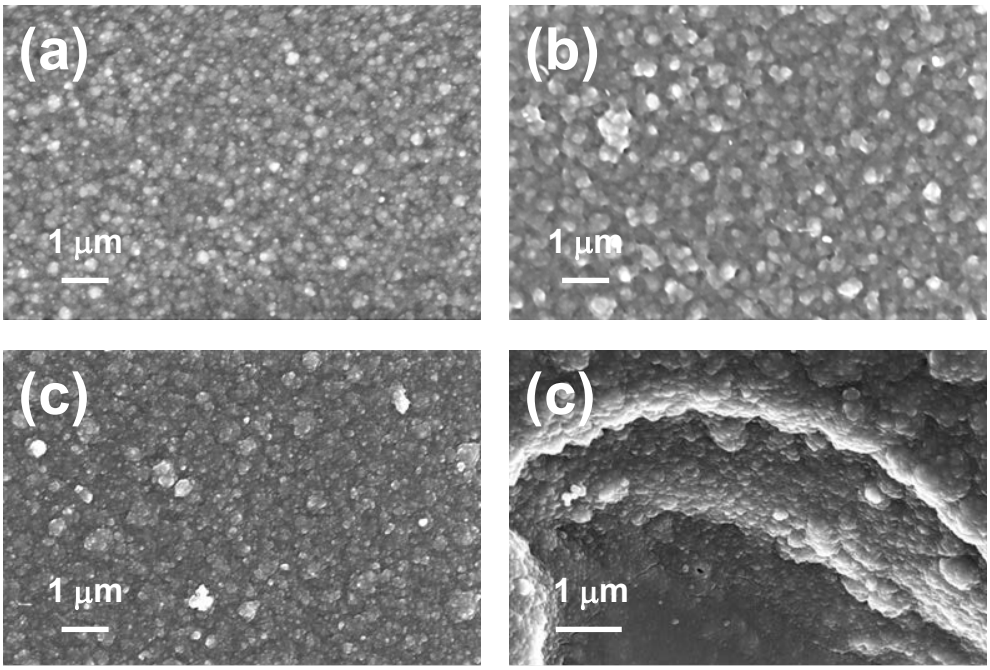

Figure 10. SEM micrographs of: (a) PTh-g-PEG_{1000} prepared using 0.1 M $LiClO_4$ and a fixed potential of 0.70 V; (b) PTh-g-PEG_{2000} prepared using 0.1 M $LiClO_4$ and a fixed potential of 0.75 V; (c) internal and (d) external side of PTh-g-PEG_{2000} prepared using 0.1 M Bu_4NPF_6 and a fixed potential of 0.80 V.

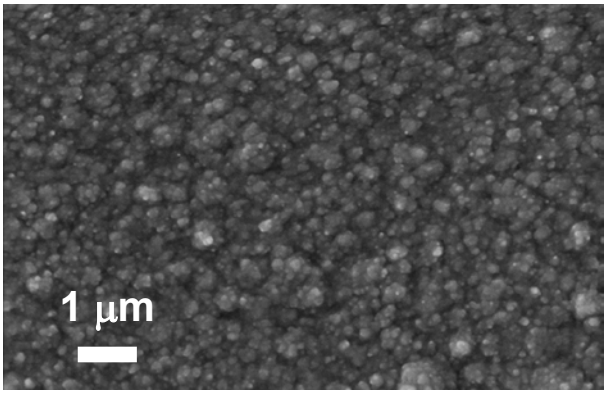

Figure 11. SEM micrograph PTh-*g*-PEG_{1000} prepared using 0.1 M $LiClO_4$ and a fixed potential of 0.75 V.

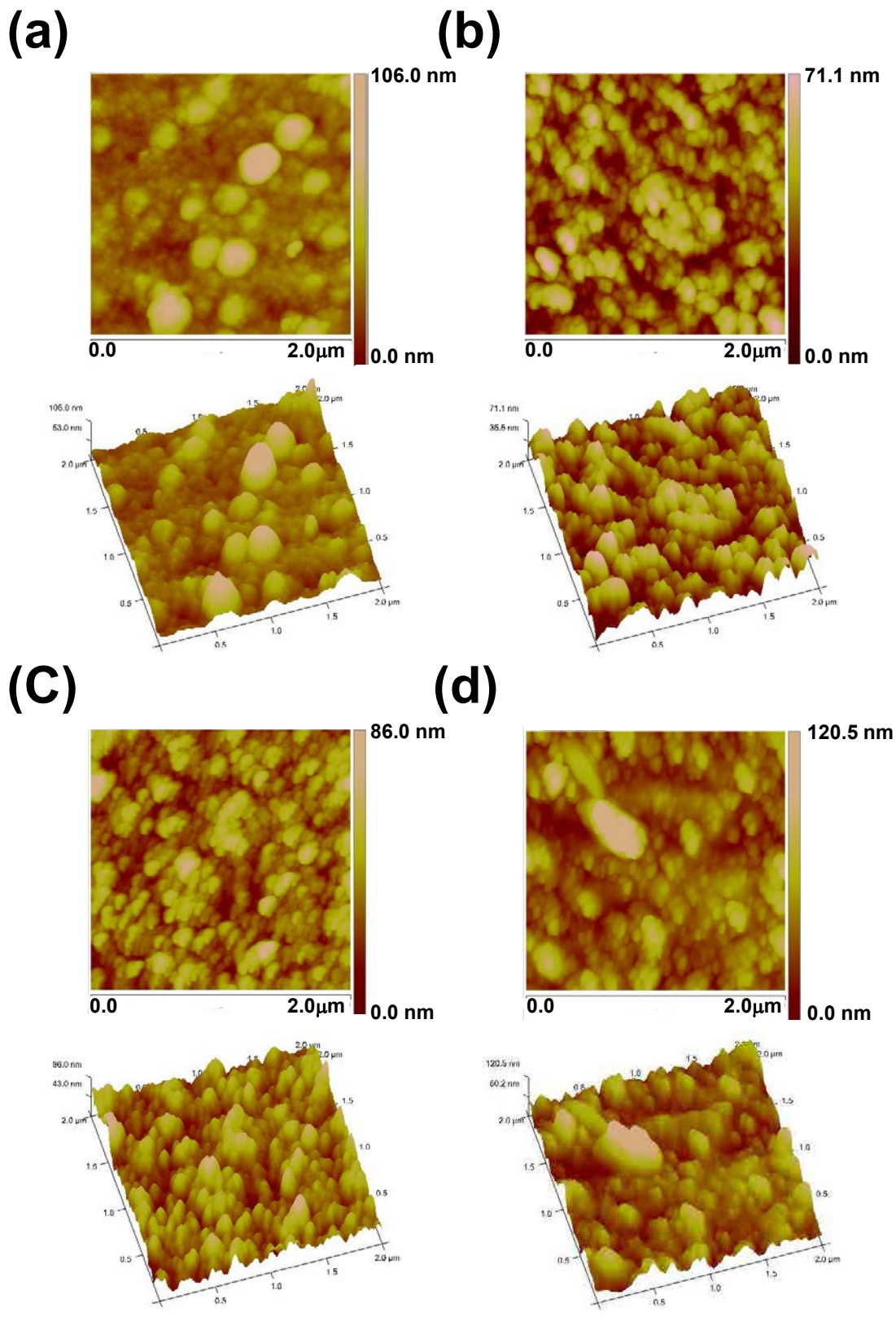

Figure 12. 2D Height and 3D topographic AFM images of: (a) PTh-g-PEG1000 prepared using 0.1 M LiClO4 and a fixed potential of 0.70 V; (b) PTh-g-PEG2000 prepared using 0.1 M LiClO4 and a fixed potential of 0.75 V; (c) PTh-g-PEG1000 prepared using 0.1 M LiClO4 and a fixed potential of 0.75 V; (d) PTh-g-PEG2000 prepared using 0.1 M Bu4NPF6 as polyelectrolyte and a fixed potential of 0.80 V.

Figures 10c and 12d display the SEM micrograph and AFM images, respectively, of PTh-g-PEG_{2000} obtained using Bu_4NPF_6 as supporting electrolyte and a polymerization potential of 0.80 V. As it can be seen, substitution of the electrolyte in the generation medium does not produce drastic changes in the morphology and topography of the copolymer. Indeed, the morphology and topography obtained using Bu_4NPF_6 are intermediate between those of discussed above for the materials generated using $LiClO_4$. On the other hand, in order to check if the morphologies displayed in Figures 10a-10c correspond only to the surface or to the whole sample, PTh-g-PEG_{2000} films were carefully separated from the electrode to examine the morphology of the internal side. As it can be seen from Figure 10d, which displays the SEM micrograph of the copolymer obtained using Bu_4NPF_6 as electrolyte, indicates that films are morphologically homogeneous.

	r_{AFM} (nm)	r_{op} (nm)	ℓ (nm)
PTh-*g*-PEG_{1000} (0.1 M $LiClO_4$, 0.70 V)	11.3±2.2	10.3±1.1	230.5±3.6
PTh-*g*-PEG_{1000} (0.1 M $LiClO_4$, 0.75 V)	14.2±0.8	11.1±0.4	489.4±14.9
PTh-*g*-PEG_{2000} (0.1 M $LiClO_4$, 0.75 V)	12.1±2.1	6.5±1.1	108.8±4.6
PTh-*g*-PEG_{2000} (0.1 M Bu_4NPF_6, 0.80 V)	14.3±1.6	7.4±1.5	204.5±5.2

Table 2. Average RMS roughness determined by atomic force microscopy and optical optical profilometry (r_{AFM} and r_{op}) and average thickness (ℓ) of the graft copolymer films.

Table 2 compares the roughness determined by AFM and optical profilometry (r_{AFM} and r_{op}). As it can be seen, the values provided by the two techniques are in very good agreement, corroborating that the films of the graft copolymers are very flat independently of the molecular weight of the PEG chain, the polymerization potential and the dopant agent. Finally, the average thickness (ℓ) of the different hybrid materials, which was measured by optical profilometry, indicates that the films are within the nanometric scale (Table 2), values ranging from ~100 to ~500 nm depending on the length of the PEG chain, the polymerization potential and the supporting electrolyte.

Electrochemical behavior

Figure 13a compares the first control voltammograms of PTh-g-PEG_{1000} and PTh-g-PEG_{2000} films prepared using polymerization potentials of 0.70 and 0.75 V,

respectively, and $LiClO_4$ as supporting electrolyte. The cyclic voltammogram of PTh-g-PEG_{1000} shows three oxidation processes: two shoulders (O_1 and O_2 in Figure 13a) with anodic peak potentials of 1.00 and 1.28 V and a well-defined anodic peak (O_3 in Figure 13a) with a potential of 1.80 V. All these processes correspond to the formation of electron-deficient species (i.e. polarons and bipolarons). The peak O_3 is related with the formation of cross-links, which block the structure of the material and reduces the mobility of the dopant anions (i.e. the formation of redox pairs is not possible at potentials higher than 1.80 V). Five oxidation processes are detected in the cyclic voltammogram of PTh-g-PEG_{2000}: the three shoulders (O_1, O_2 and O_4 in Figure 13a) with anodic peak potentials of 0.95, 1.20 and 1.65 V, and the two anodic peaks (O_3 and O_5 in Figure 13a) with anodic peak potentials of 1.38 and 1.80 V. As occurred for PTh-g-PEG_{1000}, the peaks at the higher potentials, especially the process defined by O_5, have been associated to cross-links between conjugated polymer chains.

Control voltammograms also indicate that the electroactivity, which increases with the similarity between the anodic and cathodic areas of the first control voltammograms, is higher for PTh-g-PEG_{1000} than for PTh-g-PEG_{2000}. This result indicates that the structure of the latter graf copolymer is more compact than that of the former one, making difficult the access of the dopant ions. This feature is fully consistent with AFM images displayed in Figures 12a and 12b, which reflect that the geometry of the aggregates observed at the submicrometric length-scale is simpler for PTh-g-PEG_{1000} than for PTh-g-PEG_{2000}. Both the more compact structure and the lower ability to store charge of PTh-g-PEG_{2000} should be also related a higher degree of cross-linking. Indeed, XPS results indicated that the difficulties in the polymerization of this material with respect to PTh-g-PEG_{1000} are not only due to the higher molecular weight of the PEG chain, which provokes more steric interactions and reduces the diffusion of the monomers, but also to its higher content of Br. This result combined with the control voltammograms displayed in Figure 13a has been interpreted as a higher tendency of PTh-g-PEG_{2000} to form cross-links.

Figure 13b shows the first control voltammograms of PTh-g-PEG_{2000} films prepared using $LiClO_4$ (polymerization potential: 0.75 V) and Bu_4NPF_6 (polymerization potential: 0.80 V), as supporting electrolytes. Considering that the thickness of the

latter film is practically twice that of the former one (Table 2), voltammograms displayed in Figure 13b indicate the ability to store charge is higher for the film doped with ClO_4^- than for that with PF_6^- (i.e. the access of the ClO_4^- ions into the polymeric matrix is easier than that of PF_6^- ions). This feature is fully consistent with previous studies,[28-30] which reported a higher mobility for ClO_4^- than for PF_6^- in PTh films.

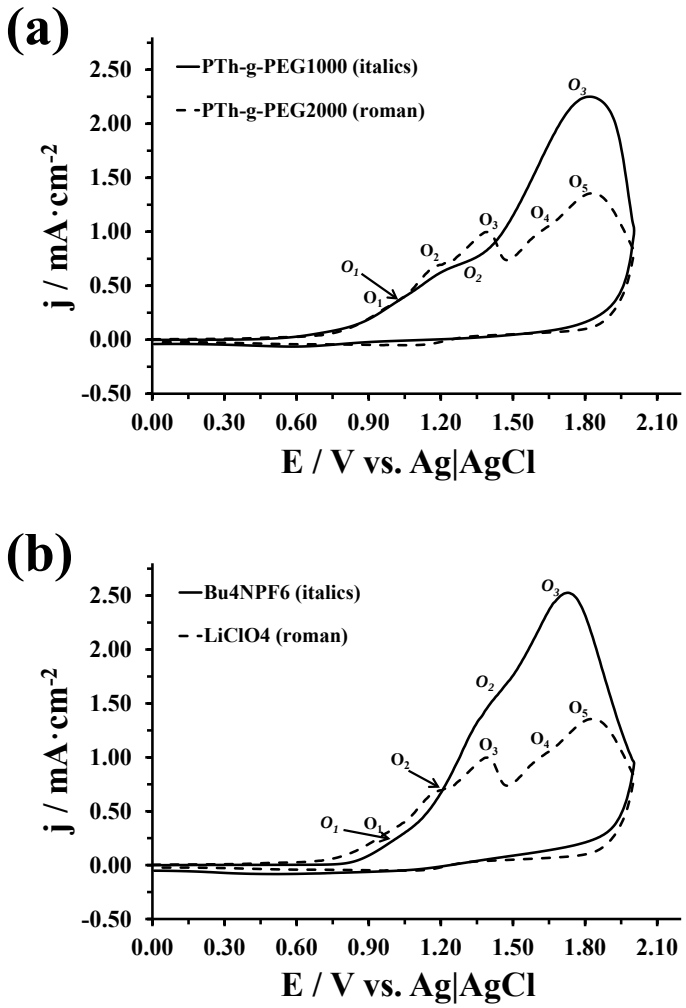

Figure 13. Control voltammograms collected using a scan rate of 50 mV·s-1 of: (a) PTh-g-PEG1000 and PTh-g-PEG2000 prepared using a fixed potential of 0.70 and 0.75 V, respectively, and 0.1 M LiClO4; (b) PTh-g-PEG2000 prepared using 0.1 M Bu4NPF6 (polymerization potential: 0.80 V) and 0.1 M LiClO4 (polymerization potential: 0.75 V).

The voltammogram of the copolymer prepared with Bu_4NPF_6 shows three oxidation processes. The anodic peak potentials of the first two shoulders (O_1 and O_2 in Figure 13b) are 1.00 and 1.45 V whereas the potential of the anodic peak is 1.72 V (O_3 in Figure 13b). As occurred previously (Figure 13a), these processes should be interpreted as the formation of polarons and bipolarons in the polymer chains. The O_1

and O_2 shoulders indicate that the first and second oxidation processes overlap, ocurring the same with the second and third processes. This feature evidences the formation of electron-deficient species in different regions of the polymer chain, as is typically observed in CPs,[47,48] even though this phenomenon is more pronounced in the graft copolymers under study. The higher definition of O_3 should be attributed to structural irregularities related with the formation of cross-links. Despite of this, both its lower electroactivity and the higher number of oxidation processes suggest that PTh-g-PEG_{2000} prepared using $LiClO_4$ presents a higher degree of branching and inter-ring linkages than PTh-g-PEG_{2000} prepared using Bu_4NPF_6.

The electrochemical stability (i.e. electrostability) of the graft copolymers was determined by recording the control voltammograms from 0.00 to 1.00 V for 10 consecutive oxidation-reduction cycles. Figure 14 compares the control voltammograms of PTh-g-PEG_{1000} and PTh-g-PEG_{2000} after 1 and 10 consecutive oxidation-reduction cycles. As it can be seen, the behavior of the two graft copolymers is very different, independently of the dopant used for the preparation of the latter. The behavior of PTh-g-PEG_{2000} is, independently of the electrolyte, similar to that previously reported for other PTh and polypyrrole derivatives.[49-52] Thus, the oxidation and reduction areas of the voltammograms decrease with the number of redox cycles evidencing a loss of electroactivity (Figures 14b and 14c), even though the electrostability is significantly higher for the material doped with PF_6^- (LEA= 29%) than for the one with ClO_4^- (LEA= 45%). This loss of electroactivity is due to the structural changes induced by the consecutive redox cycles in the CP, as was recently proved by SEM in a morphological study of a PTh derivative.[53] More specifically, molecular aggregates tend to collapse upon consecutive redox cycles producing a reduction in the porosity of the material, which explains that the access and escape of the dopant anions into the polymeric matrix become more difficult.

In contrast, the oxidation and reduction areas of the voltammograms recorded for PTh-g-PEG_{1000} doped with ClO_4^- increases considerably with the number of consecutive oxidation-reduction cycles. This phenomenon, which is maintained even during a higher number of cycles (not show), has been also attributed to structural changes. In this case, the porosity of the material increases with the number of cycles

facilitating the access and escape of the dopant ions during the oxidation and reduction processes, respectively. According to these electrochemical observations, PTh-g-PEG_{1000} should be considered as a self-electrostabilized material.

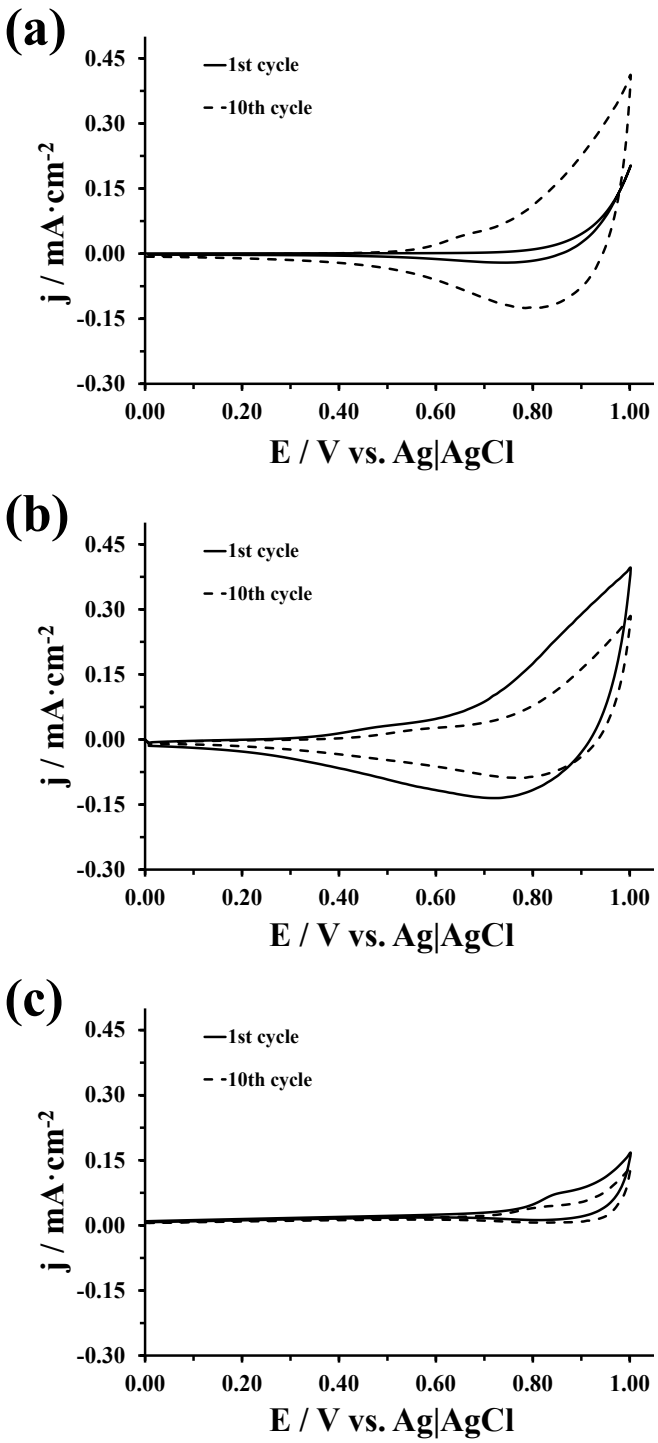

Figure 14. Control voltammograms after one and ten consecutive oxidation-reduction cycles for: (a) PTh-g-PEG1000 prepared using a fixed potential of 0.70 V and 0.1 M LiClO4; (b) PTh-g-PEG2000 prepared using a fixed potential of 0.75 V and 0.1 M LiClO4; and (c) PTh-g-PEG2000 prepared using a fixed potential of 0.80 V and 0.1 M Bu4NPF6.

Adsorption of proteins

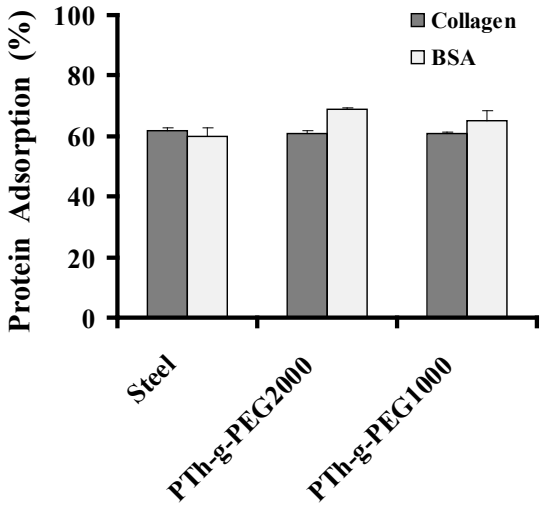

Figure 15. Adsorption (in %) of collagen and BSA onto the surface of PTh-g-PEG_{1000} and PTh-g-PEG_{2000} prepared using a fixed potential of 0.70 and 0.75 V, respectively, and 0.1 M $LiClO_4$. Three samples were analysed for each group. Bars represent the mean ± standard deviations. The asterisk indicates a significant difference with the control (steel), Turkey's test ($p < 0.05$).

In order to investigate the ability of the PTh-g-PEG_{1000} and PTh-g-PEG_{2000} surfaces to interact with different types of proteins, adsorption protein assays were carry out using collagen type I (fibrillar extracellular matrix protein) and BSA (globular plasma protein). Adsorption is a non-specific phenomenon mediated by non-specific forces, as for example electrostatic and hydrophobic interactions. The percentage of proteins adsorbed onto the surface of the two graft copolymers with respect to the amount initially added to the incubation method is represented in Figure 15. As it can be seen, the adsorption was relatively high in all cases (i.e. higher than 60%), detailed analysis revealing some interesting features. Thus, although the adsorption of collagen was similar in all cases (i.e. 61-62 %), including the control, BSA prefers PTh-g-PEG_{1000} (65%) and, especially, PTh-g-PEG_{2000} (69%) with respect to steel (61%). The difference between PTh-g-PEG_{1000} and PTh-g-PEG_{2000} should be attributed not only to the molecular weight of the PEG chain but also to the cross-links, which are more abundant in the latter than in former. Thus, the distribution of charged species (i.e. electron-deficient polarons and bipolarons, and dopant anions) in the polymeric matrix becomes more random and homogeneous when the degree of cross-linking increases. Such distribution is particularly appropriated for the adsorption of globular proteins, as

BSA, while it does not represents any advantage for the adsorption of the fibrillar proteins, such as collagen.

These results have shown to be promising on the potential of copolymers with a PTh backbone and chains of PEG grafted to the backbone to act as active surfaces for the selective adsorption of proteins. This study represents a first step towards the development of new hybrid materials for proteins separation by selective adsorption.

6.1.4 Conclusions

In summary, we have shown that hybrid materials with isolating and biocompatible PEG chains grafted to the conducting PTh backbone can be prepared by combining synthetic chemical routes with anodic polymerization processes. FTIR and XPS have been used to investigate the chemical structure and composition of the graft copolymers. The morphology and topography have been found to be influenced by the dopant agent, the molecular weight of the PEG chains and the polymerization potential, even though all the prepared materials consist in compact distributions of nanoaggregates organized in very flat surfaces. Analyses of the electrochemical properties reveal that PTh-*g*-PEG_{1000} is a self-stabilizing material, its electrochemical stability increasing with the number of consecutive oxidation-reduction cycles. Furthermore, all the hybrids undergo a high number of anodic oxidation processes, many of them related with the formation of charged species, like electron-deficient polarons and bipolarons, and cross-links. Because of cross-links affect the distribution of charged species on the flat surface or close to it, preliminary studies have been carried out to examine the performance of these materials as active surfaces for the selective adsorption of proteins. Results reveal that the affinity of these materials, especially PTh-*g*-PEG_{2000}, towards globular proteins is higher than towards fibrillar proteins, suggesting that they are promising tools for biotechnological and biomedical applications.

6.1.5 References

1. T. A. Skotheim and J. R. Reynolds, In *Handbook of Conducting Polymers*, 3rd ed.; CRC Press;Boca Raton, FL, 2007.
2. H.S.O. Chan and S.C. Ng, *Prog. Polym. Sci.*, 1998, **23** 1167.
3. S.H. Hosseini and A. Entezami, *Polym. Adv. Technol.*, 2001, **12**, 524.

4. B. Kim, L. Chen, J. Gong, and Y. Osada, *Macromolecules*, 1999, **32**, 3964.
5. Y. G. Kim, L. A. Samuelson, J. Kumar and S. K. Tripathy, *J. Macromol. Sci.*, 2002, **A39**, 1127.
6. S. C. Rasmussen, J. C. Pickens and J. E. Hutchison, *Chem. Mater.*, 1998, **10**,1990.
7. S. M. Ryan, G. Mantovani, X. Wang, D. M. Haddleton and D. J. Brayden, *Exp. Opin. Drug Deliv.*, 2008, **5**, 371.
8. S. P. Zhong, Y. P. Zhang and C. T. Lim, *Tissue Engin. Part B-Reviews*, 2012, **18**, 77.
9. C. Mangold, F. Wurm and H. Frey, *Polym. Chem.*, **2012**, *3*, 1714.
10. J. Peyre, V. Humblot, C. Methivier, J.-M. Berjeaud and C.-M. Pradier, *J. Phys. Chem. B*, 2012, **47**, 13839.
11. V. Castelletto, G. E. N. Z. Zhu and I. W. Hamley, *Langmuir*, 2010, **26**, 9986.
12. I. W. Hamley, M. J. Krysmann, V. Castelletto and L. Noirez, *Adv. Mater.*, 2008, **20**, 4394.
13. Y. Y. Xu, J. Y. Yuan, B. Fang, M. Drechsler, M. Mullner, S. Bolisetty, M Ballauf and A. H. E. Muller, *Adv. Funct. Mater.*, 2010, **20**, 4182.
14. H. L. Wang, Y. Zhang, M. Tian, L. F. Zhai, Z. Wei and T. J. Shi, *J. Appl. Polym. Sci.*, 2008, **110**, 3985.
15. J. G. Sun, S. V. Graeter, L. Yu, S. F. Duan, J. P. Spatz and D. Ding, *Biomacromolecules*, 2008, **9**, 2569.
16. K. Driesen, R. Van Deun, C. Gorller-Walrand and K. Binnemans, *Chem. Mater.*, 2004, **16**, 1531.
17. Y. Deng, Y. J. Li, J. Dai, M. D. Lang and X. Y. Huang, *J. Polym. Sci.: Polym. Chem.*, 2011, **49**, 4747.
18. E. Lee, B. Hammer, J.-K. Kim, Z. Page, T. Emrick and R. C. Hayward, *J. Am. Chem. Soc.*, 2011, **133**, 10390.
19. Y. Song, J. Kim, M. J. Im, B. J. Moon and T. Park, *Macromolecules*, 2012, **45**, 5058.
20. J. Kim, Y. Song and T. Park, *Chem. Commun.*, 2011, **47**, 4697.
21. J. Kim, A. Siva and T. Park, *Polymer*, 2011, **52**, 3704.
22. F. Liu, Y. Chen, Y. Wei, L. Li and S. Shang, *J. Appl. Polym. Sci.*, 2012, **123**, 2582.
23. M. Pomerantz, H. Yang and Y. Cheng, *Macromolecules*, 1995, **28**, 5706.
24. S. Thomas, C. Zhang and S.-S. Sun, *J. Polym. Sci.: Part A: Polym. Chem.*, 2005, **43** 4280.
25. A. Cirpan, S. Alkan, L. Toppare, Y. Hepuzer and Y. Yagci, *J. Polym. Sci.: Part: Polym. Chem.*, 2002, **40**, 4131.
26. T. A. Chen, X. Wu and R. D. Rieke, *J. Am. Chem. Soc.*, 1995, **117**, 233.
27. S. Natarajan and S. H. Kim, *Thin Solid Films*, 2006, **496**, 606.
28. H. Shi, J. Roncali and F. Garnier, *Macromolecules*, 1992, **25**, 6425.
29. J. Roncali, H. Shi and F. Garnier, *J. Phys. Chem.*, 1991, **95**, 8983.
30. M. Pohjakallio, G. Sundholm, P. Talonen, *J. Electroanalyt. Chem.*, 1996, **406**, 165.
31. S. Ahmad, M. Deepa and S. Singh, *Langmuir,* 2007, **23**, 11430.
32. S. A. Spanninga, D. C. Martin and Z. Chen, *J. Phys. Chem. C,* 2010, **114**, 14992.
33. C. D. Grande, M. C. Tria, G. Jiang, R. Ponnapati and R. Advincula, *Macromolecules* **2011**, *44*, 966.
34. E. Kiss, I. Bertoti and E. I. Vargha-Butler, *J. Colloid Interf. Sci.*, 2002, **245**, 91.
35. S. Sharma, R. W. Johnson and T. A. Desai, *Appl. Surf. Sci.*, 2003, **206**, 218.
36. K. L. Purvis, G. Lu, J. Schwartz and S. L. Bernasek, *J. Am. Chem. Soc.*, 2000, **122**, 1808.

37. J. Chastain and C. Roger, Handbook of X-ray Photoelectron Spectroscopy, 1995.
38. V. I. Nefedoc, D. Gati, B. F. Dzhurinskii, N. P. Sergushin and V. Ya, *Russ. J. Inorg. Chem.*, 1975, **20**, 2307.
39. V. B. Damodaran, C. J. Fee and K. C. Popat, *Surf. Interface Anal.*, 2012, **44**, 144.
40. N. Hebestreit, J. Hofmann, U. Rammelt and W. Plieth, *Electrochim. Acta*, 2003, **48**, 1779.
41. D. Aradilla, D. Azambuja, F. Estrany, J. I. Iribarren, C. A. Ferreira and C. Alemán, *Polym. Chem.,* 2011, **2**, 2548.
42. M Fall, M.M Dieng, J.-J Aaron, S Aeiyach and P.C Lacaze, *Synth. Met.*, 2001, **118**, 149.
43. G. Greczynski, T. Kugler and W. R. Salaneck, *Thin Solid Films,* 1999, **354**, 129.
44. G. Zotti, S. Zecchin, G. Schiavon, F. louwet, L. Groenendaal, X. Crispin, W. Osikowicz, W. Salaneck and M. Fahlman, *Macromolecules,* 2003, **36**, 3337.
45. J. M. González-Domínguez , P. Castell , S. Bespín-Gascón , A. Ansón-Casaos , A. M. Díez-Pascual , M. A. Gómez-Fatou , A. M. Benito , W. K. Maser and M. T. Martínez, *J. Mater. Chem,.* 2012, **22**, 21285.
46. K. G. Neoh, E. T. Kang and K. L. Tan, *Polym. Deg. Stabil.*, 1991, **31**, 37.
47. K. Faied, M. Leclerc, M. Nguyen, A. Diaz, *Macromolecules*, 1995, **28**, 284.
48. C. Y. Kao, B. Lee, S. S. Wielunski, M. I. McCulloch, E. Garfunkel, L. C. Feldman and V. Podzorov, *Adv. Funct. Mater.*, 2009, **19**, 1.
49. C. Ocampo, R. Oliver, E. Armelin, C. Alemán and F. Estrany, *J. Polym. Res.*, 2006, **13**, 193.
50. R. Oliver, A. Muñoz, C. Ocampo, C. Alemán, E. Armelin and F. Estrany, *Chem. Phys.*, 2007, **328**, 299.
51. M. M. Pérez-Madrigal, E. Armelin, L. J. del Valle, F. Estrany and C. Alemán, *Polym. Chem.*, 2012, **3**, 979.
52. D. Aradilla, F. Estrany, E. Armelin, R. Oliver, J. I. Iribarren and C. Alemán, *Macromol. Chem. Phys.*, 2010, **211**, 1663.
53. D. Aradilla, F. Estrany and C. Alemán, *J. Phys. Chem. C*, 2012, **115**, 8430.

6.2 Polythiophene-*g*-poly(ethylene glycol) graft copolymers for electroactive scaffolds. */**

The properties, microscopic organization and behavior as cellular matrix of all-conjugated PTh backbone and well-defined PEG grafted chains have been investigated using different experimental techniques and molecular dynamic simulations. UV-vis spectroscopy has been used to determine the optical band gap, which has been found to vary between 2.25 and 2.9 eV depending on the length of the PEG chains and the chemical nature of the dopant anion, and to detect polaron→bipolaron transitions between band gap states. The two graft copolymers have been found to be excellent cellular matrices, their behavior being remarkably better than found for other biocompatible PTh derivatives [*e.g.* PEDOT]. This is fully consistent with their hydrophilicity of the copolymers, which increases with the molecular weight of the PEG chains, and the molecular organization predicted by atomistic Molecular Dynamics (MD) simulations. Graft copolymers tethered to the surface tend to form biphasic structures in solvated environments (*i.e.* extended PTh and PEG fragments are perpendicular and parallel to the surface, respectively) while collapses onto the surface in desolvated environments. Furthermore, the electrochemical activity and the maximum of current density are remarkably higher for samples coated with cells than for uncoated samples, suggesting multiple biotechnological applications in which the transmission with cells is carried out at the electrochemical level.

*Results described in this section previously appeared in *J. Mater. Chem. B*, 2013,**1**, 4135.

**Computer simulations described in this section were performed by J. Torras.

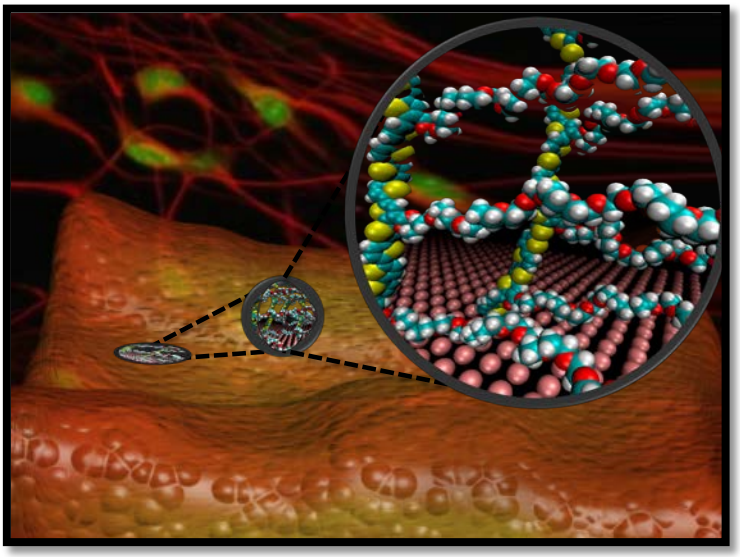

6.2.1 Introduction

The discovery of a new class of organic polymers with conducting properties in the late of 1970 opened up a new era in the field of polymer science.[1] In the last decades CPs have attracted considerable interest because of their interesting electrical, electrochemical, optical and magnetic properties.[2] Among them, polyheterocycles, such as PPy, PTh, PAni and some of their derivatives have received particular attention because they exhibit good stabilities, good conductivities and easy of synthesis.[2-4] PTh derivatives have been settled among the most promising CPs for technological applications, poly(3-hexylthiophene) and, specially, PEDOT being the most popular. PEDOT (Figure 1), which exhibits low band gap (1.6-1.7 eV), high conductivity (up to 550 $S \cdot cm^{-1}$) and good environmental stability,[5-7] has been employed to fabricate electrochromic devices,[8] fuel cells,[9] field emitters[10] and dye-sensitized solar cells (DSSCs).[11]

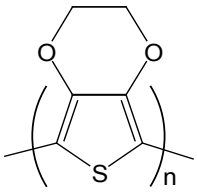

Figure 1. Molecular structure of PEDOT

Most CPs present a number of important advantages for biomedical applications, including biocompatibility, ability to entrap and controllably release biological molecules (*i.e.* reversible doping), ability to transfer charge from a biochemical reaction, and the potential to easily alter the electrical, chemical, physical, and other properties of the CPs to better suit the nature of the specific application. These unique characteristics are useful in many biomedical applications, such as biosensors, tissue-engineering scaffolds, neural probes, drug-delivery devices, and bio-actuators. Biomedical applications of CPs have been recently reviewed.[12,13] In spite of this, there is always the desire to further optimize a material when specific application. The two common properties desired for all biomedical applications are biocompatibility and redox stability (*i.e.* electroactivity and electrochemical stability), but beyond these needs, CP modifications tend to be specific for the application. For example, it is important to improve the ability of CPs to act as bioactive platform for cellular proliferation. This can be achieved physically (*i.e.* physical adsorption of

molecules that enhance proliferation of a variety of cell types) or chemically (*i.e.* functionalizing the CP with the desired molecules through chemical bonds). Functionalization of CPs with different molecules has allowed biomedical engineers to modify CPs with biological sensing elements, and to turn on and off different signaling pathways to create CPs that enhance cellular adhesion and proliferation and improve their biocompatibility.[14-17]

Among polymer-polymer hybrid materials, graft copolymers made of components with very different properties are receiving increasing attention.[18-23] Graft copolymers amplify the characteristic properties of their individual components, exhibiting unusual features because of their confined structure, compact organization and notable chain end effects. Within this context, copolymers formed by an all conjugated PTh backbone and other polymeric grafted chains have been prepared to improve the very limited processability and solubility of unsubstituted PTh [*e.g.* poly(methyl acrylate)[24,25] and PS[26,27]], to fabricate donor-π-acceptor molecular species [*e.g.* poly(styrene-*graft*-C_{60})[28]] or to prepare hydrophilic conducting surfaces [e.g. PEG monomethacrylate[29]].

In a very recent study, we reported the synthesis and characterization of hybrid materials made of well-defined PEG chains grafted to the conducting PTh backbone, which were denoted PTh-*g*-PEG_n (where *n* refers to the molecular weight of PEG chains).[30] PEG is a biocompatible hydrophilic polymer with many practical applications in biology, biotechnology and biomedicine,[31,32] that is frequently used for the fabrication of polymer-biomolecule,[33,34] polymer-polymer[35] and polymer-inorganic[36,37] hybrid materials. The fabrication of PTh-*g*-PEG_n (Figure 2) was achieved through a two-steps process, which consisted of the chemical synthesis of macromonomers (*i.e.* Th_5 substituted with PEG chains of M_w=1000 or 2000) and the anodic polymerization of such macromonomers.[30] The chemical structure, composition, morphology and electrochemical properties of the resulting materials, PTh-*g*-PEG_{1000} and PTh-*g*-PEG_{2000}, were investigated using FTIR, XPS, SEM, AFM and CV. Furthermore, the ability of these hybrids to adsorb both extracellular and plasma proteins was investigated, their affinity towards globular proteins being higher than towards fibrillar proteins.[30]

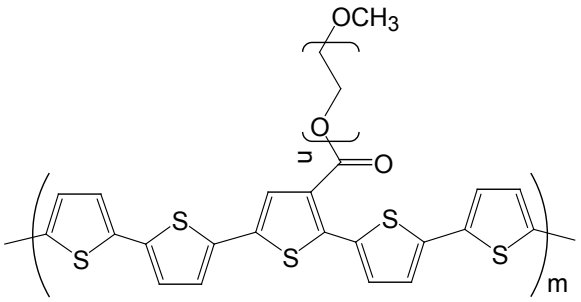

PTh-*g*-PEG_{1000}: *n*= 22

PTh-*g*-PEG_{2000}: *n*= 44

Figure 2. Molecular structure of PTh-*g*-PEG_n

This work is mainly focused in the electronic, electrochromic and superficial properties, internal organization at the molecular level and behavior as cellular matrix of PTh-*g*-PEG_{1000} and PTh-*g*-PEG_{2000}. More specifically, the electronic and electrochromic properties of the hybrids have been investigated using UV-vis spectroscopy. After this the surface wettability of the graft copolymers have been examined and compared with that of PEDOT, a polar PTh derivate that was proved to enhance cellular adhesion and proliferation,[38,39] by measuring the contact angle. Next, the relative organization of the PTh backbone and the PEG side chains in graft copolymers have been examined using atomistic MD simulations. For this purpose, an assembly formed by two copolymer molecules deposited in a surface has been simulated considering both desolvated (*i.e.* gas-phase) and aqueous solution environments. Finally, the biocompatibility and behavior of the two hybrids as biological platforms have been examined using cellular adhesion and proliferation assays. The latter issue is particularly revelant since results have allowed to demonstrate that chemical modification of PTh chains by grafting biocompatible PEG results in a material with enhanced properties as bioactive platform.

6.2.2 Methods

Synthesis. The macromonomers used for the anodic polymerization of PTh-*g*-PEG_{1000} and PTh-*g*-PEG_{2000} consisted on a Th_5 bearing a PEG chain of M_w=1000 and M_w=2000, respectively, at the central Th ring. These macromonomers, hereafter denoted Th_5-PEG_{1000} and Th_5-PEG_{2000} (Figure 3), were prepared by chemical synthesis using the route described in reference 13.

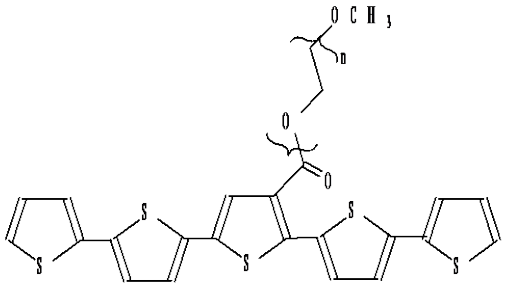

Th_5-PEG_{1000}: *n*= 22

Th_5-PEG_{2000}: *n*= 44

Figure 3. Molecular structure of Th_5-PEG_n

On the other hand, PTh-*g*-PEG_n graft copolymers were prepared by CA under a constant potential using an Autolab PGSTAT302N equipped with the ECD module (Ecochimie, The Netherlands). All polymerizations were carried out in a standard three-electrode cell under nitrogen atmosphere (99.995% in purity) at room temperature. The anodic compartment was filled with 15 mL of a $1 \cdot 10^{-3}$ M Th_5-PEG_n solution in a mixture of acetonitrile:dichloromethane (50:50 v/v) containing 0.1 M of a supporting electrolyte, while the cathodic compartment was filled with 10 mL of the same electrolyte solution. Steel AISI 316 and ITO sheets of 1.0×0.5 and 0.5×0.5 cm^2, respectively, were employed as WEs. The CE was a Pt sheet of 1.0×0.50 cm^2 while the RE was an Ag|AgCl electrode containing a KCl saturated aqueous solution (Eº = 0.222 V at 25ºC), which was connected to the working compartment through a salt bridge containing the electrolyte solution. Graft copolymers were prepared considering the following experimental conditions:

- PTh-*g*-PEG_{1000} and PTh-*g*-PEG_{2000}: $LiClO_4$ as supporting electrolyte and constant potential of 0.70 and 75 V, respectively.

- PTh-*g*-PEG_{2000}: Bu_4NPF_6 as supporting electrolyte and a potential of 0.80 V.

UV-vis. UV-vis absorption spectra of macromonomers in solution were registered using a Specord 200 spectrophotometer. Spectra of macromonomers and PTh-*g*-PEG_n films were obtained using a UV-vis-NIR Shimadzu 3600 spectrophotometer equipped with a tungsten halogen visible source, a deuterium arc UV source, a photomultiplier tube UV-vis detector, and an InGaAs photodiode and cooled PbS photocell NIR detectors. Spectra were recorded in the absorbance mode using the

integrating sphere accessory (model ISR-3100), the wavelength range being 185-3300 nm. The interior of the integrating sphere was coated with highly diffuse $BaSO_4$ reflectance standard. Uncoated ITO glass was used as reference. Hybrid material films were deposited on ITO-glass electrodes for measurements. Single-scan spectra were recorded at a scan speed of 60 nm/min. Measurements, data collection and data evaluation were controlled by the computer software UVProbe version 2.31.

Wettability. Contact angle measurements were performed using the sessile drop method, at room temperature and controlled humidity. Images of 1 μL distilled water drops were recorded after stabilization (30 s) using a CAM-200 equipment from KSV-Finland. Contact angle values were obtained as the average of five independent measures for each sample.

Optical profilometry. The thickness of the films was determined using a WYKO 9300NT optical profiler (Veeco, Plainview, NY). Different scratches were intentionally provoked on PTh-*g*-PEG_{1000} and PTh-*g*-PEG_{2000} films and measured to allow statistical analysis of data. Imaging of the films was conducted using the following optimized settings: VSI mode, full resolution, 5-mm back scan and 10-mm primary scan, 10× and 50× Michelson LR objective lens (fields of view of 2.0×) for image sizes of 237×315 μm^2 and 64×48 μm^2, respectively.

AFM. Topographic AFM images were obtained with a Molecular Imaging PicoSPM using a NanoScope IV controller under ambient conditions. The tapping mode AFM was operated at constant deflection. The row scanning frequency was set to 1 Hz and the physical tip-sample motion speed was 10 $\mu m \cdot s^{-1}$. Roughness was determined using the statistical application of the Nanoscope software, which calculates the average considering all the values recorded in the topographic image with exception of the maximum and the minimum. AFM measurements were performed on various parts of the films, which produced reproducible images similar to those displayed in this work. The scan window sizes used in this work were 5×5 μm^2.

MD simulations. Graft copolymers were simulated using an assembly of two molecules, each one containing a backbone with 20 Th rings and four grafted PEG chains with 22 repeating units (Figure 1). Accordingly, the molecular weight of the PEG

chain in these model graft copolymers corresponds to that of PTh-*g*-PEG_{1000}. The two molecules were attached to the center of a square surface (*L*= 133.98 Å) formed by 900 spherical particles (*i.e.* 30×30 particles with a distance of 4.62 Å between neighboring particles) through a bond between the α-carbon of the first backbone Th ring and one spherical particle of the surface. The distance between the spherical particles used to attach the molecules was 26.1 Å. MD simulations were performed on two model systems, which can be described as follows:

(i) The two molecules tethered to the surface in the gas-phase. This solvent-free model corresponds to the situation encountered in AFM experiments. MD simulations of this model system involved 2462 explicit particles.

(ii) The two molecules attached to the surface in aqueous solution. For this purpose, a spherical water cap with a radius of 70 Å and centered in the middle of tethered molecules was constructed and, subsequently, filled with 92513 explicit water molecules. This solvated model represents the situation found in cell attachment assays. The model involved a total of 280001 explicit particles.

The potential energy of the simulated systems was computed using the AMBER force field.[40] All the bonding and van der Waals parameters, with exception of the S–C–C–S torsion, were taken from the Generalized AMBER force-field (GAFF).[41] The parameters for the S–C–C–S torsion were extracted from a recent study in which force-field parameters compatible with AMBER were developed by computing the potential of mean forces for the inter-ring rotation of different 2,2'-bithiophene derivatives.[42] Atomic charges were adjusted using the Restrained ElectroStatic Potential (RESP) strategy.[43] The van der Waals parameters of the spherical particles used to construct the surface [R= 2.35 Å and ε= 0.90 kcal/mol] were extrapolated from previous studies devoted to investigate the structure of organic systems tethered to rigid surfaces.[44,45] Water molecules were represented using the TIP3P model.[46]

MD simulations were performed using the AMBER 12.0 program.[47] Simulations in aqueous solution were performed by applying an atom-pair distance cut-off at 12 Å to compute van der Waals and electrostatic interactions, whereas gas-phase simulations were performed without cut-off. Bond lengths involving hydrogen atoms

were constrained using the SHAKE algorithm with a numerical integration step of 2 fs.[48] The positions of the spherical particles at the surface were restrained applying a force constant of 40 kcal/mol·Å^2.

Before starting the MD run series, 5×10^3 steps of energy minimization were performed to relax conformational and structural tensions. After this, the systems in the gas-phase and in solution were progressively heated from 0 to 298 K along 45 ps of MD and, subsequently, equilibrated at the latter temperature for 15 ps. The last snapshot of the equilibration was used as the starting point for the production series. Coordinates were saved every 10 ps for further analysis for simulation lengths of 5 ns.

Cellular adhesion and proliferation. Vero cells were cultured in DMEM supplemented with 10% fetal bovine serum (FBS), 1% penicillin/streptomycin and 2 mM L-glutamine at 37ºC in a humidified atmosphere of 5% CO_2 in air. The cultured medium was changed every two days and, for sub-culture, cell monolayers were rinsed with PBS and detached by incubation with 0.25% trysin/EDTA for 5 min at 37ºC. Cell concentration was determined by counting at the Neubauer camera using 4% trypan blue as dye vital. The detached cells with viability $\geq$ 95% were used for cultures following the conditions for the adhesion and proliferation assays.

PTh-*g*-PEG_{1000} and PTh-*g*-PEG_{2000} films deposited onto steel AISI 316 sheets of 1 cm^2 were placed in plates of 24 wells and sterilized using UV irradiation for 15 min in a laminar flux cabinet. Samples were incubated with 1 mL of culture medium during 30 min under culture conditions to equilibrate the material. Finally, the medium was aspired and the material was evaluated for cell adhesion and proliferation by exposing cells to direct contact with the material surface. An aliquot of 50 mL containing 5×10^4 cells (adhesion assays) or 2×10^4 cells (proliferation assays) was deposited on the substrate of each well. The plate was incubated under culture conditions for 60 min to promote the cell attachment to the film surface. Finally, 1 mL of the culture medium was added to each well. Controls of adhesion and proliferation were simultaneously performed by culturing cells on the surface of the TCPS plates and uncoated steel. Cell adhesion and proliferation were evaluated after 24 hours and 7 days of culture,

respectively, using the MTT assay, which determines the cell viability. The viability results were normalized to TCPS control as relative percentages.

Results were derived from the average of four replicates (n= 4) for each independent experiment. ANOVA and Turkey tests were performed to determine the statistical significance, which was considered at a confidence level of 95% ($p < 0.05$).

The cells onto PTh-*g*-PEG_{1000} and PTh-*g*-PEG_{2000} films were examined by epifluorescence microscopy (BA410 Model, Motic Spain S.L.). For this purpose, Vero cells were fixed and permeabilized with cold acetic acid:methanol (1:3) for 3 min and subsequently replaced with fresh fixative for further 3 min. After drain the fixative, air-dry material was immersed in 2 mL of stain (0.1 µg/mL bisbenzimide Hoechst 33258 in PBS) and incubated for 5 min at room temperature in the dark to stain nuclei. Then, stain was removed and films were mounted in a nonfluorescent medium. The bisbenzimide fluorescence and intrinsic fluorescence of films were observed with standard fluorescence filters sets: MF31000 filter (Exciter D350/50x and Emitter D460/50m) and a MF31001 filter (Exciter D480/30x and Emitter D535/40m), respectively.

SEM. SEM studies were performed using a FIB Zeiss Neon 40 scanning electron microscope operating at 5 kV, equipped with an EDX spectroscopy system. Samples were mounted on a double-side adhesive carbon disc and sputter-coated with a thin layer of carbon to prevent sample charging problems. Before the carbon coating for examination, samples covered with cells were fixed in a 2.5% glutaraldehyde PBS solution overnight at 4ºC. Then, they were dehydrated by washing in an alcohol battery (30º, 50º, 70º, 90º, 95º and 100º) at 4ºC for 30 minutes per wash. Finally, samples were air-dried, and sputter-coated with carbon before SEM observation.

Electrochemical characterization. The electrochemical behavior of PTh-*g*-PEG_{1000} and PTh-*g*-PEG_{2000} was studied by CV considering two different environments: films directly obtained from electropolymerization (*i.e.* as prepared samples) and films covered will cells. For this purpose, a sterilized PBS (pH= 7.2) was used as electrolyte in the three-electrode cell. Steel sheets of 1 cm^2 area were used as CE and WE, an Ag|AgCl electrode being used as the RE. CVs were registered at a scan rate of 50 $mV \cdot s^{-1}$

in the potential range from -0.30 to +0.90 V. All CV assays were performed with an Autolab PGSTAT302N equipped with the ECD module (Ecochimie, The Netherlands).

The electroactivity refers to the charge storage ability and was determined by measuring the cathodic and anodic areas in the first control voltammogram (*i.e.* the electroactivity increases with the similarity between such areas). The electrochemical stability (electrostability) was evaluated by determining the loss of electroactivity with the number of consecutive oxidation-reduction cycles (*LEA*, in %):

$$LEA = \frac{\Delta Q}{Q_I} 100 \qquad (1)$$

where ΔQ is the difference between the voltammetric charges (in C) of the first and the last oxidation-reduction cycle, and Q_I is the voltammetric charge corresponding to the first cycle. In this work all *LEA* values are referred to a total of 10 consecutive oxidation-reduction cycles.

6.2.3 Results and Discussion

Electronic properties

Diluted dichloromethane solutions of Th_5-PEG_{1000} and Th_5-PEG_{2000} macromonomers (i.e. 0.09 and 0.18% w/w, respectively) show an absorbance peak in the UV-vis range at λ_{max}= 402 and 376 nm (Figure 4a), respectively, which corresponds to the π-π^* transition of the Th rings. The UV-vis spectra of Th_5-PEG_{1000} and Th_5-PEG_{2000} films, which were prepared by drop casting on an ITO plate 20 μL of a 1mM macromonomer solution in acetonitrile/dichloromethane (50/50), are included in Figure 4a. As it can be seen, the π-π^* transition of Th_5-PEG_{1000} (λ_{max}= 377 nm) and Th_5-PEG_{2000} (λ_{max}= 385 nm) shows blue and red shift, respectively, with respect to the spectra recorded for dilute solutions. Thus, the conjugation of the Th_5 fragment in films, which relies upon overlap of the π-orbitals of the coplanar Th rings, is lower and higher than in diluted solution for Th_5-PEG_{1000} and Th_5-PEG_{2000}, respectively. This feature evidences that grafted PEG chains play a predominant role in the electronic properties of macromonomers, their importance being expected to decrease upon polymerization.

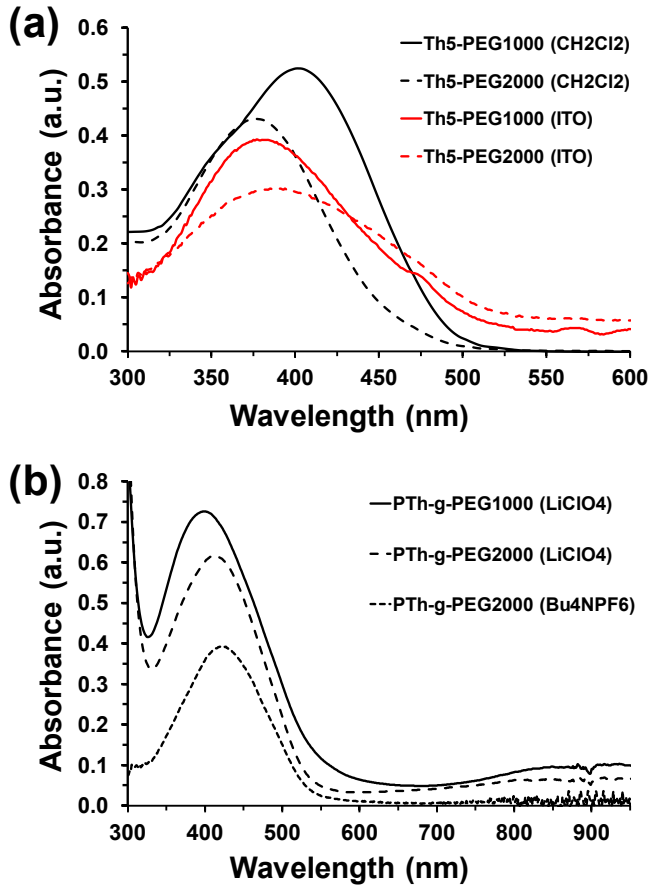

Figure 4. UV-vis spectra of: (a) Th_5-PEG_{1000} and Th_5-PEG_{2000} macromonomers in diluted dichloromethane solution and deposited as a film onto ITO substrate; and (b) PTh-g-PEG_{1000} prepared using $LiClO_4$ as supporting electrolyte and PTh-g-PEG_{2000} obtained in presence of $LiClO_4$ and Bu_4NPF_6.

Figure 4b compares the UV-vis spectra of PTh-g-PEG_{1000} prepared using $LiClO_4$ as supporting electrolyte with those of PTh-g-PEG_{2000} obtained in presence of $LiClO_4$ and Bu_4NPF_6. The shape three spectra are rather similar and show a broad band with λ_{max} at 400 (PTh-g-PEG_{1000} with $LiClO_4$), 413 (PTh-g-PEG_{2000} with $LiClO_4$) and 423 nm (PTh-g-PEG_{2000} with Bu_4NPF_6), which corresponds to the π-π^* transition. The red shift with respect to the macromonomers originates from the increment of the conjugation length produced in the backbone upon polymerization. However, the width of the band reflects the coexistence of long and short effective conjugation lengths. Moreover, both PTh-g-PEG_{1000} and PTh-g-PEG_{2000} are less conjugated than poly[3-(3,6-dioxaheptyl)thiophene], an early reported PTh derivative containing small oligo(oxyethylene) substituents [i.e. R= $-(CH_2CH_2O)_2-CH_3$], which showed λ_{max}= 435 and 445 nm when produced by chemical and electrochemical polymerization, respectively.[49] Indeed, all these systems show less conjugation than unsubstituted PTh

chemically[50] and electrochemically[51] produced (i.e. λ_{max}= 495 and 447 nm, respectively).

In a π-conjugated system, the band gap (E_g) is defined as the difference between the lowest energy in the conduction band and the highest energy in the valence band. According to the zero order approximation, this is equal to the lowest excitation energy, which can be obtained from the onset value (λ^{onset}) at the lower energy edge of the absorption spectrum (i.e.$E_g = 1240/\lambda^{onset}$). Specifically, the optical ε_g derived from the UV-vis spectra of PTh-g-PEG_{1000} (λ^{onset}= 552 nm) and PTh-g-PEG_{2000} (λ^{onset}= 542 nm) prepared using ClO_4^- as dopant is 2.25 and 2.29 eV, respectively, while that obtained for PTh-g-PEG_{2000} doped with PF_6^- (λ^{onset}= 547 nm) is 2.27 eV. According to these values, the energy gap associated to the lowest π-π^* transition of PTh-g-PEG_n graft copolymers is slightly larger than those conventional PTh derivatives substituted at the 3-position [e.g. poly(thiophene-3-methyl acetate), 1.98-2.17 eV,[52] poly(3-chlorothiophene), 2.14 eV,[53] and poly(3-bromothiophene), 1.93-1.97eV[54]]. This feature corroborates that the conjugation length at the backbone is lower for these graft copolymers than for derivatives with conventional substituents. Moreover, all these values are higher than the ε_g determined for PEDOT using electrochemical (1.98 eV)[55] or spectroscopic (1.6-1.7 eV)[5] methods (see Table 1), which is consistent with excellent electrochemical and electrical behavior of this PTh derivative.

Another interesting feature is that the oxidation band observed at ~900 nm for both PTh-g-PEG_{1000} and PTh-g-PEG_{2000} when prepared in presence of $LiClO_4$ is not detected when the supporting electrolyte is Bu_4NPF_6. This band, which can be attributed to the formation of polarons and bipolarons in PTh chains,[52] evidences the influence of the dopant agent. Thus, the two graft copolymers form complexes with the ClO_4^- dopant anions while the vanishing of the band confirms the lack of complexes with PF_6^-.

	PTh-*g*-PEG$_{1000}$	PTh-*g*-PEG$_{2000}$	PEDOT
E_g (eV)	2.25[a]	2.29[a]	1.6-1.7;[a,b] 1.98[c]
Contact angle (º)	87	76	82
Roughness (nm)	11±2	12±2	111±19
Adhesion of Vero cells (%/cm^2)	98.7±4.7[d]	101.3±4.7[d]	117.3±9.1[d,e]
Proliferation of Vero cells (%/cm^2)	149.2±9.7[d]	166.4±17.3[d]	100.0±3.7[d,e]
Electroactivity (%)	162[f]	329[f]	131[e,f]

[a] Band gap determined by UV-vis spectroscopy. [b] Taken from reference 5. [c] Band gap determined electrochemically in reference 55. [d] The relative viability of Vero cells was established in relation to the TCPS control (i.e. viability of TCPS= 100%). [e] Data taken from reference 16. [f] Enhancement of the electroactivity in films covered with cells with respect to the uncovered ones.

Table 1. Comparison of the properties determined for PTh-g-PEG1000, PTh-g-PEG2000 and PEDOT.

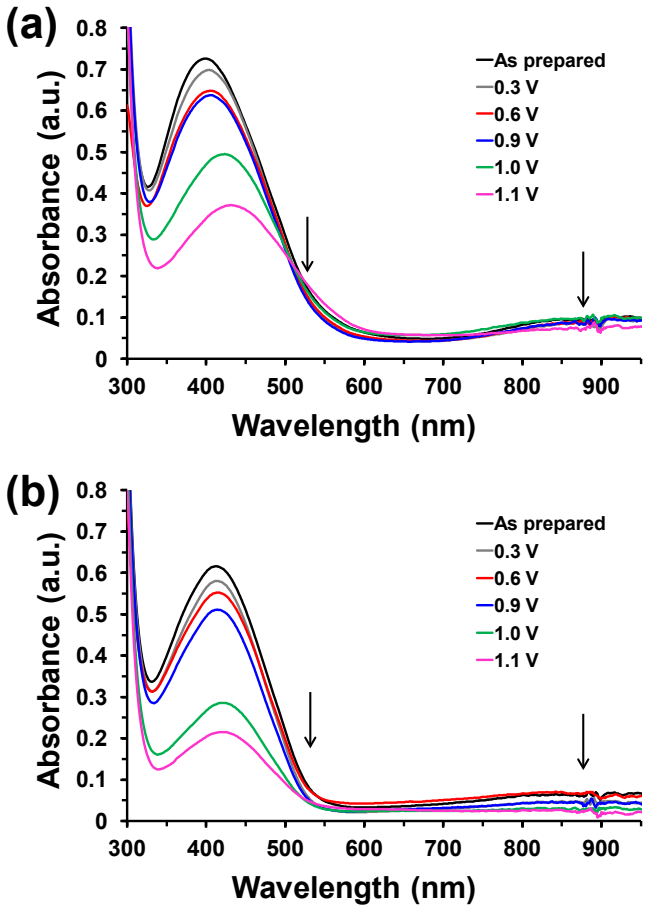

Figure 5. UV-vis spectra of (a) PTh-g-PEG$_{1000}$ and (b) PTh-g-PEG$_{2000}$ doped with ClO_4^- using as prepared samples and after re-oxidation with potentials of 0.3, 0.6, 0.9, 1.0 and 1.1 V.

Figure 5 shows the effects of additional oxidation in the electronic properties of PTh-g-PEG_{1000} and PTh-g-PEG_{2000} doped with ClO_4^-. For this purpose, after introduce the graft copolymer films in acetonitrile solutions with 0.1 M $LiClO_4$, a constant potential was applied during 10 s. UV-vis spectra were recorded after re-oxidation with potentials of 0.3, 0.6, 0.9, 1.0 and 1.1 V. As it can be seen, this oxidation process is accompanied by the reduction and the red shift of the absorbance band associated to the π-π^* transition. Thus, the λ_{max} of as prepared PTh-g-PEG_{1000} and PTh-g-PEG_{2000} films increases from 400 and 413 nm, respectively, to 431 and 422 nm after apply a constant potential of 1.1 V during 10 s. Both the red shift and the decrease of the absorbance provoked by further oxidation are consistent with a reduction of the ε_g, which is slightly more pronounced for PTh-g-PEG_{1000} than for PTh-g-PEG_{2000}. On the other hand, the second band, which is observed at ~900 nm in the as prepared samples, shifts into the NIR region after additional oxidation. According to previous studies, this variation, which is similar for the two graft copolymers, has been attributed to polaron→bipolaron transitions between band gap states.[56]

Regarding to the electrochromic properties of graft copolymers, as prepared PTh-g-PEG_{1000} and PTh-g-PEG_{2000} films doped with ClO_4^- showed a brownish orange and intense yellow color, respectively, while the latter hybrid obtained using Bu_4NPF_6 as supporting electrolyte displayed an intermediate color. Re-oxidation with potentials lower than 1.0 V does not provoke any variation in the color while films change to green and bluish green when the applied potential is 1.0 and 1.1 V, respectively. This behavior is fully consistent with that observed for conventional PThs.[57]

Surface wettability.

The average values of the contact angle (θ) determined for PTh-g-PEG_{1000} and PTh-g-PEG_{2000} films doped with ClO_4^- are θ= 87º and 76º, respectively, indicating that, as expected, the enlargement of the PEG chains increases the hydrophilicity at the surface. Zhang et al. reported that the contact angle of unsubstituted PTh obtained by electropolymerization is higher than 100º.[58] Moreover, the own authors showed that the water-repellency of PTh increases with the thickness,[58] which was attributed to the effect of the superficial morphology on the roughness. Thus, ultrathin films are compact and smooth while the surface becomes more irregular and porous as the

thickness increases, enhancing the roughness. However, the influence of the molecular weight of grafted chains in both the thickness and roughness of PTh-g-PEG_n have been found to be very small. Specifically, the AFM 2D images displayed in Figure 6 evidence that the surface of two copolymers presents nanometric aggregates. Although the frequency and size of such aggregates depend on the length of the PEG chains, the RMS roughness is very similar and noticeably low for the two materials: 11±2 and 12±2 nm for PTh-g-PEG_{1000} and PTh-g-PEG_{2000}, respectively. Similarly, optical profilometry measurements indicate that the films of the two grafted copolymer are ultrathin, the thickness being ~230 and ~110 nm for PTh-g-PEG_{1000} and PTh-g-PEG_{2000}, respectively. Accordingly, the observed $\Delta\theta$= -11º should be essentially attributed to the length of the PEG chains.

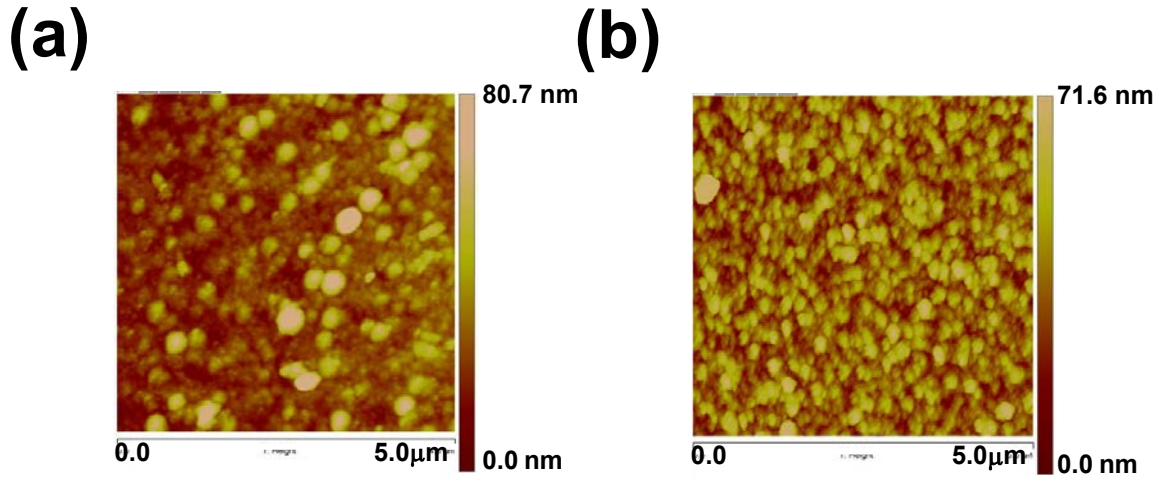

Figure 6. 2D Height AFM images of (a) PTh-g-PEG_{1000} and (b) PTh-g-PEG_{2000} prepared using $LiClO_4$ as supporting electrolyte.

In order to compare the water-affinity of PEDOT, a polar PTh derivative that behave as a good cellular matrix,[21,22] with that of PTh-g-PEG_n, ultrathin films of the former material were electrochemically prepared by CA under a constant potential of 1.40 V using acetonitrile as generation medium and $LiClO_4$ as supporting electrolyte. The thickness and roughness of the films obtained using a polymerization time of 10 s were ~240 nm and 111±19 nm, respectively. The contact angle determined for PEDOT was θ= 82º (Table 1). Considering that the roughness of PEDOT is one order of magnitude higher than those of graft copolymers, the contact angles determined for PTh-g-PEG_{1000} and PTh-g-PEG_{2000} suggest the behavior of these graft copolymers as supportive matrix for the cells growth should be excellent (see below).

Microscopic organization of PTh backbone and PEG chains.

MD simulations in the gas-phase and aqueous solution led to very different results, as is clearly evidenced by the atomistic structures displayed in Figure 7. Thus, inspection of snapshots selected at different time intervals indicates that, although the relative disposition of the PTh backbone and the PEG side groups is initially similar in the two environments, important differences appear after only 400 ps. More specifically, initially both PTh and PEG fragments are extended, even though the former are perpendicular to the rigid surface while the latter are parallel. This biphasic organization is preserved after 5 ns of MD in solution, the largest change being in this case the small conformational fluctuations underwent by the flexible PEG fragments. In contrast, in the gas-phase the graft PEG chains tend to wrap the PTh backbone and the whole system collapses onto the surface. This process starts after a few hundreds of picoseconds, being completely finished after 1 ns. Thus, the desolvated environment facilitates the formation of both short- and large-range interactions, giving place to the formation of a globular structure that also interacts with the surface.

In order to provide a more quantitative view of the conformational reorganization underwent by PTh-g-PEG_{1000} chains in the gas-phase and solution, Figure 8 represents the temporal evolution of the end-to-end distance ($d_{e\text{-}e}$) for both the PTh and PEG segments. As it can be seen in Figure 5a, which displays the variation of the $d_{e\text{-}e}$ for the PTh backbone of the two explicit molecules against the simulation time, the values obtained after thermal equilibration ($d_{e\text{-}e}$= 70.2 and 70.8 Å) remains practically constant during the whole trajectories (averages over the whole trajectory: 67.5±3.0 and 69.0±3.2 Å). In contrast, the $d_{e\text{-}e}$ drops in the gas-phase from 69.6 and 61.6 Å to ~35 Å after only 0.8 ns, which represents a drastic shrinkage of the backbone (~45-50%). After this, the PTh segment experiences a slight lengthening, which also takes 0.8 ns, allowing the system to alleviate the short-range repulsions generated by the fast initial contraction. Finally, the $d_{e\text{-}e}$ values remain relatively constant at 38.8±4.2 and 44.4±3.5 Å during the last 3.4 ns of simulation.

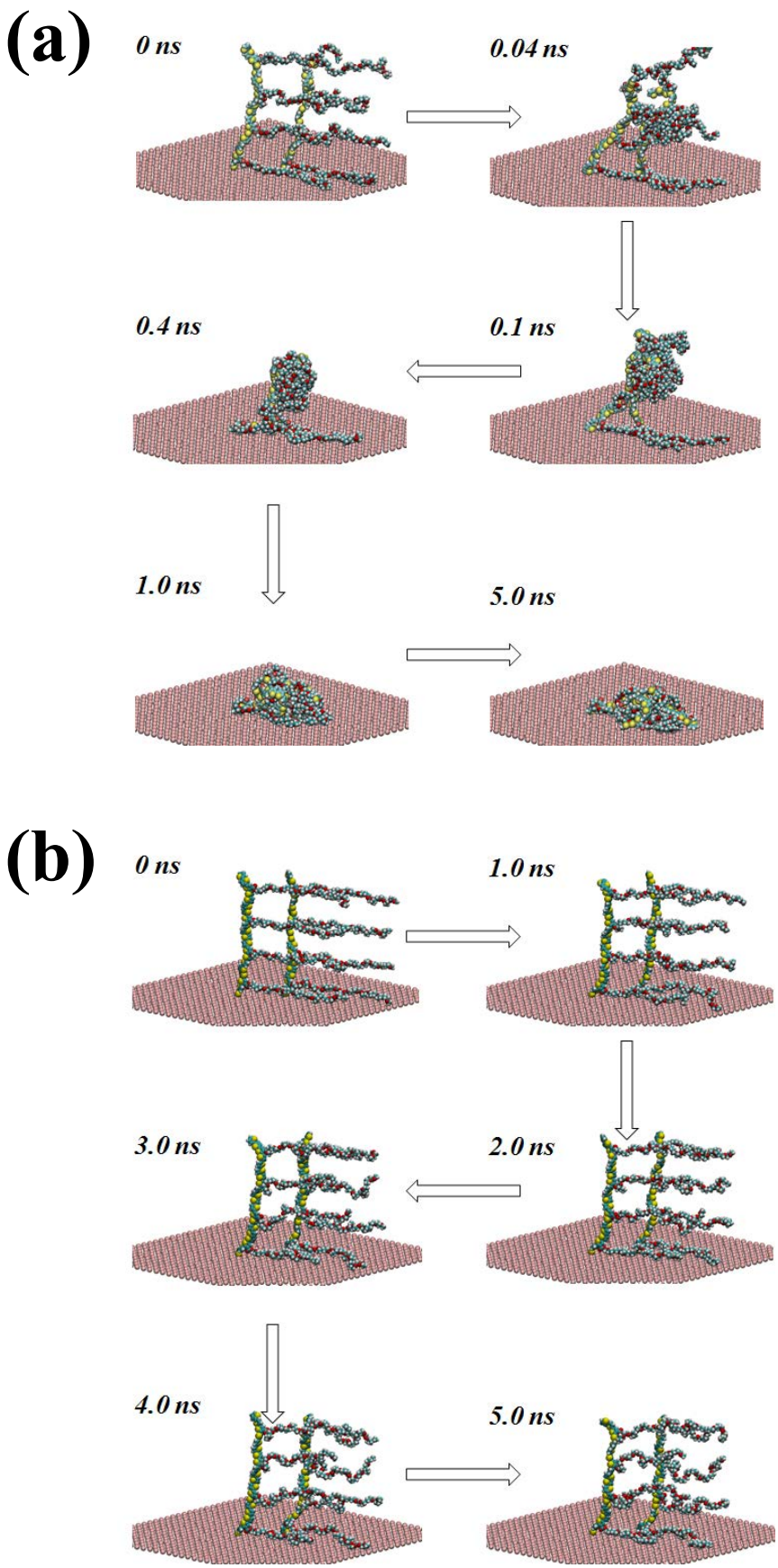

Figure 7. Selected snapshots from MD simulations (a) in the gas-phase and (b) in solution. Water molecules and hydrogen atoms have been omitted to clarify the representations.

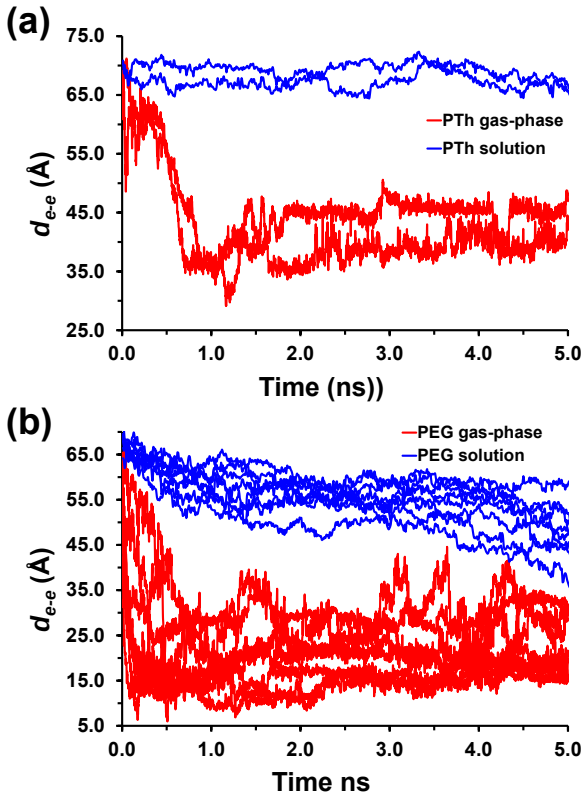

Figure 8. Temporal evolution of the end-to-end distance (d_{e-e}) determined from MD simulations of PTh-g-PEG_{1000} in the gas-phase (red lines) and solution (blue lines) for: (a) backbone PTh segments (2 explicit molecules per simulation); and (b) side PEG segments (2 explicit molecules × 4 repeat units= 8 segments per simulation).

The three-dimensional organization of the PTh-g-PEG_{1000} chains has been also examined by using the partial radial distribution functions. Figure 9a and 9b displays the partial distributions of the S···S (g_{S-S}) and O···O (g_{O-O}) pairs, respectively, in desolvated and aqueous environments, which have been calculated considering pairs of the same molecule (i.e. intramolecular pairs) and the sum of both intra- and intermolecular pairs (i.e. all pairs). As it can be seen, comparison intramolecular and all pairs $g_{S-S}(r)$ and $g_{O-O}(r)$ profiles indicates that the relatively ordered organization is, as expected, dominated by the intramolecular contribution. The $g_{S-S}(r)$ shows six well-defined peaks centered at 3.45, 4.25, 7.55, 10.85, 14.25 and 18.15 Å in aqueous solution while only four peaks centered at 3.35, 4.25, 7.05 and 10.55 Å are detected in the gas-phase, the latter two being relatively undefined. This feature clearly indicates that the PTh backbone is well organized in solution, adopting a structure that is practically perpendicular to the surface, as was displayed in Figure 4b. In contrast, such long-range order is loss in the desolvated system, the peaks at distances lower than 7.1 Å being due to the existence of short-range interactions. The $g_{O-O}(r)$ profiles show

similar trends, even though the order in the PEG chains is considerably lower than that of PTh because of its intrinsic conformational flexibility, which is restricted in PTh due to the geometric restrictions of the thiophene ring. Thus, three well-defined peaks centered at 2.85, 5.55 and 8.45 Å are displayed in solution while only two peaks at 2.95 and 5.45 Å are shown in the desolvated system, the last one broad and ill-defined.

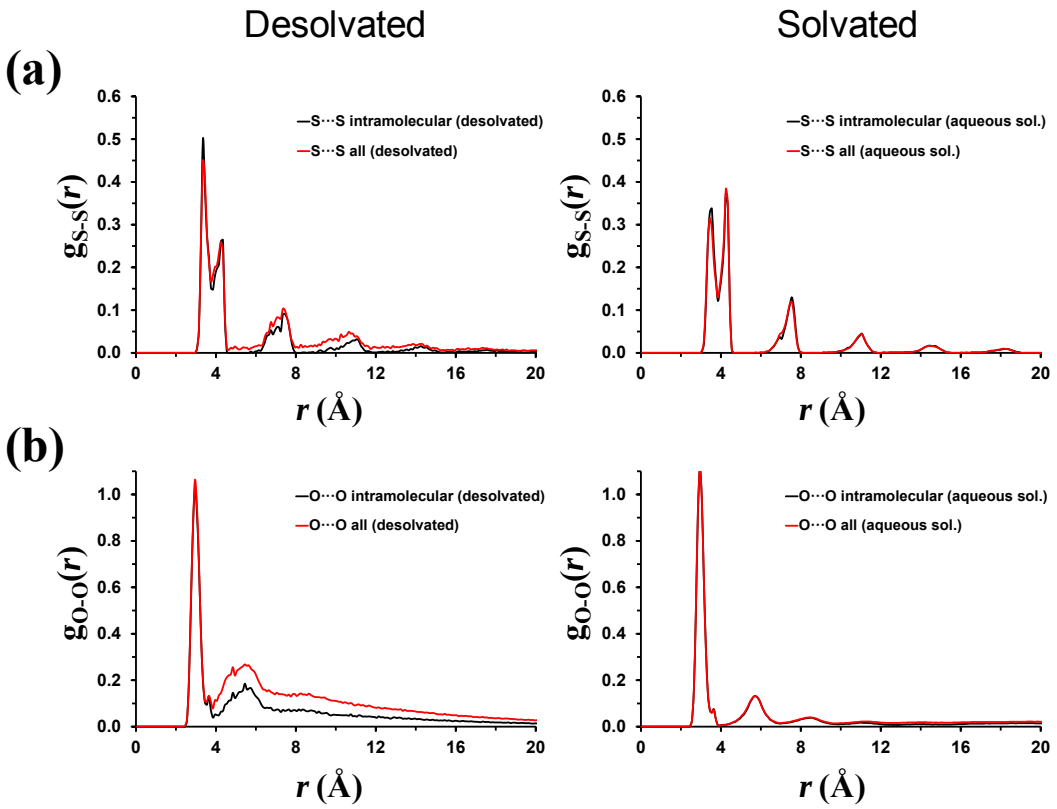

Figure 9. Partial radial distribution functions of (a) S···S and (b) O···O pairs from MD simulations of PTh-g-PEG_{1000} in the gas-phase (left) and solution (right). Two profiles are displayed in each case: intramolecular pairs (black) and all pairs (red).

Behavior as cellular matrix.

The biocompatibility of PTh-g-PEG_{1000} and PTh-g-PEG_{2000} doped with ClO_4^- was determined by cell adhesion and proliferation assays. The Vero cell line was selected because of its adherent growth and epithelial-like characteristics. Quantitative results of cellular adhesion assays are displayed in Figure 10a, steel and TCPS (or culture plate) being used as control substrates. As it can be seen, the number of cells by area adhered to the surface is significantly higher for PTh-g-PEG_{1000} and, especially, PTh-g-PEG_{2000} than for TCPS and steel. Thus, the hybrids do not show cytotoxic effects within a short period of time (i.e. 24 h), acting as excellent supportive matrices. After seven days of culture, PTh-g-PEG_{2000} retains the same behavior while that of PTh-g-PEG_{1000}

improves considerably, indicating that this material stimulates cellular proliferation more than PTh-g-PEG_{2000} and the controls. Thus, the results provided by cell proliferation assays, which are displayed in Figure 10b, reflect that the cell viability of the two hybrids is practically the same after seven days of culture and remarkably higher than that found for PEDOT.[38,39] The ability of PTh-g-PEG_{1000} and PTh-g-PEG_{2000} to behave as cellular matrices is clearly shown in the fluorescence images and SEM micrographs displayed in Figure 11, which show not only the high density of adhered cells but also their homogeneous spreading onto the surface of the substrates.

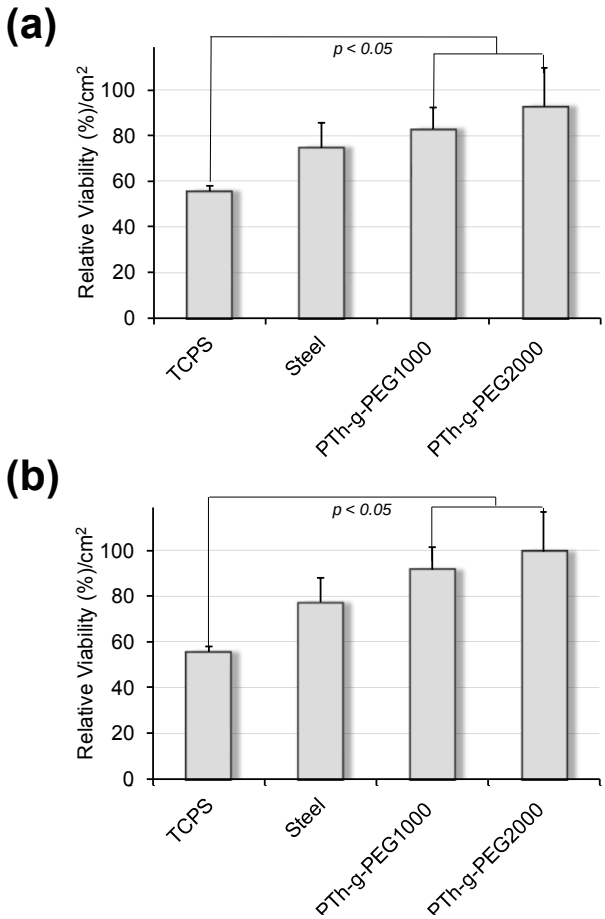

Figure 10. Cellular adhesion (a) and cellular proliferation (b) on PTh-g-PEG1000 and PTh-g-PEG2000 doped with ClO_4^-. The relative viability of Vero cells was established in relation to the TCPS control (tissue culture polystyrene). Steel was also considered as a control substrate because the individual polymers and the blend were deposited on this material. $p < 0.05$ vs TCPS.

Table 1 compares the response of PEDOT towards Vero cells[16] with those of PTh-g-PEG_{1000} and PTh-g-PEG_{2000}. In all cases viability is relative to the TCPS control. As it can be seen, the number of adhered cells by unit of area is similar for the three compounds, even though from a quantitative point of view is slightly higher for PEDOT.

However, the cell viability in proliferation assays is remarkably higher for the two graft copolymers than for PEDOT. This feature evidences that grafted PEG chains improves significantly the cell response of PTh, results in an excellent bioactive platform for tissue engineering.

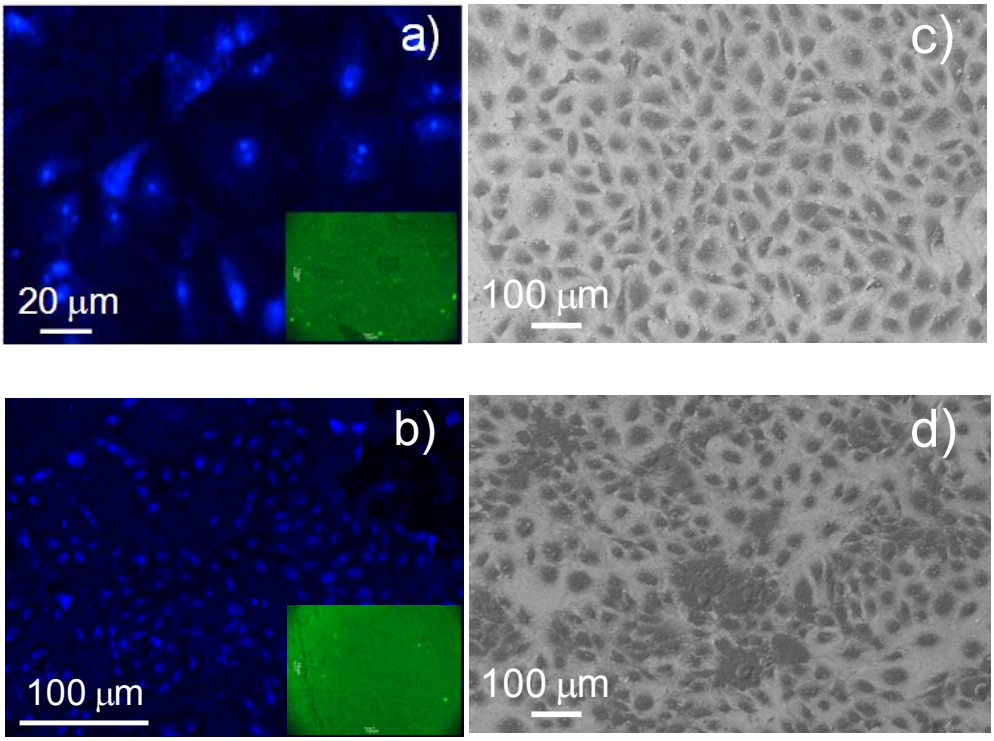

Figure 11. Fluorescence images of cell adhesion onto (a) PTh-g-PEG_{1000} and (b) PTh-g-PEG_{2000} surfaces. Cell adhesion was observed with nuclei stain using bisbenzimide. Insets show the intrinsic fluorescence of the hybrid matrix. SEM micrographs of cells adhered on the surface of (c) PTh-g-PEG_{1000} and (d) PTh-g-PEG_{2000}.

Electrochemical behavior of the cellular matrix.

Control voltammograms in PBS of PTh-g-PEG_{1000} and PTh-g-PEG_{2000} as prepared (uncovered) and covered with Vero cells in PBS are displayed in Figure 12a. The electroactivity of the covered films is significantly higher (i.e. 162 and 329%, respectively) than that of the uncovered ones, this feature being particularly remarkable for PTh-g-PEG_{2000}. The remarkable activity of covered films, which is higher than for PEDOT (Table 1), should be attributed to the exchange of ions promoted by the adhered cells during oxidation-reduction process. Although the electrochemical behavior of the two hybrids is dominated by the PTh backbone, the role played by the latter effect is expected to be more important in the hybrid with smaller PEG chains, as is evidenced in Figure 12a. On the other hand, the current density at 0.90 V increases

from 0.26 and 0.06 mA·cm^{-2} for uncovered PTh-g-PEG$_{1000}$ and PTh-g-PEG$_{2000}$, respectively, to 0.74 and 0.39 mA·cm^{-2} for the systems coated with cells. This behavior also reflects the enhancement of the electrochemical properties provoked by the adhered cells.

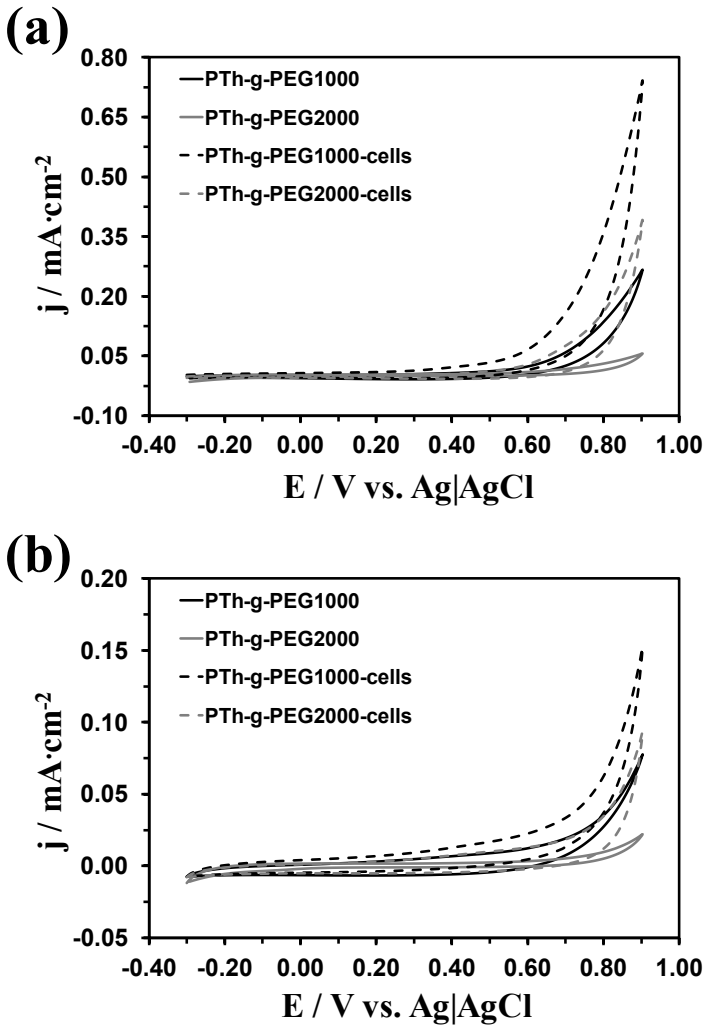

Figure 12. CVs of PTh-g-PEG$_{1000}$ (black) and PTh-g-PEG$_{2000}$ (grey) films uncovered (solid line) and coated with Vero cells (dashed lines) in PBS. Voltammograms of both the as prepared samples (a) and after ten consecutive oxidation-reduction cycles (b) are displayed.

Figure 12b compares the voltammograms recorded after 10 consecutive oxidation-reduction cycles in PBS for samples uncovered and coated with cells. As it can be seen, there is a significant reduction in the electroactivity with respect to the control voltammograms displayed in Figure 12a. The electrochemical stability of uncovered samples was slightly higher than that of samples coated with Vero cells. Thus, the LEA of uncovered and covered samples is ~65% and ~75%, respectively. This should be attributed to the fact that, in the first cycle, the electroactivity of the former

samples in the first cycle is very low compared to that of the latter ones. Accordingly, it spite of such LEA values, the electroactivity of films coated with Vero cells is considerably higher than that of the uncoated films after 10 consecutive redox cycles (i.e. 79% and 228% for PBS of PTh-g-PEG_{1000} and PTh-g-PEG_{2000}, respectively).

6.2.4 Conclusions

UV-vis spectroscopy analyses of macromonomers indicate that the electronic properties of the pentathiophene fragment are dominated by the size of the PEG chains. This effect is significantly reduced upon polymerization, the π-conjugation of the PTh backbone playing a fundamental role in graft copolymers. The optical E_g ranges from 2.25 to 2.29 eV, depending of the length of the PEG chain and the dopant agent. These values are ~0.3 eV larger than those typically found for 3-substituted PTh derivatives, indicating that PEG chains provokes a higher reduction in the conjugation length of the PTh backbone. Furthermore, the formation of polarons and bipolarons as well as the transition between such two states upon re-oxidation have been also detected by UV-vis spectroscopy.

The hydrophilicity of PTh-*g*-PEG_n increases with *n*, the contact angle measured for PTh-*g*-PEG_{2000} being even higher than that of PEDOT. This behavior is fully consistent with the structure predicted by MD simulations in hydrated environments. More specifically, simulations indicate that PTh and PEG segments are perpendicular and parallel to the surface, respectively, both showing extended conformations are relatively ordered arrangements. Due to this biphasic organization polar PEG chains are completely accessible to the water molecules of the bulk. In a desolvated environment the copolymer chains collapse onto the surface, leading to an important reduction of the molecular order.

The behavior of the two hybrids as supportive matrix has been found to very good, especially that of PTh-*g*-PEG_{2000}. The two systems promote cells growth, their behavior as matrices for cellular proliferation being significantly higher than that reported for PEDOT due to the biocompatibility of the PEG fragments.[16] Furthermore, the electrochemical activity and the maximum of current density are significantly higher for PTh-*g*-PEG_n films coated by cells than for uncoated samples. The overall of

the results suggest that the graft copolymers studied in this work have many potential biotechnological applications, especially those in which electrochemical properties are used as elements for the communication with cells (*e.g.* biosensing and transmission components in orthopedic devices).

6.2.5 References

1. H. Shirakawa, E. J. Louis, A. G. MacDiarmid, C. K. Chiang and A. J. Heeger, *Chem. Soc. Chem. Commun.*, 1977, **578**.
2. "Handbook of conducting polymers" 3rd edition, T. A. Skoteheim and J. R. Reynolds, Eds., CRC Press, Boca Raton, FL 2007.
3. K. Kundu and D. Giri, *Am. Inst. Phys.* 1996, **105**,11075.
4. S. Y. Hong and D. S. Marnick, *Macromolecules*, 1992, **25**, 4652.
5. L. B. Groenendaal, F. Jonas, D. Freitag, H. Pielartzik and J. R. Reynolds, *Adv. Mater.*, 2000, **12**, 481.
6. S. Kirchmeyer and K. Reuter, *J. Mater. Chem.*, 2005, **15** 2077.
7. Pettersson, T. Johansson, F. Carlsson, H. Arwin and O. Inganas, *Synth. Met.*, 1999, **101**, 198.
8. A. Kumar, D. M. Welsh, M. C. Morvant, F. Piroux, K. A. Abboud and J. R. Reynolds, *Chem. Mater.*, 1998, **10**, 896.
9. B. Winther-Jensen, O. Winther-Jensen, M. Forsyth and D. R. MacFarlane, *Science*, 2008, **321**, 671.
10. J. Joo, S.-H. Park, D.-S. Seo, S.-J. Lee, H.-S. Kim, K.-W. Ryu, T.-J. Lee, S.-H. Seo and C.-L. Lee, *Adv. Funct. Mater.*, 2005, **15**, 1465.
11. J. K. Koh, J. Kim, B. Kim, J. H. Kim and E. Kim, *Adv. Mater.*, 2011, **23** 1641.
12. N. K. Guimard, N. Gomez and C. E: Schmidt, *Prog. Polym. Sci.*, 2007, *prog. Polym. Sci.*, 2007, **32**, 876.
13. A. D. Bendrea, L. Cianga and I. Cianga, *J. Biomat. Appl.*, 2011, **26**, 3.
14. D. F. Li, H. J. Wang, J. X. Fu, W. Wang, X. S. Jia and J. Y. Wang, *J. Phys. Chem. B*, 2008, **112**, 16290.
15. S. Kamalesh, P. Tan, J. Wang, T. Lee, E. T. Kang, C. H. Wang, *J. Biomed. Mater. Res.*, 2000, **52**, 467.
16. G. Fabregat, G. Ballano, E. Armelin, L. J. del Valle, C. Cativiela and C. Alemán, *Polym. Chem.*, 2013, **4**, 1412.
17. M. M. Pérez-Madrigal, E. Armelin, L. J. del Valle, F. Estrany and C. Alemán, *Polym. Chem.*, 2012, **3**, 979.
18. N. Mohamed-Mahmoud and G. Olgun, *Prog. Polym. Sci.*, 2012, **37**, 1597.
19. C. J. Galvin and J. Genzer, *Prog. Polym. Sci.*, 2012, **37**, 871.
20. V. Singh, P. Kumar and R. Sanghi, *Prog. Polym. Sci.*, 2012, **37**, 340.
21. D. Neugebauer, *Polymer*, 2011*,* **56**, 521.
22. C. Feng, Y. J. Li, D. Yang, J. H. Hu, X. H. Zhang and X. Y. Huang, *Chem. Soc. Rev.*, 2011, **40**, 1282.
23. D. Uhrig and J. Mays, *Polym. Chem.*, 2011, **2**, 69.
24. P. J. Costanzo and K. K. Stokes, *Macromolecules*, 2002, **35**, 6804.
25. A. Cirpan, S. Alkan, L. Toppare, Y. Hepuzer and Y. Yag, *J. Polym. Sci. Part A: Polym. Chem.*, 2002, **40**, 4131.

26. J. Shen and K. Ogino, *Chem. Lett.*, 2005, **34**, 1616.
27. J. Shen, K. Tsuchiya and K. Ogino, *J. Polym. Sci. Part A: Polym. Chem.*, 2008, **46**, 1003.
28. X. Chen, B. Gholamskhass, X. Han, G. Vamvouinis and S. Holdcroft, *Macromol. Rapid Commun.*, 2007, **28**, 1792.
29. F. Liu, Y. Chen, Y. Wei, L. Li and S. Shang, *J. Appl. Polym. Sci.*, 2012, **123**, 2582.
30. A. D. Bendrea, G. Fabregat, L. Cianga, F. Estrany, L. J. del Valle, I. Cianga and C. Alemán, *Polym. Chem.* 2013, **4**, 2709.
31. S. P. Zhong, Y. P. Zhang and C. T. Lim, *Tissue Engin. Part B-Reviews*, 2012, **18**, 77.
32. C. Mangold, F. Wurm and H. Frey, *Polym. Chem.*, 2012, **3**, 1714.
33. J. Peyre, V. Humblot, C. Methivier, J.-M. Berjeaud and C.-M. Pradier, *J. Phys. Chem. B*, 2012, **47**, 13839.
34. I. W. Hamley, M. J. Krysmann, V. Castelletto and L. Noirez, *Adv. Mater.*, 2008, **20**, 4394.
35. Y. Y. Xu, J. Y. Yuan, B. Fang, M. Drechsler, M. Mullner, S. Bolisetty, M Ballauf and A. H. E. Muller, *Adv. Funct. Mater.*, 2010, **20**, 4182.
36. J. G. Sun, S. V. Graeter, L. Yu, S. F. Duan, J. P. Spatz and D. Ding, *Biomacromolecules*, 2008, **9**, 2569.
37. K. Driesen, R. Van Deun, C. Gorller-Walrand and K. Binnemans, *Chem. Mater.*, 2004, **16**, 1531.
38. L. J. del Valle, D. Aradilla, R. Oliver, F. Sepulcre, A. Gamez, E. Armelin, C. Alemán and F. Estrany. *Eur. Polym. J.*, 2007, **43**, 2342.
39. L. J. del Valle, F. Estrany, E. Armelin, R. Oliver and C. Alemán. *Macromol. Biosci.*, 2008, **8**, 1144.
40. W. D. Cornell, P. Cieplak, C. L. Bayly, I. R. Gould, K. M. Merz, D. M. Ferguson, D. C. Spellmeyer, T. Fox, J. W. Caldwell and P. A. Kollman, *J. Am. Chem. Soc.*, 1995, **117**, 5179.
41. J. Wang, R. M. Wolf, J. W. Caldwell and D. A. Case, *J. Comput. Chem.*, 2004, **15**, 1157.
42. J. Preat, F. Rodríguez-Ropero, J. Torras, O. Bertran, D. Zanuy and C. Alemán, *J. Comput. Chem.*, 2010, **31**, 1741.
43. P. Cieplak, W. Cornell, C. I. Bayly and P. A. Kollman, *J. Comput. Chem.*, 1995, **16**, 1357.
44. D. Curcó, D. Zanuy, R. Nussinov and C. Alemán, *J. Comput. Chem.*, 2011, **32**, 607.
45. D. Curcó, G. Revilla-López, C. Alemán and D. Zanuy, *J. Pept. Sci.*, 2011, **17**, 132.
46. W. L. Jorgensen, J. Chandrasekhar, J. D. Madura, R. W. Impey and M. L. Klein, *J. Chem. Phys.*, 1983, **79**, 926.
47. D. A. Case, T. A. Darden, T.E. Cheatham III, C. L. Simmerling, J. Wang, R. E. Duke, R. Luo, R. C. Walker, W. Zhang, K. M. Merz, B. Roberts, S. Hayik, A. Roitberg, G. Seabra, J. Swails, A. W. Goetz, I. Kolossváry, K. F. Wong, F. Paesani, J. Vanicek, R. M. Wolf, J. Liu, X. Wu, S. R. Brozell, T. Steinbrecher, H. Gohlke, Q. Cai, X. Ye, J. Wang, M.-J. Hsieh, G. Cui, D. R. Roe, D. H. Mathews, M. G. Seetin, R. Salomon-Ferrer, C. Sagui, V. Babin, T. Luchko, S. Gusarov, A. Kovalenko, P. A. Kollman, *AMBER 12*, University of California: San Francisco, 2012.
48. J. P. Ryckaert, G. Ciccotti and H. J. C. Berendsen, *J. Comput. Phys.*, 1977, **23**, 327.
49. L. H. Shi, F. Garnier and J. Roncali, *Macromolecules*, 1992, **25**, 6425.

50. H. B. Yildiz, S. Kiralp, L. Toppare, Y. Yagci, K. Ito, *Macromol. Chem. Phys.*, 2006, **100**, 124.
51. F. Alakhras and R. Holze, *Synth. Metals*, 2007, **157**, 109.
52. A. L. Gomes, J. Casanovas, O. Bertran, J. S. de C. Campos, E. Armelin and C. Alemán, *J. Polym. Res.*, 2011, **18**, 1509.
53. Y. Pang, X. Li, G. Shi and L. Jin, *Thin Solid Films*, 2008, **516**, 6512.
54. J. Casanovas, D. Aradilla, J. Poater, M. Solà, F. Estrany and C. Alemán, *Phys. Chem. Chem. Phys.*, 2012, **14**, 10050.
55. D. Aradilla, F. Estrany and C. Alemán, *J. Appl. Polym. Sci.*, 2011, **121**, 1982.
56. G. Fabregat, C. Alemán, M. T. Casas and E. Armelin, *J. Phys. Chem. B*, 2012, **116**, 5064.
57. O. Inganäs, *Chem. Soc. Rev.*, 2010, **39**, 2633.
58. R. B. Pernites, R. R. Ponnapati and R. C. Advincula, *Adv. Mater.*, 2011, **23**, 3207.

CHAPTER 7

PEDOT-CREKA NANOCOMPOSITES FOR BIOMEDICAL APPLICATIONS

7.1 Impact of incorporating a clot-binding peptide into conducting polymer properties: Composites for biomedical applications*

Biocomposites formed by a pentapeptide, CREKA, which recognizes clotted plasma proteins, entrapped into PEDOT matrix have been prepared using three very different procedures. XPs analyses indicate that PEDOT-CREKA films, prepared by CA in basic aqueous solution (pH=10.3) and deposited onto a PEDOT internal layer, present the higher concentration of peptide: one CREKA molecule per six polymer repeat units. The surface of this bilayered system shows numerous folds homogeneously distributed, which have been exhaustively characterized by SEM and AFM. Indeed, the morphology and topography of such bilayered films is completely different from those of biocomposites prepared acid aqueous and organic solutions as polymerization media. The impact of the entrapped peptide molecules in the electrochemical properties of the CP has been found to be practically negligible. In contrast, biocompatibility assays with two different cellular lines indicate that PEDOT-CREKA favours cellular proliferation, which has been attributed to the binding of the peptide to the fibrin molecules from the serum used as supplement in the culture medium. The latter assumption has been corroborated examining the ability of PEDOT-CREKA to bind fibrin. The overall of the results suggest that PEDOT-CREKA is appropriated for multiple biomedical applications combining the electrochemical properties of CP and the ability of the peptide to recognize and bind proteins.

* Results described in this section has been accepted for publication in *Appl. Mater. Interfaces.*

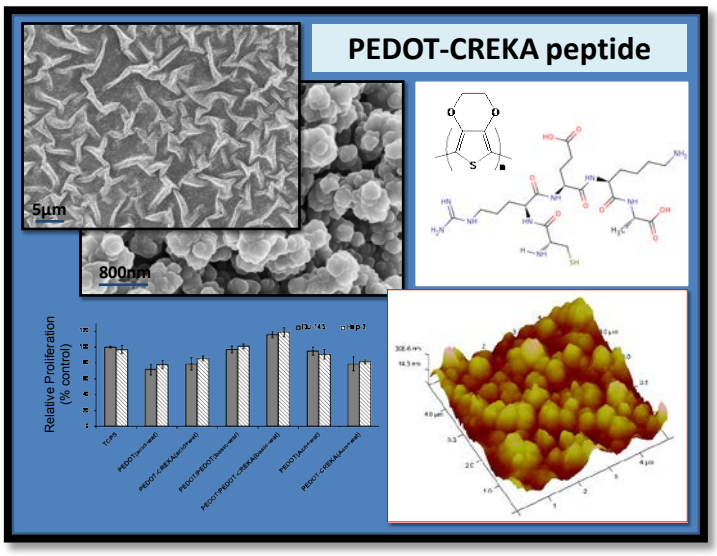

7.1.1 Introduction

CP coatings have been shown to improve the charge transfer characteristics of conventional metal electrodes and biological assays have revealed that proteins and cells preferentially adhere to coated electrodes.[1-4] As a consequence, many CPs have been used in tissue engineering applications, even though research efforts have been mainly concentrated on PPy, PEDOT and their derivatives.[5] Some extracellular matrix biomolecules, especially peptides, are known to support cell attachment and growth when incorporated into CPs or used as a coating.[6-15]

The incorporation of peptides can be carried out using different approaches. The most frequent is the incorporation of anionic peptides as dopant agents of the CPs,[5-15] which is achieved through the incorporation of the biomolecule into the monomer medium used for the polymerization process. Unfortunately, this particular class of dopants may produce significant undesirable changes in the bulk properties of the CP, reducing the electrical conductivity, the electroactivity, the electrochemical stability, etc. Other emerging non-covalent approach to modify CPs for biomedical applications is based on the use of peptides with binding specificity, which are selected from phage display libraries. For example, surface modification with Arg-Gly-Asp (RGD) of PPy doped with chloride peptide promotes the PC12 cell adhesion in serum-free media, whereas no adhesion is observed on unmodified surfaces.[12] An advantage of this entrapment approach is that, apparently, it should not modify the intrinsic properties of the CP and could be used with a wide range of different biomolecules that do not need to be negatively charged. In addition to the dopant and non-covalent entrapment approaches, modification of CPs via covalent bonds has been also explored. Multiple techniques have been used, like for example: the modification of the β-position on PPy to create strong disulfide bonds with the Cys of Arg-Gly-Asp-Cys (RGDS), enhancing osteoblast adhesion;[13,14] and the modification of the surface to immobilize peptides through covalent bonds, which have been successfully used for different biomedical applications (*e.g.* immobilize nerve growth factor[15] and promote cellular proliferation[16]).

Over the last years, Ruoslahti and coworkers have identified a series of tumor-homing peptides by using *in vivo* screening of peptide libraries.[17,18] Among the homing

peptides discovered by this procedure exists a linear peptide that contains only five amino acids with sequence Cys-Arg-Glu-Lys-Ala (CREKA).[17,18] This pentapeptide, which recognizes fibrin-fibronectin complexes, was used to design a self-amplifying nanoparticle delivery system.[19] Iron oxide nanoparticles coated with this peptide accumulate in tumor vessels, where they induce additional local clotting and thereby produce new binding sites for more nanoparticles. This amplification system enhanced homing of the nanoparticles in a mouse tumor model without causing clotting or other obvious side effects in the body. Although self-amplified tumor accumulation produced enhancement of tumor imaging, significant inhibition of tumor growth was not obtained. Determination of the bioactive conformation of CREKA through computer aided modeling tools[20,21] led to engineer a series of analogues by targeted replacements in Arg and Glu, which were replaced by the corresponding N- and C^{α}-methylated amino acids.[22] CREKA analogues nanoparticles were combined with nanoparticles coated with another tumor-homing peptide (Cys-Arg-Lys-Asp-Lys-Cys) and nanoparticles with an elongated shape (nanoworms). Treatment of mice with prostate cancer with multiple doses of these nanoworms induced tumor necrosis and highly significant reduction in tumor growth.[22]

Modification of CPs by introducing CREKA analogues, which due to their unique properties could extend the biomedical applications of these materials, is highly desirable. In this work we focus on the most appropriated approach and conditions for the incorporation of these peptides into the polymer matrix as well as on their impact on the CP properties. As the synthesis of the above mentioned CREKA analogues involves an important chemical effort, which is essentially related with the preparation of non-proteinogenic amino acids, the parent peptide CREKA has been used for the investigations reported in this work. However, as the charge distribution is the same in CREKA that in its N- and C^{α}-methylated analogues (*i.e.* all these peptides are cationic with two positively charged amino acids and only one negatively charged), the former should be considered a good model. Within this context, in this contribution we have evaluated three different approaches to modify PEDOT with CREKA. Furthermore, the influence of the peptide on the morphology, topography, electrochemical properties,

cellular activity and ability to bind fibrin has been established by comparing PEDOT with modified PEDOT, hereafter referred as PEDOT-CREKA.

7.1.2 Methods

Materials. EDOT monomer, dodecylbenzene sulfonate (SDBS) and acetonitrile (analytical reagent grade) were purchased from Aldrich and used as received without further purification. Anhydrous $LiClO_4$ (analytical reagent grade, Aldrich) was stored in an oven at 80 ºC before use in electrochemical trials. CREKA peptide with > 98% of HPLC purity was purchased from GenScript USA Inc. Ultrapure milliQ water was used to prepare all the aqueous solutions.

Synthesis.Both anodic polymerization and electrochemical assays were performed with an Autolab PGSTAT302N equipped with the ECD module (Ecochimie, The Netherlands) using a three-electrode compartment cell under nitrogen atmosphere (99.995% pure) at room temperature. Steel AISI 316 sheets of 1 cm^2 in area were used as WE and CE. To prevent interferences during the electrochemical assays, the WE and CE were cleaned with acetone before each trial. The RE was an Ag|AgCl electrode containing a KCl saturated aqueous solution [offset potential versus the standard hydrogen electrode, E^0= 0.222 Volts (V) at 25ºC], which was connected to the working compartment through a salt bridge containing the electrolyte solution.

Although all PEDOT-CREKA composites reported in this work were prepared by anodic polymerization, different approaches that differ in the procedure and/or experimental conditions were employed to identify the material with optimum properties.

1) ***PEDOT-CREKA films produced in organic environment.*** The anodic compartment of the cell was filled with 10 mL of a 0.01 M EDOT solution in acetonitrile containing 0.1 M $LiClO_4$ as supporting electrolyte and 1 mg/mL of CREKA aqueous solution, while the cathodic compartment was filled with 10 mL of the same electrolyte solution. Films were prepared by CA under a constant potential of 1.40 V, which was identified as the optimum value for the polymerization of EDOT in acetonitrile,[23] using a polymerization time θ= 200 s (*i.e.* films obtained using smaller polymerization times were very fragile and difficult to handle). The experimental conditions used for the preparation of

PEDOT films used as blank were identical to those of PEDOT-CREKA with the exception of the anodic compartment, which was filled with 5 mL of 0.01 M EDOT solution in acetonitrile containing 0.1 M $LiClO_4$ as supporting electrolyte and 5 mL of ultrapure milliQ water. Hereafter, films prepared using these conditions are denoted PEDOT-CREKA(Acn+wat) and PEDOT(Acn+wat).

2) ***PEDOT-CREKA films produced in a basic aqueous environment.*** All films were prepared by CA using an aqueous medium with pH= 10.3 (adjusted with NaOH) and a constant potential of 1.10 V, which was identified as the optimum potential for the polymerization of EDOT in water.[24] Preliminary assays indicated that films obtained by direct electrodeposition of the composite onto the steel electrode were very fragile and difficult to handle for characterization and application assays. In order to overcome this limitation, the preparation of PEDOT-CREKA films was afforded using a new approach based on a two-steps process. Initially, the steel electrode was coated with PEDOT. For this purpose, the anodic compartment was filled with 10 mL of a 20 mM EDOT monomer aqueous solution containing 10 mM SDBS as supporting electrolyte while the cathodic compartment was filled with 10 mL of the same electrolyte solution. The polymerization time selected for the electrodeposition of this coating layer was θ= 10 s (*i.e.* different trials using θ= 20 and 30 s did not improve the electrochemical properties). After this, a new layer of PEDOT-CREKA composite was electrodeposited onto the surface of the PEDOT layer. This was achieved by filling the anodic compartment with a generation solution identical to that mentioned above for the first layer but containing 1 mg/mL of CREKA peptide. The applied potential and the polymerization time were 1.10 V and θ= 20 s, respectively. PEDOT films used as the blank were prepared employing experimental conditions identical to those described above, even though two different systems were considered: (1) single-layered films obtained using a polymerization times of 10, 20 and 30 s (*i.e.* the polymerization times used for the individual layers of the bilayered system and its sum); and (2) bilayered films obtained without CREKA (*i.e.* two PEDOT layers prepared using polymerization times of 10 and 20 s). Hereafter, composite and blank films prepared using these conditions are denoted PEDOT/PEDOT-CREKA(basic-wat), PEDOT(basic-wat) and PEDOT/PEDOT(basic-wat), respectively.

3) ***PEDOT-CREKA films produced in an acid aqueous environment***. The anodic compartment of the cell was filled with 5 mL of an aqueous medium with pH= 5.4 (adjusted with HCl) containing 0.01 M EDOT, 0.1 M SDBS and 1 mg/mL of CREKA peptide. The cathodic compartment was filled with 10 mL of the same electrolyte solution. Films were generated by CA using a constant potential of 1.10 V and a polymerization time of 10 s, which was the minimum time required to obtain a complete coverage of the surface. For the preparation of the PEDOT films used for comparison, which were obtained under the same experimental conditions, the CREKA peptide was not included in the generation medium. The composite and blank films produced in this environment have been denoted PEDOT-CREKA(acid-wat) and PEDOT(acid-wat), respectively.

Analytical techniques

FTIR. The influence of the polymer matrix on the secondary structure of the entrapped peptide was performed using a FTIR 4100 Jasco spectrophotometer. Spectra were recorded in the transmittance mode. The samples were placed in an attenuated total reflection accessory with thermal control and a diamond crystal (Specac model MKII Golden Gate Heated Single Reflection Diamond ATR).

XPS. XPS analyses were performed in a SPECS system equipped with a high-intensity twin-anode X-ray source XR50 of Mg/Al (1253 eV/1487 eV) operating at 150 W, placed perpendicular to the analyzer axis, and using a Phoibos 150 MCD-9 XP detector. The X-ray spot size was 650 mm. The pass energy was set to 25 and 0.1 eV for the survey and the narrow scans, respectively. Charge compensation was achieved with a combination of electron and argon ion flood guns. The energy and emission current of the electrons were 4 eV and 0.35 mA, respectively. For the argon gun, the energy and the emission current were 0 eV and 0.1 mA, respectively. The spectra were recorded with a pass energy of 25 eV in 0.1 eV steps at a pressure below 6×10^{-9} mbar. These standard conditions of charge compensation resulted in a negative but perfectly uniform static charge. The C 1s peak was used as an internal reference with a binding energy of 284.8 eV. High-resolution XPS spectra were acquired by Gaussian–Lorentzian curve fitting after S-shape background subtraction. The surface composition was determined using the manufacturer's sensitivity factors.

High-performance liquid chromatography (HPLC). Analyses were carried out using a isocratic gradient of 0.1% trifluoroacetic acid, 10% acetonitrile, and 10% methanol in 100% water, with 1 mL/h of flux and a sample loop of 20 µL on a Licrospher (Merk) C18 column (4.6 mm x 250 mm) with 5 µm diameter particle. The HPLC system consisted on a LC-410 Perkin Elmer HPLC Pump, a LC-235 Perkin Elmer UV-VIS detector, and a Perkin Elmer (Diode Array Detector) interface. The HPLC analysis was running by 15 minutes and the chromatograms were analyzed using the Grams v.8 software (Galactic Inc.). Samples were detected by two channels of absorbance at 220 nm and 280 nm. The standard curve was prepared with different concentrations of CREKA, the area of the peaks being represented against the peptide concentration. Models were adjusted through linear regression analyses. The PEDOT-CREKA samples (2 mg of powder) were extracted in the same HPLC buffer (1 mL) overnight. After this, samples were centrifuged and the supernatant isolated for the HPLC analysis. The determination of CREKA in the sample was performed using the method of substance added. Accordingly, samples were injected in the column and the chromatogram recorded. Next, a known amount of CREKA was added to the sample, which was subsequently injected in the HPLC column. This process allowed us to determine the peaks of CREKA in the sample.

SEM. SEM studies were carried out using a FIB Zeiss Neon 40 scanning electron microscope operating at 6 kV, equipped with an EDX spectroscopy system. Samples were mounted on a double-side adhesive carbon disc and sputter-coated with a thin layer of carbon to prevent sample charging problems.

Contact stylus profilometry. The thickness of the films was determined using a Dektak 150 stylus profilometer (Veeco, Plainview, NY). Different scratches were intentionally provoked on the films and measured to allow statistical analysis of data. Imaging of the films was conducted using the following optimized settings: tip radius= 2.5 µm; stylus force= 1.5 mg; scan length= 1 µm; speed= 1.5 nm/s..

AFM. Topographic AFM images were obtained with a Dimension 3100 Nanoman AFM and Multimode from Veeco using a NanoScope IV controller under ambient conditions in tapping mode. The roughness was determined using the

statistical application of the Nanoscope software, which calculates the average considering all the values recorded in the topographic image with the exception of the maximum and the minimum. AFM measurements were performed on various parts of the films, which produced reproducible images similar to those displayed in this work. The scan window sizes were 5×5 and 25×25 μm^2.

Electrochemical characterization. Electrochemical properties of all the synthesized systems were investigated by CV. The electroactivity, which refers to the charge store ability, and the electrochemical stability (electrostability) were determined using a 0.1M PBS (pH= 7.4 adjusted with NaOH). The initial and final potentials were -0.40 V, whereas a reversal potential of 0.80 V was considered. The scan rate was 50 $mV \cdot s^{-1}$ in all cases. The electroactivity increases with the similarity between the anodic and cathodic areas of the first control voltammogram, whereas the electrostability decreases with the oxidation and reduction areas of consecutive control voltammograms. CV assays were performed with an Autolab PGSTAT302N equipped with the ECD module (Ecochimie, The Netherlands).

Biological assays

Cell adhesion and proliferation test. In vitro adhesion and proliferation assays were performed using two different cellular lines of adherent growth: (i) cells HEp-2; and (ii) cells DU145. HEp-2 and DU145 have an epithelial morphology. TCPS plate has been used as control substrate.

Cells were plated in 25 cm^2 tissue flasks and grown in DMEM supplemented with 10% FBS, penicillin G (100 U/ml) and streptomycin (100 mg/mL). Cultures were performed at 37 °C and humid atmosphere with 95% air (5% carbon dioxide). Passage 2 cultures were used for experiments. Cellular confluent cultures were dissociated with 0.05% trypsin and 0.02% EDTA in Hanks' Balanced Salt Solution, harvested by centrifugation, and counted in Neubauer camera using 0.4% trypan blue.

Adhesion and proliferation assays were performed seeding 5×10^4 and 2×10^4 cells, respectively, from an appropriate cell suspension concentration with viability >95%. PEDOT and PEDOT-CREKA films electrodeposited on 1 cm^2 steel sheets were placed in 24-well plates, and subsequently sterilized by UV-radiation during 15 min in

the laminar flow cabinet. Next, cells were seeded by a slowly pipette of the cell suspension onto the top surface of each sample, covering 80-90% of the sample's surface. In order to avoid a reduction of the seeding efficiency, no contact between cell suspensions and the sides of the wells was allowed. The plates were placed with care into an incubator, avoiding agitation. After 1 h, fresh medium (1 mL) was added into each well and the plate was returned to the incubator. Cultures to evaluate cellular adhesion and proliferation were incubated during 24 h and 7 days, respectively. All experiments were repeated at least three times.

To evaluate the cell number in the samples, the medium of each well was changed by fresh medium supplemented with MTT [5 mg/mL] and the plate returned to the incubator for 3 h. After this, the medium of each well was removed and the samples recoveries were placed in wells of a clean plate. The MTT reaction in the viable cells was determined by dissolving the formazan crystals in 1 mL of DMSO/methanol/water (70%/20%/10%, % in vol.). Then, the absorbance at 540 nm was read in a microplate reader (Biochrom Ltd., UK). Analyses were carried out using the cell adherence density in each sample in comparison to the control (%, relative of control).

To evaluate the cellular morphology, samples incubated with cells were fixed in 1 mL of 2.5% paraformaldehyde in PBS during 24 h at 4 ºC. Then, samples were progressively dehydrated using alcohols of 30º, 40º, 50º, 70º, 90º, 95º, and 100º for 30 min at 4 ºC in each one. Finally, samples were coated by carbon sputtering for the observation in the scanning electronic microscope.

Fibrin recognition. Analysis to examine the adsorption of fibrin onto the surface of PEDOT and PEDOT-CREKA composites were performed according to the following protocol. Fibrin solutions with concentrations of 2 and 10 mg/mL were prepared in a mixture of 0.1 M PBS and 0.1 M NaOH (4v:1v ratio) for 24 h. Incorporation of NaOH was required because fibrin was not soluble in 0.1 M PBS (pH= 7.4). Materials were incubated with 0.5 mL of such fibrin solutions for 24 h at 37ºC. After this, samples were washed with a 0.1 M PBS : 0.1 M NaOH (4:1) mixture. Adsorbed fibrin was removed by adding 0.2 mL of 0.1 M PBS with nonyl phenoxypolyethoxyethanol (NP-40)

surfactant (0.5% v/v) and orbital shaking at 50 rpm during 30 min and 37ºC. In order to avoid interferences between the NP40 surfactant and the Bradford reagent, the former was eliminated by precipitating the fibrin with 20 μL of trichloroacetic acid. Then, the solution with the precipitate was centrifuged for 15 min at 12000 rpm. The solid (fibrin) was washed with cold acetone and maintained in the refrigerator for 1 hour. After this, the solid was centrifuged again during 15 min at 12000 rpm. The fibrin was dried in vacuum and, finally, dissolved in 50 μL of 0.1 M PBS : 0.1 M NaOH (4v:1v) mixture for Bradford assay.

For the absorbance assays, a fibrin concentration calibration curve was carried out using fibrin standards, which were prepared using buffer solution (0.1 M PBS : 0.1 M NaOH, 4v:1v) with concentrations of protein ranging from 0.04 to 2.00 mg/mL. Next, 5 μL of each fibrin standard was added to a 96-well plate, blank wells being filled with 5μL of buffer. After this, Bradford reagent (250 μL) was added and, subsequently, mixed on shaker for 30 s. Samples were incubated at room temperature for 15 min. Finally, the absorbance was measured at 595 nm.

7.1.3 Results and Discussion

Chemical composition

The biocomposites were examined by FTIR and XPS spectroscopies. The FTIR spectra (not shown) of PEDOT-CREKA samples prepared by the different procedures described above (see Methods section) and of their PEDOT counterparts were qualitatively similar. Unfortunately, the entrapped peptide was not clearly detectable in the biocomposites. Thus, the amide I (1700-1600 cm^{-1}) and and amide II (1600-1500 cm^{-1}) regions, which arise primarily from the C=O stretching vibration and the coupling between the N-H in-plane bending and C–N stretching modes, respectively, and the N–H (free: 3500-3300 cm^{-1}; hydrogen bonded: 3350-3070 cm^{-1}) were not clearly recognizable because of the overlapping with the band associated to the Th ring (C=C and C–C stretching) and water (O–H stretching) bands. Regarding the latter, it should be mentioned that hydration occurred despite samples being stored two days in a desiccator evidencing the hydrophilicity of the materials, as was already reported.[25] The rest of the bands were assigned to those typically found in PEDOT:[26-28] C–S

stretching (837 cm^{-1}), stretching of the ethylenedioxy group (1141 and 1057 cm^{-1}) and deformation of the ethylenedioxy group (922 cm^{-1}).

Figure 1a displays the high resolution XPS spectra in the C1s, N1s, O1s and S2p regions for PEDOT/PEDOT-CREKA(basic-wat). Before to discuss the analysis, it should be mentioned that the peaks of peptide may be influenced by those of the CP and vice versa, explaining the small deviations found in some peaks with respect to the values reported in the literature.[29-42] Deconvolution of the C1s peak led to three Gaussian curves that have been attributed to the C–C and C–S bonds of PEDOT and surfactant molecules (284.5 eV), the C–O and C–N of PEDOT and peptide molecules (285.5 eV),[29-31] and to the C=O of amide (288.2 eV).[32,33] The O1s signal consists of four components with the first centered at 532.9 eV, corresponding to the C–O–C bonding in the ethylene bridge.[29,34] The peak centered at 532.1 eV is attributed to the C=O of the amide group[35] while the component at 531.2 eV is assigned to the COO^- moiety of CREKA and the SO_3^- of SDBS dopant molecules.[35] The component at 529.6 eV is associated to contamination products.[16]

The high resolution N1s spectrum, which shows two peaks centered at 399.9 and 401.4 eV, is essential to demonstrate that CREKA is embedded in PEDOT matrix. Previous studies of CP-peptide composites indicated that peaks comprised between 399 and 400 eV are due to the N–H and N–C=O bonds of the peptides.[16,32,35] The peak centered at 401.4 eV is attributed to the N-terminal free charged amino group.[32,33] The peak assigned to the C–N of Arg side group, which should appear at 399.2 eV, is overlapped with the lowest energy peak. These observations support the successful incorporation of the peptide to the CP matrix. The high resolution XPS of the S2p region for the composite, which is included in Figure 1a, shows the spin-split sulfur coupling, $S2p_{3/2}$ and $S2p_{1/2}$, for the C–S–C bond of the thiophene ring (163.6 and 164.7 eV, respectively) and its homologous with the positively charged sulfur (*i.e.* $C–S^+–C$ at 166.1 and 167.3 eV, respectively).[38-41] The components centered at 168.0 ($S2p_{3/2}$) and 169.1 eV ($S2p_{1/2}$) are attributed to the SO_3^- of SDBS (165.1 eV),[42] The component associated to the C–SH of Cys, which is expected at approximately 163.2 eV,[39] is unfortunately overlapped with some other peaks, discrimination being not possible.

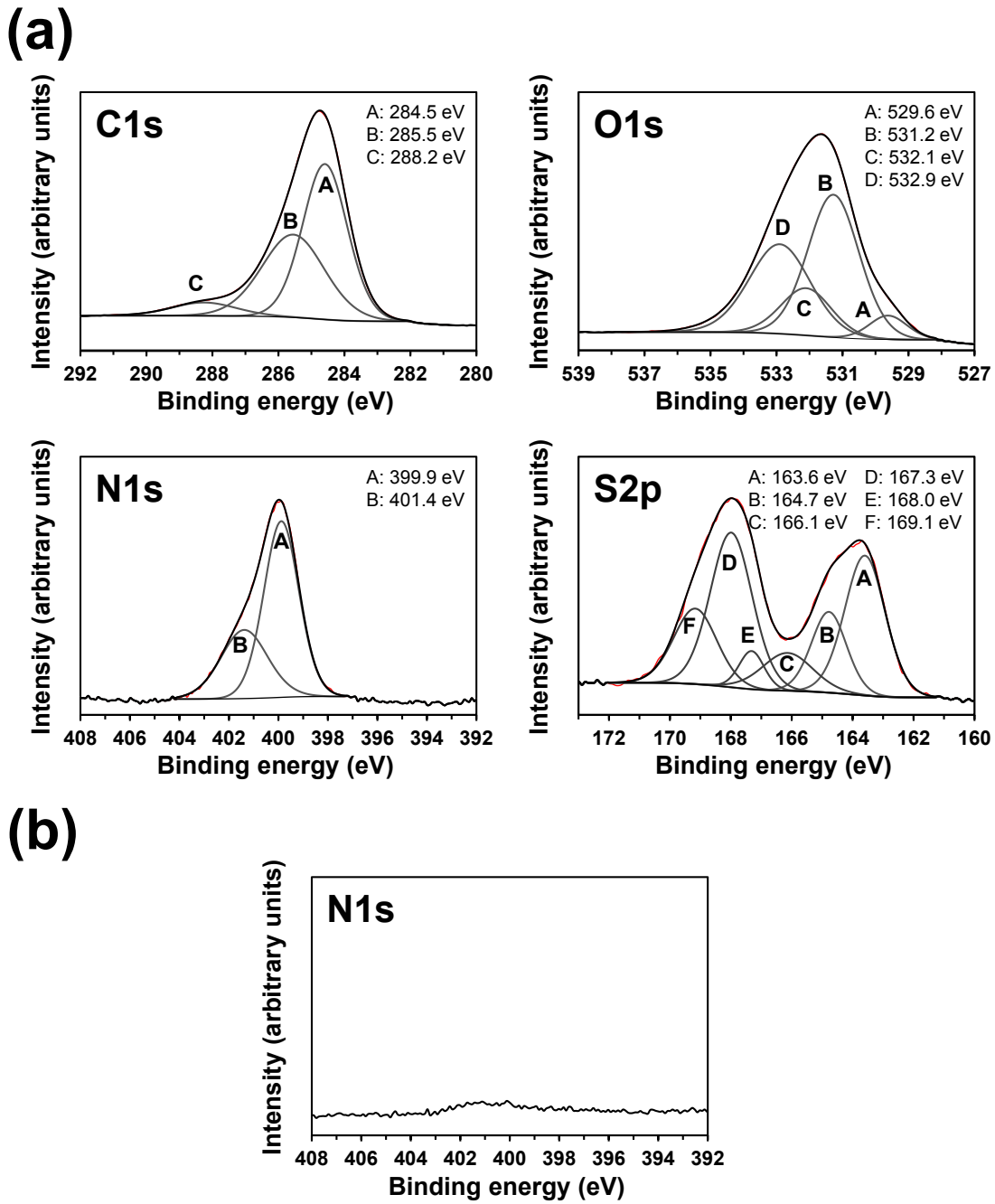

Figure 1. (a) High resolution XPS spectra for PEDOT/PEDOT-CREKA(basic-wat): C1s, O1s, N1s and S2p regions. (b) N1s region of the XPS spectra recorded for the internal PEDOT layer before the electrodeposition of the PEDOT-CREKA composite. Peaks from deconvolution are displayed in all cases.

High resolution XPS spectra for PEDOT were reported and discussed in a recent study[38] and for this reason discussion have not been included in Figure 1. However, in order to remark the absence of CREKA signals, Figure 1b displays the spectrum in the N1s region recorded for the internal PEDOT layer that was used to coat the steel electrode in PEDOT/PEDOT-CREKA(basic-wat) films. Comparison of the N1s spectra

displayed in Figures 1a and 1b corroborates the successful incorporation of CREKA into the CP matrix during the polymerization process. XPS spectra (not shown) recorded for PEDOT-CREKA(Acn+wat) and PEDOT-CREKA(acid-wat) showed the same peaks, the presence of peptide being demonstrated by the signals detected at the N1s region.

The number of EDOT units per CREKA peptide molecule in each composite was derived from the S / N ratio, where S refers to the sum of the atomic percent composition associated to the C–S–C and C–S^+–C curves at the S2p region and N is total atomic percent composition of the nitrogen atom. Results indicated that the content of CREKA in PEDOT/PEDOT-CREKA(basic-wat) films is very high with ~6 EDOT units per CREKA molecule. However, this successful ratio decreases significantly for PEDOT-CREKA(acid-wat) and PEDOT-CREKA(Acn+wat), the number of EDOT units per peptide molecule increasing one and two orders of magnitude, respectively (*i.e.* ~85 and > 350 EDOT units per peptide molecule). In general, the atomic compositions obtained by XPS using the conditions described in the Methods section correspond to the surface, the penetration of the X-ray radiation being expected to be of the order of ~10 nm. As the thickness of PEDOT-CREKA(acid-wat) and PEDOT-CREKA(Acn+wat) films is within the micrometric scale (see next subsection), HPLC analyses were carried out to examine the possible existence of a higher concentration of peptide inside the films (*i.e.* below 10 nm surface).

HPLC results for CREKA, PEDOT(Acn) and PEDOT-CREKA(Acn+wat) are displayed in Figure 2. Detection of the eluted at 220 nm produced two peaks with retention times of 3.3 and 4.8 min for CREKA (Figure 2a), whereas a single peak with a retention time of 4.8-5.0 min was identified when the eluted was detected at 280 nm (data not shown). We assumed that the peak detected at 280 nm corresponds to a honeycomb structure formed by layers of peptides, as was previously found in other polymer-peptide conjugates.[14,15] The response of PEDOT(Acn) was the same at both 220 and 280 nm, two peaks with different intensities and retention times of 4.8-5.0 min and 9.3 min being detected (Figure 2b). The chromatograms of CREKA standards have been followed by absorbance at 220 nm, the linear models for the peaks at 3.3 min (R^2= 0.9812) and 4.8 min (R^2= 0.9999) being displayed in the inset of Figure 2a. As a

consequence of the excellent correlations between the peak areas and the CREKA concentrations, the two models become indistinguishable.

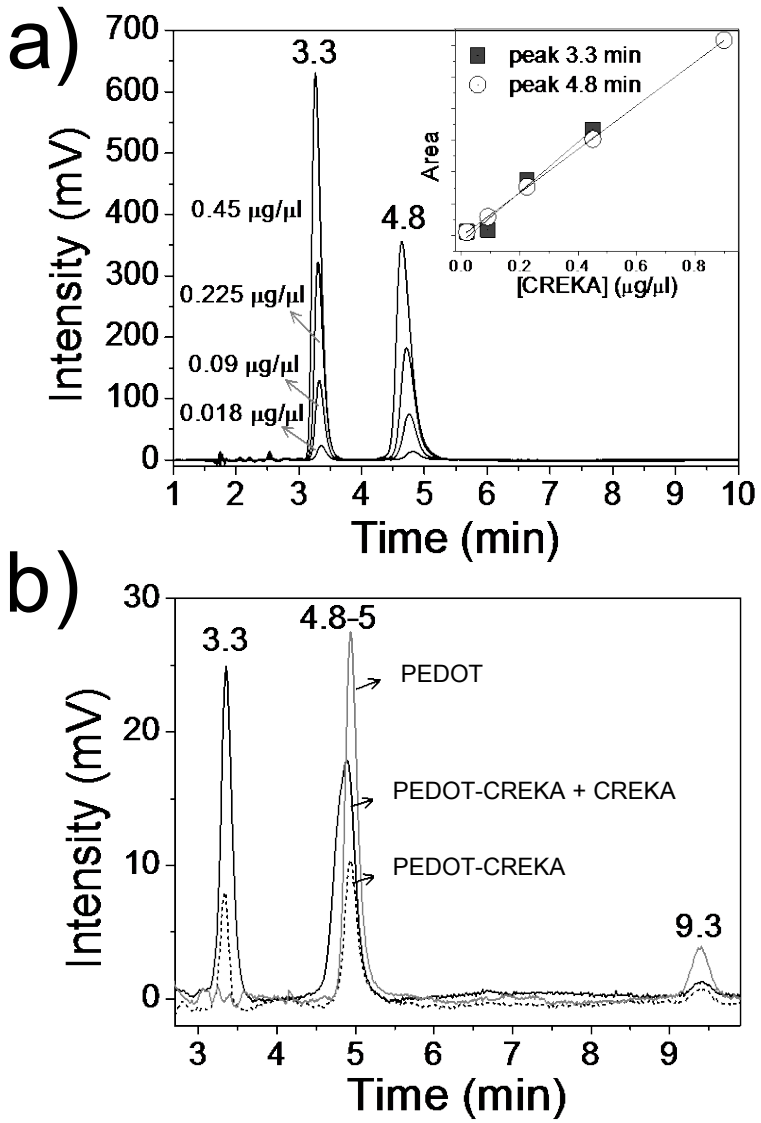

Figure 2. Detection of CREKA in PEDOT-CREKA(Acn+wat) by HPLC. (a) Chromatograms of CREKA at different concentrations show overlapping. The detection was carried out by absorbance at 220 nm. The retention times are indicated over each peak. The inset shows the linear models obtained using the two peaks of CREKA. (b) Chromatograms used to analyze the peptide extracted from PEDOT-CREKA(Acn+wat). The correspondence of peaks was determined by adding a known concentration of CREKA in the extracted sample. A PEDOT extract was used as control to identify the peaks of the CP.

The concentration of peptide extracted from PEDOT-CREKA(Acn+wat) was determined using the method of the added concentration (Figure 2b). As can be seen, the peaks of CREKA and the peptide extracted from PEDOT-CREKA(Acn+wat) are overlapped. The concentration of peptide in the latter was estimated to be 0.3-0.4%,

which corresponds to a PEDOT:CREKA mass ratio of 300:1. This ratio, which corroborates the XPS results, is significantly lower than that used for the electropolymerization of the films. These results indicate that the net positive charge of CREKA, which is removed at basic pH conditions used for the preparation of PEDOT/PEDOT-CREKA(basic-wat) films, makes difficult the entrapment of the peptide into the polymer matrix.

Morphology and topography

Figure 3a shows the morphology of PEDOT/PEDOT-CREKA(basic-wat) films, which can be described as relatively compact surface with multiple, relatively prominent and well-localized folds homogeneously distributed on it. Magnified SEM micrographs reveal differences between the folds and the regions located at the bottom of the surface. Although such two zones consist of the aggregation of pseudo-spherical granules, the attachment of such elements is clearly more compact at the bottom regions of the surface than at the folds. The average thickness and roughness determined by profilometry of PEDOT/PEDOT-CREKA(basic-wat) films, including the folds, are 3.8$\pm$1.3 μm and 582$\pm$24 nm, respectively.

The morphology of PEDOT/PEDOT(basic-wat) films (Figure 3b) is apparently very similar to that described above. Thus, the surface shows many folds homogeneously distributed. However, detailed inspection indicates that such fold are significantly more prominent than those observed in PEDOT/PEDOT-CREKA(basic-wat). The height of the folds, as determined by profilometry, is 7.0$\pm$1.4 and 2.5$\pm$1.1 μm for PEDOT/PEDOT(basic-wat) and PEDOT/PEDOT-CREKA(basic-wat), respectively. The average thickness and roughness measured for PEDOT/PEDOT(basic-wat) films by profilometry are 7.8$\pm$2.9 μm and 1.4$\pm$0.5 μm, respectively.

Inspection of the morphologies reported for PEDOT and PEDOT/PEDOT films produced in acetonitrile[43] evidenced the absence of folds. This feature suggests that the pH and the aqueous solvent used to prepared PEDOT/PEDOT-CREKA(basic-wat) and PEDOT/PEDOT(basic-wat) may play a crucial role in the formation of the folds displayed in Figures 3a and 3b. In order to get further understanding, single-layered PEDOT(basic-wat) films were generated using the same aqueous medium with pH=

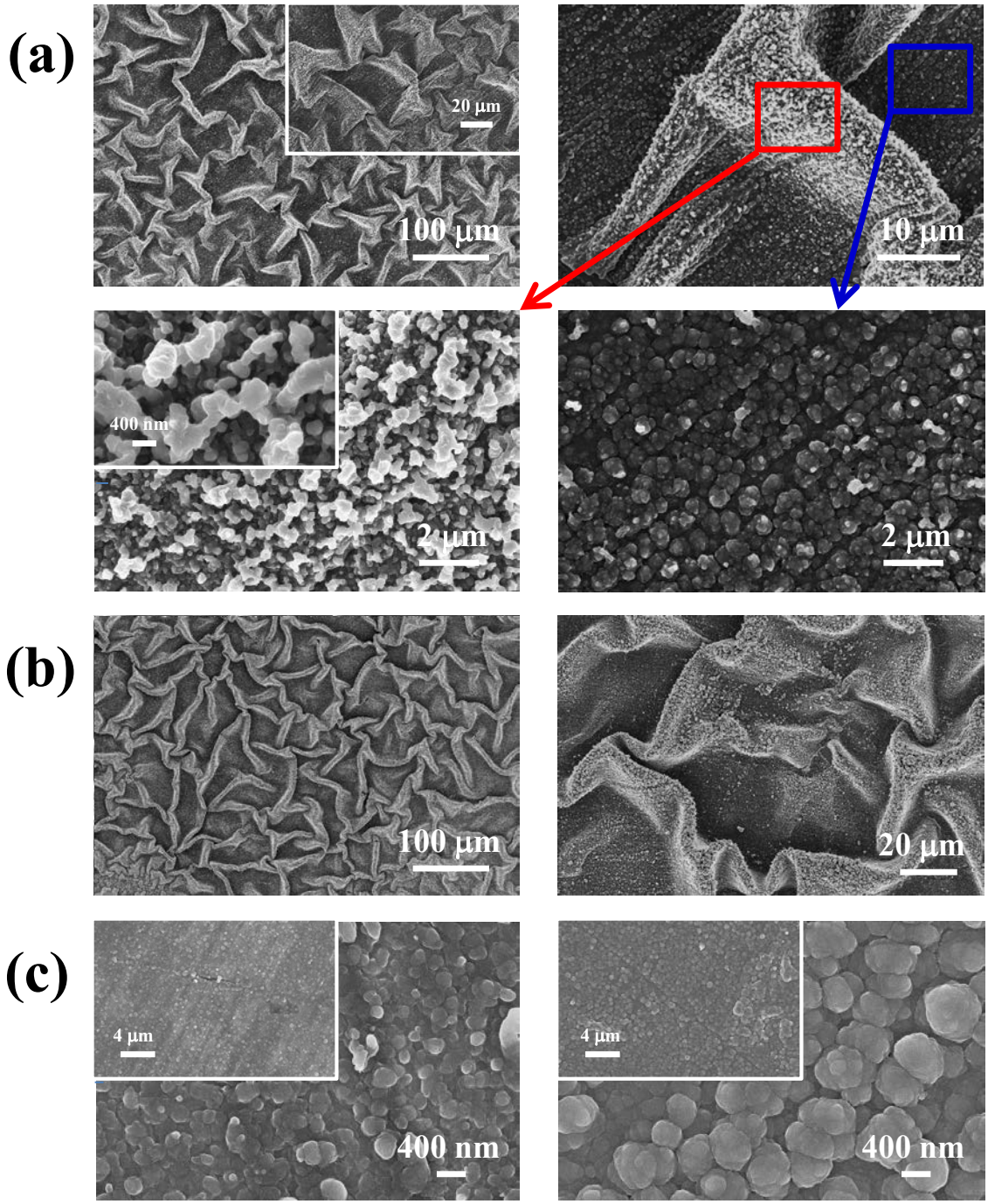

Figure 3. Low- and high-resolution SEM images of: (a) PEDOT/PEDOT-CREKA(basic-wat); (b) PEDOT/PEDOT(basic-wat); and (c) PEDOT(basic-wat) generated using polymerization times of 10 and 20 s (left and right, respectively).

10.3 and considering polymerization times of 10 and 20 s, like those used for the internal and external layer of PEDOT/PEDOT(basic-wat), respectively. SEM micrographs of these films are displayed in Figure 3c. As it can be seen, the morphologies are relatively similar to those described for the films produced in acetonitrile, a homogenous distribution of compact aggregates being observed in the two cases. Furthermore, the size of such aggregates increases with the polymerization time, as

was also observed in acetonitrile.[43] The overall of these results indicates that the formation of the folds in PEDOT/PEDOT-CREKA(basic-wat) and PEDOT/PEDOT(basic-wat) is due to the simultaneous coexistence of three factors rather than two: two-polymerization steps, basic pH and aqueous environment.

Figure 4a displays low- and high-resolution SEM images representative of the overall PEDOT(Acn+wat) morphology. This material presents a heterogeneous surface with multiple flake-like aggregates, which in turn can be described as aggregates of fiber-like sticks. This morphology looks less porous than that of the single-layered films displayed in Figure 3c. Inspection of the SEM images recorded for PEDOT-CREKA(Acn+wat) surface (not shown) does not reflect any significant difference with respect to those displayed in Figure 4a, suggesting as occurred for PEDOT/PEDOT-CREKA(basic-wat), that the entrapped peptide do not alter the surface of the CP.

In order to ascertain if the peptide affects the surface morphology of the internal side, films were detached from the steel electrodes and coated with an ultrathin layer of carbon. Low- and high-resolution SEM images of the internal side of PEDOT(Acn+wat) and PEDOT-CREKA(Acn+wat) are shown in Figures 4b and 4c, respectively. As it can be seen, entrapped CREKA affects both the texture and morphology of PEDOT. The more noticeable results are the homogeneous smooth texture and the practical absence of small nodular outcrops in PEDOT-CREKA(Acn+wat) films, whereas these are frequently and homogeneously present in PEDOT(Acn+wat). These nodules correspond to the typical PEDOT agglomerates previously mentioned, their absence in PEDOT-CREKA(Acn+wat) suggesting a more compact internal surface. The similarity between PEDOT(Acn+wat) and PEDOT-CREKA(Acn+wat) in the external surface morphology has been attributed to the fact that peptide molecules incorporate to the polymer matrix at the first stages of the polymerization process. The average thickness and roughness measured by profilometry for PEDOT-CREKA(Acn+wat) is 2.4 ± 0.5 μm and 429 ± 97 nm respectively, these values being very similar to those determined for PEDOT(Acn+wat).

Figure 4d shows the morphologies of PEDOT(acid-wat) and PEDOT-CREKA(acid-wat), which are similar to that reported for PEDOT produced in organic media (*e.g.*

acetonitrile solution).[44] Thus, the SEM micrographs reflect a porous structure formed by a dense network of thin fiber-like morphologies connecting small clusters of aggregated molecules that are located at very different levels. In spite of this, it should be noted the occasional apparition of small regions in which the surface becomes smooth (*i.e.* more compact), which has been attributed to the effect of the acid pH.

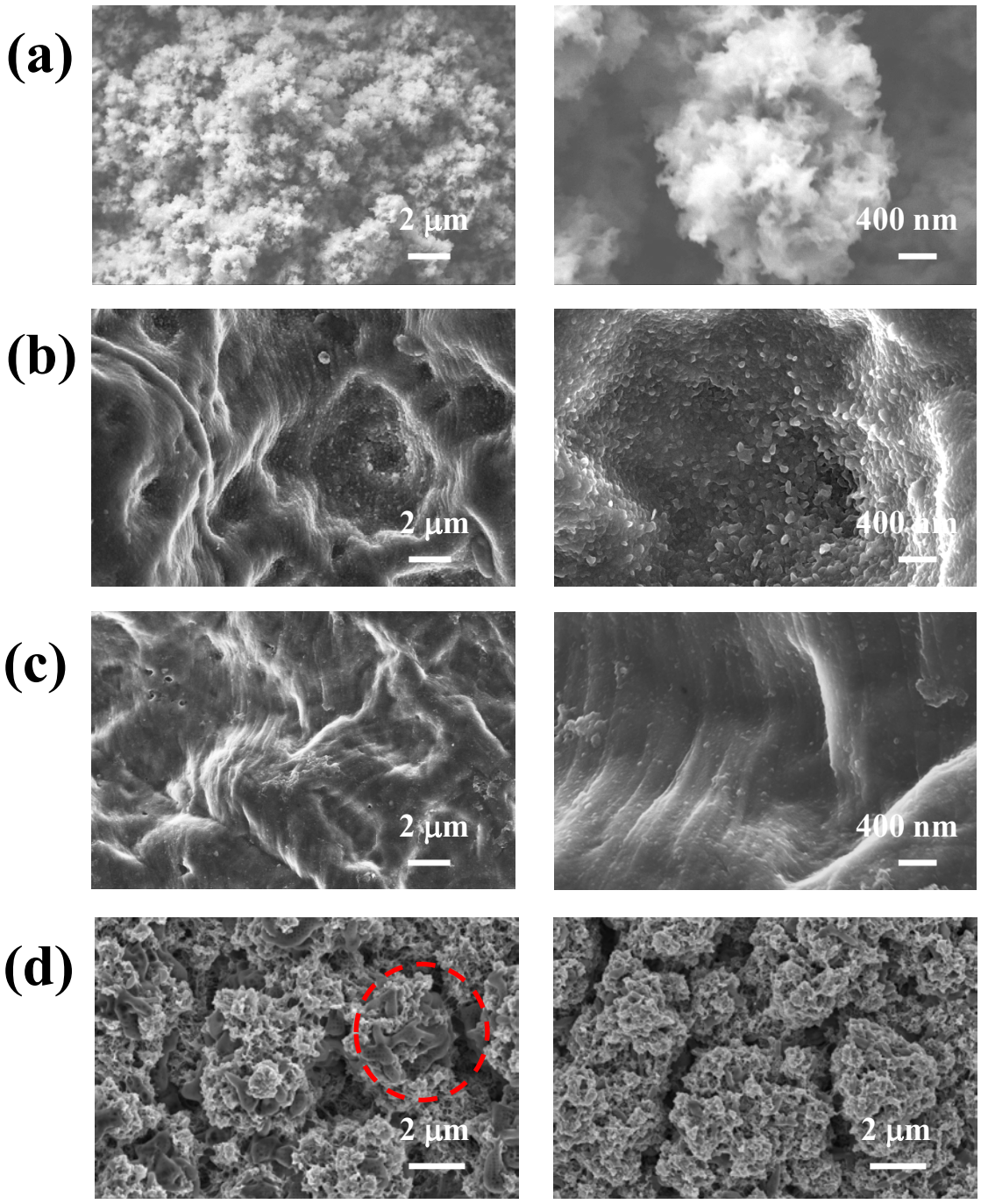

Figure 4. Low- and high-resolution SEM images (left and right, respectively) of (a) the external surface morphology of PEDOT(Acn+wat), and the internal surface morphology of (b) PEDOT(Acn+wat) and (c) PEDOT-CREKA(Acn+wat). Internal surfaces of PEDOT(Acn+wat) and PEDOT-CREKA(Acn+wat) films were coated with an ultrathin layer of carbon. (d) SEM

micrographs of PEDOT(acid-wat) and PEDOT-CREKA(acid-wat) (left and right, respectively). The red circle shows a smooth region.

Figures 5a-5d display AFM micrographs of PEDOT/PEDOT-CREKA(basic-wat) and PEDOT/PEDOT(basic-wat). The topography of the internal PEDOT layer (Figure 5a) can be described as a dense distribution of sharp peaks grouped in clusters (*i.e.* independent mountain ranges separated by valleys). This surface topography is very similar to that obtained for PEDOT films polymerized in acetonitrile at 1.40 V and using 10 s as polymerization time,[45] even though the roughness of the latter (r= 73$\pm$6 nm) was slightly higher than that determined in this work for the film generated at 1.10 V and using a basic aqueous environment (r= 29$\pm$5 nm). The topographic image of the PEDOT/PEDOT-CREKA(basic-wat) surface (Figure 5b) evidences that the size and number of the clusters observed for the internal layers increases and decreases, respectively, upon the deposition of the composite external layer. Thus, the latter does not provoke a homogeneous growing, in terms of height, of the clusters formed in the internal layer but an aggregation of clusters, which enhances the difference with respect to the plateau regions (*i.e.* the surface is less leveled). Consistently, the roughness experiences a significant increment (r= 126$\pm$28 nm). The surface topography of PEDOT/PEDOT(basic-wat) reveals a similar effect in absence of CREKA peptide (Figure 5c), even though it is less pronounced. Thus, the size of the aggregates is intermediate between those displayed in Figures 5a and 5b. Similarly, the roughness (r= 74$\pm$2 nm) is intermediate between those of the internal PEDOT layer and PEDOT/PEDOT-CREKA(basic-wat). It should be emphasized that the topographies displayed in Figures 5b and 5c correspond to a bottom surface regions rather than to the folds observed by SEM for the two bilayered systems (see Figures 3a and 3b). Figure 5d displays the AFM image (25 μm $\times$ 25 μm) of one of the folds observed in PEDOT/PEDOT-CREKA(basic-wat). The height of the fold, which has been estimated using the cross-sectional profile of the topography image (included in Figure 5d), is $\sim$3.3 μm, this value being in good agreement with the value obtained using cross sectional SEM (3.8 μm).

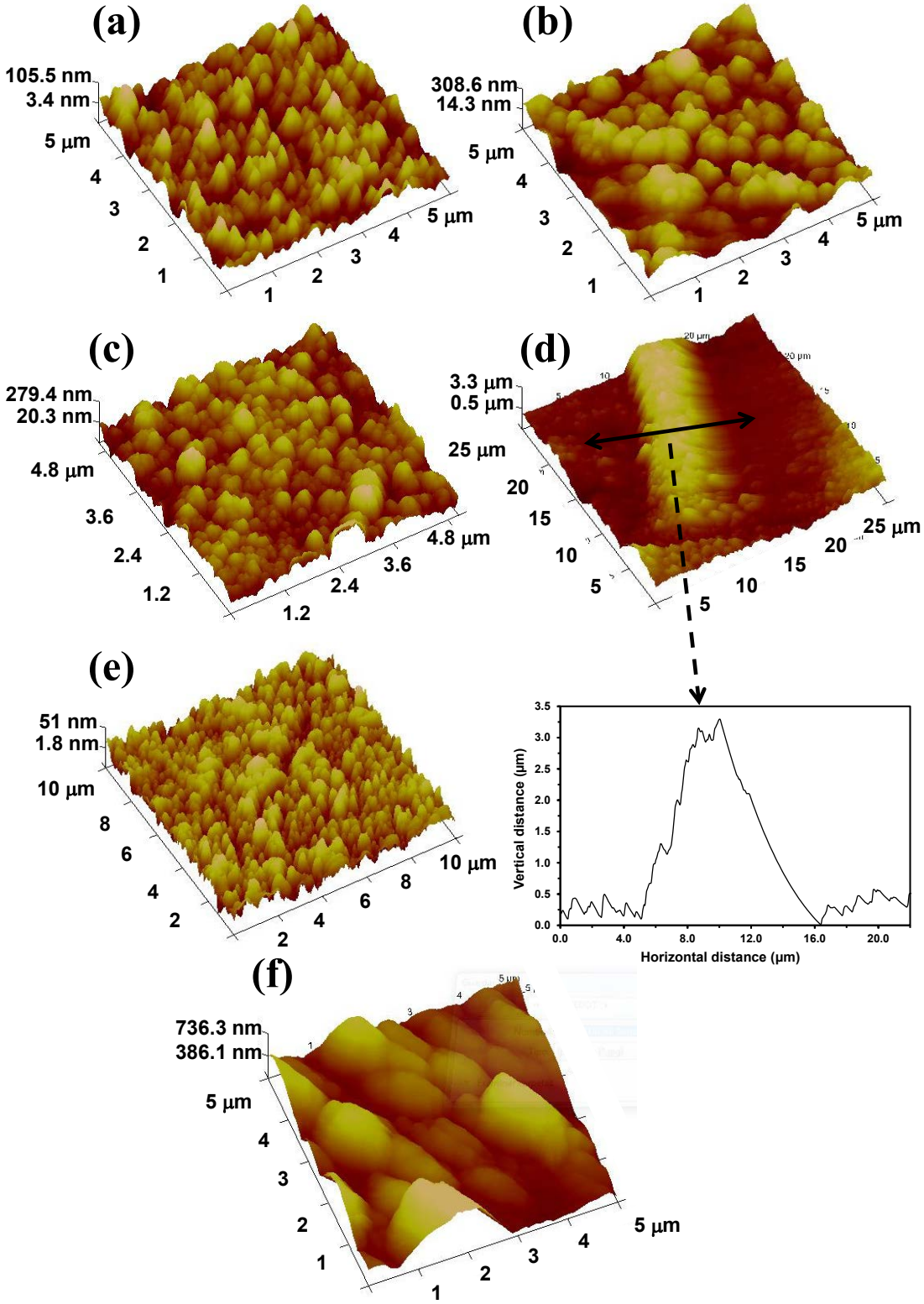

Figure 5. AFM micrographs (3D topography) of the: (a) internal PEDOT layer of PEDOT/PEDOT-CREKA(basic-wat) and PEDOT/PEDOT(basic-wat); (b) surface of PEDOT/PEDOT-CREKA(basic-wat) (bottom surface region); (c) surface of PEDOT/PEDOT(basic-wat) (bottom surface region); (d) surface of PEDOT/PEDOT-CREKA(basic-wat) (region with fold); (e) surface of PEDOT(acid-wat); and (f) surface of PEDOT-CREKA(Acn-wat). The cross-sectional profile of the topography image is included in (d).

The AFM image displayed in Figure 5e for PEDOT-CREKA(acid-wat) evidences a surface topography very similar to that of the internal PEDOT layer of PEDOT/PEDOT-CREKA(basic-wat) films. This consists of a relatively dense distribution of sharp peaks that are grouped forming small clusters. As PEDOT chains exclusively involve α-α linkages (*i.e.* the β positions of the thiophene ring are occupied by the fused dioxane ring), the clusters are attributed to the formation of compact molecular aggregates of linear chains that are stabilized by the dopant agent. The roughness of PEDOT-CREKA(acid-wat) (r= 51$\pm$6) is intermediate between those of the internal layer of PEDOT/PEDOT-CREKA(basic-wat) and PEDOT produced in acetonitrile using $LiClO_4$ as supporting electrolyte (r= 29$\pm$5 and 73$\pm$6 nm, respectively).[45] Finally, the AFM images of PEDOT-CREKA(Acn+wat) (Figure 5f) and PEDOT(Acn+wat) (not shown) are very similar, resembling those reported for micrometric PEDOT films produced in acetonitrile using a constant potential of 1.40 V, a polymerization time higher than 100 s and $LiClO_4$ as supporting electrolyte.[45] The topography consists on a reduced number of compact and, simultaneously, large blocks of aggregated polymer chains emerging over flat regions. Also, the surface roughness of PEDOT-CREKA(Acn+wat) and PEDOT(Acn+wat) (r= 392$\pm$34 and 381$\pm$29 nm, respectively) are higher than those for the rest of the films described in Figure 5.

Charge store ability and electrochemical stability

The CVs of PEDOT/PEDOT(basic-wat) and PEDOT/PEDOT-CREKA(basic-wat) in a physiological environment (0.1 M PBS, pH= 7.4), which were recorded in the potential range from -0.40 to 0.80 V, are displayed in Figure 6a. Comparison with the voltammogram obtained for the PEDOT internal layer of such 2-layered films, which is included in Figure 6a, indicates that the maximum anodic current density (j_{max}), which is reached at the reversal potential, increases significantly upon the incorporation of the second layer (*i.e.* from 0.75 mA·cm^{-2} to ~1.0 mA·cm^{-2}, which represents an increment of ~35%). Furthermore, the second layer provokes an increment of the electroactivity. More specifically, the ability to store charge increases by 20% and 17% when the second layer is deposited onto the internal layer in PEDOT/PEDOT(basic-wat) and PEDOT/PEDOT-CREKA(basic-wat), respectively. Accordingly, the electrochemical properties of PEDOT/PEDOT(basic-wat) and PEDOT/PEDOT-CREKA(basic-wat) are very

similar indicating that the influence of the entrapped CREKA peptide molecules is significantly lower than that produced by bilayered structure of the film. This behaviour is fully consistent with those previously reported for different PEDOT-containing multilayered films produced in organic solvents.[43,44]

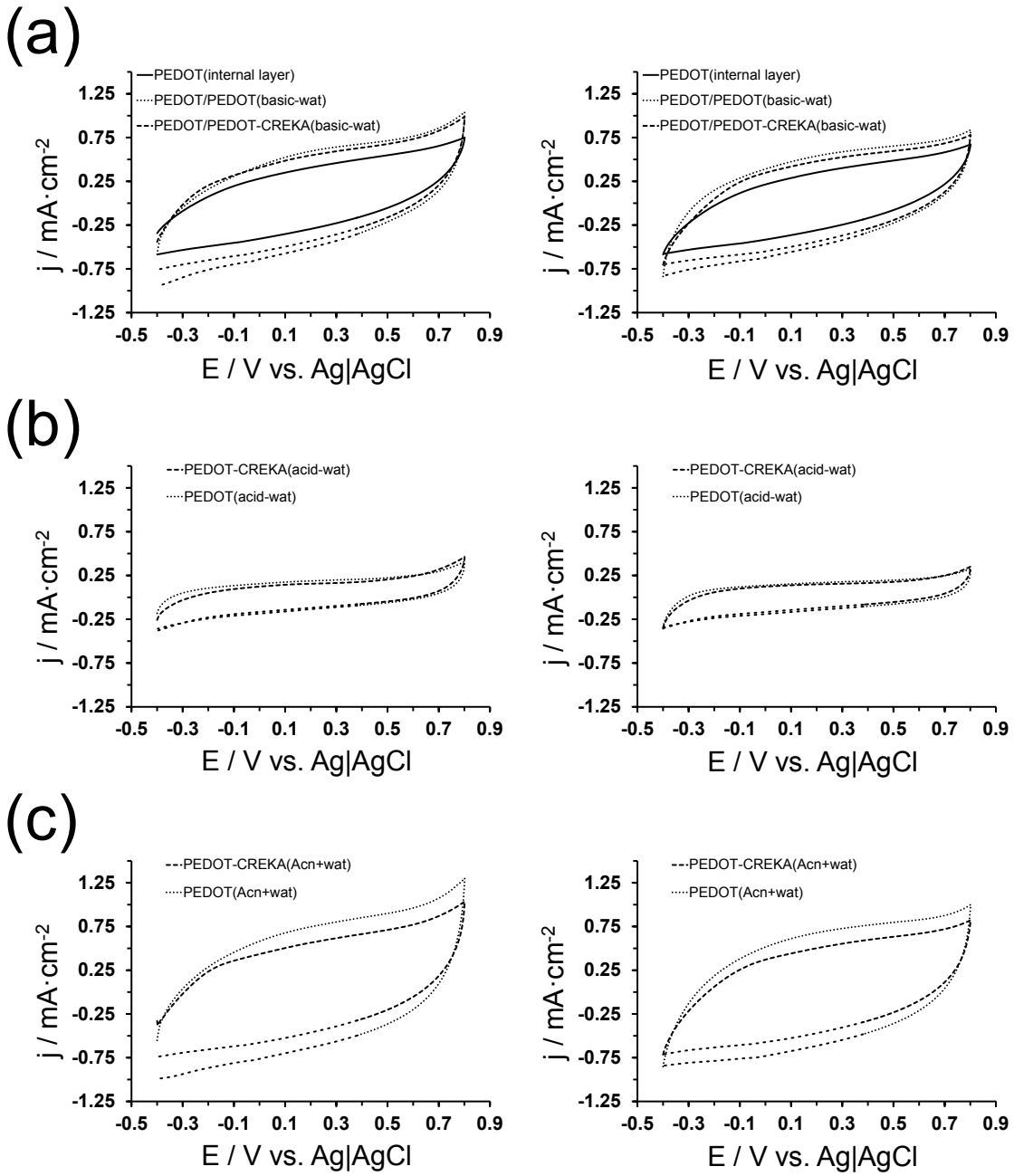

Figure 6. Initial control voltammogram (left) and voltammogram after five consecutive oxidation-reduction cycles (right) in 0.1 M PBS (pH= 7.4) of: (a) internal PEDOT layer, PEDOT/PEDOT(basic-wat) and PEDOT/PEDOT-CREKA(basic-wat); (b) PEDOT(acid-wat) and PEDOT-CREKA(acid-wat); and (c) PEDOT(Acn+wat) and PEDOT-CREKA(Acn+wat).

In order to evaluate the electrochemical stability of the films produced in a basic aqueous environment, control voltammograms have been compared with those

recorded after five oxidation-reduction cycles in PBS, which are included in Figure 6a. The loss of ability to store charge is higher for 2-layered films than for the internal PEDOT layer. Thus, the electroactivity of PEDOT/PEDOT(basic-wat) and PEDOT/PEDOT-CREKA(basic-wat) decreases 12% and 18% after five consecutive redox cycles while that of the internal PEDOT layer decreases by only 9%. This result is in agreement with previous observations, which reflected that the interfaces between layers found in multilayered films have a negative effect in the electrostability.[46] Despite its relatively high concentration, CREKA does not affect the redox capabilities of PEDOT as is reflected by the considerable resemblance between PEDOT/PEDOT(basic-wat) and PEDOT/PEDOT-CREKA(basic-wat) in terms of both electroactivity and electrostability.

Figure 6b compares the control voltammograms and the voltammograms after five consecutive redox cycles in 0.1 M PBS (pH= 7.4) recorded for PEDOT(acid-wat) and PEDOT-CREKA(acid-wat). As was expected, the small concentration of peptide incorporated into the polymeric matrix generated in an acid aqueous environment does not provoke significant changes in terms electroactivity and electrostability. Thus, the ability to store charge of PEDOT(acid-wat) and PEDOT-CREKA(acid-wat) are practically identical, whereas the loss of electroactivity after five cycles is of 16% and 14% for the former and the latter, respectively. Furthermore, comparison of the voltammograms displayed in Figures 6a and 6b indicates that the electroactivity of the films obtained in a basic environment is ~65% higher than that of films generated in an acid medium.

The most electroactive films are those generated in a mixture of acetonitrile and water using $LiClO_4$ as supporting electrolyte (Figure 6c). Thus, the ability to store charge of PEDOT(Acn+wat) and PEDOT-CREKA(Acn+wat) is 28% and 5% higher than that of PEDOT/PEDOT(basic-wat) and PEDOT/PEDOT-CREKA(basic-wat), respectively. In this case, the substitution of a small amount of perchlorate dopant anions by CREKA peptides has a noticeable impact in the electroactivity, which was not observed in PEDOT-CREKA(acid-wat) when a small concentration of SDBS dopant was replaced by peptide molecules. This feature should be attributed to the excellent properties of the perchlorate anion as dopant agent, which in turn are due to its small size, high mobility and charge concentration.[23,47] The loss of electroactivity after 5 redox cycles amounts

to 15% and 18% for PEDOT(Acn+wat) and PEDOT-CREKA(Acn+wat), indicating that their electrochemical stability is very similar to that of PEDOT(basic-wat) and PEDOT/PEDOT-CREKA(basic-wat).

Biocompatibility

The abilities of PEDOT/PEDOT-CREKA(basic-wat), PEDOT-CREKA(acid-wat) PEDOT-CREKA(Acn+wat) and the corresponding PEDOT substrates without CREKA to cellular adhesion and proliferation were compared by considering two different cellular lines: HEp-2 and DU-145. These carcinogenic cells were selected due to their fast growth. Quantitative results of cellular adhesion assays are displayed in Figure 7a, TCPS (or culture plate) being used as control substrate. Results indicate that the peptide does not provoke any effect in the adhesion of the cells, which was found to be similar in all cases to that obtained for the control TCPS. After 7 days of culture, the cellular activity was re-evaluated. Results, which are displayed in Figure 7b, show a similar number of viable cells per unit of material for TCPS, PEDOT-CREKA(acid-wat), PEDOT-CREKA(Acn+wat), PEDOT(acid-wat) and PEDOT(Acn+wat). Although the entrapment of CREKA in the polymer matrix was expected to favour cellular adhesion and/or proliferation through the binding to the fibrin molecules from the serum used as supplement in the culture medium, the peptide concentration was, unfortunately, too low in PEDOT-CREKA(acid-wat) and PEDOT-CREKA(Acn+wat) (*i.e.* 0.3-0.4%).

In contrast, the number of proliferated cells per area of PEDOT/PEDOT(basic-wat) and, especially, PEDOT/PEDOT-CREKA(basic-wat) increases appreciably with respect to the number of adhered cells per area of the same material. The fact that such improvement is observed for both bilayered films indicate that enhancement of the proliferation must be partially attributed to the high surface roughness achieved when the polymerization medium consists on a basic aqueous solution. However, the percentage of proliferated cells is ~20% higher for PEDOT/PEDOT-CREKA(basic-wat) than for PEDOT/PEDOT(basic-wat) evidencing that the concentration of peptide in the former is high enough to promote cell viability.

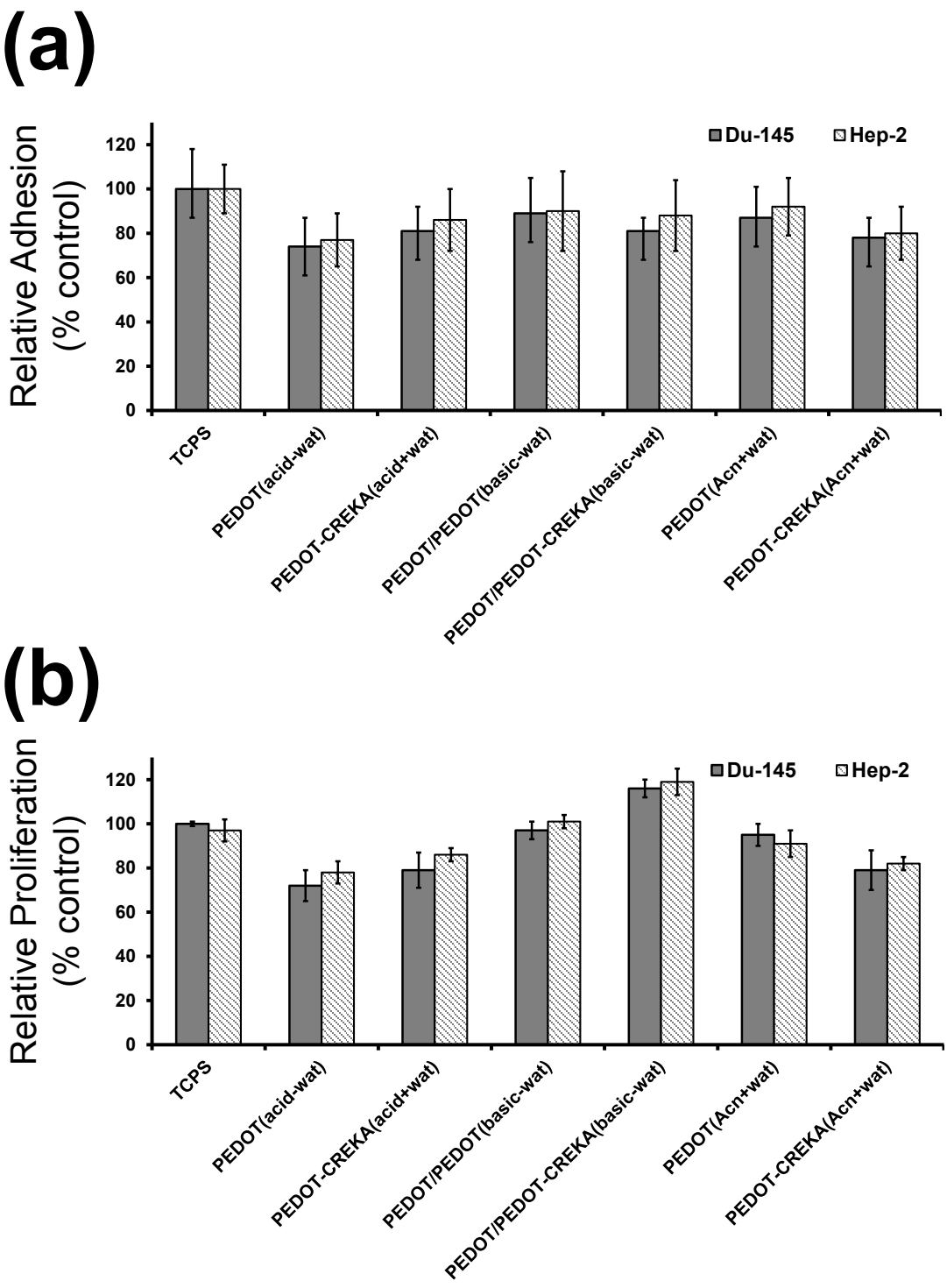

Figure 7. Cellular adhesion (a) and cellular proliferation (b) on the surface of PEDOT(acid-wat), PEDOT-CREKA(acid-wat), PEDOT/PEDOT(basic-wat), PEDOT/PEDOT-CREKA(basic-wat), PEDOT(Acn+wat) and PEDOT-CREKA(Acn+wat). TCPS was used as control substrate. DU-145 and HEp-2 cells were cultured during 24 h (adhesion assay) and 7 days (proliferation assay). The experiments were performed using six samples for each substrate.

Figure 8 shows SEM micrographs adhered and subsequently proliferated on the surface of PEDOT(Acn+wat) and PEDOT-CREKA(Acn+wat) films. The cellular mechanism operating for the adhesion of the cells onto the surface of the two bilayered films is

similar. In both cases the cells connect to the surface with filopodia. The spreading of the cells was achieved through an intimate contact between cells and surface of the films. Thus, abundant cytoplasmatic filopodias were detected forming bridges between the agglomerates of the material at the surface of the films.

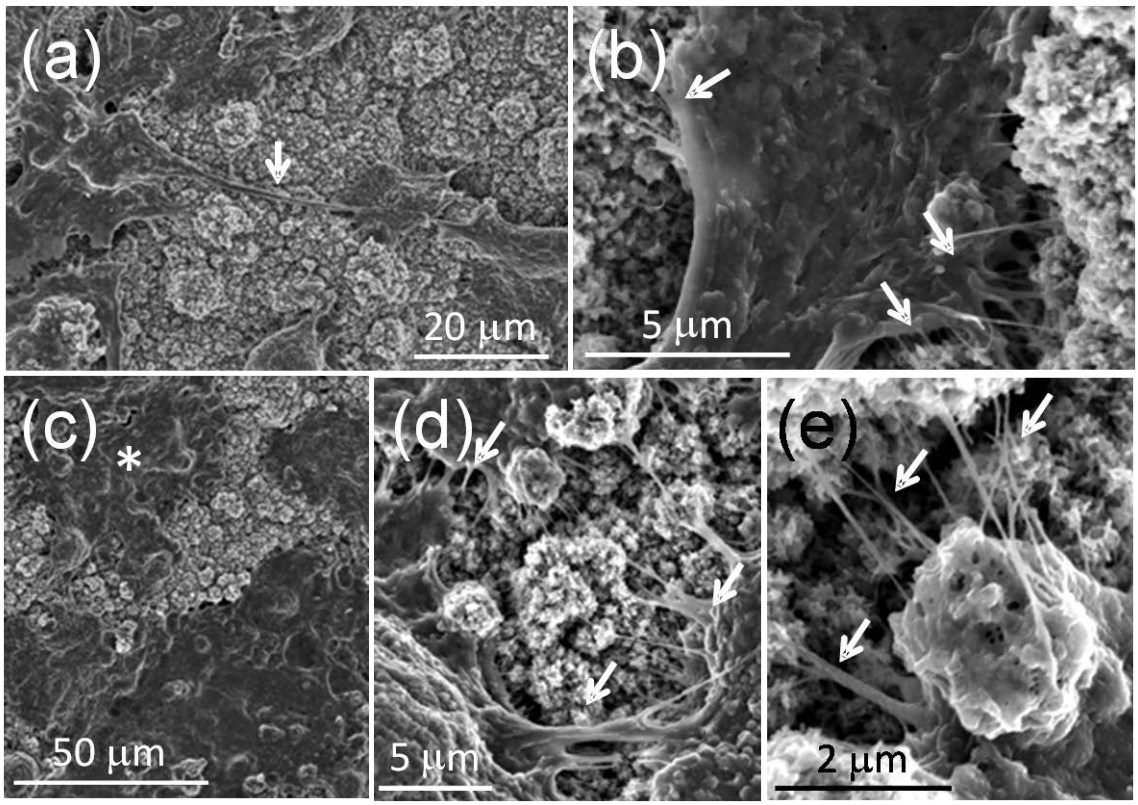

Figure 8. Adhesion and proliferation of DU-145 cells onto PEDOT(Acn+wat) (a,b) and PEDOT-CREKA(Acn+wat) (c-e) surfaces. (a) Clustered cells are connected by bridge cytoplasmatic elements (arrow), which is a prerequisite to colonize the material. (b) The cells spread filopodias (arrows) to adhere to PEDOT(Acn+wat) surface. (c) Cells grouped in clusters (asterisk) to adhere to PEDOT-CREKA(Acn+wat) surface. (e and f) The filopodias are the cytoplasmatic elements responsible of cellular adhesion to PEDOT-CREKA(Acn+wat).

Binding of fibrin

Assays to evaluate the adsorption of fibrin have been carried out using the composite prepared in a basic aqueous environment only, which showed the higher concentration of CREKA. Figure 9a represents the absorbance at 595 nm – fibrin concentration calibration curve used to evaluate the ability of PEDOT/PEDOT-CREKA(basic-wat) to bind protein with respect to PEDOT/PEDOT(basic-wat), which has been used as blank

The fibrin-binding capabilities of PEDOT/PEDOT(basic-wat) and PEDOT/PEDOT-CREKA(basic-wat) are compared in Figures 9b and 9c. Results provided by the binding

assay using the 2 mg/mL fibrin solution (Figure 9b) indicates that affinity of PEDOT/PEDOT-CREKA(basic-wat) towards the proteins is 50% higher than that of PEDOT/PEDOT(basic-wat). However, the amount of fibrin recovered from the solution was extremely low in both cases (*i.e.* ~2-3%). This situation changes drastically when samples are immersed in 10 mg/mL fibrin solutions, the amount of protein adsorbed by PEDOT/PEDOT-CREKA(basic-wat) and PEDOT/PEDOT(basic-wat) being 10.8% and 6.9%. These results corroborate our previous assumption about the influence of CREKA in cellular proliferation. More specifically, the higher performance of PEDOT/PEDOT-CREKA(basic) as bioactive cellular platform (Figure 7b) is due to the binding between the peptide entrapped into the CP matrix and the binding of fibrin molecules from the culture medium, promoting cell proliferation.

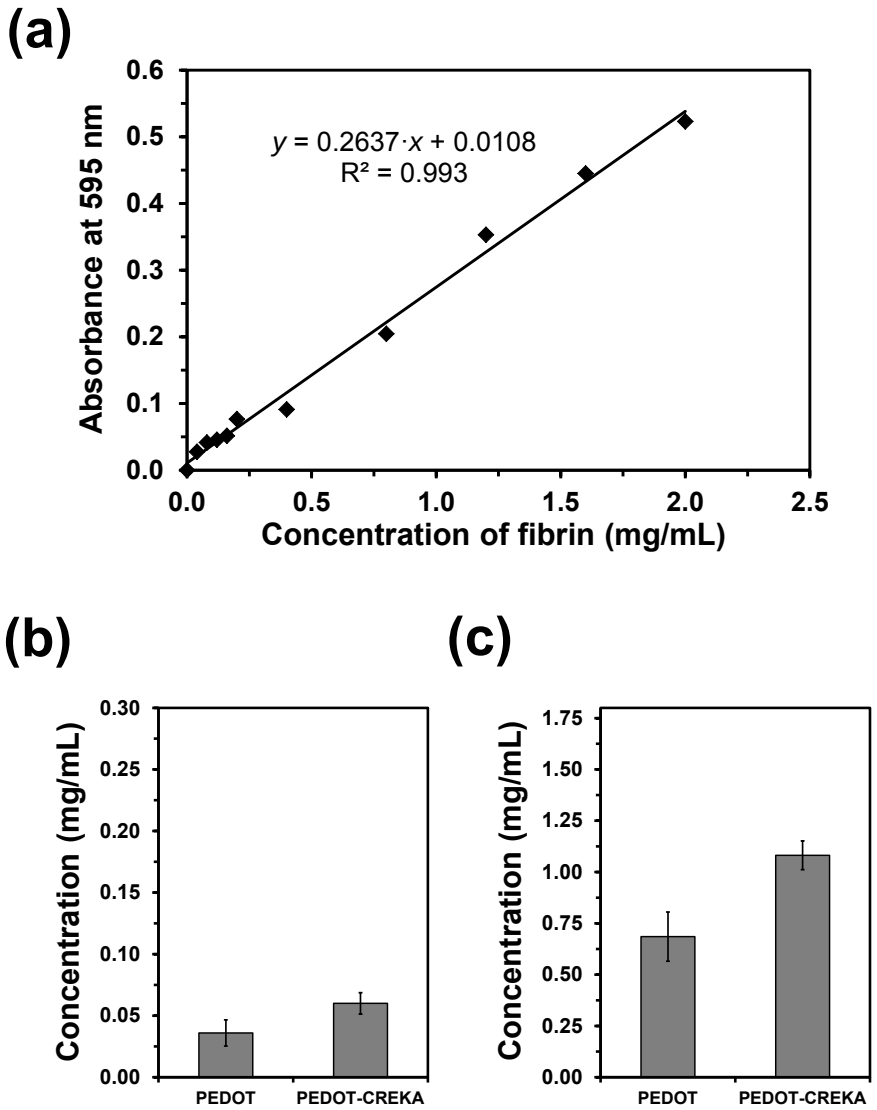

Figure 9. (a) Calibration curve representing the absorbance at 595 nm against the concentration of fibrin. The concentration of protein adsorbed by PEDOT/PEDOT(basic-wat)

and PEDOT/PEDOT-CREKA(basic-wat) films when immersed in solutions with 2 and 10 mg/mL of fibrin are displayed in (b) and (c), respectively.

7.1.4 Conclusions

PEDOT-CREKA composites have been prepared using different experimental conditions, which have been found to have a large impact not only on the content of entrapped peptide but also on the morphology and properties. The content of peptide has been determined to be relatively high in PEDOT/PEDOT-CREKA(basic-wat) bilayered films (*i.e.* one CREKA molecule per ~6 EDOT units) and very low for PEDOT-CREKA(acid-wat) and PEDOT-CREKA(Acn+wat) single-layered systems (*i.e.* one CREKA molecule per ~85 and > 350 EDOT units).

The surface morphology of PEDOT/PEDOT-CREKA(basic-wat) films consists on a homogeneous distribution of compact, relatively prominent and well-localized folds, whereas PEDOT-CREKA(Acn+wat) and PEDOT-CREKA(acid-wat) surfaces present flake-like aggregates and clustered aggregates of thin fiber-like networks, respectively. These morphologies result from the different polymerization conditions (*i.e.* solvent, pH, potential, dopant anion and single- or bi-layered structure) while entrapment of the peptide into the CP matrix does not affect the surface morphology. On the other hand, the influence of peptide in the electrochemical properties of the CP is very small for the biocomposites prepared using SDBS, the electroactivity and electrochemical stability of PEDOT/PEDOT-CREKA(basic-wat) being significantly higher than those of PEDOT-CREKA(acid-wat). In contrast, CREKA clearly reduces the electroactivity of PEDOT(Acn+wat), which has been attributed to the charge and large size of peptide molecules with respect to those of the perchlorate anions.

Results obtained in this work suggest that PEDOT/PEDOT-CREKA biocomposites could be used for different biomedical applications in which the integration of the intrinsic properties of PEDOT and the benefit induced by the peptides represents an advantage (*e.g.* implants for tissue engineering, nerve regeneration and components for orthopedic devices). However, our most immediate objective consist on the preparation and characterization of bilayered biocomposites based on the combination of PEDOT and some recently developed CREKA analogues that were

found to induce tumor necrosis.[22] Thus, such new biocomposites, which are being prepared using the same experimental that PEDOT/PEDOT-CREKA(basic-wat), are expected to add selective cellular response, increasing the range of potential biomedical applications.

7.1.5 References

1. R. A. Green, C. M. Williams, N. H. Lovell and L. A. Poole-Warren, *J. Mater. Sci.: Mater. Med.,* 2008, **19**, 1625.
2. X. Cui, V. A. Lee, Y. Raphael, J. A. Wiler, J. F. Hetke, D. J. Anderson and D. C. Martin, *J. Biomed. Mater. Res.*, 2001, **56**, 261.
3. X. Cui and D. C. Martin, *Sensors Actuators A,* 2003, **103**, 384.
4. A-D. Bendrea, G. Fabregat, L. Cianga, F. Estrany, L. J. del Valle, I. Cianga and C. Alemán, *Polym. Chem.*, 2013, **4**, 2709.
5. N. K. Guimard, N. Gomez and C. E. Schmidt, *Prog. Polym. Sci.*, 2007, **32**, 876.
6. Y. Zhong, X. Yu, R. Gilbert and R.V. Bellamkonda, *J. Rehabil. Res. Dev.*, 2001, **38**, 627.
7. X. Cui, J. Wiler, M. Dzaman, R. A. Altschuler and D. C. Martin, *Biomaterials*, 2003, **24**, 777.
8. B. Garner, A. J. Hodgson, G. G. Wallace and P. A. Underwood, *J. Mat. Sci. Mater. Med.*, 1999, **10**, 19.
9. R. A. Green, N. H. Lovell and L. A. Poole-Warren, *Biomaterials*, 2009, **30**, 3637.
10. X. Y. Cui and D. C. Martin, *Sensors Actuators B*, 2003, **89**, 92.
11. Y. H. Xiao, X. Y. Cui, J. M. Hancock, M. Bouguettaya, J. R. Reynolds and D. C. Martin, *Sensors Actuators B*, 2004, **99**, 437.
12. A. B. Sanghvi, K. P-H. Miller, A. M. Belcher and C. E. Schmidt, *Nat. Mater.*, 2005, **4**, 496.
13. E. De Giglio, L. Sabbatini and P. G. Zambonin, *J. Biomater. Sci. Polym. Ed.*, 1999, **10**, 845.
14. E. De Giglio, L. Sabbatini, S. Colucci and G. Zambonin, *J. Biomater. Sci. Polym. Ed.*, 2000, **11**, 1073.
15. N. Gomez and C. E. Schmidt, *J. Biomed. Mater. Res. A*, 2007, **81**, 135.
16. G. Fabregat, G. Ballano, E. Armelin, L. J. del Valle, C. Cativiela and C. Alemán, *Polym. Chem.*, 2013, **4**, 1412.
17. R. Pasqualini and E. Ruoslahti, *Nature*, 1996, **380**, 364.
18. J. A. Hoffman, E. Giraudo, M. Singh, L. Zhang, M. Inoue, K. Porkka, D. Hanahan and E. Ruoslahti, *Cancer Cell*, 2003, **4**, 383.
19. D. Simberg, T. Duza, J. H. Park, M. Essler, J. Pilch, L. Zhang, A. M. Derfus, M. Yang, R. M. Hoffman, S. Bathia, M. J. Sailor and E. Ruoslahti, *Proc. Natl. Acad. Sci. U S A*, 2007, **104**, 932.
20. D. Zanuy, A. Flores-Ortega, J. Casanovas, D. Curcó, R. Nussinov and C. Alemán, *J. Phys. Chem. B.*, 2008, **112**, 8692.
21. D. Zanuy, D. Curcó, R. Nussinov and C. Alemán, *Biopolymers*, 2009, **92**, 83.
22. L. Agemy, K. N. Sugahara, V. R. Kotamraju, K. Gujraty, O. M. Girard, Y. Kono et al, *Blood*, 2010, **116**, 2847.
23. C. Ocampo, R. Oliver, E. Armelin, C. Alemán and F. Estrany, *J. Polym. Res.*, 2006, **13**, 193.
24. D. Aradilla, F. Estrany, D. S. Azambuja, M. T. Casas, J. Puiggalí, C. A. Ferreira and C. Alemán, *Eur. Polym. J.,* 2010, **46**, 977.
25. C. Sivakumar and K. L. Phani, *Chem. Commun.,* 2011, **47**, 3535.
26. S. Liu, H. Liu, K. Bandyopadhyay, Z. Gao and L. Echegoyen, *J. Org. Chem.*, 2000, **65**, 3292.
27. C. Kvarnstrom, H. Neugebauer, S. Blomquist, H. J. Ahonen, J. Kankare and A. Ivaska, *Electrochim. Acta*, 1999, **44**, 2739.
28. S. Garreau, G. Louarn, J. P. Buisson, G. Froyer and S. Lefrant, *Macromolecules*, 1999, **32**, 6807.

29. S. Ahmad, M. Deepa and S. Singh, *Langmuir*, 2007, **23**, 11430.
30. G-F. Wang, X-M. Tao, J. H. Xin and B. Fei, *Nanoscale Res. Lett.*, 2009, **4**, 613.
31. S. A. Spanninga, D. C. Martin and Z. Chen, *J. Phys. Chem. C*, 2010, **114**, 14992.
32. D. Bhattacharyya and K. K. Gleason, *Chem. Mater.,* 2011, **23**, 2600.
33. J. S. Stevens, A. C. de Luca, M. Pelendritis, G. Terenghi, S. Downes, S. L. M Schroeder, *Surf Interface Anal.,* 2013, **45**, 1238.
34. N. Sakmeche, S. Aeiyach, J-J. Aaron and M. Jouini, *Langmuir*, 1999, **15**, 2566.
35. R. Flamia, G. Lanza, A. M. Salvi, J. E. Castle and A. M. Tamburro, *Biomacromolecules*, 2005, **6**, 1299.
36. T. Strother, R. J. Hamers and L. M. Smith, *Nucleic Acids Res.,* 2000, **28**, 3535.
37. G. Iucci, M. Dettin, C. Battocchio, R. Gambaretto, C. Di Bello and G. Polzonetti, *Mater. Sci. Eng. C.*, 2007, **27**, 1201.
38. D. Aradilla, D. Azambuja, F. Estrany, J. I. Iribarren, C. A. Ferreira and C. Alemán, *Polym. Chem.*, 2011, **2**, 2548.
39. J. F. Moulder, W. F. Stickle, P. E. Sobol and K. D. Bomben, Handbook of X-ray Photoelectron Spectroscopy: a Reference Book of Standard Spectra for Identification and Interpretation of XPS Data, Perkin-Elmer Corporation, Eden Prairie, MN, 1995.
40. G. Greczynski, T. Kugler and W. R. Salaneck, *Thin Solid Films*, 1999, **354**, 129.
41. G. Zotti, S. Zecchin and G. Schiavon, *Macromolecules*, 2003, **36**, 3337.
42. S. R. Taffarel and J. Rubio, *Minerals Engineering*, 2010, **23**, 771.
43. D. Aradilla, F. Estrany and C. Alemán, *J. Appl. Polym. Sci.*, 2011, **121**, 1982.
44. D. Aradilla, F. Estrany, E. Armelin and C. Alemán, *Thin Solid Films*, 2010, **518**, 4203.
45. D. Aradilla, F. Estrany, E. Armelin and C. Alemán, *Thin Solid Films*, 2012, **520**, 4402.
46. F. Estrany, D. Aradilla, R. Oliver and C. Alemán, *Eur. Polym. J.*, 2007, **43**, 1876.
47. C. Alemán, R. Oliver, E. Brillas, J. Casanovas and F. Estrany, *Chem. Phys.,* 2006, **323**, 407.

CHAPTER 8

CONCLUSIONS

CHAPTER 8. Conclusions

The main conclusions of this Thesis can be summarized as follows:

1) Conducting Polymers for Sensor Applications

- **a.** Application of the LbL templating self-assembly technique to NMPy and NCPy allows to produce core-shell particles of controlled size and thickness. These core-shell particles are easily converted in hollow microspheres by removing the template.
- **b.** The morphology of *N*-substituted PPy derivatives, particularly PNCPy and PNMPy, can be precisely controlled through the polymerization method. Compact films, solid microspheres with a porous internal structure, and core-shell microspheres with an ultrathin shell have been prepared using anodic, chemical oxidative, and LbL polymerization processes, respectively.
- **c.** Trilayered PEDOT/PNMPy/PEDOT hollow microspheres have been prepared by chemical synthesis. The chemical, morphological, topographical and electrochemical properties of these 3-layered microspheres have been determined and compared with those of microstructures prepared individual CPs.
- **d.** PEDOT/PNMPy/PEDOT hollow microspheres have been successfully used for the electrochemical detection of DA. The anodic oxidation peak response of these 3-layered microstructures provide better peak resolution than that obtained for PNMPy monolayers activated with AuNPs.
- **e.** All the 3-layered films prepared in this work, with exception of PNCPy/PEDOT/PNCPy, present a porous surface morphology that is expected to facilitate the access and escape of ions into the polymeric matrix during oxidation and reductions processes, respectively.
- **f.** Biosensors constructed using *N*-substituted PPy derivatives are able to detect DA concentrations lower than that found in the synapse (1.6 mM), i.e. in the scale of μM without loss of current sensitivity.
- **g.** DA detection studies using composites made of AuNPs combined with *N*-substituted PPy derivatives indicate that the metallic nanoparticles are not essential for the sensing abilities of the CPs. However, AuNPs facilitate the electronic

transference and the charge migration processes, which associated to DA oxidation, through the CPs.

h. The electrochemical response of PNCPy towards DA is more effective than that of PNMPy. However, among the studied CPs, PEDOT is the most appropriated for the selective detection of DA in presence of AA and UA.

i. The performance of PEDOT for the selective detection of DA cannot be improved by adding a coating of AuNPs at the surface or by incorporating interphases inside the film through multiple step polymerization techniques.

j. A rational design process has been used to attach a hydroxymethyl substituent to the dioxane ring of every PEDOT repeat unit. The sensitivity towards DA of the resulting material, PHMeDOT, is better than that of PEDOT when these materials are deposited on ITO.

k. Among 3-layered films, PEDOT/PNMPy/PEDOT and PEDOT/PNMPy/PEDOT/AuNP show the best response towards DA in terms of both sensitivity and anodic oxidation peak resolution.

l. AuNPs improve moderately the sensitivity of submicrometric PEDOT/PNMPy/PEDOT multi-layered films towards DA molecules. This catalytic activity does not increase with the concentration of nanoparticles.

m. The selectivity of PEDOT/PNMPy/PEDOT electrodes can be improved without alter their sensibility using a pre-treatment based on the application of consecutive oxidation-reduction cycles.

n. The limit of detection of PEDOT/PNMPy/PEDOT electrodes is around 10 μM in presence of AA and UA, decreasing to 2-3 μM in absence of the interferents.

o. Submicrometric PEDOT/PNMPy/PEDOT film coated with AuNP has been successfully used to identify DA in samples with real interferents made of human urine. This result suggests that these films are appropriated for biomedical applications related with the fabrication of effective sensors for the treatment of neurological disorders.

-2) Peptide-Conducting Polymer Conjugates as Bioactive Platforms

- **a.** Synthetic amino acids bearing an EDOT group in the side chain have been designed and successfully conjugated with PEDOT chains through a potentiostatic procedure to obtain new hybrid materials.
- **b.** Conjugates based on chemical similarity concepts preserve the electrical and electrochemical properties of the CP. This strategy is more appropriated than typical non-covalent approaches, which usually produce materials with worse properties than the individual CPs.
- **c.** Small changes in the chemical structure of conjugated peptides provoke small but non-negligible alterations in the electrochemical, hydrophilic and electronic properties of the peptide-CP conjugate.
- **d.** The behaviour of PEDOT-I as bioactive platform is more effective than that of PEDOT, indicating that conjugates based on chemical similarity concepts result in cellular matrices with excellent electrochemical and electrical responses.

3) PEG-Conducting Polymer Conjugates as Bioactive Platforms

- **a.** Conjugated hybrid materials consisting on graft copolymers with a PTh backbone and chains of PEG grafted to the backbone have been prepared using a mixed strategy that combines anodic polymerization and chemically synthesis of macromonomers.
- **b.** The morphology and topography of PTh-*g*-PEG$_n$ have been found to be influenced by the dopant agent, the molecular weight of the PEG chains and the polymerization potential, even though compact distributions of nanoaggregates organized in very flat surfaces were obtained in all cases.
- **c.** The electrochemical properties of PTh-*g*-PEG$_{1000}$ are particularly exciting. This is a self-stabilizing material that increases the ability to exchange charge reversibly with the number of consecutive redox cycles.
- **d.** Although the π-conjugation of the PTh plays a fundamental role in the electronic properties of PTh-*g*-PEG$_n$ graft copolymers, PEG chains provokes a considerably reduction in the backbone conjugation length leading to lower optical values that those typically found for 3-substituted PTh derivatives.

e. The hydrophilicity of PTh-*g*-PEG_n increases with *n*, the contact angle measured for PTh-*g*-PEG_{2000} being even higher than that of PEDOT homopolymer.

f. The affinity of PTh-*g*-PEG_{2000} towards globular proteins is clearly higher than towards fibrillar proteins, suggesting that this is a promising candidate for the selective adsorption of proteins.

g. The behaviour of PTh-*g*-PEG_n graft copolymers as supportive matrix for cells proliferation is better than that reported for PEDOT homopolymer due to the biocompatibility of the PEG fragments.

h. The electrochemical activity and the maximum of current density for PTh-*g*-PEG_n films coated by cells are significantly higher than for uncoated samples, suggesting that these graft copolymers are potential candidates for the biotechnological applications in which electrochemical properties are used as elements for the communication with cells.

4) PEDOT-CREKA Nanocomposites for Biomedical Applications

a. PEDOT-CREKA nanocomposites have been prepared under different experimental conditions (*i.e.* solvent, pH, potential, dopant anion and single- or bi-layered structure), which determine the content of entrapped peptide, morphology and properties.

b. PEDOT/PEDOT-CREKA(basic-wat) films consists on a homogeneous distribution of compact, relatively prominent and well-localized folds, whereas PEDOT-CREKA(Acn+wat) and PEDOT-CREKA(acid-wat) surfaces present flake-like aggregates and clustered aggregates of thin fiber-like networks, respectively.

c. The influence of peptide in the electrochemical properties of the CP is very small for the biocomposites prepared using SDBS, the electroactivity and electrochemical stability of PEDOT/PEDOT-CREKA(basic-wat) being significantly higher than those of PEDOT-CREKA(acid-wat).

d. Biocompatibility assays indicate that PEDOT-CREKA favours cellular proliferation, which is due to the binding of the peptide to the fibrin molecules from the serum used as supplement in the culture medium. The latter has been corroborated examining the ability of PEDOT-CREKA to bind fibrin.

ANNEX I

CAPTIONS FOR FIGURES

CHAPTER 1

Figure 1. General classification of CPs according to their chemical structure. 4

Figure 2. Surface morphology of thick PPy films assessed using scanning electron microscopy (SEM) (left) and the corresponding cyclic voltammograms (CV), indicating electrical activity of the polymers (right). A) doped with ions Cl-, B) doped with poly(vinyl sulfate), C) doped with dermatan sulfate, D) doped with collagen (inset: thin film of collagen-PPy). (Data taken from reference 31). 5

Figure 3. Two degenerate ground state structures of trans-PA. 6

Figure 4. Formation of polaron and bipolaron (p-type doping) in polyheterocycles. A = S, NH or O. 7

Figure 5. Mechanism for heterocycle polymerization. A = S, NH or O. 8

Figure 6. Principal strategies to modify CPs for biomedical applications. 12

CHAPTER 4

CHAPTER 4.1

Figure 1. Scheme showing the synthesis of doped and hollow PNMPy spheres. 43

Figure 2. Raman spectra of (a) PNMPy-FeCl3, (b) PNMPy-DBSA, (c) PPy-FeCl3, and (d) PPy-DBSA core-shell particles. Inset arrow indicates the Cα=Cβ bond-stretching vibration associated to the loss of symmetry in the molecule due to the irreversible oxidation of the Py ring. Exciting radiation: 632.8 nm. 46

Figure 3. High resolution XPS spectra of PNMPy/PSS core-shell and PS uncoated microspheres: (a) C 1s region; (b) N 1s region; and (c) Cl 2p region. 48

Figure 4. CVs of (a) GCE; (b) AuNPs-modified GCE, (c) PNMPy-modified GCE and (d) PNMPy/AuNPs-modified GCE in absence and presence of different DA concentrations. Scan rate: 100mV·s^{-1}. Supporting electrolyte: 0.1M PBS. Voltammograms were obtained by scanning from -0.40 to 0.80V at a scan rate of 100 mV·s^{-1}. 51

Figure 5. Electrochemical oxidation of DA to DQ. 51

Figure 6. CVs of PNMPy/AuNPs-modified GCE without dopamine and with 1.5 µM (6, 7, 8 and 9 cycles). 52

CHAPTER 4.2

Figure 1. Molecular structure of PNCPy. 59

Figure 2. (a) SEM micrograph of the surface of a film prepared by anodic polymerization. (b) Low- and (c) high-resolution SEM images of microspheres obtained using oxidative polymerization in emulsion medium, the pseudo-spherical nanoaggregates coating the microspheres being displayed in (d). (e) TEM micrographs

of an isolated microsphere. (f) SEM image of the FIB-section of a microsphere (inset: high resolution micrograph showing the remarkable porosity). 63

Figure 3. UV-vis spectra of PNCPy obtained using 20, 30, 50, 100 and 300 s of polymerization time and by CA. Numbers depicted on the graph are referred to the maximum wavelength obtained for each transition band. 64

Figure 4. Particle size distribution of the PNCPy microspheres obtained by chemical oxidative polymerization in emulsion medium. 65

Figure 5. Size distribution of the nanoaggregates located at the surface of the PNCPy microspheres produced by chemical oxidative polymerization in emulsion medium. 65

Figure 6. EDX analysis of the nanoaggregates located at the surface of the PNCPy microspheres produced by chemical oxidative polymerization in emulsion medium. 66

Figure 7. (a) and (b) SEM micrograph of PS microparticles before and after sulfonation reaction, respectively. (c-d) SEM and (e-f) TEM micrographs of PNCPy/PSS core-shell particles (inset: crystalline structure, shadowed with Pt). 67

Figure 8. Scheme showing the synthesis of PNCPy core shell microspheres. 68

Figure 9. (a) SEM micrograph of the transversal section of a PNCPy/PSS core-shell particle. (b) and (c) TEM images of free-standing hollow PNCPy microspheres. (d) SEM micrograph of the damage produced by the removal of the PSS template in PNCPy/PSS core-shell microspheres. 69

Figure 10. FTIR spectra of PNCPy synthesized by chemical and electrochemical polymerization methods compared to the monòmer, NCPy, absorption bands. 70

CHAPTER 4.3

Figure 1. Scheme showing the synthesis of hollow PEDOT/PNMPy/PEDOT spheres. 77

Figure 2. FTIR spectra of PSS microspheres (black dashed curve), PNMPy (blue curve) and PEDOT (red curve) synthesized by oxidative chemical polymerization. 80

Figure 3. SEM micrographs of PS core-shell particles with one layer of PEDOT (a-b-c), PEDOT/PNMPy bilayers (d-e-f) and PEDOT/PNMPy/PEDOT trilayers (g-h-i). 82

Figure 4. (a) SEM micrographs and (b) EDX analyses of the hollow and open microspheres composed by PEDOT/PNMPy/PEDOT multilayered films. Scale bar of inset corresponds to 100 nm. 83

Figure 5. TEM images of (a) PEDOT, (b) PEDOT/PNMPy and (c and d) PEDOT/PNMPy/PEDOT hollow spheres doped with $FeCl_4$.PEDOT/PNMPy/PEDOT spheres are partially collapsed. 84

Figure 6. AFM images of: (a) PEDOT/PNMPy/PEDOT core-shell microspheres and (b and c) PEDOT/PNMPy/PEDOT hollow microspheres. The image displayed in (c) corresponds to a detailed view of the region selected in (b), which was used to determine the RMS roughness. 85

Figure 7. UV-vis spectra of PEDOT/PNMPy/PEDOT hollow microspheres obtained by oxidative chemical synthesis. 86

Figure 8. (a) Control voltammograms of GCEs uncoated and coated with PEDOT/ PNMPy/PEDOT hollow microspheres after re-doping with $LiClO_4$. (b) Comparison of DA detection intensity from 0 to 2 mM in 0.1M PBS, employing PEDOT/PNMPy/PEDOT microspheres re-doped with $LiClO_4$. (c) Calibration curve for DA detection in the concentration range from 0.5 to 2 mM in 0.1M PBS with PEDOT/PNMPy/PEDOT hollow microspheres. Red and black lines correspond to the first and fifth oxidation-reduction cycles, respectively. Numbers inside rectangular forms indicate the loss of intensity from the first to the fifth redox cycle, in percentatge. 88

CHAPTER 4.4

Figure 1. Electrochemical oxidation of DA to DQ. 98

Figure 2. Variation of the W_{ox} per unit of area of PNCPy (filled diamonds) and PNMPy (empty diamonds) deposited on stainless steel from 10 mM monomer solutions in acetonitrile with 0.1 M $LiClO_4$ at a constant potential of 1.40 V, against the Q_{pol}. 100

Figure 3. CVs for the oxidation of (a) PNMPy and (b) PNMPy/AuNP modified GCEs in the absence and presence of different DA concentrations (from 1 to 10 mM). Scan rate: 100 mV/s. Initial and final potential: -0.40 V; reversal potential: +0.80 V. For each graphic, labels a, b, c, d and e refer to DA concentrations of 0, 1, 3, 6 and 10 mM, respectively. 101

Figure 4. CVs for the oxidation of (a) PNCPy- and (b) PNCPy/AuNP-modified GCEs in the absence and presence of different DA concentrations (from 1 to 10 mM). Scan rate: 100 mV/s. Initial and final potential: -0.40 V; reversal potential: +0.80 V. For each graphic, labels a, b, c, d and e refer to DA concentrations of 0, 1, 3, 6 and 10 mM, respectively. 102

Figure 5. Variation of (a) the oxidation potential and (b) the current density for the oxidation peak of DA against the neurotransmitter concentration measured using PNMPy (filled triangles), PNMPy/AuNP (filled squares), PNCPy (empty triangles) and PNCPy/AuNP modified GCEs (empty squares). 103

Figure 6. Electrochemical oxidation of DQ to DC. 103

Figure 7. Control voltammograms for 10 consecutive oxidation-reduction cycles of (a) PNMPy/AuNP and (b) PNCPy/AuNP modified GCEs in presence of 10 mM DA. 105

Figure 8. Variation of the *EA* after 10 consecutive oxidation-reduction cycles for PNMPy (filled triangles), PNMPy/AuNP (filled squares), PNCPy (empty triangles) and PNCPy/AuNP modified GCEs (empty squares) against the DA concentration. 105

Figure 9. CVs for the oxidation of (a) PNMPy and PNMPy/AuNP modified GCEs and (b) PNCPy and PNCPy/AuNP modified GCE in presence of a 100 μM DA concentration. Scan rate: 100 mV/s. Initial and final potential: -0.40 V; reversal potential: +0.80 V. The second consecutive oxidation-reduction cycle is also displayed for the PNMPy modified GCE. 106

Figure 10. Four structures of lower energy derived from quantum mechanical calculations for (a) 1-NMPy···DQ, (b) 2-NMPy···DQ and (c) 3-NMPy···DQ complexes. (d) Atomistic model proposed for the detection of DA by PNMPy. 107

Figure 11. Structures derived from QM calculations for (a) 1-NCPy···DQ, (b) 2-NCPy···DQ and (c) 3-NCPy···DQ complexes. (d) Atomistic model proposed for the detection of DA by PNCPy. 110

CHAPTER 4.5

Figure 1. TEM micrograph of AuNPs (scale bar: 100 nm). 119

Figure 2. SEM micrographs of PEDOT/PNMPy/PEDOT, PNMPy/PEDOT/PNMPy, PEDOT/PNCPy/PEDOT and PNCPy/PEDOT/PNCPy 3-layered films: surface (left) and cross-section (right). 121

Figure 3. First control voltammograms of bare GC and modified GC/AuNP electrodes in the absence and presence of 1 mM DA. Supporting electrolyte: 0.1 M PBS. Voltammograms were obtained by scanning from -0.40 to 0.80 V at a scan rate of 50 $mV \cdot s^{-1}$. 124

Figure 4. Electrochemical oxidation reactions for (a) DA, (b) AA and (c) UA. 124

Figure 5. Control voltammograms of 1 mM DA in 0.1 M PBS at 3-layered and 3-layered/AuNP electrodes after one and five consecutive oxidation-reduction cycles (solid and dashed line, respectively). Voltammograms were obtained by scanning from -0.40 to 0.80 V at a scan rate of 50 $mV \cdot s^{-1}$. 128

Figure 6. Variation of the (a) peak oxidation potential and the (b) peak intensity at 3-layered and 3-layered/AuNP electrodes against the number of consecutive oxidation-reduction cycles of 1 mM DA in 0.1 M PBS. 130

Figure 7. Representation of the D_0 (Eqn 1) derived from the CVs (scan rate: 50 $mV \cdot s^{-1}$) recorded at 3-layered and 3-layered/AuNP electrodes for the following solutions: (a) 1 mM DA in 0.1 M PBS; and (b) mixture with 100 μM DA, 200 μM AA and 100 μM UA in 0.1 M PBS. 132

Figure 8. (a) Control voltammograms of 1 mM DA in 0.1 M PBS at submicrometric electrodes based on PEDOT/PNMPy/PEDOT films. (b) Variation of the peak intensity (solid lines) and peak oxidation potential (dashed lines) of 1 mM DA in 0.1 M PBS at submicrometric electrodes based on PEDOT/PNMPy/PEDOT films against the number of consecutive oxidation-reduction cycles. 134

Figure 9. Voltammograms of 1 mM DA in 0.1 M PBS after five consecutive oxidation-reduction cycles recorded at electrodes based on submicrometric PEDOT/PNMPy/PEDOT films. Voltammograms were obtained by scanning from -0.40 to 0.80 V at a scan rate of 50 $mV \cdot s^{-1}$. 135

Figure 10. (a) Variation of the *EA* (in %) against the number of consecutive oxidation-reduction cycles for submicrometric 3l-5s and 3l-5s/AuNP-4 films in 0.1 M PBS. Control

voltammograms at electrochemically degraded (b) 3l-5s and (c) 3l-5s/AuNP-4 electrodes of 1 mM DA in 0.1 M PBS (red line) and of 0.1 M PBS (black line). 137

Figure 11. Control voltammograms of 1 mM DA in 0.1 M PBS at electrochemically degraded (a) 3l-5s and (b) 3l-5s/AuNP-4 electrodes after one and consecutive detection cycles (solid and dashed line, respectively). Voltammograms were obtained by scanning from -0.40 to 0.80 V at a scan rate of 50 $mV \cdot s^{-1}$. 138

Figure 12. Control voltammograms at (a) 3l-5s and (b) 3l-5s/AuNP-4 electrodes of 1 mM DA in 0.1 M PBS obtained by scanning from -0.40 to 0.80 V at a scan rate of 50, 100, 200, 400, 600 and 1200 $mV \cdot s^{-1}$. 139

Figure 13. Variation of the anodic peak intensity, oxidation peak potential, cathodic peak current and reduction peak potential against the square root of the scan rate for (a) 3l-s5 and (b) 3l-5s/AuNP-4 in presence of 1 mM DA in 0.1 M PBS. 140

Figure 14. Variation of the D_0 (Eqn 1) against the scan rate. 141

Figure 15. (a) Calibration curve for DA concentrations ranging from 1 to 100 μM (inset: from 1 to 10 μM) in 0.1 M PBS at 3l-5s and 3l-5s/AuNP-4 electrodes. (b) Calibration curve for DA concentrations ranging from 1 to 100 μM in 0.1 M PBS with 200 μM AA and 100 μM UA, acting as interferents, at 3l-5s and 3l-5s/AuNP-4 electrodes. CVs are displayed in Figures 16 and 17. 142

Figure 16. Control voltammograms at (a) 3l-5s and (b) 3l-5s/AuNP-4 electrodes of DA concentrations ranging from 1 to 100 μM in 0.1 M PBS. The voltammogram in absence of DA is also displayed (red line). Voltammograms were obtained by scanning from -0.40 to 0.80 V at a scan rate of 50 $mV \cdot s^{-1}$. These results were used for the calibration curves displayed in Figure 15a. 143

Figure 17. Control voltammograms at (a) 3l-5s and (b) 3l-5s/AuNP-4 electrodes of DA concentrations ranging from 1 to 100 μM in 0.1 M PBS with 200 μM AA and 100 μM UA acting as interferents. The voltammogram in absence of DA is also displayed (red line). Voltammograms were obtained by scanning from -0.40 to 0.80 V at a scan rate of 50 $mV \cdot s^{-1}$. These results were used for the calibration curves displayed in Figure 15b. 144

Figure 18. (a) Calibration curve for DA concentrations ranging from 10 to 400 μM in human urine samples at 3l-5s and 3l-5s/AuNP-4 electrodes. (b) Control voltammograms at 3l-5s/AuNP-4 electrode of DA concentrations ranging from 10 to 400 μM in human urine samples. Voltammograms were obtained by scanning from -0.40 to 0.80 V at a scan rate of 50 $mV \cdot s^{-1}$. 145

CHAPTER 4.6

Figure 1. Molecular structure of PNMPy, PNCPy and PEDOT. 152

Figure 2. Electrochemical oxidation reactions for (a) DA, (b) AA and (c) UA. 155

Figure 3. Control voltammograms of a solution mixture with 100 μM DA, 200 μM AA and 100 μM UA in 0.1 M PBS at (a) 1-CP and 1-CP/AuNP electrodes. The electroche-

mical response to the same solution mixture (solid black line) and to 0.1 M PBS (dotted black line) at bare (a) GC and (b) GC/AuNP electrodes is also displayed. All voltammograms were obtained by scanning from -0.40 to 0.80 V at a scan rate of 50 mV·s^{-1}. 157

Figure 4 Control voltammograms of a solution mixture with 100 μM DA, 200 μM AA and 100 μM UA in 0.1 M PBS at (a) 2-CP and 2-CP/AuNP electrodes. All voltammograms were obtained by scanning from -0.40 to 0.80 V at a scan rate of 50 mV·s^{-1}. 159

Figure 5. Optimized structures for (a) 7-EDOT···DQ, (b) 7-EDOT···dAA and (c) 7-EDOT···dqU complexes with $\Delta E \leq 1.5$ kcal/mol. Intermolecular C–H···O interactions are indicated. Distances are listed in Å. 164

Figure 6. Molecular structure of PHMeDOT. 165

Figure 7. (a) FTIR spectra of PHMeDOT and HMeDOT. (b) UV-vis spectrum of PHMeDOT electrodeposited on ITO. (c) Voltammograms for PHMeDOT films deposited on ITO after one and ten consecutive oxidation-reduction cycles. Voltamograms were recorded in water with 0.1 M PBS at 50 mV/s and 25ºC. 167

Figure 8. (a) High and low (inset) resolution SEM micrographs and (b) AFM image of PHMeDOT films electrodeposited on GC under a constant potential of 1.50 V using an acetonitrile solution containing 0.1 M monomers with 0.1 M TBATFB and a θ=6 s. 169

Figure 9. Control voltammograms of a solution mixture with 100 μM DA, 200 μM AA and 100 μM UA in 0.1 M PBS at 1-PEDOT and 1-PHMeDOT deposited on (a) GC and (b) ITO. The electrochemical response to the same solution mixture at the modified ITO electrodes after five consecutive oxidation-reduction cycles is also displayed in (b). All voltammograms were obtained by scanning from -0.40 to 0.80 V at a scan rate of 50 mV·s^{-1}. 171

CHAPTER 5

CHAPTER 5.1

Figure 1. Scheme showing the preparation of PEDOT-I. 180

Figure 2. Reagents and conditions for the synthesis of I: (a) $POCl_3$, DMF, 0ºC 2h, rt overnight, 94%; (b) Hippuric acid, NaOAc, Ac_2O, rt 30 min, 1, 80ºC 4h, 68%; (c) MeONa, MeOH, rt 30 min, 97%; (d) H_2, Wilkinson's catalyst, MeOH/CH_2Cl_2 8/2, 45ºC 12h, 99%; (e) Boc_2O, DMAP, THF, 35ºC 24h, 95%; (f) NH_2-NH_2, THF/MeOH 1/1, rt 24h, 93%. 185

Figure 3. (a) Scheme displaying the synthetic process used to prepare PEDOT-I (see text). The first step corresponds to the generation of nanometric PEDOT films while the second one consists on the incorporation of I to the end of the PEDOT chains. (b) Control voltammograms for the oxidation of PEDOT films deposited on steel electrodes in a 0.1 M $LiClO_4$ acetonitrile solution containing (solid black line) and non-containing (dashed black line) 1 mM I. Initial and final potentials: –0.50 V; reversal potential: 1.90 V. Scan rate: 10 mV s^{-1}. Temperature: 25ºC. The control voltammogram of an uncoated steel electrode in a 0.1 M $LiClO_4$ acetonitrile solution containing 1 mM I (solid gray line)

is also displayed. The oxidation potentials related with the formation of PEDOT-I and the electrochemical degradation of the films are labeled as A and B, respectively. 189

Figure 4. FTIR spectra of PEDOT (black line) and PEDOT-I (θ_2= 20 s; red line) 191

Figure 5. High-resolution XPS spectra for PEDOT-I (θ_2= 20 s): C1s (top), O1s (middle) and N1s (bottom) regions. Peaks from deconvolution are also displayed. 193

Figure 6. SEM micrographs of (a) PEDOT and (b) PEDOT-I (θ_2= 30 s). (c) AFM image of PEDOT. 196

Figure 7. UV-vis spectra of: (a) I; and (b) PEDOT (black line), PEDOT-I (θ_2= 20 s; dark gray) and doped PEDOT (additional 20 s of oxidation at 1.34 V; light gray). 197

Figure 8. (a) Control voltammograms for the oxidation of PEDOT and PEDOT-I (θ_2= 20 s) and doped PEDOT films. The voltammogram of the bare steel AISI 316 substrate is also displayed for reference. Voltammograms were recorded in water with 0.1 M PBS at 25 mV/s and 25ºC. Initial and final potentials: –0.40 V; reversal potential: +0.60 V. (b) Variation of *EA* (in %) against the number of consecutive oxidation-reduction cycles for PEDOT, PEDOT-I (θ_2= 20 s) and doped PEDOT in water with 0.1 M PBS. 199

Figure 9. Cellular adhesion (a) and cellular proliferation (b) on PEDOT, doped PEDOT and PEDOT-I (θ_2= 20 s) using HEp-2, LLC-MK2, MDCK and Vero eukaryotic cell lines. The relative viability was established in relation to the TCPS control. Steel was also considered as a control substrate because the individual polymers and the blend were deposited on this material. $p < 0.05$ vs a) TCPS, b) Steel, c) PEDOT, and d) doped PEDOT. 201

Figure 10. SEM micrograps of (a) MDCK, (b) LLC-MK2, (c) Vero and (d) Hep-2 cells cultured for seven days on the surface of PEDOT-I (θ_2= 20 s). The substrate surfaces (domains without cells) are marked with asterisks (*). The connections or interactions between the cell and the surface are indicated by arrows: lamedipodia in the low resolution image of (d) and fillopodia in the insets of (a) and (d). Insets in (b) and (c) display intercellular communication processes. 202

CHAPTER 5.2

Figure 1. Schematic description of the process used for obtaining the conjugates designed by chemical similarity in this work: (a) PEDOT-I and (b) PEDOT-II. 209

Figure 2. Chemical structure of: (a) Ac-**I**-NHMe and Ac-**II**-NHMe; (b) Ac-Abu-NHMe and Ac-Ala-NHMe; and (c) $(EDOT)_n$-I and $(EDOT)_n$-II. 210

Figure 3. Reagents and conditions used to obtain **II**: (a) *n*-BuLi 1.6M, THF, -78ºC 10 min, diethyl-(*N-tert*-butoxycarbonyl)-iminomalonate, THF, -78ºC 1h, 58%; (b) i): KOH 2N/MeOH, rt 2h, ii): Δ50ºC 30 min, 99%; (c) $TMSCH_2N_2$, Toluene/MeOH, rt 30 min, 97%. 216

Figure 4. (a) Control voltammograms for PEDOT*, PEDOT-I and PEDOT-II after (a) 2 and (b) 50 consecutive oxidation-reduction cycles. Voltammograms were recorded in a 0.1 M PBS solution at 25 mV/s and 25ºC. Initial and final potentials: –0.50 V; reversal

potential: +0.80 V. The reduction peak at -0.4 V has been attributed to the reduction of oxygen. 218

Figure 5. Variation of *EA* (in %) against the number of consecutive oxidation-reduction cycles for PEDOT*, PEDOT-I and PEDOT-II in a 0.1 M PBS solution. 219

Figure 6. EIS spectra (Nyquist impedance plots) over a frequency of 100 kHz to 10 mHz of PEDOT*, PEDOT-I and PEDOT-II in a 0.1 M PBS solution. 220

Figure 7. (a) SEM micrograph PEDOT-II. (b) Contact angle measurements of steel, PEDOT*, PEDOT-I and PEDOT-II. 222

Figure 8. Minimum energy conformations of representative minima of (a) Ac-II-NHMe and (b) Ac-I-NHMe calculated at the ωB97X-D/6-311++G(d,p) level. The intramolecular hydrogen bonds and N–H···π interactions are indicated by dashed lines and arrows, respectively. Geometric parameters associated to these interactions (*i.e.* H···O distance and ∠N–H···O angle in hydrogen bonds and the distance between the H and the center of mass of the thiophene ring in N–H···π) are indicated. 228

Figure 9. Minimum energy conformations of representative minima of (a) **II** and (b) **I** calculated at the ωB97X-D/6-311++G(d,p) level. The intramolecular interactions are indicated by dashed lines. Geometric parameters associated to these interactions (*i.e.* H···O distance and ∠N/C–H···O angle in hydrogen are indicated. 232

Figure 10. Absorption (absorbance expressed within an arbitrary unit) spectra of (a) **I** and (b) **II**. For each system, thick black and grey lines represent the experimentally recorded and simulated spectra, respectively. The curves (thin black lines) and wavelength (in nm) at the maxima resulting from the deconvolution process are also shown. 233

Figure 11. Difference of the total electronic densities (excited - ground) corresponding to the first two electronic transitions (λ^1 and λ^2). Blue (green) regions indicate an increase (decrease) of electron density upon electronic transition. 234

Figure 12. Electronic spectra calculated for the more stable conformations (*i.e.* $\Delta G <$ 1.5 kcal/mol; see Tables 5 and 6) of **I** (a) and **II** (b). 236

Figure 13. Absorption (absorbance expressed within an arbitrary unit) spectra of doped and dedoped PEDOT*, PEDOT-I and PEDOT-II. The main absorbance peaks are indicated by arrows. 237

Figure 14. Variation of the E_g derived from both DFT and TD-DFT calculations in the gas-phase (black) and acetonitrile solution (red) against 1/*n*, where *n* is the number of EDOT units, in (a) $(EDOT)_n$-I and (b) $(EDOT)_n$-II. The solid lines correspond to the linear regressions used to extrapolate this electronic property towards conjugates with infinite PEDOT chains. 238

Figure 15. Variation of the IP derived from DFT calculations in the gas-phase (black) and acetonitrile solution (red) against 1/*n*, where *n* is the number of EDOT units, in (a) $(EDOT)_n$-I and (b) $(EDOT)_n$-II. The solid lines correspond to the linear regressions used

to extrapolate this electronic property towards conjugates with infinite PEDOT chains. 240

CHAPTER 6.

CHAPTER 6.1

Figure 1. Molecular structure of P(3HT-*b*-3EGT). 249

Figure 2. Molecular structure of PTh-g-PEG_{1000} and PTh-g-PEG_{2000}. 250

Figure 3. (a) Scheme displaying the processes used to prepare PTh-g-PEG1000 and PTh-g-PEG2000. (b) Reagents and conditions for the synthesis of pentathiophene macromonomers. (c) Conditions used for the preparation of the graft copolymers by electropolymerization. 254

Figure 4. ^{1}H-NMR spectrum in acetone-d_6 of (a) Th_5-PEG_{1000} and (b) Th_5-PEG_{2000} macromonomers. 257

Figure 5. FTIR spectra of: (a) Th5-PEG1000 and PTh-g-PEG1000; and (b) Th5-PEG2000 and PTh-g-PEG2000. 258

Figure 6. FTIR spectra of: (a) Th5-PEG1000 and PTh-g-PEG1000; and (b) Th5-PEG2000 and PTh-g-PEG2000. 259

Figure 7. (a) Control voltammograms for the oxidation of a 1 mM of Th_5-PEG_{2000} solution in acetonitrile:dichloromethane (50:50 v/v) with 0.1 M $LiClO_4$ (black line) or 0.1 M Bu_4NPF_6 (gray line), and of 1 mM of Th_5-PEG_{1000} solution in acetonitrile:dichloromethane (50:50 v/v) with 0.1 M $LiClO_4$ (black dashed line). Voltammograms were recorded using a 0.5×0.25 cm^2 ITO electrode. Initial and final potentials: 0.00 V; reversal potential: 2.00 V. Scan rate: 50 mV/s. The derivative of the potential for the voltammograms recorded for the Th_5-PEG_{2000} and Th_5-PEG_{1000} solutions are displayed in (b) and (c), respectively. The anodic (O) processes are indicated for each case. 261

Figure 8. High-resolution XPS spectra for PTh-g-PEG_{1000} (left) and PTh-g-PEG_{2000} (right): C1s, O1s, S2p and Cl2p regions. Peaks from deconvolution, which are labeled with letters, are discussed in Table 1. 264

Figure 9. XPS spectra in the Br3d region for PTh-*g*-PEG_{1000} and PTh-*g*-PEG_{2000} prepared using $LiClO_4$ as electrolyte. 266

Figure 10. SEM micrographs of: (a) PTh-g-PEG_{1000} prepared using 0.1 M $LiClO_4$ and a fixed potential of 0.70 V; (b) PTh-g-PEG_{2000} prepared using 0.1 M $LiClO_4$ and a fixed potential of 0.75 V; (c) internal and (d) external side of PTh-g-PEG_{2000} prepared using 0.1 M Bu_4NPF_6 and a fixed potential of 0.80 V. 267

Figure 11. SEM micrograph PTh-*g*-PEG_{1000} prepared using 0.1 M $LiClO_4$ and a fixed potential of 0.75 V. 267

Figure 12. 2D Height and 3D topographic AFM images of: (a) PTh-g-PEG_{1000} prepared using 0.1 M $LiClO_4$ and a fixed potential of 0.70 V; (b) PTh-g-PEG_{2000} prepared using 0.1

M $LiClO_4$ and a fixed potential of 0.75 V; (c) PTh-g-PEG_{1000} prepared using 0.1 M $LiClO_4$ and a fixed potential of 0.75 V; (d) PTh-g-PEG_{2000} prepared using 0.1 M Bu_4NPF_6 as polyelectrolyte and a fixed potential of 0.80 V. 268

Figure 13. Control voltammograms collected using a scan rate of 50 $mV \cdot s^{-1}$ of: (a) PTh-g-PEG_{1000} and PTh-g-PEG_{2000} prepared using a fixed potential of 0.70 and 0.75 V, respectively, and 0.1 M $LiClO_4$; (b) PTh-g-PEG_{2000} prepared using 0.1 M Bu_4NPF_6 (polymerization potential: 0.80 V) and 0.1 M $LiClO_4$ (polymerization potential: 0.75 V). 271

Figure 14. Control voltammograms after one and ten consecutive oxidation-reduction cycles for: (a) PTh-g-PEG_{1000} prepared using a fixed potential of 0.70 V and 0.1 M $LiClO_4$; (b) PTh-g-PEG_{2000} prepared using a fixed potential of 0.75 V and 0.1 M $LiClO_4$; and (c) PTh-g-PEG_{2000} prepared using a fixed potential of 0.80 V and 0.1 M Bu_4NPF_6. 273

Figure 15. Adsorption (in %) of collagen and BSA onto the surface of PTh-g-PEG_{1000} and PTh-g-PEG_{2000} prepared using a fixed potential of 0.70 and 0.75 V, respectively, and 0.1 M $LiClO_4$. Three samples were analysed for each group. Bars represent the mean $\pm$ standard deviations. The asterisk indicates a significant difference with the control (steel), Turkey's test ($p < 0.05$). 274

CHAPTER 6.2

Figure 1. Chemical structure of PEDOT. 280

Figure2. Chemical structure of PTh-*g*-PEG_n. 282

Figure 3. Molecular structure of Th_5-PEG_n. 283

Figure 4. UV-vis spectra of: (a) Th_5-PEG_{1000} and Th_5-PEG_{2000} macromonomers in diluted dichloromethane solution and deposited as a film onto ITO substrate; and (b) PTh-*g*-PEG_{1000} prepared using $LiClO_4$ as supporting electrolyte and PTh-*g*-PEG_{2000} obtained in presence of $LiClO_4$ and Bu_4NPF_6. 289

Figure 5. UV-vis spectra of (a) PTh-*g*-PEG_{1000} and (b) PTh-*g*-PEG_{2000} doped with ClO_4^- using as prepared samples and after re-oxidation with potentials of 0.3, 0.6, 0.9, 1.0 and 1.1 V. 291

Figure 6. 2D Height AFM images of (a) PTh-*g*-PEG_{1000} and (b) PTh-*g*-PEG_{2000} prepared using $LiClO_4$ as supporting electrolyte. 293

Figure 7. Selected snapshots from MD simulations (a) in the gas-phase and (b) in solution. Water molecules and hydrogen atoms have been omitted to clarify the representations. 295

Figure 8. Temporal evolution of the end-to-end distance ($d_{e\text{-}e}$) determined from MD simulations of PTh-*g*-PEG_{1000} in the gas-phase (red lines) and solution (blue lines) for: (a) backbone PTh segments (2 explicit molecules per simulation); and (b) side PEG segments (2 explicit molecules $\times$ 4 repeat units= 8 segments per simulation). 296

Figure 9. Partial radial distribution functions of (a) S···S and (b) O···O pairs from MD simulations of PTh-*g*-PEG_{1000} in the gas-phase (left) and solution (right). Two profiles are displayed in each case: intramolecular pairs (black) and all pairs (red). 297

Figure 10. Cellular adhesion (a) and cellular proliferation (b) on PTh-*g*-PEG_{1000} and PTh-*g*-PEG_{2000} doped with ClO_4^-. The relative viability of Vero cells was established in relation to the TCPS control (tissue culture polystyrene). Steel was also considered as a control substrate because the individual polymers and the blend were deposited on this material. $p < 0.05$ *vs* TCPS. 298

Figure 11. Fluorescence images of cell adhesion onto (a) PTh-*g*-PEG_{1000} and (b) PTh-*g*-PEG_{2000} surfaces. Cell adhesion was observed with nuclei stain using bisbenzimide. Insets show the intrinsic fluorescence of the hybrid matrix. SEM micrograps of cells adhered on the surface of (c) PTh-*g*-PEG_{1000} and (d) PTh-*g*-PEG_{2000}. 299

Figure 12. CVs of PTh-*g*-PEG_{1000} (black) and PTh-*g*-PEG_{2000} (grey) films uncovered (solid line) and coated with Vero cells (dashed lines) in PBS. Voltammograms of both the as prepared samples (a) and after ten consecutive oxidation-reduction cycles (b) are displayed. 300

CHAPTER 7.

Figure 1. (a) High resolution XPS spectra for PEDOT/PEDOT-CREKA(basic-wat): C1s, O1s, N1s and S2p regions. (b) N1s region of the XPS spectra recorded for the internal PEDOT layer before the electrodeposition of the PEDOT-CREKA composite. Peaks from deconvolution are displayed in all cases. 318

Figure 2. Detection of CREKA in PEDOT-CREKA(Acn+wat) by HPLC. (a) Chromatograms of CREKA at different concentrations show overlapping. The detection was carried out by absorbance at 220 nm. The retention times are indicated over each peak. The inset shows the linear models obtained using the two peaks of CREKA. (b) Chromatograms used to analyze the peptide extracted from PEDOT-CREKA(Acn+wat). The correspondence of peaks was determined by adding a known concentration of CREKA in the extracted sample. A PEDOT extract was used as control to identify the peaks of the CP. 320

Figure 3. Low- and high-resolution SEM images of: (a) PEDOT/PEDOT-CREKA(basic-wat); (b) PEDOT/PEDOT(basic-wat); and (c) PEDOT(basic-wat) generated using polymerization times of 10 and 20 s (left and right, respectively). 322

Figure 4. Low- and high-resolution SEM images (left and right, respectively) of (a) the external surface morphology of PEDOT(Acn+wat), and the internal surface morphology of (b) PEDOT(Acn+wat) and (c) PEDOT-CREKA(Acn+wat). Internal surfaces of PEDOT(Acn+wat) and PEDOT-CREKA(Acn+wat) films were coated with an ultrathin layer of carbon. (d) SEM micrographs of PEDOT(acid-wat) and PEDOT-CREKA(acid-wat) (left and right, respectively). The red circle shows a smooth region. 324

Figure 5. AFM micrographs (3D topography) of the: (a) internal PEDOT layer of PEDOT/PEDOT-CREKA(basic-wat) and PEDOT/PEDOT(basic-wat); (b) surface of PEDOT/PEDOT-CREKA(basic-wat) (bottom surface region); (c) surface of PEDOT/PEDOT(basic-

wat) (bottom surface region); (d) surface of PEDOT/PEDOT-CREKA(basic-wat) (region with fold); (e) surface of PEDOT(acid-wat); and (f) surface of PEDOT-CREKA(Acn-wat). The cross-sectional profile of the topography image is included in (d). 326

Figure 6. Initial control voltammogram (left) and voltammogram after five consecutive oxidation-reduction cycles (right) in 0.1 M PBS (pH= 7.4) of: (a) internal PEDOT layer, PEDOT/PEDOT(basic-wat) and PEDOT/PEDOT-CREKA(basic-wat); (b) PEDOT(acid-wat) and PEDOT-CREKA(acid-wat); and (c) PEDOT(Acn+wat) and PEDOT-CREKA(Acn+wat). 328

Figure 7. Cellular adhesion (a) and cellular proliferation (b) on the surface of PEDOT(acid-wat), PEDOT-CREKA(acid-wat), PEDOT/PEDOT(basic-wat), PEDOT/PEDOT-CREKA(basic-wat), PEDOT(Acn+wat) and PEDOT-CREKA(Acn+wat). TCPS was used as control substrate. DU-145 and HEp-2 cells were cultured during 24 h (adhesion assay) and 7 days (proliferation assay). The experiments were performed using six samples for each substrate. 331

Figure 8. Adhesion and proliferation of DU-145 cells onto PEDOT(Acn+wat) (a,b) and PEDOT-CREKA(Acn+wat) (c-e) surfaces. (a) Clustered cells are connected by bridge cytoplasmatic elements (arrow), which is a prerequisite to colonize the material. (b) The cells spread filopodias (arrows) to adhere to PEDOT(Acn+wat) surface. (c) Cells grouped in clusters (asterisk) to adhere to PEDOT-CREKA(Acn+wat) surface. (e and f) The filopodias are the cytoplasmatic elements responsible of cellular adhesion to PEDOT-CREKA(Acn+wat). 332

Figure 9. (a) Calibration curve representing the absorbance at 595 nm against the concentration of fibrin. The concentration of protein adsorbed by PEDOT/PEDOT(basic-wat) and PEDOT/PEDOT-CREKA(basic-wat) films when immersed in solutions with 2 and 10 mg/mL of fibrin are displayed in (b) and (c), respectively. 333

CAPTIONS FOR TABLES

CHAPTER 1

Table 7. Comparision of chemical and electrochemical CP polymerization. 9

Table 8. Advantages and limitations of CPs in biomedical applications. 11

CHAPTER 4

CHAPTER 4.4

Table 1. Relative energy, binding energy and inter-ring dihedral angles of the four structures of lower energy calculated for *n*-NMPy···DQ complexes, where *n* ranges from 1 to 3. Molecular geometries have been obtained at the HF/6-31+G(d,p) level, while ΔE and ΔE_{int} were derived from single point calculations at the B3LYP/6-311++G(d,p) level. 108

Table 2. Relative energy, binding energy and inter-ring dihedral angles of the four structures calculated for *n*-NCPy···DQ complexes, where *n* ranges from 1 to 3. Molecular geometries have been obtained at the HF/6-31+G(d,p) level, while ΔE and ΔE_{int} were derived from single point calculations at the B3LYP/6-311++G(d,p) level. 111

CHAPTER 4.5

Table 1. Summary of the electrochemical behavior of a solution mixture with 100 μM DA, 200 μM AA and 100 μM UA in 0.1 M PBS at CP and CP/AuNP electrodes. Both the peak potential and the peak intensity for the oxidation of each analyte are displayed. 125

Table 2. Summary of the electrochemical behavior of 1 mM DA in 0.1 M PBS at micrometric and submicrometric 3-layered and 3-layered/AuNP electrodes (see text for nomenclature). Both the peak potential and the peak intensity for the oxidation of DA to DQ are displayed. 129

Table 3. Sensitivity and resolution obtained for the determination of DA, AA and UA in 0.1 M PBS using different 3-layered and 3-layered/AuNP electrodes. CVs are displayed in Figure 5 while the values of the peak current and peak potentials are listed in Table 4. 129

Table 4. Summary of the electrochemical behavior of a solution mixture with DA (100 μM), AA (200 μM) and UA (100 μM) in 0.1 M PBS at 3-layered and 3-layered/AuNP electrodes. Both the peak potential and the peak intensity for the oxidation of each analyte are displayed. 130

CHAPTER 4.6

Table 1. Sensitivity and Resolution obtained for the determination of DA, AA and UA in 0.1 M PBS using different 1-CP and 1-CP/AuNP electrodes. CVs are displayed in Figure 3. 158

Table 2. Sensitivity and Resolution obtained for the determination of DA, AA and UA in 0.1 M PBS using different 2-CP and 2-CP/AuNP electrodes. CVs are displayed in Figure 4. 160

Table 3. Relative energy and binding energy of the structures of lower energy calculated for 7-EDOT···X complexes with X= DQ, dAA and qdU. Molecular geometries and energy parameters have been obtained at the B3LYP/6-31++G(d,p) level. 163

Table 4. Sensitivity and Resolution obtained for the determination of DA, AA and UA in 0.1 M PBS using 1-PEDOT and 1-PHMeDOT electrodeposited on GC and ITO. CVs are displayed in Figure 9. 172

CHAPTER 5

CHAPTER 5.1

Table 1. Weight percent composition (C, O and N) obtained by EDX spectroscopy analyses at the surface of PEDOT and PEDOT-I (θ_2= 30 s) films. 192

Table 2. Atomic percent composition (C1s, O1s, N1s, S2p and Cl2p) obtained by XPS for PEDOT and PEDOT-I nanometric films. 194

Table 3. Contribution (in %) of the N1s peaks at 399.9 and 402.0 eV obtained by XPS for PEDOT and PEDOT-I films. 195

Table 4. Specific capacitance for PEDOT, doped PEDOT and PEDOT-I (θ_2= 20 s) obtained from CV assays (Eqn 2) using different scan rates. 200

CHAPTER 5.2

Table 1. Dihedral angles, relative energy and free energy of the minimum energy conformations obtained for Ac-II-NHMe (Figure 2a) at the ωB97X-D/6-311++G(d,p) level. The dihedral angles associated to the amide moieties (ω_0 and ω) remained close to 180º in all cases (not shown). 224

Table 2. Dihedral angles, relative energy and free energy of the minimum energy conformations obtained for Ac-Ala-NHMe (Figure 2b) at the ωB97X-D/6-311++G(d,p) level. The dihedral angles associated to the amide moieties (ω_0 and ω) remained close to 180º in all cases (not shown). 224

Table 3. Dihedral angles, relative energy and free energy of the minimum energy conformations obtained for Ac-I-NHMe (Figure 2a) at the ωB97X-D/6-311++G(d,p) level. The dihedral angles associated to the amide moieties (ω_0 and ω) remained close to 180º in all cases (not shown). 226

Table 4. Dihedral angles, relative energy and free energy of the minimum energy conformations obtained for Ac-Abu-NHMe (Figure 2b) at the ωB97X-D/6-311++G(d,p) level. The dihedral angles associated to the amide moieties (ω_0 and ω) remained close to 180º in all cases (not shown). 227

Table 5. Dihedral angles, relative energy and free energy of the minimum energy conformations obtained for **II** (Figure 1) at the ωB97X-D/6-311++G(d,p) level. The dihedral angles associated to the amide moieties (ω_0 and ω) remained close to 180º in all cases (not shown). 230

Table 6. Dihedral angles, relative energy and free energy of the minimum energy conformations obtained for **I** (Figure 1) at the ωB97X-D/6-311++G(d,p) level. The dihedral angles associated to the amide moieties (ω_0 and ω) remained close to 180º in all cases (not shown). 230

Table 7. Maximum vertical absorption wavelengths (λ_{max}) and oscillator strengths (*f*) of EDOT, **I** and **II** computed at the PCM(acetonitrile)/CAM-B3LYP /6-311++G(d,p) level of theory. The conformations with $\Delta G<1.5$kcal/mol are highlighted by a light grey background. 236

CHAPTER 6.

CHAPTER 6.1

Table 1. Assignment of the peaks obtained in the high-resolution XPS spectra recorded for PTh-g-PEG_k with k= 1000 and 2000 (Figure 8) and atomic percent composition (C1s, O1s, S2p and Cl2p). 265

Table 2. Average RMS roughness determined by atomic force microscopy and optical optical profilometry (r_{AFM} and r_{op}) and average thickness (ℓ) of the graft copolymer films. 269

CHAPTER 6.2

Table 1. Comparison of the properties determined for PTh-g-PEG1000, PTh-g-PEG2000 and PEDOT. 291